

Springer Theses

Recognizing Outstanding Ph.D. Research

Ruth Pöttgen

Search for Dark Matter with ATLAS

Using Events with a Highly Energetic
Jet and Missing Transverse
Momentum in Proton-Proton
Collisions at $\sqrt{s} = 8 \text{ TeV}$

 Springer

Springer Theses

Recognizing Outstanding Ph.D. Research

Aims and Scope

The series “Springer Theses” brings together a selection of the very best Ph.D. theses from around the world and across the physical sciences. Nominated and endorsed by two recognized specialists, each published volume has been selected for its scientific excellence and the high impact of its contents for the pertinent field of research. For greater accessibility to non-specialists, the published versions include an extended introduction, as well as a foreword by the student’s supervisor explaining the special relevance of the work for the field. As a whole, the series will provide a valuable resource both for newcomers to the research fields described, and for other scientists seeking detailed background information on special questions. Finally, it provides an accredited documentation of the valuable contributions made by today’s younger generation of scientists.

Theses are accepted into the series by invited nomination only and must fulfill all of the following criteria

- They must be written in good English.
- The topic should fall within the confines of Chemistry, Physics, Earth Sciences, Engineering and related interdisciplinary fields such as Materials, Nanoscience, Chemical Engineering, Complex Systems and Biophysics.
- The work reported in the thesis must represent a significant scientific advance.
- If the thesis includes previously published material, permission to reproduce this must be gained from the respective copyright holder.
- They must have been examined and passed during the 12 months prior to nomination.
- Each thesis should include a foreword by the supervisor outlining the significance of its content.
- The theses should have a clearly defined structure including an introduction accessible to scientists not expert in that particular field.

More information about this series at <http://www.springer.com/series/8790>

Ruth Pöttgen

Search for Dark Matter with ATLAS

Using Events with a Highly Energetic Jet
and Missing Transverse Momentum
in Proton-Proton Collisions at $\sqrt{s} = 8$ TeV

Doctoral Thesis accepted by
the Johannes Gutenberg University, Mainz, Germany

Author
Dr. Ruth Pöttgen
Fysikum
Stockholms Universitet (SU)
Stockholm
Sweden

Supervisor
Prof. Stefan Taprogge
Institute for Physics
Johannes Gutenberg University
Mainz
Germany

ISSN 2190-5053

Springer Theses

ISBN 978-3-319-41044-9

DOI 10.1007/978-3-319-41045-6

ISSN 2190-5061 (electronic)

ISBN 978-3-319-41045-6 (eBook)

Library of Congress Control Number: 2016942522

© Springer International Publishing Switzerland 2016

This work is subject to copyright. All rights are reserved by the Publisher, whether the whole or part of the material is concerned, specifically the rights of translation, reprinting, reuse of illustrations, recitation, broadcasting, reproduction on microfilms or in any other physical way, and transmission or information storage and retrieval, electronic adaptation, computer software, or by similar or dissimilar methodology now known or hereafter developed.

The use of general descriptive names, registered names, trademarks, service marks, etc. in this publication does not imply, even in the absence of a specific statement, that such names are exempt from the relevant protective laws and regulations and therefore free for general use.

The publisher, the authors and the editors are safe to assume that the advice and information in this book are believed to be true and accurate at the date of publication. Neither the publisher nor the authors or the editors give a warranty, express or implied, with respect to the material contained herein or for any errors or omissions that may have been made.

Printed on acid-free paper

This Springer imprint is published by Springer Nature

The registered company is Springer International Publishing AG Switzerland

Für meine Großeltern

Supervisor's Foreword

One of the biggest present mysteries in fundamental science is the so far unknown nature of Dark Matter, which amounts to about one-quarter of the energy–matter density of our universe. So far no unambiguous direct detection of Dark Matter has been made in laboratory on earth. A favourite candidate for dark matter particles is the so-called weakly interacting massive particle (WIMP), behaving in several ways similar to neutrinos (albeit possibly having a much larger mass).

This thesis addresses the hunt for Dark Matter in the laboratory, making use of the Large Hadron Collider (LHC) as the energy frontier machine of this decade, to possibly produce and study candidates for Dark Matter under controlled conditions. If these were to be produced in proton-proton collisions, they would however escape a direct detection by the LHC experiments. The question thus arises: how to detect the undetectable in an experiment such as the ATLAS detector? The answer is given by the so-called “mono- X ” signature, which implies the (pair) production of WIMPs together with another (detectable) object X in the final state of the reaction. There are several possibilities for the object X , however, in most cases the largest sensitivity is obtained when X is a hadronic jet. One of the major challenges in this search is the careful estimation of irreducible backgrounds, dominated by the production of Z -boson together with jets, where the former decay in neutrino-antineutrino pairs. As part of this thesis a detailed, data-driven determination has been performed, together with a thorough determination of systematic uncertainties.

The results are interpreted in two different but related theoretical frameworks: One is the canonical approach of an effective field theory that allows for a straightforward comparison to other searches for Dark Matter. The other is a new approach with respect to previous LHC searches: using a simplified model, which is more robust at LHC energies than the effective theory ansatz. The absence of an observed excess in the full data set at a centre-of-mass energy of 8 TeV as recorded by ATLAS in 2012 was used to set more stringent bounds on relevant parameters of both models, compared to earlier results from LHC.

Furthermore, this book describes major contributions to the understanding and the improvement (as well as its operation) of a crucial component of the ATLAS experiment for its full physics program: the ATLAS trigger system. Without its reliable and efficient trigger ATLAS would not be able to select the interesting events out of the huge rate of inelastic proton-proton collisions delivered by the LHC, i.e. the necessary search for the needle in the haystack.

In 2015, the LHC resumed its operation (in the so-called “run II”) providing proton-proton collisions at the unprecedented centre-of-mass energy of 13 TeV. Part of this book contains a sensitivity study made in the context of this thesis, clearly showing the significantly enlarged discovery potential for WIMPs.

The analysis in this thesis documents the state-of-art results from run-I of the LHC in the search for WIMPs as candidates for Dark Matter in the mono-jet signature. The results are complementary to those of direct detection experiment, aiming at e.g. recording the recoil of a nucleus when hit by a WIMP. These are presented in a thorough scientific manner and in an extremely comprehensible way, embedded in the overall scientific context also beyond particle physics. This book will surely serve as a compendium for future young research students in the analysis of run-II data from ATLAS (and other experiments).

Mainz, Germany
June 2016

Prof. Stefan Tapprogge

Abstract

Any physics analysis at a collider experiment heavily relies on an efficient trigger system to filter out potentially interesting events. To ensure stable operation, a continuous and detailed real-time monitoring is essential. Two such online monitoring features for the Central Trigger of the ATLAS experiment at the Large Hadron Collider (LHC) at the European centre for particle physics, CERN, are developed as part of this thesis and are presented in detail. To prepare the ATLAS experiment for the second run of the LHC starting in 2015, among other systems the Central Trigger hardware will be upgraded to remove resource limitations and allow for the connection of newly installed systems. This thesis reports on the corresponding changes and extensions in the simulation of the Central Trigger, the implementation of which is part of this work.

A further part of this thesis presents a search for Dark Matter candidates. Cosmological observations indicate that about 80 % of the matter content of the universe consist of a form of non-luminous matter which is traceable only due to its gravitational interaction and for which the Standard Model of particle physics does not provide a viable candidate. A number of experiments searches for evidence of Weakly Interacting Massive Particles (WIMPs), that in a natural way could account for the observed present day abundance of this Dark Matter. In recent years, also the search for WIMP pair production at hadron colliders has gathered momentum. A possible signal signature at a collider is a jet originating from initial state radiation and recoiling against a pair of WIMPs, leading to events with a highly energetic jet and a large amount of missing transverse momentum due to the WIMPs leaving the detector without interacting. The signal is thus expected to manifest itself as an excess above the Standard Model prediction at large missing transverse energy (E_T^{miss}).

The search for WIMP candidates presented in this thesis uses such mono-jet events, based on 20 fb^{-1} of proton-proton collision data collected in 2012 with the ATLAS detector at a centre-of-mass energy of $\sqrt{s} = 8 \text{ TeV}$. The main Standard Model backgrounds are estimated in a semi-data driven way. The event selection is optimized with respect to the sensitivity for a WIMP signal and the search is

performed in eight signal regions of increasing E_T^{miss} . No significant excess is observed and model independent limits both at 90 % and 95 % confidence level (CL) are set on the cross section for new physics. In addition, 90 % CL limits are derived on the suppression scale of an effective field theory (EFT) for various operators and compared to the results from other search experiments. The collider limits for all considered effective operators are stronger than the bounds from other experiments at low WIMP masses in the case of spin-independent interactions, and over a large mass range for spin-dependent interactions. In the light of concerns about the applicability of an EFT at LHC energies, the results are furthermore interpreted in terms of a simplified model with an s -channel vector mediator.

A simulation based sensitivity study on the prospects of the Dark Matter search with mono-jet events at a centre-of-mass energy of 14 TeV is presented and expected limits at 95 % CL as well as discovery potentials are given. It is found that already with the first few fb^{-1} of $\sqrt{s} = 14$ TeV data the expected limits can improve by a factor of 2. The discovery potential ultimately reaches up to suppression scales of 2.6 TeV, while for $\sqrt{s} = 8$ TeV it is of the order of 700 GeV.

Contents

1	Introduction	1
	References	4
Part I Theory and Motivation		
2	The Standard Model of Particle Physics	7
2.1	Survey of Fundamental Particles and Their Interactions	7
2.2	Electroweak Interaction and Symmetry Breaking	10
2.3	Quantum Chromodynamics	15
2.4	Open Questions and Extensions	17
	References	19
3	Dark Matter	21
3.1	Basics of Cosmology	21
3.2	Relic Density	24
3.3	Evidence for Dark Matter	26
3.4	Dark Matter Candidates	31
3.5	WIMP Searches	34
	3.5.1 Direct Detection	34
	3.5.2 Indirect Detection	39
	References	40
4	Proton-Proton Collisions	45
4.1	Terminology	45
4.2	Parton Density Functions	46
4.3	Cross Sections	49
4.4	Event Simulation	54
	4.4.1 Final State Particle Generation	55
	4.4.2 Event Generators	57
	References	58

5	Mono-Jet Events as Dark Matter Signature at Colliders	61
5.1	Mono-Jet Signature of WIMP Pair Production	61
5.2	Effective Field Theory for Maverick Dark Matter	62
5.2.1	Validity of the Effective Theory	65
5.3	Simplified Models	67
5.4	Standard Model Background Processes	68
5.5	Mono-X Results After 2011	69
	References	71

Part II Experimental Facilities

6	The Large Hadron Collider	75
6.1	The Accelerator Complex	75
6.2	The LHC Bunch Structure	76
6.3	Luminosity	77
6.4	The LHC Experiments	78
6.5	Performance and Perspectives	79
	References	81
7	The ATLAS Experiment	83
7.1	General Information	83
7.1.1	The Coordinate System	83
7.1.2	Variables Used to Describe Particle Properties	84
7.1.3	Detector Overview	84
7.2	Tracking System	86
7.2.1	The Pixel Detector	87
7.2.2	The Semi-Conductor Tracker	87
7.2.3	The Transition Radiation Tracker	88
7.3	Calorimeter System	88
7.3.1	Electromagnetic Calorimeter	89
7.3.2	Hadronic Calorimeter	91
7.4	Muon System	92
7.5	Special Systems	93
7.5.1	Forward Detectors	94
7.5.2	Beam Pickup Systems	94
7.5.3	Beam Conditions Monitors	94
7.6	Trigger System	95
7.6.1	Overview	95
7.6.2	Level-1 Trigger	96
7.6.3	Central Trigger	99
7.7	Data Handling	102
7.7.1	Data Taking	102
7.7.2	Data Processing and Storage	103
7.8	Detector Simulation	104

7.9 Object Reconstruction 105

7.9.1 Electrons 105

7.9.2 Muons 106

7.9.3 Jets 107

7.9.4 Missing Transverse Energy 109

7.10 Luminosity Determination 111

References 113

Part III Operation and Upgrade of the Central Trigger

8 Operation of the Central Trigger During Run-I 117

8.1 Orbit Monitoring 118

8.2 Bunch Group Monitoring 119

8.2.1 Histogram Digitisation 120

8.2.2 Comparing Bunch Patterns 122

8.2.3 Application to Real Data 125

8.3 Testing of Trigger Menus 129

References 130

9 Upgrade of the Central Trigger 131

9.1 Upgrade of the Hardware During the Long-Shutdown-I 132

9.2 Central Trigger Simulation 134

9.2.1 Event Format 135

9.2.2 Inputs and Internal Objects 137

9.2.3 Simulation of Special Triggers 137

9.2.4 Trigger Decision 138

9.2.5 Output 138

9.2.6 Modifications for Running on Data 139

9.2.7 Data Quality Monitoring 139

9.3 Upgrade of the Central Trigger Simulation 141

9.3.1 Updated Event Format 141

9.3.2 New Software Packages 143

9.3.3 Adaption to New Hardware 145

References 146

Part IV Analysis

10 Analysis Strategy 149

10.1 Signal Characteristics and Parameters 149

10.2 Estimation of Main Background Contributions 150

10.2.1 Transfer from Control Regions 150

10.2.2 Method for Combination of $Z(\rightarrow \nu\bar{\nu})$ +jets
Estimates 154

10.3 Small Background Contributions 155

10.4 Statistical Analysis 156

References 158

11	Data and Simulated Samples	159
11.1	Data	159
11.2	Simulated Samples	160
11.2.1	Signal Process	161
11.2.2	Background Processes	162
	References	168
12	Physics Objects Definitions	171
12.1	Jets	171
12.2	Electrons	172
12.3	Muons	173
12.4	Missing Transverse Energy	174
	References	175
13	Event Selection	177
13.1	Preselection	177
13.2	Optimisation Studies	179
13.2.1	Quantification of Sensitivity	179
13.2.2	Cut Studies	182
13.3	Complete Signal Region Selection	192
	References	193
14	Background Estimation	195
14.1	Systematic Uncertainties	196
14.1.1	Trigger	196
14.1.2	Jet Energy Scale and Resolution	196
14.1.3	Lepton Uncertainties	197
14.1.4	Soft Terms in Missing Transverse Energy	198
14.1.5	Pile-Up	199
14.1.6	Track Veto	199
14.1.7	Luminosity	199
14.1.8	Background Subtraction in the Control Regions	199
14.1.9	PDF	200
14.1.10	Shower Modeling	201
14.1.11	Matching Scale	201
14.1.12	Renormalisation and Factorisation Scales	201
14.1.13	Electroweak Radiative Corrections on the W to Z Ratio	202
14.2	Estimation of $Z(\rightarrow \nu\bar{\nu}) + \text{jets}$ Background	202
14.2.1	Estimation from a $Z + \text{jets}$ Control Region with Two Muons	202
14.2.2	Estimation from a $Z + \text{jets}$ Control Region with Two Electrons	214
14.2.3	Estimation from a $W + \text{jets}$ Control Region with a Muon	220

14.2.4	Estimation from a $W + \text{jets}$ Control Region with an Electron.	229
14.2.5	Combination of $Z(\rightarrow \nu\bar{\nu}) + \text{jets}$ Estimates	236
14.3	Estimation of $W^{\pm}(\rightarrow \ell^{\pm}\bar{\nu}) + \text{jets}$ Backgrounds	238
14.3.1	$W^{\pm}(\rightarrow \mu^{\pm}\bar{\nu}) + \text{jets}$ Estimation from a $W + \text{jets}$ Control Region with a Muon.	238
14.3.2	$W^{\pm}(\rightarrow e^{\pm}\bar{\nu}) + \text{jets}$ and $W^{\pm}(\rightarrow \tau^{\pm}\bar{\nu}) + \text{jets}$ Estimation from a $W + \text{jets}$ Control Region with an Electron.	239
14.4	$Z(\rightarrow \ell^+ \ell^-) + \text{jets}$ Backgrounds Taken from Simulation	246
14.5	Top and Diboson Backgrounds	247
14.6	Multi-jet and Non-collision Background	248
	References	249
15	Results and Interpretation	251
15.1	Background Summary and Model Independent Results	251
15.2	Inputs for Limit Calculation	256
15.2.1	Luminosity	257
15.2.2	Jet Energy Scale and Resolution.	257
15.2.3	E_T^{miss} Soft Terms.	258
15.2.4	Beam Energy.	258
15.2.5	Factorisation and Renormalisation Scale	259
15.2.6	PDF	259
15.2.7	ISR and FSR.	260
15.3	Dark Matter Limits	261
15.3.1	Effective Operator Limits	261
15.3.2	Simplified Model	271
15.4	Results Summary.	274
	References	274
16	Prospects with Future LHC Data	277
16.1	Estimation of Event Yields	277
16.2	Reach of the Mono-Jet Search in the EFT Framework	279
16.3	Comparison to a Simplified Model.	283
16.4	Summary of 14TeV Studies	284
	References	285
Part V Conclusion		
17	Conclusion.	289
Appendix A: Signal Simulation Samples.		
		293
Appendix B: Signal Tables		
		299
Curriculum Vitae		
		321

Chapter 1

Introduction

The idea that all matter is made of not further divisible particles dates back to the greek philosopher Democritus and his teacher Leucippus, who called these fundamental particles *atoms*. The actual beginning of what today is known as elementary particle physics, however, can rather be placed in 1897, when J.J. Thomson discovered that cathode rays were actually made of negatively charged particles, which he initially called *corpuscles* [1]. He thought of the atom as a “plum pudding”, with the electrons immersed in a positively charged paste. This picture was, however, disproved by Rutherford’s scattering experiment [2], which showed that the positive charge is located in the core of the atom, the nucleus. By 1932, with the discovery of the neutron by Chadwick [3], the picture of what atoms and therefore all matter is made of seemed to be complete: The nucleus of an atom consists of protons and neutrons and is surrounded by a cloud of electrons, rendering the atom as a whole neutral.

In the first half of the 20th century, however, a large number of seemingly elementary particles of different masses, charges and spin were discovered. This called for an underlying theory to establish order in this *zoo* of particles. In a remarkable interplay between theoretical predictions and experimental evidence, the Standard Model of particle physics was developed and has since been confirmed with great precision by a vast amount of experimental data. It describes the fundamental building blocks that constitute all particles observed in nature or created in the laboratory and the interactions between these building blocks. The building blocks are fermions with half-integer spin and they form three families (or generations) with masses increasing from one family to the other. Each family comprises a charged *lepton*, a neutral lepton called *neutrino*, and two *quarks*. Quarks (and antiquarks) do not exist as free particles but only in bound states of either two or three, referred to as *mesons* or *baryons*. Protons and neutrons are examples of such baryons, consisting of different combinations of three first-generation quarks. With the electron also belonging to the first family, all matter of our everyday life is composed of first-generation fundamental fermions.

In addition to the building blocks, there are force carriers mediating the electromagnetic, weak and strong force. Gravitation is not included in the Standard Model, although many attempts to do so have been made. The final piece of the Standard Model is the Higgs-boson, which is predicted by the theory to explain how the fundamental particles acquire mass. With the discovery of a Higgs-like particle at the Large Hadron Collider (LHC) at the European centre for particle physics, CERN, in Geneva in 2012, the Standard Model in itself is complete.

There are, however, phenomena the Standard Model provides no explanation for. Among these are the question why there are three families with vastly different masses, why there is only matter left in the universe when originally matter and antimatter were produced in equal amounts, or why the scales of the different interactions differ by so many orders of magnitude. A very striking shortcoming of the Standard Model is the fact that the particles it contains account for merely about 20% of the matter in the universe—the remaining 80% are *Dark Matter* for which the Standard Model provides no viable particle candidate in sufficient abundance. Even when taking Dark Matter into account, there remain approximately 70% of the matter-energy-content of the universe unaccounted for. They are referred to as *Dark Energy* and are even less understood than Dark Matter.

One of the first to postulate Dark Matter was F. Zwicky in 1933 [4], based on his observation that galaxies in a galaxy cluster moved much faster than was to be expected from the amount of visible matter. Today, there is compelling evidence from astrophysical observations on very different cosmological scales for the existence of Dark Matter. Among the most convincing ones are the shape of rotation curves of stars in galaxies, observations made on galaxy cluster collisions, implications from the measurement of the cosmic microwave background and structure formation in the early universe. In all of these cases, the observed data cannot be explained by the amount of visible matter alone under the assumption that general relativity holds at these scales. While there have been attempts to establish other explanations—as for example modified gravitational laws—for one or the other observation, the virtue of the hypothesis of Dark Matter is that it is able to explain all the observed phenomena consistently.

However, to date, there is no experimental hint of what Dark Matter is made of. There is, on the other hand, a plethora of models beyond the Standard Model predicting new particles that could be candidates for Dark Matter. A very popular class are Weakly Interacting Massive Particles (WIMPs), that are supposed to interact only weakly with normal matter and have masses similar to those of the electroweak scale. As such, they can naturally account for the observed present-day abundance of Dark Matter. Such particles are searched for by a variety of experiments and recently the Dark Matter search at particle colliders has gathered momentum as well. The typical signature are events with a deficit of transverse momentum caused by the Dark Matter particles escaping the detector without interaction with the material. At a hadron collider like the LHC, events with a highly energetic jet and missing transverse momentum provide good sensitivity to such a signal due to the large cross section for jet production. The search for Dark Matter in these *mono-jet* events with

the data collected by the ATLAS experiment at the LHC in 2012 will be presented in this thesis.

The development and progress in particle physics over the past century was only possible by probing deeper into the constituents of matter, i.e. going to smaller and smaller scales. This corresponds to going to higher energies—the larger the energy, the smaller the structures that can be probed, which is why elementary particle physics has become known as *high energy physics* (HEP). The instrument of choice are particle accelerators and colliders—by colliding particles and studying the collision products insight can be gained into the constituents of matter and their interactions.

A large number of theories exist proposing solutions to the shortcomings of the Standard Model and many of them predict new particles heavier than the ones known to date. To be able to investigate these theories, a collider with a centre-of-mass energy large enough to produce these new particles is needed. The currently most powerful collider is CERN's LHC, designed to provide a large discovery potential with proton-proton collisions at a centre-of-mass energy of up to 14 TeV, reaching instantaneous luminosities of more than $10^{34} \text{ cm}^{-2} \text{ s}^{-1}$.

The collider, however, is only one ingredient—in order to fully exploit the tremendous physics potential of the LHC, a well-understood and efficiently operated detector to measure the collision products, providing high-quality data is equally important. The ATLAS detector at the LHC is such a device: It is a general purpose detector, designed to cover a broad spectrum of physics analyses, ranging from testing predictions of the Standard Model to exploring models for physics beyond the Standard Model. Apart from instrumentation to identify particles and measure their properties, a vital part of any collider experiment is a highly reliable and efficient trigger system. Collisions at the LHC occur at a nominal rate of up to 40 MHz and have to be reduced to the order of a few hundred Hz, singling out the most interesting events to make the best possible use of the available band width. For an effective data taking all parts of the detector have to be constantly monitored—especially the trigger system without which data taking is not possible. The ATLAS trigger system reduces the event rate in three distinct steps, the core piece of the first trigger level is the Central Trigger Processor (CTP) which makes the actual decision whether or not the detector is read out for a given collision. Moreover, the CTP serves as the interface to the LHC machine and forwards the timing signals to the ATLAS detector, which makes detailed monitoring of the timing at the CTP necessary. Two such monitoring features were developed as part of the work documented in this thesis.

During the first years of data taking from 2010 to early 2013, the LHC has delivered collisions at centre-of-mass energies of 7 and 8 TeV. In 2015, it will resume operation after a two-years shutdown during which the machine and the experiments have been upgraded to be ready for operation at up to 14 TeV. This will open up even larger possibilities for new physics to be discovered and to further deepen the understanding of the Standard Model. Together with other systems of the ATLAS detector, the Central Trigger is currently undergoing a hardware upgrade to ensure the continued high performance and the achievement of the experiment's physics goals. The corresponding changes and extensions to the event format and the Central

Trigger simulation have been implemented in a backward compatible way as part of the work documented in this thesis.

The theoretical foundation and motivation for the analysis presented in this thesis will be presented in part I: Chap. 2 will give a summary of the Standard Model and the open questions it leaves. In particular, evidence and searches for Dark Matter will be discussed in Chap. 3. The basics of proton-proton collisions will be presented in Chaps. 4 and 5 will give an introduction of how the mono-jet signature in such collisions can be used to search for Dark Matter. Part II compiles information on the LHC in Chap. 6 and the ATLAS experiment in Chap. 7. In part III, different timing monitoring features of the Central Trigger are presented in Chap. 8 together with the procedure for testing of trigger menus. In Chap. 9 the upgrade of the Central Trigger simulation for the LHC run-II is described and the changes to the event format are discussed. In part IV, the analysis of mono-jet events and the results of the search for WIMP Dark Matter candidates are presented. First, the general analysis strategy is outlined in Chap. 10 and the data and simulation samples used are given in Chap. 11. Chapter 12 defines the physics objects used in the analysis and in Chap. 13 the event selection and its optimisation is summarised. A detailed description of the estimation of Standard Model processes and the corresponding systematic uncertainties is given in Chap. 14, while in Chap. 15 the results and their interpretation are presented and discussed. Finally, in Chap. 16, prospects for the mono-jet Dark Matter search at 14 TeV are illustrated. Chapter 17 concludes the thesis.

References

1. Thomson J (1897) Cathode rays. *Philos Mag* 44:293–316. doi:[10.1080/14786449708621070](https://doi.org/10.1080/14786449708621070)
2. Rutherford E (1911) The scattering of alpha and beta particles by matter and the structure of the atom. *Philos Mag* 21:669–688. doi:[10.1080/14786440508637080](https://doi.org/10.1080/14786440508637080)
3. Chadwick J (1932) The existence of a neutron. *R Soc Lond Proc Ser A* 136:692–708. doi:[10.1098/rspa.1932.0112](https://doi.org/10.1098/rspa.1932.0112)
4. Zwicky F (1933) Die Rotverschiebung von extragalaktischen Nebeln. *Helv Phys Acta* 6:110–127

Part I
Theory and Motivation

Chapter 2

The Standard Model of Particle Physics

This chapter will review the current theoretical model of elementary particle physics, based largely on references [1–4]. Section 2.1 will give an overview of the particle content of this *Standard Model* of particle physics as well as the interactions between them. The set of observed particles has recently been completed by the discovery of a particle which so far appears to be compatible with the long searched for *Higgs*-boson, which had been predicted as part of the mechanism generating masses of the fundamental particles via spontaneous symmetry breaking. The electroweak interaction and the Higgs-mechanism are discussed in Sect. 2.2, followed by a brief overview of the strong interaction in Sect. 2.3. Despite of being one of the most successful theories in the history of science, the Standard Model has a number of shortcomings that will be highlighted in Sect. 2.4, as one of them is the motivation for the analysis documented in this work.

Throughout this thesis, natural units will be used, i.e. $\hbar = c = 1$.

2.1 Survey of Fundamental Particles and Their Interactions

The Standard Model (SM) of particle physics describes the fundamental building blocks of matter and their interactions. All visible matter is made of two kinds of elementary particles (i.e. without any substructure): *leptons* and *quarks*. They are *fermions*, i.e. they carry half-integer spin, and they interact via three fundamental forces: the electromagnetic, the weak and the strong interaction, with the first two being unified in the electroweak force. The incorporation of the fourth fundamental force, gravitation, into the Standard Model is still an unresolved challenge. However, at the involved mass scales its strength is negligible compared to that of the other interactions. The interactions between quarks and leptons are mediated by the

Table 2.1 Overview of the three fundamental forces described by the Standard Model, the corresponding gauge bosons and charges

Interaction	Gauge boson	Mass (GeV)	Charge
Strong	8 gluons (g)	0	Colour (r,g,b)
Electromagnetic	Photon (γ)	0	Electrical
Weak	Z	~ 91.2	Weak isospin
	W^\pm	~ 80.4	

exchange of particles with integer spin—the gauge bosons. There is one such boson for the electromagnetic interaction, the massless photon (γ), which couples to the electric charge but is itself uncharged. The weak interaction is mediated by three bosons, the electrically neutral Z -boson and the positively and negatively charged W^\pm -bosons, that each couple to the 3-component of the weak isospin. There are 8 electrically neutral and massless gluons (g) that mediate the strong force. The corresponding charge is called *colour* and comes in three variants (commonly labeled *red*, *green* and *blue*) and the corresponding anticolours. Gluons themselves carry colour charge, which allows them to interact with each other, leading to a short range for the strong force. The electromagnetic force, on the other hand, has infinite reach, since the photon is massless, while the weak interaction is short-ranged due to the mass of the Z and W bosons—roughly 91 and 80 GeV, respectively. Table 2.1 summarises the three interactions.

There are six leptons, grouped into three families, each family consisting of one (negatively) charged lepton and a neutrino which only carries weak charge. Each lepton has an anti-particle for which the additive quantum numbers have the opposite sign. The masses of the charged leptons—electron (e), muon (μ) and tau (τ)—increase in this order from approximately 511 keV over 105 MeV to 1.7 GeV [4]. Neutrinos are treated as massless in the SM. However, the observation of neutrino oscillations (cf. [5]) indicates that they have a non-vanishing mass. The current experimental upper bound is $m_\nu < 2\text{ eV}$ [6, 7].

Quarks exist in six *flavours* and are also grouped into three families. The first family consists of the *up*(u)- and *down*(d)-quark, the names of which refer to their 3-component of the *isospin*, which is $+1/2$ for the up-quark and $-1/2$ for the down-quark.¹ In analogy, the other families also comprise one *up*-type and one *down*-type quark. The *up*-type quarks have an electric charge of $2/3|e|$, the *down*-type quarks of $-1/3|e|$. As for the leptons, the quark masses increase throughout the families, the *up*-type quark of the third family, the *top*(t)-quark, being the heaviest fundamental particle with a mass of roughly 173 GeV [4]. All stable matter surrounding us is made up of fermions of the first family: atoms consist of electrons, proton and neutrons, the

¹The isospin was originally introduced to treat neutron and proton as the same particles (*nucleons*) with different isospin orientation ($\pm 1/2$). In the quark model, the isospin of the nucleon results from the isospin of its constituents.

latter two being compositions of u - and d -quarks. The particles of the other families and compounds of them always decay into lighter particles.

Besides the electric and weak charge, quarks carry colour charge, i.e. they take part in the strong interaction. Again, there exists an anti-quark to each quark which carries anti-colour. Quarks do not exist as free particles in nature but occur only in bound states of two or three (anti-)quarks. Those composite particles are referred to as *hadrons* and can be classified into two main groups: *Mesons* consist of one quark and one anti-quark, *baryons* of three quarks (and anti-baryons of three anti-quarks). All observed hadrons appear to be colourless (*white*), i.e. colour singlet states, which is realised by combining either colour and anticolour for the mesons or red, green and blue (antired, antigreen, antiblue) for the baryons.

In Table 2.2, the fundamental fermions and some of the quantum numbers are listed. (The concept of weak isospin will be discussed in Sect. 2.2.)

Within the SM, the fundamental interactions are described in gauge theories, the underlying principle being that the corresponding Lagrangian density has to be invariant under certain local gauge transformations which define a symmetry. These transformations—or their representation as matrices, respectively—are the *generators* of the corresponding symmetry group. In order to have a global symmetry hold also locally, vector-boson fields, the *gauge fields*, have to be introduced, one for each generator of the symmetry group. This shall be illustrated here using the example of quantum electrodynamics (QED), the quantum field theory of electromagnetism. The Dirac equation for a free particle with charge q and mass m , described by a wave function $\psi(x)$ is given by

$$(i\gamma^\mu \partial_\mu - m)\psi(x) = 0. \quad (2.1)$$

Performing a local phase transformation of the form $\psi'(x) = e^{iq\chi(x)}\psi(x)$ leads to

$$\begin{aligned} (i\gamma^\mu \partial_\mu - m)\psi'(x) &= e^{iq\chi(x)} \underbrace{(i\gamma^\mu \partial_\mu - m)\psi(x)}_{=0} - q\gamma^\mu (\partial_\mu \chi(x))\psi'(x) \\ &= q\gamma^\mu A'_\mu \psi'(x) \neq 0, \end{aligned} \quad (2.2)$$

Table 2.2 Overview over the fundamental fermions of the Standard Model and some of their quantum numbers: weak isospin I , its third component I_3 , electric charge Q_f and weak hypercharge Y

	Fermions			I	I_3	Q_f [e]	Y
Leptons	$\begin{pmatrix} \nu_e \\ e \end{pmatrix}_L$	$\begin{pmatrix} \nu_\mu \\ \mu \end{pmatrix}_L$	$\begin{pmatrix} \nu_\tau \\ \tau \end{pmatrix}_L$	$\frac{1}{2}$	$+\frac{1}{2}$ $-\frac{1}{2}$	0 -1	-1
	e_R	μ_R	τ_R	0	0	-1	-2
Quarks	$\begin{pmatrix} u \\ d' \end{pmatrix}_L$	$\begin{pmatrix} c \\ s' \end{pmatrix}_L$	$\begin{pmatrix} t \\ b' \end{pmatrix}_L$	$\frac{1}{2}$	$+\frac{1}{2}$ $-\frac{1}{2}$	$+\frac{2}{3}$ $-\frac{1}{3}$	$\frac{1}{3}$
	u_R	c_R	t_R	0	0	$+\frac{2}{3}$	$\frac{4}{3}$
	d_R	s_R	b_R			$-\frac{1}{3}$	$-\frac{2}{3}$

with $A'_\mu(x) = -\partial_\mu\chi(x)$. This means, the transformed wave function does not fulfil the Dirac equation for a free particle, but for a particle in an electromagnetic field. To establish the invariance of the Dirac equation under a local phase transformation, the field has to be transformed as well, $A'_\mu(x) = A_\mu(x) - \partial_\mu\chi(x)$ and the derivative is replaced by the covariant derivative: $\partial_\mu \rightarrow D_\mu = \partial_\mu + iqA_\mu$. In this way,

$$(i\gamma^\mu D_\mu - m)\psi(x) = 0 \quad (2.3)$$

is rendered invariant under the simultaneous transformation of ψ and the gauge field A_μ .

Generalising this formalism, the Standard Model is described by a $SU(2)_L \otimes U(1)_Y \otimes SU(3)_C$ gauge symmetry. The $SU(3)_C$ -term denotes the underlying symmetry of the strong interaction, with the three degrees of freedom of the colour charge (hence the index C). The $SU(3)$ has 8 generators, which are associated to eight gluons. The first two terms incorporate the gauge symmetry of the electroweak interaction, which has four generators. A local gauge symmetry forbids mass terms in the Lagrangian density, which means that the gauge bosons have to be massless. The $SU(3)$ of the strong interaction is an exact symmetry, and hence the gluons are massless. However, only one of the experimentally observed vector bosons of the electroweak interaction, the photon, is massless. W - and Z -bosons on the other hand are massive, indicating that the gauge symmetry is broken. The mechanism for this spontaneous symmetry breaking predicts the existence of another fundamental boson, which has to have spin 0. It is commonly referred to as the Higgs-boson, named after Peter Higgs who was one of the first ones to predict its existence [8–10]. Such a scalar boson was discovered by the ATLAS [11] and CMS [12] collaborations in 2012 and so far all measurements of its properties are consistent with those predicted for a Standard Model Higgs-boson. More details on the symmetry breaking mechanism will be discussed in Sect. 2.2.

2.2 Electroweak Interaction and Symmetry Breaking

Historically, the electromagnetic and weak interaction were considered two separate phenomena, until they were unified in the electroweak theory of Glashow, Salam and Weinberg [13–15], similar to the unification of electric and magnetic interactions by Maxwell [16].

A number of experimental observations on particle decays (especially β -decays) had to be incorporated when building a theory of the weak interaction. The short range of the interaction suggested, that the corresponding exchange particles had to be massive. For a long time, only *charged current* interactions were known, in which the charge of the leptons or quarks involved changes by ± 1 . Therefore, there should be at least two exchange particles, with charge $+1$ and -1 , named W^+ and W^- , respectively. Assuming—in analogy to the electromagnetic interaction—that these particles have spin 1, the interaction in general can be described by a combination of a

vector (V) and an axial-vector (A) operator. The strength of the different contributions is described by coefficients c_V and c_A , respectively, i.e. the interaction will contain a term of the form $\gamma^\mu (c_V + c_A \gamma^5)$. A parity-conserving interaction, which couples equally to left- and right-handed particles, can only be either purely vectorial ($c_A = 0$) or purely axial-vectorial ($c_V = 0$).² If both coefficients have the same absolute value, parity is *maximally violated*.

Any spinor u describing a fermion can be decomposed into a left-handed (u_L) and a right-handed (u_R) component in the following way:

$$u = u_L + u_R = \frac{1}{2}(\mathbb{1} - \gamma^5)u + \frac{1}{2}(\mathbb{1} + \gamma^5)u, \quad (2.4)$$

where $\mathbb{1}$ denotes the 4×4 unity matrix, and $P_{R/L} = \frac{1}{2}(\mathbb{1} \pm \gamma^5)$ are the helicity projection operators. It is experimentally found that only left-handed fermions participate in the charged currents, i.e. $c_V = 1$ and $c_A = 1$. Parity is maximally violated in these interactions, the theory is therefore also referred to as *V-A* - theory.³ Moreover, it is found that the coupling strength is the same for all fermions. This is different from *neutral currents*, which do not change the electric charge of the participating fermions. They were first observed at the Gargamelle bubble chamber at CERN 1973 [17] and attributed to the exchange of a neutral vector boson, Z^0 . It was subsequently found that the coupling strength depends on the charge of the fermions. The unified description of these phenomena within the electroweak theory is based on the introduction of a new quantum number, called *weak isospin* (I), and the consistent application of the isospin formalism. Left-handed fermions are grouped into doublets of weak isospin $I = 1/2$, with 3-component $\pm 1/2$, cf. Table 2.2. Right-handed fermions are weak isospin singlets, $I = I_3 = 0$, since they do not participate in charged current interactions.

Transitions between left-handed charged leptons and neutrinos or *up*- and *down*-type quarks are possible by emission of a charged W^\pm -boson. Since the 3-component of the weak isospin thereby changes by one unit, the W -bosons must have $I = 1$ and $I_3 = \pm 1$. To explain the transitions between different generations, the electroweak eigenstates of down-type quarks are interpreted not as the actual quark mass eigenstates (d , s , b) but mixtures of those, labelled d' , s' and b' , according to the unitary *Cabibbo–Kobayashi–Maskawa* (CKM) matrix [18, 19]:

$$\begin{pmatrix} d' \\ s' \\ b' \end{pmatrix} = \begin{pmatrix} V_{ud} & V_{us} & V_{ub} \\ V_{cd} & V_{cs} & V_{cb} \\ V_{td} & V_{ts} & V_{tb} \end{pmatrix} \begin{pmatrix} d \\ s \\ b \end{pmatrix} \quad (2.5)$$

The diagonal elements describe the transitions within one generation and are close to unity. Transitions between families are accordingly strongly suppressed.

²In case of the electromagnetic force it is a pure vector interaction.

³A $V + A$ —theory would describe an interaction only right-handed particles take part in.

Within the isospin formalism, there should be another boson with $I_3 = 0$ and the same couplings to fermions as W^\pm , which does not change the 3-component, i.e. it mediates transitions that do not change the fermion flavour, just like the neutral currents. However, this boson cannot be identical to the Z^0 , since the couplings of the latter are different for fermions with different electrical charge. To solve this problem, a fourth field is introduced, which is a weak isospin singlet, $I = I_3 = 0$, i.e. it couples to fermions without changing the 3-component of their isospin. Experimentally, indeed, two such bosons are observed: the photon and the Z -boson. The basic idea of electroweak unification is thus to express the observed bosons as mixtures of the two bosons with $I_3 = 0$. In the language of gauge theories this is expressed as follows.

The electric charge and the weak isospin are related via the Gell–Mann–Nishijima relation [20, 21]:

$$Y = 2(I_3 + Q), \quad (2.6)$$

where Y is called the *weak hypercharge*.

The symmetry group of the electroweak interaction is $SU(2)_L \otimes U(1)_Y$. $SU(2)_L$ is the weak isospin group describing transformations of the left-handed isospin doublets. $U(1)_Y$ is the hypercharge group, which is essentially a phase transformation. To ensure local gauge invariance a triplet of vector fields, W_μ^i , $i = 1, 2, 3$, is introduced for the $SU(2)_L$ and a single vector field, B_μ , for the $U(1)_Y$.

The covariant derivative reads

$$D^\mu = \partial^\mu + ig\vec{T} \cdot \vec{W}^\mu + i\frac{g'}{2}YB^\mu, \quad (2.7)$$

with couplings g and g' for the $SU(2)_L$ and $U(1)_Y$, respectively. For left-handed fermions, \vec{T} is given by $\vec{T} = \frac{\vec{\tau}}{2}$, where τ_i , $i = 1, 2, 3$ are the Pauli-matrices. $T_i = \tau_i/2$, $i = 1, 2, 3$ are the generators of $SU(2)_L$. For right-handed fermions, $\vec{T} = \vec{0}$. The generator of the hypercharge group is $Y/2$.

With this, the relations for the observable vector bosons are expressed as:

$$W_\mu^\pm = \frac{1}{\sqrt{2}}(W_\mu^1 \mp iW_\mu^2), \quad (2.8)$$

$$Z_\mu = W_\mu^3 \cos \theta_W - B_\mu \sin \theta_W, \quad (2.9)$$

$$A_\mu = W_\mu^3 \sin \theta_W + B_\mu \cos \theta_W. \quad (2.10)$$

Here, the *weak mixing angle* θ_W , is related to the coupling constants in the following way:

$$\sin \theta_W = \frac{g'}{\sqrt{g^2 + g'^2}} \quad (2.11)$$

and has been measured to $\sin^2 \theta_W = 0.23119(14)$ [4]. As will be seen later, the mixing angle also relates the masses of the heavy gauge bosons as

$$\cos \theta_W = \frac{m_W}{m_Z}. \quad (2.12)$$

Moreover, there is a fundamental relation between the elementary charge e and the coupling constants:

$$e = g' \cos \theta_W = g \sin \theta_W. \quad (2.13)$$

The couplings to the W bosons are $g_W = gI_3$ for all fermions, the fermion dependent couplings to the Z -boson are given as

$$g_Z(f) = \frac{g}{\cos \theta_W} (I_3 - Q_f \sin^2(\theta_W)), \quad (2.14)$$

with the values of I_3 and Q_f as given in Table 2.2. For the neutral currents the values of the coefficients for vector and axial-vector interaction are given by $c_V(f) = I_3 - 2Q_f \sin^2(\theta_W)$ and $c_A(f) = I_3$. Accordingly, neutral current interactions are not maximally CP violating.

In 1983, the W - and Z -bosons were discovered at CERN [22, 23]. The bosons in Eqs. (2.8)–(2.10), however, are still massless, since they are linear combination of massless fields. In order to introduce a mechanism for the Gauge bosons to acquire mass, the Lagrangian including the interaction of the fields with fermions and the terms for kinetic energy is studied, which can be written as

$$\mathcal{L} = \mathcal{L}_F + \mathcal{L}_G = \sum_{f=l,q} f^\dagger i \not{D} f - \frac{1}{4} W_{\mu\nu}^i W_i^{\mu\nu} - \frac{1}{4} B_{\mu\nu} B^{\mu\nu} \quad \text{with } \not{D} = \gamma^\mu D_\mu. \quad (2.15)$$

The field tensors are given as

$$W_{\mu\nu}^i = \partial_\mu W_\nu^i - \partial_\nu W_\mu^i - g \varepsilon_{ijk} W_\mu^j W_\nu^k \quad (2.16)$$

$$B_{\mu\nu} = \partial_\mu B_\nu - \partial_\nu B_\mu. \quad (2.17)$$

Writing the covariant derivative for left- and right-handed fermions (f_L and f_R) explicitly, the Lagrangian reads

$$\begin{aligned} \mathcal{L} = & f_L^\dagger \gamma^\mu \left(i \partial_\mu + g \frac{\tau^i}{2} W_\mu^i + \frac{g'}{2} Y B_\mu \right) f_L + f_R^\dagger \gamma^\mu \left(i \partial_\mu + \frac{g'}{2} Y B_\mu \right) f_R \\ & - \frac{1}{4} W_{\mu\nu}^i W_i^{\mu\nu} - \frac{1}{4} B_{\mu\nu} B^{\mu\nu}. \end{aligned} \quad (2.18)$$

To introduce the mass terms for the heavy bosons, the simplest extension is to introduce two complex scalar fields ϕ^+ and ϕ^0 , that form an isospin doublet,

$$\Phi = \begin{pmatrix} \phi^+ \\ \phi^0 \end{pmatrix}, \quad (I = 1/2, Y = 1). \quad (2.19)$$

According to Eq. (2.6), the above values of I and Y indeed yield charge +1 and 0. The Lagrangian for the Higgs-field is given by

$$\begin{aligned} \mathcal{L}_{Higgs} &= (\partial^\mu \Phi)^\dagger (\partial_\mu \Phi) - V(\Phi^\dagger, \Phi), \\ V(\Phi^\dagger, \Phi) &= m^2 \Phi^\dagger \Phi + \lambda (\Phi^\dagger \Phi)^2, \quad m^2, \lambda \in \mathbb{R}. \end{aligned} \quad (2.20)$$

The shape of the potential $V(\Phi^\dagger, \Phi)$ depends on the choice of the parameters m and λ . λ has to be greater than 0 to ensure stability of the vacuum. When in addition $m^2 = -\mu^2 < 0$ is chosen, the potential has a local maximum at the origin and degenerate minima on a circle around it. By adapting a particular ground state the symmetry is spontaneously broken. In particular, in the configuration where the expectation value of the charged Higgs-field vanishes, the ground state can be written as

$$\Phi_0 \equiv \langle \Phi_0 \rangle = \frac{1}{\sqrt{2}} \begin{pmatrix} 0 \\ v \end{pmatrix}, \quad v = \frac{\mu}{\sqrt{\lambda}}. \quad (2.21)$$

Considering a small excitation:

$$\Phi(x) = \frac{1}{\sqrt{2}} \begin{pmatrix} 0 \\ v + \eta(x) \end{pmatrix}, \quad (2.22)$$

and inserting it into the Lagrangian yields

$$\begin{aligned} \mathcal{L} &= \left[\frac{1}{2} (\partial^\mu \eta) (\partial_\mu \eta) - \mu^2 \eta^2 \right] - \frac{1}{4} W_{\mu\nu}^i W_i^{\mu\nu} \\ &\quad - \frac{1}{4} B_{\mu\nu} B^{\mu\nu} + \frac{1}{2} \cdot \frac{g^2 v^2}{4} (|W_\mu^+|^2 + |W_\mu^-|^2) + \frac{1}{2} \cdot \frac{v^2}{4} |g' B_\mu - g W_\mu^3|^2. \end{aligned} \quad (2.23)$$

There is a real Goldstone boson, η , with mass $m_\eta = \sqrt{2}\mu$, which is identified with the Higgs-boson. In addition, the mass terms for the other bosons result from the Lagrangian as well:

$$m_\gamma = 0, \quad (2.24)$$

since there is no masses for the electromagnetic four-potential. Moreover,

$$m_W = \frac{1}{2} g v \quad (2.25)$$

and with $g' B_\mu - g W_\mu^3 = -\sqrt{g^2 + g'^2} Z_\mu$:

$$m_Z = \frac{1}{2} v \sqrt{g^2 + g'^2}. \quad (2.26)$$

From the last two equations the relation Eq. (2.12) for the masses of W and Z bosons and the weak mixing angle is obtained. A measurement of all three parameters thus allows testing the SM predictions. The parameter μ which defines the Higgs mass cannot be predicted by the theory. The recently discovered Higgs-candidate particle has a mass of roughly 126 GeV , thus fixing the value of μ .

The masses of the fundamental fermions can be generated by Yukawa couplings to the Higgs-field, adding another term to the Lagrangian:

$$\mathcal{L}_{Yukawa} = -h_{d_{ij}} \bar{q}_{L_i} \Phi d_{R_j} - h_{u_{ij}} \bar{q}_{L_i} \tilde{\Phi} u_{R_j} - h_{l_{ij}} \bar{l}_{L_i} \Phi e_{R_j} + h.c. \quad (2.27)$$

with $\tilde{\Phi} = -i\sigma_2\Phi^*$ and q_L (l_L) and u_R , d_R (e_R) being the quark (lepton) $SU(2)_L$ doublets and singlets. The mass of a fermion f is given by

$$m_f = \frac{1}{\sqrt{2}} h_f v, \quad (2.28)$$

i.e. the coupling h_f is proportional to the fermion mass.

2.3 Quantum Chromodynamics

The quark model had initially been introduced by Gell-Mann [24] (and independently by Zweig) in 1964 to explain the multitude of observed hadrons as built up off fundamental constituents—the quarks. This hypothesis was corroborated experimentally by the results of deep inelastic scattering (DIS) experiments studying the structure of the proton, which indicated that the proton should consist of three charged constituents [25]. However, there remained scepticism about the model mainly due to two reasons: No free quarks were observed and states like the Δ^{++} baryon, hypothesised to consist of three u -quarks with the same spin, should not exist due to the Pauli principle. Already at the time the notion of *confined quarks* was brought up but lacked any form of explanation. A remedy for the dilemma of apparent violation of the Pauli principle had been proposed by Greenberg in 1964 [26]: He introduced a new quantum number which came to be known as colour. Nevertheless, only when the J/Ψ was discovered in 1974 [27, 28] and required the introduction of a fourth quark, the quark model became more popular. It was further strengthened by the observation of additional states including the new quark and the subsequent discovery of the particles of the third family which was completed 1995 with the discovery of the top quark [29, 30]. Deep inelastic scattering showed that there are electrically neutral constituents inside the proton that are identified with the mediators of the strong force, the gluons. Further evidence for gluons was found for example in the *jet* structure characteristics of inelastic scattering at high energies [31]. Based on these observations the current picture of a proton is as follows: Its ‘macroscopic’ properties like charge and spin are defined by its *valence quarks* content. The valence quarks of a proton are two u - and one d -quark. They are held together by the strong

force, i.e. by the exchange of gluons. These gluons can again fluctuate into quark-antiquark pairs, which form the *quark sea*, or split into gluons. The gluons, valence- and sea-quarks are commonly referred to as *partons*.

The 8 generators of the $SU(3)_C$ symmetry of the strong interaction can be represented via the Gell-Mann matrices λ_ρ , $\rho = 1, 2, \dots, 8$. The commutators of these matrices define the totally antisymmetric structure functions f^{abc} of the $SU(3)$:

$$[\lambda^a, \lambda^b] = 2i f^{abc} \lambda^\gamma. \quad (2.29)$$

The covariant derivative is given as

$$D_\mu = \partial_\mu - ig_s \frac{\lambda_\rho}{2} G_\mu^\rho, \quad (2.30)$$

with the ρ -component G_μ^ρ of the gluon field. Using this, the Lagrangian of quantum chromodynamics (QCD) can be formulated as

$$\mathcal{L}_{QCD} = \sum_q \bar{q}(i\not{D} - m_q)q - \frac{1}{4} G_{\mu\nu}^\rho G_\rho^{\mu\nu}. \quad (2.31)$$

The ρ th gluon field tensor is written as

$$G_{\mu\nu}^\rho = \partial_\mu G_\nu^\rho - \partial_\nu G_\mu^\rho + g_s f^{\rho\beta\gamma} G_\mu^\beta G_\nu^\gamma. \quad (2.32)$$

The strong coupling constant α_s is related to the coupling g_s above as

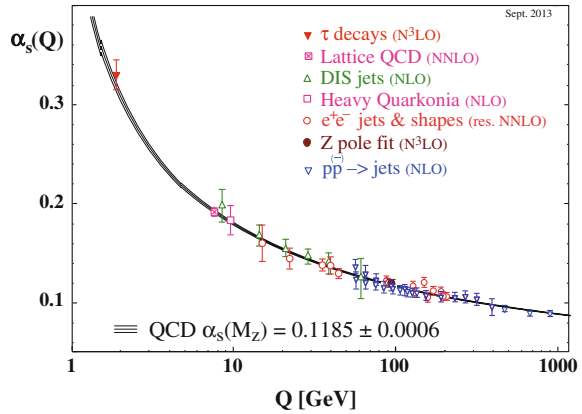
$$\alpha_s = \frac{g_s^2}{4\pi}. \quad (2.33)$$

The last term in Eq. (2.32) describes the self-coupling of gluons with each other due to the fact that they carry colour charge as well (more precisely, one colour and one anticolour charge). This leads to special features of the strong interaction. At small distances, the self-coupling of gluons leads to “anti-screening” effects, resulting in a weakening of the coupling constant α_s . This is referred to as *asymptotic freedom*, as the quarks are quasi-free and can be treated perturbatively. On the other hand, the coupling constant becomes large for large distances, which leads to the so-called *confinement* of quarks in hadrons: When trying to separate two quarks, the energy needed becomes so large, that it exceeds the threshold for the creation of new quark-antiquark pairs, which then again form colourless states with the original quarks. This process is also referred to as *hadronisation*.

The dependence of the strong coupling constant on the energy—parameterised as momentum transfer Q —can in leading order be expressed as

$$\alpha_s(Q) = \frac{12\pi}{(33 - 2n_f) \log \frac{Q^2}{\Lambda^2}}, \quad (2.34)$$

Fig. 2.1 Summary of measurements of α_s , illustrating the running of the coupling constant as a function of the energy scale Q [4]



with some arbitrary scale Λ for which α_s is assumed to be known. The number n_f is the number of quark flavours accessible at the chosen energy scale, i.e. for which $Q^2 > m_q^2$. Due to this energy dependence α_s is called a *running coupling constant*.

From Eq. (2.34), it can be seen that, in case $n_f < 17$, for $Q \rightarrow \infty$ the coupling strength approaches 0—the quarks are asymptotically free. On the other hand, α_s grows for small values of Q and becomes greater than 1 for values of Q below a few hundred MeV. In this regime, no perturbation expansion is possible any more, confinement sets in. A typical scale is the mass of the Z -boson: $\alpha_s(m_Z) = 0.1185(6)$ [4]. The running of the coupling constant is also apparent from Fig. 2.1 which shows measurements of its value at various scales.

2.4 Open Questions and Extensions

The Standard Model of particle physics is surely one of the most successful theories in physics. So far, it withstands all tests and has been experimentally verified with tremendous precision. One of its latest triumphs is the discovery of a Higgs-boson candidate particle which to date appears to have the properties predicted by the SM. But even if it does, there remain several phenomena that cannot be explained within the SM and hence require the existence of some kind of yet undiscovered physics—commonly referred to as *new physics* or *physics beyond the SM* (BSM).

Within the SM, neutrinos are treated as massless, but observation of neutrino oscillation demands that neutrinos in fact do have a non-vanishing mass, albeit a very small one.

Another challenge for the SM is the so-called *hierarchy problem*: The standard model gives no explanation for the enormous difference between the electroweak scale ($\mathcal{O}(100 \text{ GeV})$), the scale at which electroweak and strong forces become equally strong (due to the running coupling constants) which is of the order of 10^{16} GeV and

the Planck scale of $\sim 10^{19}$ GeV, at which also the gravitational interaction becomes as strong as the other forces. Similarly, while the masses of the fundamental particles can be generated via the Higgs-mechanism in electroweak symmetry breaking, the theory gives no explanation for the large range of the masses. Moreover, additional particles are needed in order to cancel diverging loop-corrections to the Higgs mass. There is also no explanation within the SM as to why there are three generations of fundamental fermions.

The origin of the matter-antimatter asymmetry in the universe is another open question in particle physics: If at the big bang particles and antiparticles were created in the same amount, they should all have annihilated again. However, the annihilation appears to be asymmetric as there is today only matter observed in the universe while the antimatter has disappeared. This requires CP violation by an amount that cannot be accommodated in the SM.

Finally, cosmological and astrophysical observations lead to the conclusion, that radiation and matter made of SM particles only account for about 5% of the mass and energy content in the universe. Roughly 27% are attributed to non-luminous *dark matter* and the remaining roughly 68% are so-called *dark energy*. Neither of these last two components finds any explanation within the SM. Dark matter will be discussed in more detail in Chap. 3.

One proposed explanation for several of the phenomena listed above provides the theory of *super-symmetry* (SUSY), in which the particle content is doubled by assigning a super-partner to each SM particle. The partners of fermions—*sfermions*—are bosons and the partners of gauge bosons—*gauginos*—are fermions. For example, the SUSY-partner of a neutrino would be called a *sneutrino*, that of a *W*-boson a *Wino*. Electrically neutral mixtures of gauginos are referred to as *neutralinos*.

Another class of extensions to the Standard Model are theories of extra spacial dimensions. In most of these models, the usual $(3 + 1)$ -dimensional spacetime—referred to as a *brane*—is embedded in the *bulk*, a $(3 + \delta + 1)$ -dimensional spacetime, i.e. adding δ extra spacial dimensions. Such scenarios are often proposed as solutions to the hierarchy problem, for example in the Arkani-Hamed, Dimopoulos and Dvali (ADD) model [32], where all of the large extra dimensions (LED) are compactified on some topology with size R , which leads to the fundamental Planck scale being lowered to approximately the electroweak scale. Another possibility to achieve this are *warped* extra dimensions, i.e. extra dimensions with large curvature, as in the so-called Randall–Sundrum model [33]. In the aforementioned models, it is assumed that the SM fields propagate in the brane only, and only gravity is allowed to propagate in the bulk. In addition, there are *universal* extra dimensions models (UED) with flat extra dimension that are much smaller than the ones in the ADD model, for example. In these UED models all particles can propagate in the extra dimensions.

In Chap. 3, Dark Matter candidates that these models provide will be discussed.

References

1. Griffiths D (1987) Introduction to elementary particles. Wiley, New York
2. Schmueser P (2013) Feynman-Graphen und Eichtheorien für Experimentalphysiker. 2nd edn. Springer, Heidelberg
3. Povh B, Rith K, Scholz Ch, Zetsche F, Rodejohann W (2013) Teilchen und Kerne: Eine Einführung in die physikalischen Konzepte; 9th edn. Springer, Spektrum
4. Beringer J et al (2012) Review of particle physics. Phys Rev D 86:010001. doi:[10.1103/PhysRevD.86.010001](https://doi.org/10.1103/PhysRevD.86.010001)
5. Ahmad QR et al (2002) Direct evidence for neutrino flavor transformation from neutral-current interactions in the sudbury neutrino observatory. Phys Rev Lett 89:011301. doi:[10.1103/PhysRevLett.89.011301](https://doi.org/10.1103/PhysRevLett.89.011301)
6. Kraus C et al (2005) Final results from phase II of the Mainz neutrino mass search in tritium beta decay. Eur Phys J C40:447–468. doi:[10.1140/epjc/s2005-02139-7](https://doi.org/10.1140/epjc/s2005-02139-7). arXiv:[hep-ex/0412056](https://arxiv.org/abs/hep-ex/0412056) [hep-ex]
7. Aseev VN et al (2011) An upper limit on electron antineutrino mass from Troitsk experiment. Phys Rev D84:112003. doi:[10.1103/PhysRevD.84.112003](https://doi.org/10.1103/PhysRevD.84.112003). arXiv:[1108.5034](https://arxiv.org/abs/1108.5034) [hep-ex]
8. Higgs PW (1964) Broken symmetries and the masses of gauge bosons. Phys Rev Lett 13:508–509. doi:[10.1103/PhysRevLett.13.508](https://doi.org/10.1103/PhysRevLett.13.508)
9. Englert F, Brout R (1964) Broken symmetry and the mass of gauge vector mesons. Phys Rev Lett. 13:321–323. doi:[10.1103/PhysRevLett.13.321](https://doi.org/10.1103/PhysRevLett.13.321)
10. Guralnik GS, Hagen CR, Kibble TWB (1964) Global conservation laws and massless particles. Phys Rev Lett. 13:585–587. doi:[10.1103/PhysRevLett.13.585](https://doi.org/10.1103/PhysRevLett.13.585)
11. The ATLAS Collaboration (2012) Observation of a new particle in the search for the Standard Model Higgs boson with the ATLAS detector at the LHC. Phys Lett. B716:1–29. doi:[10.1016/j.physletb.2012.08.020](https://doi.org/10.1016/j.physletb.2012.08.020). arXiv:[1207.7214](https://arxiv.org/abs/1207.7214) [hep-ex]
12. The CMS Collaboration (2012) Observation of a new boson at a mass of 125 GeV with the CMS experiment at the LHC. Phys Lett. B716:30–61. doi:[10.1016/j.physletb.2012.08.021](https://doi.org/10.1016/j.physletb.2012.08.021). arXiv:[1207.7235](https://arxiv.org/abs/1207.7235) [hep-ex]
13. Weinberg S (1967) A model of leptons. Phys Rev Lett 19:1264–1266. doi:[10.1103/PhysRevLett.19.1264](https://doi.org/10.1103/PhysRevLett.19.1264)
14. Glashow SL (1961) Partial symmetries of weak interactions. Nucl Phys 22:579–588. doi:[10.1016/0029-5582\(61\)90469-2](https://doi.org/10.1016/0029-5582(61)90469-2)
15. Goldstone J, Salam A, Weinberg S (1962) Broken symmetries. Phys Rev. 127:965–970. doi:[10.1103/PhysRev.127.965](https://doi.org/10.1103/PhysRev.127.965)
16. Maxwell JC (1865) A dynamical theory of the electromagnetic field. In: Philosophical transactions of the royal society of London. vol 155, pp. 459–512. doi:[10.1098/rstl.1865.0008](https://doi.org/10.1098/rstl.1865.0008). eprint: <http://rstl.royalsocietypublishing.org/content/155/459.full.pdf+html>. <http://rstl.royalsocietypublishing.org/content/155/459.short>
17. Hasert F et al (1973) Observation of neutrino like interactions without muon or electron in the gargamelle neutrino experiment. Phys Lett B 46:138–140. doi:[10.1016/0370-2693\(73\)90499-1](https://doi.org/10.1016/0370-2693(73)90499-1)
18. Kobayashi M, Maskawa T (1973) CP Violation in the renormalizable theory of weak interaction. Prog Theor Phys 49:652–657. doi:[10.1143/PTP.49.652](https://doi.org/10.1143/PTP.49.652)
19. Cabibbo N (1963) Unitary symmetry and leptonic decays. Phys Rev Lett 10:531–533. doi:[10.1103/PhysRevLett.10.531](https://doi.org/10.1103/PhysRevLett.10.531)
20. Gell-Mann M (1956) The interpretation of the new particles as displaced charge multiplets. II Nuovo Cimento. 4.2:848–866. doi:[10.1007/BF02748000](https://doi.org/10.1007/BF02748000). ISSN: 0029-6341
21. Nakano T, Nishijima K (1953) Charge independence for V-particles. Prog Theor Phys. 10.5:581–582. doi:[10.1143/PTP.10.581](https://doi.org/10.1143/PTP.10.581). eprint: <http://ptp.oxfordjournals.org/content/10/5/581.full.pdf+html>. <http://ptp.oxfordjournals.org/content/10/5/581.short>
22. Arnison G et al (1983) Experimental observation of isolated large transverse energy electrons with associated missing energy at $s^{*}(1/2) = 540$ -GeV. Phys Lett B 122:103–116. doi:[10.1016/0370-2693\(83\)91177-2](https://doi.org/10.1016/0370-2693(83)91177-2)

23. Arnison G et al (1983) EXperimental observation of lepton pairs of invariant mass around 95-GeV/c**2 at the CERN SPS collider. Phys Lett B 126:398–410. doi:[10.1016/0370-2693\(83\)90188-0](https://doi.org/10.1016/0370-2693(83)90188-0)
24. Gell-Mann M (1964) A schematic model of baryons and mesons. Phys Lett 8:214–215. doi:[10.1016/S0031-9163\(64\)92001-3](https://doi.org/10.1016/S0031-9163(64)92001-3)
25. Kendall HW, Panofsky WKH (1971) The structure of the proton and the neutron. Sci Am. 224.6:60–77. <http://www.nature.com/scientificamerican/journal/v224/n6/pdf/scientificamerican0671-60.pdf>
26. Greenberg OW (1964) Spin and unitary-spin independence in a paraquark model of baryons and mesons. Phys Rev Lett. 13:598–602. doi:[10.1103/PhysRevLett.13.598](https://doi.org/10.1103/PhysRevLett.13.598)
27. Aubert JJ et al (1974) Experimental observation of a heavy particle J. Phys Rev Lett. 33(23):1404–1406. doi:[10.1103/PhysRevLett.33.1404](https://doi.org/10.1103/PhysRevLett.33.1404)
28. Augustin JE et al (1974) Discovery of a narrow resonance in e^+e^- annihilation. Phys Rev Lett. 33(23):1406–1408. doi:[10.1103/PhysRevLett.33.1406](https://doi.org/10.1103/PhysRevLett.33.1406)
29. Abe F et al (1995) Observation of top quark production in pp collisions with the collider detector at fermilab. Phys Rev Lett. 74(14):2626–2631. doi:[10.1103/PhysRevLett.74.2626](https://doi.org/10.1103/PhysRevLett.74.2626)
30. Abachi S et al (1995) Observation of the top quark. Phys Rev Lett. 74(14):2632–2637. doi:[10.1103/PhysRevLett.74.2632](https://doi.org/10.1103/PhysRevLett.74.2632)
31. Jacob MRM, Landshoff PV (1980) The inner structure of the proton. Sci Am. 3:66–75
32. Arkani-Hamed N, Dimopoulos S, Dvali G (1998) The Hierarchy problem and new dimensions at a millimeter. Phys Lett. B429:263–272. doi:[10.1016/S0370-2693\(98\)00466-3](https://doi.org/10.1016/S0370-2693(98)00466-3). [arXiv:hep-ph/9803315](https://arxiv.org/abs/hep-ph/9803315) [hep-ph]
33. Randall L, Sundrum R (1999) A Large mass hierarchy from a small extra dimension. Phys Rev Lett. 83:3370–3373. doi:[10.1103/PhysRevLett.83.3370](https://doi.org/10.1103/PhysRevLett.83.3370). [arXiv:hep-ph/9905221](https://arxiv.org/abs/hep-ph/9905221) [hep-ph]

Chapter 3

Dark Matter

In this chapter, some essential background information for the interpretation of the data analysis presented in part IV is compiled. Section 3.1 gives a short introduction to cosmology, with more details on the derivation of the present abundance of a thermal relic in Sect. 3.2. In Sect. 3.3, some of the most striking evidence for the existence of dark matter is presented. Possible particle candidates are discussed in Sect. 3.4 and the status of the searches for generic weakly interacting massive particles is summarised in Sect. 3.5. The contents of this chapter is largely inspired by the summaries in [1].

3.1 Basics of Cosmology

Today, there is a broad consensus among cosmologists about the general picture of the evolution of the universe, according to which it came into existence roughly 10^{10} years ago in the *Big Bang*. At that time, it was in a highly compressed state, and the standard model of cosmology successfully describes its evolution to the present day state. The model, which goes back to the discovery of Hubble's law [2, 3], explains many of the observed properties of the universe, among those the thermal history, the present abundances of elements, the background radiation and large scale structures.

The model is based on three fundamental building blocks: the Einstein equation of general relativity, which connects the matter and energy content of the universe to its geometry, the metric, which gives a description of the structure of the spacetime, and the equations of state, containing the specification of the physical properties of the matter and energy content.

With a few assumptions, the Einstein field equation can be derived almost from first principles. One requirement is that the equation should be invariant under coordinate transformations, another is that it should reproduce Newtonian gravity in the limit of weak fields. Moreover, the equation should be a second order differential equation

linear in the second derivatives in analogy to the Poisson equation for Newtonian gravity. Using this, one finds

$$R_{\mu\nu} - \frac{1}{2}g_{\mu\nu}R = -\frac{8\pi G_N}{c^4}T_{\mu\nu} + \Lambda g_{\mu\nu}. \quad (3.1)$$

The left hand side of the above equation contains the information on the geometry: $R_{\mu\nu}$ is the Ricci tensor, $R = g_{\mu\nu}R^{\mu\nu}$ the Ricci scalar and $g_{\mu\nu}$ the metric tensor. The right hand side of (3.1) describes the energy content: $T_{\mu\nu}$ is the energy-momentum tensor, G_N is the gravitational constant, c the speed of light and Λ the *cosmological constant*. It was first introduced by Einstein in order to obtain a stationary solution, but was abandoned when the expansion of the universe was discovered. The Λ -term in Eq. (3.1) constitutes a ‘vacuum energy’, creating a gravitational field in the absence of matter, thus relating to the spacetime itself, rather than to the matter content. The cosmological constant has experienced a revival in the light of data from type Ia supernova, which indicate that the expansion of the universe is accelerating [4]. This could be explained by a term like the second one on the right hand side of the Einstein equation (3.1). Moreover, the measurement of the cosmic microwave background, which will be discussed in Sect. 3.3, yields indications for the existence of *dark energy*, which can be associated with the cosmological constant.

To solve the Einstein equation one is required to specify the symmetry of the problem. Mathematically, solving the equation is greatly simplified by assuming homogeneity and isotropy of the universe. As this assumption is justified by experimental observations, it can be used to define the metric. The line element then takes the form

$$ds^2 = -cdt^2 + a(t)^2 \left(\frac{dr^2}{1 - kr^2} + r^2 d\Omega^2 \right), \quad (3.2)$$

where $a(t)$ is called the *scale factor* and k is a constant which can take the values $+1$, 0 or -1 and describes the spatial curvature; $k = 0$ corresponding to the case of usual flat Euclidian space.

Solving the Einstein equations with this metric, one of its components yields

$$\left(\frac{\dot{a}}{a} \right)^2 + \frac{k}{a^2} = \frac{8\pi G_N}{3} \rho_{tot}, \quad (3.3)$$

one of the *Friedmann equations* [5]. Commonly, the Hubble parameter is defined by

$$H(t) = \frac{\dot{a}(t)}{a(t)}. \quad (3.4)$$

A recent estimate of the present value of the Hubble parameter, the *Hubble constant* H_0 , is $63.7 \pm 1.2 \text{ km s}^{-1} \text{ Mpc}^{-1}$ [6].

The expansion of the universe and the resulting increase in the scale factor $a(t)$ lead to a cosmological redshift of the light coming from distant galaxies. If light of

wavelength λ_e is emitted and the observed wavelength is λ_o , the redshift parameter z is defined by

$$1 + z \equiv \frac{\lambda_o}{\lambda_e}. \quad (3.5)$$

It can be shown [7] that the relation to the scale factor is given by

$$1 + z = \frac{a(t_o)}{a(t_e)}, \quad (3.6)$$

with t_o and t_e being the time of observation and emission, respectively.

From Eq. (3.3), it follows that the universe is flat, i.e. $k = 0$, for

$$\rho_{tot} = \frac{3H^2}{8\pi G_N} \equiv \rho_c, \quad (3.7)$$

where ρ_c is called the *critical density*. It is customary to quote the abundance Ω_X of some species X in the universe in units of the critical density:

$$\Omega_X \equiv \frac{\rho_X}{\rho_c}, \quad (3.8)$$

and defining

$$\Omega \equiv \sum_i \Omega_i \quad (3.9)$$

with which the Friedmann equation (3.3) takes the form

$$\Omega - 1 = \frac{k}{H^2 a^2}. \quad (3.10)$$

From the above expression it can be seen that the value of k defines whether Ω is greater than, smaller than or equal to 1. For example, $\Omega = 1$ corresponds to a flat universe. For $\Omega < 1$, the universe is called *open*, for $\Omega > 1$ it is *closed*.

The evolution of a component of the matter-energy-content depends on the respective equations of state which differ for different components. When defining the present day quantity

$$\Omega_K \equiv -\frac{k}{H^2 a^2}, \quad (3.11)$$

(such that $\Omega + \Omega_K = 1$ in Eq. (3.10)), it follows from Eq. (3.6) that the value of this quantity at an earlier time (i.e. at larger redshift) is given by $\Omega_K (1 + z)^2$. For the matter content of the universe, the density (Ω_M) scales as $(1 + z)^3$, since for a constant comoving number density the physical mass density is diluted with the changing volume. For photons, also the energy is reduced by the redshift, hence the radiation density (Ω_R) scales as $(1 + z)^4$. For a general component X obeying an

equation of state of the form $p_X = \alpha_X \rho_X$ the density scales as $(1+z)^{3(1+\alpha_X)}$. For example, for the cosmological constant, $\alpha_\Lambda = -1$, such that the density remains constant.

This leads to the following expression for the expansion rate as a function of the redshift z :

$$\frac{H^2(z)}{H_0^2} = \left[\Omega_X(1+z)^{3(1+\alpha_X)} + \Omega_K(1+z)^2 + \Omega_M(1+z)^3 + \Omega_R(1+z)^4 \right]. \quad (3.12)$$

Measuring the cosmological parameters today allows one to project back in time. This projection holds until one reaches an epoch where interactions that lead to interchanges between the different species can occur. This should correspond to the time of neutrino decoupling, which happened shortly before the formation of light elements in *Big Bang nucleosynthesis* (BBN). Probing further back is only possible with additional assumptions about particle interactions and perhaps even about physical laws themselves.

A very short summary of the current picture of the history of the universe is given below.

It is assumed that at a temperature of $T \sim 10^{16}$ GeV symmetry breaking of some unified group into the Standard Model gauge group $SU(3)_C \otimes SU(2)_L \otimes U(1)_Y$ occurred. This gauge symmetry breaks further into $SU(3)_C \otimes U(1)_Q$ during electroweak symmetry breaking at $T \sim 10^2$ GeV. At $T \sim 10^1 - 10^3$ GeV, potential weakly interacting dark matter candidates *freeze out* (see Sect. 3.2). For $T \sim 0.3$ GeV, quarks and gluons become confined into hadrons in the *QCD phase transition*. Neutrino freeze-out takes place at $T \sim 1$ MeV, until at $T \sim 100$ keV, in the primary nucleosynthesis protons and neutrons begin to form light elements (D, ^3He , ^4He , Li). Some of the strongest constraints on the Big Bang theory come from Big Bang nucleosynthesis and it is one major success of the model to predict the observed abundances remarkably well. At $T \sim 1$ eV, matter and radiation density are equalised, leading to the beginning of structure formation. The cosmic microwave background (see Sect. 3.3) results from photon decoupling at $T \sim 0.4$ eV. The current-day temperature of 2.7 K corresponds to about 10^{-4} eV.

3.2 Relic Density

An important quantity in the discussions that are to follow in this chapter is the present density of a thermal relic from the early universe. The standard calculation of this *relic density* will be outlined in this section.

Qualitatively, the process can be understood in the following way: A given species of particles has to have a sufficient interaction rate to remain in thermodynamic equilibrium. If the interaction rate decreases below the expansion rate of the universe, interactions do not take place any more and the particle species *decouples*. This is

also referred to as the *freeze-out*, the temperature at which this occurs is called the freeze-out temperature, T_F .

The starting point for deriving the relic density of a non-relativistic particle species is the Boltzmann equation:

$$\frac{dn}{dt} + 3Hn = -\langle\sigma v\rangle(n^2 - n_{eq}^2), \quad (3.13)$$

where n is the particle number density and n_{eq} is the one for thermal equilibrium. H is the Hubble parameter, and $\langle\sigma v\rangle$ is the product of the annihilation cross section and the relative velocity of the annihilating particles; brackets mean thermal average. For the non-relativistic case this can be expanded in powers of v^2 :

$$\langle\sigma v\rangle = a + b\langle v^2\rangle + \mathcal{O}(\langle v^4\rangle) \approx a + 6b/x \quad (3.14)$$

with $x := \frac{m}{T}$. The equilibrium number density of a species of mass m ¹ at some temperature T can be expressed in the Maxwell–Boltzmann approximation as

$$n_{eq} = g\left(\frac{mT}{2\pi}\right)^{3/2} e^{-m/T}. \quad (3.15)$$

Here, g denotes the number of degrees of freedom.

The Boltzmann equation (3.13) is solved in two distinct regimes: long before and long after the freeze-out, i.e. $x \ll x_F$ and $x \gg x_F$, with $x_F = m/T_F$, for details see for example [8]. Matching the respective solutions yields the following expression for the relic density of some generic relic X in terms of the critical density and the scaled Hubble parameter h , defined by $H_0 = 100 h \text{ km s}^{-1} \text{ Mpc}^{-1}$:

$$\Omega_X h^2 \approx \frac{1.07 \times 10^9 \text{ GeV}^{-1}}{M_{Pl}} \frac{x_F}{\sqrt{g_F^*}} \frac{1}{(a + 3b/x_F)}. \quad (3.16)$$

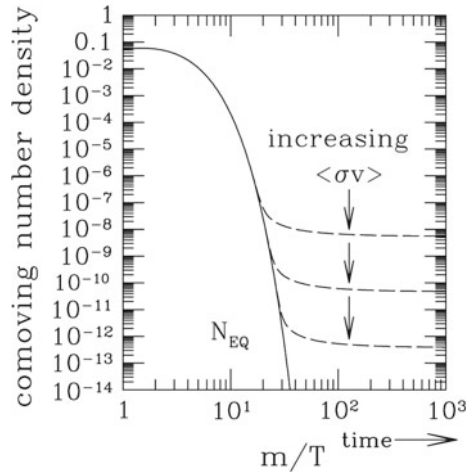
The number of relativistic degrees of freedom at freeze-out is given by g_F^* , M_{Pl} is the Planck mass. To estimate the relic density within this approximation one thus has to calculate the annihilation cross section and extract the mass-dependent parameters a and b , which allows to derive x_F . In an order-of-magnitude estimation Eq. (3.16) can be re-written as

$$\Omega_X h^2 \approx \frac{3 \times 10^{-27} \text{ cm}^3 \text{ s}^{-1}}{\langle\sigma v\rangle}, \quad (3.17)$$

from which it can be readily seen that the present abundance of the species X is determined by the annihilation cross section at the time of freeze-out. In particular, for larger annihilation cross section, the relic density is smaller, as a larger fraction of X could annihilate. Analogously, a small annihilation cross section results in a larger

¹ m is assumed to be large enough for the particle to be non-relativistic.

Fig. 3.1 Evolution of the comoving number density and freeze-out in the early universe [9]



relic abundance. This is also illustrated in Fig. 3.1, in this version taken from [9], which shows the evolution of the comoving number density² as a function of x . The number density decreases exponentially with increasing x , until the interaction rate becomes too small and the component freezes out, i.e. the comoving number density does not change any more. This happens the earlier, the lower the annihilation cross section is, which is sometimes referred to as the ‘survival of the weak’.

It has to be kept in mind that the above relations were derived under certain simplifying assumptions that are not valid generally. The relic density can be changed significantly with respect to the result obtained in the standard calculation by the presence of a scalar field in the early universe, as shown in [10]. There are three other cases in which the treatment outlined above does not hold, which are detailed in [11]: There could be resonant enhancement, the relic particle could be close to a mass threshold, allowing for additional annihilation or there could be *coannihilations*, when there is another species which shares a quantum number with species X and has a similar mass.

3.3 Evidence for Dark Matter

The existence of non-luminous matter as such is firmly established by a variety of cosmological observations at different scales. Without any claim to completeness some of the most intriguing hints shall be described in the following.

On galactic scales, the measurement of *rotation curves* of galaxies offers the perhaps most convincing evidence for the existence of dark matter (DM). The rotation curve shows the orbital velocity of stars and gas in the galaxy in dependence of the

²Since the universe is expanding, the density has to be considered w.r.t. to the ‘expanding volume’.

distance from the galactic centre. It can be measured by combining optical surface photometry with observations of the 21 cm hydrogen line.

From Newtonian dynamics, the rotation velocity, $v(r)$, is calculated as

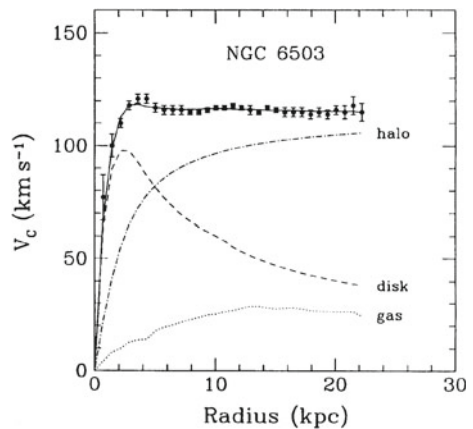
$$v(r) = \sqrt{\frac{G_N M(r)}{r}}, \quad (3.18)$$

with $M(r)$ given by the mass density distribution $\rho(r)$ as $M(r) = 4\pi \int dr \rho(r)r^2$. Thus, at distances greater than the radius of the optical disk, the rotation curves should fall as $\propto 1/\sqrt{r}$. However, the observed curves show a significantly different behaviour, as presented in Fig. 3.2 for the galaxy NGC 6503 [12]: The rotation curves are flat at large distances, even far beyond the optical disk. The data points are clearly not described by what is to be expected from the disk and the gas in the galaxy. This suggests that there should be a halo of non-luminous matter with $M(r) \propto r$ and $\rho(r) = 1/r^2$, respectively. Such a halo is also indicated in Fig. 3.2.

The DM profiles at small radii are less well known and there are large uncertainties in their description, but this does not diminish the evidence for the existence of a spherical dark matter halo in principle.

There is a large number of other indications for dark matter on sub- or inter-galactic scales, all relating to the fact that the matter-to-light ratio appears to be larger than what would be expected from visible matter. Among those are the weak modulation of strong lensing around some elliptical galaxies, hinting at a substructure on scales of $\sim 10^6$ sun masses. Within the Milky Way, an observation referred to as the *Oort discrepancy*, e.g. [13], named after J. Oort who was the first to describe it in 1932 [14], leads to the conclusion that there appears to be more matter than observed in the form of stars, given the gravitational potential one has to assume to account for their distribution. Distant galaxies appear as subjects of weak gravitational lensing by foreground structures that is not fully accounted for by the visible objects in some

Fig. 3.2 Rotation Curve of galaxy NGC 6503 [12]. The measured data points are shown in comparison to the fitted profiles for gas, disk and dark matter



cases. Further evidence is derived from the velocity dispersions of dwarf spheroidal galaxies and spiral galaxy satellites.

The first to bring up the idea of dark matter was Swiss astronomer Fritz Zwicky in 1933 [15]. He measured the velocity distribution of galaxies in the Coma Cluster via their Doppler-shifted spectra. Applying the virial theorem, he inferred the gravitational potential and thereby the mass of the cluster. Combining this with a measurement of the total luminosity, he derived a mass-to-light ratio for the Coma cluster that was larger than the one in the solar neighbourhood by two orders of magnitude. This led him to the conclusion that there must be additional matter in the Coma cluster which does not emit light, “missing matter”.

Other methods to estimate the mass of a cluster include the study of weak gravitational lensing effects or of the X-ray emission profile. While different methods give dark matter density profiles consistent among each other and also with numerical simulations, there remains some uncertainty in the prediction of the profiles in cluster cores.

Figure 3.3, taken from Ref. [16], shows a combination of images of the galaxy cluster 1E 0657-56, obtained with different techniques. The cluster is the product of a collision between two galaxy clusters. The optical image showing the galaxies in orange and white is overlaid with pink shading which indicates the mass distribution as obtained from X-ray emission from the hot gas. The blue regions mark where the highest mass concentration is found, as inferred from gravitational lensing. It can be seen that the ‘normal’ baryonic matter (pink) is clearly shifted with respect to the centre of the mass distribution, the blue shading can thus be interpreted as the dark matter distribution. While the hot gas shows a distortion due to the collision which can be explained by a drag force similar to air resistance, the dark matter distribution still shows a spherical distribution, indicating that it did not interact with the gas nor with itself (except for gravitational effects). Consequently, the dark matter was not slowed down in contrast to the gas, which explains the separation of the two components after the collision. This is seen as the strongest argument for dark matter

Fig. 3.3 The “Bullet Cluster”: product of the collision of two galaxy clusters. The dark matter halo shown in *blue* is inferred from gravitational lensing effects [16]



being involved: If the hot gas would contribute the largest fraction to the total mass, the separation of it and the regions of highest mass density could not be explained. According to Ref. [17], the spatial offset of the centres of total and baryonic mass corresponds to an 8σ significance. This is taken as proof that the largest fraction of matter in the cluster is unseen.

While evidence for the existence of dark matter on scales of the size of galaxies or galaxy clusters is intriguing, these observations do not provide means to estimate the total amount of dark matter in the universe. It can, however, be extracted from the analysis of the cosmic microwave background (CMB).

The CMB consists of photons created in the early universe, which can propagate undisturbed since they decoupled from matter approximately 380000 years after the Big Bang. George Gamow and his collaborators predicted the existence of CMB in 1948 [18] and it was discovered (unintentionally) by Penzias and Wilson in 1965 [19, 20]. Today, the CMB has been measured to exhibit the spectrum of a black body with a temperature of 2.7255(6) K [6] and to deviate from isotropy only at the level of 10^{-5} . It is these small anisotropies that are the key to constraining cosmological parameters and thereby test cosmological models.

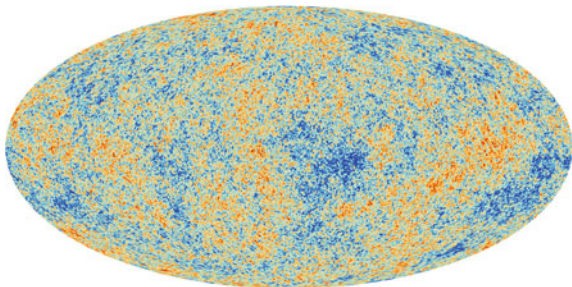
In order to do so, the temperature fluctuations are parameterised as an expansion in spherical harmonics $Y_{\ell m}(\theta, \phi)$:

$$\frac{\delta T}{T}(\theta, \phi) = \sum_{\ell=2}^{+\infty} \sum_{m=-\ell}^{\ell} a_{\ell m} Y_{\ell m}(\theta, \phi). \quad (3.19)$$

The temperature fluctuations appear to be Gaussian to a good approximation, which means that all the information contained in maps of the CMB can be compressed into the power spectrum. Constraints on cosmological parameters are then obtained by fitting a model to this spectrum and extracting the best-fit values for the parameters by maximising an N -dimensional likelihood, where N is the number of parameters.

The most recent measurements of the CMB are from the ESA PLANCK satellite [21], whose CMB sky map is shown in Fig. 3.4. The fluctuations are of the order of a few hundred μK . Figure 3.5 shows the corresponding expansion of the temperature fluctuations as a function of the multipole moment ℓ , which is corresponding to the angular scale $\phi \sim \pi/\ell$, i.e. small numbers of ℓ are linked to large angular scales and

Fig. 3.4 Foreground cleaned map of the temperature fluctuations of cosmic microwave background as measured by the PLANCK satellite. The colour scheme corresponds to a range of -300 – $300\mu\text{K}$ [21, 22]



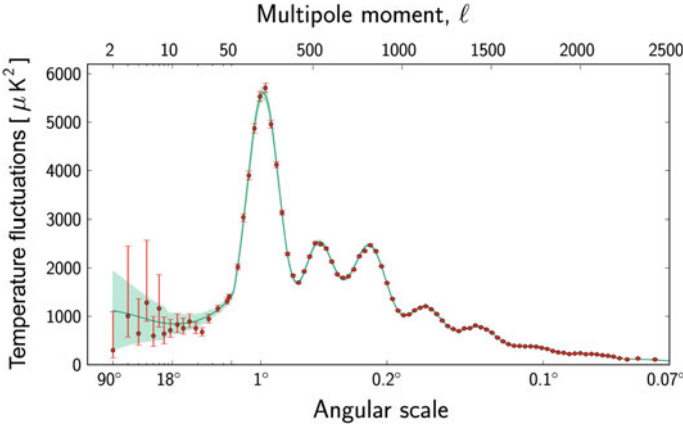


Fig. 3.5 The temperature fluctuations of the CMB as measured by PLANCK [22, 24]

vice versa. The measured data are shown together with the best fit model. The error bars include experimental uncertainties as well as cosmic variance,³ indicated by the green band around the fit model. There is very good agreement between the data and the model.

The fit included 6 primary parameters [24], from which a number of additional parameters can be derived.

Important information is obtained from the position, shape and relative height of the peaks, which are referred to as *acoustic peaks*, since they originate from acoustic waves in the photon-baryon fluid before recombination and photon decoupling. These oscillations lead to spatial variations in the CMB temperature and standing waves manifest themselves as harmonic peaks in the multipole expansion. For example, the position of the first peak is sensitive to the curvature of the universe and to a small extent also to the amount of dark energy. The shape is determined by the density of baryons and dark matter, which are two of the primary fit parameters. They are estimated to be

$$\Omega_b h^2 = 0.02207(33) \quad \text{and} \quad \Omega_c h^2 = 0.1196(31) \quad (3.20)$$

at 68 % confidence level [24]. This is, within uncertainties, compatible with the result from the WMAP satellite [25], which measured for example $\Omega_c h^2 = 0.1120(56)$.

Moreover, the CMB measurements are consistent with a flat universe, as the total energy density is close to the critical one. However, this requires a non-vanishing amount of dark energy which was derived from the Planck data to be $\Omega_\Lambda = 0.686(20)$.

³Cosmic variance refers to the uncertainty due to the fact that the sample size for observations on the scale of the entire universe is naturally very limited, as there is only one universe to be observed [23].

The fact that the second peak appears suppressed with respect to the first and the third can be explained by a substantial amount of dark baryons. The existence of a third peak as well as its relative height provides further information on the dark matter density.

The best fit values from the Planck data yield the following picture of the composition of the matter-energy-content of the universe: 68.3% is dark energy, dark matter accounts for 26.7% and only 4.9% is baryonic matter.

Another indirect hint to the existence of an additional matter component from the study of structure formation in the early universe. This is mostly done by N-body simulations, which have greatly profited from the vast increase in computing power over the last decades. There is broad agreement that the formation of structures cannot be modelled correctly without assuming the presence of dark matter. The standard model of cosmology is thus often referred to as the Λ CDM, as it contains both the cosmological constant as well as cold dark matter as essential ingredients to explain the evolution of the universe to its present state.

Plenty of phenomena on very different scales have been observed with very different techniques and are attributed to the existence of non-baryonic dark matter. There exist other attempts of explanations, like modified gravity (for example [26–28]), for many of the observations, but to date those approaches do not incorporate all observations in a consistent way. Dark matter so far remains the only solution able to account for all observed phenomena. However, there has been no particle candidate observed yet that exhibits the required properties to constitute the relic abundance of dark matter.

3.4 Dark Matter Candidates

Studies of structure formation in the universe give important constraints on the nature of dark matter candidates. One is that dark matter should have been non-relativistic when the formation of galaxies started, which is referred to as *cold* dark matter (in contrast to *hot* relativistic or *warm* dark matter).

The dark matter particles have to have the right mass and abundance to yield the observed relic density. Moreover, a viable dark matter candidate has to be stable on cosmological time scales since otherwise it would have decayed by now. As the name “dark” indicates, it should have no electromagnetic and only very small weak interactions.

Among the fundamental particles of the Standard Model, there is only one potential dark matter candidate: the neutrino. While neutrinos fulfil the latter two requirements, they are essentially ruled out as the only or dominant dark matter component by the first two.

The neutrino abundance is not large enough to account for the amount of dark matter derived from the observations outlined in Sect. 3.3. Since the upper limit on neutrino masses is ~ 2 eV [6], the total neutrino density is bounded from above by

$$\Omega_\nu h^2 \lesssim 0.07. \quad (3.21)$$

The combination of CMB and large-scale structure data yields a tighter limit of $\Omega_\nu h^2 \lesssim 0.0062$ at 95% confidence level [6].

Another argument against neutrinos as the dominant dark matter component is that they are relativistic particles and as such have to be considered as *hot* dark matter.

In 1993, Dodelson and Widrow suggested *sterile* neutrinos as possible dark matter candidates [29]. Such particles should be similar to SM neutrinos, except that they should not take part in the weak interaction, which can be readily achieved by assuming they are right-handed. They are, however, allowed to mix with the SM neutrinos, just as those do among each other as well, which is also the basis for the production of sterile neutrinos in the early universe. Due to this mixing, the sterility is not perfect, allowing the particles to decay into SM neutrinos and photons. The study of possible decays together with the analysis of their contribution to the total energy density yield stringent constraints [30], for example on the mass of sterile neutrinos which is restricted to $\sim 1 \text{ keV} \sim 10 \text{ MeV}$. The authors of [30] conclude that the ranges for couplings and masses left open by these constraints still allow for species of sterile particles with an abundance sufficient to account for all the non-baryonic dark matter. Moreover, such particles would allow to circumvent other laboratory or astrophysical constraints. However, sterile neutrinos would be very difficult to detect due to their almost non-existing interaction with any other SM particle.

Another class of hypothetical DM candidates are *axions*, originally proposed in the context of a solution to the strong CP problem.⁴ Data from laboratory searches, stellar cooling and supernova 1987A imply that axions have to have masses below roughly 0.01 eV. Their interactions with SM particles are expected to be very weak, which indicates they were not in thermal equilibrium in the early universe. The assumptions made about their production mechanism strongly affect the calculation of their relic density, rendering it with a large uncertainty. However, there exist ranges for which axions comply to all present-day constraints.

A general class of DM candidates are *Weakly Interacting Massive Particles*, WIMPs, often denoted as χ , with masses of the order of a few GeV to TeV and cross sections at the electroweak scale. If these particles are assumed to be produced thermally in the early universe their relic density after the freeze-out can be calculated reliably within standard cosmology, c.f. Sect. 3.1, and is given approximately by the following expression where logarithmic corrections have been neglected:

$$\Omega_\chi h^2 \sim \text{const.} \frac{T_0^3}{M_{Pl}^3 \langle \sigma_A v \rangle} \sim \frac{0.1 \text{ pb} \cdot c}{\langle \sigma_A v \rangle}. \quad (3.22)$$

In the above expression, T_0 is the CMB temperature today, M_{Pl} the Planck mass, c the speed of light, σ_A is the annihilation cross section of a pair of WIMPs into SM

⁴Theory allows CP violation in the strong interaction, but it is not observed in experiments. For example, one consequence would be a large electric dipole moment of the neutron, which is however measured to be consistent with 0.

particles which is averaged, as indicated by the brackets $\langle \dots \rangle$, over the relative WIMP velocity distribution in the centre-of-mass system of the two WIMPs. Independent of the other properties of the WIMPs, freeze-out occurs at $T_F \sim m_\chi/20$ (cf. Fig. 3.1), meaning that the WIMPs are non-relativistic at the time of decoupling. From relation (3.22), it follows that for WIMPs with masses and cross sections at the scale typical for the weak interaction the calculated relic density is compatible with the measured value. This intriguing feature is also referred to as the *WIMP miracle* and is the reason why WIMPs are popular candidates for particle dark matter.

There is a number of models for physics beyond the Standard Model that contain dark matter candidates in the form of a WIMP. One example is super-symmetry: In the *minimal super-symmetric Standard Model* (MSSM), R -parity is conserved, where the quantum number R is defined as $3(B - L) + 2S$, with the baryon number B , the lepton number L and the spin S . With the R -parity being defined as $P_R = (-1)^R$, it follows that SM particles have R -parity of 1 and supersymmetric particles have R -parity of -1 . The requirement of R -parity conservation means that the lightest super-symmetric particles (LSP) cannot decay, which makes them viable dark matter candidates if they are neutral. Two possible candidates are hence the sneutrino or a neutralino. Sneutrinos are basically ruled out by experiments, since the calculated scattering cross section with a nucleon is much larger than the bounds from direct detection experiments [31]. Other supersymmetric scenarios exist in which *gravitinos*, the superpartners of the graviton, are the LSP and are stable. Since they only interact gravitationally, however, they would be very difficult to observe. The phenomenological properties of gravitinos are similar to those of *axinos*—the superpartners of the axion. For a long time, it was thought that axinos could only be warm or hot dark matter, but depending on the reheating temperature after inflation, they might also constitute cold dark matter [32–34].

Some models for extra spatial dimensions also provide dark matter candidates. A common feature of the models mentioned in Sect. 2.4 is that the compactification of the extra dimensions results in a quantisation of the momenta of the fields that propagate in the bulk, namely in units of $p^2 \sim 1/R^2$, when R is the size of the (compactified) extra dimensions. This means that for each bulk field, there is a set of Fourier expanded modes, which are referred to as *Kaluza–Klein* (KK) states. In the four-dimensional spacetime, these states manifest as a series (or *tower*) of particles with masses $m_n = n/R$, where n counts the mode number. These new states only differ in mass, all other quantum numbers are the same. The lightest Kaluza–Klein particle (LKP) can be stabilised based on momentum conservation in the higher dimensional space in a similar way as is done via R -parity conservation for the LSP.

There are many other types of dark matter candidates, among them light scalar dark matter [35, 36] or dark matter predicted within little Higgs models [37, 38], but they are not to be discussed here.

While there are numerous models that naturally provide candidates for dark matter, they all come with assumptions and in some cases a large number of additional parameters. It is thus desirable to analyse experimental data in a more general way without restricting the interpretation to one specific model. One approach to do so by

means of an effective field theory will be described in Sect. 5.2 and will be employed in the analysis presented in this work.

In Sect. 3.5, an overview of different search approaches and current results for WIMP searches is given.

3.5 WIMP Searches

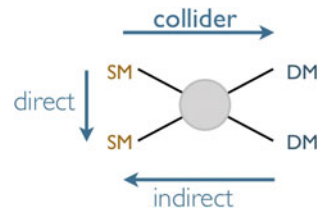
There are three general classes of search experiments for a WIMP signal: direct detection experiments that are looking for nuclear recoils in a target volume, indirect searches aiming for the detection of annihilation products of WIMP pairs, and collider searches, where the production of WIMPs would be detectable as a signal of missing transverse energy. The relation of the different search approaches is shown schematically in Fig. 3.6. The general techniques for direct and indirect searches and an overview of recent results are given in the following sections. The presentation of the collider searches is deferred to Sect. 5.5, when the basics of proton-proton collisions and the signal model will have been introduced.

3.5.1 Direct Detection

All direct detection experiments are based on the experimental indications that WIMPs are gravitationally trapped within galaxies, with an adequate density profile to yield the observed rotation curves. In the Milky Way, the mean velocity relative to the galactic centre is expected to be roughly the same as for stars, which is of the order of a few hundred kilometres per second in the region of the solar system. Assuming these velocities, the interaction of WIMPs with ordinary matter is via elastic scattering off nuclei. Given that WIMPs should typically have masses between 10 GeV and 10 TeV, the recoil energies will be in the range of 1–100 keV.

On the one hand, the interaction rate of WIMPs with nuclei in a detector will depend on the number of target nuclei in the detector volume, which is given as the ratio of the detector mass, m_{Det} , and the atomic mass of the nucleus, $m_{A,i}$, for a specific species i :

Fig. 3.6 Illustration of the relation of different search approaches for dark matter



$$N_i = \frac{m_{Det}}{m_{A,i}}. \quad (3.23)$$

On the other hand, the rate depends on the product of the interaction cross section and the local WIMP flux. This flux, in turn, is linked to the local density of dark matter ρ_{DM} , the mean WIMP circular velocity v_c , the galactic escape velocity v_{esc} , and the WIMP mass, m_χ . Commonly used standard values [39] are $\rho_{DM} = 0.3 \text{ GeV/cm}^3$, $v_c = 220 \text{ km/s}$, and $v_{esc} = 544 \text{ km/s}$. With these assumptions, the interaction rate depends mainly on two unknown parameters: the WIMP mass and the interaction cross section. Hence, results such as exclusion curves are typically plotted in a plane of these two variables. The rate can be approximated by

$$R \sim \sum_i N_i n_\chi \langle \sigma_{i\chi} \rangle, \quad (3.24)$$

with N_i as defined above, $n_\chi = \rho_\chi/m_\chi$ is the local WIMP number density and $\langle \sigma_{i\chi} \rangle$ the interaction cross section with a nucleus of species i , averaged over the WIMP velocity relative to the detector.

The WIMP-nucleon scattering is commonly classified as either *spin-dependent* (SD) or *spin-independent* (SI) interactions, based on the type of the coupling. Axial-vector interactions belong to the first group as they result from couplings to the spin content (J) of the nucleon such that the cross section is proportional to $J(J+1)$ and rather independent of the mass of the nucleus. Thus, there is no significant gain from using a heavier target material (typically ^{19}Fe , ^{23}Na , ^{73}Ge , ^{127}I , ^{129}Xe , ^{131}Xe and ^{133}Ce). This is different for the spin-independent interactions like scalar or vector couplings: Here, the cross section increases approximately as the square-root of the mass of the nucleus, making heavy target materials like Ge and Xe preferable. In these cases, the spin-independent interaction is usually stronger than the spin-dependent one.

Expected signal rates are far below the typical radioactive backgrounds, which requires the laboratories to be stationed deep underground, the detectors to be shielded against residual radiation due to muons or radioactivity from the rocks, and to use materials with very low intrinsic radioactivity.

The sensitivity of direct detection experiments is highest if the WIMP mass is close to the nucleus mass. At very small WIMP masses the sensitivity decreases drastically, as such light WIMPs will not cause any recoil of the much heavier nuclei. On the other hand, given the fact that the WIMP flux scales as $1/m_\chi$ for fixed mass density, the sensitivity also drops at high values of m_χ .

There are two ways a WIMP signal is expected to manifest itself in direct detection experiments: One is the change of the recoil direction within the course of a day due to the changing direction of the Earth passing through the WIMP cloud, the other is an annual modulation of the recoil rate, originating from the movement of the Earth around the sun and its velocity adding to or subtracting from that of the sun. The first effect is only observable with gaseous detectors or anisotropic response

scintillators. The second effect is of the order of a few percent and is only detectable by experiments with a heavy target material.

Different techniques for the detection of the nuclear recoil and also combinations of those are in use in the large number of direct detection experiments. The three basic types are observation of scintillation, phonons or ionisation. Many experiments make use of two techniques at the same time, exploiting the fact that the nuclear recoil and background from for example electronic recoil have a different energy sharing between the two channels. This is illustrated schematically in Fig. 3.7 [40]: nuclear and electronic recoils occupy different region in the phase space of the two detection channels (left), which offers the possibility to define a criterion to discriminate between the two types of events (right).

An overview of the current experimental search status is presented in Fig. 3.8. There are claims of positive results in the region below 100 GeV WIMP mass by DAMA/LIBRA [41], CoGeNT [42] and CRESST [43] and CDMS-II [44]. These are challenged by exclusion limits (90%CL) from other experiments, especially Xenon100 [45], LUX [46] and SuperCDMS [47].

DAMA uses a matrix of 25 highly pure NaI crystals, for a total detector mass of 250 kg, and detects the scintillation light with photomultipliers. The setup was found to be very stable, allowing to measure down to a threshold of 2 keV. The experiment observes a modulation in the rate with a period of one year and a maximum around the end of May, which is in good agreement with expectations from the motion of the Earth around the sun. However, an independent confirmation is needed to establish this as a true dark matter signal. One possibility—which is in preparation in form of the DM-Ice detector at the South Pole—is to repeat the measurement at a different location (ideally a different hemisphere), to make sure it is not a local effect.

CoGeNT employs commercial Ge detectors, which allow to measure recoils as soft as 400 eV. The collaboration has reported an excess of events below 3 keV, the origin of which is not clear yet. There also is an 2.8σ significance for an annular

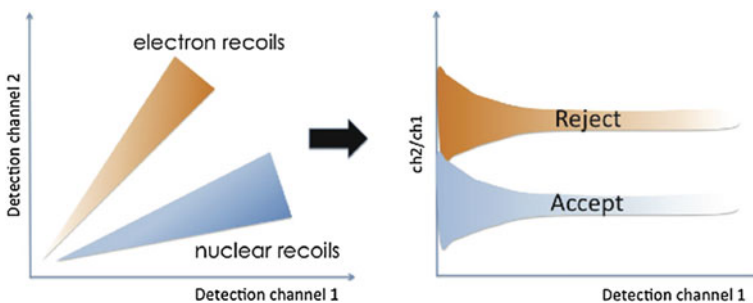


Fig. 3.7 Schematic illustration of the principle of making use of two observation techniques that provide discrimination between nuclear recoil and background. Events from nuclear and electronic recoil populate the plane of channel 1 versus channel 2 differently (*left*), allowing to define a rejection criterion (*right*) [40]

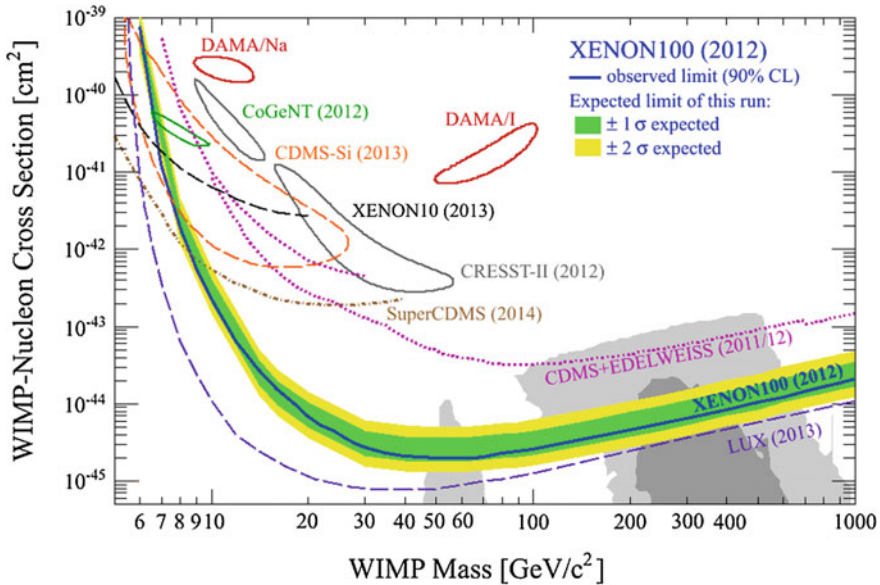


Fig. 3.8 Overview of current limits on spin-independent WIMP-nucleon scattering cross section. Shown are various positive claims [41–44] as well as 90%CL exclusion limits [45–48]. Taken from [49]

modulation which might turn out compatible with the DAMA result, but needs to be confirmed with more data.

CDMS-II (Cryogenic Dark Matter Search) is an example for an experiment using two different techniques to discriminate nuclear from electronic recoil: The ionisation and phonon signals are collected on either side of the 19 Ge and 11 Si detectors, which are cooled to a temperature of less than 50 mK. The Ge detectors weigh 230 g each, the Si detectors 100 g. The ionisation yield for the nuclear recoil is much lower than for the electronic recoil, allowing for the discrimination strength. In 2010, results from the final exposure [50], corresponding to 612 kg-days were published: Two events were observed in the signal region, consistent with a fluctuation of the background estimate. A dedicated publication from 2012 [51] reports a negative result for the search for annual modulation. A separate analysis of only the Si detector data was published in 2013 [44]. Three candidate events were found in a blind analysis of 140 kg-days, where the background estimate was 0.41 events. This results in an 5.4% probability for the three events in the signal region being caused by the known backgrounds. Testing the background-only against the background+WIMP hypothesis while taking the measured recoil energies into account yields a probability of 0.19% for the background-only hypothesis.

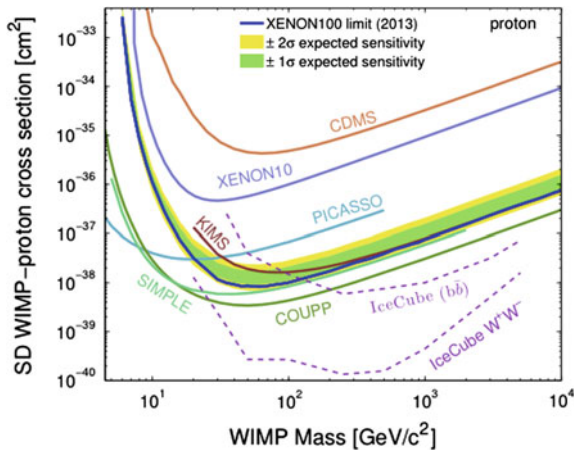
CRESST-II is another experiment reporting a positive result at small WIMP masses. The target material are 10 kg of calcium tungstate (CaWO_4), consisting of cylindrical crystals with a mass of 300 g each. It uses a combination of phonon

observation and scintillation to distinguish possible signal events from the background. They detect 67 events in the signal region and find that these cannot be accounted for by known backgrounds, which are estimated to a total of about 44 events. Improvements on the background estimation are ongoing.

There are a number of experiments using both scintillation and ionisation, often in the form of double phase time projection chambers (TPCs). Typical target materials are Ar and Xe. The core of the detector contains the liquid with a layer of gas on top in a cryostat. When an interaction takes place in the liquid phase, a first scintillation signal, called S1, is created together with ionisation electrons. These are extracted into the gaseous phase by electric fields, where they create a secondary scintillation signal, S2, proportional to the primary ionisation charge. The ratio of S2/S1 provides discrimination against most of the backgrounds. Examples for experiments using these techniques are XENON and LUX, which provide the strongest limits on the WIMP-nucleon scattering cross section today. The most recent results from LUX, released in 2013 [46], are based on 85.3 live-days with a fiducial mass of 118 kg and strongly disfavour the positive claims by the other experiments. Xe has a natural blend of both spin-even and spin-odd isotopes, such that it can probe both spin-independent as well as spin-dependent interactions. A summary of results in the spin-dependent case is shown in Fig. 3.9 [52]. The most recent result by XENON [52] pushes the limits into the region where SIMPLE [53], PICASSO [54], and COUPP [55] set limits (the lines from IceCube will be discussed in the next section). These experiments use different detection principles than the ones described before: The COUPP detector is a bubble chamber containing 3.5 l of CF_3I . Temperature and pressure inside the chamber can be adjusted such that bubble nucleation by electronic recoils is avoided, providing an excellent background rejection. The nuclear recoils can be distinguished from α -decays because they generate a different sound.

PICASSO uses a variant of the bubble chamber technique: superheated droplets of C_4F_{10} are immersed in a gel. Nuclear recoils and α -decays will result in an explosion

Fig. 3.9 Overview of current limits on spin-dependent WIMP-nucleon scattering cross section for various experiments [52–57]. See text for details [52]



of a droplet, causing a sound signal. SIMPLE uses the same technique as PICASSO, but with C_2ClF_5 droplets.

3.5.2 Indirect Detection

Looking for annihilation products of WIMPs, such as gamma rays, neutrinos, positron, anti-protons or anti-nuclei, is a way of indirectly searching for dark matter. The corresponding experiments provide complementary information to direct detection searches since they might have a larger reach to high masses and are sensitive to models with different couplings.

The basic assumption is that WIMPs are slowed down and captured in heavy objects like the Earth or the sun, and due to the increased density in these objects are more likely to annihilate. Thereby, for example, neutrinos can be created and interact in the Earth, causing upwards going muons which can be detected in neutrino telescopes such as IceCube [58] or SuperKamiokande [59]. These limits can again be interpreted in terms of the WIMP-nucleon scattering cross section, since this initiates the process of WIMPs being captured in the sun. IceCube has derived limits both for the case of WIMPs annihilating to $b\bar{b}$ and W^+W^- [57]. These are also shown in Fig. 3.9. The W^+W^- hypothesis results in the most stringent limits above WIMP masses of roughly 30 GeV.

Dwarf spheroidal galaxies, faint objects which are assumed to be satellites of the Milky Way, are observed to have a large mass-to-light ratio of the order of 100. If this is due to dark matter accumulated in them, they are promising targets for the observation of gamma rays. In a recent publication [60], the FERMI Large Area Telescope (LAT) presents a survey of 25 such galaxies in the Milky Way, making use of 4 years of data taking. No significant signal in γ -rays is found, and 15 of the galaxies are combined to derive some of the strongest limits on the annihilation cross section into various SM particles for WIMP masses between 2 GeV and 10 TeV, as is shown in Fig. 3.10.

FERMI LAT also published data on the observation of the centre of the Milky Way, which were analysed in [61] and a bump in the γ -ray spectrum at roughly 130 GeV was observed. Since the first publication, the local and global significance has been reduced [62], but still more data are needed to either verify or discard this as a dark matter signal.

Several experiments (PAMELA [63], FERMI [64], AMS [65]), observe an excess in the positron fraction in charged cosmic rays. While this in principle could be due to dark matter annihilation, it would require dark matter particles with a cross section and mass incompatible with the expectation for a thermal relic. Moreover, no excess is observed in the anti-proton flux, which requires models of leptophilic dark matter. Due to these drawbacks, nearby astrophysical sources like pulsars are considered the more likely explanation, but more data is needed to confirm either hypothesis.

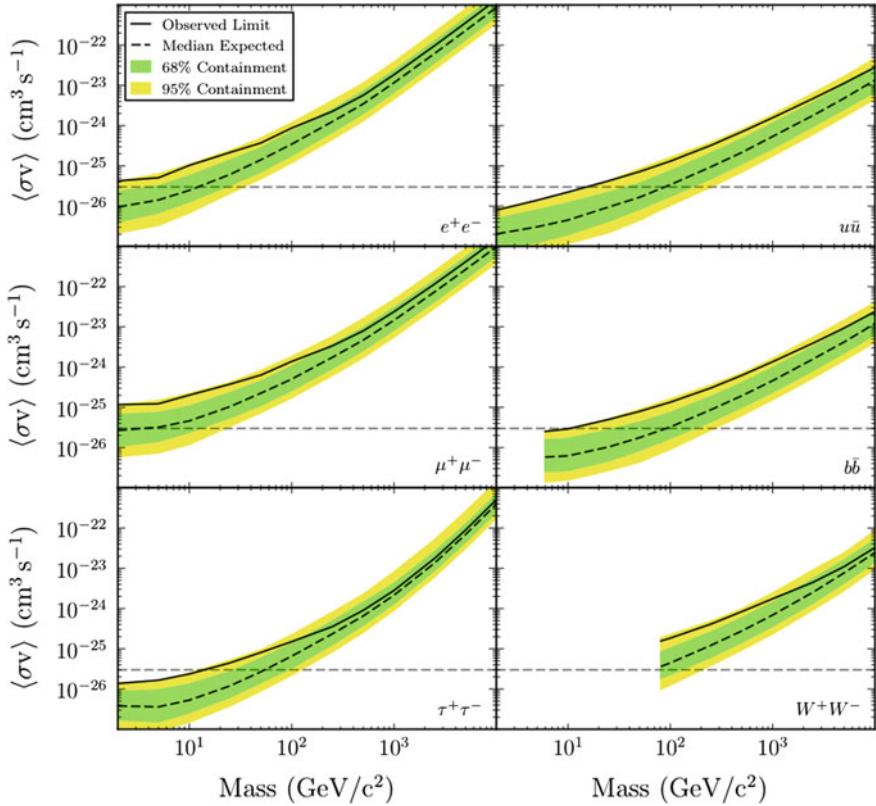


Fig. 3.10 Limits by FERMI LAT on the WIMP annihilation cross section for various annihilation channels [60]

References

1. Bertone G, Hooper D, Silk J (2005) Particle dark matter: evidence, candidates and constraints. *Phys Rep* 405:279–390. doi:[10.1016/j.physrep.2004.08.031](https://doi.org/10.1016/j.physrep.2004.08.031). [arXiv:hep-ph/0404175](https://arxiv.org/abs/hep-ph/0404175) [hep-ph]
2. Lemaître G (1931) Expansion of the universe, a homogeneous universe of constant mass and increasing radius accounting for the radial velocity of extra-galactic nebulae. *MNRAS* 91:483–490
3. Hubble E (1929) A relation between distance and radial velocity among extra-galactic nebulae. *Proc Natl Acad Sci* 15:168–173. doi:[10.1073/pnas.15.3.168](https://doi.org/10.1073/pnas.15.3.168)
4. Riess AG et al (2001) The farthest known supernova: support for an accelerating universe and a glimpse of the epoch of deceleration. *Astrophys J* 560:49–71. doi:[10.1086/322348](https://doi.org/10.1086/322348). [arXiv:astro-ph/0104455](https://arxiv.org/abs/astro-ph/0104455)
5. Friedman A (1999) On the curvature of space. *Gen Relativ Gravit* 31(12):1991–2000. doi:[10.1023/A:1026751225741](https://doi.org/10.1023/A:1026751225741). ISSN: 0001-7701
6. Beringer J et al (2012) Review of particle physics. *Phys Rev D* 86(1):010001. doi:[10.1103/PhysRevD.86.010001](https://doi.org/10.1103/PhysRevD.86.010001)

7. Bergstrom L (2000) Nonbaryonic dark matter: observational evidence and detection methods. *Rep Prog Phys* 63:793 (2000). doi:[10.1088/0034-4885/63/5/2r3](https://doi.org/10.1088/0034-4885/63/5/2r3). [arXiv:hep-ph/0002126](https://arxiv.org/abs/hep-ph/0002126) [hep-ph]
8. Kolb EW, Turner MS (1990) The early universe. *Front Phys* 69:1–547
9. Hooper D (2009) TASI 2008 lectures on dark matter. Technical Report, pp 709–764. [arXiv:0901.4090](https://arxiv.org/abs/0901.4090) [hep-ph]
10. Salati P (2003) Quintessence and the relic density of neutralinos. *Phys Lett B* 571:121–131. doi:[10.1016/j.physletb.2003.07.073](https://doi.org/10.1016/j.physletb.2003.07.073). [arXiv:astro-ph/0207396](https://arxiv.org/abs/astro-ph/0207396) [astro-ph]
11. Griest K, Seckel D (1991) Three exceptions in the calculation of relic abundances. *Phys Rev D* 43(10):3191–3203. doi:[10.1103/PhysRevD.43.3191](https://doi.org/10.1103/PhysRevD.43.3191)
12. Begeman K, Broeils A, Sanders R (1991) Extended rotation curves of spiral galaxies: dark haloes and modified dynamics. *Mon Not R Astron Soc* 249:523
13. Bahcall JN, Flynn C, Gould A (1992) Local dark matter from a carefully selected sample. *Astrophys J* 389:234–250. doi:[10.1086/171201](https://doi.org/10.1086/171201)
14. Oort JH (1932) The force exerted by the stellar system in the direction perpendicular to the galactic plane and some related problems. *Bull Astron Inst Neth* 6:249
15. Zwicky F (1933) Die Rotverschiebung von extragalaktischen Nebeln. *Helv Phys Acta* 6:110–127
16. Hupp E, Roy S, Watzke M (2006) NASA Finds Direct Proof of Dark Matter. Press Release. NASA Press Release 06-297. http://www.nasa.gov/home/hqnews/2006/aug/HQ_06297_CHANDRA_Dark_Matter.html
17. Clowe D et al (2006) A direct empirical proof of the existence of dark matter. *Astrophys J* 648:L109–L113. doi:[10.1086/508162](https://doi.org/10.1086/508162). [arXiv:astro-ph/0608407](https://arxiv.org/abs/astro-ph/0608407) [astro-ph]
18. Gamow G (1948) The origin of elements and the separation of galaxies. *Phys Rev* 74:505–506. doi:[10.1103/PhysRev.74.505.2](https://doi.org/10.1103/PhysRev.74.505.2)
19. Penzias AA, Wilson RW (1965) A measurement of excess antenna temperature at 4080 Mc/s. *Astrophys J* 142:419–421. doi:[10.1086/148307](https://doi.org/10.1086/148307)
20. Dicke RH et al (1965) Cosmic black-body radiation. *Astrophys J* 142:414–419. doi:[10.1086/148306](https://doi.org/10.1086/148306)
21. Ade P et al (2013) Planck 2013 results. I. Overview of products and scientific results. *ArXiv Pre-Prints*. doi:[10.1051/0004-6361/201321529](https://doi.org/10.1051/0004-6361/201321529). [arXiv:1303.5062](https://arxiv.org/abs/1303.5062) [astro-ph.CO]
22. The PLANCK Collaboration/ESA (2014) PLANCK Images. http://www.sciops.esa.int/index.php?project=PLANCK&page=Planck_images. Accessed August 2014
23. Somerville RS et al (2004) Cosmic variance in the great observatories origins deep survey. *Astrophys J* 600:L171. doi:[10.1086/378628](https://doi.org/10.1086/378628). [arXiv:astro-ph/0309071](https://arxiv.org/abs/astro-ph/0309071) [astro-ph]
24. Ade P et al (2013) Planck 2013 results. XV. CMB power spectra and likelihood. *ArXiv Pre-Prints*. [arXiv:1303.5075](https://arxiv.org/abs/1303.5075) [astro-ph.CO]
25. Komatsu E et al (2011) Seven-year wilkinson microwave anisotropy probe (WMAP) observations: cosmological interpretation. *Astrophys J Suppl Ser* 192(2):18. <http://stacks.iop.org/0067-0049/192/i=2/a=18>. [arXiv:1001.4538](https://arxiv.org/abs/1001.4538) [astro-ph.CO]
26. Milgrom M (1983) A modification of the Newtonian dynamics as a possible alternative to the hidden mass hypothesis. *Astrophys J* 270:365–370. doi:[10.1086/161130](https://doi.org/10.1086/161130)
27. Moffat J (2006) Scalar-tensor-vector gravity theory. *JCAP* 0603:004. doi:[10.1088/1475-7516/2006/03/004](https://doi.org/10.1088/1475-7516/2006/03/004). [arXiv:gr-qc/0506021](https://arxiv.org/abs/gr-qc/0506021) [gr-qc]
28. Toth VT (2010) Cosmological consequences of modified gravity (MOG). *ArXiv Pre-Prints*. [arXiv:1011.5174](https://arxiv.org/abs/1011.5174) [gr-qc]
29. Dodelson S, Widrow LM (1994) Sterile-neutrinos as dark matter. *Phys Rev Lett* 72:17–20. doi:[10.1103/PhysRevLett.72.17](https://doi.org/10.1103/PhysRevLett.72.17). [arXiv:hep-ph/9303287](https://arxiv.org/abs/hep-ph/9303287) [hep-ph]
30. Abazajian K, Fuller GM, Patel M (2001) Sterile neutrino hot, warm, and cold dark matter. *Phys Rev D* 64:023501. doi:[10.1103/PhysRevD.64.023501](https://doi.org/10.1103/PhysRevD.64.023501). [arXiv:astro-ph/0101524](https://arxiv.org/abs/astro-ph/0101524) [astro-ph]
31. Falk T, Olive KA, Srednicki M (1994) Heavy sneutrinos as dark matter. *Phys Lett B* 339:248–251. doi:[10.1016/0370-2693\(94\)90639-4](https://doi.org/10.1016/0370-2693(94)90639-4). [arXiv:hep-ph/9409270](https://arxiv.org/abs/hep-ph/9409270) [hep-ph]
32. Covi L, Kim JE, Roszkowski L (1991) Axinos as cold dark matter. *Phys Rev Lett* 82:4180–4183. doi:[10.1103/PhysRevLett.82.4180](https://doi.org/10.1103/PhysRevLett.82.4180). [arXiv:hep-ph/9905212](https://arxiv.org/abs/hep-ph/9905212) [hep-ph]

33. Covi L et al (2001) Axinos as dark matter. JHEP 0105:033. doi:[10.1088/1126-6708/2001/05/033](https://doi.org/10.1088/1126-6708/2001/05/033). [arXiv:hep-ph/0101009](https://arxiv.org/abs/hep-ph/0101009) [hep-ph]
34. Covi L et al (2004) Axino dark matter and the CMSSM. JHEP 0406:003. doi:[10.1088/1126-6708/2004/06/003](https://doi.org/10.1088/1126-6708/2004/06/003). [arXiv:hep-ph/0402240](https://arxiv.org/abs/hep-ph/0402240) [hep-ph]
35. Boehm C, Ensslin T, Silk J (2004) Can annihilating dark matter be lighter than a few GeVs? J Phys G 30:279–286. doi:[10.1088/0954-3899/30/3/004](https://doi.org/10.1088/0954-3899/30/3/004). [arXiv:astro-ph/0208458](https://arxiv.org/abs/astro-ph/0208458) [astro-ph]
36. Boehm C, Fayet P (2004) Scalar dark matter candidates. Nucl Phys B 683:219–263. doi:[10.1016/j.nuclphysb.2004.01.015](https://doi.org/10.1016/j.nuclphysb.2004.01.015). [arXiv:hep-ph/0305261](https://arxiv.org/abs/hep-ph/0305261) [hep-ph]
37. Birkedal-Hansen A, Wacker JG (2004) Scalar dark matter from theory space. Phys Rev D 69:065022. doi:[10.1103/PhysRevD.69.065022](https://doi.org/10.1103/PhysRevD.69.065022). [arXiv:hep-ph/0306161](https://arxiv.org/abs/hep-ph/0306161) [hep-ph]
38. Cheng H-C, Low I (2003) TeV symmetry and the little hierarchy problem. JHEP 0309:051. doi:[10.1088/1126-6708/2003/09/051](https://doi.org/10.1088/1126-6708/2003/09/051). [arXiv:hep-ph/0308199](https://arxiv.org/abs/hep-ph/0308199) [hep-ph]
39. Green AM (2012) Astrophysical uncertainties on direct detection experiments. Mod Phys Lett A 27(1230004):30004. doi:[10.1142/S0217732312300042](https://doi.org/10.1142/S0217732312300042). [arXiv:1112.0524](https://arxiv.org/abs/1112.0524) [astro-ph.CO]
40. Arneodo F (2013) Dark matter searches. ArXiv Pre-Prints (2013). [arXiv:1301.0441](https://arxiv.org/abs/1301.0441) [astro-ph.IM]
41. Bernabei R et al (2013) Final model independent result of DAMA/LIBRA-phase I. Eur Phys J C 73:2648. doi:[10.1140/epjc/s10052-013-2648-7](https://doi.org/10.1140/epjc/s10052-013-2648-7). [arXiv:1308.5109](https://arxiv.org/abs/1308.5109) [astro-ph.GA]
42. Aalseth CE et al (2013) CoGeNT: a search for low-mass dark matter using p-type point contact germanium detectors. PRD 88(1):012002. doi:[10.1103/PhysRevD.88.012002](https://doi.org/10.1103/PhysRevD.88.012002). [arXiv:1208.5737](https://arxiv.org/abs/1208.5737) [astro-ph.CO]
43. Angloher G et al (2012) Results from 730 kg days of the CRESST-II dark matter search. Eur Phys J C 72:1971. doi:[10.1140/epjc/s10052-012-1971-8](https://doi.org/10.1140/epjc/s10052-012-1971-8). [arXiv:1109.0702](https://arxiv.org/abs/1109.0702) [astro-ph.CO]
44. CDMS Collaboration (2013). Silicon detector dark matter results from the final exposure of CDMS II. Phys Rev Lett 111:251301. doi:[10.1103/PhysRevLett.111.251301](https://doi.org/10.1103/PhysRevLett.111.251301). [arXiv:1304.4279](https://arxiv.org/abs/1304.4279) [hep-ex]
45. Aprile E et al (2012) Dark matter results from 225 live days of XENON100 data. Phys Rev Lett 109(18):181301. doi:[10.1103/PhysRevLett.109.181301](https://doi.org/10.1103/PhysRevLett.109.181301). [arXiv:1207.5988](https://arxiv.org/abs/1207.5988) [astro-ph.CO]
46. Akerib D et al (2014) First results from the LUX dark matter experiment at the Sanford underground research facility. Phys Rev Lett 112:091303. doi:[10.1103/PhysRevLett.112.091303](https://doi.org/10.1103/PhysRevLett.112.091303). [arXiv:1310.8214](https://arxiv.org/abs/1310.8214) [astro-ph.CO]
47. Agnese R et al (2014) Search for low-mass wimps with superCDMS. Phys Rev Lett 112:241302. doi:[10.1103/PhysRevLett.112.241302](https://doi.org/10.1103/PhysRevLett.112.241302). [arXiv:1402.7137](https://arxiv.org/abs/1402.7137) [hep-ex]
48. Armengaud E et al (2011) Final results of the EDELWEISS-II WIMP search using a 4-kg array of cryogenic germanium detectors with interleaved electrodes. Phys Lett B 702(5):329–335. ISSN: 0370-2693. <http://dx.doi.org/10.1016/j.physletb.2011.07.034>
49. Schumann M (2014) Dual-phase liquid xenon detectors for dark matter searches. JINST 9:C08004. doi:[10.1088/1748-0221/9/08/C08004](https://doi.org/10.1088/1748-0221/9/08/C08004). [arXiv:1405.7600](https://arxiv.org/abs/1405.7600) [astro-ph.IM]
50. CDMS Collaboration (2010) Dark matter search results from the CDMS II experiment. Science 327:1619. doi:[10.1126/science.1186112](https://doi.org/10.1126/science.1186112). [arXiv:0912.3592](https://arxiv.org/abs/0912.3592) [astro-ph.CO]
51. CDMS Collaboration (2012) Search for annual modulation in low-energy CDMS-II data. ArXiv Pre-Prints (2012). [arXiv:1203.1309](https://arxiv.org/abs/1203.1309) [astro-ph.CO]
52. Aprile E et al (2013) Limits on spin-dependent WIMP-nucleon cross sections from 225 live days of XENON100 data. Phys Rev Lett 111(2):L021301. doi:[10.1103/PhysRevLett.111.021301](https://doi.org/10.1103/PhysRevLett.111.021301). [arXiv:1301.6620](https://arxiv.org/abs/1301.6620) [astro-ph.CO]
53. Felizardo M et al (2012) Final analysis and results of the phase II SIMPLE dark matter search. Phys Rev Lett 108(20):201302. doi:[10.1103/PhysRevLett.108.201302](https://doi.org/10.1103/PhysRevLett.108.201302). [arXiv:1106.3014](https://arxiv.org/abs/1106.3014)
54. Archambault S et al (2012) Constraints on low-mass WIMP interactions on 19F from PICASSO. Phys Lett B 711:153–161. doi:[10.1016/j.physletb.2012.03.078](https://doi.org/10.1016/j.physletb.2012.03.078). [arXiv:1202.1240](https://arxiv.org/abs/1202.1240) [hep-ex]
55. Behnke E et al (2012) First dark matter search results from a 4-kg CF3I bubble chamber operated in a deep underground site. Phys Rev D 86(5):052001. doi:[10.1103/PhysRevD.86.052001](https://doi.org/10.1103/PhysRevD.86.052001). [arXiv:1204.3094](https://arxiv.org/abs/1204.3094) [astro-ph.CO]
56. Kim SC et al (2012) New limits on interactions between weakly interacting massive particles and nucleons obtained with CsI(Tl) crystal detectors. Phys Rev Lett 108(18):181301. doi:[10.1103/PhysRevLett.108.181301](https://doi.org/10.1103/PhysRevLett.108.181301). [arXiv:1204.2646](https://arxiv.org/abs/1204.2646) [astro-ph.CO]

57. The IceCube Collaboration (2012). Search for dark matter annihilations in the Sun with the 79-string IceCube detector. ArXiv Pre-Prints. [arXiv:1212.4097](https://arxiv.org/abs/1212.4097) [astro-ph.HE]
58. Abbasi R et al (2010) Calibration and characterization of the IceCube photomultiplier tube. Nucl Instrum Meth A 618:139–152. doi:[10.1016/j.nima.2010.03.102](https://doi.org/10.1016/j.nima.2010.03.102). [arXiv:1002.2442](https://arxiv.org/abs/1002.2442) [astro-ph.IM]
59. Fukuda S et al (2003) The Super-Kamiokande detector. Nucl Instrum Methods Phys Res Sect A: Accel Spectrom Detect Assoc Equip 501(2–3):418–462. [http://dx.doi.org/10.1016/S0168-9002\(03\)00425-X](http://dx.doi.org/10.1016/S0168-9002(03)00425-X). ISSN: 0168-9002
60. Ackermann M et al (2014) Dark matter constraints from observations of 25 Milky Way satellite galaxies with the fermi large area telescope. Phys Rev D 89:042001. doi:[10.1103/PhysRevD.89.042001](https://doi.org/10.1103/PhysRevD.89.042001). [arXiv:1310.0828](https://arxiv.org/abs/1310.0828) [astro-ph.HE]
61. Weniger C (2012) A tentative gamma-ray line from dark matter annihilation at the fermi large area telescope. JCAP 1208:007. doi:[10.1088/1475-7516/2012/08/007](https://doi.org/10.1088/1475-7516/2012/08/007). [arXiv:1204.2797](https://arxiv.org/abs/1204.2797) [hep-ph]
62. Weniger C (2013) Gamma-ray lines in the Fermi-LAT data? ArXiv Pre-Prints. [arXiv:1303.1798](https://arxiv.org/abs/1303.1798) [astro-ph.HE]
63. Adriani O et al (2009) An anomalous positron abundance in cosmic rays with energies 1.5–100 GeV. Nature 458:607–609. doi:[10.1038/nature07942](https://doi.org/10.1038/nature07942). [arXiv:0810.4995](https://arxiv.org/abs/0810.4995) [astro-ph]
64. Ackermann M et al (2012) Measurement of separate cosmic-ray electron and positron spectra with the fermi large area telescope. Phys Rev Lett 108(1):011103. doi:[10.1103/PhysRevLett.108.011103](https://doi.org/10.1103/PhysRevLett.108.011103). [arXiv:1109.0521](https://arxiv.org/abs/1109.0521) [astro-ph.HE]
65. Aguilar M et al (2014) Electron and positron fluxes in primary cosmic rays measured with the alpha magnetic spectrometer on the international space station. Phys Rev Lett 113(12):121102. doi:[10.1103/PhysRevLett.113.121102](https://doi.org/10.1103/PhysRevLett.113.121102). <http://link.aps.org/doi/10.1103/PhysRevLett.113.121102>

Chapter 4

Proton-Proton Collisions

This chapter is intended to give an overview of the basics of the description and simulation of proton-proton (pp) collisions. The terminology is introduced in Sect. 4.1. Section 4.2 contains a brief discussion of parton density functions and Sect. 4.3 introduces the basic concepts for the calculation of hadron-hadron cross sections. The simulation of collision events is described in Sect. 4.4 and an overview of the generators most relevant for this work is given.

4.1 Terminology

The compositeness of hadrons complicates the description of a hadron-hadron collision with respect to that for events at a lepton collider, i.e. the collisions of elementary particles. In a typical pp collision, primarily two partons interact in a *hard scattering process*, while the remnants of the initial hadrons give rise to additional activity, as is illustrated in Fig. 4.1 [1]. This complicated picture can be decomposed into different sub-processes and stages, as is described in the following.

In Fig. 4.1, the two incoming protons are indicated by three green lines (for the valence quarks) and a green ellipse (symbolising the proton itself) each. The *hard process* between two of the partons is depicted as the big red circle in the figure. Both before and after the interaction, partons can produce additional QCD radiation by gluon splitting ($g \rightarrow gg$, $g \rightarrow q\bar{q}$) or by gluon radiation from quarks ($\bar{q} \rightarrow \bar{q}g$). This is referred to as *initial state radiation* (ISR) and *final state radiation* (FSR), depending on where the radiation is emitted. The products of the hard scattering repeatedly emit further QCD radiation and a *parton shower* (PS) evolves, indicated in red. The small red circles symbolise decays of particles produced in the hard interaction (two top quarks and a Higgs-boson in this example). The coloured particles produced in the parton shower eventually combine into colourless hadrons—a process called *hadronisation* and indicated by the light green blobs. These primary hadrons finally decay into stable particles. The resulting collimated bundles of hadrons are called *jets*.

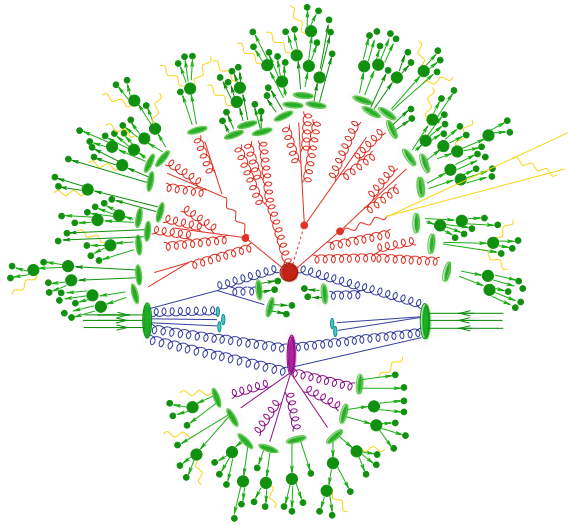


Fig. 4.1 Illustration of a pp collision. Two partons from the incoming protons (*large green ellipses*) undergo initial state radiation and interact in the hard process (*big red blob*). A parton shower (*red*) emerges from the products of the hard interaction. The resulting partons hadronise into colourless states (*light green blobs*) that subsequently decay into stable particles (*green circles*). A secondary interaction between proton remnants is shown as a *purple blob*, again creating a parton shower (*purple*), which hadronises, followed by decays into stable particles. This is part of the underlying event, together with the beam remnants (*light blue blobs*). Electromagnetic radiation (*yellow*) can be emitted by charged particles at any stage [1]

The lower hemisphere of Fig. 4.1 shows a secondary interaction between remnants of the protons as a purple ellipse. Again, a parton shower is produced (purple lines), resulting in hadronisation and decay into stable particles. Such interactions, that occur in addition to the hard process, are typically much softer than the primary interaction and are part of the *underlying event*, as are the remaining beam remnants, depicted as blue ellipses.

During all stages of the event development electromagnetic radiation off charged particles can take place, as is shown by the yellow lines.

4.2 Parton Density Functions

As seen in Sect. 4.1, the hard interaction in a pp collision is not between the protons as a whole but between two of their constituents. Hence, not the entire centre-of-mass energy (\sqrt{s}) of the two protons is available in the hard process but instead only the partonic centre-of-mass energy, $\sqrt{\hat{s}}$. The square of the partonic centre-of-mass energy is related to the beam energy via $\hat{s} = x_1 x_2 s$, where x_1 and x_2 are the *Björken* x -variables of the two partons, which can be interpreted as the fraction of the proton

momentum the partons each carry.¹ The probability density to find a parton p with a certain momentum fraction x at a given momentum transfer Q^2 is given by the *parton density function* (PDF), $f_p(x, Q^2)$.

QCD does not predict the structure of the proton and therefore the PDFs cannot be calculated ab initio, but have to be measured from experimental data. Historically, most of the information came from Deep Inelastic Scattering (DIS) in fixed-target lepton-nucleon scattering experiments and from the HERA electron-proton collider at DESY. The fixed-target data include scattering of electrons, muons and neutrinos on targets of hydrogen and deuterium as well as nuclear targets. In addition, recently more and more collider data on J/Ψ , W^\pm , Z/γ^* , jet, $b\bar{b}$ and $t\bar{t}$ production are included. Table 19.2 in reference [2] gives an overview of the main processes used in PDF fits. Figure 4.2 shows the coverage in the x - Q^2 -plane for different types of experiments. Fixed-target and HERA data cover regions down to x -values of approximately 10^{-5} , mostly at momentum transfers below a few hundred GeV^2 . It can be seen that the LHC already with operation at $\sqrt{s} = 7\text{TeV}$ opens the possibility for constraining PDFs in regions at higher Q^2 , not accessible to the other experiments.

The energy dependence of the PDFs is given by the *DGLAP* equations [4–6]:

$$\begin{aligned} \frac{\partial q_i(x, Q^2)}{\partial \log Q^2} &= \frac{\alpha_s}{2\pi} \int_x^1 \frac{dz}{z} \left\{ P_{q_i q_j}(z, \alpha_s) q_j\left(\frac{x}{z}, Q^2\right) + P_{q_i g}(z, \alpha_s) g\left(\frac{x}{z}, Q^2\right) \right\} \quad (4.1) \\ \frac{\partial g(x, Q^2)}{\partial \log Q^2} &= \frac{\alpha_s}{2\pi} \int_x^1 \frac{dz}{z} \left\{ P_{g q_j}(z, \alpha_s) q_j\left(\frac{x}{z}, Q^2\right) + P_{g g}(z, \alpha_s) g\left(\frac{x}{z}, Q^2\right) \right\}. \end{aligned}$$

In the above expression, $g(x, Q^2)$ is the gluon PDF, $q_i(x, Q^2)$ the quark PDF and $P_{ab}(z, \alpha_s)$ are the *splitting functions*, which can be expanded in perturbation theory:

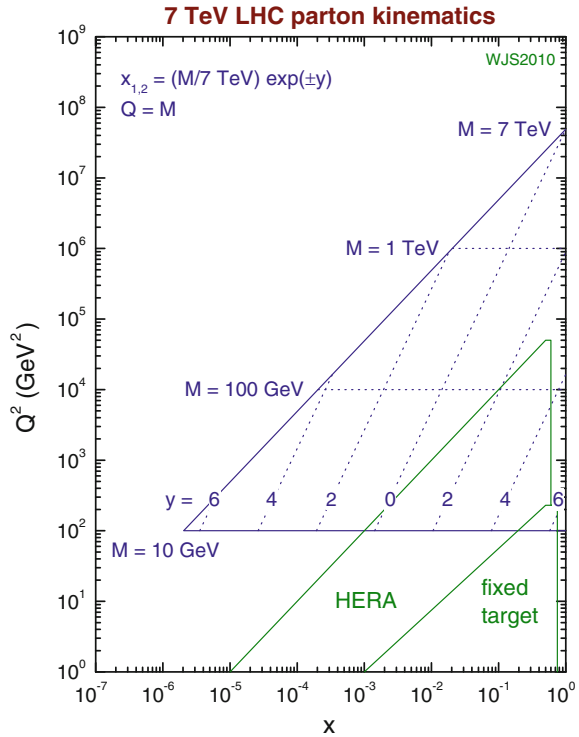
$$P_{ab}(x, \alpha_s) = P_{ab}^{(0)}(x) + \frac{\alpha_s}{2\pi} P_{ab}^{(1)}(x) + \dots \quad (4.2)$$

Expressions for the splitting functions at leading order (LO) and next-to-leading order (NLO) can be found for example in [7]. For the evolution in x , there are no such equations, but it has to be obtained from the fits to the data.

Several collaborations continuously work to improve the PDF fits with the most recent data. The PDF4LHC working group has benchmarked six PDF sets as particularly useful for the LHC [8], namely from the groups ABKM [9], CTEQ [10], GJR [11], HERAPDF [12], NNPDF [13] and MSTW [14]. The general procedure is similar for all the collaborations. They typically start from a parametrisation of the input PDFs at a low scale (1–2 GeV) which is of the form $xf = x^a(\dots)(1-x)^b$ with a total of 10–30 free parameters. The Neural Net PDF group (NNPDF) uses MonteCarlo replica of the experimental data to train a neural network to obtain a

¹The Björken variable was originally introduced as a convenient dimensionless quantity in the determination of the structure functions of the proton. However, in the limit of vanishing transverse momentum and rest masses of the partons, x is equivalent to the fraction of the proton momentum that the parton carries.

Fig. 4.2 Graphical illustration of the coverage in (x, Q^2) for different experiments. The *blue lines* indicate the corresponding values of invariant mass M and rapidity y of particles produced at the LHC at a centre-of-mass energy of 7 TeV [3]



parametrisation of the low-scale PDF. The input distributions are then evolved up in Q^2 by means of the DGLAP equations. Since the PDFs are an important ingredient to the calculation of cross sections—as will be discussed in Sect. 4.3—they can be used to predict cross sections that are then fitted to the experimental data, which allows to determine the parameters and thereby provide PDFs.

The PDF fitting collaborations typically publish not only central values for the PDFs but also associated *error sets* in which the uncertainties on the experimental input data are incorporated. Furthermore, the uncertainties include effects due to the choice of parametrisation and finite order calculations. A broadly used technique for the quantification of the PDF uncertainties is the *Hessian method* [15]: A matrix with dimension equal to the number of free fit parameters is diagonalised, resulting in a corresponding number of orthonormal eigenvectors, which are now mixtures of the free parameters. Alternative PDF sets—the error sets—are obtained by moving in the “+” and “-” direction of each eigenvector, i.e. changing the parameter values and hence the PDF accordingly. This results in a number of error sets twice as large as the number of fit parameters. How these error sets are used to estimate the uncertainty on a specific quantity will be described in the context of the signal uncertainties in Sect. 15.2.6.

Figure 4.3 shows the PDFs from the MSTW [3] and NNPDF [16] collaborations for both $Q^2 = 10 \text{ GeV}^2$ (left) and $Q^2 = 10^4 \text{ GeV}^2$ (right). The general trends are the same for both families. The valence quark PDFs dominate at high x -values, while the sea-quarks and especially the gluons dominate at low x . By comparing the left plots with the right ones, it is evident that for higher Q^2 the contributions at low x become larger. This can be qualitatively understood as being an effect of increasing resolution: The higher the momentum transfer Q^2 , the smaller the distances that are probed, i.e. what appeared to be one parton at lower energies turns out to be several partons with accordingly smaller momentum fractions x .

The predictions for various processes can differ significantly beyond what is covered by their uncertainties between the different PDF sets, due to several reasons [17]: The fits are not based on the same data sets, they use different values for the strong coupling constant α_s and the charm and beauty quark masses, the schemes for heavy quark production are not the same and differing choices of PDF parametrisation and model constraints are made. In reference [8], furthermore, a prescription is given for the estimation of PDF uncertainties on physical quantities. The authors advocate the use of mainly PDF sets from the CTEQ, MSTW and NNPDF sets, as those include collider data in addition to results from fixed target experiments and HERA and provide specific sets for varying values of $\alpha_s(m_Z)$.

Several PDF sets have been updated since the publication of references [8, 17]. Comparisons for some of the most recent sets can be found in reference [18]. Figure 4.4 is taken from that reference. It shows the ratio of parton-parton luminosities² with respect to the NNPDF2.3 PDF set with their respective uncertainties as function of the invariant mass $M_X = \sqrt{\hat{s}} = \sqrt{x_1 x_2 s}$ of the final state at centre-of-mass energies of 8 TeV. All PDFs are calculated at NNLO, using their default α_s values. The three sets agree within their uncertainties, which are smallest at values of M_X around 100 GeV and become very large at $M_X \geq 1 \text{ TeV}$, especially for the gluon-gluon luminosity.

PDF sets are made available in the LHAPDF library [19]. It provides the central value as well as the error sets and can hence be used for PDF re-weighting and estimation of PDF uncertainties. The version 6.1.3 of this package will be used within this work.

4.3 Cross Sections

Basis for the calculation of cross sections is *Fermi's Golden Rule*, which states that a transition rate for a process is given by the absolute square of the quantum mechanical amplitude integrated over the available phase space [20]. For example, for a scattering process of the form $2 \rightarrow n$, i.e. two incoming and n outgoing particles, the cross section can be expressed as:

²The parton luminosities are defined as $\Phi_{ij}(M_X^2) = \frac{1}{s} \int_{\tau}^1 \frac{dx_1}{x_1} f_i(x_1, M_X^2) f_j(\tau/x_1, M_X^2)$, $\tau \equiv M_X^2/s$, with $f(x, M^2)$ is a PDF at scale M^2 .

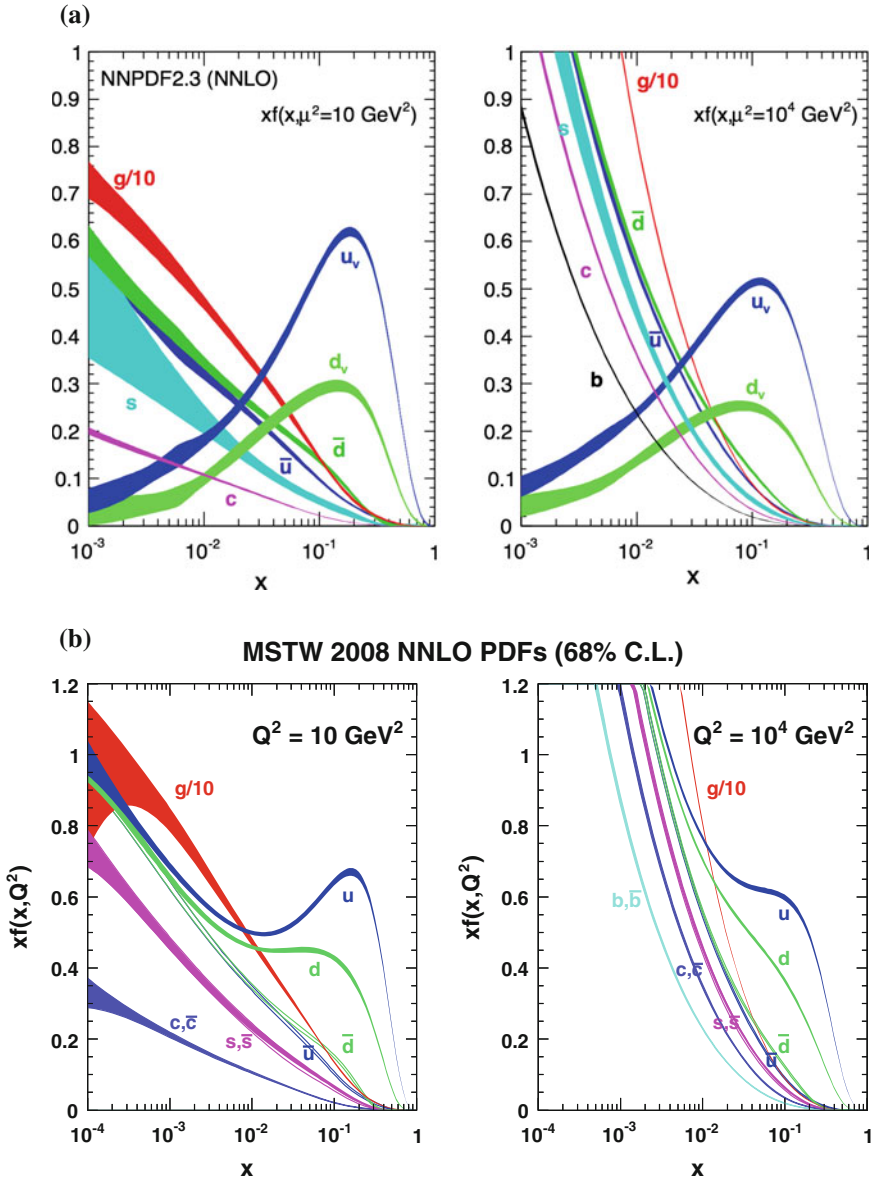


Fig. 4.3 Parton distribution functions for quarks, antiquarks and gluons from (a) NNPDF [16] and (b) MSTW [3], both at $Q^2 = 10 \text{ GeV}^2$ (left) and $Q^2 = 10^4 \text{ GeV}^2$ (right). The PDFs for quark and antiquark of non-valence quark flavours are assumed to be identical

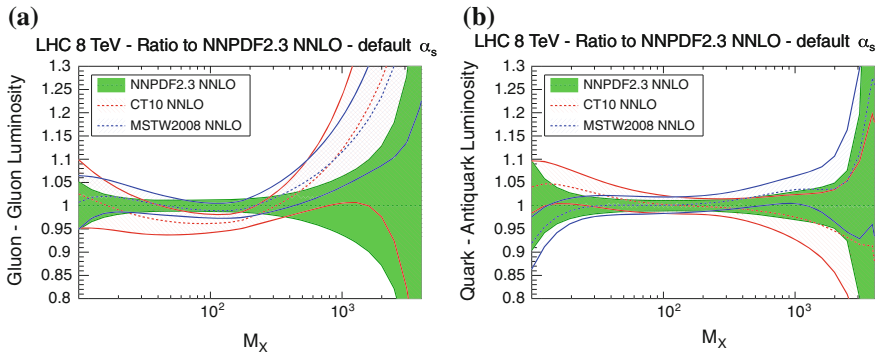


Fig. 4.4 Parton-parton luminosities for different PDF families relative to NNPDF2.3 NNLO. Shown are the **a** gluon-gluon and **b** quark-antiquark luminosities with their uncertainties [18]

$$\sigma = \frac{S}{4\sqrt{(p_1 \cdot p_2)^2 - (m_1 m_2)^2}} \int |\mathcal{M}|^2 (2\pi)^4 \delta^4(p_1 + p_2 - p_3 \cdots - p_n) \times \prod_{j=3}^n 2\pi \delta(p_j^2 - m_j^2) \Theta(p_j^0) \frac{d^4 p_j}{(2\pi)^4}. \quad (4.3)$$

Here, the incoming particles are labelled 1 and 2 the outgoing particles $3 \dots n$. S is a factor correcting for double counting in case there are identical particles in the final state. The δ - and Θ -functions impose the kinematic constraints: four-momentum conservation is ensured by the factor $\delta^4(p_1 + p_2 - p_3 \cdots - p_n)$, each outgoing particle is forced to be on its mass shell by the factor $\delta(p_j^2 - m_j^2)$ and the outgoing energies have to be positive as is ensured by the Θ -function. The matrix element amplitude \mathcal{M} is calculated by means of the *Feynman calculus*. The corresponding *Feynman-rules* are illustrated by *Feynman-diagrams*, consisting of lines for each particle and vertices describing the couplings between them. Each element of such a graph corresponds to a specific term in the amplitude for the depicted process. If there are several diagrams for the same process, the corresponding amplitudes have to be added, following the Feynman-rules, to take interferences into account. This shall be illustrated for the simple example of electron–electron scattering in the following. Figure 4.5 shows the two leading order diagrams for this process, i.e. the ones with the lowest number of vertices (two in this case). Mathematically, the electrons are represented by spinors u (incoming) and \bar{u} (outgoing), which are solutions to the Dirac equation. Each vertex contributes a factor proportional to the coupling, $ig\gamma^\mu$, where g is related to the electromagnetic coupling constant α via $g = \sqrt{4\pi\alpha}$. At each vertex, momentum conservation has to hold, leading again to δ -functions in the expression for the amplitude. The photon *propagator* is given by $\frac{-ig_{\mu\nu}}{q^2}$, where q is the momentum flowing through the internal photon line. Over these momenta has to be integrated, such that the amplitude for the diagram on the left-hand side reads:

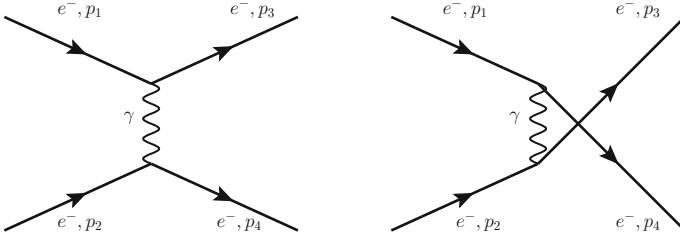


Fig. 4.5 Leading order Feynman diagrams for electron–electron scattering

$$\begin{aligned}
 \mathcal{M}_1 &= (2\pi)^4 \int [\bar{u}(p_3)(ig\gamma^\mu)u(p_1)] \frac{-ig_{\mu\nu}}{q^2} [\bar{u}(p_4)(ig\gamma^\nu)u(p_2)] \\
 &\quad \times \delta^4(p_1 - p_3 - q)\delta^4(p_2 - p_4 + q)d^4q \\
 &= \frac{ig^2}{(p_1 - p_3)^2} [\bar{u}(p_3)\gamma^\mu u(p_1)] [\bar{u}(p_4)\gamma_\mu u(p_2)] (2\pi)^4 \delta^4(p_1 + p_2 - p_3 - p_4).
 \end{aligned} \tag{4.4}$$

The remaining δ -function is omitted in the further amplitude calculation as it is already part of the phase space constraints in Eq. (4.3). The amplitude for the second diagram is obtained analogously by exchanging the momenta p_3 and p_4 . When adding both diagrams (i.e. their amplitudes), a relative “-”-sign has to be introduced since they differ only in the exchange of two particles. The full amplitude then reads

$$\begin{aligned}
 \mathcal{M} &= \frac{ig^2}{(p_1 - p_3)^2} [\bar{u}(p_3)\gamma^\mu u(p_1)] [\bar{u}(p_4)\gamma_\mu u(p_2)] \\
 &\quad - \frac{ig^2}{(p_1 - p_4)^2} [\bar{u}(p_4)\gamma^\mu u(p_1)] [\bar{u}(p_3)\gamma_\mu u(p_2)].
 \end{aligned} \tag{4.5}$$

What enters the cross section is the amplitude squared, $|\mathcal{M}|^2 = |\mathcal{M}_1 - \mathcal{M}_2|^2$, such that both diagrams and interference between them is considered. It should be noted, that the electron–electron scattering could also proceed via the exchange of a Z -boson, i.e. in the diagrams in Fig. 4.5 the photon line has to be replaced by a Z and the coupling and propagator terms have to be adopted accordingly. However, for momentum transfer well below the mass of the Z -boson, this can be safely ignored.

The diagrams in Fig. 4.5 are only the most simple versions of the scattering process—in addition there could be initial or final state radiation or various loop diagrams, some of which are illustrated in Fig. 4.6. All of these have in common that they include a larger number of vertices and hence coupling factors—they are of higher order. In the case of QED, with $\alpha \sim 1/137$, the amplitudes for the higher order diagrams will be suppressed accordingly. However, as becomes apparent from Fig. 4.6, there typically is a large number of higher order diagrams and it grows dramatically when more loops or additional radiation is included. Therefore, these

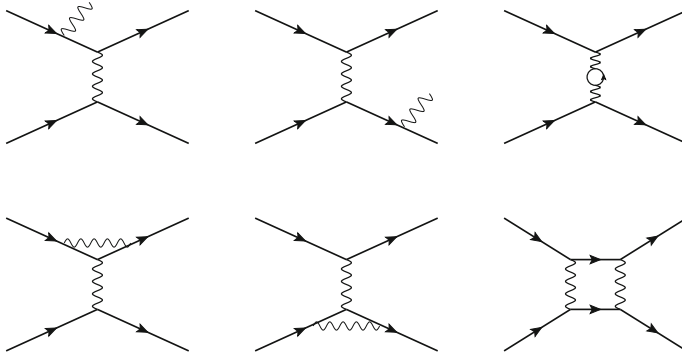


Fig. 4.6 Sub-set of next-to-leading order Feynman diagrams for electron–electron scattering

higher order diagrams can result in sizeable contributions to the total cross section. Many processes have nowadays been calculated to next-to-leading (NLO) and even next-to-next-to-leading order (NNLO), to make the theory predictions more precise.

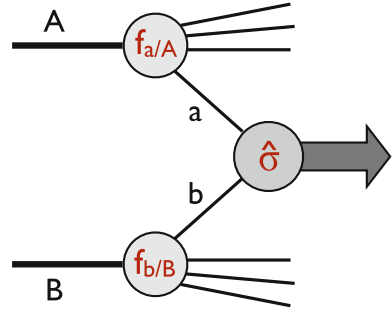
For QCD, the Feynman calculus can be applied in much the same way as illustrated above using the corresponding Feynman rules (see for example reference [20]), provided that one is in a regime where the strong coupling constant is sufficiently small such that the higher order histograms are perturbative corrections to the LO ones.

The procedure outlined above can be used to describe and calculate processes at the level of fundamental particles, but the calculation of hadron–hadron cross sections requires one more ingredient which is known as the *factorisation theorem*. It goes back to the work of S. Drell and T.-M. Yan [21] on the annihilation of a quark–antiquark pair into a pair of massive leptons—the Drell–Yan process. They postulated, that the hadronic cross section, $\sigma(AB \rightarrow \mu^+ \mu^- + X) \equiv \sigma_{AB}$, can be calculated by reweighting the partonic sub-process, $\hat{\sigma}(q\bar{q} \rightarrow \mu^+ \mu^-) \equiv \hat{\sigma}_{ab}$, with the parton density functions $f_{q/H}$ obtained from DIS:

$$\sigma_{AB} = \int dx_a dx_b f_{a/A}(x_a) f_{b/B}(x_b) \hat{\sigma}_{ab}. \quad (4.6)$$

This is illustrated in Fig. 4.7. The procedure was successfully extended to other hard processes. However, when trying to calculate corrections from gluon emission, large logarithms arise when the gluons are emitted collinear with the incoming quarks, such that the perturbation expansion does not converge. It was realised later on, that this could be remedied by factorising these logarithms into the definition of the PDFs via the DGLAP equations. Factorisation theorems were derived and showed that in general for all hard scattering processes all logarithms appearing in the corrections can be absorbed into renormalised PDFs in this way. Finally, it was recognised that the

Fig. 4.7 Illustration of the factorisation theorem for a hadron–hadron collision. Adapted from [15]



remaining finite corrections had to be derived for each process separately, resulting in corrections of order α_s^n . This leads to the following refined formulation of Eq. (4.6):

$$\sigma_{AB} = \int dx_a dx_b f_{a/A}(x_a, \mu_F^2) f_{b/B}(x_b, \mu_F^2) \times [\hat{\sigma}_0 + \alpha_s(\mu_R^2) \hat{\sigma}_1 + \dots]_{ab} . \quad (4.7)$$

In this expression, μ_R is the renormalisation scale for the strong running coupling constant and μ_F is the factorisation scale, which marks the transition between long- and short-distance physics.

The actual cross section should of course be independent of the choices of μ_R and μ_F , which is true in the limit that all orders in perturbation theory are considered. In this case, the scale dependencies of the PDFs and the coupling constant are exactly compensated by the dependence of the coefficients. If not all orders are considered (as is usually the case), a reasonable choice has to be made for the scales, typically a scale characteristic for the process, for example the di-lepton mass in case of the Drell–Yan process. Often, $\mu_R = \mu_F$ is assumed. The numerical results will differ for different choices of the scales, which reflects one uncertainty in the cross section due to the neglect of higher orders. In many cases, the LO calculation can only provide a first rough estimation of the cross section because of the often large uncertainties due to the renormalisation and factorisation scales. For some processes, there are also additional partonic processes that only contribute at higher orders. A measure for the correction that an NLO calculation would give is the *k-factor*, which is simply the ratio of NLO to LO calculation. Often, this *k-factor* is calculated not only for the inclusive cross section but also as a function of some kinematic variable.

4.4 Event Simulation

For the comparison of the observed data to predictions from theory, simulations of the hadronic process as well as the detector response are needed. The software tools to do so are generally referred to as *event generators* or simply *generators*. The simulation

proceeds in several steps: first, the generation of the final state particles in a collision, then their passing through the detector and finally the digitisation. Afterwards, the simulated data sets can be passed to the reconstruction software in the same way as actual recorded data. In this section, only the first step will be described, details on the detector simulation and digitisation are given in Sect. 7.8. Most of the information given in this section is based on [22].

4.4.1 Final State Particle Generation

The event generation is a complex task, given the large number of particles produced in hadron–hadron collisions and their momenta ranging over many orders of magnitude. A special challenge is the simulation of the non-perturbative soft QCD processes involved, which requires some sort of phenomenological approximation.

As was outlined in Sect. 4.1, a collision event can be divided into different regimes of momentum transfer, that can be simulated separately using different approaches. The method of choice for all regimes are Monte Carlo (MC) techniques [23].

The matrix element of the hard process between two incoming partons in which a relatively small number of outgoing particles is produced can be calculated in perturbation theory (to some limited order), using for example Feynman diagrams as described in the previous section. Choices have to be made for the factorisation and renormalisation scales as well as the PDF set to be used when calculating the hadronic cross section. Typically, each generator has a default PDF, but allows to use a different one via the LHAPDF library. A general recommendation is to use a PDF of the same perturbative order as the matrix element calculation. Often, a characteristic scale Q^2 for the process to be calculated is chosen and renormalisation and factorisation scales are set to this value. The scale Q^2 also is the starting scale for the initial and final state parton showers. As was mentioned in the previous section, for production of an s -channel resonance with mass M as in the Drell–Yan process the typical choice is $Q^2 = M^2$, while for the pair production of massless particles with a transverse momentum p_T , typically $Q^2 = p_T^2$ is chosen.

Starting from the scale of the hard process, parton shower algorithms describe, with the help of the DGLAP equations, the evolution down to scales of ~ 1 GeV, at which the partons become confined in hadrons. These parton showers account for higher order effects that are not covered by the fixed order matrix element calculation of the hard process. The final state parton showers are simulated by a step-wise Markov chain [24], probabilistically adding one more parton at a time, where the probability for the parton to evolve from a higher to a lower scale without radiating a gluon or splitting is given by the *Sudakov form factor*. The description of the initial state parton shower is a backward evolution by dressing the interacting partons with further radiation. Again, a probabilistic Markov chain is formulated by means of the DGLAP equations which can be used to derive the probability that a parton with a given momentum fraction at a certain scale has come from a higher momentum

fraction at a lower scale. This is done iteratively until the scale reaches the non-perturbative regime and a model describing the remnant of the hadron is employed.

A special challenge in the MC generation is the coherent combination of the matrix element calculation and the parton shower, where double counting has to be avoided. Different schemes for this *matching* exist, for example the CKKW technique [25, 26]. Typically, some *matching scale* is defined which separates the regimes treated by the matrix element calculations and the parton shower, respectively.

The partons produced in the final state shower have to be combined into colourless states, taking the colour connections between them and the beam remnants into account. Since this process happens at scales beyond the perturbativity of QCD, phenomenological models have to be used. While this involves more free parameters than the previous steps, it can be regarded as universal to a good approximation, meaning that the parameters can be tuned on one data set and then be used for other simulations. There are two general classes of such models: the *cluster model* and the *string model*. While the former constructs an intermediate stage of cluster objects, the latter transforms partonic systems directly into hadrons. The produced hadrons may be instable, i.e. have a proper life time smaller than 10 ps, so that their decays have to be simulated as well.

Due to the compositeness of hadrons and the large collision energy additional parton-parton interactions can take place, which are part of the underlying event. The additional interactions are assumed to be $2 \rightarrow 2$ QCD processes with a transverse momentum above a certain threshold $p_{T,\min}$. The total interaction cross section can be calculated using the factorisation scheme and the partonic cross sections for these $2 \rightarrow 2$ processes. It is found to diverge for small values of $p_{T,\min}$ and exceed the total hadronic cross section, which can be understood since an event with two interactions counts twice in the interaction cross section but only once in the total hadronic cross section. The average number of interactions can then be calculated as the ratio of the two cross sections, and hence is a function of $p_{T,\min}$:

$$\langle n \rangle(p_{T,\min}) = \frac{\sigma_{\text{int}}(p_{T,\min})}{\sigma_{\text{tot}}}. \quad (4.8)$$

The cutoff $p_{T,\min}$ can be interpreted in the following way: If the transverse momentum decreases, the transverse wavelength increases accordingly and individual colour charges are not resolved any more, such that the effective coupling is reduced. This is referred to as *colour screening* and can be implemented in the simulation by suppressing scattering processes below the scale $p_{T,\min}$. The value of this scale and other parameters and dependencies of the UE modelling have to be adjusted to describe the experimental data well. A set of these parameters is called an *underlying event tune*. Similarly, tunes for the parton shower and hadronisation modelling are adapted to data.

In most cases, event samples are generated for one specific process of interest at a time, say the production of a Z-boson with some number n of additional partons. Typically, the generation is done at LO for this process. It should be noted that for event generators the meaning of *order* is often slightly different than the one

encountered before in the context of perturbation theory. For generators, it means that the considered process is calculated without loop corrections. The process itself, however, can as in the example above include a high multiplicity of initial state radiation partons (i.e. jets) and as such be technically of higher order in QCD.

At this stage in the simulation, the events can be filtered such that only events fulfilling certain properties are retained. For example, when generating leptonic Z-boson decays, cuts can be placed on the mass of the boson or its transverse momentum. Such *generator cuts* can be useful to ensure suitable statistics in different regions of phase space without consuming too much computing power.

4.4.2 Event Generators

There is a number of general-purpose generators available for LHC physics. Moreover, there exist more specialised programs for particular processes. In the following, the generators most relevant for this work be introduced.

SHERPA SHERPA [27]³ is one example of a general-purpose generator. The main focus in the development SHERPA are the perturbative parts of the event generation. SHERPA makes use of two full-fledged matrix element generators that feature highly advanced phase-space integration techniques, making SHERPA one of the generators most advanced in the automated generation of tree-level matrix elements. The description of the parton shower has been improved by implementation of new techniques and SHERPA provides its own hadronisation model. Moreover, it comprises modelling of hadron and τ decays as well as QED FSR and the simulation of the underlying event based on multiple-parton scattering. SHERPA can be used to model all SM processes as well as a variety of extensions to BSM physics.

MadGraph MadGraph is a matrix element generator. While nowadays there is a version of MadGraph [28] that allows for the inclusion of loop diagrams, for samples used in this work the predecessor version [29], which is a leading order generator, was used. MadGraph automatically generates matrix elements as for example decays or $2 \rightarrow n$ scattering. The user simply specifies the process of interest by giving the initial and final state particles and MadGraph generates the Feynman diagrams and the code needed for the calculation of the matrix element at a certain point in phase space. This code serves as basis for the calculation of cross sections or decay widths, or for event generation. For the simulation of parton showers, underlying event etc. the output has to be passed on to an external programme, for example PYTHIA.

PYTHIA PYTHIA is another general-purpose generator which has been developed over more than 30 years. Its latest version 8 [30] begins to be used more often, while the previous version 6 [31] still is used in combination with some generators that do not feature the appropriate interface to PYTHIA8 yet.

³Simulation of High-Energy Reactions of PArticles.

PYTHIA provides more than 200 hard-coded subprocesses, mainly $2 \rightarrow 1$ or $2 \rightarrow 2$, and a few $2 \rightarrow 3$, that can be switched on individually. Unlike for example SHERPA, PYTHIA does not have automated code generation for new processes, instead it is designed such that it allows external input to the greatest possible extent. One standard example would be the generation of *Les Houches Event* (LHE) [32] files by general-purpose matrix-element generator like MadGraph (see above). These can be used as input to PYTHIA for the simulation of parton showering, underlying event etc. The soft processes included in PYTHIA are elastic, single and double diffractive and non-diffractive processes, which together provide an inclusive description of the total pp cross section. PYTHIA is thus often used for the generation of events with multiple collisions in addition to the hard process of interest, so called *pile-up* events.

Herwig++ Herwig++ [33] improves on the former Herwig⁴ programme. It automatically generates the hard process and models decays with full spin correlations also for many BSM models. It produces angular ordered parton showers and provides an built-in hadronisation model. The underlying event is modelled by multiple parton interactions and Herwig++ features sophisticated models for the decay of hadrons and τ leptons.

MC@NLO As the name indicates, MC@NLO [34–39] calculates the hard process in NLO—however, only in QCD; the calculations in QED are LO. It provides its own algorithm for parton showering and includes spin correlations for most processes. For the modelling of the underlying event, MC@NLO is typically interfaced to Herwig++. MC@NLO is an example of a specialised generator, the processes currently implemented are: Higgs boson, single vector boson, vector boson pair, heavy quark pair, single top (with and without associated W or charged Higgs), lepton pair and associated Higgs+W/Z production in hadron collisions.

AcerMC AcerMC [40] is another specialised generator that can be interfaced to for example PYTHIA(6) or Herwig for ISF/FSR, hadronisation and decays, underlying event and beam remnants. Its purpose is the generation of SM background processes at pp collisions. Therefore, for a number of selected processes, a library for the corresponding matrix elements and phase space modules is provided. The code for the matrix element calculation is based on MadGraph.

References

1. Siegert F (2010) Monte-Carlo event generation for the LHC. PhD thesis, Durham University. Durham E-Theses. <http://etheses.dur.ac.uk/484/>
2. Beringer J et al (2012) Review of particle physics. Phys Rev D 86(1): 010001. doi:10.1103/PhysRevD.86.010001
3. Stirling WJ, Private communication
4. Gribov VN, Lipatov LN (1972) Deep inelastic e p scattering in perturbation theory. Sov J Nucl Phys 15:438–450

⁴Hadron Emission Reactions With Interfering Gluons.

5. Dokshitzer YL (1977) Calculation of the structure functions for deep inelastic scattering and e^+e^- annihilation by perturbation theory in quantum chromodynamics. *Sov Phys JETP* 46:641–653
6. Altarelli G, Parisi G (1977) Asymptotic freedom in parton language. *Nucl Phys B* 126:298. doi:[10.1016/0550-3213\(77\)90384-4](https://doi.org/10.1016/0550-3213(77)90384-4)
7. Ellis RK, Stirling WJ, Webber B (1996) QCD and collider physics. *Camb Monogr Part Phys Nucl Phys Cosmol* 8:1–435
8. Botje M et al (2011) The PDF4LHC working group interim recommendations. *ArXiv Pre-Prints*. [arXiv:1101.0538](https://arxiv.org/abs/1101.0538) [hep-ph]
9. Alekhin S, Blumlein J, Moch SO (2011) Parton distributions and tevatron jet data. *ArXiv Pre-Prints*. [arXiv:1105.5349](https://arxiv.org/abs/1105.5349) [hep-ph]
10. Lai HL et al (2010) New parton distributions for collider physics. *Phys Rev D* 82:074024. doi:[10.1103/PhysRevD.82.074024](https://doi.org/10.1103/PhysRevD.82.074024). [arXiv:1007.2241](https://arxiv.org/abs/1007.2241) [hep-ph]
11. Gluck M, Jimenez-Delgado P, Reya E (2008) Dynamical parton distributions of the nucleon and very small- x physics. *Eur Phys J C* 53:355–366. doi:[10.1140/epjc/s10052-007-0462-9](https://doi.org/10.1140/epjc/s10052-007-0462-9). [arXiv:0709.0614](https://arxiv.org/abs/0709.0614) [hep-ph]
12. F. Aaron et al (2010) Combined measurement and QCD analysis of the inclusive ep scattering cross sections at HERA. *J High Energy Phys* 1:109 doi:[10.1007/JHEP01\(2010\)109](https://doi.org/10.1007/JHEP01(2010)109). <http://dx.doi.org/10.1007/JHEP01>
13. Ball RD et al (2013) Parton distributions with LHC data. *Nucl Phys B* 867:244–289. doi:[10.1016/j.nuclphysb.2012.10.003](https://doi.org/10.1016/j.nuclphysb.2012.10.003). [arXiv:1207.1303](https://arxiv.org/abs/1207.1303) [hep-ph]
14. Martin AD et al (2009) Parton distributions for the LHC. *Eur Phys J C* 63:189–285. doi:[10.1140/epjc/s10052-009-1072-5](https://doi.org/10.1140/epjc/s10052-009-1072-5). [arXiv:0901.0002](https://arxiv.org/abs/0901.0002) [hep-ph]
15. Campbell JM, Huston J, Stirling W (2007) Hard Interactions of Quarks and Gluons: a primer for LHC physics. *Rept Prog Phys* 70:89. doi:[10.1088/0034-4885/70/1/R02](https://doi.org/10.1088/0034-4885/70/1/R02). [arXiv:hep-ph/0611148](https://arxiv.org/abs/hep-ph/0611148) [hep-ph]
16. <https://nnpdf.hepforge.org/>. Accessed July 2014
17. Cooper-Sarkar A (2011) PDFs for the LHC. *ArXiv Pre-Prints*. [arXiv:1107.5170](https://arxiv.org/abs/1107.5170) [hep-ph]
18. Ball RD et al (2013) Parton distribution benchmarking with LHC data. *JHEP* 1304:125. doi:[10.1007/JHEP04\(2013\)125](https://doi.org/10.1007/JHEP04(2013)125). [arXiv:1211.5142](https://arxiv.org/abs/1211.5142) [hep-ph]
19. Whalley MR, Bourilkov D, Group RC (2005) The Les Houches accord PDFs (LHAPDF) and LHAGLUE. *ArXiv Pre-Prints*. [arXiv:hep-ph/0508110](https://arxiv.org/abs/hep-ph/0508110) [hep-ph]
20. Griffiths D (1987) *Introduction to elementary particles*. Wiley, New York
21. Drell S, Yan TM (1971) Partons and their applications at high-energies. *Annals Phys* 66:578. doi:[10.1016/0003-4916\(71\)90071-6](https://doi.org/10.1016/0003-4916(71)90071-6)
22. Buckley A et al (2011) General-purpose event generators for LHC physics. In: *Phys Rept* 504:145–233. doi:[10.1016/j.physrep.2011.03.005](https://doi.org/10.1016/j.physrep.2011.03.005). [arXiv:1101.2599](https://arxiv.org/abs/1101.2599) [hep-ph]
23. Landau D, Binder K (2005) *A guide to monte carlo simulations in statistical physics*. Cambridge University Press, New York. ISBN: 0521842387
24. Norris JR (1998) *Markov chains*. Cambridge series in statistical and probabilistic mathematics. Cambridge University Press, New York. ISBN: 978-0-521-48181-6
25. Krauss F (2002) Matrix elements and parton showers in hadronic interactions. *JHEP* 0208:015. doi:[10.1088/1126-6708/2002/08/015](https://doi.org/10.1088/1126-6708/2002/08/015). [arXiv:hep-ph/0205283](https://arxiv.org/abs/hep-ph/0205283) [hep-ph]
26. Gleisberg T et al (2004) SHERPA 1. alpha: a Proof of concept version. *JHEP* 0402:056. doi:[10.1088/1126-6708/2004/02/056](https://doi.org/10.1088/1126-6708/2004/02/056). [arXiv:hep-ph/0311263](https://arxiv.org/abs/hep-ph/0311263) [hep-ph]
27. Gleisberg T et al (2009) Event generation with SHERPA 1.1. *JHEP* 02:007. [arXiv:0811.4622](https://arxiv.org/abs/0811.4622) [hep-ph]
28. Alwall J et al (2014) The automated computation of tree-level and next-to-leading order differential cross sections, and their matching to parton shower simulations. *JHEP* 1407:079. doi:[10.1007/JHEP07\(2014\)079](https://doi.org/10.1007/JHEP07(2014)079). [arXiv:1405.0301](https://arxiv.org/abs/1405.0301) [hep-ph]
29. Alwall J et al (2011) MadGraph 5: going Beyond. *JHEP* 1106:128. doi:[10.1007/JHEP06\(2011\)128](https://doi.org/10.1007/JHEP06(2011)128). [arXiv:1106.0522](https://arxiv.org/abs/1106.0522) [hep-ph]
30. Sjostrand T, Mrenna S, Skands PZ (2008) A brief introduction to PYTHIA 8.1. *Comput Phys Commun* 178:852–867. doi:[10.1016/j.cpc.2008.01.036](https://doi.org/10.1016/j.cpc.2008.01.036). [arXiv:0710.3820](https://arxiv.org/abs/0710.3820) [hep-ph]

31. Sjostrand T, Mrenna S, Skands P (2006) PYTHIA 6.4 physics and manual. JHEP 05:026. [arXiv:hep-ph/0603175](https://arxiv.org/abs/hep-ph/0603175)
32. Alwall J et al (2007) A Standard format for Les Houches event files. Comput Phys Commun 176:300–304. doi:[10.1016/j.cpc.2006.11.010](https://doi.org/10.1016/j.cpc.2006.11.010). [arXiv:hep-ph/0609017](https://arxiv.org/abs/hep-ph/0609017) [hep-ph]
33. Corcella G et al (2001) HERWIG 6: an event generator for hadron emission reactions with interfering gluons (including supersymmetric processes). JHEP 01:010. [arXiv:hep-ph/0011363](https://arxiv.org/abs/hep-ph/0011363)
34. Frixione S, Webber BR (2002) Matching NLO QCD computations and parton shower simulations. JHEP 0206:029. doi:[10.1088/1126-6708/2002/06/029](https://doi.org/10.1088/1126-6708/2002/06/029). [arXiv:hep-ph/0204244](https://arxiv.org/abs/hep-ph/0204244) [hep-ph]
35. Frixione S, Webber B (2006) The MC@NLO 3.2 event generator. ArXiv Pre-Prints. [arXiv:hep-ph/0601192](https://arxiv.org/abs/hep-ph/0601192)
36. Frixione S, Nason P, Webber BR (2003) Matching NLO QCD and parton showers in heavy quark production. JHEP 0308:007. doi:[10.1088/1126-6708/2003/08/007](https://doi.org/10.1088/1126-6708/2003/08/007). [arXiv:hep-ph/0305252](https://arxiv.org/abs/hep-ph/0305252) [hep-ph]
37. Frixione S et al (2006) Single-top production in MC@NLO. JHEP 0603:092. doi:[10.1088/1126-6708/2006/03/092](https://doi.org/10.1088/1126-6708/2006/03/092). [arXiv:hep-ph/0512250](https://arxiv.org/abs/hep-ph/0512250) [hep-ph]
38. Frixione S et al (2008) Single-top hadroproduction in association with a W boson. JHEP 0807:029. doi:[10.1088/1126-6708/2008/07/029](https://doi.org/10.1088/1126-6708/2008/07/029). [arXiv:0805.3067](https://arxiv.org/abs/0805.3067) [hep-ph]
39. Frixione S et al (2011) NLO QCD corrections in Herwig++ with MC@NLO. JHEP 1101:053. doi:[10.1007/JHEP01\(2011\)053](https://doi.org/10.1007/JHEP01(2011)053). [arXiv:1010.0568](https://arxiv.org/abs/1010.0568) [hep-ph]
40. Kersevan BP, Richter-Was E (2013) The Monte Carlo event generator AcerMC versions 2.0 to 3.8 with interfaces to PYTHIA 6.4, HERWIG 6.5 and ARIADNE 4.1. Comput Phys Commun 184:919–985. doi:[10.1016/j.cpc.2012.10.032](https://doi.org/10.1016/j.cpc.2012.10.032). [arXiv:hep-ph/0405247](https://arxiv.org/abs/hep-ph/0405247) [hep-ph]

Chapter 5

Mono-Jet Events as Dark Matter Signature at Colliders

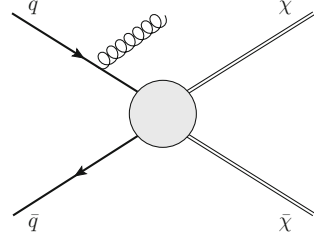
In this chapter, a possible signature of Dark Matter pair production at colliders is discussed. The general features are described in Sect. 5.1 and the signal description in an effective field theory (EFT) framework is introduced in Sect. 5.2, where also the applicability of this EFT is briefly discussed. An alternative approach using a simplified model with a light mediator is presented in Sect. 5.3. The Standard Model background contributions are described in Sect. 5.4 and an overview of the collider results before 2012 is given in Sect. 5.5.

5.1 Mono-Jet Signature of WIMP Pair Production

If WIMP dark matter annihilates into SM particles or scatters off nuclei, as described in Sect. 3.5, it should also be possible to pair-produce WIMPs by colliding SM particles. In the very simplistic picture of Fig. 3.6, dark matter would not be detectable at a collider, since the WIMPs are assumed to be stable¹ and they themselves will not interact in the detector. Instead, there has to be some additional activity to make it possible to trigger the event. Commonly, the initial state radiation of a particle recoiling against the WIMP system is assumed, leading to a configuration like the one in Fig. 5.1. The experimental signature accordingly is a high- p_T object and a large amount of missing transverse energy due to the escaping WIMP pair. The ISR object can be a heavy boson, a photon or a jet, where especially the latter has a large cross section at hadron colliders. These topologies are commonly referred to as *mono-X* signatures. They can also result from other extensions to the Standard Model, as for example large extra dimensions (cf. Sect. 2.4), which were among the

¹The stability requirement is also what makes pair production the dominant process: If single WIMP production would contribute with a sizeable cross section, the reverse process of a WIMP decaying into SM particles would have to be possible as well.

Fig. 5.1 Initial state radiation of a SM particle recoiling against the WIMP pair, which gives rise to missing transverse energy



first models that were constrained by mono- X and especially mono-jet searches at colliders [1–4].

In recent years, a model independent approach [5, 6] to search for a dark matter signal in mono- X topologies has become popular. The interaction between WIMPs and SM quarks and gluons is described in an effective field theory, which allows for a straight-forward comparison to both direct and indirect detection experiments (cf. Sect. 5.2). Given the large cross section for mono-jet events at hadron colliders, these were historically the first signatures to be interpreted in this way. The first publications were on collider data reanalysed by the theory community [6–10], but the framework was quickly adopted by the experiments themselves as well [11–13].

5.2 Effective Field Theory for Maverick Dark Matter

As was discussed in Sect. 3.4, many models for physics beyond the Standard Model (BSM) predict viable dark matter candidates. Instead of restricting the interpretation to one specific model, a model-independent effective field theory approach, as introduced in Ref. [6], is used in this work.

The cases considered in Ref. [6] are real and complex scalar as well as Majorana and Dirac fermionic WIMPs. Even though the theoretical description does not depend on a specific BSM model, there are a few assumptions made: The dark matter particles are assumed to be the only new particles accessible to the collider—hence the term ‘maverick’ dark matter. In particular, the mediating particles are too heavy to be produced directly. Moreover, the WIMP is assumed to be odd under some Z_2 symmetry, such that only couplings between an even number of WIMPs can occur. The WIMP is further assumed to be a singlet under the gauge groups of the SM, i.e. it has no tree-level couplings to the gauge bosons. From this, it follows that all factors containing SM fields have to be invariant under SM gauge transformations as well. Couplings to the Higgs-boson are not considered.

Under the assumptions above, the simplest class of operators contains lepton or quark bilinears. The former contribute only minimally in direct detection or collider searches and are not considered further. The quark bilinear operators considered are of the form $\bar{q}\Gamma q$, with $\Gamma \in \{1, \gamma^5, \gamma^\mu, \gamma^\mu\gamma^5, \sigma^{\mu\nu}\}$. In addition, operators with couplings to colour field strengths are considered.

The effective theory defined by these operators is non-renormalisable, and hence will break down at an energy scale of the order of the mass of the particles that have been integrated out. This *suppression scale* is parameterised by the quantity M_* , which depends on the masses and couplings of the mediating particles and hence on the specifics of the UV-completion. The simplest completion that comes to mind for mediating an interaction between two WIMPs and SM particles is the exchange of a single mediator of mass M_{Med} with a coupling g_{SM} to SM particles and g_χ to the WIMPs. In this case, M_* will be related to the parameters of the UV-complete model by $M_* \sim M_{Med} / \sqrt{g_{SM} g_\chi}$.

The complete list of operators is given in Fig. 5.2 [6]. The coefficients are derived such that comparisons with direct detection become easier. The (pseudo-)scalar quark bilinears are normalised by the quark mass m_q , which mitigates contributions from flavour changing processes. These operators will be dominated by heavy quark contributions. The gluon field strength operators are normalised by a factor of α_s , hinting at their origin as loop processes. The powers of M_* are chosen to yield the correct dimension in the action.

The virtue of the effective field theory is that it allows one to convert the limits on the suppression scale into limits on the WIMP-nucleon scattering cross section. Not all operators contribute in the limit of low momentum transfer, the formulas

Name	Operator	Coefficient
D1	$\bar{\chi}\chi\bar{q}q$	m_q/M_*^3
D2	$\bar{\chi}\gamma^5\chi\bar{q}q$	im_q/M_*^3
D3	$\bar{\chi}\chi\bar{q}\gamma^5q$	im_q/M_*^3
D4	$\bar{\chi}\gamma^5\chi\bar{q}\gamma^5q$	m_q/M_*^3
D5	$\bar{\chi}\gamma^\mu\chi\bar{q}\gamma_\mu q$	$1/M_*^2$
D6	$\bar{\chi}\gamma^\mu\gamma^5\chi\bar{q}\gamma_\mu q$	$1/M_*^2$
D7	$\bar{\chi}\gamma^\mu\chi\bar{q}\gamma_\mu\gamma^5q$	$1/M_*^2$
D8	$\bar{\chi}\gamma^\mu\gamma^5\chi\bar{q}\gamma_\mu\gamma^5q$	$1/M_*^2$
D9	$\bar{\chi}\sigma^{\mu\nu}\chi\bar{q}\sigma_{\mu\nu}q$	$1/M_*^2$
D10	$\bar{\chi}\sigma_{\mu\nu}\gamma^5\chi\bar{q}\sigma_{\alpha\beta}q$	i/M_*^2
D11	$\bar{\chi}\chi G_{\mu\nu}G^{\mu\nu}$	$\alpha_s/4M_*^3$
D12	$\bar{\chi}\gamma^5\chi G_{\mu\nu}G^{\mu\nu}$	$i\alpha_s/4M_*^3$
D13	$\bar{\chi}\chi G_{\mu\nu}\tilde{G}^{\mu\nu}$	$i\alpha_s/4M_*^3$
D14	$\bar{\chi}\gamma^5\chi G_{\mu\nu}\tilde{G}^{\mu\nu}$	$\alpha_s/4M_*^3$

Name	Operator	Coefficient
C1	$\chi^\dagger\chi\bar{q}q$	m_q/M_*^2
C2	$\chi^\dagger\chi\bar{q}\gamma^5q$	im_q/M_*^2
C3	$\chi^\dagger\partial_\mu\chi\bar{q}\gamma^\mu q$	$1/M_*^2$
C4	$\chi^\dagger\partial_\mu\chi\bar{q}\gamma^\mu\gamma^5q$	$1/M_*^2$
C5	$\chi^\dagger\chi G_{\mu\nu}G^{\mu\nu}$	$\alpha_s/4M_*^2$
C6	$\chi^\dagger\chi G_{\mu\nu}\tilde{G}^{\mu\nu}$	$i\alpha_s/4M_*^2$
R1	$\chi^2\bar{q}q$	$m_q/2M_*^2$
R2	$\chi^2\bar{q}\gamma^5q$	$im_q/2M_*^2$
R3	$\chi^2 G_{\mu\nu}G^{\mu\nu}$	$\alpha_s/8M_*^2$
R4	$\chi^2 G_{\mu\nu}\tilde{G}^{\mu\nu}$	$i\alpha_s/8M_*^2$

Fig. 5.2 List of all effective operators considered in Ref. [6]. The labels D, C and R denote Dirac fermionic, complex and real scalar DM, respectively

for the relevant ones are given below.² They are derived from the expectation value of the partonic operator in the nucleon [14], taking into account the kinematics of WIMP-nucleon scattering.

$$\sigma_{\chi N}^{D1} = 1.60 \times 10^{-37} \text{ cm}^2 \left(\frac{\mu_\chi}{1 \text{ GeV}} \right)^2 \left(\frac{20 \text{ GeV}}{M_*} \right)^6 \quad (5.1)$$

$$\sigma_{\chi N}^{D5,C3} = 1.38 \times 10^{-37} \text{ cm}^2 \left(\frac{\mu_\chi}{1 \text{ GeV}} \right)^2 \left(\frac{300 \text{ GeV}}{M_*} \right)^4 \quad (5.2)$$

$$\sigma_{\chi N}^{D8,D9} = 4.7 \times 10^{-39} \text{ cm}^2 \left(\frac{\mu_\chi}{1 \text{ GeV}} \right)^2 \left(\frac{300 \text{ GeV}}{M_*} \right)^4 \quad (5.3)$$

$$\sigma_{\chi N}^{D11} = 3.83 \times 10^{-41} \text{ cm}^2 \left(\frac{\mu_\chi}{1 \text{ GeV}} \right)^2 \left(\frac{100 \text{ GeV}}{M_*} \right)^6 \quad (5.4)$$

$$\sigma_{\chi N}^{C1,R1} = 2.56 \times 10^{-36} \text{ cm}^2 \left(\frac{\mu_\chi}{1 \text{ GeV}} \right)^2 \left(\frac{10 \text{ GeV}}{m_\chi} \right)^4 \left(\frac{10 \text{ GeV}}{M_*} \right)^4 \quad (5.5)$$

$$\sigma_{\chi N}^{C5,R3} = 7.40 \times 10^{-39} \text{ cm}^2 \left(\frac{\mu_\chi}{1 \text{ GeV}} \right)^2 \left(\frac{10 \text{ GeV}}{m_\chi} \right)^4 \left(\frac{60 \text{ GeV}}{M_*} \right)^4 \quad (5.6)$$

In the above equations, μ_χ is the reduced mass of the WIMP-nucleon system. Depending on the type of interaction, the operators will contribute either to spin-dependent or to spin-independent WIMP-nucleon scattering. In this work, a subset of these is considered, see Table 5.1. All of the operators for fermionic DM that contribute in WIMP-nucleon scattering are considered, covering different initial states and types of interaction, both spin-dependent as well as spin-independent. Out of the operators for scalar DM, only C-operators are considered, since the cross sections for the real scalar DM operators are suppressed by a factor of 2. The operators C1 and C5 will be studied, which are the pendants to D1 and D11 for fermionic DM.

For the vector- and axial-vector couplings (D5 and D8), formulas for the conversion into limits on the annihilation cross section are given in Ref. [8]:

$$\sigma_V v_{rel} = \frac{1}{16\pi M_*^4} \sum_q \sqrt{1 - \frac{m_q^2}{m_\chi^2}} \left(24(2m_\chi^2 + m_q^2) + \frac{8m_\chi^4 - 4m_\chi^2 m_q^2 + 5m_q^4}{m_\chi^2 - m_q^2} v_{rel}^2 \right), \quad (5.7)$$

$$\sigma_A v_{rel} = \frac{1}{16\pi M_*^4} \sum_q \sqrt{1 - \frac{m_q^2}{m_\chi^2}} \left(24m_q^2 + \frac{8m_\chi^4 - 22m_\chi^2 m_q^2 + 17m_q^4}{m_\chi^2 - m_q^2} v_{rel}^2 \right). \quad (5.8)$$

²There is a slight difference in Eq. (5.3) with respect to Eq. (5) in Ref. [6]: the prefactor is 4.7×10^{-39} instead of 9.18×10^{-40} , see Footnote 6 in Ref. [12].

Table 5.1 Operators considered in this work

Label	Initial state	Type	Spin-dependence	Dimension
D1	$q\bar{q}$	Scalar	SI	7
D5	$q\bar{q}$	Vector	SI	6
D8	$q\bar{q}$	Axial-vector	SD	6
D9	$q\bar{q}$	Tensor	SD	6
D11	gg	Scalar	SI	7
C1	$q\bar{q}$	Scalar	SI	6
C5	gg	Scalar	SI	6

SI means spin-independent, *SD* spin-dependent. The tensor operator describes a magnetic-moment coupling

Here, v_{rel} is the relative velocity of the two annihilating WIMPs, and $\langle v_{rel}^2 \rangle = 0.24$. This will be used in Chap. 15 to compare to results from indirect detection experiments.

5.2.1 Validity of the Effective Theory

In general, the use of an effective theory is only justified when the scale of the process to describe is much lower than the scale of the underlying microscopic process. If this holds, the process can be described by a set of effective operators with some ultra-violet (UV) cutoff scale, which has to be much higher than the typical momentum transfer occurring in the process considered. While for the small momentum transfers involved in the direct detection of dark matter the use of an effective theory is well justified, its applicability at collider energies, especially at the LHC, has become subject of discussions in the past years. It has been pointed out in various publications, for example in Refs. [6, 15–20], that the use of the EFT at LHC-like energies has to be handled with care. A very detailed discussion of the subject can also be found in Ref. [21] and the following remarks are largely based on the studies therein.

The suppression scale relates to the mass of an s -channel mediator and the couplings as

$$M_* = \frac{M_{Med}}{\sqrt{g_\chi g_{SM}}}. \quad (5.9)$$

As a minimal requirement for the EFT to be applicable, the momentum transfer in the interaction, Q_{tr} , has to be smaller than the mediator mass, $Q_{tr} < M_{Med}$, leading to

$$M_* > \frac{Q_{tr}}{\sqrt{g_\chi g_{SM}}}. \quad (5.10)$$

The upper bound on the couplings which render the theory still perturbative is given by $g_\chi, g_{\text{SM}} < 4\pi$. This leads to

$$M_* > \frac{Q_{tr}}{4\pi}. \quad (5.11)$$

In order to produce a pair of WIMPs of mass m_χ (in an s -channel process), the momentum transfer has to be at least twice as large as the WIMP mass, $Q_{tr} > 2m_\chi$, yielding the following minimal constraint for the EFT to be valid within the kinematic boundaries:

$$M_* > \frac{m_\chi}{2\pi}. \quad (5.12)$$

In Ref. [21], the condition (5.10) is proposed to be used as a means to quantify the error one makes by assuming full validity of the EFT. For a given initial limit on the suppression scale M_*^{init} , there might be events which do not fulfill the requirement (5.10), removing those events leaves a fraction of valid events R_v^i . This fraction can be used to rescale the limits, yielding a new value of M_*^i , in the following way:

$$M_*^i = [R_v^i]^{1/(2(d-4))} M_*^{init}. \quad (5.13)$$

Here, d is the dimension of the operator (7 for D1 and D11, 6 for the other operators). This procedure is repeated using M_*^i in the requirement of Eq. (5.10), retrieving a new fraction of valid events and a new value of M_*^i and so forth, until either all events that are left fulfil the requirement or no events are left (i.e. $R_v^i = 1$ or $R_v^i = 0$). When denoting the product of the validity fractions of each iteration step (i.e. the overall fraction of valid events) as $R_v^{tot} = \prod_i R_v^i$, the final limit on the suppression scale can be written as

$$M_*^{final} = [R_v^{tot}]^{1/(2(d-4))} M_*^{init}. \quad (5.14)$$

For the dimension 6 operators a validity fraction of 50% would thus mean a deterioration in the limit by about 16%, for example.

The result of the iterative procedure depends, however, on the assumption made for the couplings. In Eq. (5.11), those are set to their maximum perturbative value of 4π . This is of course a peculiar—although valid—configuration when considering a weakly coupled theory. Other choices of the coupling lead to stronger constraints on the validity. One common choice in the literature is $\sqrt{g_{\text{SM}}g_\chi} = 1$, which result in $Q_{tr} < M_*$ as a requirement for validity. But this, again, is just one arbitrary choice.

Moreover, the discussion above relates to the assumption of an s -channel mediator in the UV-completion, which is not straight forward to introduce for all the operators. For example, the gg -operator D11 would still need an effective vertex to couple the two gluons to the mediator. A more detailed discussion can be found in Ref. [22]. For the results of this work, the indication of validity has been restricted to the minimalistic requirement (5.12).

5.3 Simplified Models

As discussed in the previous section, the assumptions made for the use of the effective theory do not hold in all regions of phase space at the LHC. Hence, it is necessary to move one step further in the direction of a UV complete theory and use simplified models for the interpretation of experimental results. The price to pay for being safe from the validity point of view is to introduce (at least one) additional parameter(s) (the mass of the mediator), i.e. to become more model dependent.

One of the simplest possibilities is to introduce a light s -channel mediator with a mass M_{Med} , a width Γ and couplings g_{SM} , g_χ to SM fermions and WIMPs, respectively. This was done in for example Ref. [8] and large parts of the following discussion are taken from there. A Feynman diagram for such a process is displayed in Fig. 5.3.

In the case of an s -channel process, resonance enhancement will occur for mediator masses well within the kinematic range, i.e. when the mediator can be produced on-shell. The smaller the decay width, the stronger this enhancement. However, for the $2 \rightarrow 2$ process considered here, the width cannot be arbitrarily small due to the open decay channels to WIMPs and jets. The value used in Ref. [8] and adopted later in this work is $\Gamma = M_{Med}/(8\pi)$, which corresponds to a mediator with couplings $g_{SM}g_\chi = 1$ and only one decay channel into quarks of one flavour and helicity and thus can be regarded as a lower bound on the width.

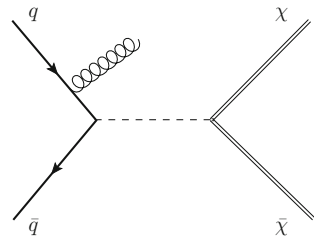
For very light mediators, colliders will have a disadvantage compared to direct detection experiments as can be seen from how the cross section scales with the mediator mass. For the collider process, the cross section is related to the parameters of the model as follows [8]:

$$\sigma(pp \rightarrow \bar{\chi}\chi + X) \sim \frac{g_{SM}^2 g_\chi^2}{(q^2 - M_{Med}^2)^2 + M_{Med}^2 \Gamma^2/4} E^2. \quad (5.15)$$

Here, E is roughly the partonic centre of mass energy and q is the four momentum transfer. For the direct detection, the following relation holds [8]:

$$\sigma(\chi N \rightarrow \chi N) \sim \frac{g_{SM}^2 g_\chi^2}{M_{Med}^4} \mu_{\chi N}^2, \quad (5.16)$$

Fig. 5.3 Feynman diagram for mono-jet signature of WIMP pair production via an s -channel process



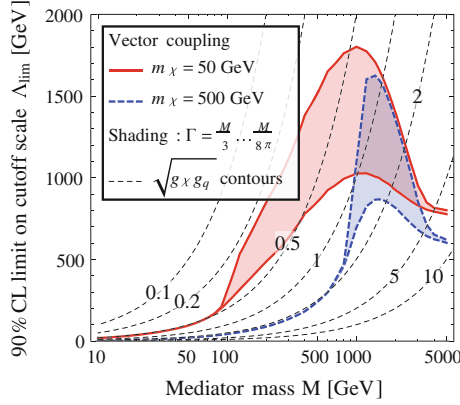


Fig. 5.4 Limits on $\Lambda \equiv M/\sqrt{g_{SM}g_\chi}$ as a function of the mediator mass M for s -channel vector-type interactions. Results for $m_\chi = 50$ GeV are shown in red, for $m_\chi = 500$ GeV in blue. The coloured bands indicate the range between the minimum width $\Gamma = M/(8\pi)$ and the maximum $\Gamma = M/3$. Contours of constant coupling are shown as grey dashed lines. The couplings are assumed to be the same for all quark flavours. Taken from Ref. [8]

with $\mu_{\chi N}$ denoting the reduced mass of the WIMP and the target nucleus.

For $M_{Med}^2 \ll q^2$, the collider limit on the coupling product does not depend on M_{Med} any more, whereas the limit from direct detection becomes stronger for small values of the mediator mass.

Even though the couplings are the actual model parameters, limits will also be given (analogous to M_*) in terms of $\Lambda \equiv M_{Med}/\sqrt{g_{SM}g_\chi}$, which is what determines the scattering cross section and was also used in Ref. [8]. In this reference, a vector-type interaction, mediated by a vector boson with equal couplings to all quark flavours is used to re-interpret the ATLAS results from Ref. [23]. The limits obtained for WIMP masses of $m_\chi = 50$ GeV and $m_\chi = 500$ GeV for different choices of the width of the mediator between $M_{Med}/(8\pi)$ and $M_{Med}/3$ are presented in Fig. 5.4. For large mediator masses the limits approach those obtained in the EFT, for intermediate masses resonant enhancement is observed for $M_{Med} > 2m_\chi$. This is indeed more pronounced for smaller widths. Below $2m_\chi$ the mediator has to be produced off-shell, leading to a decrease in cross section and hence weaker limits. The dependence on the width disappears and the lines follow the coupling contours, in agreement with the conclusion that for small masses the limit on the coupling will not depend on the mediator mass.

5.4 Standard Model Background Processes

So far, only the signal was addressed in this chapter. One of the main differences between the direct searches and the collider experiments are the background levels. Direct search experiments are low-background or zero-background experiments:

Their aim is to reject any background completely such that any observed event should be a signal event. At the collider, the situation is different: For the mono-jet signature (and similarly for the other mono-X signatures), there are irreducible and unavoidable backgrounds. They cannot be removed completely, but have to be estimated precisely. The irreducible background to mono-jet events is the production of a Z -boson in association with jets, where the Z subsequently decays into a neutrino-antineutrino pair, which leave the detector without interacting, giving rise to missing transverse energy. This is the exact same signature as expected for a signal event.

Another source of large backgrounds are W +jets events, where the W decays leptonically, giving rise to missing E_T due to the (anti)neutrino, and the lepton from the decay is not identified. In the case of $W^\pm(\rightarrow \tau^\pm\bar{\nu})$ + jets events, the τ can either decay leptonically or hadronically, leading to another jet. Leptonic W -decays with identified leptons can be removed by vetoing on leptons, but it might happen that the lepton is outside of the detector acceptance or not properly reconstructed. Such events also fit the mono-jet signature.

$Z(\rightarrow \nu\bar{\nu})$ +jets and $W^\pm(\rightarrow \ell^\pm\bar{\nu})$ + jets events together account for about 95 % of the backgrounds at E_T^{miss} of 150 GeV. The remaining contributions are mostly pair or single production of top quarks and diboson processes. Contributions from leptonic Z -decays are very small since there is typically not much missing energy in these events. The same holds for QCD multi-jet events, whose contribution is negligible at large missing E_T (above 250 GeV). Another small contribution below 250 GeV of missing E_T are events from non-collision backgrounds, but at higher E_T^{miss} these are also negligible.

5.5 Mono-X Results After 2011

Naturally, the first mono-X channel to be explored at the LHC was the mono-jet signature, as it promises highest sensitivity in many cases because of the large cross section compared to, for example, mono-photon. Observed limits from ATLAS [12], CMS [3] and CDF [11] based on data prior to 2012 are compared to direct detection results in Fig. 5.5 [12]. The ATLAS and CMS results correspond to the full data set collected in 2011 at a centre-of-mass energy of 7 TeV. For both types of interactions it can be seen that for the operators considered here (for Dirac fermionic WIMPs only) the LHC limits vary only slightly in the range of WIMP masses up to a few hundred GeV. This can be understood since the kinematics for the production of light WIMPs at LHC energies are the same, independent of the WIMP mass. This is not true any more for higher WIMP masses, where the limits are found to degrade due to the smaller cross section.

For spin-dependent interactions (left), the collider limits are stronger than the direct search results over a large range of WIMP masses, the limits for the operator D9 are about one order of magnitude stronger than those for D8. For spin-independent interactions, the collider limits provide additional information at low WIMP masses, where the direct detection experiments are not sensitive. The strongest limits are

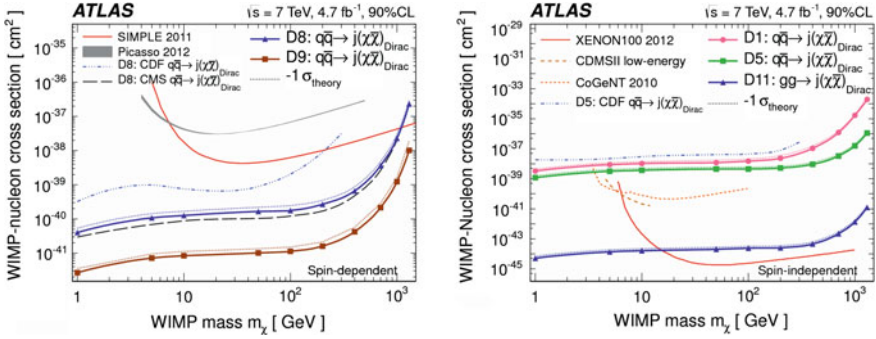


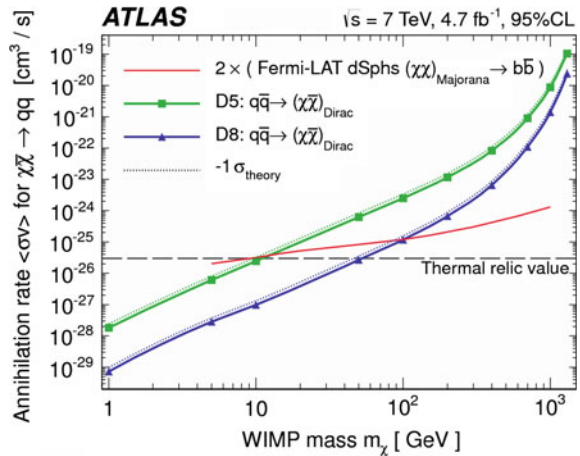
Fig. 5.5 Limits on the WIMP-nucleon scattering cross section from mono-jet analyses at CDF [11], CMS [3] and ATLAS [12] in comparison to direct detection experiments, both for spin-dependent (*left*) and spin-independent (*right*) interactions [12]

obtained for the gluon-gluon operator D11, the operators D1 and D5 give similar limits, about five orders of magnitude weaker than D11. For the ATLAS limits, the impact of theoretical uncertainties is illustrated by a dashed line and it is observed that the effect is very small.

A similar situation is found for the comparison to the indirect detection results from the Fermi-LAT, as shown in Fig. 5.6 [12]: the collider bounds from ATLAS are competitive at low WIMP masses, below 10 or 100 GeV for the operator D5 and D8, respectively.

Figure 5.7 [24] shows results from mono-photon searches in ATLAS [24] and CMS [25], compared to the mono-jet results [3, 11, 12] and the direct detection limits. The picture with respect to the direct detection experiments is basically the same as for the mono-jet analyses. ATLAS and CMS find very similar limits for the

Fig. 5.6 Comparison of the WIMP annihilation cross section limits obtained in the ATLAS mono-jet search to results from Fermi-LAT. The Fermi-LAT limits are for Majorana-fermionic WIMPs, hence the factor of 2 [12]



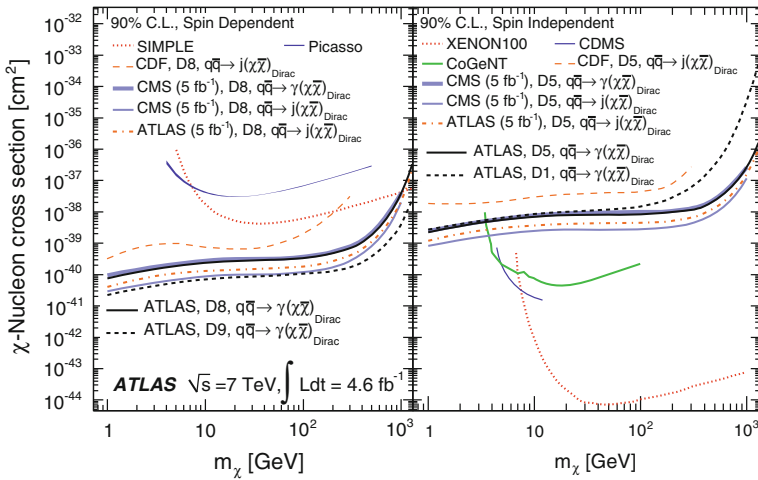


Fig. 5.7 Limits on spin-dependent (*left*) and spin-independent (*right*) WIMP-nucleon scattering cross section from various mono-jet and mono-photon analyses in comparison to direct detection results [24]

mono-photon channel. The mono-jet searches of both experiments provide stronger limits, as is to be expected due to the much higher cross section. The gluon-gluon operator D11 can not be probed with mono-photon events.

References

1. Aaltonen T et al (2008) Search for large extra dimensions in final states containing one photon or jet and large missing transverse energy produced in pp collisions at $\sqrt{s} = 1 : 96$ TeV. Phys Rev Lett 101(18):181602. doi:[10.1103/PhysRevLett.101.181602](https://doi.org/10.1103/PhysRevLett.101.181602)
2. Abazov V et al (2003) Search for large extra dimensions in the monojet + missing E_T channel at DØ. Phys Rev Lett 90:251802. doi:[10.1103/PhysRevLett.90.251802](https://doi.org/10.1103/PhysRevLett.90.251802). arXiv:[hep-ex/0302014](https://arxiv.org/abs/hep-ex/0302014) [hep-ex]
3. The CMS Collaboration (2011). Search for new physics with a mono-jet and missing transverse energy in pp collisions at $\sqrt{s} = 7$ TeV. Phys Rev Lett 107:201804. doi:[10.1103/PhysRevLett.107.201804](https://doi.org/10.1103/PhysRevLett.107.201804). arXiv:[1106.4775](https://arxiv.org/abs/1106.4775) [hep-ex]
4. The ATLAS Collaboration (2011). Search for new phenomena with the monojet and missing transverse momentum signature using the ATLAS detector in $\sqrt{s} = 7$ TeV proton-proton collisions. Phys Lett B 705:294–312. doi:[10.1016/j.physletb.2011.10.006](https://doi.org/10.1016/j.physletb.2011.10.006). arXiv:[1106.5327](https://arxiv.org/abs/1106.5327) [hep-ex]
5. Goodman J et al (2011) Constraints on light majorana dark matter from colliders. Phys Lett B 695:185–188. doi:[10.1016/j.physletb.2010.11.009](https://doi.org/10.1016/j.physletb.2010.11.009). arXiv:[1005.1286](https://arxiv.org/abs/1005.1286) [hep-ph]
6. Goodman J et al (2010) Constraints on dark matter from colliders. Phys Rev D 82:116010. doi:[10.1103/PhysRevD.82.116010](https://doi.org/10.1103/PhysRevD.82.116010). arXiv:[1008.1783](https://arxiv.org/abs/1008.1783) [hep-ph]
7. Rajaraman A et al (2011) LHC bounds on interactions of dark matter. Phys Rev D 84:095013. doi:[10.1103/PhysRevD.84.095013](https://doi.org/10.1103/PhysRevD.84.095013). arXiv:[1108.1196](https://arxiv.org/abs/1108.1196) [hep-ph]

8. Fox PJ et al (2012) Missing energy signatures of dark matter at the LHC. Phys Rev D 85:056011. doi:[10.1103/PhysRevD.85.056011](https://doi.org/10.1103/PhysRevD.85.056011). arXiv:[1109.4398](https://arxiv.org/abs/1109.4398) [hep-ph]
9. Cheung K et al (2012) Global constraints on effective dark matter interactions: relic density, direct detection, indirect detection, and collider. JCAP 1205:001. doi:[10.1088/1475-7516/2012/05/001](https://doi.org/10.1088/1475-7516/2012/05/001). arXiv:[1201.3402](https://arxiv.org/abs/1201.3402) [hep-ph]
10. Bai Y, Fox PJ, Harnik R (2010) The tevatron at the frontier of dark matter direct detection. JHEP 1012:048. doi:[10.1007/JHEP12\(2010\)048](https://doi.org/10.1007/JHEP12(2010)048). arXiv:[1005.3797](https://arxiv.org/abs/1005.3797) [hep-ph]
11. Aaltonen T et al (2012) A search for dark matter in events with one jet and missing transverse energy in $p\bar{p}$ collisions at $\sqrt{s} = 1 : 96$ TeV. Phys Rev Lett 108:211804. doi:[10.1103/PhysRevLett.108.211804](https://doi.org/10.1103/PhysRevLett.108.211804). arXiv:[1203.0742](https://arxiv.org/abs/1203.0742) [hep-ex]
12. The ATLAS Collaboration (2013). Search for dark matter candidates and large extra dimensions in events with a jet and missing transverse momentum with the ATLAS detector. JHEP 1304:075. doi:[10.1007/JHEP04\(2013\)075](https://doi.org/10.1007/JHEP04(2013)075). arXiv:[1210.4491](https://arxiv.org/abs/1210.4491) [hep-ex]
13. The CMS Collaboration (2012). Search for dark matter and large extra dimensions in mono-jet events in pp collisions at $\sqrt{s} = 7$ TeV. JHEP 1209:094. doi:[10.1007/JHEP09\(2012\)094](https://doi.org/10.1007/JHEP09(2012)094). arXiv:[1206.5663](https://arxiv.org/abs/1206.5663) [hep-ex]
14. Belanger G et al (2009) Dark matter direct detection rate in a generic model with micrOMEGAS 2.2. Comput Phys Commun 180:747–767. doi:[10.1016/j.cpc.2008.11.019](https://doi.org/10.1016/j.cpc.2008.11.019). arXiv:[0803.2360](https://arxiv.org/abs/0803.2360) [hep-ph]
15. Cotta R et al (2013) Bounds on dark matter interactions with electroweak gauge bosons. Phys Rev D 88:116009. doi:[10.1103/PhysRevD.88.116009](https://doi.org/10.1103/PhysRevD.88.116009). arXiv:[1210.0525](https://arxiv.org/abs/1210.0525) [hep-ph]
16. Dreiner H et al (2013) Illuminating dark matter at the ILC. Phys Rev D 87(7):075015. doi:[10.1103/PhysRevD.87.075015](https://doi.org/10.1103/PhysRevD.87.075015). arXiv:[1211.2254](https://arxiv.org/abs/1211.2254) [hep-ph]
17. Shoemaker IM, Vecchi L (2012) Unitarity and monojet bounds on models for DAMA, CoGeNT, and CRESST-II. Phys Rev D 86:015023. doi:[10.1103/PhysRevD.86.015023](https://doi.org/10.1103/PhysRevD.86.015023). arXiv:[1112.5457](https://arxiv.org/abs/1112.5457) [hep-ph]
18. Fox PJ, Williams C (2013) Next-to-leading order predictions for dark matter production at hadron colliders. Phys Rev D 87(5):054030. doi:[10.1103/PhysRevD.87.054030](https://doi.org/10.1103/PhysRevD.87.054030). arXiv:[1211.6390](https://arxiv.org/abs/1211.6390) [hep-ph]
19. Haisch U, Kahlhoefer F, Unwin J (2013) The impact of heavy-quark loops on LHC dark matter searches. JHEP 1307:125. doi:[10.1007/JHEP07\(2013\)125](https://doi.org/10.1007/JHEP07(2013)125). arXiv:[1208.4605](https://arxiv.org/abs/1208.4605) [hep-ph]
20. Fox PJ et al (2011) LEP shines light on dark matter. Phys Rev D 84:014028. doi:[10.1103/PhysRevD.84.014028](https://doi.org/10.1103/PhysRevD.84.014028). arXiv:[1103.0240](https://arxiv.org/abs/1103.0240) [hep-ph]
21. Busoni G et al (2014) On the validity of the effective field theory for dark matter searches at the LHC. Phys Lett B 728:412–421. doi:[10.1016/j.physletb.2013.11.069](https://doi.org/10.1016/j.physletb.2013.11.069). arXiv:[1307.2253](https://arxiv.org/abs/1307.2253) [hep-ph]
22. The ATLAS Collaboration (2015). Search for new phenomena in final states with an energetic jet and large missing transverse momentum in pp collisions at $\sqrt{s} = 8$ TeV with the ATLAS detector. submitted to EPJC. arXiv:[1502.01518](https://arxiv.org/abs/1502.01518) [hep-ex]
23. The ATLAS Collaboration (2011). Search for new phenomena in monojet plus missing transverse momentum final states using 1 fb⁻¹ of pp collisions at $\sqrt{s}=7$ TeV with the ATLAS detector. Technical report ATLAS-CONF-2011-096. Geneva: CERN
24. The ATLAS Collaboration (2013). Search for dark matter candidates and large extra dimensions in events with a photon and missing transverse momentum in pp collision data at $\sqrt{s} = 7$ TeV with the ATLAS detector. Phys Rev Lett 110(1):011802. doi:[10.1103/PhysRevLett.110.011802](https://doi.org/10.1103/PhysRevLett.110.011802)
25. The CMS Collaboration (2012). Search for dark matter and large extra dimensions in pp collisions yielding a photon and missing transverse energy. Phys Rev Lett 108(26)–261803. doi:[10.1103/PhysRevLett.108.261803](https://doi.org/10.1103/PhysRevLett.108.261803)

Part II
Experimental Facilities

Chapter 6

The Large Hadron Collider

The Large Hadron Collider (LHC) [1] at the European Laboratory for Particle Physics (CERN¹) near Geneva, Switzerland, is a hadron accelerator, designed to provide unprecedented centre-of-mass-energies and luminosities for the discovery of new physics. Furthermore, it allows for measurements of parameters of the Standard Model in hitherto inaccessible regions of phase space.

A large fraction of the physics programme is based on proton-proton collisions, for which energies of up to 14 TeV and luminosities of more than $10^{34} \text{ cm}^{-2}\text{s}^{-1}$ are foreseen. In addition, the accelerator provides the possibility of colliding lead (Pb) ions at energies of up to 2.8 TeV per nucleon and luminosities of $10^{27} \text{ cm}^{-2}\text{s}^{-1}$. These collisions are used to study the formation of a quark-gluon-plasma under conditions similar to those in the early universe.

Section 6.1 gives an overview of the accelerator complex, while Sect. 6.3 gives the definition of the luminosity in terms of collider parameters. The filling scheme of the LHC, which is subject to certain constraints from the pre-accelerator chain, is described in Sect. 6.2. A short overview of the four large LHC experiments is given in Sect. 6.4, and the run-I performance as well as the expectations for run-II are presented in Sect. 6.5.

6.1 The Accelerator Complex

Before being filled into the LHC, the protons have to be accelerated. This pre-acceleration proceeds in several steps, the complete injection chain is shown in Fig. 6.1. The protons are extracted by ionising hydrogen and are first fed into a linear accelerator, Linac2. Subsequently, they pass through the Booster, the proton

¹Conseil Européen pour la Recherche Nucléaire.

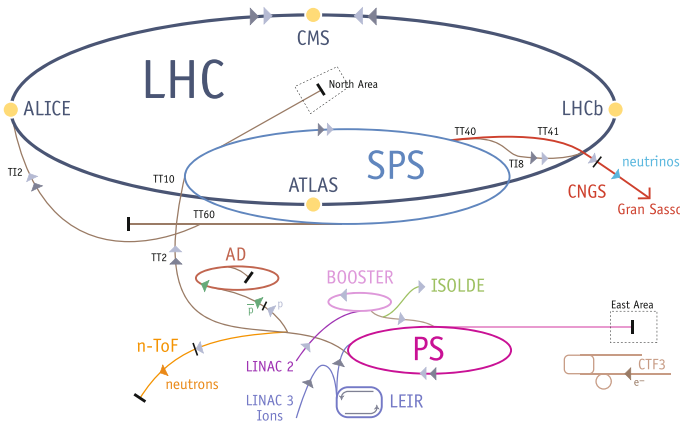


Fig. 6.1 The CERN accelerator complex. For a description of the proton acceleration chain see text [2]

synchrotron (PS) and the super proton synchrotron (SPS), and are finally filled into the LHC ring via two transfer lines. Their energy is increased in each step, from 50 MeV after Linac2 to 1.4, 25 and 450 GeV of injection energy into the LHC, where they are to be accelerated to up to 7 TeV per beam.

The collider is situated in the 27 km long tunnel that formerly hosted CERN's Large Electron-Positron Collider (LEP), approximately 100 m underground. The magnetic fields needed to steer the particles around the ring are provided by 1232 superconducting NbTi dipole magnets. They are cooled to a temperature of 1.9 K by superfluid helium and generate fields stronger than 8 T. In addition to the dipole magnets for steering, there are 392 quadrupole magnets for focussing the beams. At the interaction points the two beams are brought into collision with a certain angle, since head-on collisions would result in a large number of parasitic interactions.

6.2 The LHC Bunch Structure

The LHC can be operated with different filling schemes. In this section, a baseline scheme for the operation at 25 ns bunch spacing is described as an example. The information is largely based on reference [3].

All filling schemes must meet certain requirements; the most important one is a window of at least $3 \mu\text{s}$ without filled bunches to allow for the beam dump kicker rise time. This is known as the *beam dump gap* or *abort gap*.

Figure 6.2 illustrates the filling scheme, where bunch 1 is defined to be the first bunch after the abort gap. In total, there are 3564 possible bunch positions, each with a length of 25 ns. The ring is filled in batches of 3 or 4 *bunch trains*—consisting of 72 bunches each—from the SPS with the following pattern:

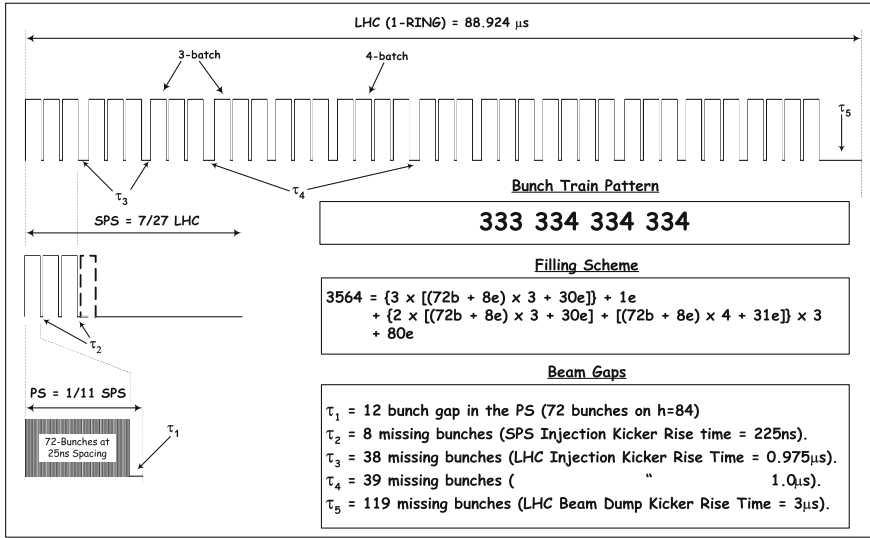


Fig. 6.2 Schematic illustration of the LHC bunch distribution for a 25 ns bunch spacing filling scheme [3]

333 334 334 334,

which makes for 39 bunch trains in total and thus 2808 filled bunches. Within one batch, there is a spacing of 8 bunches between the trains (τ_2 in Fig. 6.2), corresponding to the SPS injection kicker rise time. The batches are separated by 38 bunches (τ_3 , rise time of the LHC injection kicker) or by 39 bunches in between the 333 or 334 packets (τ_4). Finally, there is the abort gap, which comprises 119 empty bunches, corresponding to the rise time of the beam dump kicker (3 μ s). In a filling scheme with 50 ns bunch spacing in the trains, the maximum number of filled bunches is 1380.

6.3 Luminosity

From the experiments point of view one of the most important figures of merit of the accelerator is the *luminosity* it can deliver. The instantaneous luminosity of a particle accelerator relates the event rate of a process to its cross section: $R = L \cdot \sigma$, $[L] = \text{s}^{-1} \text{cm}^{-2}$.

The luminosity can be calculated from beam parameters according to the following formula [1]:

$$L = \frac{N_p^2 n_b f \gamma}{4\pi \epsilon \beta^*} F, \tag{6.1}$$

where N_p is the number of particles per bunch, and n_b the number of bunches in one beam. The beam revolution frequency f and the relativistic γ -factor enter in the numerator, while the normalised transverse beam emittance ε and the beta function at the collision point, β^* , appear in the denominator. The numerator gives the number of interactions per time interval, while the denominator describes the intersection area of the two beam profiles, that are assumed to be Gaussian in this case. The additional factor F accounts for a geometrical correction due to the crossing angle with which the beams are brought into collision. In Eq. (6.1), the beams are assumed to be round and have the same parameters.

As seen in the previous section, for the LHC, there can be as much as 2808 colliding bunches, and the number of protons per bunch can exceed 10^{11} . The revolution frequency is approximately 11 kHz.

Apart from the instantaneous luminosity, the (time-) integrated luminosity, $\mathcal{L} = \int L dt$, is also of interest for the experiments. It is a measure for the amount of data produced in a certain period of time and is measured in inverse cross section units, i.e. in 1/pb, 1/fb, etc.

6.4 The LHC Experiments

The LHC provides particle collisions at four interaction points. There, the four large LHC experiments are located: CMS [4] (Compact Muon Solenoid) and ATLAS [5] (A Large Toroidal Lhc ApparatuS) are so-called general purpose experiments, while LHCb [6] and ALICE [7] (A Large Ion Colliding Experiment) pursue a more specialised physics programme.

As the name indicates, LHCb focuses on physics involving bottom or beauty quarks. It was designed for luminosities of $10^{32} \text{ cm}^{-2}\text{s}^{-1}$, which requires a luminosity levelling when the LHC is producing higher luminosities: The beams are focused less compared to ATLAS or CMS before entering the collision area of LHCb to reduce the instantaneous luminosity.

ALICE is the only LHC experiment primarily designed to study heavy-nucleus collisions. These provide unique possibilities for investigating the behaviour of strongly interacting particles in the extreme environment of very high temperatures and energy densities.

The leading principle in the design of ATLAS and CMS was the aim to cover a range of physics measurements and searches as wide as possible in order to be able to take full advantage of the discovery potential of the LHC. They were devised to operate at the highest luminosities the LHC can provide. There are a number of smaller experiments situated around the LHC ring: The Total elastic and diffractive cross-section measurement experiment (TOTEM) [8] consists of 4 detector pairs at different positions on either side of the CMS experiment at very small angles to the beam pipe in order to capture so-called forward physics that escape the larger detectors. It studies the structure of the proton while at the same time monitoring the LHC luminosity. Similarly, LHCf [9] (LHC forward), is installed 140 m away from

the interaction point on both sides of the ATLAS detector. It is intended to study particle cascades similar to cosmic rays that are caused by particles from the proton collisions produced almost collinear to the beam.

6.5 Performance and Perspectives

The information in this section is based in large parts on references [10, 11].

In March 2010, the LHC started taking data at a centre-of-mass energy of 7 TeV. From the machine point of view this was essentially a commissioning phase, used to gain experience with and establish confidence in the operational procedures and the machine protection systems. In June 2010, bunches with the nominal intensity around 10^{11} protons were used for the first time and subsequently the number of bunches was increased gradually, reaching a value of 368 by the end of 2010. The peak luminosity achieved was $2.1 \times 10^{32} \text{ cm}^{-2} \text{ s}^{-1}$ and the integrated luminosity delivered to ATLAS and CMS was approximately 0.04 fb^{-1} .

In 2011, still at a beam energy of 3.5 TeV, the LHC performance limits were further explored. The bunch spacing in the trains was reduced to 50 ns and the number of bunches was steadily increased, reaching the maximum possible value of 1380 at 50 ns spacing. Further adjustment of the beam parameters and increase of the bunch intensities led to a peak instantaneous luminosity of $3.7 \times 10^{33} \text{ cm}^{-2} \text{ s}^{-1}$. The total integrated luminosity of proton-proton collisions in 2011 amounts to about 5 fb^{-1} .

2012 was the first year mainly devoted to collection of a large data set. The beam energy was increased to 4 TeV, the bunch spacing was kept at 50 ns and there were typically 1380 bunches in the machine. In Fig. 6.3 the peak luminosities for all LHC fills during the 2012 proton-proton run are displayed. It can be seen that following

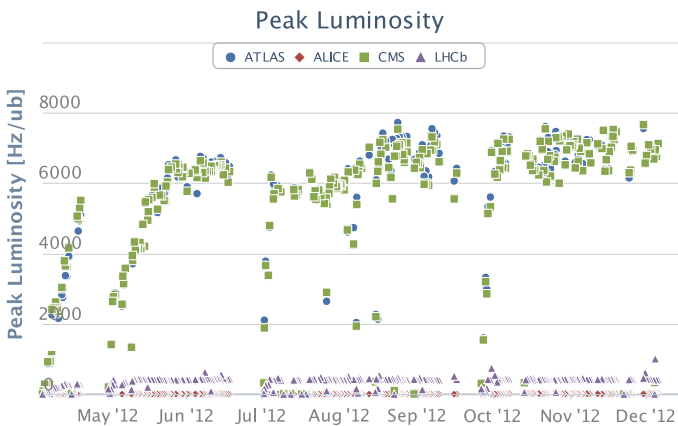


Fig. 6.3 Peak luminosity of the LHC for all fills in 2012 [12]

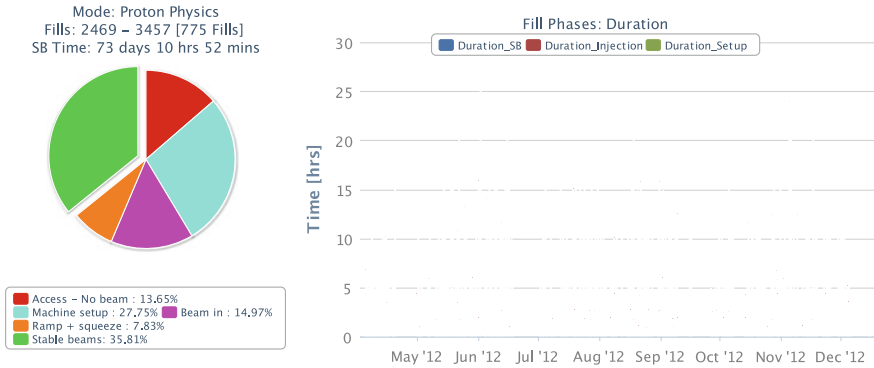


Fig. 6.4 Availability of the LHC in 2012 [12]

a rapid increase in the beginning, the peak luminosities continuously reach values above $6 \times 10^{33} \text{ cm}^{-2} \text{ s}^{-1}$, reaching the record value of almost $8 \times 10^{33} \text{ cm}^{-2} \text{ s}^{-1}$.

Figure 6.4 illustrates the good performance of the LHC during 2012 in terms of availability for physics data taking. The pie chart on the left shows the fraction of time spent in different states: the largest fraction, almost 36%, is for stable beams (SB), i.e. operation suitable for physics, corresponding to more than 73 days. Only about 14% had to be spent on interventions, i.e. without any beam. A bit more than a quarter of the time was used for machine setup. The time needed to bring the beams into collision mode after the injection (Ramp and Squeeze) amounted to about 8% of the total operation time. The histogram on the right in Fig. 6.4 shows the duration of the various LHC fills that made it into stable beams, split into the time spent for setting up the machine (green), injection of the beams (maroon) and stable beam operation (blue). For most of the fills the stable beam operation is the largest fraction.

In early 2013, the LHC entered an approximately 2 years shutdown—the long shutdown 1, or LS1. The primary goal is the consolidation of the superconducting splices in the roughly 1700 interconnects of the magnets in order to allow for an increase of the beam energy to 6.5 and 7 TeV. In addition, a large amount of maintenance and other consolidation projects is performed; for a list of key projects see for example reference [10].

The centre-of-mass energy at the re-start of data taking in spring 2015 will most likely be 13 TeV. The LHC will be operated with a 25 ns bunch spacing. The instantaneous luminosities will reach or even exceed the design value of $10^{34} \text{ cm}^{-2} \text{ s}^{-1}$. An integrated luminosity of about 25 fb^{-1} is expected for the end of 2015—about as much as during the three years of run-I.

References

1. Evans L, Bryant P (2008) LHC machine. J Instrum 3:S08001. <http://stacks.iop.org/1748-0221/3/i=08/a=S08001>
2. CERN (2009) LHC the guide. <http://cds.cern.ch/record/1165534/files/CERN-Brochure-2009-003-Eng.pdf>
3. Bailey R, Collier P (2003) Standard filling schemes for various LHC operation modes. Technical report LHC-PROJECT-NOTE-323. Geneva: CERN
4. The CMS Collaboration (2008) The CMS experiment at the CERN LHC. JINST 3:S08004. doi:[10.1088/1748-0221/3/08/S08004](https://doi.org/10.1088/1748-0221/3/08/S08004)
5. The ATLAS Collaboration (2008) The ATLAS experiment at the CERN large Hadron collider. JINST 3:S08003. doi:[10.1088/1748-0221/3/08/S08003](https://doi.org/10.1088/1748-0221/3/08/S08003)
6. Alves AA et al (2008) The LHCb detector at the LHC. JINST 3:S08005. doi:[10.1088/1748-0221/3/08/S08005](https://doi.org/10.1088/1748-0221/3/08/S08005)
7. Carena F et al (2014) The ALICE data acquisition system. Nucl Instrum Meth A741:130162. doi:[10.1016/j.nima.2013.12.015](https://doi.org/10.1016/j.nima.2013.12.015)
8. Anelli G et al (2008) The TOTEM experiment at the CERN large Hadron collider. JINST 3:S08007. doi:[10.1088/1748-0221/3/08/S08007](https://doi.org/10.1088/1748-0221/3/08/S08007)
9. Adriani O et al (2008) The LHCf detector at the CERN large Hadron collider. JINST 3:S08006. doi:[10.1088/1748-0221/3/08/S08006](https://doi.org/10.1088/1748-0221/3/08/S08006)
10. Lamont M (2013) Status of the LHC. J. Phys: Conf Ser 455.1:012001. <http://stacks.iop.org/1742-6596/455/i=1/a=012001>
11. Lamont M (2013) The LHC's first long run. Technical report 54381. Geneva: CERN. <http://cerncourier.com/cws/article/cern/54381>
12. LHC Performance and Statistics (2014) <http://lhc-statistics.web.cern.ch/LHC-Statistics/index.php>. Accessed 78 Sept 2014

Chapter 7

The ATLAS Experiment

This chapter will first give a general overview of the ATLAS detector in Sect. 7.1 and describe the components relevant for the analysis presented in this work in more detail in Sects. 7.2–7.5. A dedicated Sect. 7.6 will cover the trigger system and focus especially on the central trigger of the first trigger level, the operation and upgrade of which part of this work was dedicated to. A brief overview of the data structures and processing is given in Sect. 7.7. Section 7.8 outlines the detector simulation framework. The reconstruction of physics objects is detailed in Sects. 7.9 and 7.10 summarises the luminosity determination.

7.1 General Information

7.1.1 The Coordinate System

The nominal collision or interaction point within ATLAS defines the origin of the coordinate system. The x -axis is pointed radially towards the centre of the LHC ring, while the y -axis points upwards, and the z -axis points along the beam pipe such that the coordinate system is right-handed. The side of the detector that is located at positive values of z is referred to as the A-side, the one at negative z as C-side.

In the transverse x - y -plane the azimuthal angle ϕ is measured relative to the x -axis. The polar angle θ is measured with respect to the z -axis. Since differences $\Delta\theta$ are not Lorentz-invariant, the pseudo-rapidity η , defined as $\eta = -\ln(\tan(\theta/2))$, is mostly used for position specification.

7.1.2 Variables Used to Describe Particle Properties

The rapidity y of a massive particle is defined as

$$y = \frac{1}{2} \ln \frac{E + p_z}{E - p_z}, \quad (7.1)$$

where E is the energy and p_z the longitudinal momentum of the particle. The pseudo-rapidity results from taking the rapidity to the limit of massless particles.

An often used quantity is the distance ΔR in the η, ϕ -plane, defined as $\Delta R = \sqrt{\Delta\eta^2 + \Delta\phi^2}$. The transverse momentum p_T is calculated from the components in the x - y -plane as $p_T = \sqrt{p_x^2 + p_y^2}$, and analogously for the transverse energy.

Since the incoming protons (and the partons within) to first approximation have momentum parallel to the beam axis only, momentum conservation requires the sum of the transverse momenta of all particles in the final state to be zero. In case there are invisible particles like neutrinos (or yet to be discovered stable, weakly-interacting particles), the sum of momenta in the transverse plane for the visible particles will not be zero, and the negative vectorial sum, $-\mathbf{E}_T^{\text{miss}}$ is called the *missing transverse momentum*. Its magnitude is denoted by $E_T^{\text{miss}} = \sqrt{E_{x,\text{miss}}^2 + E_{y,\text{miss}}^2}$ and is referred to as *missing transverse energy*.

The transverse mass m_T of a W boson decaying into a charged lepton ℓ and a neutrino ν is calculated as $m_T = \sqrt{2p_T^\ell E_T^{\text{miss}}(1 - \cos \Delta\phi(\ell, E_T^{\text{miss}}))}$, using the missing E_T and the transverse momentum of the lepton p_T as well as the angle between the two.

7.1.3 Detector Overview

ATLAS [2] is a magnetic spectrometer with a cylindrical as well as a forward-backward symmetry in multiple layers as is typical for multi-purpose detectors. It is designed to reconstruct and identify all products emerging from the collisions at the LHC. The design exploits the fact that different kinds of particles have different types of interactions with the detector materials and thereby can be distinguished based on the signals they leave in various detector components—if at all. For example, muons as *minimum ionising particles* interact only little with the detector material and are the only particles to reach the outermost part of the detector—apart from particles like neutrinos that do not interact at all. ATLAS is divided into three main parts: the detectors closest to the beam pipe are tracking detectors, followed by the calorimeters and finally the muon system. A cut-away view of the ATLAS detector is shown in Fig. 7.1. The cylindrical detector parts in the central region of the detector form the *barrel*, while the regions beyond that are referred to as the *end-caps*.

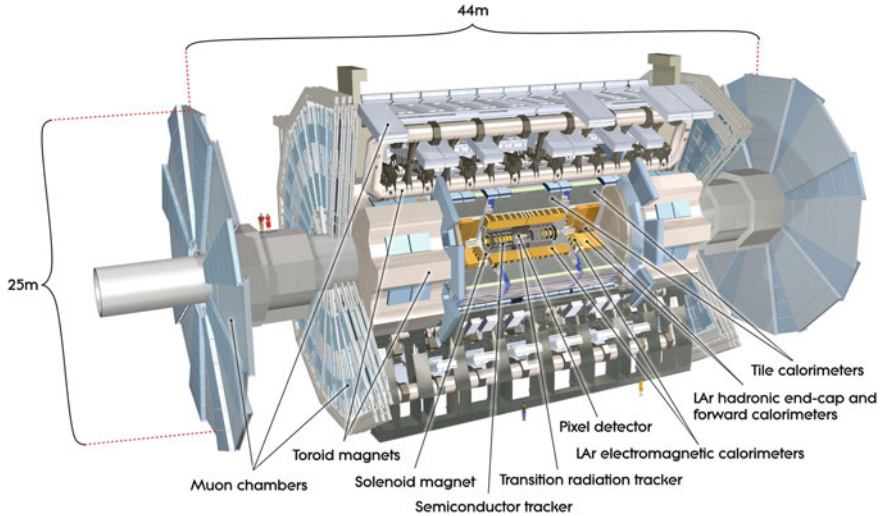


Fig. 7.1 Schematic view of the ATLAS detector [1]

The inner detector (ID) tracking system itself consists of three sub-detectors exploiting different techniques for particle registration: the pixel detector, the semiconductor tracker (SCT) and the transition radiation tracker (TRT). They are used for the reconstruction of trajectories (in the following also referred to as *tracks*) of charged particles as well as the position of an interaction, the *vertex*, and for electron identification. To measure the particle momenta based on the curvature of the reconstructed tracks, the ID tracking system is embedded in a 2 T strong solenoidal magnetic field.

ATLAS uses two different types of calorimeters: the electromagnetic calorimeter is a liquid-argon (LAr) sampling calorimeter while the hadronic calorimeter uses scintillator tiles. The electromagnetic calorimeter has an accordion-geometry allowing for full coverage in ϕ . It has a high granularity and is segmented in the longitudinal direction allowing for a high energy and position resolution. In the end-caps, the LAr technology is used also for the hadronic calorimeters. The forward calorimeter (FCAL) is a LAr calorimeter for both electromagnetic and hadronic energy measurement.

The ATLAS muon system is immersed into a toroidal magnetic field, generated by three magnets: one in the central region (0.5 T) and one in each of the end-cap regions (1 T). High momentum resolution is provided by three layers of high precision tracking chambers. This is helped by minimising multiple scattering due to the air core and the light and open structure of the muon system. A further key component are trigger chambers that have a timing resolution of 1.5–4 ns.

To single out potentially interesting events, ATLAS uses a three-level trigger system. The different levels use subsequently more and higher granularity information, reducing the rate stepwise from the \sim GHz interaction rate (at the design luminosity

of $10^{34} \text{ cm}^{-2} \text{ s}^{-1}$) to below 75 kHz at the first level and then further to the order of a few kHz and a few hundred Hz after levels 2 and 3, respectively. The third trigger level is referred to as event filter (EF). Event filter and level 2 are collectively known as the high-level trigger (HLT).

7.2 Tracking System

A schematic view of the inner detector tracking system with its three sub-detectors is shown in Fig. 7.2, its description in the following is based largely on Chap. 4 of Ref. [2]. The two innermost sub-detectors, the pixel detector and the SCT, provide high spatial resolution for track reconstruction in the region of $|\eta| < 2.5$. They are divided in a barrel part, in which they form concentric cylinders around the beam pipe, and an end-cap part, where they are grouped in disks perpendicular to the z -axis. In the region $|\eta| < 2.0$, the ID is completed by the TRT, with its straws parallel to the beam pipe in the barrel region and perpendicular to it, pointing radially outwards, in the end-caps.

The magnetic field for momentum measurements is generated by the central solenoid magnet and has a strength of 2 T.

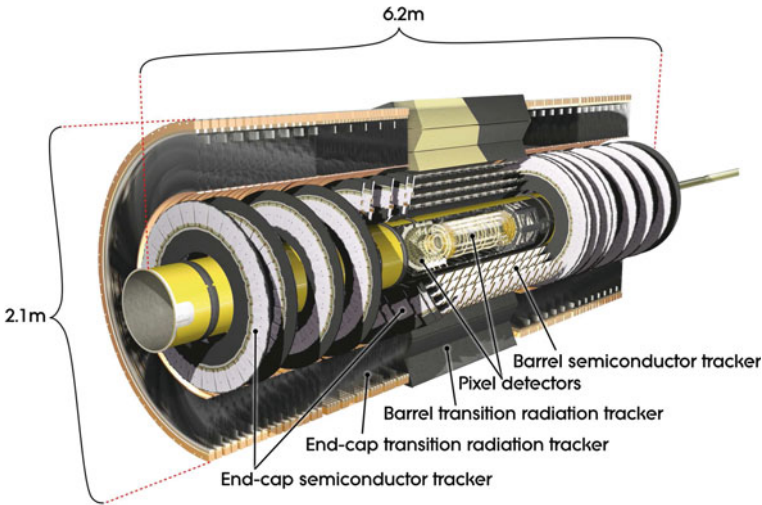
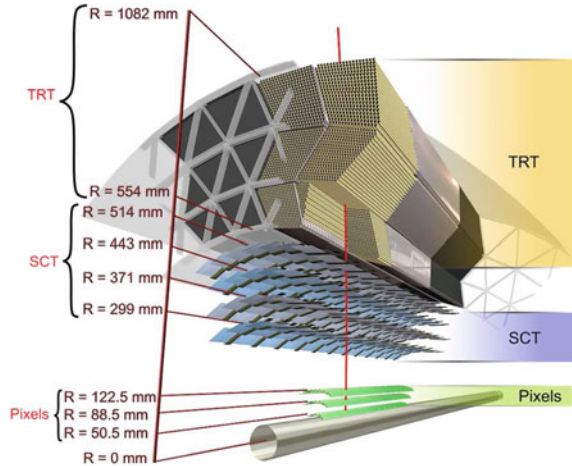


Fig. 7.2 Schematic view of the ATLAS inner detector [2]

Fig. 7.3 Drawing of a track of 10 GeV p_T traversing the ATLAS inner detector at $\eta = 0.3$ [2]



7.2.1 The Pixel Detector

The pixel detector comprises three layers (disks) in the barrel (end-cap) region. Positioned at a radial distance of 5 cm from the z -axis, the innermost pixel layer is the detector part closest to the interaction point. The outermost layer is located at $R = 12$ cm. The pixel detector provides the highest granularity of the three ID systems. In total, there are 1744 sensors with 46080 read-out pixels each, yielding approximately 80 million read-out channels. The pixels have a minimum size of $50 \times 400 \mu\text{m}^2$ in $(R - \phi) \times z$. In the barrel, an intrinsic accuracy of $10 \mu\text{m} \times 115 \mu\text{m}$ is achieved, while in the end-cap disks tracks can be reconstructed with an accuracy of $10 \mu\text{m} \times 115 \mu\text{m}$ in $(R - \phi) \times R$.

The high precision of the pixel detector is vital for the measurement of impact parameters and for the reconstruction of primary interaction and secondary decay vertices. The latter are needed in order to tag heavy-flavour quarks and τ -leptons via their decays. Here, especially the innermost layer plays an important role. The position of the pixel layers relative to the beam pipe and the other inner detector systems in the barrel region is depicted in Fig. 7.3.

7.2.2 The Semi-Conductor Tracker

The semi-conductor tracker is a silicon micro-strip detector with multiple layers, each layer consisting of two sets of strips with a stereo angle between each other, allowing for a two-dimensional position measurement. There are four such layers in the barrel region with one set of strips running parallel to the beam axis. The innermost layer is at a radial distance of about 30 cm from the z -axis, the outermost

layer at 51.4 cm. The spatial resolution achieved in the barrel region is $17\ \mu\text{m}$ in $(R - \phi)$ and $580\ \mu\text{m}$ in z . In the end-cap region, there are 9 disks with one set of strips running radially. They provide a spatial resolution of $17\ \mu\text{m}$ in $(R - \phi)$ and $580\ \mu\text{m}$ in R . There are 15912 sensors in total, each with 768 strips, resulting in approximately six million read-out channels for the SCT.

7.2.3 The Transition Radiation Tracker

In addition to contributing to the high precision track measurement, the TRT has the unique ability to identify electrons via the detection of transition radiation photons. The detector consists of straw tubes filled with a Xe-based gas mixture and interleaved with polypropylene fibres (barrel) or foils (end-caps), which serve as the transition radiation material. In the barrel, the TRT extends roughly from 55 to 108 cm in radial direction. In the end-cap it is arranged in two sets of wheels, extending from $z \simeq 0.8\ \text{m}$ to $z \simeq 2.7\ \text{m}$. The TRT provides track measurement in $(R - \phi)$ up to $|\eta| = 2.0$, based on a large number of typically 36 hits per track in the straw tubes. The accuracy of this position information is $130\ \mu\text{m}$ per straw. In total, it features about 350000 read-out channels.

The TRT is an important component for the momentum measurement since the high number of hits and the larger track length compensate for the lower precision per point compared to the silicon detectors. In addition, it has the merit of providing additional power for electron identification: the number of transition-radiation photons depends on the mass of the traversing particle, lower mass giving more photons, i.e. higher intensity. Thus, by applying two different thresholds, radiation from the very light electrons can be distinguished from, e.g. radiation emitted due to a pion, so that it is possible to discriminate between different types of particles.

7.3 Calorimeter System

Figure 7.4 shows a cut-away view of the calorimeter systems in ATLAS, consisting of the electromagnetic, hadronic and forward calorimeters. The following description is taken in large parts from Chap. 5 of Ref. [2].

The coverage in $|\eta|$ is up to 4.9, stretching over a range of various radiation environments and requirements of physics processes. The techniques that are employed for calorimetry are adapted to these different conditions depending on the η region: in the central region that corresponds to the coverage of the inner detector, the electromagnetic calorimeter has a fine granularity to allow for measurements of electrons and photons with high precision. The remaining parts of the calorimeter are mostly needed for reconstruction of jets and missing transverse energy, for which a lower granularity is sufficient.

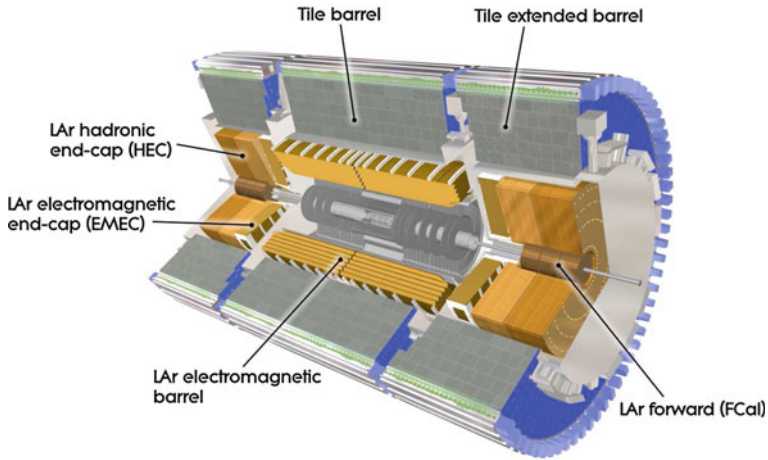


Fig. 7.4 Schematic view of the ATLAS calorimeters [2]

Another key feature of calorimeters is their containment for electromagnetic and hadronic showers, i.e. their depth. The total thickness of the EM calorimeters is at least 22 radiation lengths (X_0) in the central and 24 X_0 in the forward region. In terms of interaction length λ , the total thickness of electromagnetic and hadronic calorimeter combined amounts to approximately 10λ . This was found to be sufficient to reduce punch-through into the muon system and to measure highly energetic jets with good resolution. These features and the high $|\eta|$ -coverage assure a precise measurement of the missing transverse energy which is important for many searches for new physics, including the one presented in this work.

7.3.1 Electromagnetic Calorimeter

In the central region with $|\eta| < 1.475$, the electromagnetic (EM) calorimeter consists of two half-barrels, that extend in radial direction from 2.8 to 4 m. The half-barrels consist of 16 modules each, such that each module covers an angle $\Delta\phi = 22.5^\circ$. On each side of the detector there are two coaxial wheels: the outer one covers the region from $|\eta| = 1.375$ to $|\eta| = 2.5$, followed by the inner wheel that extends the coverage to $|\eta| = 3.2$. In total, they extend over radii from about 0.3 to 2.1 m. These wheels are referred to as the electromagnetic end-cap calorimeter (EMEC). The wheels are each segmented into eight wedge-shaped modules.

The EM calorimeter is a lead-LAr sampling calorimeter with kapton electrodes that are interleaved with lead absorber plates. Due to the accordion-shape of the electrodes the calorimeter is perfectly symmetric in ϕ , without any azimuthal cracks.

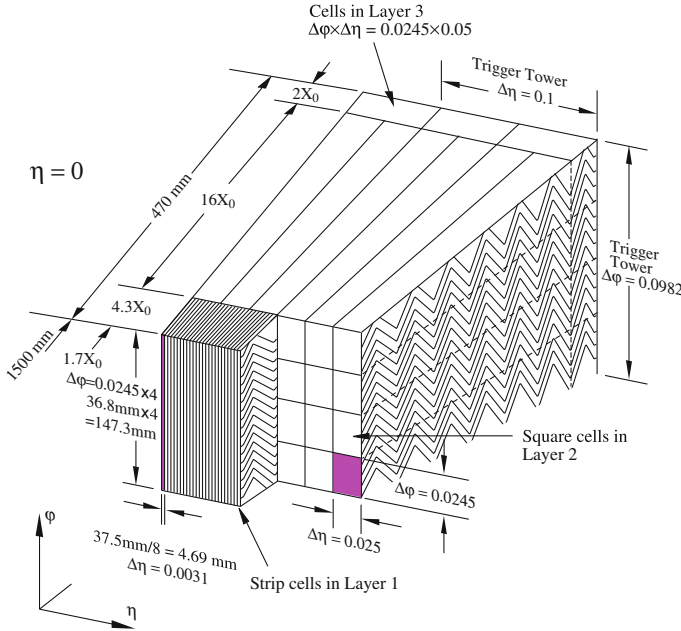


Fig. 7.5 Schematic view of a module of the electromagnetic calorimeter [2]

A special feature of the ATLAS calorimeter is its longitudinal segmentation: in the region $|\eta| < 2.5$, which is the one most relevant for precision measurements, the calorimeter has three segments, the first layer being finely segmented in η , which allows for a precise position measurement. Combining this information for photon-clusters with the information from the second calorimeter layer yields the η -direction of photons, which do not leave tracks in the inner detector. The fine segmentation of the first layer also allows to reconstruct individual photons from a particle decay into 2 photons with high accuracy even when they are close together. The largest fraction of an electromagnetic shower energy is collected in the second calorimeter layer, the third layer collects merely the tail of the shower and therefore has a coarser segmentation. The layout and cell dimensions of the different segments for a barrel module are shown in Fig. 7.5. In the end-cap inner wheel there are two segments with a coarser lateral granularity.

To correct for energy losses of electrons and photons before they enter the calorimeter, there is a presampler in the region $|\eta| < 1.8$, which consists of a 1.1 cm (0.5 cm) thick layer of LAr in the barrel (end-cap) region.

Including the presampler cells, a barrel module features 3424 and a module in the MEC roughly 4000 read-out cells.

The energy resolution in the EM calorimeter is parameterised in the following way:

$$\frac{\sigma}{E} = \frac{a}{\sqrt{E}} \oplus \frac{b}{E} \oplus c. \tag{7.2}$$

Here, a , b and c are η -dependent parameters. a is called the sampling term, b the noise term and c the constant term. The design value for the sampling term is approximately $10\%/\sqrt{E(\text{GeV})}$ at low $|\eta|$; at larger $|\eta|$ it is expected to worsen due to the increased amount of material in front of the calorimeter. The noise term is about $350 \times \cosh \eta \text{ MeV}$ for a typical cluster in the barrel for a mean number of interactions per bunch crossing of $\langle \mu \rangle = 20$. At high energies, the relative energy resolution approaches the constant term, which is 0.7% per design.

7.3.2 Hadronic Calorimeter

ATLAS features three hadronic calorimeters, that use different techniques and/or materials depending on the respective detector region.

The **tile calorimeter** is a sampling calorimeter that uses steel as the absorber and scintillating tiles as active material. It consists of a central barrel at $|\eta| < 1.0$ with a length of 5.8m and two extended barrels, each 2.6m long, in the region $0.8 < |\eta| < 1.7$, all of which are azimuthally divided into 64 modules. The inner radius of the tile calorimeter is 2.28m, the outer radius 4.25m. As the EM calorimeter, the tile calorimeter is segmented in three layers in depth: for the barrel the respective thicknesses in hadronic interaction length λ are 1.5, 4.1 and 1.8, for the extended barrels the corresponding numbers are 1.5, 2.6, and 3.3. The tiles are read out using photomultipliers on two sides by wavelength shifting fibres.

The **hadronic end-cap calorimeter** (HEC) covers an $|\eta|$ -range from 1.5 to 3.2, thus it overlaps slightly with the tile as well as the forward calorimeter. Copper plates serve as absorber and LAr as active medium. There are two wheels on each detector side, all of them divided in two segments in depth. Each wheel consists of 32 wedge-shaped modules. The energy resolution of the barrel and end-cap hadronic calorimeters is given as

$$\frac{\sigma_E}{E} = \frac{50\%}{\sqrt{E(\text{GeV})}} \oplus 3\% \quad (7.3)$$

Finally, there is the **forward calorimeter** (FCal). It is recessed by about 1.2m with respect to the EMEC front face in order to reduce neutron albedo in the inner detector cavity. This requires high density material in the FCal to compensate the limitation in depth. The FCal is divided into three modules per end-cap: the first one is made of copper and optimised for electromagnetic measurements, the other two use tungsten to measure mainly hadronic energy deposition. The modules consist of a metal matrix that contains the electrode structures, i.e. concentric rods and tubes, in longitudinal channels. The active medium is LAr and it is filled in the gaps between the rods and tubes in the channels. The energy resolution is

$$\frac{\sigma_E}{E} = \frac{100\%}{\sqrt{E(\text{GeV})}} \oplus 10\% \quad (7.4)$$

7.4 Muon System

The core piece of the muon system are the superconducting toroid magnets that provide the magnetic field needed for the momentum measurement based on the muon tracks. These tracks are reconstructed with high-precision tracking chambers. Additionally, the muon system is equipped with trigger chambers, providing fast signals. The different components are shown in the cut-away view in Fig. 7.6. The summary of the main features given here is based on Chap. 6 of Ref. [2].

The magnet system consist of three magnets, each containing 8 coils: the large barrel toroid in the region $|\eta| < 1.4$ and one end-cap toroid on each side of the detector at $1.6 < |\eta| < 2.7$. The latter are inserted into the central toroid and rotated by an angle of 22.5° , such as to provide radial overlap. Thus, the bending power in the transition region between the two systems is optimised. The resulting field is mostly orthogonal to the trajectories of traversing muons. While the eight coils of the central toroid each have their own cryostat, the end-cap coils on each side are immersed in one common cryostat. Reflecting the ϕ -symmetry of the toroids, the muon system is divided into octants.

In the barrel region, the chambers form three cylindric layers around the beam axis with radii of 5, 7.5 and 10 m, approximately. In order to allow for services to the solenoid magnet, the calorimeters and the inner detector, there is a gap in coverage at $|\eta| \simeq 0$. In the end-caps, there are four wheels perpendicular to the beam axis at distances $\sim 7.4, 10.8, 14, 21.5$ m, instrumented with chambers. They are arranged

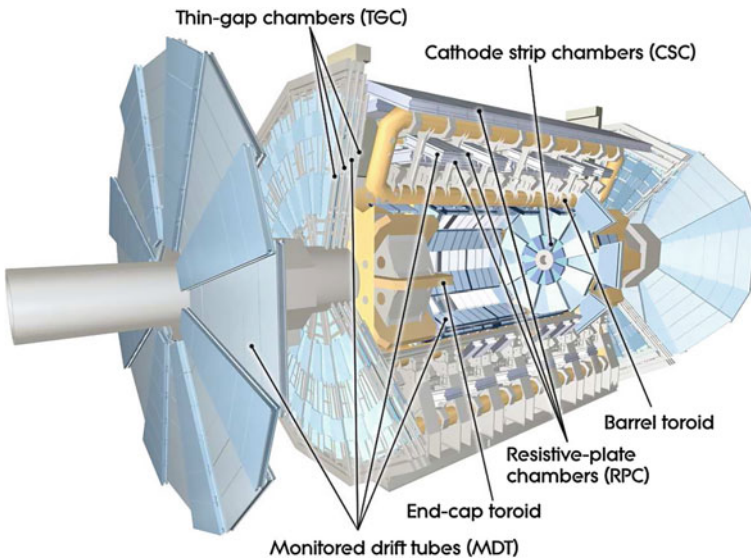


Fig. 7.6 Schematic view of the ATLAS muon systems [2]

in such a way that a straight track typically would traverse three layers of muon chambers.

There are two different types of muon chambers used for the position measurement: Monitored Drift Tube chambers (MDTs) provide the track coordinates in most of the detector regions within $|\eta| < 2.7$. They have the advantage of being simple in construction, have predictable mechanical deformations and provide very accurate measurements. One chamber contains three to eight layers of tubes; the average resolution is about $35\ \mu\text{m}$ per chamber. In the forward region, Cathode Strip Chambers (CSCs) are used in the innermost layer at $2.0 < |\eta| < 2.7$. These are multi-wire proportional chambers where the cathodes are divided into orthogonal strips. Thus, they measure both coordinates simultaneously, with a precision of $40\ \mu\text{m}$ in the bending and $5\ \text{mm}$ in the transverse plane. Compared to the MDTs they have a higher granularity and their time resolution is better, hence they are better suited for the high-rate environment close to the beam pipe.

For an accurate track reconstruction and momentum measurement a very good and stable alignment of the muon chambers with respect to each other and to the other detector components is vital. Thus, already during assembly, high precision techniques were employed and a sophisticated optical alignment system is in place within as well as between the chambers. The design performance goal is a 10% resolution for a 1 TeV track when using only the muon spectrometer for the track reconstruction. This means that a sagitta along the z -axis of $500\ \mu\text{m}$ has to be measured with a precision better than $50\ \mu\text{m}$.

In addition to the tracking chambers, there are fast muon chambers used for triggering, that deliver signals within 15–25 ns after the passage of a particle. Thus, they can be used to tag the beam-crossing. Moreover, they deliver well-defined p_T thresholds and provide the coordinate measurement in the direction orthogonal to the one measured by the tracking chambers. Two different techniques are used: in the barrel region $|\eta| < 1.05$, Resistive Plate Chambers (RPCs) are installed while the trigger information in the forward region, up to $|\eta| = 2.4$ is provided by Thin Gap Chambers (TGCs).

7.5 Special Systems

This section gives a brief overview of other systems integrated in the ATLAS trigger and readout system. There are detectors measuring particles at very large absolute values of pseudo-rapidity as well as systems providing information about the LHC beams.

7.5.1 *Forward Detectors*

The forward region of the ATLAS detector is equipped with three additional detector systems: two for luminosity measurements and one for the measurement of the centrality in heavy-ion collisions.

The main online luminosity monitor for ATLAS is LUCID (LUminosity measurement using a Cerenkov Integrating Detector), situated at a distance of 17 m on either side of the interaction point, which detects inelastic pp scattering in the forward region.

At ± 240 m from the interaction point the ALFA detector (Absolute Luminosity For ATLAS) is located. Its scintillating fibre trackers are located in Roman pots which can be moved as close as 1 mm to the beam. Due to the large distance to the ATLAS detectors, the signals from the ALFA system are at the edge of the latency allowed for inclusion in the first level trigger system (see Sect. 7.6.1).

The Zero-Degree Calorimeter (ZDC) is located on both sides of the interaction point at 140 m distance, which is the point of transition between two separate beam pipes into one common straight section pipe. The ZDC can measure neutral particles at $|\eta| \geq 8.2$, using alternating layers of quartz rods and tungsten plates.

7.5.2 *Beam Pickup Systems*

At 175 m on either side of the ATLAS interaction point, there is a BPTX station, consisting of four electrostatic button pick-up detectors [3], arranged symmetrically in the transverse plane around the beam pipe. ATLAS uses the signals for timing purposes, in particular to adjust the phase of the bunch clock sent by the LHC. A signal from one of the stations indicates a bunch passing through ATLAS, a coincidence of signals on both sides can be used to trigger on paired (i.e. potentially colliding) LHC bunches.

7.5.3 *Beam Conditions Monitors*

In order to prevent potential damage to the experiments from mis-directed beams, various beam monitoring systems are in place. One of them is the ATLAS Beam Conditions Monitor system (BCM) [4]. Its diamond sensors are installed at a distance of $z = 1.84$ m on either side of the interaction point at $|\eta| = 4.2$. Due to the symmetric configuration, signals originating from collisions at the IP will reach both BCM systems at the same time, $\Delta t = 0$, while stray protons reach the systems with a time difference of $\Delta t = 2z/c \simeq 12.5$ ns. Signals from the BCM system are used as input to the ATLAS trigger system, as they allow for example to trigger on beam gas or halo events.

7.6 Trigger System

Bunch crossings at the LHC occurred with a rate of roughly 15 MHz during run-I, but only a very small fraction are interesting events for physics analyses and the rate with which events can be read out and recorded for permanent storage is limited. Thus, the LHC experiments need a high performance trigger system to make best use of the bandwidth available and select interesting events as efficiently as possible. In the following, an overview of the trigger system will be given, based largely on Chap. 8 in Ref. [2]. Special emphasis will be given to the first trigger level and especially the central trigger, as parts of this work relate to its operation and upgrade.

7.6.1 Overview

The general architecture of the ATLAS trigger system is shown in Fig. 7.7. The rate reduction is performed in three steps: at the first trigger level (L1), a very limited subset of the detector information is used in order to take a decision within $2.5 \mu\text{s}$. To achieve this, the first level operates purely hardware-based, using custom-built electronics. The core piece which takes the actual trigger decision—the level-1 accept or L1A—is the Central Trigger Processor (CTP). It combines low-granularity infor-

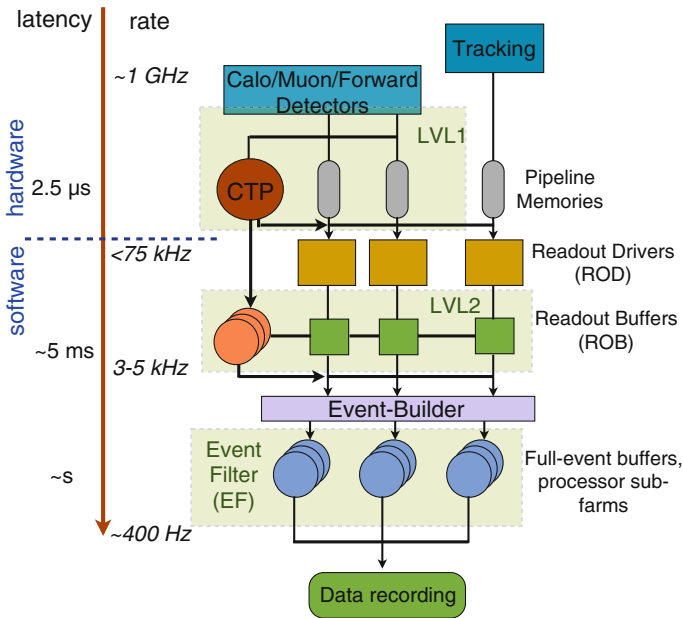


Fig. 7.7 Schematic view of the ATLAS trigger system. Adapted from Fig. 1 in Ref. [5]

mation from the calorimeter and muon triggers; no track information is exploited at L1. The maximum output rate of the L1 is limited to 75 kHz by the detector read-out. If an event is accepted at L1, so-called Region-of-Interest (RoI) information is passed on to the second trigger level (L2) and summary information is sent to the data acquisition system (DAQ). The RoI's are the η - ϕ —regions in which interesting activity in the calorimeter or muon system was detected. Information on the type of activity and the energy involved is also included. The second level uses software algorithms to process the full-granularity information from the RoI's, including also the tracker information. This reduces the rate down to the order of a few kHz with a latency of about 5 ms. If events pass the L2, event building is performed and in a final step offline reconstruction algorithms are run in the Event Filter (EF), the third trigger level, which reduces the rate to $\mathcal{O}(100\text{ Hz})$. The processing of an event at EF level proceeds within a few seconds. The second and third level are commonly referred to as High Level Trigger or HLT.

According to the signature detected, the events are assigned to different *data streams*—if they contain jets, τ -leptons or missing energy, they are written to the `JetTauEtmiss` stream, if they contain electrons or photons, they are assigned to the `Egamma` stream etc. An event can also end up in different streams if it contains the corresponding objects.

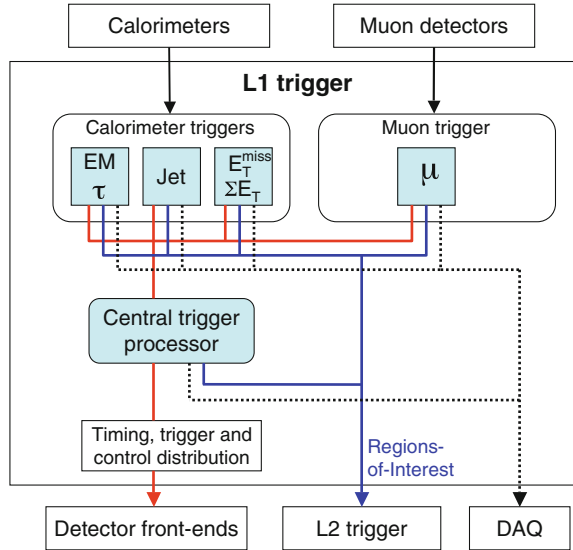
7.6.2 Level-1 Trigger

At the first trigger level, the decision is taken based on information from the trigger muon chambers (c.f. Sect. 7.4) and the calorimeter systems. The muon trigger chambers provide the number of candidates above a certain p_T threshold, there are six freely programmable thresholds in total. From the calorimeters, information on electron/photon¹ (e/γ) cluster energies, jets or hadronically decaying τ -leptons in terms of multiplicities above threshold are obtained as well as flags for the sums of total and missing transverse energy. For the e/γ and τ trigger there is the possibility to require isolation as well.

All this information is combined in the Central Trigger Processor together with additional information from the forward detectors and beam-pickup systems to form *trigger items*, which are logical combinations of requirements on the input data and are defined in the *trigger menu*. The maximum number of inputs allowed to be used in a menu is 160 and the total number of items is limited to 256, both by the CTP hardware. An overview of the first trigger level is shown in Fig. 7.8.

¹Since no tracking information is used at L1, electrons and photons cannot be distinguished at this stage.

Fig. 7.8 Schematic view of the ATLAS level-1 trigger system. The L1 decision is taken by the Central Trigger Processor based on inputs from calorimeter and muon triggers. Shown in red, blue and black, are the paths to the detector front-ends, L2 trigger and data acquisition system, respectively [2]

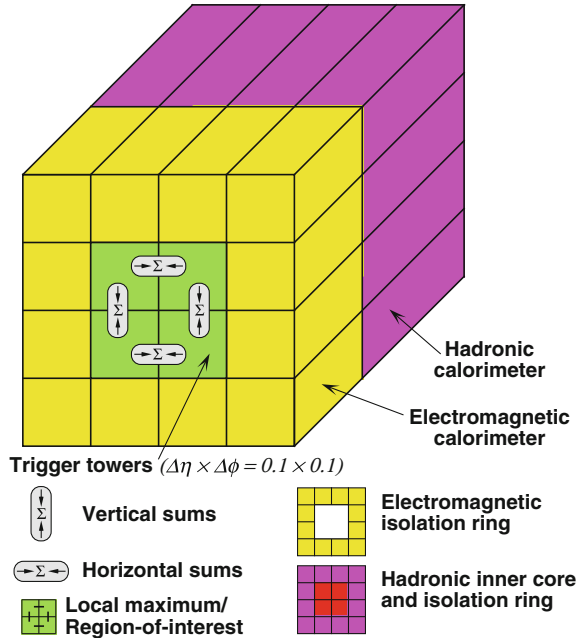


7.6.2.1 Calorimeter Trigger

For each bunch crossing, the first level calorimeter trigger, *L1Calo*, evaluates roughly 7000 analogue trigger towers and sends the results to the CTP. The towers are of dimensions 0.1×0.1 in $\Delta\eta \times \Delta\phi$ in most regions of the detector, a bit larger in the forward regions, and include energies from the electromagnetic and hadronic calorimeters.

The *L1Calo* system has three main sub-systems: the pre-processor, the jet/energy processor (JEP) and the cluster processor (CP). With the pre-processor, the analogue input signals are digitised and a digital filter is applied to assign them to the correct bunch crossing. Moreover, it determines the transverse energy values that are the actual inputs to the trigger algorithms from look-up tables (LUT). The CP is responsible for the identification of e/γ and τ candidates whose E_T lies above a certain programmable threshold and which might be required to be isolated. The τ and e/γ identification is performed up to $|\eta| < 2.5$, which is the region for precision measurement with the tracking system and the electromagnetic calorimeter. Figure 7.9 shows a graphical illustration of the applied trigger algorithm: a sliding-window algorithm scans over all possible 4×4 combinations of trigger towers, searching for 2×2 clusters for which at least one of the possible sums of two electromagnetic towers (2 horizontal, 2 vertical) is above a predefined threshold. In the case of τ triggers, the 2×2 tower clusters from both the electromagnetic and the hadronic calorimeter are added and compared to a given threshold. Isolation is implemented by checking the energies of the surrounding ring of 12 towers in both the electromagnetic as well as the hadronic calorimeter against a programmable veto threshold. In case of e/γ , also the 2×2 tower core in the HCal is used for isolation requirements.

Fig. 7.9 Graphical illustration of the algorithm to identify electron/photons or τ 's [2]



In order to avoid multiple counting of the same cluster candidate, the sum of the four central electromagnetic and hadronic towers has to be a local maximum with respect to its 8 closest neighbours. The position of this local maximum is what is sent as RoI information to L2. There are 8 sets of threshold and isolation criteria reserved for e/γ candidates and 8 sets that can be used for either e/γ or τ triggers.

The jet trigger elements sent to the JEP are 0.2×0.2 sums in $\Delta\eta \times \Delta\phi$ including both the electromagnetic and the hadronic calorimeter. They are used to identify jets and to calculate global sums of scalar and missing transverse energy. For the jet triggers, information up to $|\eta| < 3.2$ is used, whereas the missing and total transverse energy triggers include the forward calorimetry up to $|\eta| < 4.9$ which is especially important for the missing E_T calculation. The FCal is also used for forward-jet triggers.

The jet trigger algorithm can be defined to use windows of two, three or four jet elements width, corresponding to window sizes of 0.4, 0.6, or 0.8 in η and ϕ . The transverse energy sum in the windows is calculated and compared to a predefined threshold. Multiple counting is again avoided by considering only local maxima, which also define the RoI coordinates. Eight combinations of threshold value and window size can be defined. In addition, there are four thresholds for the total transverse energy and eight for the missing transverse energy to be reported to the central trigger.

In both processors, the multiplicities of the respective object above the various thresholds are counted and subsequently sent to the CTP. In case of an L1A, the

input data, intermediate calculations and trigger results from the L1Calo system are read out and sent to the data acquisition system. Moreover, the multiplicities, types and positions of τ , jet and e/γ candidates are sent to the RoI builder for use by the second trigger level.

7.6.2.2 Muon Trigger

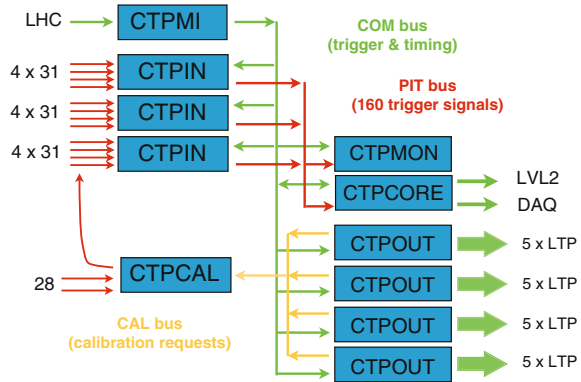
The muon trigger uses information from the RPCs in the barrel and the TGCs in the end-caps, based on three trigger stations each. The algorithm looks for coincidences in different trigger stations within one *road*, which tracks the path of a muon from the interaction point through the detector. The width of this road depends on the p_T threshold that is to be applied—the higher the threshold the narrower the road. There is a total of six programmable thresholds, three for the low- p_T (6–9 GeV) and three for the high- p_T (9–35 GeV) triggers. The information from the barrel and end-cap triggers is combined in the muon-to-CTP interface (MUCTPI), which subsequently sends multiplicity information for the 6 thresholds to the CTP. There are three bits for the multiplicity information of a threshold, allowing for a maximum value of 7. Multiplicities larger than 7 are sent as a value of 7 as well. The MUCTPI also performs residual overlap removal between barrel and end-cap trigger sectors and in ϕ -direction between neighbouring barrel trigger sectors. It sends information not only to the CTP but also to the L2 and DAQ. A formatted copy of the information on candidate muon tracks together with the candidate multiplicity are provided to the DAQ. The 16 highest p_T candidates are forwarded to the L2.

7.6.3 Central Trigger

As mentioned above, the Central Trigger Processor is the piece of the L1 trigger where the actual decision (L1A) is made following the item logic defined in the trigger menu. Moreover, trigger summary information is sent to the L2 trigger and the DAQ. The CTP also provides per-bunch as well as accumulated scaler data for monitoring purposes and is responsible for the distribution of timing signals.

The inputs used by the CTP are the information on candidate threshold multiplicities and energy flags from the calorimeter and muon systems as well as inputs from other systems like forward detectors and beam pick-up systems. Internally, the CTP provides random triggers from two random generators, two prescaled clocks and eight bunch group triggers. The bunch groups (BG) are lists of *bunch crossing identifiers* (BCID) sorted into certain categories. For example, the *empty* BG contains all those bunch crossings that do not contain any protons, the *filled* or *physics* BG are those BCIDs for which collisions are expected in ATLAS.

Fig. 7.10 Schematic view of the central trigger system, its boards and the signal distribution. Adapted from Fig. 11 in Ref. [6]



7.6.3.1 Architecture

The central trigger system consists of a number of modules in a standard VME crate which are connected via bus lines as presented in Fig. 7.10. The CTPMI module is the machine interface and receives the timing signals from the LHC, i.e. the 40 MHz bunch clock as well as the orbit signal, which is issued with the revolution frequency of the LHC. Before reaching the CTPMI, the signals are passed through the RF2TTC (radio-frequency to trigger, timing and control) interface module, where they are cleaned and delays can be applied to adjust phase drifts. Such drifts occur for example due to temperature differences affecting the lengths of the fibres used to transmit the LHC signals across the ring to the ATLAS counting room. For standalone running, the CTPMI module is also capable of generating the timing signals internally. Moreover, it generates the *event counter reset* (ECR). The signals are transmitted via the COM bus (for common, green).

The inputs from external systems arrive at one of three CTPIN boards, each of which provides four connectors, allowing for a total of 372 inputs. The input signals are synchronised with the bunch clock and aligned with respect to each other. Each CTPIN also features monitoring scalars that can be incremented when either a single signal or a given pattern of inputs is present. A subset of 160 inputs is selected via switch matrices and transmitted via the Pattern-In-Time (PIT, red) bus to the CTPCORE module, which takes the trigger decision, and to the CTPMON module for per-bunch monitoring. The interface to the sub-detectors are four CTPOUT modules, which receive the trigger signals from the COM bus and fan them out to the local trigger processors (LTPs) of the sub-detector TTC partitions via 5 CTP links each. In turn, the CTPOUT modules receive the BUSY signals and calibration requests from the sub-detectors. The BUSY is sent to the COM bus, while the calibration requests are routed via the CAL bus (yellow) to the CTPCAL module. From there, the calibration requests are sent via front-panel to one of the CTPIN boards. In addition, the CTPCAL module provides front-panel inputs for beam-pick-up systems and test triggers, for example.

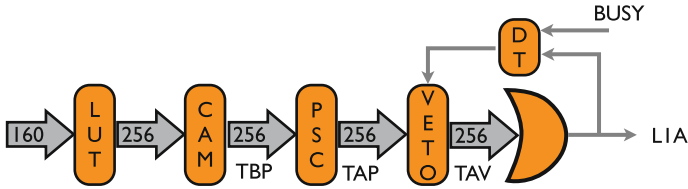


Fig. 7.11 Schematic view of the trigger path in the CTPCORE module. Adapted from Fig. 14 in [6]

7.6.3.2 L1A Generation and Readout Data

The trigger path of the CTPCORE module is shown in Fig. 7.11. The 160 inputs from the PIT bus are fed into look-up tables (LUTs), which return 256 *trigger conditions*, for example that 2 muons have passed a threshold of 4 GeV. Such a condition would be labeled 2MU4. The output of the LUTs are further combined using content-addressable memories (CAM), yielding up to 256 triggers before prescales (TBP) according to the logic in the trigger menu. The items can include conditions on the internal triggers like the bunch group. For example, items that are to be considered only when they fired in a bunch crossing with actual collisions can be ANDed with the physics bunch group. The next step in the L1A generation is the prescaling, done with the help of 24-bit prescalers (PSC) and yielding the 256 triggers after prescales (TAP). Finally, the triggers can be masked or vetoed, where the veto mask is the logical OR of a general programmable mask, the dead-time and the general BUSY of the detector. The L1A signal is the logical OR of the resulting triggers after veto (TAV).

There are two types of dead-time the CTPCORE can generate: the *simple* dead-time with a programmable fixed number of untriggered BCs after each L1A, and the *complex* dead-time, which is implemented as a leaky-bucket algorithm and thus limits the number of L1A in a given time interval. Two leaky-bucket algorithms can be defined for trigger items with different priority. Higher priority means that an item is affected less by dead-time.

In addition to the L1A, the CTP generates a number of other signals. The trigger type word is built from the TAVs. It contains information on which kind of triggers fired in the respective event and can be used to steer the event data processing. The CTP also creates identifiers for the event fragments: the L1ID or event number, and the BCID. The BCID is reset by the bunch counter reset (BCR) signal received from the TTC system. The event counter reset signal (ECR) generated by the CTPMI resets the L1ID. To keep the event numbering unique, the *extended* L1ID is formed from an 8-bit ECR counter and the 24-bit L1ID. The current *luminosity block* is also part of the data sent by the CTP. A luminosity block (or lumiblock) is defined as the shortest time interval for which the integrated luminosity after dead-time and prescaling can be determined. This helps to reduce data loss, since in case of a detector failure only the affected lumiblocks have to be discarded. Therefore, the luminosity blocks should be as small as possible, while still containing enough data to estimate the

luminosity reliably. In ATLAS, the duration is typically of the order of one to two minutes. At a luminosity block transition, the generation of triggers is paused until the lumiblock number in a register of the CTPCORE is incremented. For each event, the value from this register is included in the readout data.

The information for the triggering bunch is sent to the L2 trigger system, while a superset including information from a programmable number of bunches before and after the triggering bunch is sent to the read-out system (ROS) from where it can be obtained for debugging and monitoring purposes.

Per-bunch monitoring of PIT signal rates is performed in the CTPMON module. It decodes and selects the inputs that are to be monitored. It is even possible to monitor groups of inputs, for example when one input is just one multiplicity bit and thus has no real meaning on its own. The counts (or rates) of each input is monitored on a bunch-by-bunch bases.

7.7 Data Handling

In this section, a short introduction to data taking with ATLAS and how these data is processed and stored shall be given.

7.7.1 Data Taking

The data taking with ATLAS is steered by the `RunControl` system (RC) [7], which is the software that steers the detector during data taking, getting and reacting to feedback from all the subsystems, sending central commands and communicating between the systems. Once all parts of the ATLAS detector are ready for data taking and the LHC is in stable beam mode, a *run* can be started. Each run is assigned a unique *run number*. The trigger and data acquisition system (TDAQ) is configured for each run via the OKS [8] conditions data base. Here, for example, the parameters for the dead-time algorithms are defined.

As described in Sect. 7.6.3.2, a run is further divided into luminosity blocks to minimise data loss in case of detector failure. The luminosity blocks can later be flagged according to different data quality criteria and this information is summarised in *good runs lists* (GRL) for use by physics analysis. During a run, information on the state of the various detector components is constantly written to the online conditions data base COOL.² This is needed for the reconstruction of the event data later.

²<https://twiki.cern.ch/twiki/bin/view/Persistence/Cool>.

7.7.2 Data Processing and Storage

ATLAS uses a software framework called Athena [9], which is based on the C++ Gaudi framework [10] originally developed for LHCb. The software is split into *projects* each of which contains a number of *packages* to structure the code and which again can have levels of sub-packages. The lowest level packages contain the actual C++ source code, following a common design.

The Athena software is used for digitisation and reconstruction of actual data as well as in simulation. The processing happens in several steps, and derivatives of the raw data are produced, eventually providing also data formats that can be used outside of Athena to simplify analysis tasks. The main processing steps and data formats are described in the following.

If an event passes the full trigger chain, the complete detector is read out, delivering the RAW data in byte-stream format. In this format, one event is about 1.6 MB. The processing of the enormous amount of data created by the LHC experiments is done on the *Grid* [11], a world wide network of computing resources, structured in different layers, or *tiers*. The first stage of the data processing happens at the *Tier-0* at CERN: first calibrations are applied and reconstruction algorithm produce the Event Summary Data (ESD) within about 48 h. The ESD still contain all event information, now in the form of detector level objects like tracks and their hits, calorimeter cells and clusters, entries in the muon system. The size of a single event is still at the level of 1 MB. This is drastically reduced by approximately a factor of 10 when producing Analysis Object Data (AOD) which—as the name indicates—contains the information needed for physics analysis, i.e. objects like electrons, muons, jets and their properties like energy, momentum, position.

The Tier-0 copies the RAW data to permanent storage devices at CERN and also to Tier-1's for storage or reprocessing. The reconstruction output is also distributed to the Tier-1's, of which there are 10. They are used to run time-consuming calibration and alignment jobs, or to re-run reconstruction, which is necessary from time to time since with the understanding of the detector evolving and necessitating updates of the calibration and alignment and the adaption of algorithms. The Tier-1's store the most up-to-date versions of the ESDs and AODs on disk for analysis and can be used for large analysis jobs. Moreover, the data is further distributed to approximately 35 Tier-2's, which are the main facilities to run analysis jobs on AODs and simulation jobs. The Tier-2's keep the AOD's available on disk, together with other data formats, such as Derived Physics Data (DPD). These contain a further reduced subset of the data, storing only certain objects and only information on these objects relevant for the specific analysis. The typical event size in these DPDs is of the order of 10 kB. The data used for the analysis presented in this work are D3PDs, which contain the event and object information in form of n-tuples or *trees* that can be processed with ROOT [12]. There are also Tier-3's that provide access to the grid resources and local storage for the end-user data.

7.8 Detector Simulation

The generation of final state particles in the collision simulation has been described in Sect. 4.4. The output of the event generators, i.e. the particles not decaying immediately, are used as input to the detector simulation [13] in form of standardised HepMC files [14]. The interaction of the particles in and their passing through the detector are simulated with the help of the GEANT4 [15, 16] particle simulation toolkit and databases containing the detector geometry and conditions. In the final step, the *digitisation*, the energy deposits are converted into voltages and currents as would be obtained in the real detector. The result is written out in a format identical to the one used for data taking such that the simulated events can be passed through the same reconstruction software.

GEANT4 contains descriptions for numerous physical processes as well as for the transportation of particles through detectors geometries. The numerical models for interactions—both electromagnetic as well as hadronic—are collected in *physics lists*; they comprise a large set of particles, materials and elements and can be used in a wide energy range. The GEANT4 toolkit is used in conjunction with a detailed description of the ATLAS detector. Two databases are used to store the information on the geometry: The *geometry database* contains basic constants as for example volume dimensions, rotations and positions, material properties like density, and it also contains links to external files that store, for example, the magnetic field maps. Various conditions data like calibrations, dead channels, or misalignment are stored in the *conditions database*. Misaligned or distorted geometries can be used to study systematic effects. Many layouts are available given that the description is constantly evolving as the material budget is updated over time.

Each particle is propagated through the detector and energy deposits in the sensitive regions are recorded as *hits*, which store the amount of deposited energy, the position and time, and are written to the *hit file*. These hits are converted into detector responses, called *digits*, in the digitisation step. A digit is produced when the current or voltage of a read-out channel exceeds a predefined threshold within a certain time window. In the real detector, these digits are the inputs to the read-out drivers (RODs) of the detector electronics. In the simulation, the ROD functionality is emulated and for each sub-system a Raw Data Object (RDO) is created. It is in the digitisation step, that hits from the hard scattering process are overlaid with those from beam gas or beam halo interactions, cavern backgrounds, minimum-bias events or long-lived particles, and that detector noise is added to the event. The L1 trigger decision is simulated as well, but without discarding events.³

In the simulation, for each event *truth* information is stored. At the generator level, the truth information contains a history of the interactions from incoming to outgoing particles and whether a particle is to be passed through the detector simulation or not. If it is, then truth tracks and decay information is stored, for example the location of photon conversion. During digitisation, Simulated Data Objects (SDOs) are created from the truth record, matching the hits to the truth particles. In the reconstruction,

³The simulation of the Central Trigger will be discussed in detail in Sect. 9.2.

this information is processed further and can be used in the analysis of simulated data to study for example the detector efficiency or systematic effects.

The detailed simulation of an event in the detector is a very computing power and time intensive process, simulation of one event can take up to several minutes. In order to provide simulation samples with sufficient statistics, therefore, various fast simulation programs have been developed. One of them which is particularly relevant for this work is ATLFast-II [17]. Here, the simulation step is sped up but the events are still passed through the full reconstruction.⁴ The reduction in computing time is achieved by using a simplified detector geometry either in the inner detector or the calorimeter or both.

7.9 Object Reconstruction

In this section, a brief overview of the reconstruction of the objects that are used in the analysis presented in part IV of this work will be presented. Electrons will be discussed in Sect. 7.9.1, muons in Sect. 7.9.2, jets in Sect. 7.9.3 and missing transverse energy in Sect. 7.9.4.

7.9.1 Electrons

The analysis presented in this work will only use electrons reconstructed in the central part of the detector, within $|\eta| < 2.47$. Therefore, only the reconstruction procedure for this region will be outlined in this section, based on the description in Ref. [18].

The starting point for the reconstruction are clusters in the electromagnetic calorimeter, EM clusters. These are searched for by a sliding-window algorithm with a window size of 0.075×0.125 in $\Delta\eta \times \Delta\phi$, corresponding to 3×5 towers of size 0.025 in both $\Delta\eta$ and $\Delta\phi$. The tower energy corresponds to the sum of energies of cells from all calorimeter layers. If this energy exceeds 2.5 GeV, the tower is considered as a seed for an EM cluster.

Once a cluster is found, it is checked whether it can be matched to a well-reconstructed inner detector track that is extrapolated into the EM calorimeter. Depending on whether or not such a track exists and is consistent with being due to a converted photon the cluster is considered as an electron, converted photon or unconverted photon. If it is compatible with an electron, the cluster energy is determined from calorimeter cells corresponding to 3×7 cells in the second layer of the EMB or 5×5 cells in case of the EMEC. The energy is calibrated in several steps [19], following slightly different procedures in data and simulation. A simulation based response calibration to restore the original energy is derived using multivari-

⁴There is another fast simulation that does not apply the actual reconstruction but smears truth objects according to the detector resolutions to get an approximation for the physics objects.

ate techniques and applied to the cluster energy in simulation. In data, uniformity corrections and a longitudinal inter-calibration between the calorimeter layers is performed before the response calibration is applied. On top of the simulation based correction, calibration factors are derived from $Z \rightarrow e^+e^-$ events in data. For the simulation, smearing factors derived from the same event sample are applied to reproduce the slightly worse resolution in data.

To discriminate against backgrounds mimicking real electrons, different sets of identification criteria are defined based on variables describing the transverse and longitudinal shower profiles. Three reference criteria are labelled *loose*, *medium* and *tight* and provide increasing background rejection. The corresponding cuts have been refined during run-I to account for the changed pile-up conditions, leading to ++ *menus* of criteria. The definitions used for the 2012 data taking can be found in Ref. [19].

7.9.2 Muons

For the reconstruction of muons ATLAS relies on the information from the muon system (MS), the inner detector (ID) and to some degree from the calorimeters, as described in Ref. [20]. The reconstruction of tracks in the MS proceeds in two steps: firstly, each layer of muon chambers is checked for a local track segment and subsequently the local segments are combined into complete tracks. In the ID, the tracks have to fulfil the following requirements in order to be considered as stemming from a muon:

- at least 5 SCT hits
- at most 2 active Pixel or SCT sensors traversed without hits
- at least 9 TRT hits in the region of full TRT acceptance.

The information from MS, ID and calorimeter is combined in different ways, yielding four different *types* of muons. For *Stand-Alone* (SA) muons, only tracks from the MS are used and interpolated to the point of closest approach to the beam pipe. The advantage is that SA muons can be used beyond the coverage of the tracking system. The main type of muons are *combined* (CB) muons, for which tracks reconstructed independently in the ID and MS are combined. *Segment-tagged* (ST) muons are reconstructed by starting from an ID track and extrapolating it to the MS. If the extrapolated track can be matched to at least one local segment, the track is considered corresponding to a muon. This provides the possibility to increase the acceptance for muons that crossed only one MS chamber layer. Finally, there are *calorimeter-tagged* (CaloTag) muons. In this case, a track from the ID is associated to an energy deposit in the calorimeter compatible with a minimum ionising particle. As no information from the MC is used, this muon type can be used to recover acceptance in un-instrumented regions of the MS. Among the types listed above, the CB muons are the ones of highest purity.

The reconstruction of all types including MS tracks (SA, CB, ST) is performed with two different algorithms (*chains*). When using chain 1, a statistical combination of the parameters of ID and MS tracks is performed. This chain is therefore labelled STACO. Chain 2 does a global refit of the hits from both systems; it is referred to as MuId.

The muon reconstruction efficiency is close to 99% within $|\eta| < 2.5$ and samples of $J/\Psi \rightarrow \mu^+\mu^-$, $\Upsilon \rightarrow \mu^+\mu^-$ and $Z \rightarrow \mu^+\mu^-$ are used to study the momentum scale and resolution.

7.9.3 Jets

Jets have been introduced in Sect. 4.1 as collimated bundles of hadrons emerging from the fragmentation of partons. As such, they will leave energy deposits in the calorimeters. These *calorimeter jets* are reconstructed from clusters in the calorimeter, which are the jet *constituents*. In the simulation, *truth jets* are formed with the same algorithm but using the stable particles after the hadronisation as constituents. Labelling the energy measured for a calorimeter jet E_{reco} and the one for the corresponding truth jet E_{truth} , the *jet energy resolution* (JER) is given by

$$\frac{\sigma}{E} = \sqrt{\left\langle \left(\frac{E_{\text{reco}} - E_{\text{truth}}}{E_{\text{truth}}} \right)^2 \right\rangle - \left\langle \frac{E_{\text{reco}} - E_{\text{truth}}}{E_{\text{truth}}} \right\rangle^2}. \quad (7.5)$$

The jet energy response \mathcal{R} is define as

$$\mathcal{R} = \left\langle \frac{E_{\text{reco}}}{E_{\text{truth}}} \right\rangle. \quad (7.6)$$

In the following, the jet reconstruction used for the analysis presented in this work will be described, which is largely based on Ref. [21].

The jets are reconstructed from topological calorimeter clusters or *topo-clusters* [22]. The cluster formation makes use of the signal-to-noise ratio (S/B) of each cell. Here, the cell noise includes in addition to electronic noise also contributions from pile-up, which improves the calorimeter performance in the presence of pile-up. The further benefit of the topological clusters is that they fully exploit the fine segmentation of the ATLAS calorimeter in following the shower development. The clustering starts from a seed cell with a signal-to-noise ratio greater than 4. Iteratively, neighbouring cells are included in the cluster if they feature an S/B greater than 2. The first neighbouring cells with a smaller S/B are still included in the cluster, but the iteration stops there. Once the clusters have been formed in that way, it is checked whether they are consistent with actually being overlapping clusters in which case they are split. The splitting is based on finding local maximum cells that have to have an energy above 500 MeV. New clusters are formed around these cells, using

only cells that are included in the parent clusters. Cells that end up in several clusters belonging to two different local maxima are added to each of them with weights that depend on their energy and distance to the cluster centroids. The energy of a topo-cluster is the sum of all the included cell energies, while its mass is set to 0. The position is derived by weighting the η and ϕ of all constituent cells with their absolute energy.

In this way, the topo-clusters are reconstructed at the electromagnetic scale (EM scale), i.e. at the baseline scale for the energy deposited by electromagnetic showers. Since the ATLAS calorimeter is non-compensating, the energy measured for hadronic showers is lower than the true energy. There are different techniques to correct for this, the one applied in the jet reconstruction for this analysis is called *local cluster weighting* (LCW or short LC). In this scheme, the clusters are classified as being either mainly electromagnetic or mainly hadronic, and calibration factors derived from single charged or neutral pion simulations are applied to each cell. The weights depend on the cluster energy and the energy density in the cell. The clusters formed and calibrated in this way are the inputs to the jet finding algorithm.

One of the most-used algorithms for jet reconstruction in ATLAS is the anti- k_t algorithm [23]. It is a sequential clustering algorithm, recombining the jet constituents (i.e. LC calibrated topo-clusters in this case) based on a distance measure. The basic idea is to define distances d_{ij} between constituents i and j as well as the distance of a constituent i to the beam (B), d_{iB} , and then find the smallest of these distances considering all constituents. If the smallest distance is a d_{ij} , the two constituents are recombined, if d_{iB} is the smallest distance, then constituent i is considered a jet and removed from the list of constituents. There are different recombination schemes, the default in ATLAS is the four-momentum recombination scheme, i.e. the four-momenta of the recombined constituents are added to give the four-momentum of the jet. The procedure is repeated until all constituents are recombined.

For the anti- k_t algorithm, the distance measures are defined as

$$\begin{aligned} d_{ij} &= \min(k_{t,i}^{2p}, k_{t,j}^{2p}) \frac{\Delta_{ij}^2}{R^2}, \\ d_{iB} &= k_{t,i}^{2p}, \end{aligned} \tag{7.7}$$

with $\Delta_{ij} \equiv (y_i - y_j)^2 + (\phi_i - \phi_j)^2$ and $k_{t,i}$, y_i and ϕ_i being the transverse momentum, rapidity and azimuthal angle of constituent i . R is a radius parameter and p is a parameter defining the relative power of energy versus geometrical scales. In the case of the anti- k_t algorithm, $p = -1$. The negative sign of p causes the clustering to proceed from the hardest to the softest constituents and the results are circular hard jets. If there are two jets close together, the harder one will stay circular while the softer jet will miss the overlap region. Positive values of p and in particular $p = 1$ correspond to k_t -clustering algorithms, which sum the softest constituents first and subsequently add the harder constituents. In both cases, the jets have the important properties of being infra-red and collinear safe, i.e. the final set of jets does not

change when an infinitely soft parton is added or a parton splits into a collinear pair of partons.

The choice of the radius parameter is a compromise between gathering all constituents belonging to a jet, i.e. emerging from the same parton, and not being affected too much by the underlying event. The jets for this thesis are reconstructed with the `FastJet` software [24], using the anti- k_t algorithm, the four-momentum recombination scheme and a distance parameter $R = 0.4$.

In addition to the local cluster weighting, further calibration is applied to the jet energy scale (JES) in several steps [21]. First, the jets are corrected for the energy offset caused by pile-up interactions [25].⁵ In a next step, the jet direction is adjusted to point back to the reconstructed vertex instead of the nominal interaction point. Then, the inverse of the jet energy response obtained from simulation after including the LCW calibration is applied as a correction factor in bins of pseudo-rapidity. Finally, a residual correction derived from in-situ measurements is applied to jets in data. All of these in-situ measurements are based on transverse momentum balancing techniques between the jet and a well-measured reference object. These objects can be Z-bosons, photons, a system of low p_T jets or another jet. After the final calibration step, the jets are referred to as LC+JES calibrated. The threshold for reconstruction as a jet is $p_T > 7 \text{ GeV}$.

7.9.4 Missing Transverse Energy

There are different possibilities to reconstruct the missing transverse energy, here, only the one applied for the E_T^{miss} variant used in part IV of this work shall be described in some detail, based on information from Ref. [26].

Generally, the E_T^{miss} can be split into two constituents, one comprising energy deposits in the calorimeter, the other contributions from the muon system. The x - and y -component of the missing transverse energy can accordingly be written as

$$E_i^{\text{miss}} = E_i^{\text{miss,calo}} + E_i^{\text{miss,\mu}} \quad , \quad \text{with } i = x, y. \quad (7.8)$$

With this, one obtains for the magnitude and ϕ -coordinate the following:

$$E_T^{\text{miss}} = \sqrt{(E_x^{\text{miss}})^2 + (E_y^{\text{miss}})^2} \quad , \quad \phi^{\text{miss}} = \arctan(E_y^{\text{miss}}/E_x^{\text{miss}}). \quad (7.9)$$

The E_T^{miss} flavour used in this work is an object based missing transverse energy: calorimeter cells are attributed to one reconstructed object (in a specific order of priority) and calibrated accordingly. The order is as follows: electrons, photons, hadronically decaying τ 's, jets and finally muons. These priorities help to resolve

⁵The pile-up correction technique has been updated for the 2012 data set, the remaining corrections are derived in the same way as in 2011. Final results for the 2012 JES calibration are not available yet.

ambiguities and overlaps between objects. For example, if a cell was already associated to an electron, it will not be considered for any other object. Cells that are not associated to any object are included in the missing E_T calculation in the so-called *cell out* term, $E_T^{\text{miss,cellOut}}$.

The calorimeter term can thus be written as the following sum

$$E_i^{\text{miss,calo}} = E_i^{\text{miss,e}} + E_i^{\text{miss,\gamma}} + E_i^{\text{miss,\tau}} + E_i^{\text{miss,jets}} + E_i^{\text{miss,softjets}} + E_i^{\text{miss,calo,\mu}} + E_i^{\text{miss,cellOut}}$$

with $i = x, y$.

(7.10)

Each term corresponds to the negative sum of the cell energies that have been calibrated according to the object they are associated to, including cells up to $|\eta| = 4.5$:

$$E_x^{\text{miss,term}} = - \sum_{j=1}^{N_{\text{cell}}^{\text{term}}} E_j \sin \theta_j \cos \phi_j$$

$$E_y^{\text{miss,term}} = - \sum_{j=1}^{N_{\text{cell}}^{\text{term}}} E_j \sin \theta_j \sin \phi_j$$
(7.11)

where $N_{\text{cell}}^{\text{term}}$ is the total number of cells associated to a term, E_j the energy of cell j , and θ_j and ϕ_j are that cell's polar and azimuthal angle, respectively.

The first three terms in Eq. 7.10 are built out of cells associated to electrons, photons or hadronically decaying τ 's, respectively. The jet term includes cells belonging to jets with a $p_T > 20 \text{ GeV}$, while cells associated to jets with $7 \text{ GeV} < p_T < 20 \text{ GeV}$ enter the *soft jet* term. The calorimeter muon term accounts for the energy loss of muons in the calorimeter and the *cellOut* term, finally, sums all topocluster cells that do not enter any of the other terms.

For the calculation of the muon term, the momenta of muon tracks within $|\eta| < 2.7$ are considered:

$$E_i^{\text{miss,\mu}} = - \sum_{\text{muons}} p_i^\mu, \quad \text{with } i = x, y.$$
(7.12)

To suppress contributions from fake muons, in the region of coverage by the tracking system ($|\eta| < 2.5$) only combined muons are used (cf. Sect. 7.9.2). Special attention has to be given to the treatment of the energy loss of muons in the calorimeter, which is different for isolated and non-isolated muons, respectively. A muon is considered isolated if there is no reconstructed jet within a distance $\Delta R = 0.3$. If the muon is isolated, the energy deposited in the calorimeter is *not* added to the calorimeter term but is included in the p_T of the muon and hence in the muon term. For non-isolated muons, however, the energy lost in the calorimeter is added to the $E_T^{\text{miss,calo,\mu}}$ term and only the muon momentum measured in the spectrometer, i.e. after energy loss, is used for the muon term. In the region $2.5 < |\eta| < 2.7$ only the muon spectrometer measurement is used for both isolated and non-isolated muons. There are small

inactive regions also inside the muon spectrometer acceptance, namely at $|\eta| = 0$ and $|\eta| \sim 1.2$. The contribution for muons at $|\eta| \sim 1.2$ can be recovered from segments matched to inner detector tracks.

To each cell considered in the E_T^{miss} calculation, a calibration is applied depending on the object the cell was associated with. For the $E_T^{\text{miss},e}$ term, *medium* electrons with a p_T greater than 10 GeV are used that have the default electron calibration applied. The photons considered in $E_T^{\text{miss},\gamma}$ have to fulfil the *tight* requirements and have a $p_T > 10$ GeV at the EM scale [27]. The τ -term is reconstructed from τ -jets that pass the *tight* identification for τ 's [28] and have a transverse momentum calibrated with the local hadronic scheme (LCW) above 10 GeV. The same scheme is used for the calibration of the jet and cellOut terms. The jets entering the $E_T^{\text{miss},\text{jet}}$ term in addition have the jet energy scale factor applied.

7.10 Luminosity Determination

The search for rare new physics processes requires a data set with large statistic. A measure for the amount of data delivered to an experiment is the integrated luminosity. Its determination is described in detail in Ref. [29] and shall be summarised in this section.

Equation (6.1) can be rewritten in the following form:

$$\mathcal{L} = \frac{n_b f_r n_1 n_2}{2\pi \Sigma_x \Sigma_y} \quad (7.13)$$

with the number of colliding bunches n_b , and the number of protons in bunch 1(2), $n_1(n_2)$. Σ_x and Σ_y are a measure for the horizontal and vertical beam width.

On the other hand, the luminosity can be expressed as the ratio of the rate (R_{inel}) and cross section σ_{inel} for inelastic pp collisions

$$\mathcal{L} = \frac{R_{inel}}{\sigma_{inel}} = \frac{\mu n_b f_r}{\sigma_{inel}}. \quad (7.14)$$

In the second part of the above equation it was used that for a storage ring the rate can be expressed in terms of revolution frequency, number of bunches and average number of interaction per bunch, μ .

As outlined in Sect. 7.5, ATLAS uses a number of different detectors for luminosity determination. They all measure the interaction rate per bunch crossing with a certain efficiency ε , yielding the visible interaction rate $\mu_{vis} = \varepsilon\mu$, corresponding to the visible cross section $\sigma_{vis} = \varepsilon\sigma_{inel}$. With this, Eq. (7.14) becomes

$$\mathcal{L} = \frac{\mu_{vis} n_b f_r}{\sigma_{vis}}. \quad (7.15)$$

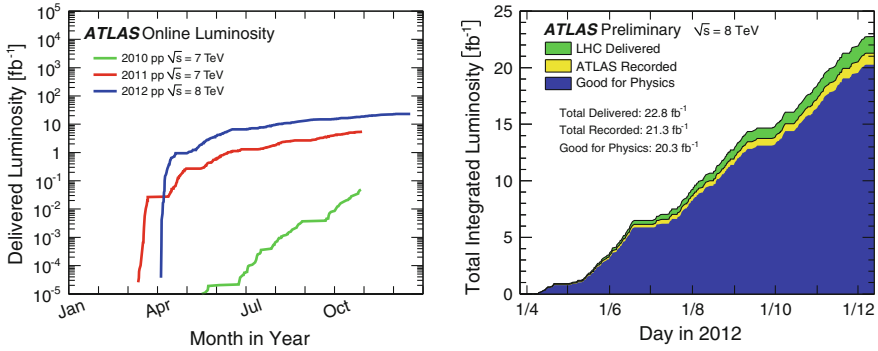


Fig. 7.12 *Left* cumulative luminosity of pp collisions versus day delivered to ATLAS during stable beams for 2010 (*green*), 2011 (*red*) and 2012 (*blue*). *Right* accumulated luminosity as a function of day in 2012. Total delivered, recorded and deemed good for physics are shown in *green*, *yellow* and *blue* [30]

The calibration of the luminosity scale for a given detector thus returns to a measurement of the visible cross section. Combining Eqs. (7.13) and (7.15) yields the following expression:

$$\sigma_{vis} = \mu_{vis} \frac{2\pi \Sigma_x \Sigma_y}{n_1 n_2}. \quad (7.16)$$

The bunch population product $n_1 n_2$ is determined by beam current measurements provided by the LHC group. The other parameters in Eq. (7.16) are measured in beam separation scans or *van der Meer* (vdM) scans. In such a scan, the beams are separated in well defined steps both in the horizontal and the vertical direction and the visible interaction rate is measured as a function of the separation. The peak values give an estimate of μ_{vis} in Eq. (7.16), the widths of the obtained curves provide a measure of $\Sigma_{x,y}$.

In this way, the visible cross section for each of the luminosity detectors was measured several times during run-I to provide adequate luminosity calibration over the entire data taking period. With the detectors calibrated, the luminosity for each lumiblock or any other period of time can be derived, taking dead-time and trigger prescales into account. The left plot in Fig. 7.12 shows the luminosity collected by ATLAS for all three years of run-I data taking. This illustrates how confidence in and understanding of the accelerator has improved since the first 7 TeV data taking in March 2010. The LHC has delivered luminosities of roughly 36 pb^{-1} during the first full year of data taking 2010, 5 fb^{-1} in 2011 and 20 fb^{-1} during the 2012 running. On the right in Fig. 7.12 the accumulated luminosity in 2012 is displayed. The total luminosity delivered by the LHC is shown in green, the fraction recorded by ATLAS is displayed in yellow. The blue histogram shows the fraction of data suitable for physics analysis, which amounts to approximately 90% of the total delivered luminosity.

For this 2012 data set that is to be used in the analysis presented in this work, the luminosity uncertainty on the total luminosity is $\pm 2.8\%$. It is derived, following the same methodology as that detailed in Ref. [29], from a preliminary calibration of the luminosity scale derived from beam-separation scans performed in November 2012.

References

1. The ATLAS Collaboration (2008) Computer generated images of ATLAS. <http://cds.cern.ch/record/1095924>
2. The ATLAS Collaboration (2008) The ATLAS experiment at the CERN large Hadron collider. JINST 3:S08003. doi:[10.1088/1748-0221/3/08/S08003](https://doi.org/10.1088/1748-0221/3/08/S08003)
3. Ohm C, Pauly T (2010) The ATLAS beam pick-up based timing system. Nucl Instrum Methods A623:558–560. doi:[10.1016/j.nima.2010.03.069](https://doi.org/10.1016/j.nima.2010.03.069). arXiv:0905.3648 [physics.ins-det]
4. Cindro V et al (2008) The ATLAS beam conditions monitor. J Instrum 3(02):P02004. <http://stacks.iop.org/1748-0221/3/i=02/a=P02004>
5. Schoerner-Sadenius T (2003) The Trigger of the ATLAS experiment. Mod Phys Lett A 18:2149–2168. doi:[10.1142/S0217732303011800](https://doi.org/10.1142/S0217732303011800). arXiv:hep-ex/0307078 [hep-ex]
6. Ask S et al (2008) The ATLAS central level-1 trigger logic and TTC system. J Instrum 3(08):P08002. <http://stacks.iop.org/1748-0221/3/i=08/a=P08002>
7. Lehmann-Miotto G et al (2010) Configuration and control of the ATLAS trigger and data acquisition. In: Nuclear instruments and methods in physics research section A: accelerators, spectrometers, detectors and associated equipment 623.1 (2010). 1st international conference on technology and instrumentation in particle physics, pp 549–551. ISSN: 0168-9002. doi:[10.1016/j.nima.2010.03.066](https://doi.org/10.1016/j.nima.2010.03.066). <http://www.sciencedirect.com/science/article/pii/S0168900210006303>
8. Soloviev I (2002) OKS Documentation (User’s Guide, Tools Manual, Reference Manual). Technical report. ATLAS DAQ/EF P-1 Technical Note 33. Geneva: CERN. <http://atlas-onlsw.web.cern.ch/Atlas-onlsw/components/configdb/docs/oks-ug/2.0/pdf/OksDocumentation.pdf>
9. ATLAS Computing: technical design report (2005) Technical Design Report ATLAS. Geneva: CERN. See also <http://atlas-computing.web.cern.ch/atlas-computing/packages/athenaCore/athenaCore.php>
10. Barrand G et al (2000) GAUDI - the software architecture and framework for building LHCb data processing applications, pp 92–95
11. Eck C et al (2005) LHC computing Grid: Technical Design Report. Version 1.06 (20 June 2005). Technical Design Report LCG. Geneva: CERN
12. Antcheva I et al (2009) ROOT - a C++ framework for petabyte data storage, statistical analysis and visualization. Comput Phys Commun 180.12. 40 YEARS OF CPC: a celebratory issue focused on quality software for high performance, grid and novel computing architectures, pp 2499–2512. ISSN: 0010-4655. doi:[10.1016/j.cpc.2009.08.005](https://doi.org/10.1016/j.cpc.2009.08.005). <http://www.sciencedirect.com/science/article/pii/S0010465509002550>
13. The ATLAS Collaboration (2010) The ATLAS simulation infrastructure. Eur Phys J C 70:823–874. doi:[10.1140/epjc/s10052-010-1429-9](https://doi.org/10.1140/epjc/s10052-010-1429-9). arXiv:1005.4568 [physics.ins-det]
14. Dobbs M, Hansen JB (2001) The HepMC C++ Monte Carlo event record for high energy physics. Comput Phys Commun 134:41–46. doi:[10.1016/S0010-4655\(00\)00189-2](https://doi.org/10.1016/S0010-4655(00)00189-2)
15. Agostinelli S, others (2003) GEANT4: a simulation toolkit. Nucl Instrum Methods A506:250–303. doi:[10.1016/S0168-9002\(03\)01368-8](https://doi.org/10.1016/S0168-9002(03)01368-8)
16. Allison J et al (2006) Geant4 developments and applications. IEEE Trans Nucl Sci 53:270. doi:[10.1109/TNS.2006.869826](https://doi.org/10.1109/TNS.2006.869826)
17. The ATLAS Collaboration (2007) Performance of the ATLAS fast simulation ATLFAST. Technical report. ATL-PHYS-INT-2007-0-5. Geneva: CERN

18. The ATLAS Collaboration (2014) Electron and photon energy calibration with the ATLAS detector using LHC Run 1 data. ArXiv Pre-Prints. [arXiv:1407.5063](https://arxiv.org/abs/1407.5063) [hep-ex]
19. The ATLAS Collaboration (2014) Electron efficiency measurements with the ATLAS detector using the 2012 LHC proton-proton collision data. Technical report. ATLAS-CONF-2014-032. Geneva: CERN
20. The ATLAS Collaboration (2014) Measurement of the muon reconstruction performance of the ATLAS detector using 2011 and 2012 LHC proton-proton collision data. ArXiv Pre-Prints. [arXiv:1407.3935](https://arxiv.org/abs/1407.3935) [hep-ex]
21. The ATLAS Collaboration (2014) Jet energy measurement and its systematic uncertainty in proton-proton collisions at $\sqrt{s} = 7$ TeV with the ATLAS detector. ArXiv Pre-Prints. [arXiv:1406.0076](https://arxiv.org/abs/1406.0076) [hep-ex]
22. Lampl W et al (2008) Calorimeter Clustering Algorithms: Description and Performance. Technical report. ATL-LARG-PUB-2008-002. ATL-COM-LARG-2008-003. Geneva: CERN
23. Cacciari M, Salam GP, Soyez G (2008) The anti-kt jet clustering algorithm. JHEP 04:063. doi:[10.1088/1126-6708/2008/04/063](https://doi.org/10.1088/1126-6708/2008/04/063). [arXiv:0802.1189](https://arxiv.org/abs/0802.1189) [hep-ph]
24. Cacciari M, Salam GP (2006) Dispelling the N3 myth for the kt jet-finder. Phys Lett B641:57–61. doi:[10.1016/j.physletb.2006.08.037](https://doi.org/10.1016/j.physletb.2006.08.037). [arXiv:hep-ph/0512210](https://arxiv.org/abs/hep-ph/0512210) [hep-ph]
25. The ATLAS Collaboration (2013) Pile-up subtraction and suppression for jets in ATLAS. Technical report. ATLAS-CONF-2013-083. Geneva: CERN
26. The ATLAS Collaboration (2012) Performance of missing transverse momentum reconstruction in proton-proton collisions at 7 TeV with ATLAS. Eur Phys J C72:1844. doi:[10.1140/epjc/s10052-011-1844-6](https://doi.org/10.1140/epjc/s10052-011-1844-6). [arXiv:1108.5602](https://arxiv.org/abs/1108.5602) [hep-ex]
27. The ATLAS Collaboration (2010) Electron and photon reconstruction and identification in ATLAS: expected performance at high energy and results at 900 GeV. Technical report. ATLAS-CONF-2010-005. Geneva: CERN
28. The ATLAS Collaboration (2010) Tau Reconstruction and Identification Performance in ATLAS. Technical report. ATLAS-CONF-2010-086. Geneva: CERN
29. The ATLAS Collaboration (2013) Improved luminosity determination in pp collisions at $\sqrt{s} = 7$ TeV using the ATLAS detector at the LHC. Eur Phys J C73:2518. doi:[10.1140/epjc/s10052-013-2518-3](https://doi.org/10.1140/epjc/s10052-013-2518-3). [arXiv:1302.4393](https://arxiv.org/abs/1302.4393) [hep-ex]
30. ATLAS Experiment - Public Results (2014) <https://twiki.cern.ch/twiki/bin/view/AtlasPublic/LuminosityPublicResults>. Accessed Sep 2014

Part III
Operation and Upgrade of the Central
Trigger

Chapter 8

Operation of the Central Trigger During Run-I

As described in Sect. 7.6.3, the Central Trigger receives the timing signals from the LHC and is responsible for their distribution through the experiment. Any shift, glitch or misalignment of the timing signals will lead to a loss of data, since for example the event fragments cannot be assembled correctly anymore. In this sense, the CTP constitutes a single point of failure, and a detailed monitoring of the timing signals is essential for an effective data taking and good quality data.

Various monitoring features not only for the timing but for different parts of the system are in place, which are typically implemented as C++ code. The monitoring can roughly be grouped into two categories: there is *online* monitoring, which is running constantly during data taking, and *offline* monitoring, which performs checks on the collected data after the recording. The online monitoring analyses the status of the system continuously and provides real time feedback in form of numbers, histograms and log messages, for example. This provides the possibility to detect and solve problems in due course and to prevent loss of data. On the other hand, the information stored in the histograms and log files during the data taking can also be used afterwards for debugging purposes. The offline monitoring is used for data quality checks to identify and flag lumiblocks that are not fit for physics analysis.

In the following, two online timing monitoring features that have been developed and implemented as part of this work will be presented: Sect. 8.1 discusses the monitoring of the *orbit signal*, in Sect. 8.2 the *bunch group* monitoring is described. Before deploying any new software at the experiment, the functionality and stability is ensured by testing the software with a copy of the Central Trigger system in the laboratory.

8.1 Orbit Monitoring

The orbit signal is issued once per LHC turn, i.e. once every 3564 bunch clock ticks, as there are 3564 bunch crossings (BC) within one LHC turn. Together with the 40 MHz bunch clock the orbit signal is needed for the definition of the bunch crossing identifier (BCID). Thus, a missed or wrongly issued orbit signal will lead to an incorrect assignment of the BCID. The BCID is used to cross check whether event fragments with the same L1ID originate from the same bunch crossing. If the BCID assignment is off, this cross check will not work. It is therefore important to catch any irregularity in the orbit signal as quickly as possible. For this purpose, there are two 12-bit counters in the CTPMI module, counting the numbers of short and long orbits, respectively, where a short orbit is one with less than 3564 bunch clock ticks, a long orbit correspondingly one with more than 3564 ticks. In addition, there is one 12-bit register storing the length of the shortest orbit detected (in units of bunch clock ticks), and one 16-bit register for the length of the longest orbit.

The counters and registers are accessible via `Read` and `Reset` methods. These methods are called whenever the `probe` function is issued by the `RunControl`, cf. Sect. 7.7.1. The `probe` function can be used by all sub-systems as a trigger for regular status and monitoring updates. It is typically called with a period of 10 s during data taking. In case of the orbit monitoring, the entries read from the counters and registers are filled into histograms that are constantly updated during a data taking run and published to the ATLAS monitoring web page. In case an irregular orbit is detected, a warning message is issued. After each reading, the counters and registers are reset, and the orbit monitoring is gapless.

There are two types of histograms for the orbit monitoring: one shows the state of the irregular orbit counters as a function of time since the beginning of a run, the other displays the distribution of the length of the irregular orbits that have been detected (in BCs). There is one histogram of each type for the short and the long orbits, respectively.

The correct filling of the histograms and issuing of warnings is verified by sending test patterns to the CTPMI module with deliberately wrong orbit lengths. An example of the plots simulated in this way is shown for the short orbits in Fig. 8.1. On the left-hand side, the number of counts of short orbits as a function of time is shown. Every 10 s, when the `probe` function is called, the counters are read out and reset afterwards. This is why the number of counts is not constantly increasing but even decreasing from time to time—the entries correspond to the state of the counter since the last reset. This kind of timeline histograms is useful to know at which time during the run something went wrong in order to correlate it with potential other problems that were seen around the same time.

Another interesting information is the length of the irregular orbits. If it is always the same, i.e. the orbit signal is shortened or lengthened by a fixed number of BCs, this can indicate a different kind of problem—for example reflections in a cable—than randomly scattered values. Hence, the distribution of the short and long orbits is also monitored separately, a simulated example is shown for the short orbits in

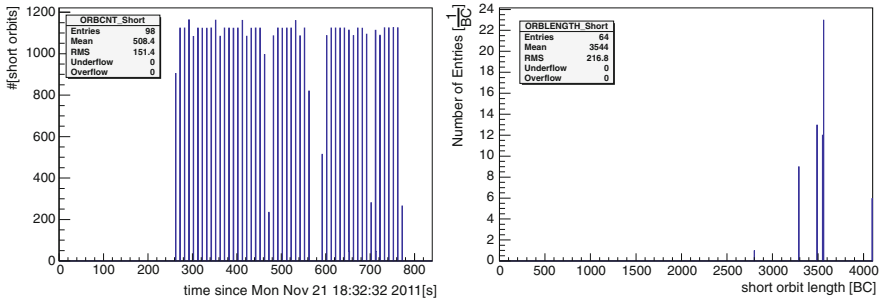


Fig. 8.1 Simulated short orbit signal monitoring histograms: the number of orbits with less than 3564 BC ticks read from the counters as a function of time since the beginning of the run (*left*) and distribution of the short orbit lengths (*right*)

the right panel of Fig. 8.1. In a run without any such timing problem, the histograms will remain empty and this has been the case in all runs since the monitoring was introduced. The histograms are, however, still useful, as they help to exclude a wrong orbit signal as the cause of timing problems when they are empty.

8.2 Bunch Group Monitoring

For the formation of trigger items, the classification of the bunch crossings into bunch groups is used, as is described in Sect. 7.6.3. Triggers for physics analysis may be combined with a logical AND with the *physics bunch group*, which contains those bunch crossings for which bunches should collide at the ATLAS interaction point. In this case, the trigger is only accepted if it fires in a bunch crossing where collisions are indeed expected. On the other hand, this means, that when the BCIDs are misaligned or an incorrect bunch group is loaded during a run, data will be lost. To prevent this, a monitoring of the physics bunch group as been developed and will be described in the following. The functionality is implemented in a C++ class called `CTPMBNCIDMatch`.

The monitoring relies on the fact that some of the triggers are known to be well timed-in, i.e. they almost exclusively fire in bunch crossings where there are actual collisions in ATLAS. Candidates for such triggers are the inputs from the electromagnetic calorimeter, labeled `EMX`, where X indicates the threshold in GeV. For example, an electromagnetic calorimeter trigger with a threshold of 3 GeV will be referred to as `EM3`. Information from the BCM described in Sect. 7.5.3 can also be used to reconstruct the physics bunch group. The BCM sends bits encoding several configurations of hits in the two systems on either side of the detector. Apart from inputs indicating whether or not there was an in-time hit on one side and an out-of-time hit on the other side, labeled `BCM_AtO` and `BCM_CtOA`, respectively, there is also a 3-bit input encoding combinations of in-time hits on both sides, called `BCM_Comb`. The

latter is especially suitable for the monitoring discussed here since it is expected to give high rates only in the collision bunches. This is not true to the same extent for the muon triggers, that suffer from large background, typically giving signals 1 BC after the collision, also referred to as afterglow. Analogously to the EM triggers, the muon triggers are labeled MUX for a certain thresholds X in GeV.

An important feature of the triggers suitable for this monitoring is that the rate in collision BCs is well above the background level to distinguish unambiguously between collision and other BCs. This disfavors the use of EM triggers with a high threshold, which will have a much lower rate than those with lower thresholds.

The triggers that are to be used for the monitoring during a specific run can be selected via the OKS database [1] at the beginning of the run from a predefined list. The default setting is to use EM3 and BCM_Comb.

The inputs for the monitoring are rate histograms produced from the counters in the CTPMON module, that are able to monitor the rates of each trigger input for each BCID, i.e. with a rate of 40 MHz. Some examples from run 214553 [2] are shown in Fig. 8.2. These histograms show the average rate accumulated during a run per BCID. The plots on the right hand side are zoomed-in versions of the left plots, the top row shows the histograms for EM3, the middle row for BCM_Comb and the bottom row for MU4. The plot for EM3 shows two clearly separated bands—one at a rate of roughly 2 kHz and one close to 0. In the zoomed plot the clear pattern of alternating filled and unfilled bunches is visible. A similar scenario is observed for the BCM_Comb trigger: here as well appears one band at high rate and the zoomed plot shows the alternating filling pattern, only that in this case the low rate is essentially 0 due to the combination of different requirements in this trigger that effectively reduces the fake rate. On the contrary, the plot for the muon trigger shows two bands with non-zero rates. This is caused by the leakage of triggers into empty bunch crossings. It is thus not easily possible to reconstruct the collision bunches from histograms like the one for MU4.

8.2.1 Histogram Digitisation

In order to re-derive the physics bunch group, histograms like the one for EM3 are ‘digitised’, i.e. the bin contents are set to either 1 or 0, depending on whether the rate is above or below a certain threshold. This threshold is derived in an iterative procedure from mean and RMS values of the bands in the histogram. For the well timed-in triggers that are to be used, there is typically only one high and one low band, which is due to background. The basic idea is to quantify the position and spread of the two bands and to place the threshold in between, safely away from either of the bands. This is done by first projecting the histograms onto the y-axis, such that a bump is obtained for each band. Then the mean value of the projection is obtained via the corresponding method implemented in ROOT. In the typical case of two clearly separated bands, the mean will lie somewhere in the region in between and can be used directly as the threshold for the digitisation. Depending on the running

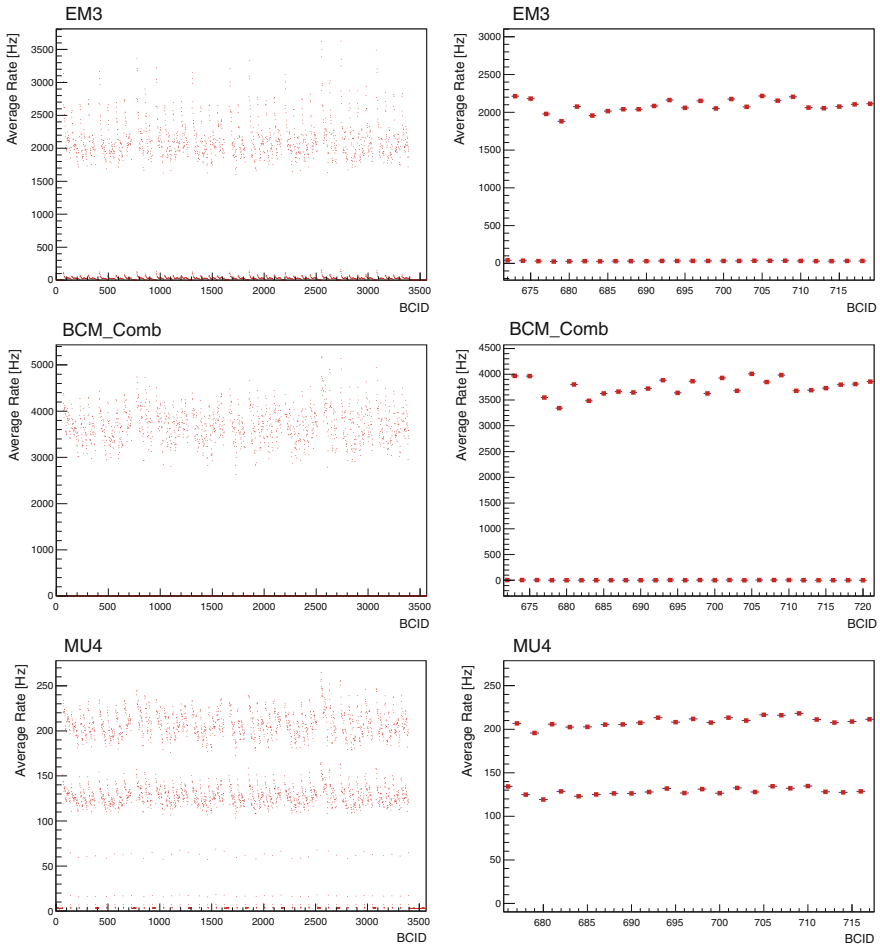


Fig. 8.2 Example per-bunch monitoring histograms from the CTPMON module for run 214553 [2]. The plots on the right hand side are zoomed-in versions of the ones on the left. The *top* row shows the EM3 trigger, the *middle* row BCM_Comb and the *bottom* row MU4

conditions and triggers used, however, there might be more involved configurations, some of which are attempted to be caught by considering various relations between mean and RMS values as detailed in the following.

In addition to the mean of the complete projection, the mean and RMS values of the regions above and below the mean are estimated using the same method in ROOT. In the following, the mean of the projection will be referred to as μ with RMS r , the mean above (below) this value will be labeled μ_H (μ_L) and the corresponding RMS value r_H (r_L). In the simplest case of two well separated bands, μ_H should give the mean value of the upper band and r_H its spread and analogously μ_L and r_L for the lower band. In the following, different special cases will be discussed in the order in

which they are checked in the code. They are considered exclusively, i.e. when one condition is met, the following are not checked further.

The first complication considered is the case where one of the RMS values is larger than the corresponding mean value, which might occur if there are actually two bands in the region above or below μ . The procedure to resolve these is the following: if $r_H > \mu_H$, then $\mu_{temp} = 0.5(\mu + \mu_H)$ is defined, and the mean and RMS values for the histogram region above μ_{temp} are determined. If this RMS value is still larger than the corresponding mean, the procedure is repeated, using μ_{temp} instead of μ . This is repeated until $r_{temp} < \mu_{temp}$, but at most 50 times. After this, the threshold, t , is set either to μ_{temp} , in case the RMS is 0, or to the mean value above μ_{temp} , reduced by four times the corresponding RMS value, i.e. $t = \mu_{temp,H} - 4r_{temp,H}$. The iteration is done in an analogous fashion in case that $r_L > \mu_L$, the threshold being set to either μ_{temp} or $\mu_{temp,L} + 3r_{temp,L}$. The cut values are defined empirically and were found to give good discrimination in the most often occurring cases, although not capturing all special configurations.

The next case considered is that either μ_H or μ_L differ by only 5% from μ . This is interpreted as only one band being present, which could occur, for example, when there are only very few colliding bunches in a run. In this case, the single band found is considered background and the threshold is set to $t = \mu + 5r$.

In case that $\mu > \mu_L + 5r_L$ and $\mu < \mu_H - 5r_H$, i.e. there are most likely two well defined and widely separated bands, the threshold is set to the mean value μ .

If $\mu_L < 0.01\mu_H$, i.e. the spacing between the bands is large, the threshold is set to $\mu_H - 5r_H$.

In case none of the above conditions is met, the threshold is initially set to $\mu_L + 5r_L$. In addition, the following boundaries are defined: $b_H = \mu_H - 3.5r_H$ and $b_L = \mu_L + 3.5r_L$. If necessary, the threshold is decreased iteratively until it is below at least one of the boundaries.

In all cases, corresponding log messages are generated. Once the threshold is defined, the CTPMON rate histograms can be digitised and the resulting pattern of colliding bunches (i.e. the bins filled with 1) can be compared to the bunch group loaded in the configuration, as will be explained in the next section.

8.2.2 Comparing Bunch Patterns

The comparison of the BCID patterns for colliding bunches is based on finding gaps between the bunch trains and comparing their number, size and position. A reference histogram is created from a list containing the physics BCIDs, which is obtained from the configuration database. The histogram again has 3564 bins and the contents for the bins corresponding to the physics bunches are set to 1. The list and hence the reference histogram are updated whenever the `UpdateBunchgroup` method is called. This typically happens once in the beginning of the run, as soon as the filling scheme of the LHC is fixed. In a normal run, the bunch group should not change after the `ATLASReady` command has been sent, i.e. data taking has started. Only if

a wrong bunch group was loaded in the beginning, it will be necessary to issue the `UpdateBunchgroup` command again, which is an extremely rare case.

The physics BCIDs stored in the list are searched for gaps, where a gap is defined as 8 or more empty BCIDs, which is the typical minimum distance between bunch trains. The beginning and endings of these gaps are stored separately. In case an unequal number of beginnings and endings or no gap at all is found, a warning message is issued. The size, first position and multiplicity of the largest gap is also stored. In a run with the nominal filling pattern of the LHC (see Fig. 6.2), the largest gap will be the abort gap, but in filling schemes with less colliding bunches, there might be larger gaps in between.

For each of the digitised rate histograms, the collision BCIDs are searched for gaps in the same way as for the reference. The gaps are compared to what is obtained for the loaded bunch group and depending on the outcome a positive or negative value is returned. These values are stored in a two-dimensional histogram with the triggers considered for the checks on the y-axis and the run time (in seconds) on the x-axis. The interval with which the checks are performed can be configured for each run via the configuration data base. The values encoding the result of the pattern comparison at a certain time are filled as the bin contents of the corresponding bin of this histogram. An example simulated with the laboratory setup by sending test patterns via an LTP is shown in Fig. 8.3 and the possible values and their meaning is given in Table 8.1. A positive value corresponds to a global shift of the bunch pattern by this number of BCs, which can accordingly go up to 3563. If a discrepancy is found but no global shift detected, different cases are labeled by negative numbers. A value of -200 means that in the digitised rate histogram no colliding bunch was

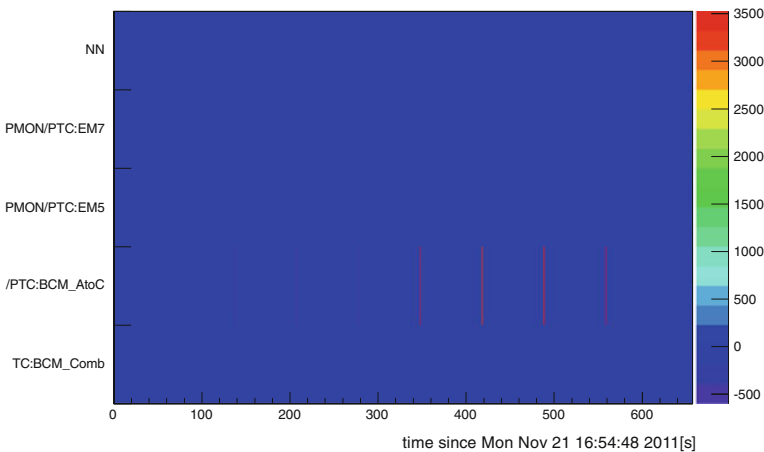


Fig. 8.3 Simulated example of the bunch group monitoring based on CTPMON rate histograms. Discrepancies between the pattern observed for the triggers on the y-axis and the loaded bunch group are shown as a function of run time in seconds. For the encoding in positive and negative numbers, see Table 8.1

Table 8.1 Encoding of outcomes of pattern comparison between reference from database and results from histogram digitisation

Value	Meaning
≥ 0	The complete pattern is shifted by this number of BCs
-200	No filled bunches found in digitised histogram
-400	Unequal number of gap beginnings and endings
-600	Not as many gaps as expected from reference
-800	No gaps found in digitised histogram
-1000	Largest gap not the same as in reference

found. In case an unequal number of beginnings and endings is determined, a value of -400 is returned, -600 signals that the number of gaps detected is different than the one from the loaded bunch group. If no gaps at all are found in the BCID pattern from the digitised histogram, this is encoded by a value of -800 . A difference in the number or size of the largest gap found results in a return value of -1000 .

The plot in Fig. 8.3 shows two of these cases for illustration: for the `BCM_AtOC` trigger, in the first roughly 5 min, entries occur with a value of -600 , indicating that an incorrect bunch group seems to be loaded, as the number of gaps is different. Following this, there are positive entries, signalling a global shift of the same pattern. This means that the correct bunch group is loaded now, but the timing is shifted. The transition was caused by sending an `UpdateBunchgroup` command. The naming of the triggers in this case has of course no real meaning, the setup was chosen such that the input signals were sent to the PIT line corresponding to the `BCM_AtOC`. The pattern generator of the LTP was fed with a file corresponding to one orbit (3564 BCs) and set to continuous mode, such that it sent this orbit over and over again. This of course does not result in bands for the low and high rates, but rather a 40 MHz rate in the colliding bunches and zero rate in the others. In this case, the reconstruction of the bunch pattern works very well, but in actual data taking much more tricky situations can occur. A few examples will be given in the next section.

Another way of cross checking the bunch group is to use the information from the beam pick-up systems, BPTX. There are two rate histograms produced from the CTPMON counters, one for each of the BPTX systems, they are labeled `BPTX0` and `BPTX1`. Examples for these histograms are shown in Fig. 8.4, `BPTX0` is displayed on the left, `BPTX1` on the right. In both histograms, the abort gap at the high BCIDs is clearly visible.

The threshold finding is applied to these histograms and typically works very reliably, given the clear separation between high and low rates. For BCIDs which feature a high rate (i.e. are set to 1 in the digitisation) in both histograms, collisions are expected in ATLAS. In this way, the BCIDs of the physics bunch group can be extracted and a histogram is created setting the bin contents for these BCIDs to 1 and the others to 0. The reference histogram created from the loaded bunch group is subtracted from this histogram for the paired bunches, yielding a histogram like the

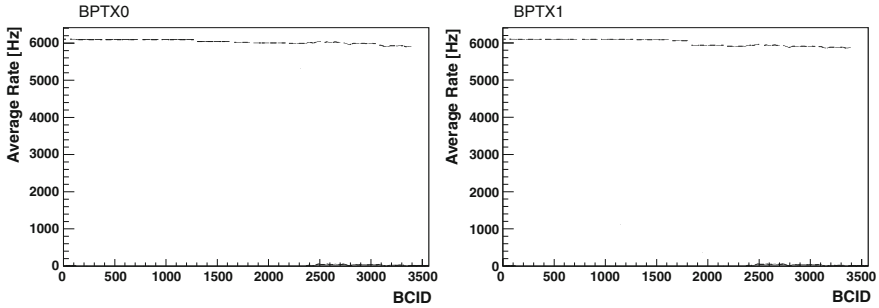
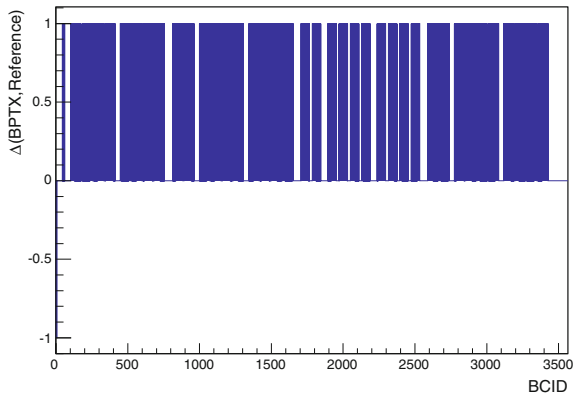


Fig. 8.4 CTPMON rate histograms for run 1,91,715 from October 2011 [2]

Fig. 8.5 Simulated CTPMON bunch group monitoring histogram based on BPTX rates. The difference between the paired bunches derived from the two BPTX systems and the expected bunch pattern of the physics bunch group is shown for each BCID



one in Fig. 8.5, which is a simulation produced with the laboratory setup. The LTP pattern generator is again used to produce the bunch group pattern to be compared to the one from the configuration. In actual data taking, this histogram typically has only bin contents of 0.

8.2.3 Application to Real Data

As mentioned above, in the case of two clearly separated, narrow bands, the collision bunch pattern can be reconstructed reliably from suitable trigger inputs. In this section, some more involved scenarios are presented in which the monitoring might not always work. The runs selected for this are runs which had only a small number of colliding bunches, specifically 190504, 190728, 191381 and 191628. All these runs are from the end of the 2011 proton-proton run at a centre-of-mass energy of 7 TeV, some further information is compiled in Table 8.2. The bunch group monitoring was not yet active in these runs, but the algorithm for threshold finding was tested on them offline. In Fig. 8.6 some examples of CTPMON rate histograms are shown for (from top to bottom) EM3, EM5, EM7 and BCM_Comb. The plots on the

Table 8.2 Example runs with low number of colliding bunches from the 2011 7 TeV proton-proton run

Run number	N_b	Date	Recorded luminosity (nb ⁻¹)
1,90,504	58	Oct 7, 2011	261.8
1,90,728	2	Oct 10, 2011	50.2
1,91,381	4	Oct 20–21, 2011	485.2
1,91,628	10	Oct 25, 2011	456.1

right show the region close to the lower band in the plots on the left. While from the plot on the left it seems there are two easy to separate bands, the zoom on the right reveals that there are a few more bunches with a slightly higher rate than the background level. When tested offline on the EM3 histogram, the threshold finding algorithm outlined above places the threshold below these values, leading to higher number of collision bunches than foreseen by the bunch group. For EM5 and EM7, the threshold is placed too close to the upper band, such that less colliding bunches are obtained after digitisation. For BCM_Comb, finally, the threshold is so low that all bunches are considered as colliding.

In Fig. 8.7 the EM5 rate histogram for run 1,90,728 with two colliding bunches is shown. On the left plot, only one bunch (101) appears to have a rate above the background level, zooming in on smaller rates, as shown in the right plot, reveals that the first bunch also has a slightly higher rate. The algorithm, however, is not capable of resolving this, such that only one colliding bunch is detected in this histogram.

Figure 8.8 displays the EM5 rate histograms for run 1,91,381 (left) with 4 and run 1,91,628 (right) with 10 colliding bunches. In run 191381, the rate is so low, that the first bunch with a rate slightly above the background ends up above threshold and 5 instead of 4 bunches are detected. For the histogram for run 1,91,628, the algorithm works despite the small number of colliding bunches.

The above examples show that while the derivation of the bunch pattern based on the CTPMON rate histograms provides a valuable cross check of the bunch group in well defined cases, there is a large number of configurations where the algorithm for threshold determination might not work. The conditions that lead to these configurations are not always obvious and can be hard to reconstruct. One complication is the fact, that the rate histograms are in fact profile plots, showing the average rate since the beginning of the run. Thus, if the histogram shows a rate for a certain BCID, this rate could have been stable around this value for the entire duration of the run, or it might have had widely different values at different times during the run, averaging to the value observed. The different scenarios considered in the threshold derivation as discussed in Sect. 8.2.1 were introduced one after the other as need was discovered to treat such special cases, as for example for runs with a small number of colliding bunches. The information in the log files will give additional information as to how reliable the derived digitisation is. In general, it is useful to perform the procedure for several input triggers, as it might be that for one

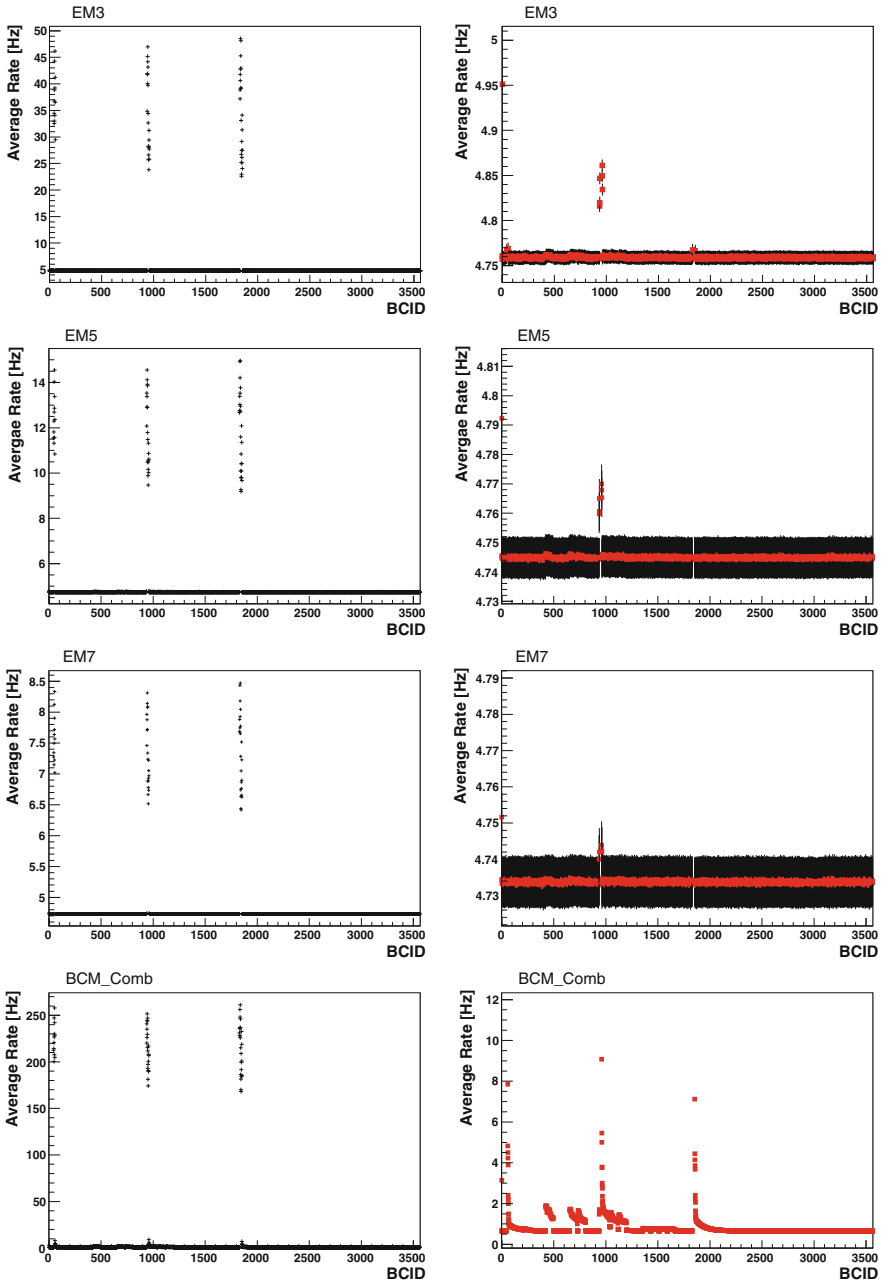


Fig. 8.6 CTPMON rate histograms for run 190504 for different input triggers: EM3 in the first, EM5 in the second, EM7 in the third and BCM_Comb in the last row. The plots on the *right* are zoomed version of the plots on the *left* [2]

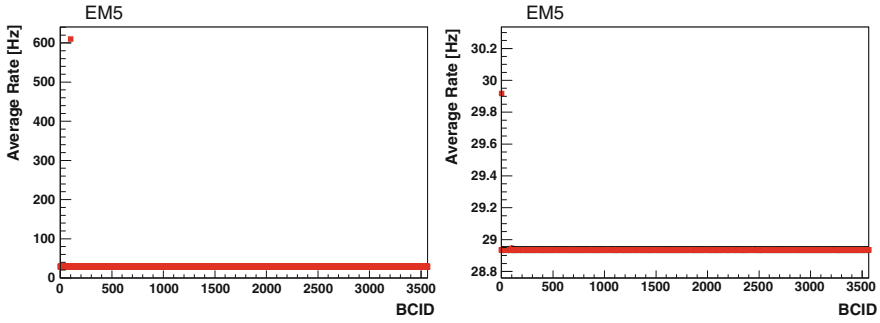


Fig. 8.7 CTPMON rate histograms for run 1,90,728 for EM5. The plot on the *right* is a zoomed version of the one on the *left* [2]

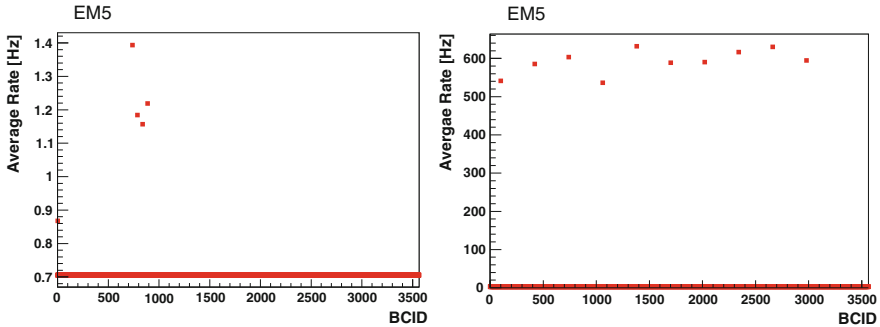


Fig. 8.8 CTPMON rate histograms for EM5 from run 1,91,381 and 1,91,628 [2]

of them the algorithm is not working, but the others might show that there is no real problem with the bunch group. For example considering EMX triggers with different values for x (but typically not larger than 10) can be helpful, as some problems of the algorithm are more pronounced for inputs with higher or lower rate, depending on the configuration.

The monitoring was deployed in the end of the 7 TeV run and has been successfully running during data taking ever since. During the 2012 data taking, there have been no problems with wrong bunch groups observed, which leads to the 2D monitoring histogram being typically empty, except for cases where the threshold finding algorithm does not work. These cases can, however, be readily identified by means of the log messages and by comparing the results for different triggers. In summary, the monitoring has proven to be useful for the DAQ system in delivering convincing information that there were no timing or other problems in the bunch groups. The challenging task of dealing with varying scenarios has been solved successfully.

The monitoring using the CTPMON rates will continue to be used in run-II. Due to the higher centre-of-mass energy, rates for low threshold triggers will increase, but the thresholds will be raised considerably, probably rendering the CTPMON rates

largely unchanged. The list of inputs to be used will have to be adapted accordingly. For bunch patterns with 25 ns spacing, additional cases for the threshold finding algorithm might have to be adjusted. The pattern comparison with the reference is expected to work unchanged, as it is based on the gaps in the pattern, which will be there also for trains of 25 ns.

8.3 Testing of Trigger Menus

The trigger menu typically has to be adapted when the running conditions change significantly, for example, if the number of bunches or protons per bunch is increased, such that the rates increase and thresholds have to be raised in order to not surpass the maximum rate of 75 kHz. This happens most often in the beginning of data taking after a longer shut-down period and when switching from proton-proton to proton-lead or lead-lead collisions. There are of the order of 10–15 menus to be tested within the course of a year of data taking, which has been done as part of this work. Before deploying a L1 trigger menu for the use in actual data taking it has to be ensured that it complies with the hardware limitations of the CTP. Two obvious requirements are that there are no more than 160 inputs used and not more than 256 items created. However, there can be further limitations on these numbers, depending on the diversity and complexity of the items. This is mostly related to the fact that inputs that are to be combined have to be routed to the same LUT. This might make it necessary to send the same input to more than one LUT, if it is used by many items, reducing the effective number of inputs. This might in turn mean, that not all of the items can be formed. The maximum number of inputs that can be used in one single item is limited by the number of LUT inputs. If an item requires more inputs, it cannot be built and has to be removed from the menu.

The testing of L1 menus proceeds in the following steps: first, it is checked whether already a switch matrix exists that allows to place the inputs such that all required items can be formed. If this is not the case, a new switch matrix is created, provided that the menu does not fail the above requirements. In the next step, test inputs for the CTP are derived from a simulation file and these are then fed into the CTP and processed according to the menu to be tested. The output is compared to the results in the simulation file. Thus, there are two files needed for the menu testing: the `xml` file containing the trigger menu and a simulated bytestream file that contains the trigger decision for some events according to the menu in question. These files are provided by the trigger experts.

Important tools to perform the testing are the `TriggerMenuCompiler`¹ and the `TriggerTool`.² The `TriggerMenuCompiler` translates the human readable `xml` menu file into the configuration and memory files needed by the CTP. The `TriggerTool` is used to interact with the compiler and to handle the configuration.

¹<https://svnweb.cern.ch/trac/atlasoff/browser/Trigger/TrigConfiguration/TriggerMenuCompiler>.

²<https://twiki.cern.ch/twiki/bin/view/Atlas/TriggerTool>.

The test patterns are generated with a programme called RunCtpTest.³ With another script, the test patterns are loaded into the CTPIN test memories, by-passing the actual inputs, and the resulting trigger decision is compared to the one from the bytestream file. If they are the same, the test was successful.

References

1. Soloviev I (2002) OKS documentation (User's guide, tools manual, reference manual). Tech. rep. ATLAS DAQ/EF P-1 Technical Note 33. Geneva: CERN. <http://atlas-onlsw.web.cern.ch/Atlas-onlsw/components/configdb/docs/oks-ug/2.0/pdf/OksDocumentation.pdf>
2. *CoCa files for dataset L1CT*. <https://atlasdaq.cern.ch/info/mda/coca/L1CT>. Accessed: Sept 2014

³<https://svnweb.cern.ch/trac/atlasdaq/browser/L1/ctp/L1CTApps>.

Chapter 9

Upgrade of the Central Trigger

When the LHC will resume operation in spring 2015 it will be with a higher centre-of-mass energy of up to 14 TeV and higher instantaneous luminosities of more than $10^{34} \text{ cm}^{-2}\text{s}^{-1}$. This will require a larger number of and more complex level-1 trigger items, especially since the maximum L1 rate will be limited to 100 kHz by the read-out rate of the sub-detectors. To ensure that the physics goal of the experiment will still be reached, a number of upgrades are foreseen for the detector, the trigger system and especially the Central Trigger.

A topological processor [1], referred to as L1Topo, will be installed at the first trigger level with the aim of improving the selection of multi-object signatures at high luminosity. This topological processor will receive inputs from the calorimeter trigger as well as coarse muon trigger information and is capable of applying cuts on, for example, the spatial separation between objects. The merger modules of the calorimeter trigger will be exchanged to provide the inputs to the L1Topo system and the interface of the muon trigger system to the CTP will be adapted accordingly. Figure 9.1 shows the layout of the upgraded level-1 trigger system with the changes indicated in red.

In Table 9.1, the usage of CTP resources by a typical 2012 trigger menu is presented. Many of the parameters are at their limits, leaving no room for more inputs or items, for example. Overcoming these resource limitations is the primary motivation for the upgrade of the CTP. Table 9.1 thus also lists the numbers for the parameters foreseen for the upgraded CTP. In particular, the number of inputs, trigger items and bunch groups will be doubled.

Parts of the work for this thesis have been on aspects of the upgrade of the Central Trigger, especially on the event format and the Central Trigger simulation. Therefore, more details on the changes to the actual hardware will be described in Sect. 9.1, while Sect. 9.2 gives an introduction to the Central Trigger simulation that has been used during run-I. Gaining a thorough understanding of this was the foundation for the changes and extensions for the event format and the simulation that have been developed and implemented as part of this work and will be discussed in Sect. 9.3.

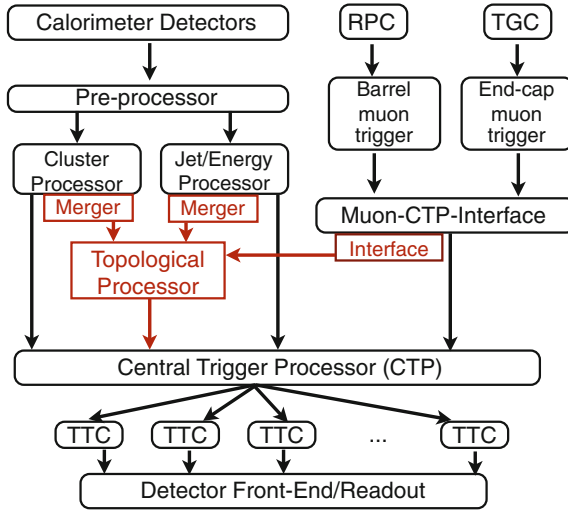


Fig. 9.1 Schematic view of the upgraded level-1 trigger system. Changes compared to the previous layout are shown in *red*. Adapted from [2]

Table 9.1 CTP resources usage by a typical 2012 trigger menu. In addition, the numbers foreseen for the upgraded CTP are shown [3]

	Used	Available	Upgrade
CTPIN input cables	9	12	12
CTP PIT bus lines	160	160	320
CTPCORE trigger items	241	256	512
CTPCORE bunch groups	8	8	16
CTPCORE front panel inputs	–	–	192
Maximum number of bits in OR	6	12	15
per-bunch item counters	12	12	256
Output cables to TTC	20	20	25

9.1 Upgrade of the Hardware During the Long-Shutdown-I

The extension of the CTP functionality for the LHC run-II requires substantial changes to the hardware: the CTPCORE and CTPOUT modules as well as the COM backplane will be replaced and the firmware of the CTPIN and CTPMON modules has to be adapted.

The PIT bus will not be exchanged but will be operated at the double data rate (DDR), i.e. transmitting data at a rate of 80 MHz, which allows for an effective number of 320 instead of 160 trigger inputs. The price to pay is an additional latency of two BCs. The 320 inputs will be used for the trigger item formation by the *CTPCORE+* module, the new version of the CTPCORE module, a block diagram of which is

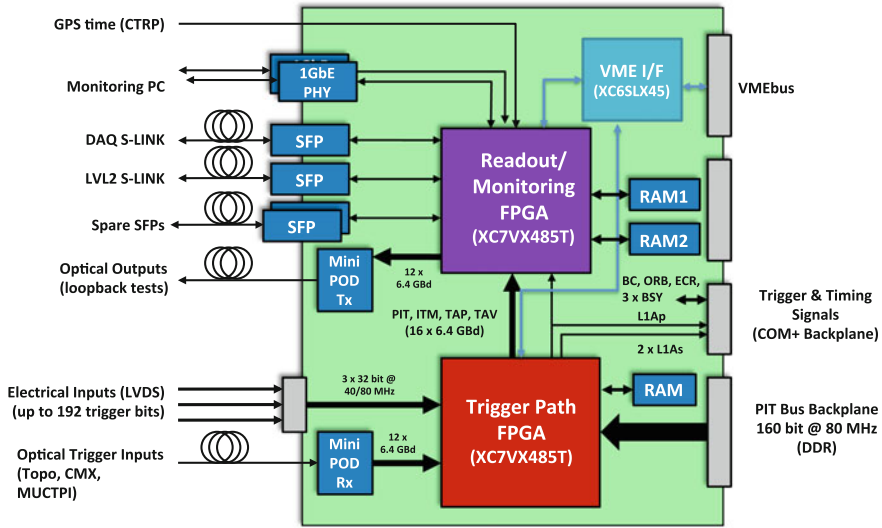


Fig. 9.2 Block diagram of the CTPCORE+ module. See text for more details [4]

shown in Fig. 9.2. Apart from the electrical inputs via the PIT bus, there will be connectors at the front panel of the CTPCORE+ for 96 additional inputs. These will be operated at DDR, making for a total of 192 additional inputs. A special virtue of these direct inputs is their lower latency compared to the ones via the CTPIN and PIT bus, which is especially important for latency critical systems like the ALFA detectors and also for the topological processor. The new CTP will thus have a total number of 512 inputs, which is more than three times the current number. The CPTCORE+ module also has two connectors for optical inputs, that are however not foreseen to be used for run-II but are put in place for possible future use.

The new module will have the capacity of forming 512 trigger items and feature 256 per-bunch counters for the monitoring of trigger item rates. There will be 16 instead of 8 bunch groups and four random trigger generators instead of two.

The upgrade further foresees the partitioning of the LIA generation in the CTPCORE+. There will be one primary and two secondary partitions, all sharing a common trigger menu and timing, but with their own selection of items out of this menu. Only the primary partition will be used for physics data taking, the purpose of the secondary partitions is to allow for independent commissioning and calibration of subsystems. The trigger path of the upgraded system is shown in Fig. 9.3. The $2 \times 160 + 192 = 512$ trigger input bits are fed into the LUTs which are capable of forming up to 512 trigger conditions, which are then combined into up to 512 trigger items in the CAM. Afterwards, the 16 bunch groups can be used in the bunch group masking and prescales are applied. The busy handling and veto is done by each partition individually, leading to the generation of three LIAs. However, only

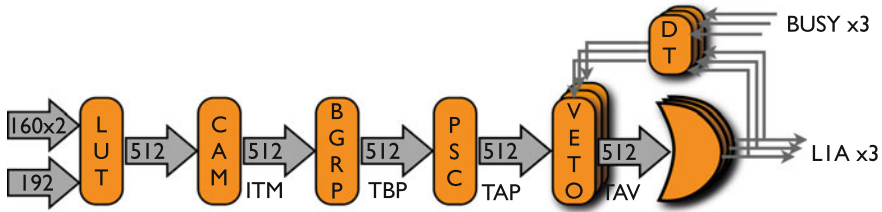
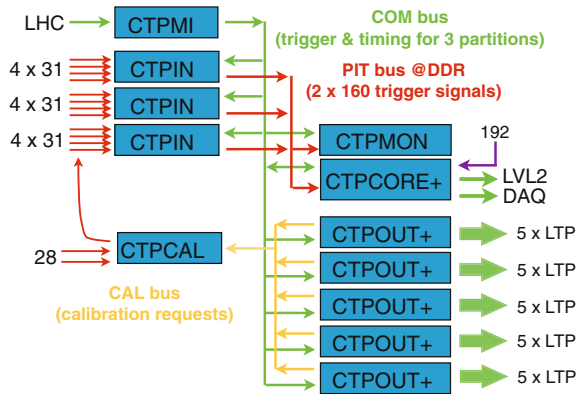


Fig. 9.3 Schematic view of the upgraded trigger path in the CTPCORE+ module [5]

Fig. 9.4 Schematic view of the upgraded Central Trigger system [3]



the event fragment from the primary partition will be forwarded to the DAQ and high level trigger.

In order to accommodate three instead of one partition, the COM backplane will be replaced and then will also allow for the connection of an additional output module. The four CTPOUT modules will be replaced by 5 CTPOUT+ modules, which will be capable of per-bunch busy monitoring. A schematic view of the upgraded CTP architecture is displayed in Fig. 9.4.

9.2 Central Trigger Simulation

The changes to the hardware for the upgraded CTP require adaption and extension of the Central Trigger simulation. In the following, the general functionality of the simulation during run-I will be described to give the basis for the discussion of the updates that have been implemented as part of this work and which will be described in Sect. 9.3.

It has to be pointed out, that the Central Trigger simulation is not a detailed simulation of the actual hardware, but rather of the logic of the trigger items. It is used in the production of MonteCarlo samples as well as in data quality checks,

where the input bits are used to rebuild the items according to the trigger menu and to compare to the results from actual data taking. In the following, first, the procedure for running the CT simulation in MonteCarlo production will be described and then the modifications for running on data will be explained. Closely related to the simulation is the data format used for the event information of the CTP, since the simulation has to produce the same output objects as are obtained in the actual data taking. Hence, the next section will be a brief description of the event format used for the CTP until the end of run-I.

9.2.1 Event Format

In principle, the event format of the CTP is freely programmable in the CTPCORE, but for practical reasons a default format is used, which complies with the general ATLAS raw event or ROD format [7]. However, the CTP format [6] still has a number of parameters that can be specified, such as the number of bunch crossing around the triggering bunch to be read out or the position of the triggering bunch. The information transmitted in a fragment can be grouped into two categories: data that changes with each bunch crossing and data that stays the same for at least parts of the run. For the latter, there are 66 programmable 32-bit words that are being filled into the event fragment with the *marker word mechanism*. Some of the marker words are reserved for constant values according to the ROD event format, which defines the header and trailer words. Other marker words contain information that changes from run to run or even during a run.

The general structure of the event format is a header, followed by the data payload and a trailer (Fig. 9.5). There remain 51 words that can be used to transmit any information considered worth storing. The first header word is an S-Link [8] fragment start marker, followed by the marker word for the actual header start. The size of the header is 9 words in total, and this information is stored in the third header word. The fourth word contains the format version number, which consists of the ROD format version number in bits (31...16), the current version being 3.1, and a user defined format version number in the remaining 16 bits. The four lowest bits are the CTP format version number, bits (9...4) contain the position of the triggering bunch and bits (15...10) the number of extra words that will be sent after the bunch crossing data. Following the format version number is a word for the source identifier: it holds the sub-detector ID, which is 0×77 (using hexadecimal format) in case of the CTP, in bits (23...16). The lower 16 bits are used to distinguish between information that is to be sent to the data acquisition and monitoring system or to the higher trigger levels (RoI information). A value of 0 means DAQ, 1 means RoI. The bits (31...24) are set to 0×00 . The next three words are for the run number, the extended L1ID and the BCID, respectively. Since only 12 bits are needed for the BCID, the remaining bits are left free. The next header word is used to send the L1 trigger type (TT) in the 8 lowest bits. The last word foreseen by the ROD event format is called *detector event type* (DETT). In the CTP event format it is used to store the lumiblock number

S-link fragment start	B0F0 0000	stripped off when reading from S-link		HEADER
start of header marker	EE12 34EE			
header size	0000 0009	number of header words without S-link start marker		
format version number	0301 EEEV	EEE: #(extra words) (15..10), L1A pos. (9..4), V: CTP format version		
source identifier DAQ	0077 0000			
source identifier RoI	0077 0001			
run number	XXXX XXXX	changes with every run		
extended LVL1 ID	EELL LLLL	EE: ECR, LLLLL: LVL1 ID		
BCID	UUUU UB BB	UUUUU: unused, BBB: 12 bits for BCID		
LVL1 trigger type	UUUU UUTT	UUUUUU: unused, TT: 8 bits for trigger type		
detector event type	HHHH LLLL	HHHH: HLT counter, LLLL: lumiblock number		
time stamp (seconds)	XXXX XXXX			PAYLOAD
time stamp (nanoseconds)	NNNN NNNU	U: unused, NNNNNNN: counts of 5 ns		
PIT (31..0)	XXXX XXXX			
⋮	⋮			
PIT (159..128)	XXXX XXXX			
additional PIT word	UUUU TGGB	U: unused, T: RNDM, PCLK, GG: bunch group, B: BCID		
TBP (31..0)	XXXX XXXX			
⋮	⋮			
TBP (255..224)	XXXX XXXX			
TAP (31..0)	XXXX XXXX			
⋮	⋮			
TAP (255..224)	XXXX XXXX			
TAV (31..0)	XXXX XXXX			
⋮	⋮			
TAV (255..224)	XXXX XXXX			
time since previous L1A	XXXX XXXX	optionally, but used per default		
turn counter	XXXX XXXX	optionally, but used per default		
additional word 3	XXXX XXXX	optionally		
⋮	⋮			
additional word 51	XXXX XXXX	optionally		
status element: error	0000 0000	not used by CTP		TRAILER
status element: information	0000 0000	not used by CTP		
number of status elements	0000 0002			
number of data elements DAQ	XXXX XXXX	calculated by CTPCORE readout data block formatter		
number of data elements RoI	XXXX XXXX	calculated by CTPCORE readout data block formatter		
position of status elements	0000 0001	1 means after data words		
S-link fragment stop marker	E0F0 0000	stripped of when reading from S-link		

Fig. 9.5 Illustration of the CT event format used at the end of run-I. Adapted from [6]

in bits (15...0) and the *HLT counter* in bits (31...16). The HLT counter specifies the lumiblock number at which the HLT prescales and some other conditions should be changed.

The trailer comprises 5 words and in addition one S-Link fragment stop marker word. The first two trailer words are intended as status words by the ROD format, the first one for errors, the second for other information, but neither is used in by the CTPCORE. The next trailer word contains the number of status words, which is 2. The next word gives the number of data elements, the last one specifies the position of the status word—in this case after the payload. The data payload contains the bunch crossing information: there are two words for the absolute time stamp, one gives the seconds, the other the nanoseconds. These are followed by the trigger input information: $5 \times 32 = 160$ for the trigger inputs from the CTPIN plus one word

containing additional information. This comprises the 4 lowest bits of the BCID in bits (3...0), the 8 bunch group trigger bits (11...4), 2 bits for the prescaled clock triggers (13...12) and two for the random triggers (15...14). The trigger input information is followed by eight words for the TBPs ($8 \times 32 = 256$), and the same number of words for the TAPs and TAVs. These $6 + 3 \times 8 = 30$ words are repeated for each bunch crossing in the read-out slice for the DAQ/MON events, RoI information is only sent for the triggering bunch. After this trigger information there can be a configurable number of freely programmable marker words. One of these words contains the time difference to the previous L1A in BCs, another the turn counter value, which gives the number of LHC turns completed since the last reset.

9.2.2 *Inputs and Internal Objects*

The input objects used by the simulation are *CableWords*, 32 bit variables corresponding to the bit pattern arriving at one of the CTPIN connectors. These inputs are retrieved from a Transient Data Store (TDS) called StoreGate.¹ Such a TDS is useful for the handling of data objects that are transmitted between different parts of the software. In this case, the inputs to the CT simulation are the outputs of other simulations, for example the calorimeter and muon triggers, which are written to StoreGate from where the CT simulation can retrieve them. The classes defining the objects that are exchanged between different systems are part of the `TrigT1Interfaces` package.²

In addition, information from the trigger configuration is extracted from the data base, comprising the thresholds and items with their prescales as defined in the trigger menu as well as the PIT assignment of the input bits. For convenience, simulation internal objects are defined that link this information together: the `CTPTriggerThreshold` stores the multiplicity of a given threshold and the corresponding start and end bits on the PIT bus. Similarly, the `CTPTriggerItem` holds the prescale information and position (or CTP ID) for a certain item. The `ThresholdMap` and `ItemMap`, respectively, link these CT simulation internal objects to the corresponding trigger configuration objects. The classes for the internal objects are part of the `TrigT1CTP` package.³

9.2.3 *Simulation of Special Triggers*

The simulation also creates a map for the bunch groups, the prescaled clock triggers and the random triggers. They are called *internal* or *special* since they are not received

¹<https://twiki.cern.ch/twiki/bin/view/AtlasComputing/StoreGate>.

²<https://svnweb.cern.ch//cern/wsvn/atlasoff/Trigger/TrigT1/TrigT1Interfaces/>.

³<https://svnweb.cern.ch//cern/wsvn/atlasoff/Trigger/TrigT1/TrigT1CTP/>.

as inputs from other systems but are created inside the CTPCORE module. There is one class for each of the three special trigger types, all derived from the same base class and as such implementing the same two methods: `execute` and `evaluate`. These classes are also part of the `TrigT1CTP` package.

The `BunchGroupTrigger` class holds a vector of the BCIDs for a given bunch group and has a counter member variable that is set to the current BCID via the `execute` method. The `evaluate` method returns `true` when the current BCID is part of the respective bunch group and `false` otherwise.

The rate (R) for each of the `RandomTriggers` is obtained from the configuration data base. The `execute` method in this case sets a counter to a random number, the `evaluate` method checks whether the counter value is greater than $1 - 1/R$ and returns `true` if that is the case.

Similarly, a rate is obtained for the `PrescaledClockTrigger` and a counter is initialised to this value. With each `execute` call it is reduced by 1 until it becomes ≤ 0 , then it is set to the initial value again. The `evaluate` method returns `true` when the counter is ≤ 0 , `false` otherwise.

9.2.4 Trigger Decision

For the generation of the L1A in the simulation, first, the multiplicities of the trigger thresholds have to be determined from the `cableWords` obtained from `StoreGate`. Each threshold from the trigger configuration ‘knows’ the bits on the input cables it was sent over. Thus, the multiplicity for each `CTPTriggerThreshold` can be derived from the bit pattern in the `cableWords` and stored in the `ThresholdMap`. Subsequently, the `execute` method for all internal triggers is called.

The core of the decision taking is the `CTPTriggerItemNode` class in `TrigT1CTP` which only contains one method, called `evaluate`, which recursively checks all the logical conditions within a trigger item and returns `true` when the item is found to have fired in this event. The function distinguishes between four types of logical nodes: AND, OR, NOT and OBJ. An OBJ is the end point of the recursion, it can be an internal trigger or a threshold. The `evaluate` function works its way back until it reaches the OBJs, checks whether they have fired or not and evaluates the logical combinations. If an item has fired, its prescale counter is increased by 1.

9.2.5 Output

The generation of the simulation outputs according to the Central Trigger event format is done by the `ResultBuilder` in `TrigT1CTP`. There are two types of output objects created: the `CTPSlink` contains the information that is to be sent on to the higher trigger levels and the class is part of the `TrigT1Interfaces` package, the `CTP_RDO` (*raw data object*) is to be sent to the DAQ for data quality monitoring.

It is contained in the `TrigT1Result` package.⁴ The `CTPSlink` contains only the information for the triggering bunch, whereas for the `CTP_RDO` the information is repeated for each bunch crossing in the read-out window.

The `ResultBuilder` constructs the 32-bit PIT words from the information in the `ThresholdMap`, setting the bits for each threshold corresponding to the multiplicity. Similarly, the TBP words for the trigger items are constructed from the `ItemMap`. The bit corresponding to the `CTPID` (the item number, 0...255) of a certain item is set to 0 or 1, depending on whether the item fired or not. If the prescale counter of an item is equal to its prescale, then the bit is set to 1 in the TAP words, otherwise it is 0. The TAV words in the simulation are the same as the TAP words, as no dead-time is simulated. Finally, the `ResultBuilder` also creates the trigger type word and the output objects are written to `StoreGate` for use by other parts of the software.

9.2.6 *Modifications for Running on Data*

When running the simulation for data quality checks, the `CableWords` are re-derived from data and written to `StoreGate`. The simulation itself works very much in the same way: the threshold multiplicities are derived and the trigger decision is rebuilt according to the logic in the trigger menu. The result can then be compared to the trigger bits in data. The only further difference is that the bunch groups are read from the ATLAS conditions data base, that stores the actual running conditions, and not from the configuration. The part of the software that creates the `CableWords` from data is called `DeriveSimulationInputs` and resides in the `TrigT1CTMonitoring` package.⁵ This class holds a three-dimensional array representing the $3 \times 4 \times 32$ inputs received via the CTPIN modules which is filled according to the PIT words recorded. The mapping of the PIT bits to the CTPIN input bits is obtained from the ATLAS conditions data base and links the PIT bit number to the name of the trigger threshold to which this bit belongs, the corresponding CTPIN slot and connector as well as the bit on the CTPIN cable. With this information, the cable array can be filled according to the fired PIT bits. From this array, in turn, the `CableWords` can be created and written to `StoreGate`.

9.2.7 *Data Quality Monitoring*

A number of cross checks on the CTP information is performed during T0 processing of the recorded data. Apart from checking the consistency with other systems, there are sanity and self-consistency checks on the CTP internal information.

⁴<https://svnweb.cern.ch/cern/wsvn/atlasoff/Trigger/TrigT1/TrigT1Result/>.

⁵<https://svnweb.cern.ch/cern/wsvn/atlasoff/Trigger/TrigT1/TrigT1CTMonitoring/>.

In total, 12 histograms are produced per default. The timestamp stored in the event fragment is compared to the timing information reconstructed from the turn counter value and the BCID and two histograms are produced, one shows the distribution of the time difference in μs , the other the time difference as a function of the lumiblock number. Two more histograms show the time since the start of the lumiblock an event belongs to and the time until the next lumiblock, respectively. There is one 2D histogram showing the average rate for each PIT line for each bunch crossing within the readout window. The triggering bunch is bunch number 0 in this case. A similar histogram shows the average rate for the BC (relative to the triggering bunch) in which a PIT line fired for the first time (within the readout window). Then there are two histograms showing the bits for each of the status words. Since the CTP is not using these words to send information, there should be no entries in these histograms. In addition, the difference in the BCID stored in the header and the extra PIT word is displayed. The time since the previous L1A is monitored as well as the trigger type. The last histograms shows how often a trigger item fires for all trigger items.

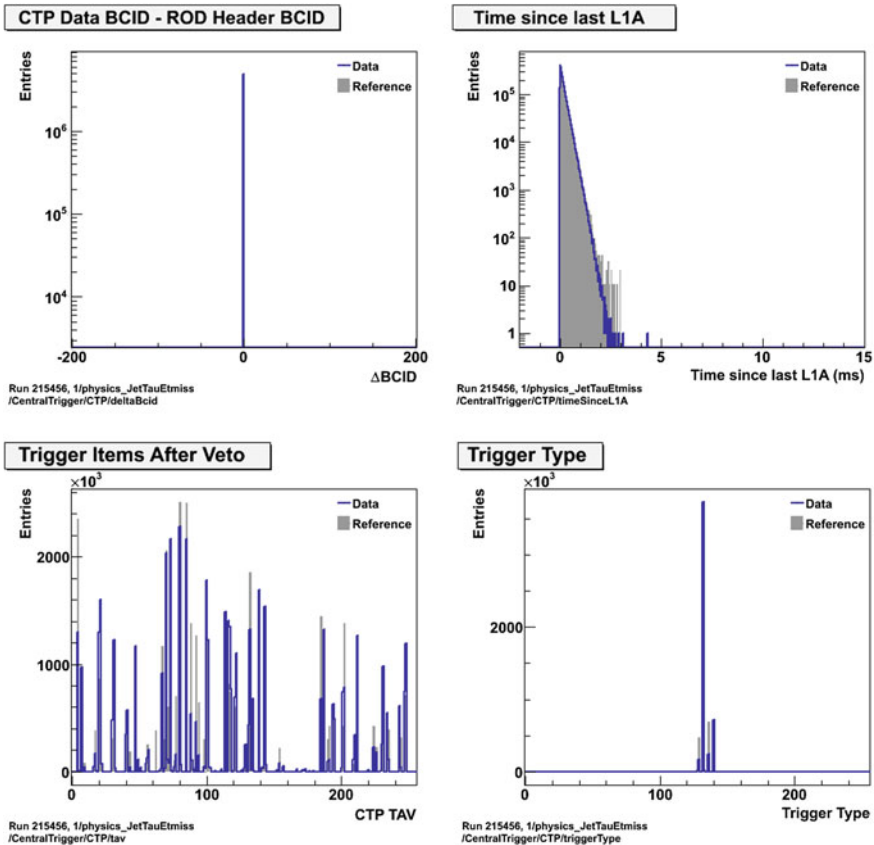


Fig. 9.6 Some of the CT monitoring histograms comparing the outcome of the re-simulation to data, for the JetTauEtmis stream of run 215456 [9]

The results of re-running the simulation on data as described in the previous section can be compared to what was seen in data to check whether there are striking differences. In Fig. 9.6 examples of such comparisons are shown from the 8 TeV run 2,15,456.⁶ The top row shows the difference in the BCID stored at different places in the event format on the left, which should be 0 both in data and simulation, and the time since the last L1A in ms on the right. This is an indicator of whether or not there was large dead-time in the run. The bottom row displays in the left histogram how often a trigger item after veto with a certain CTPID has triggered. Since there is no dead-time included in the simulation, differences are to be expected here. Similarly, the distribution of the trigger type which is presented in the bottom right plot is not expected to agree perfectly, since the trigger type is formed from the TAVs. For the future, it might be interesting to include a histogram for the TBPs and TAPs, as there is better agreement to be expected between data and simulation for those. Especially the TBPs should be exactly the same for data and re-simulation.

9.3 Upgrade of the Central Trigger Simulation

The upgrades foreseen in the hardware require updates of different aspects linked to the CT simulation. The data format will change, the increased number of inputs and items as well as the changes in the internal triggers have to be implemented and an interface to inputs from the topological processor has to be provided. These developments were done as part of this work and will be presented in the following sections.

9.3.1 Updated Event Format

The event format will not undergo dramatic changes but some of the bit assignments will be different. A schematic view of the updated event format is presented in Fig. 9.7 with the changes highlighted in red. While the header and trailer will not change (the ROD format stays the same), the number of data words will increase corresponding to the larger number of inputs and items. The inputs received via the PIT bus and the front panel inputs (FPI) will, in the following, be collectively referred to as TIPS (trigger inputs). There will be 17 TIP words in total, 16 for the 512 external inputs and one for the extra information of internal triggers. Here, the assignment will be the following: the 16 highest bits will be used for the 16 bunch groups, bits (15...12) will contain the information for the four random triggers, and the 12 lowest bits will be used to store the full BCID, as there will be no prescaled clock triggers any more. The number of words for the trigger items at all three stages in the trigger path will double as well, such that there are 16 words each for TBP, TAP, and TAV.

⁶https://atlasdqm.cern.ch/webdisplay/tier0/1/physics_JetTauEtmisss/run_215456/run/CentralTrigger/CTP/.

S-link fragment start	B0F0 0000	stripped off when reading from S-link	HEADER
start of header marker	EE12 34EE		
header size	0000 0009	number of header words without S-link start marker	
format version number	0301 EEEV	EEE: #(extra words) (15..10), L1A pos. (9..4), V: CTP format version	
source identifier DAQ	0077 0000		
source identifier RoI	0077 0001		
run number	XXXX XXXX	changes with every run	
extended LVL1 ID	EELL LLLL	EE: ECR, LLLLL: LVL1 ID	
BCID	UUUU UBBB	UUUUU: unused, BBB: 12 bits for BCID	
LVL1 trigger type	UUUU UUTT	UUUUUU: unused, TT: 8 bits for trigger type	
detector event type	HHHH LLLL	HHHH: HLT counter, LLLL: lumiblock number	
time stamp (seconds)	XXXX XXXX		PAYLOAD
time stamp (nanoseconds)	NNNN NNNU	U: unused, NNNNNNN: counts of 5 ns	
TIP (31..0)	XXXX XXXX		
⋮	⋮		
TIP (511..480)	XXXX XXXX		
additional TIP word	GGGG TBBB	GGGG: bunch group, T: RNDM, B: full BCID	
TBP (31..0)	XXXX XXXX		
⋮	⋮		
TBP (511..480)	XXXX XXXX		
TAP (31..0)	XXXX XXXX		
⋮	⋮		
TAP (511..480)	XXXX XXXX		
TAV (31..0)	XXXX XXXX		
⋮	⋮		
TAV (511..480)	XXXX XXXX		
time since previous L1A	XXXX XXXX	not optional any more	
turn counter	XXXX XXXX	not optional any more	
additional word 3	XXXX XXXX	optionally	
⋮	⋮		
additional word 51	XXXX XXXX	optionally	
status element: error	0000 0000	not used by CTP	TPRAILER
status element: information	0000 0000	not used by CTP	
number of status elements	0000 0002		
number of data elements DAQ	XXXX XXXX	calculated by CTPCORE readout data block formatter	
number of data elements RoI	XXXX XXXX	calculated by CTPCORE readout data block formatter	
position of status elements	0000 0001	1 means after data words	
S-link fragment stop marker	E0F0 0000	stripped of when reading from S-link	

Fig. 9.7 Schematic view of the CTP event format as foreseen for run-II. Changes with respect to run-I are highlighted in *red*. Adapted from [6]

Given the large number of data words, the size of the event fragment will increase considerably. The data transition is, however, limited to 40 Mwords/s, with 1 word consisting of 32 bits. On the other hand, an L1 output rate of up to 100 kHz has to be possible. This limits the maximum size of one fragment to 400 words. The total length of the fragment (in number of words) is given by the following expression:

$$\begin{aligned}
 N_{tot} &= N_{head} + N_{time} + N_{extra} + N_{BC} + N_{trailer} \\
 &= 9 + 2 + N_{extra} + n_{BC} \cdot (17 + 3 \cdot 16) + 5 \\
 &= 16 + N_{extra} + 65n_{BC},
 \end{aligned} \tag{9.1}$$

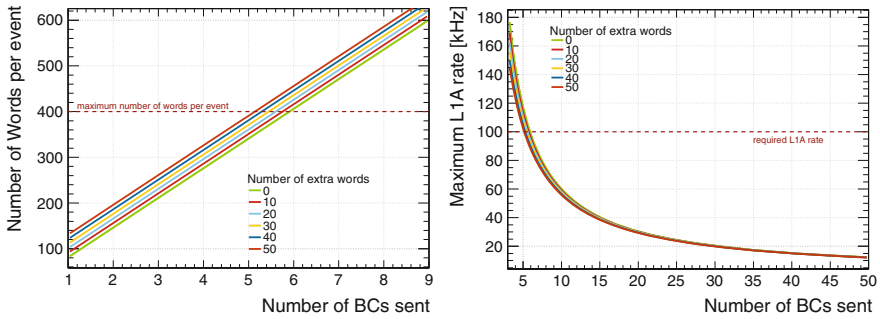


Fig. 9.8 Dependency of the CTP fragment size (*left*) and the maximum L1A rate (*right*) on the number of extra words and the size of the read-out window

where N_{head} and $N_{trailer}$ are the number of header and trailer words, respectively, N_{time} are the two words reserved for the time stamp information, N_{extra} is the number of additional words added after the payload, n_{BC} is the size of the read-out window in BCs and N_{BC} is the total number of words needed for the input and item information for each BC. The left plot in Fig. 9.8 shows the size of the event fragment for different numbers of extra words as a function of the number of BCs that are transmitted. It is seen that up to 4 BCs can be sent safely, while a read-out slice of 5 BCs can be critical depending on the number of extra words. Any larger number of BCs sent is not feasible. The dependence on the number of extra words is much weaker: when sending only 4 BCs or less, there is no limitation to the number of extra words (out of the 51 available) that can be sent.

The same information is shown in the right plot in terms of the maximum L1 rate: for numbers of BCs larger than 5, the maximum rate of 100kHz cannot be achieved. If larger numbers of BCs are to be sent, a smaller L1 rate has to be accepted.

9.3.2 New Software Packages

The parameters defining the event format as well as other parameters of the CT have been hardcoded in many parts of the ATLAS software. This made changes and updates tedious and error-prone. To circumvent such difficulties in the future, two new software packages are introduced that compile essential CT parameters. These are accessible by other parts of the software, such that the values of the parameters can be managed centrally and updates become transparent to the users. As these packages are intended to be used as central ‘dictionaries’ not only for the Central Trigger but also for other L1 systems, the packages are generically called `L1CommonCore` and `L1Common`. For technical reasons, the parameters are split into two packages that belong to different parts of the ATLAS software. The `L1CommonCore` package contains basic parameters that are not expected to change very often, as for example

the number of inputs and items. Other parameters that are more likely to change especially in the beginning of operation, such as the input cabling, are stored in the `L1Common` package.

The packages contain records of all values a parameter has had in certain versions to ensure backward compatibility. The design of the packages shall be illustrated using the example of the event data format. Despite the versions discussed in this chapter already, there have been slightly different versions in the earlier stages of data taking, which are detailed in Ref. [6]. The `L1CommonCore` package contains the parameters for all the different versions in an `xml` file and from this, C++ classes and python headers are derived automatically. The `xml` file contains the parameters as a DOCTYPE called `CTSpecs`, the single elements are denoted as `CTSpec`. They have three mandatory elements—a name, a type and a value—and one optional element: a comment. In addition, they have a namespace attribute, `ns`, which is mandatory and specifies the version the value of this parameter corresponds to. An example of such a `CTSpec` element looks like this:

```
<CTSpec ns='v0'>
  <name>"MaxTrigItems"</name>
  <type>u32</type>
  <value>256</value>
  <comment>"Maximum number of items that can be formed in the CTPCORE"</comment>
</CTSpec>
```

If the value of a parameter does not change with a new version of the CT event format (as, e.g., the number of items for the first versions `v0-v3`), no new element has to be created. The python script that generates the header and class files will take the latest available value for a parameter for a given version. For example, if version `v4` is required, for all parameters that exist with attribute `'v4'` the corresponding value will be used. If a parameter only exists with attributes `'v0'` and `'v2'`, the one for `'v2'` will be used, as it is assumed to be the most up to date value. Note that this implies that when a parameter is reverted to a value it had in an earlier version, it is still necessary to create a new element with the newest version as an attribute.

It is also important to note that every parameter has to have a version `'v0'`, even if it was introduced only later (as, for example, the turn counter value). The value for `'v0'` should then be set to an appropriate place holder value (like 999) to make it clear in downstream code that this parameter has no relevance for the given version of the event format.

The information contained in the `L1CommonCore` package was mostly inspired by the contents of the `CTPfragment`⁷ package and the `CTPdataformat` definition therein. The `L1CommonCore` package extends this to be usable for any version of the CT event format without the need to know specifics about the format. The user can simply create an object `CTPdataformatVersion` by passing the desired version number in the constructor and from this has access to all the parameters for the desired version. The Central Trigger simulation is one of the first use cases for these packages.

⁷<https://svnweb.cern.ch/trac/atlastdaq/browser/DAQ/DataFlow/CTPfragment>.

9.3.3 *Adaption to New Hardware*

The updated simulation has to include the inputs arriving at the front panel of the CTPCORE (FPI), for example from the L1Topo processor. A new class `FrontPanelCTP` has been introduced in `TrigT1Interfaces` which provides the `CableWords` in a similar fashion as for the CTPIN inputs. The main difference is that the direct inputs are over-clocked by a factor of 2, such that there are in total six `CableWords`, three for each DDR clock. This is important when extracting the multiplicities from the `CableWords`.

The situation is slightly different for the inputs from the CTPIN boards: the inputs themselves are not over-clocked; at any time there arrives the same signal at a given input line. The over-clocking happens only afterwards, when the inputs are forwarded via the PIT bus. From the point of view of the simulation, this results simply in double the number of PIT signals (320), the treatment in the code, like the extraction of multiplicities, stays essentially the same.

In order to be able to build items containing information from the topological processor as well as the usual calorimeter or muon trigger, inputs from both systems have to go into the same LUT. Each LUT has 16 inputs and it is foreseen to use bits (11...0) for the PIT signals and bits (15...12) for the FPIs. Therefore, the 512 input bits (as they are written to the event format, for example), will not be grouped into 320 PIT plus 192 FPI, but will be a mixture of both. It is therefore convenient to introduce a new class combining the inputs, which is called `TIP` for trigger input. This class is part of the `TrigConfL1Data`⁸ configuration package. A `TIP` object knows whether it is a PIT or FPI and to which DDR clock it belongs. This is especially important when re-deriving the `CableWords` from the `TIPs` when running on data.

Changes are also required in the simulation of the internal triggers. In run-II, there will be no prescaled clock triggers any more, so they have to be disabled in the simulation as well. On the other hand, there will be four (instead of two) random trigger generators and 16 bunch groups (instead of 8). The increased number of these triggers is easily incorporated by extending the internal trigger map accordingly. The `ResultBuilder` is adapted to write the correct bits into the output objects.

The mechanism for the prescaling of trigger items will also change in run-II. During run-I, a counter-based and hence deterministic prescaling was done. After the long shutdown, a random prescaling will be used. For this, there is one pseudo-random binary sequence generator per trigger item, each with its own seed. The 24 lower bits (of 31 in total) will be used, corresponding to range of 0 to $2^{24} - 1$. Each item is assigned a *cut value*, C , and is accepted if the sequence generated has a value smaller than C . The corresponding prescaling factor is given by $ps = 2^{24}/(C + 1)$ and is thus typically a non-integer number. The cut value will thus be what defines the prescaling, while an integer approximation will be given in the trigger menu as well for reasons of readability. The goodness of this approximation decreases with higher prescale factors. For an integer approximation of 50, the actual value would be 50.0000476, corresponding to an error of 0.0001 %. For 5,00,000, the non-integer

⁸<https://svnweb.cern.ch/cern/wsvn/atlasoff/Trigger/TrigConfiguration/TrigConfL1Data/>.

value is 4,93,447—an error of 1.3%. However, in the simulation code the actual cut value given in the configuration will be used. For reasons of backward compatibility, the `ItemMap` will continue to store the prescale factor instead of the cut, but the exact value, not the approximation. When evaluating whether an item is accepted or not, the prescale factor is converted back into the cut and compared to the prescale counter of the item. This counter is set to a random number for each event. This should provide a close simulation of the prescaling in actual data taking, although only in the overall statistics, not on an event-by-event basis as the random numbers will not be the same for data and simulation for a given event.

The `ResultBuilder` is also updated to construct the output objects according to the new event format. In order to keep the simulation backward compatible, the simulation and all the code relating to it have been rewritten to make use of the `L1CommonCore` and `L1Common` packages. This allows to specify the version of the CTP that is to be used and run the simulation with the adequate settings. In this way, it will be possible also in the future to run on the data from run-I or produce MC samples corresponding to the old CTP. Moreover, this facilitates the implementation of further changes to the data format or other CTP parameters.

All these changes concerning the hardware and item formation inside the CTP have been implemented. Further adaption of the simulation might be necessary before run-II to account for changes in the output of other systems (i.e. external input to the simulation). For example, the integration of the `L1Topo` inputs has to be finalised once the output format of the `L1Topo` simulation is defined, which was not yet the case on the timescale of this work. However, the basic interface is there in form of the `FrontPanelCTP` class, which is expected to make the actual integration straight-forward. Once actual data with the new event format becomes available, the `DeriveSimulationInput` algorithm will have to be tested.

References

1. Simioni E et al (2012) Topological and central trigger processor for 2014 LHC luminosities. In: 18th IEEE-NPSS Real time conference (RT), pp 1–5. doi:[10.1109/RTC.2012.6418353](https://doi.org/10.1109/RTC.2012.6418353)
2. Ask et al S (2008) The ATLAS central level-1 trigger logic and TTC system. In: *J Instrum*, vol 3(08), 08002p. <http://stacks.iop.org/1748-0221/3/i=08/a=P08002>
3. Haas S Private communication
4. Haas S, Ghibaudi M, Private communication
5. Haas S, Spiwoeks R, Private communication
6. Haas S, Pauly T, Pöttgen R, Spiwoeks R (2014) The event format of the ATLAS central trigger processor
7. Vandelli W (2014) The raw event format in the ATLAS Trigger and DAQ
8. van der Bij HC et al (1998) S-LINK: a Prototype of the ATLAS Read-out Link. In: Presented at the fourth workshop on electronics for LHC experiments, Rome, 21–25 Sept 1998
9. Tier 0 Processing DQ Monitoring. <https://atlasdqm.cern.ch/webdisplay/>. Accessed Sept 2014

Part IV

Analysis

Chapter 10

Analysis Strategy

This chapter will give an overview of the general signal characteristics and how their differences with respect to Standard Model processes can be exploited to define a set of basic criteria for a signal region definition in Sect. 10.1. This section also contains a reminder of the parameters that limits will be set on. Section 10.2 will describe the estimation of the main backgrounds from W and Z production in association with jets, including the combination of several estimates of the $Z(\rightarrow \nu\bar{\nu})$ +jets process. The different estimation procedures for other background contributions are presented in Sect. 10.3. In Sect. 10.4 a short overview of the limit setting procedure is given.

10.1 Signal Characteristics and Parameters

As discussed in Sect. 5, the signature of events with a large amount of missing transverse energy and a hard ISR jet is a promising topology for the search of Dark Matter in the form of pair-produced WIMPs. The signal is expected to become visible as an excess over the Standard Model prediction in regions of large E_T^{miss} . The events are tagged by the presence of a highly energetic jet. No isolated leptons occur for such a signal process, which is why the search will be performed with events that do not contain identified electrons or muons. These are the basic requirements for the definition of *signal regions*. The number of observed data events in these signal regions will be compared to the SM expectation. In case no significant excess is found in data, limits on the cross section for new physics can be derived.

These limits can be converted into limits on the signal model parameters. For the effective field theory described in Sect. 5.2, the parameter to be constrained is the suppression scale, M_* , since the cross section for a given operator and a given WIMP mass depends only on this scale. One of the main advantages of the effective theory is that it allows to convert limits on M_* into limits on the WIMP-nucleon scattering cross section as well as on the annihilation rate of dark matter particles

into quarks, providing the possibility to compare with results from direct and indirect search experiments. Given the concerns about the applicability of the EFT at the LHC experiments, in addition to the EFT a simplified model with an s -channel mediator of mass M_{Med} will be considered, cf. Sect. 5.3. Here, limits will be set on the product of the couplings to SM particles and WIMP, $\sqrt{g_{SM}g_\chi}$. In analogy to the effective theory, the scale $\Lambda = M_{Med}/\sqrt{g_{SM}g_\chi}$ is defined and limits on it will be derived. In this way, the results between both models can be related.

10.2 Estimation of Main Background Contributions

The largest Standard Model background process, the production of Z -bosons in events with ISR jets, where the Z decays into a neutrino-antineutrino pair, is irreducible since it results in exactly the same signature as a signal would. Another large background contribution are leptonic W decays accompanied by jets from ISR, in which the lepton escapes the dedicated vetoes or—in case of $W^\pm(\rightarrow \tau^\pm\bar{\nu})$ +jets—decays hadronically. A precise estimation of these backgrounds is vital for the comparison to the observed number of events. Since purely simulation based predictions suffer from large experimental and theoretical uncertainties (of the order of 20–30%), a semi-data driven approach is adopted in this analysis. As this is one of the most crucial and also most complex parts of the analysis, the method shall be outlined in some detail in the following.

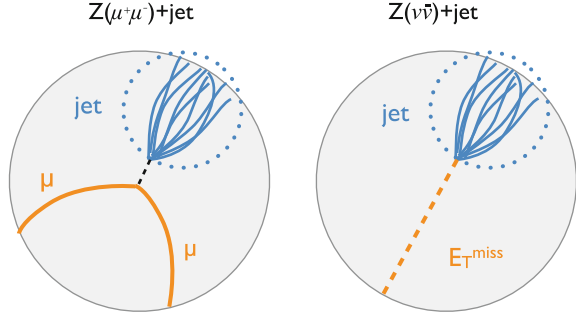
10.2.1 Transfer from Control Regions

In order to minimise the dependence on the modelling of the mainly contributing SM processes in the simulation, the predictions are to be corrected to data. Control regions (CR) are defined by explicitly selecting W or Z decays in both the electron and muon channel, while keeping the same requirements on jets and E_T^{miss} as in the signal region. After the removal of background contributions in the CRs, the expected number of background events in the signal region can be estimated by correcting for the acceptance of the control region specific cuts with respect to the common cuts between control and signal region.

All four processes are used to estimate the $Z(\rightarrow \nu\bar{\nu})$ +jets contribution in the signal region, resulting in four independent estimates that can be combined to give a more precise estimate of the largest background. The underlying idea is, that $Z(\rightarrow \nu\bar{\nu})$ +jets can be modelled by $W^\pm(\rightarrow \ell^\pm\bar{\nu})$ +jets and $Z(\rightarrow \ell^+\ell^-)$ +jets processes if the leptons are treated as E_T^{miss} , i.e. as neutrinos. This is illustrated for $Z(\rightarrow \mu^+\mu^-)$ +jets in Fig. 10.1. The leptons are removed from the calculation of missing E_T , meaning that their energy will be considered missing as well.

Moreover, a control region of $W^\pm(\rightarrow \mu^\pm\bar{\nu})$ +jets events is used to estimate $W^\pm(\rightarrow \mu^\pm\bar{\nu})$ +jets in the signal region. Similarly, the $W^\pm(\rightarrow e^\pm\bar{\nu})$ +jets background

Fig. 10.1 Sketch illustrating the use of $Z(\rightarrow \mu^+\mu^-)$ +jets events to emulate $Z(\rightarrow \nu\bar{\nu})$ +jets events



contamination is estimated using a $W^\pm(\rightarrow e^\pm\bar{\nu})$ +jets control region. The same control region is also used to assess the $W^\pm(\rightarrow \tau^\pm\bar{\nu})$ +jets contribution. In principle, both W control regions could be used to estimate the $W^\pm(\rightarrow \tau^\pm\bar{\nu})$ +jets background, but only the $W^\pm(\rightarrow e^\pm\bar{\nu})$ +jets CR will be used in this work, since for both processes the missing E_T corresponds to the neutrino p_T , while in the case of $W^\pm(\rightarrow \mu^\pm\bar{\nu})$ +jets the missing E_T is the boson p_T .

The general procedure is as follows: The control region selection is applied to data to select candidate events for the respective W or Z process, in the following also referred to as *control region process* (CRP). This gives a number of events, N_{data}^{CR} , which still has to be corrected for background contributions. Contaminations from top and diboson production processes (N_{top}^{CR} and N_{VV}^{CR}) are removed by subtracting the contributions estimated from simulated samples, i.e. calculating $N_{data}^{CR} - N_{top}^{CR} - N_{VV}^{CR}$. The remaining events can still contain (small) contributions from other W or Z processes. In order to remove those, the fraction of events due to the control region process, $N_{CRP}^{CR, MC}$, with respect to all W or Z events in the control region, $N_{all W/Z MC}^{CR}$, is used to scale the number of events. This fraction is given as

$$f_{CRP} = \frac{N_{CRP}^{CR, MC}}{N_{all W/Z MC}^{CR}}, \quad (10.1)$$

and is taken from the simulation. With this, the number of observed data events, $N_{CRP}^{CR, data}$, for the control region process can be expressed as

$$N_{CRP}^{CR, data} = (N_{data}^{CR} - N_{top}^{CR} - N_{VV}^{CR}) \cdot f_{CRP}. \quad (10.2)$$

To obtain the number of events in the signal region, the above number first has to be corrected for the acceptance of the cuts that are needed to single out the control region process in data, i.e. the cuts on the lepton kinematics and boson related quantities. This acceptance is taken from simulation as the ratio of events passing the complete CR selection with respect to the number of events passing the *preselection* ($N_{CRP}^{preselect., MC}$), i.e. all cuts that are identical to the signal region selection:

$$A_{CR\ cuts} = \frac{N_{CRP}^{CR, MC}}{N_{CRP}^{presel., MC}}. \quad (10.3)$$

Finally, a *transfer factor* (TF) is applied to correct for the remaining differences to the actual signal region selection, including the veto on the good leptons. This transfer factor is again a ratio taken from simulation, namely the number of events for the process that is to be estimated in the SR, the *process of interest* (PoI), $N_{PoI}^{SR, MC}$, and the number of events after the preselection of the control region process:

$$TF = \frac{N_{PoI}^{SR, MC}}{N_{CRP}^{presel., MC}}. \quad (10.4)$$

This transfer factor accounts for possible differences between the control region process and the process of interest, for example due to the presence of a lepton in one but not the other or due to different cross sections if W control regions are used to estimate $Z(\rightarrow \nu\bar{\nu})+\text{jets}$. For the estimation of $Z(\rightarrow \nu\bar{\nu})+\text{jets}$ from Z control regions, this ratio also corrects for the different branching ratios.

With the quantities defined above, the signal region estimate, $N_{PoI}^{SR, est.}$, can be written as

$$N_{PoI}^{SR, est.} = \frac{N_{CRP}^{CR, data}}{A_{CR\ cuts}} \cdot TF. \quad (10.5)$$

It is worth noting, that (10.5) is equivalent to the following:

$$\begin{aligned} N_{PoI}^{SR, est.} &= N_{CRP}^{CR, data} \cdot \frac{N_{CRP}^{presel., MC}}{N_{CRP}^{CR, MC}} \cdot \frac{N_{PoI}^{SR, MC}}{N_{CRP}^{presel., MC}} \\ &= (N_{data}^{CR} - N_{top}^{CR} - N_{VV}^{CR}) \cdot \frac{N_{CRP}^{CR, MC}}{N_{all\ W/Z\ MC}^{CR}} \cdot \frac{N_{CRP}^{presel., MC}}{N_{CRP}^{CR, MC}} \cdot \frac{N_{PoI}^{SR, MC}}{N_{CRP}^{presel., MC}} \\ &= (N_{data}^{CR} - N_{top}^{CR} - N_{VV}^{CR}) \cdot \frac{N_{PoI}^{SR, MC}}{N_{all\ W/Z\ MC}^{CR}}, \end{aligned} \quad (10.6)$$

i.e. the estimate in the signal region is obtained by scaling the observed events in the control region that have been corrected for top and diboson contributions by the MC ratio of events for the process of interest after the signal region cuts divided by the number of events from all W and Z processes in the control region.

In this form, one of the main advantages of this method becomes clearly visible: The simulation enters the background estimation only as a ratio¹ which leads to (partial) cancellation of systematic uncertainties, both experimental and theoretical. For example, the luminosity uncertainty which would affect the normalisation of

¹With the exception of the top and diboson processes.

the samples if they were used directly, has no effect on the ratio.² Similarly, the effect of mis-modelling of detector related uncertainties, such as jet energy scale and resolution, and theoretical uncertainties—PDF or renormalisation and factorisation scales—is reduced.

Another way of reading Eq. 10.6 is that the simulation is normalised to the data. Since the transfer factor is applied bin-by-bin, not only the normalisation, but also the shape is corrected to match the one observed in data, minimising effects from potential MC mis-modelling.

The selection efficiencies for leptons in general can be different for data and simulation. The performance groups thus provide scale factors (SF), as a function of the detector region and the p_T of the leptons, that have to be applied as event weights in the simulation in order to get the same efficiency in both data and MC. This has to be taken into account in the transfer factor method described in this section. In the respective control regions, the scale factors are applied according to the position and p_T of the selected leptons. When estimating $W^\pm(\rightarrow \ell^\pm \bar{\nu})$ +jets in the signal region, the numerator of the transfer factor in (10.4) has to be modified appropriately as well. This is done by considering

$$N_{PoI}^{SR, MC} = N^{\text{before veto}} - \sum_{i=1}^{N^{\text{fail veto}}} SF_i = N^{\text{pass veto}} + \sum_{i=1}^{N^{\text{fail veto}}} (1 - SF_i) \quad (10.7)$$

Here, $N^{\text{before veto}}$ is the number of simulated events before the veto is applied, $N^{\text{pass veto}}$ is the number of events that pass the veto, and $N^{\text{fail veto}}$ is the number of events that contain identified leptons and thus are rejected by the veto. Each of these events is assigned a weight corresponding to the SF for the respective lepton. Typically, the scale factors are close to 1, so that this is a small correction.

Combining Eqs. 10.6 and 10.7 and using, for example, $W^\pm(\rightarrow \mu^\pm \bar{\nu})$ +jets as PoI and the $W^\pm(\rightarrow \mu^\pm \bar{\nu})$ +jets CR to estimate it, the complete formula for the estimation of $W^\pm(\rightarrow \mu^\pm \bar{\nu})$ +jets in the signal region reads:

$$N_{W(\mu\nu)}^{SR, est} = \left(N_{data}^{W(\mu\nu) CR} - N_{top}^{W(\mu\nu) CR} - N_{VV}^{W(\mu\nu) CR} \right) \cdot \frac{N_{W(\mu\nu)}^{SR, MC} + \sum_{i=1}^{N_{W(\mu\nu)}^{SR fail veto, MC}} (1 - SF_i)}{\sum_{j=1}^{N_{all W/Z MC}^{W(\mu\nu) CR}} SF_j}, \quad (10.8)$$

where the scale factors have to be applied event by event.

Similarly, for the estimation of $Z(\rightarrow \nu \bar{\nu})$ +jets from the $W^\pm(\rightarrow \mu^\pm \bar{\nu})$ +jets control region, one can write:

²This is not strictly true when triggers with different luminosities are used in different regions, but this is not the case here.

$$N_{Z(\nu\nu)}^{SR, est} = \left(N_{data}^{W(\mu\nu)CR} - N_{top}^{W(\mu\nu)CR} - N_{VV}^{W(\mu\nu)CR} \right) \cdot \frac{N_{Z(\nu\nu)}^{SR, MC}}{\sum_{i=1}^{N_{all W/Z MC}^{W(\mu\nu)CR}} SF_i} . \quad (10.9)$$

Here, no additional scale factors are needed in the numerator since there are essentially no real leptons in the $Z(\rightarrow \nu\bar{\nu})+\text{jets}$ simulation.

10.2.2 Method for Combination of $Z(\rightarrow \nu\bar{\nu})+\text{jets}$ Estimates

As described in Sect. 10.2.1, there are two estimates for the $Z(\rightarrow \nu\bar{\nu})+\text{jets}$ background from each $W^\pm(\rightarrow \ell^\pm\bar{\nu})+\text{jets}$ and $Z(\rightarrow \ell^+\ell^-)+\text{jets}$ control region, yielding four estimates in total. Typically, using a $Z+\text{jets}$ control region to estimate $Z(\rightarrow \nu\bar{\nu})+\text{jets}$ leads to smaller systematic uncertainties since the processes are more similar, as was seen in reference [1]. However, the W control regions provide much higher statistics, which is of special importance when going to regions of large E_T^{miss} . In this way, all four estimates can contribute to an improvement of the measurement when combining them. For this purpose, a BLUE (*best linear unbiased estimator*) method as described in reference [2] is applied.

In this approach, the final estimate y is assumed to be linear combination of the (four) individual measurements y_i , $i = 1 \dots 4$, each of which is assigned a weight w_i to account for their relative uncertainties, i.e.

$$y = \sum_{i=1}^4 w_i y_i \quad \text{or} \quad y = \vec{w}^T \cdot \vec{y}, \quad \text{with} \quad \sum_{i=1}^4 w_i = 1. \quad (10.10)$$

The latter relation follows from the requirement that the estimate shall be unbiased. The uncertainty on the final estimate y due to a systematic source a , $\sigma_{y,a}$, can be written as

$$\sigma_{y,a}^2 = \sum_{i=1}^4 \sum_{j=1}^4 w_i w_j V_{ij}^a \quad (10.11)$$

and accordingly the total uncertainty is given by

$$\sigma_y^2 = \sum_{i=1}^4 \sum_{j=1}^4 w_i w_j V_{ij} \quad \text{or} \quad \sigma_y^2 = \vec{w}^T V \vec{w}. \quad (10.12)$$

In the above equations, V^a is the covariance matrix of the four measurements for a source a of systematic uncertainty, and $V = \sum_a V_a$ is the covariance matrix for the total uncertainty. These matrices have the variances of the individual measurements (due to a source a) on the diagonal, $V_{ii} = \sigma_i^2$, and the correlation terms in the off-diagonal elements, $V_{ij, i \neq j} = \rho_{ij} \sigma_i \sigma_j$.

The weights \vec{w} can be derived by minimising a generalised χ^2 of the following form

$$\chi^2 = [y\vec{e} - \vec{y}]^T V^{-1} [y\vec{e} - \vec{y}], \quad (10.13)$$

where \vec{e} is a unit-vector, resulting in

$$\vec{w} = \frac{V^{-1} \cdot \vec{e}}{\vec{e}^T \cdot (V^{-1} \cdot \vec{e})}. \quad (10.14)$$

The BLUE method can yield negative values for some of the weights in Eq. (10.14) if some estimates have much larger uncertainties than the others and the correlations are close to 1. This leads to the final estimate lying outside of the range covered by the individual values, which seems peculiar at first sight. However, it can be understood as follows [2]: In the case of strong (positive) correlations, the individual measurements will likely lie on the same side of the true value, which means that the best linear estimate will require extrapolation beyond the measurement closest to the true value. This in turn means that one or several of the weights have to be negative (and thus the sum of the remaining weights will be greater than 1).

When building the covariance matrices for various sources of uncertainties, the correlations will be approximated to be either 0 or 100% in the following way: Systematic uncertainties of a given source are treated fully correlated between different individual estimates. For the experimental uncertainties this is done since all measurements use the same detector. In case of the theoretical uncertainties it is less obvious. It is likely that the uncertainties are correlated to some extent but not to 100%. For example, the same PDF has been used for all W and Z simulation, thus, there is reason to assume there will be some correlation. As the exact correlations are not known, 100% will be assumed here. For the statistical uncertainties, the situation is slightly more complicated. While the uncertainties due to data statistics for the background subtraction and the denominator of the transfer factor are uncorrelated (since the control regions are orthogonal), the numerator of the transfer factor is the same for all $Z(\rightarrow \nu\bar{\nu})$ +jets estimates and hence is treated fully correlated.

10.3 Small Background Contributions

The diboson as well as $t\bar{t}$ and single top production are only small contributions to the total background in the signal region. Therefore, their normalisation is taken directly from the simulation. The same holds for $Z(\rightarrow \ell^+\ell^-)$ +jets processes that are efficiently suppressed by the lepton veto and the requirement of large E_T^{miss} in the signal region.

Multi-jet processes that can enter the signal region when a jet is missed or its energy is mis-measured, are largely suppressed by the requirement of large E_T^{miss} . The remaining small contribution at the lower end of the considered E_T^{miss} range is estimated in a data-driven way, since there are no simulation samples with sufficient

statistics available due to the large cross section of such events at a hadron collider. Moreover, the cross section predictions suffer from large theory uncertainties, which makes a direct estimation from data preferable.

The small residual non-collision background that is left after dedicated cleaning cuts and that also only contributes at the lowest considered $E_{\text{T}}^{\text{miss}}$ values is estimated in a data-driven way as well. At higher $E_{\text{T}}^{\text{miss}}$ (> 250 GeV) it is completely negligible [3].

10.4 Statistical Analysis

The agreement of data and estimated backgrounds can be quantified in terms of *hypothesis tests*. The signal+background hypothesis, called H_1 , is tested against the background only hypothesis, H_0 . The *p-value* of such a test gives the probability of finding data that is equally or less compatible with the hypothesis H_1 than the observed data under the assumption of H_0 . Accordingly, a small *p-value* means that the observed data is unlikely to be explained by H_0 . The *significance* (σ) of a discrepancy is defined with the help of the *p-value*: It gives the number of standard deviations of a Gaussian distribution such that the corresponding integral in the tail is equal to the *p-value*. For example, a 5σ significance corresponds to a *p-value* of 2.87×10^{-7} .

In case no significant excess is observed, limits on the model parameters for the effective theory and the simplified model are estimated, as mentioned in Sect. 10.1. In this analysis, a modified frequentist approach is adopted and an overview of the procedure and tools used for limit setting shall be given in this section.

Limit setting in principle corresponds to inverting the result of a hypothesis test. If the *p-value* is smaller than some predefined boundary, the hypothesis is rejected. This boundary is defined by the desired *confidence level* (CL) of the test such that the *p-value* has to be smaller than $1-\text{CL}$. For setting exclusion limits on a *parameter of interest* (POI) at a certain confidence level, the parameter of interest is scanned and the hypothesis test is repeated for each scan point until the corresponding *p-value* becomes smaller than $1-\text{CL}$. In the analysis to be conducted here, the parameter of interest is the signal strength μ . In order to calculate the *p-value*, a test statistic, t_μ , has to be defined, which is a measure of the compatibility of data and H_1 , under the assumption of a signal strength μ . The *p-value* is then given as

$$p = \int_{t_{\mu,obs}}^{\infty} f(t_\mu|\mu) dt_\mu. \quad (10.15)$$

Here, $t_{\mu,obs}$ is the value of the test statistic in data, $f(t_\mu|\mu)$ is the probability density function (p.d.f.) of the test statistic under the assumption of a certain value of μ . In general, $f(t_\mu|\mu)$ as to be derived by computing intensive simulations of toy experiments. There are, however, cases for which asymptotic formulas can be derived, as detailed in reference [4].

Starting from the assumption that a set of N measured quantities $\vec{x} = (x_1, \dots, x_N)$ is described by a joint p.d.f. $f(\vec{x}; \vec{\psi})$, where $\vec{\psi} = (\psi_1, \dots, \psi_n)$ are n parameters of unknown value, the likelihood function is given by the p.d.f. evaluated at \vec{x} but considered a function of the parameters, i.e. $L(\vec{\psi}) \equiv f(\vec{x}, \vec{\psi})$. Apart from the parameter(s) of interest, $\vec{\mu}$, there may be additional parameters that have to be determined from data but are of no interest for the final result. Such parameters are referred to as *nuisance parameters* and will be collectively labelled θ . Systematic uncertainties are a typical case of nuisance parameters. A way to remove the nuisance parameters from the problem is to construct the *profile likelihood*:

$$L_P(\vec{\mu}) = L(\vec{\mu}, \hat{\theta}(\vec{\mu})). \quad (10.16)$$

Here, $\hat{\theta}(\vec{\mu})$ is given by the $\vec{\theta}$ that maximise L for a given $\vec{\mu}$. The test statistics in reference [4] are based on the *profile likelihood ratio*

$$\lambda(\mu) = \frac{L_P}{L(\hat{\mu}, \hat{\theta})}, \quad (10.17)$$

where in the above expression for simplicity only one POI (μ) is considered. The values $\hat{\mu}$ and $\hat{\theta}$ maximise L globally, i.e. they are the maximum likelihood estimators. From this, it follows that $0 \leq \lambda(\mu) \leq 1$, and λ close to 1 indicates good agreement between the hypothesised value of μ and the data.

An often used test statistic for limit setting in LHC searches is a *one-sided* profile likelihood test statistic defined in the following way:

$$t_\mu = \begin{cases} -2 \ln \lambda(\mu) & \hat{\mu} \leq \mu \\ 0 & \hat{\mu} > \mu \end{cases}. \quad (10.18)$$

The test statistic is set to 0 for $\mu < \hat{\mu}$, since—when setting upper limits—data with $\hat{\mu} > \mu$ would not be considered less compatible with μ than the data obtained. Therefore, $\mu < \hat{\mu}$ is not included in the rejection region of the test. When defining the test statistic in this way, larger values of t_μ correspond to less compatibility between μ and the data. In reference [4], asymptotic formulas are derived for this test statistic and they are implemented in the hypothesis testing functionality of `ROOTStats` [5, 6]. This implementation is used in this thesis via the `HistFitter` tool [7] to perform the limit scan and to calculate limits using the CL_s -method [8, 9]. In this method, not the p -value itself is used to define the limit but rather $CL_s = p_{sb}/(1 - p_b) < 1 - CL$, i.e. the ratio of p -value for the signal+background hypothesis divided by $1-p$ -value for the background only hypothesis has to be smaller than $1-CL$. This definition has the advantage of being more robust against background fluctuations and prevents the setting of exclusion limits when there is no sensitivity [10]. Systematic uncertainties are included as nuisance parameters.

References

1. The ATLAS Collaboration (2013) Search for dark matter candidates and large extra dimensions in events with a jet and missing transverse momentum with the ATLAS detector. JHEP 1304:075. doi:[10.1007/JHEP04\(2013\)075](https://doi.org/10.1007/JHEP04(2013)075). [arXiv:1210.4491](https://arxiv.org/abs/1210.4491) [hep-ex]
2. Lyons L, Gibaut D, Clifford (1988) How to combine correlated estimates of a single physical quantity. Nucl Instrum Meth A270:110. doi:[10.1016/0168-9002\(88\)90018-6](https://doi.org/10.1016/0168-9002(88)90018-6)
3. The ATLAS Collaboration (2015) Search for new phenomena in final states with an energetic jet and large missing transverse momentum in pp collisions at $\sqrt{s} = 8$ TeV with the ATLAS detector. submitted to EPJC 2015. [arXiv:1502.01518](https://arxiv.org/abs/1502.01518) [hep-ex]
4. Cowan G et al (2011) Asymptotic formulae for likelihood-based tests of new physics. Eur Phys J C71:1554. doi:[10.1140/epjc/s10052-011-1554-0](https://doi.org/10.1140/epjc/s10052-011-1554-0). [arXiv:1007.1727](https://arxiv.org/abs/1007.1727) [physics.data-an]
5. Moneta L et al (2010) The RooStats project". In: Proceedings of the 13th International workshop on advanced computing and analysis techniques in physics research. February 22-27, Jaipur, India, p. 57. <http://acat2010.cern.ch/>. Published online at <http://pos.sissa.it/cgi-bin/reader/conf.cgi?confid=93>. [arXiv:1009.1003](https://arxiv.org/abs/1009.1003) [physics.data-an]
6. Schott for the RooStats Team G (2012) RooStats for searches. In: ArXiv Pre-Prints. [arXiv:1203.1547](https://arxiv.org/abs/1203.1547) [physics.data-an]
7. Baak M et al (2014) HistFitter software framework for statistical data analysis. In: ArXiv Pre-Prints. Eur Phys J C. [arXiv:1410.1280](https://arxiv.org/abs/1410.1280) [hep-ex]
8. Read AL (2002) Presentation of search results: the $CL_{(s)}$ technique. Tech Rep J Phys G G28:2693–2704
9. Read AL (2000) Modified frequentist analysis of search results (the CL_s method). CERN-OPEN-2000-205
10. Beringer J et al (2012) Review of particle physics. Phys Rev D 86:010001. doi:[10.1103/PhysRevD.86.010001](https://doi.org/10.1103/PhysRevD.86.010001)

Chapter 11

Data and Simulated Samples

The samples used in this analysis are all derived from the official ATLAS AOD production. They are D3PDs provided centrally by the ATLAS SUSY analysis group. The data sample analysed in this thesis is described in Sect. 11.1, details on the simulated samples both for the Standard Model background processes as well as for the signal are given in Sect. 11.2.

11.1 Data

The raw data sample that is the basis of this work was recorded by the ATLAS detector between April and December 2012 and corresponds to the data taking periods A–E, G–J, and L, which comprise run numbers from 200804 to 215643. Table 11.1 gives an overview of the data taking periods, their corresponding run numbers and integrated luminosities. The total luminosity of the data set after applying basic data quality requirements is 20.3 fb^{-1} .

For the signal regions and most of the control regions, data from the `JetTauEtmiss` stream selected with an unrescaled E_T^{miss} trigger with a threshold of 80 GeV at event filter level is used. In some electron control regions data is selected from the `EGamma` stream with a logical OR of two single electron triggers: one with a threshold of 24 GeV at the event filter level and an additional isolation requirement (`EF_e14vhi_medium1`) and one with a threshold of 60 GeV (`EF_e60_medium1`). Both trigger require medium quality of the electrons. The corresponding integrated luminosity is the same as for the `JetTauEtmiss` stream.

Table 11.1 Data periods from the 2012 data taking that are used for the analysis

Period	Dates	Run numbers	\mathcal{L}_{int} (pb ⁻¹)
A	Apr-04 : Apr-20	200804 : 216432	892
B	May-01 : Jun-18	202660 : 205113	5474
C	Jul-01 : Jul-24	206248 : 207397	1614
D	Jul-24 : Aug-23	207447 : 209025	3532
E	Aug-23 : Sep-17	209074 : 210308	2808
G	Sep-26 : Oct-08	211522 : 212272	1380
H	Oct-13 : Oct-26	212619 : 213359	1617
I	Oct-26 : Nov-02	213431 : 213819	1126
J	Nov-02 : Nov-26	213900 : 215091	2890
L	Nov-30 : Dec-06	215414 : 215643	961
A-L	Apr-04 : Dec-06	200804 : 215643	22754

11.2 Simulated Samples

The simulated samples for this analysis have been produced with the ATLAS offline software release Athena 17.2, during the so-called MC12a production campaign.¹ They all use the same description of the detector that corresponds to the status at the beginning of the data taking period in 2012.² The detector simulation is based on GEANT4 [1], as described in Sect. 7.8. While some of the background samples are produced with a full detector simulation, the signal samples and the remaining background samples use the fast detector simulation, ATLFASII (cf. Sect. 7.8).

To simulate multiple interactions in a bunch crossing (pile-up), all of the simulated samples are overlaid in the digitisation step with additional minimum bias events. These events are generated using PYTHIA8 [2] with the AM2 tune [3] and the MSTW2008LO [4] PDF set. The average number of interactions $\langle \mu \rangle$ ranges from 0 to 40, which does not describe data for different running conditions equally well. Thus, the simulated samples are reweighted in order to correct the pile-up distribution to match the one observed in data. This is done with the help of the PileupReweighting tool,³ which is also used to derive the weights for each simulated sample based on the good runs list. The tool assigns event weights based on the average number of interactions.

¹<https://twiki.cern.ch/twiki/bin/viewauth/AtlasProtected/AtlasProductionGroupMC12a>.

²<https://twiki.cern.ch/twiki/bin/viewauth/Atlas/MC12aWiki>.

³<https://twiki.cern.ch/twiki/bin/viewauth/AtlasProtected/ExtendedPileupReweighting>.

11.2.1 Signal Process

Samples for the signal process of WIMP pair production in events with ISR jets are generated using `MadGraph5` [5] interfaced to `PYTHIA6` [6] using the MLM matching scheme [7]. Two sets of samples are produced: One with a matching scale (called *qcut*) at 80 GeV (QCUT80) and one with $qcut = 300$ GeV (QCUT300) in order to provide reasonable statistics at high E_T^{miss} . This effectively places the same cut on the p_T of the leading parton, hence the samples can be combined by selecting the leading parton at truth-level and cutting on its p_T . To be safe from turn-on effects, a cut value of 350 GeV is chosen, meaning that events with $p_T^{\text{lead. parton}} > 350$ GeV in the QCUT80 sample will be discarded and the same is done for events with $p_T^{\text{lead. parton}} < 350$ GeV in the QCUT300 sample.

The PDF set used in the sample generation is `CTEQ6L1` [8], which is a rather old PDF set and nowadays not deemed suitable for processes at the LHC any more. Instead, the recommendation for leading order PDF sets is to use `MSTW2008LO` [9]. Thus, all signal samples are reweighted to `MSTW20081068c1`. For this, version 6.1.3 of the `LHAPDF` library of PDF sets [10] is used. A weight is assigned to each event based on the scale of the event (Q^2), the momentum fractions (x_1, x_2) and types of the two interacting partons (all of which is stored in the `D3PDFs`), and the original and alternate PDF to be used.

As discussed in Sect. 5.2, there is a total of 20 effective operators describing the production of either Dirac fermionic or complex scalar WIMP pairs, (cf. Fig. 5.2), but only a subset of those contributes to direct detection in the limit of low momentum transfer [11]. This motivated the choice of using D1, D5, D8, D9, and D11 for the Dirac fermionic dark matter, and C1 and C5 for complex scalar dark matter, cf. Sect. 5.2. For the operator D8 only truth samples are generated. The only difference between D8 and D5 is the cross section and there is thus no need for separate fully simulated samples. C1 and C5 are the equivalents to D1 and D11 for the case of scalar dark matter.

For each operator, samples for WIMP masses of 50, 100, 200, 400, 700, 1000 and 1300 GeV are produced. For small WIMP masses the acceptances are the same at LHC energies for D1, D5 (D8) and D11. For D9 and the scalar DM operators this was found to not be true to the same extend [12] and hence additional samples for $m_\chi = 10$ GeV are added. The samples with their cross sections, numbers of generated events, the corresponding integrated luminosity and the sample ID are listed in Table A.1 for the complex scalar DM operators and in Table A.2 for the operators for Dirac fermionic DM.

In addition to the simulation for the effective operators, samples are produced for the simplified model described in Sect. 5.3. The same setup as for the EFT is used and the samples are again reweighted to `MSTW20081068c1`. Mediator masses of 10, 50, 100, 300, 600 GeV and 1, 3, 6, 10, 30 TeV, as well as WIMP masses between 10 GeV and 1.3 TeV are generated, see Tables A.3 and A.4. Two different widths are

considered for the mediator: $\Gamma = M_{Med}/3$ and $\Gamma = M_{Med}/(8\pi)$, motivated by the same choice made in reference [13], cf. Sect. 5.3.

11.2.2 Background Processes

For the $Z(\rightarrow \nu\bar{\nu})$ +jets, $Z(\rightarrow \ell^+\ell^-)$ +jets and $W^\pm(\rightarrow \ell^\pm\bar{\nu})$ +jets processes, samples have been generated with SHERPA [14], using the CT10 [15] NLO PDF set. SHERPA⁴ as a complete MC generator has its own models for showering, fragmentation and underlying event. The matching between the matrix element level and the parton shower is done following the CKKW matching scheme [16, 17].

In addition to the inclusive SHERPA samples, samples have been produced in slices of boson p_T to ensure sufficient statistics up to high E_T^{miss} , which are the most important regions of phase space for this analysis. The samples with a p_T cut of 280 GeV or more are generated with a full detector simulation, for the samples describing decays into τ -leptons, all of the sliced samples use full simulation. The other W/Z +jets samples are done using ATLFASTII. Moreover, the samples were produced in three exclusive heavy quark flavour compositions (veto on b and c quarks, allow for c but veto b, allow for b only).⁵ The $Z(\rightarrow \ell^+\ell^-)$ +jets samples are generated with a generator level cut of 40 GeV on the invariant mass of the di-lepton system.

All W/Z +jets samples are normalised to the NNLO cross sections from DYNLO [18, 19] using k -factors of 1.12 for Z +jets and 1.1 for W +jets. Tables 11.2, 11.3, 11.4, 11.5, 11.6, 11.7 and 11.8 list the W/Z +jets samples together with their effective cross section and the corresponding integrated luminosity. The effective cross section is corrected for the generator cut efficiencies and the k -factor, and the luminosity is calculated using this cross section and the weighted number of events. The weighted numbers include the pile-up weights as well as generator weights, which differ from 1 for MC@NLO [20] and SHERPA. They are calculated as the sum of weights for all generated events, $N_{gen} = \sum_i^{N_{gen}} (w_{pu,i} \cdot w_{mc,i})$.

For the simulation of top-quark pair production, MC@NLO interfaced to HERWIG+JIMMY [21, 22] for the underlying event is used; the PDF set is CT10. The mass of the top quark is assumed to be 172.5 GeV, for which a cross section of $253_{-14.5}^{+13.3}$ pb for top pair production in pp collisions at $\sqrt{s} = 8$ TeV is predicted. The calculation was done at NNLO in QCD, hence the corresponding k -factors are 1 [23–28]. Table 11.9 lists the top process samples with their effective cross section and integrated luminosity, calculated in the same way as for the W/Z +jets samples. There are two $t\bar{t}$ samples: one for the fully hadronic decay channel (45.7% of the total cross section), and one for the decays involving leptons (54.3%).

The simulation of single top quark production is done using different generators for the t -channel on the one hand and the s -channel and Wt processes on the other

⁴Acronym for Simulation for High-Energy Reactions of PArticles [16].

⁵This is mainly to improve the description of variables used in flavour tagging algorithms and hence of minor relevance for this analysis.

Table 11.2 $Z(\rightarrow \nu\bar{\nu})$ +jets samples used for the analysis

Name	σ (pb)	\mathcal{L}_{int} (fb $^{-1}$)
ZnunuMassiveCBPt0_BFilter	197.2	34.6
ZnunuMassiveCBPt0_CFilterBVeto	1879.1	5.1
ZnunuMassiveCBPt0_CVetoBVeto	4630.2	3.0
ZnunuMassiveCBPt70_140_BFilter	15.7	81.2
ZnunuMassiveCBPt70_140_CFilterBVeto	65.7	11.0
ZnunuMassiveCBPt70_140_CVetoBVeto	105.2	12.1
ZnunuMassiveCBPt140_280_BFilter	2.4	84.5
ZnunuMassiveCBPt140_280_CFilterBVeto	9.3	48.0
ZnunuMassiveCBPt140_280_CVetoBVeto	13.5	51.9
ZnunuMassiveCBPt280_500_BFilter	0.2	246.3
ZnunuMassiveCBPt280_500_CFilterBVeto	0.6	91.1
ZnunuMassiveCBPt280_500_CVetoBVeto	0.8	286.1
ZnunuMassiveCBPt500_BFilter	0.0	1046.3
ZnunuMassiveCBPt500_CFilterBVeto	0.0	318.4
ZnunuMassiveCBPt500_CVetoBVeto	0.0	1066.0

Table 11.3 $Z(\rightarrow \mu^+\mu^-)$ +jets samples used for the analysis

Name	σ (pb)	\mathcal{L}_{int} (fb $^{-1}$)
ZmumuMassiveCBPt0_BFilter	34.8	31.5
ZmumuMassiveCBPt0_CFilterBVeto	352.5	4.1
ZmumuMassiveCBPt0_CVetoBVeto	856.4	3.3
ZmumuMassiveCBPt70_140_BFilter	2.7	108.7
ZmumuMassiveCBPt70_140_CFilterBVeto	11.7	20.5
ZmumuMassiveCBPt70_140_CVetoBVeto	18.6	27.4
ZmumuMassiveCBPt140_280_BFilter	0.4	97.0
ZmumuMassiveCBPt140_280_CFilterBVeto	1.7	53.8
ZmumuMassiveCBPt140_280_CVetoBVeto	2.4	58.6
ZmumuMassiveCBPt280_500_BFilter	0.0	137.8
ZmumuMassiveCBPt280_500_CFilterBVeto	0.1	101.6
ZmumuMassiveCBPt280_500_CVetoBVeto	0.1	79.9
ZmumuMassiveCBPt500_BFilter	0.0	1199.4
ZmumuMassiveCBPt500_CFilterBVeto	0.0	343.1
ZmumuMassiveCBPt500_CVetoBVeto	0.0	1174.1

Table 11.4 $Z(\rightarrow e^+e^-)+$ jets samples used for the analysis

Name	σ (pb)	\mathcal{L}_{int} (fb $^{-1}$)
ZeeMassiveCBPt0_BFilter	34.9	31.5
ZeeMassiveCBPt0_CFilterBVeto	352.2	4.1
ZeeMassiveCBPt0_CVetoBVeto	850.9	3.3
ZeeMassiveCBPt70_140_BFilter	2.7	108.9
ZeeMassiveCBPt70_140_CFilterBVeto	11.7	19.1
ZeeMassiveCBPt70_140_CVetoBVeto	18.6	27.4
ZeeMassiveCBPt140_280_BFilter	0.4	97.0
ZeeMassiveCBPt140_280_CFilterBVeto	1.6	54.1
ZeeMassiveCBPt140_280_CVetoBVeto	2.4	58.6
ZeeMassiveCBPt280_500_BFilter	0.0	138.6
ZeeMassiveCBPt280_500_CFilterBVeto	0.1	101.3
ZeeMassiveCBPt280_500_CVetoBVeto	0.1	80.2
ZeeMassiveCBPt500_BFilter	0.0	1126.6
ZeeMassiveCBPt500_CFilterBVeto	0.0	345.3
ZeeMassiveCBPt500_CVetoBVeto	0.0	1470.0

Table 11.5 $Z(\rightarrow \tau^+\tau^-)+$ jets samples used for the analysis

Name	σ (pb)	\mathcal{L}_{int} (fb $^{-1}$)
ZtautauMassiveCBPt0_BFilter	34.6	31.7
ZtautauMassiveCBPt0_CFilterBVeto	352.8	4.1
ZtautauMassiveCBPt0_CVetoBVeto	858.0	3.3
ZtautauMassiveCBPt70_140_BFilter	2.7	109.0
ZtautauMassiveCBPt70_140_CFilterBVeto	11.7	20.5
ZtautauMassiveCBPt70_140_CVetoBVeto	18.6	27.4
ZtautauMassiveCBPt140_280_BFilter	0.4	96.5
ZtautauMassiveCBPt140_280_CFilterBVeto	1.7	54.0
ZtautauMassiveCBPt140_280_CVetoBVeto	2.4	58.6
ZtautauMassiveCBPt280_500_BFilter	0.0	141.3
ZtautauMassiveCBPt280_500_CFilterBVeto	0.1	102.1
ZtautauMassiveCBPt280_500_CVetoBVeto	0.1	80.0
ZtautauMassiveCBPt500_BFilter	0.0	1180.5
ZtautauMassiveCBPt500_CFilterBVeto	0.0	355.0
ZtautauMassiveCBPt500_CVetoBVeto	0.0	1465.7

Table 11.6 $W^\pm(\rightarrow \mu^\pm \bar{\nu})$ +jets samples used for the analysis

Name	σ (pb)	\mathcal{L}_{int} (fb $^{-1}$)
WmunuMassiveCBPt0_BFilter	156.2	27.9
WmunuMassiveCBPt0_CJetFilterBVeto	518.0	5.6
WmunuMassiveCBPt0_CJetVetoBVeto	11513.8	2.4
WmunuMassiveCBPt70_140_BFilter	12.8	33.5
WmunuMassiveCBPt70_140_CJetFilterBVeto	55.3	12.5
WmunuMassiveCBPt70_140_CJetVetoBVeto	211.1	6.0
WmunuMassiveCBPt140_280_BFilter	2.2	94.6
WmunuMassiveCBPt140_280_CJetFilterBVeto	7.5	57.0
WmunuMassiveCBPt140_280_CJetVetoBVeto	24.9	18.6
WmunuMassiveCBPt280_500_BFilter	0.2	120.3
WmunuMassiveCBPt280_500_CJetFilterBVeto	0.5	88.8
WmunuMassiveCBPt280_500_CJetVetoBVeto	1.4	78.0
WmunuMassiveCBPt500_BFilter	0.0	179.2
WmunuMassiveCBPt500_CJetFilterBVeto	0.0	75.4
WmunuMassiveCBPt500_CJetVetoBVeto	0.1	141.4

Table 11.7 $W^\pm(\rightarrow \tau^\pm \bar{\nu})$ +jets samples used for the analysis

Name	σ (pb)	\mathcal{L}_{int} (fb $^{-1}$)
WtaunuMassiveCBPt0_BFilter	155.8	27.9
WtaunuMassiveCBPt0_CJetFilterBVeto	561.2	5.3
WtaunuMassiveCBPt0_CJetVetoBVeto	11453.0	2.0
WtaunuMassiveCBPt70_140_BFilter	12.8	33.5
WtaunuMassiveCBPt70_140_CJetFilterBVeto	55.3	12.5
WtaunuMassiveCBPt70_140_CJetVetoBVeto	210.0	6.1
WtaunuMassiveCBPt140_280_BFilter	2.2	94.7
WtaunuMassiveCBPt140_280_CJetFilterBVeto	7.6	56.5
WtaunuMassiveCBPt140_280_CJetVetoBVeto	24.8	18.8
WtaunuMassiveCBPt280_500_BFilter	0.2	120.1
WtaunuMassiveCBPt280_500_CJetFilterBVeto	0.5	87.3
WtaunuMassiveCBPt280_500_CJetVetoBVeto	1.4	78.7
WtaunuMassiveCBPt500_BFilter	0.0	179.0
WtaunuMassiveCBPt500_CJetFilterBVeto	0.0	74.9
WtaunuMassiveCBPt500_CJetVetoBVeto	0.1	142.1

Table 11.8 $W^\pm (\rightarrow e^\pm \bar{\nu})$ +jets samples used for the analysis

Name	σ (pb)	\mathcal{L}_{int} (fb $^{-1}$)
WenuMassiveCBPt0_BFilter	155.6	28.0
WenuMassiveCBPt0_CJetFilterBVeto	597.2	5.1
WenuMassiveCBPt0_CJetVetoBVeto	11439.9	2.4
WenuMassiveCBPt70_140_BFilter	12.8	33.5
WenuMassiveCBPt70_140_CJetFilterBVeto	55.9	12.4
WenuMassiveCBPt70_140_CJetVetoBVeto	209.3	6.1
WenuMassiveCBPt140_280_BFilter	2.2	94.7
WenuMassiveCBPt140_280_CJetFilterBVeto	7.7	56.1
WenuMassiveCBPt140_280_CJetVetoBVeto	24.7	18.9
WenuMassiveCBPt280_500_BFilter	0.2	120.1
WenuMassiveCBPt280_500_CJetFilterBVeto	0.5	86.8
WenuMassiveCBPt280_500_CJetVetoBVeto	1.4	77.2
WenuMassiveCBPt500_BFilter	0.0	179.4
WenuMassiveCBPt500_CJetFilterBVeto	0.0	74.6
WenuMassiveCBPt500_CJetVetoBVeto	0.1	28.7

Table 11.9 $t\bar{t}$ and single top samples used for the analysis

Name	σ (pb)	\mathcal{L}_{int} (fb $^{-1}$)
SingleTopSChanWenu	0.6	279.1
SingleTopSChanWmunu	0.6	279.0
SingleTopSChanWtaunu	0.6	279.1
SingleTopWtChanIncl	22.4	79.0
singletop_tchan_e	9.5	27.1
singletop_tchan_mu	9.5	27.1
singletop_tchan_tau	9.5	26.6
ttbar_LeptonFilter	137.4	84.1
ttbar_allhad	115.6	8.0

hand. The s -channel and Wt processes are simulated in the same way as the $t\bar{t}$ samples, i.e. using MC@NLO together with HERWIG+JIMMY and CT10. For the t -channel processes, AcerMC [29] with PYTHIA6 and the CTEQ6L1 PDF is used. This is accounting for the fact that the b -quark spectator is mis-modelled in MC@NLO [30, 31].

Samples modelling the production of pairs of electroweak gauge bosons are generated with the same setup as the W and Z samples, i.e. SHERPA and CT10, using a full detector simulation. Their effective cross sections and integrated luminosities are listed in Table 11.10. Except for the samples including a photon, the b - and c -quarks are treated as massive quarks. The $V\gamma$ samples ($V = W$ or $V = Z$) are generated

Table 11.10 Diboson samples used for the analysis

Name	σ (pb)	\mathcal{L}_{int} (fb ⁻¹)
enugammaPt10	163.1	72.3
munugammaPt10	162.7	71.5
tautaugammaPt10	32.3	124.3
taunugammaPt10	163.0	40.3
llll_ZZ	8.7	435.0
eegammaPt10	32.3	274.7
mumugammaPt10	32.3	284.6
nunugammaPt20	9.0	610.8
gammaVtoqq	6.8	90.0
llnunu_WW_MassiveCB	5.6	1987.1
llnunu_ZZ_MassiveCB	0.5	2078.5
lllnu_WZ_MassiveCB	10.2	367.9
lnununu_WZ_MassiveCB	1.5	358.4
ZWtoeeqq_MassiveCB	1.5	160.0
ZZtoeeqq_MassiveCB	0.2	169.6
ZWtomumuqq_MassiveCB	1.5	160.2
ZZtomumuqq_MassiveCB	0.2	169.0
ZWtotatauqq_MassiveCB	1.5	161.4
ZZtotatauqq_MassiveCB	0.2	173.1
ZWtonunuqq_MassiveCB	2.8	88.6
ZZtonunuqq_MassiveCB	1.7	96.0
WWtoenuqq_MassiveCB	7.7	142.7
WZtoenuqq_MassiveCB	2.0	146.5
WWtomunuqq_MassiveCB	7.7	142.4
WZtomunuqq_MassiveCB	2.0	146.3
WWtotaunuqq_MassiveCB	7.7	142.9
WZtotaunuqq_MassiveCB	2.0	145.6

with a cut on the photon p_T of 10 GeV, except for the sample where the Z decays into neutrinos, where the cut is at 20 GeV. Apart from that, there is a lower cut at 7 GeV on the invariant mass which is increased to 40 GeV for the $Z\gamma$ samples with charged leptons in the final state. The VV samples ($V \neq \gamma$) are normalised to NLO cross section calculations [32].

The production of a photon together with jets is simulated using PYTHIA8 with the AU2 tune and the CTEQ6L1 PDF set. They are produced in exclusive bins of

Table 11.11 γ +jets samples used for the analysis

Name	σ (pb)	\mathcal{L}_{int} (fb $^{-1}$)
gammajet_binned20	117865.5	0.0
gammajet_binned40	11377.5	0.1
gammajet_binned80	862.2	1.2
gammajet_binned150	68.0	14.7
gammajet_binned300	2.8	362.0

photon p_T with lower bin boundaries of 20, 40, 80, 150 and 300 GeV. The last sample starting from 300 GeV is inclusive. The effective cross section and integrated luminosity of the samples are listed in Table 11.11.

References

1. Agostinelli S, Others (2003) GEANT4: a simulation toolkit. Nucl Instrum Methods A506:250–303. doi:[10.1016/S0168-9002\(03\)01368-8](https://doi.org/10.1016/S0168-9002(03)01368-8)
2. Sjostrand T, Mrenna S, Skands PZ (2008) A brief introduction to PYTHIA 8.1. Comput Phys Commun 178:852–867. doi:[10.1016/j.cpc.2008.01.036](https://doi.org/10.1016/j.cpc.2008.01.036). arXiv:[0710.3820](https://arxiv.org/abs/0710.3820) [hep-ph]
3. The ATLAS Collaboration (2011) Further ATLAS tunes of PYTHIA6 and Pythia 8. Technical report. ATL-PHYS-PUB-2011-014. Geneva: CERN
4. Martin AD et al (2009) Parton distributions for the LHC. Eur Phys J C63:189–285. doi:[10.1140/epjc/s10052-009-1072-5](https://doi.org/10.1140/epjc/s10052-009-1072-5). arXiv:[0901.0002](https://arxiv.org/abs/0901.0002) [hep-ph]
5. Alwall J et al (2011) MadGraph 5: going beyond. JHEP 1106:128. doi:[10.1007/JHEP06\(2011\)128](https://doi.org/10.1007/JHEP06(2011)128). arXiv:[1106.0522](https://arxiv.org/abs/1106.0522) [hep-ph]
6. Sjostrand T, Mrenna S, Skands P (2006) PYTHIA 6.4 physics and manual. JHEP 05:026. arXiv:[hep-ph/0603175](https://arxiv.org/abs/hep-ph/0603175)
7. Alwall J et al (2008) Comparative study of various algorithms for the merging of parton showers and matrix elements in hadronic collisions. Eur Phys J C53:473–500. doi:[10.1140/epjc/s10052-007-0490-5](https://doi.org/10.1140/epjc/s10052-007-0490-5). arXiv:[0706.2569](https://arxiv.org/abs/0706.2569) [hep-ph]
8. Pumplin J, Others (2002) New generation of parton distributions with uncertainties from global QCD analysis. JHEP 0207:012. doi:[10.1088/1126-6708/2002/07/012](https://doi.org/10.1088/1126-6708/2002/07/012). arXiv:[hep-ph/0201195](https://arxiv.org/abs/hep-ph/0201195) [hep-ph]
9. Buckley A, Ferrando J, Gwenlan C, Private communication
10. Whalley MR, Bourilkov D, Group RC (2005) The Les Houches accord PDFs (LHAPDF) and LHAGLUE. ArXiv Pre-Prints. arXiv:[hep-ph/0508110](https://arxiv.org/abs/hep-ph/0508110) [hep-ph]
11. Goodman J et al (2010) Constraints on dark matter from colliders. Phys Rev D82:116010. doi:[10.1103/PhysRevD.82.116010](https://doi.org/10.1103/PhysRevD.82.116010). arXiv:[1008.1783](https://arxiv.org/abs/1008.1783) [hep-ph]
12. Abdallah J et al (2013) Search for new phenomena with mono-jet plus missing transverse energy signature in proton-proton collisions at $\sqrt{s} = 8$ TeV with the ATLAS detector. Technical report. ATL-COM-PHYS-2013-1578. Geneva: CERN
13. Fox PJ et al (2012) Missing energy signatures of dark matter at the LHC. Phys Rev D85:056011. doi:[10.1103/PhysRevD.85.056011](https://doi.org/10.1103/PhysRevD.85.056011). arXiv:[1109.4398](https://arxiv.org/abs/1109.4398) [hep-ph]
14. Gleisberg T et al (2009) Event generation with SHERPA 1.1. JHEP 02:007. arXiv:[0811.4622](https://arxiv.org/abs/0811.4622) [hep-ph]
15. Lai H-L et al (2010) New parton distributions for collider physics. Phys Rev D 82:074024. doi:[10.1103/PhysRevD.82.074024](https://doi.org/10.1103/PhysRevD.82.074024). arXiv:[1007.2241](https://arxiv.org/abs/1007.2241) [hep-ph]

16. Gleisberg T et al (2004) SHERPA 1. alpha: a proof of concept version. JHEP 0402:056. doi:[10.1088/1126-6708/2004/02/056](https://doi.org/10.1088/1126-6708/2004/02/056). [arXiv:hep-ph/0311263](https://arxiv.org/abs/hep-ph/0311263) [hep-ph]
17. Krauss F (2002) Matrix elements and parton showers in hadronic interactions. JHEP 0208:015. doi:[10.1088/1126-6708/2002/08/015](https://doi.org/10.1088/1126-6708/2002/08/015). [arXiv:hep-ph/0205283](https://arxiv.org/abs/hep-ph/0205283) [hep-ph]
18. Catani S et al (2009) Vector boson production at hadron colliders: a fully exclusive QCD calculation at NNLO. Phys Rev Lett 103:082001. doi:[10.1103/PhysRevLett.103.082001](https://doi.org/10.1103/PhysRevLett.103.082001). [arXiv:0903.2120](https://arxiv.org/abs/0903.2120) [hep-ph]
19. Catani S, Grazzini M (2007) An NNLO subtraction formalism in hadron collisions and its application to Higgs boson production at the LHC. Phys Rev Lett 98:222002. doi:[10.1103/PhysRevLett.98.222002](https://doi.org/10.1103/PhysRevLett.98.222002). [arXiv:hep-ph/0703012](https://arxiv.org/abs/hep-ph/0703012) [hep-ph]
20. Frixione S, Webber B (2006) The MC@NLO 3.2 event generator. ArXiv Pre-Prints. [arXiv:hep-ph/0601192](https://arxiv.org/abs/hep-ph/0601192)
21. Corcella G, Others (2002) HERWIG 6.5 *release note*. [arXiv:hep-ph/0210213](https://arxiv.org/abs/hep-ph/0210213)
22. Butterworth JFJ, Seymour M (1996) Multiparton interactions in photoproduction at HERA. Z Phys C72:637–646. [arXiv:hep-ph/9601371](https://arxiv.org/abs/hep-ph/9601371)
23. Cacciari M et al (2012) Top-pair production at hadron colliders with next-to-next-to-leading logarithmic soft-gluon resummation. Phys Lett B710:612–622. doi:[10.1016/j.physletb.2012.03.013](https://doi.org/10.1016/j.physletb.2012.03.013). [arXiv:1111.5869](https://arxiv.org/abs/1111.5869) [hep-ph]
24. Baernreuther P, Czako M, Mitov A (2012) Percent level precision physics at the tevatron: first genuine NNLO QCD corrections to $q\bar{q} \rightarrow t\bar{t} + X$. Phys Rev Lett 109:132001. doi:[10.1103/PhysRevLett.109.132001](https://doi.org/10.1103/PhysRevLett.109.132001). [arXiv:1204.5201](https://arxiv.org/abs/1204.5201) [hep-ph]
25. Czako M, Mitov A (2012) NNLO corrections to top-pair production at hadron colliders: the all-fermionic scattering channels. JHEP 1212:054. doi:[10.1007/JHEP12\(2012\)054](https://doi.org/10.1007/JHEP12(2012)054). [arXiv:1207.0236](https://arxiv.org/abs/1207.0236) [hep-ph]
26. Czako M, Mitov A (2013) NNLO corrections to top pair production at hadron colliders: the quark-gluon reaction. JHEP 1301:080. doi:[10.1007/JHEP01\(2013\)080](https://doi.org/10.1007/JHEP01(2013)080). [arXiv:1210.6832](https://arxiv.org/abs/1210.6832) [hep-ph]
27. Czako M, Fiedler P, Mitov A (2013) Total top-quark pair-production cross section at Hadron colliders through $O(\alpha_s^4)$. Phys Rev Lett 110.25:252004. doi:[10.1103/PhysRevLett.110.252004](https://doi.org/10.1103/PhysRevLett.110.252004). [arXiv:1303.6254](https://arxiv.org/abs/1303.6254) [hep-ph]
28. Czako M, Mitov A (2011) Top++: a program for the calculation of the top-pair cross-section at Hadron colliders. ArXiv Pre-Prints. [arXiv:1112.5675](https://arxiv.org/abs/1112.5675) [hep-ph]
29. Kersevan BP, Richter-Was E (2013) The Monte Carlo event generator AcerMC versions 2.0 to 3.8 with interfaces to PYTHIA 6.4, HERWIG 6.5 and ARIADNE 4.1. Comput Phys Commun 184:919–985. doi:[10.1016/j.cpc.2012.10.032](https://doi.org/10.1016/j.cpc.2012.10.032). [arXiv:hep-ph/0405247](https://arxiv.org/abs/hep-ph/0405247) [hep-ph]
30. Re E (2014) Overview of MC generators for single top. <https://indico.cern.ch/getFile.py/access?contribId=7&resId=0&materialId=slides&confId=136488>. Accessed July 2014
31. Hirschi-Bühl D (2014) Comparison of t-channel signal generators. <https://indico.desy.de/getFile.py/access?contribId=28&sessionId=18&resId=0&materialId=slides&confId=5178>. Accessed July 2014
32. Campbell JM, Ellis RK, Williams C (2011) Vector boson pair production at the LHC. JHEP 1107:018. doi:[10.1007/JHEP07\(2011\)018](https://doi.org/10.1007/JHEP07(2011)018). [arXiv:1105.0020](https://arxiv.org/abs/1105.0020) [hep-ph]

Chapter 12

Physics Objects Definitions

This analysis uses reconstructed jets, electrons, muons as well as missing transverse energy. In Sect. 7.9 general information on the reconstruction of these objects in ATLAS is given. This section is intended to provide more analysis specific information on the definition of the various objects and which requirements they have to meet in order to be considered in the analysis. This is done for jets in Sect. 12.1, for electrons and muons in Sects. 12.2 and 12.3, respectively, and for the missing transverse energy in Sect. 12.4.

12.1 Jets

Jet candidates are reconstructed from topological clusters that are calibrated with the LC+JES scheme using the anti- k_r clustering algorithm [1] with a distance parameter of 0.4, cf. Sect. 7.9.3. On top of the LC+JES calibration, the jet energy scale is further corrected with the help of the `ApplyJetCalibration`¹ package, which provides corrections to the four-momentum of a given jet. This includes further pile-up corrections based on the jet area as well as more refined in-situ calibrations derived during the course of the data taking that were not yet included in the reconstruction for the data and simulation samples listed in Chap. 11. Any cut on the transverse momentum of the jets is done after this calibration. For a jet to be considered in the analysis it has to have (calibrated) p_T exceeding 30 GeV and must be within $|\eta| < 4.5$.²

The main backgrounds to jets coming from real pp -collisions are calorimeter noise and non-collision events like cosmic ray muons or beam-induced events. Muons from

¹<https://twiki.cern.ch/twiki/bin/viewauth/AtlasProtected/ApplyJetCalibration2012>.

²Only for event cleaning and E_T^{miss} calculation jets starting from $p_T > 20$ GeV are considered.

cosmic radiation may traverse the earth above the ATLAS detector and leave energy deposits or tracks in the detector. Moreover, the beam core is surrounded by a halo of protons and these can produce secondary particle showers when hitting one of the LHC collimators. Muons produced this way can also reach the detector. Similarly, muons can be produced in beam-gas scattering. Typically, such muons are traveling parallel to the beam axis and will likely only leave signals in one of the calorimeters or in the tracker. To reduce the contamination from these backgrounds, a number of quality requirements is placed on any jet with a calibrated p_T above 20 GeV within the full η range. If any of these jets does not pass the selection, the event is rejected. The quality requirements are detailed in Table 1(a) of reference [2] and correspond to the *looser* jet quality criterion, which was designed to provide an efficiency above 99.8% while retaining a rejection of fake jets as high as possible. The *looser* jet quality is the performance group's recommendation for physics analysis.³

Analyses with final states of higher object multiplicities than the one described in this work are hardly affected by the non-collision backgrounds. However, the mono-jet topology can easily result from one of the sources described above. Hence, additional cuts are applied to further suppress non-collision backgrounds. The highest p_T jet has to fulfil additional requirements: Its p_T has to be greater than 120 GeV and it has to be central with $|\eta| < 2.0$. Furthermore, its charge fraction (f_{ch}) has to be greater than 10% of the maximum energy fraction in one calorimeter layer (f_{max}). The charge fraction is defined as the ratio of the sum of p_T of tracks associated to the jet and the calibrated jet p_T . This cleaning is discussed in more detail in Ref. [3].

12.2 Electrons

Electron candidates are discarded if the associated cluster is affected by a dead front-end board in the first or second calorimeter sampling, by the presence of a dead high-voltage region affecting the three samplings or by the presence of a masked cell in the core of the cluster.

The performance group defines different working points in terms of identification efficiency and fake rejection for electrons. The baseline categories (*loose*, *medium*, *tight*) are defined in reference [4]. The cut variables and values have been adapted to the different running conditions in 2011 and 2012, the latest working points are summarised in the so called *++menu*.⁴

Different definitions for electrons are used in this analysis: In the signal regions, where leptons are vetoed, a relatively loose selection is applied (resulting in a tighter veto), while in the electron control regions, where good electrons are explicitly selected, the selection cuts are harder.

Electron candidates in the signal regions (*SR electrons* or *veto electrons*) are required to be of medium++ quality, have a p_T greater than 7 GeV and be within $|\eta| < 2.47$. No isolation is required and no overlap removal with jets is performed.

³<https://twiki.cern.ch/twiki/bin/viewauth/AtlasProtected/HowToCleanJets2011>.

⁴<https://twiki.cern.ch/twiki/bin/viewauth/AtlasProtected/TechnicalitiesForMedium1>.

Table 12.1 Electron definitions in different regions

SR	Loose CR	Tight CR
$p_T > 7 \text{ GeV}$	$p_T > 20 \text{ GeV}$	$p_T > 25 \text{ GeV}$
$ \eta < 2.47$	$ \eta < 2.47$ $1.37 < \eta < 1.56$ excluded	$ \eta < 2.47$ $1.37 < \eta < 1.56$ excluded
Medium++	Medium++	Tight++
–	–	Isolation
No overlap removal	Overlap removal	Overlap removal

In the $Z(\rightarrow e^+e^-)+\text{jets}$ control region, where exactly 2 good electrons are required, a good electron has to have medium++ quality, a p_T larger than 20 GeV and fulfill $|\eta| < 2.47$, while the region $1.37 < |\eta| < 1.56$ is excluded. No isolation is required. The same criteria are applied to the electron in the $W^\pm(\rightarrow e^\pm\bar{\nu})+\text{jets}$ control region used to estimate $W^\pm(\rightarrow \tau^\pm\bar{\nu})+\text{jets}$ or $W^\pm(\rightarrow e^\pm\bar{\nu})+\text{jets}$, which will be referred to as $W^\pm(\rightarrow e^\pm\bar{\nu})+\text{jets}$ control region B.

A different control region definition, $W^\pm(\rightarrow e^\pm\bar{\nu})+\text{jets}$ control region A, is used to estimate $Z(\rightarrow \nu\bar{\nu})+\text{jets}$ from $W^\pm(\rightarrow e^\pm\bar{\nu})+\text{jets}$, and here the requirements are more stringent: The electron has to pass the tight++ identification cuts and the p_T threshold is raised to 25 GeV. In addition, the electron is required to be isolated: The scalar sum of the transverse momenta of tracks with $\Delta R < 0.3$ around the electron candidate has to be smaller than 5 % of its transverse momentum. In addition, the sum of transverse energies of topological clusters (calibrated at EM scale) in a cone of radius $R < 0.3$ that has been corrected for pile-up and leakage has to be less than 5 % of the candidate p_T .

In the $W^\pm(\rightarrow e^\pm\bar{\nu})+\text{jets}$ control regions an overlap removal between good electrons and jets is performed such that the jet is discarded in case it is within $\Delta R < 0.2$ from the electron candidate.

Table 12.1 summarises the definitions used in different regions.

12.3 Muons

In this analysis, both *segment tagged* and *combined* muons from the STACO chain are used. The inner detector track associated to the muon candidate has to fulfil the following requirements⁵ according to the performance group's recommendation:

- number of pixel hits + number of crossed dead pixel sensors > 0
- number of SCT hits + number of crossed dead SCT sensors > 4

⁵https://twiki.cern.ch/twiki/bin/viewauth/AtlasProtected/MCPAnalysisGuidelinesData2012#Selection_Guidelines.

Table 12.2 Muon definitions in different regions

SR	CRs
Combined or segment tagged	
Matched to inner detector track	
$ \eta < 2.5$	
$p_T^{Cone20} < 1.8 \text{ GeV}$	
$p_T > 7 \text{ GeV}$	$p_T > 20 \text{ GeV}$

- number of pixel holes + number of SCT holes < 3
- within $0.1 < |\eta| < 1.9$:
 - number of TRT hits + number of TRT outliers > 5
 - AND number of TRT outliers $< 0.9 \times (\text{number of TRT hits} + \text{number of TRT outliers})$

Only isolated muons are considered: the scalar sum of the transverse momentum of tracks in a cone with radius 0.2 around the muon candidate has to be less than 1.8 GeV.

As for electrons, there are slightly different muon candidate definitions for signal and control regions. In the signal regions, *segment tagged* and *combined* muons fulfilling the above requirements are considered, as long as they have a p_T exceeding 7 GeV and are within $|\eta| < 2.5$. In the following, such muons will be referred to as *signal region muons* or *veto muons*.

In the muon control regions ($W^\pm (\rightarrow \mu^\pm \bar{\nu}) + \text{jets}$ and $Z (\rightarrow \mu^+ \mu^-) + \text{jets}$), the same criteria are applied with the only difference being a harder cut on the transverse momentum at $p_T > 20 \text{ GeV}$ (Table 12.2).

12.4 Missing Transverse Energy

Here, a few adjustments to the definition of missing transverse energy specific to this analysis shall be described. The `ReFFinal` variant of the missing E_T that is used in this analysis is an object based E_T^{miss} , i.e. energy deposits are attributed to electrons, photons, hadronically decaying taus, jets, soft jets or muons, as described in Sect. 7.9.4. However, since this analysis does not use reconstructed τ -leptons, an E_T^{miss} variant is used that does not include τ 's as reconstructed objects. Instead, the energy from τ -jets is included in the jet term. This variant is referred to as `Egamm10NoTau`. Moreover, for this analysis, the muon term of `ReFFinal` (cf. Eq. 7.8) is not included in the E_T^{miss} , resulting in a purely calorimeter based missing E_T .

In the signal region, where muons (and electrons) are vetoed, the full detector E_T^{miss} (i.e. including the muon term) and the calorimeter E_T^{miss} are essentially the same (except for small contributions from muons surviving the veto). For $Z (\rightarrow \nu \bar{\nu}) + \text{jets}$ events, the E_T^{miss} in the signal region corresponds to the boson p_T , thus, the E_T^{miss} in

Table 12.3 E_T^{miss} definition depending on the SR process to be estimated and the control region to be used. The ‘+jets’ notation has been omitted for practical reasons

SR process	E_T^{miss} equivalent	CR	E_T^{miss} variant
$Z(\nu\bar{\nu})$	Boson p_T	$Z(\mu^+\mu^-)$ $Z(e^+e^-)$ $W(\mu^\pm\bar{\nu})$ $W(e^\pm\bar{\nu})$ A	Calorimeter Corrected Calorimeter Corrected
$W(\mu^\pm\bar{\nu})$	Boson p_T	$W(\mu^\pm\bar{\nu})$	Calorimeter
$W(e^\pm\bar{\nu})$	Neutrino p_T	$W(e^\pm\bar{\nu})$ B	Calorimeter
$W(\tau^\pm\bar{\nu})$	Neutrino p_T	$W(e^\pm\bar{\nu})$ B	Calorimeter

the control regions used to estimate this process is also desired to be the boson p_T . In other words, the leptons in the $W^\pm(\rightarrow \ell^\pm\bar{\nu})$ +jets and $Z(\rightarrow \ell^+\ell^-)$ +jets control regions are to be treated as ‘invisible’, i.e. they are removed from the E_T^{miss} calculation. For the muon control regions, this is already achieved by using the calorimeter E_T^{miss} as described above. In the electron control regions, it is done with the help of the `MissingEtUtility` package.⁶ The weights with which the electrons enter the E_T^{miss} calculation are set to 0 and the missing E_T is recomputed from the remaining objects.

Since for $W^\pm(\rightarrow e^\pm\bar{\nu})$ +jets or $W^\pm(\rightarrow \tau^\pm\bar{\nu})$ +jets the missing E_T corresponds to the neutrino p_T , the electrons are not removed from the E_T^{miss} calculation in the $W^\pm(\rightarrow e^\pm\bar{\nu})$ +jets control region used to assess these processes. Table 12.3 gives an overview over the different E_T^{miss} variants used in the various control regions.

References

1. Cacciari M, Salam GP, Soyez G (2008) The anti-kt jet clustering algorithm. JHEP 04:063. doi:10.1088/1126-6708/2008/04/063. arXiv:0802.1189 [hep-ph]
2. The ATLAS Collaboration (2012) Selection of jets produced in proton-proton collisions with the ATLAS detector using 2011 data. Technical report. ATLAS-CONF-2012-020. Geneva: CERN
3. Abdallah J et al (2013) Search for new phenomena with mono-jet plus missing transverse energy signature in proton-proton collisions at $\sqrt{s} = 8\text{TeV}$ with the ATLAS detector. Technical report. ATL-COM-PHYS-2013-1578. Geneva: CERN
4. The ATLAS Collaboration (2012) Electron performance measurements with the ATLAS detector using the 2010 LHC proton-proton collision data. Eur Phys J C72:1909. arXiv:1110.3174 [hep-ex]

⁶<https://twiki.cern.ch/twiki/bin/viewauth/AtlasProtected/MissingETUtility>.

Chapter 13

Event Selection

In this section, the selection of events in the signal region will be outlined. First, the requirements imposed to select good quality data and basic cuts to suppress backgrounds are described in Sect. 13.1. Section 13.2 summarises studies on a potential optimisation of the selection to increase the sensitivity to the WIMP signal. The final signal region selection is given in Sect. 13.3.

13.1 Preselection

Since this analysis uses information from all detector parts to reconstruct the physics objects as described in Chap. 12, only data recorded with a fully functional detector, i.e. passing detector quality criteria, is used. The corresponding lumiblock numbers from each run are centrally provided in form of a standard good-runs-list (GRL).¹ In the signal regions, events are selected by an E_T^{miss} trigger with a threshold of 80 GeV at the event filter (EF) level, `EF_xe80_tclcw`, that was unrescaled during the complete data taking period. The corresponding thresholds at L1 and L2 are 60 and 65 GeV, respectively. As the naming indicates, this trigger uses topoclusters at EF level that are LCW-calibrated. In particular, this means that no information from the muon system is included in the calculation, i.e. muons will be treated as missing E_T in the trigger. The trigger reaches an efficiency of 98 % at 151 GeV offline E_T^{miss} [1].

To ensure that a recorded event is consistent with a pp -collision, there has to be a reconstructed vertex with at least 2 tracks associated to it. Additional cleaning is applied to the remaining events, following recommendations from the data quality

¹The GRL used for this analysis is `data12_8TeV.periodAllYear_DetStatus-v61-pro14-02_DQDefects-00-01-00_PHYS_StandardGRL_All_Good.xml`.

group²: Events in a time window around a noise burst in the LAr calorimeter, events with corrupted tile calorimeter data, and events with partly missing event information due to a restart of a sub-system during a run, are rejected with the help of event flags provided in the D3PDs. In case of a saturation in one of the tile calorimeter cells which causes the E_T^{miss} to be badly measured the event is discarded. This is done using a centrally provided software tool called `TileTripReader`.³

A dedicated tool is used to deal with masked tile calorimeter modules, the `BCHCleaningTool`,⁴ which defines two working points for the cleaning cuts, called *tight* and *medium*. The *tight* cleaning considers any jet that points to the core or the edges of a dead module as bad, while the *medium* cleaning flags jets pointing to the core as bad and jets pointing to the edges only if they do not pass additional cuts on the fraction of jet energy coming from cells classified as bad and on the fraction of energy deposited in the electromagnetic calorimeter (f_{EM}). If one of the two leading jets falls into an area with a masked module and does not pass the *tight* cleaning, the event is discarded. For additional sub-leading jets, the *medium* cleaning is applied. Again, the event is rejected if one of these additional jets does not pass the cuts.

In the signal regions, events containing at least one veto-quality electron or muon (as defined in Sects. 12.2 and 12.3) are rejected. In addition to the lepton vetoes, a veto on isolated tracks is employed to suppress background contributions from $W^\pm(\rightarrow \tau^\pm \nu) + \text{jets}$ [1, 2].

Multi-jet events can enter the signal (or control) regions when a jet is mis-measured, yielding high E_T^{miss} . In this case, there will be a jet close to the E_T^{miss} . To suppress such events, all jets (as defined in Sect. 12.1) have to be well separated from the direction of E_T^{miss} , which is enforced by a cut on the minimal difference in ϕ between the E_T^{miss} and any good jet, $|\Delta\phi_{\text{min}}(\text{jet}_i, E_T^{\text{miss}})|$. The distribution of this variable is shown in Fig. 13.1: The shape comparison between signal, main background contributions and data shows the data having the largest entries at small values of $|\Delta\phi_{\text{min}}(\text{jet}_i, E_T^{\text{miss}})|$, while the signal and larger backgrounds peak at the maximum value of π , in consistency with the topology of an ISR jet recoiling against invisible particles. The larger entries at $|\Delta\phi_{\text{min}}(\text{jet}_i, E_T^{\text{miss}})| < 0.5$ in data⁵ can be explained by the contamination from multi-jet events with one jet being mis-measured giving rise to an E_T^{miss} (in the direction of the jet) large enough to pass the cut of 150 GeV. Thus, already with a cut of $|\Delta\phi_{\text{min}}(\text{jet}_i, E_T^{\text{miss}})| > 0.5$ multi-jet events can be suppressed efficiently. However, as also is visible from Fig. 13.1, cutting at $|\Delta\phi_{\text{min}}(\text{jet}_i, E_T^{\text{miss}})| > 1.0$ reduces the top background without affecting the signal efficiency significantly. While this will not have a large impact on the signal sensitivity due to the small size of the top contamination in the signal region, it is

²<https://twiki.cern.ch/twiki/bin/viewauth/Atlas/DataPreparationCheckListForPhysicsAnalysis>.

³<https://twiki.cern.ch/twiki/bin/viewauth/Atlas/TileTripReader>.

⁴<https://twiki.cern.ch/twiki/bin/viewauth/AtlasProtected/BCHCleaningTool>.

⁵Data is used for illustration since there is no multi-jet simulation with sufficient statistics due to the high cross section for multi-jet productions at a pp -collider.

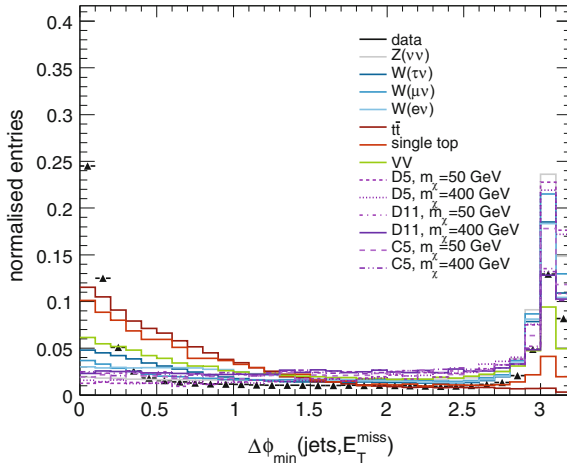


Fig. 13.1 Minimum azimuthal separation between E_T^{miss} and any good jet for the main background processes and several signal points after preselection. The signal samples are shown with *dashed lines* in various shades of *violet*, the (dominant) $Z(\rightarrow \nu\bar{\nu})+\text{jets}$ background is shown in *grey*, *blue lines* are for $W+\text{jets}$ backgrounds, *reds* for the *top* contribution and *green* for the diboson processes. Data is shown as *black* points. All histograms are normalised to unit area

relevant in the control regions when allowing for large jet multiplicities. Therefore, the cut value of $|\Delta\phi_{\text{min}}(\text{jet}_i, E_T^{\text{miss}})| > 1.0$ was chosen. The E_T^{miss} is required to be at least 150 GeV.

13.2 Optimisation Studies

While for earlier publications of the mono-jet analysis [3–5] a generic selection was used to retain sensitivity to a broad spectrum of new physics models, this analysis includes a modified selection optimised for the WIMP signature, where an ISR jet is recoiling against the WIMP pair. Studies were performed as to which extent differences in the event topologies can be exploited to enhance the sensitivity for the WIMP signal. The quantity used as a measure for the sensitivity will be introduced in Sect. 13.2.1, the actual study of different cut sets is discussed in Sect. 13.2.2.

13.2.1 Quantification of Sensitivity

As a measure for the sensitivity the following quantity was used, following the reasoning in [6]:

$$S := \frac{\varepsilon(t)}{S_{\text{min}}}, \quad (13.1)$$

where t characterises a certain set of cuts and ε the selection efficiency of the signal for this set of cuts. The quantity S_{min} is given as

$$S_{min} = \frac{a^2}{8} + \frac{9b^2}{13} + a\sqrt{B} + \frac{b}{2}\sqrt{b^2 + 4a\sqrt{B} + 4B} \quad (13.2)$$

with a and b being the number of standard deviations required for discovery and exclusion limits, respectively, and B is the number of background events which again is a function of the chosen set of cuts, $B = B(t)$. As discussed in Ref. [6], the advantage of this quantification of the sensitivity compared to for example the well established S/\sqrt{B} or $S/\sqrt{S+B}$ is that it allows for selection optimisation independent of the—perhaps unknown—cross section of the signal. In addition, the optimisation is done for exclusion and discovery at the same time. Here, the main steps for arriving at Eq. 13.2 as detailed in Ref. [6] are reviewed.

The starting point is the standard case of hypothesis testing: the hypothesis for new physics with parameters m , H_m , is to be tested against the default background-only hypothesis, H_0 . To perform the hypothesis test, a so-called *critical region* is defined, in which H_0 will be rejected. The *significance level* α is defined as the probability to reject H_0 when it is true. The *power function* for the test, $1 - \beta(m)$, is the probability of actually claiming a discovery when H_m is true. Finally, the *sensitivity region* is defined as $1 - \beta_\alpha(m) > CL$, where α and the desired confidence level CL have to be defined before doing the experiment. This region of sensitivity defines a region of parameter space where the experiment will certainly give an answer: either this region will be excluded (at the defined confidence level) or a discovery will be made.

In Ref. [6] these definitions are then applied to the case of a counting experiment. The probabilities for obtaining a certain number of events, n , under the assumption of H_0 or H_m , respectively, is given by a Poisson distribution:

$$p(n|H_0) = e^{-B} B^n / n!, \quad (13.3)$$

$$p(n|H_m) = e^{-B-S_m} (B + S_m)^n / n!, \quad (13.4)$$

where S_m is the number of signal events. The critical region for a counting experiment would be defined as $n > n_{min}$, where n_{min} depends on B and α . The power of such a tests grows monotonically with S_m and the equation for the sensitivity region thus translates into $S_m > S_{min}$. In other words, once a value of S_{min} is reached, the power function will always be greater than CL for any m .

When doing a Gaussian approximation to the Poisson distribution, S_{min} can be expressed as $S_{min} = a\sqrt{B} + b\sqrt{B + S_{min}}$ and solving for S_{min} yields

$$S_{min} = \frac{b^2}{2} + a\sqrt{B} + \frac{b}{2}\sqrt{b^2 + 4a\sqrt{B} + 4B}.$$

Assuming that the cut efficiency is independent of the parameters m , the number of signal events can be expressed as $S_m(t) = \varepsilon(t) \cdot L \cdot \sigma_m$ which leads to the following expression for the minimal required signal cross section:

$$\sigma_{min} = \frac{\frac{b^2}{2} + a\sqrt{B(t)} + \frac{b}{2}\sqrt{b^2 + 4a\sqrt{B(t)} + 4B(t)}}{\varepsilon(t) \cdot L}. \tag{13.5}$$

The smaller the necessary cross section, the higher the sensitivity, hence the following expression should be maximised:

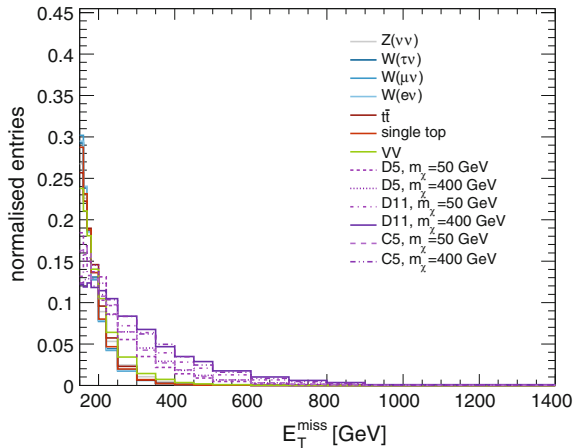
$$\frac{\varepsilon(t)}{\frac{b^2}{2} + a\sqrt{B(t)} + \frac{b}{2}\sqrt{b^2 + 4a\sqrt{B(t)} + 4B(t)}}. \tag{13.6}$$

The denominator is already close to Eq. 13.2, the remaining changes are due to an empirical fit to account for differences between the tail integrals of the Gaussian and the Poisson distribution, respectively. (See Fig. 6 of Ref. [6].)

Since for a discovery a significance of 5σ is required and exclusion limits are typically set at 95 % confidence level, the values chosen in Eq. 13.2 are $a = 5$ and $b = 2$.

It should be pointed out, that this approach does not provide means to compare different signals with potentially different cross section, since the cross section does not enter in the calculation. In other words, obtaining a larger value of S for one signal does not mean that the experiment will be more sensitive to this signal than to others, since the cross sections might differ largely. In the case of the different WIMP signal points for example, the cut efficiencies $\varepsilon(t)$ will in general be larger for higher values of m_χ due to the correspondingly harder E_T^{miss} spectrum, but the cross section will be smaller so that the overall sensitivity will turn out smaller for higher masses. Maximising S , however, provides the optimal selection for a given single signal point.

Fig. 13.2 E_T^{miss} for the main background processes and several signal points after preselection. The signal samples are shown with dashed lines in various shades of violet, the $Z(\rightarrow \nu\bar{\nu})$ +jets background is shown in grey, blue lines are for W +jets backgrounds, reds for the top contribution and green for the diboson processes. Histograms are normalised to unit area



13.2.2 Cut Studies

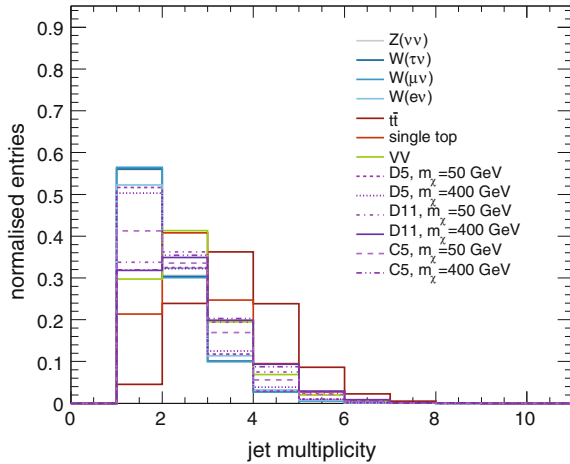
In the following, the preselection cuts outlined in Sect. 13.1 will be applied as a baseline. The cuts to be studied will be applied in addition to this baseline. For the comparison of different selections, three operators are chosen: the quark-antiquark vector operator (D5) which is a benchmark model and often used by other experiments as well, e.g. [7, 8], the gluon-gluon operator (D11) which is of special interest at colliders, and the C5 operator for complex scalar DM. For each operator, three different WIMP masses are considered: 50, 400 and 1000 GeV, to sample the complete mass range covered in this analysis. The aim of the studies, however, is not to define separate selections for each signal point, but to provide an overview of potential differences between signal and background and general trends in the sensitivity when varying certain cuts.

As already discussed previously, the largest and irreducible background contribution are events with a jet from ISR and a Z boson decaying into two neutrinos. While the event topology is the same for this process and the signal events, the signal is expected to manifest itself as an excess of events with high missing transverse energy, as shown in Fig. 13.2. The different dashed lines in various shades of violet are for the WIMP signal samples, the $Z(\rightarrow \nu\bar{\nu})$ +jets background is shown in grey, blue lines are for W +jets backgrounds, while top and diboson contributions are shown in red and green, respectively.⁶ The histograms are normalised to unit area in order to facilitate the shape comparison. It can be clearly seen that the spectra for the WIMP signal samples are harder than the ones for the backgrounds. There are also some differences between the different operators, for example the spectra for D5 are softer than for the other two. Increasing the WIMP mass corresponds to a harder E_T^{miss} spectrum for all operators, since more energy escapes with the heavier WIMPs.

Higher E_T^{miss} means in turn, that on average the ISR jets will have higher momentum in the signal than in the background, and are hence more likely to split or radiate further jets. It is thus to be expected that the jet multiplicity will on average be higher for the signal process. This is confirmed by the jet multiplicity distribution in Fig. 13.3 (the colour scheme is the same as for Fig. 13.2): Comparing signal and Z or W processes shows the shift of the distribution to higher values for the WIMP samples. This is more pronounced for the C5 and especially the D11 operator than for D5, but the trend is also visible for D5. Moreover, it can be seen that also the diboson and especially the top processes feature a higher average jet multiplicity—even higher than the signal samples in case of the top background. This can be understood since for these cases jets can arise not only from ISR but also in the final state. Previous versions of the mono-jet analysis had a veto on events with more than 2 jets. As is visible in Fig. 13.3, this cut reduces the top contamination by approximately 50%. However, the top (and diboson) backgrounds are a very small contamination in the

⁶The $Z(\rightarrow \ell^+\ell^-)$ +jets backgrounds are not included in this plot to reduce the number of lines. Their contribution in the signal regions is very small and can be neglected in this context.

Fig. 13.3 Jet multiplicity for the main background processes and several signal points after the preselection. The signal samples are shown with *dashed lines* in various shades of *violet*, the (dominant) $Z(\rightarrow \nu\bar{\nu})$ +jets background is shown in *grey*, *blue lines* are for W +jets backgrounds, *reds* for the *top* contribution and *green* for the diboson processes. All histograms are normalised to unit area



signal region due to the lepton vetoes (of the order of 1–2%), an increase thus is not a serious concern.

The QCD multi-jet background is not included in Fig. 13.3 because there is no simulation with sufficient statistics available—the large missing E_T required in this analysis removes the multi-jet background efficiently. The remaining contamination is further reduced by the cut on the minimum azimuthal distance between the E_T^{miss} and any good jet, $|\Delta\phi_{\min}(\text{jet}_i, E_T^{\text{miss}})|$, cf. Fig. 13.1.

The plots in Fig. 13.4 show the development of the jet multiplicity distribution with E_T^{miss} for three main background contributions ($Z(\rightarrow \nu\bar{\nu})$ +jets, $W^\pm(\rightarrow \tau^\pm\nu)$ +jets, $W^\pm(\rightarrow \mu^\pm\nu)$ +jets) on the left and the three WIMP operators at $m_\chi = 400$ GeV on the right. The histograms are normalised such that the maximum entry is 1. This shows that the higher jet multiplicities are related to the harder E_T^{miss} spectra for the signal. D5 as the operator that yields the softest spectrum among the three also features the lowest average jet multiplicity.

The larger average jet multiplicity for the signal also implies differences in other variables: In general, the p_T - E_T^{miss} -balance in signal events will be different than for background processes.

The leading jet will have a smaller transverse momentum with respect to the missing transverse energy, as is illustrated in Fig. 13.5a. The distributions for the WIMP samples show a tail towards values smaller than 1 which is not as pronounced for the W or Z backgrounds. The distributions peak close to 1, except for the top and diboson processes for which a shift to smaller values and a tail to values above 1 is observed. This can again be explained by the slightly different topology involving jets in the final states: The jets can point in opposite hemispheres, such that the E_T^{miss} is decreased with respect to the leading jet p_T . Figures 13.5b, c show the ratio for events with exactly one and more than one jet, respectively. It can clearly be seen that the tails in the distributions mostly originate from events with several jets.

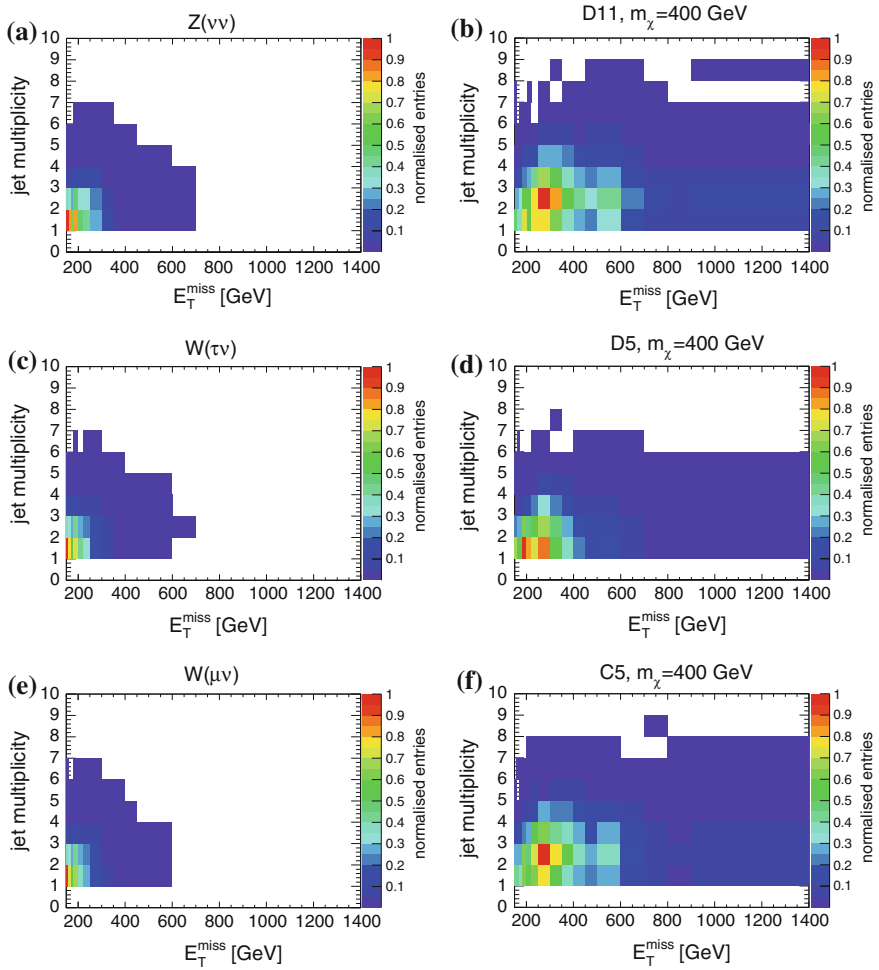


Fig. 13.4 Distribution of jet multiplicity as a function of E_T^{miss} for the main background processes (*left*) and three signal points at $m_\chi = 400$ GeV (*right*). Histograms are normalised such that the maximum is 1. **a** $Z(\rightarrow \nu\bar{\nu})+\text{jets}$. **b** D11, $m_\chi = 400$ GeV. **c** $W^\pm(\rightarrow \tau^\pm\nu)$ +jets. **d** D5, $m_\chi = 400$ GeV. **e** $W^\pm(\rightarrow \mu^\pm\nu)$ +jets). **f** C5, $m_\chi = 400$ GeV

The aforementioned topology difference of top and diboson with respect to the other processes is also visible in Fig. 13.6: Fig. 13.6a shows the ratio of the sub-leading and leading jet p_T , and it can be seen that while the signal and W and Z backgrounds have the largest entries at small values, the top and diboson distributions are shifted to larger values, especially for $t\bar{t}$. This can be interpreted as the final states being less ‘mono-jet like’, in the sense that the leading jet is less dominating. Figure 13.6b shows the vectorial sum of the E_T^{miss} and all transverse jet momenta within a cone of radius $\Delta R = 2.0$ around the leading jet. For a perfectly balanced

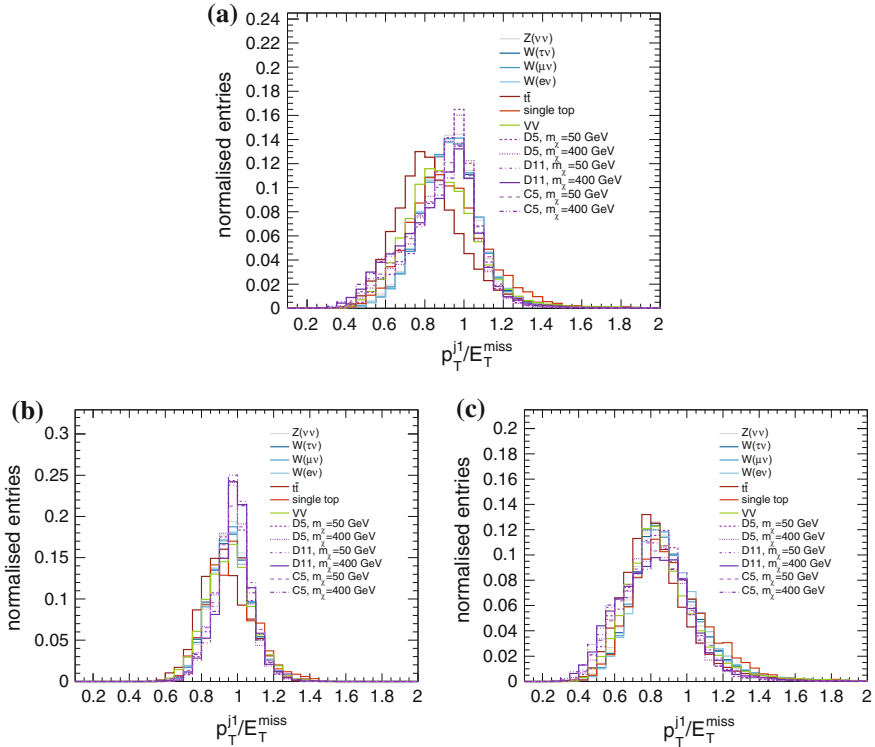


Fig. 13.5 The ratio of leading jet p_T and E_T^{miss} in events with any number of jets (a), exactly one jet (b), and more than one jet. The signal samples are shown with *dashed lines* in various shades of violet, the (dominant) $Z(\rightarrow \nu\bar{\nu})$ +jets background is shown in grey, blue lines are for W +jets backgrounds, reds for the top contribution and green for the diboson processes. All histograms are normalised to unit area. a Inclusive jet multiplicity. b Exactly one jet. c More than one jet

mono-jet event, this sum should be 0, the larger it is, the less ‘mono-jet like’ is the event. Again, as is to be expected, the top processes show a distribution with a larger tail towards higher values and which is less peaked at small values than for the other processes.

In summary, a possible gain in sensitivity can be achieved with respect to previous versions of the mono-jet analysis by not restricting the jet multiplicity and by using asymmetric cut values for leading jet p_T and E_T^{miss} . These options will be studied in more detail in the following. Additional cuts on the ratio of sub-leading and leading jet p_T or the vectorial sum of jet p_T ’s and E_T^{miss} may improve the suppression of top (and diboson) backgrounds, but cannot help to discriminate between signal and the dominating backgrounds from $Z(\rightarrow \nu\bar{\nu})$ +jets and $W^\pm(\rightarrow \ell^\pm\bar{\nu})$ +jets. They will thus not be considered further for the signal region optimisation.

In Fig. 13.7 the quantity S introduced in equation (13.1) is displayed in the plane of (upper) cuts on the jet multiplicity and (lower) cuts on the E_T^{miss} for the three

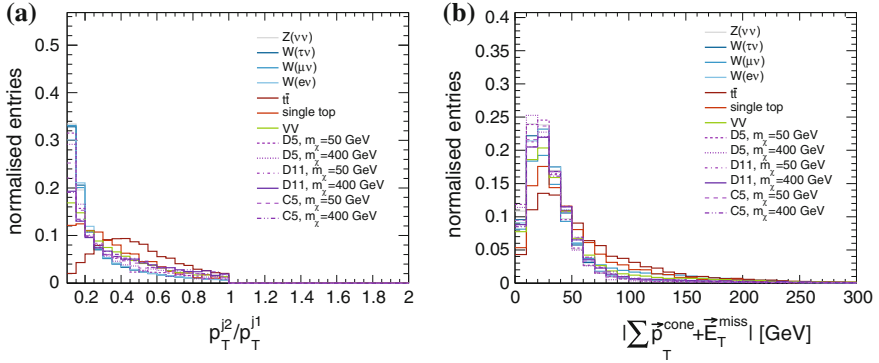


Fig. 13.6 Energy and p_T balance for the main background processes and several signal points after preselection: The ratio of the two leading jet p_T 's (a) and the vectorial sum of the E_T^{miss} and the jet p_T 's in a cone of radius $\Delta R = 2.0$ around the leading jet (b). The signal samples are shown with dashed lines in various shades of violet, the (dominant) $Z(\rightarrow \nu\bar{\nu})$ +jets background is shown in grey, blue lines are for W +jets backgrounds, reds for the $t\bar{t}$ contribution and green for the diboson processes. All histograms are normalised to unit area. a Ratio of sub-leading and leading jet p_T . b Vectorial difference of E_T^{miss} and jet p_T 's

operators and two of the mass values. The plots have been normalised such that the maximum value in each of them is 1.⁷ They demonstrate that in general the sensitivity will be higher when not restricting the jet multiplicity, with the gain being smallest for D5. For values of the multiplicity above 5, the changes in sensitivity become marginal, since there are hardly any events with so many jets, see Fig. 13.3. Moreover, the plots show that the optimal cut value on E_T^{miss} differs for the different operators. In particular, it is interesting to note that cutting ever harder in E_T^{miss} will not necessarily increase the sensitivity, since at some point the signal efficiency becomes too small. For D5, for example, which has the softest E_T^{miss} spectrum of the three, the optimal cut is lower than for the other operators. Correspondingly, for higher values of m_χ it is beneficial to cut harder on E_T^{miss} . Figure 13.8 shows for the same signal points the evolution of the sensitivity as a function of E_T^{miss} for various cuts on the jet multiplicity, i.e. projections on the x -axis for single y -bins in Fig. 13.7. The values of S are not normalised to the maximum, though, and instead magnified by an arbitrary factor of 10^6 for the sake of readability.⁸ These plots illustrate again that the sensitivity can be increased by releasing the jet veto. For C5 and D11, there is a considerable increase when going from $N_{\text{jet}} < 3$ to $N_{\text{jet}} < 4$ and also $N_{\text{jet}} < 5$. The higher jet multiplicities do not differ much in terms of sensitivity since the gain in signal efficiency is small. For D5, the gain from releasing the jet veto is rather

⁷This is legitimate since—as pointed out in Sect. 13.2.1— S can not be compared between different samples. Only the difference in S for various sets of cuts for a separate sample matters.

⁸It should again be noted that the absolute values of S have no real meaning, only the relative variations are of interest.

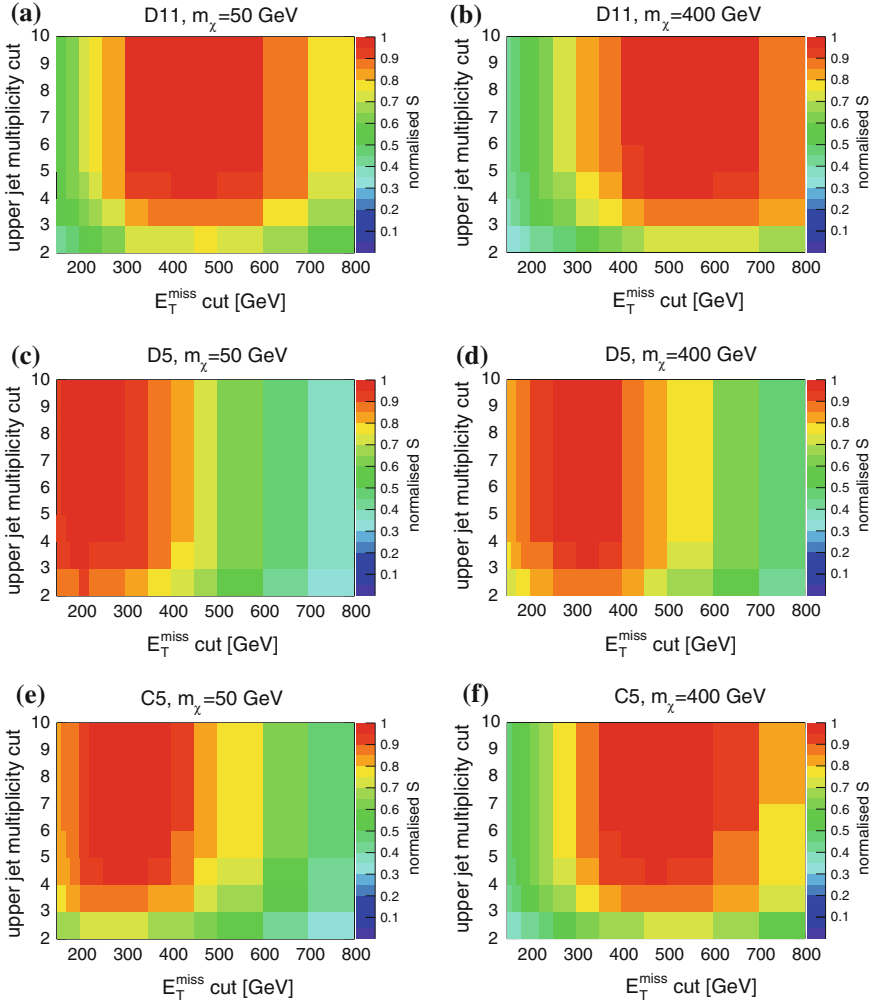


Fig. 13.7 Sensitivity S as a function of the cuts on jet multiplicity and E_T^{miss} for three operators at $m_\chi = 50$ GeV (left) and $m_\chi = 400$ GeV (right). D11 is shown in the top row, D5 in the middle and C5 at the bottom. Histograms are normalised such that the maximum is 1. **a** D11, $m_\chi = 50$ GeV. **b** D11, $m_\chi = 400$ GeV. **c** D5, $m_\chi = 50$ GeV. **d** D5, $m_\chi = 400$ GeV. **e** C5, $m_\chi = 50$ GeV. **f** C5, $m_\chi = 400$ GeV

small. It can also be deduced from these plots that the optimal cut on E_T^{miss} does not depend on the cut on the jet multiplicity.

In Fig. 13.9, S (normalised to the maximum) is shown in the plane of cuts on leading jet p_T and E_T^{miss} , respectively. Only configurations with $E_T^{\text{miss}} > p_T$ are considered. Again, the left column shows the three operators for a WIMP mass of 50 GeV, the right column for 400 GeV. The same trends for the behaviour with respect to E_T^{miss} as discussed for Fig. 13.7 are observed. The optimal cut value in E_T^{miss} , moreover, is

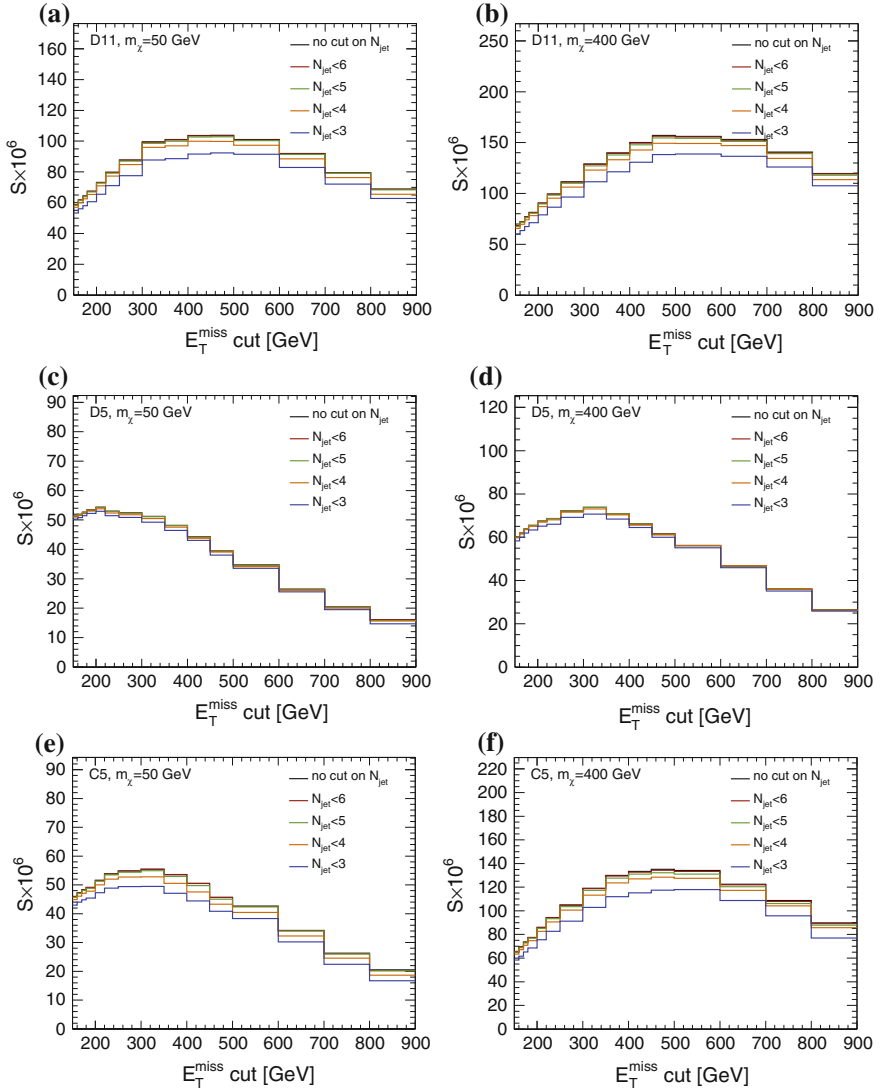


Fig. 13.8 Sensitivity S as a function of E_T^{miss} for different cuts on the jet multiplicity for three operators at $m_\chi = 50$ GeV (left) and $m_\chi = 400$ GeV (right). D11 is shown in the top row, D5 in the middle and C5 at the bottom. S is scaled by the arbitrary factor of 10^6 for the sake of readability. **a** D11, $m_\chi = 50$ GeV. **b** D11, $m_\chi = 400$ GeV. **c** D5, $m_\chi = 50$ GeV. **d** D5, $m_\chi = 400$ GeV. **e** C5, $m_\chi = 50$ GeV. **f** C5, $m_\chi = 400$ GeV

independent of the cut on leading jet p_T . In particular, applying symmetric cuts on leading jet p_T and E_T^{miss} , as was done in previous versions of the mono-jet analysis, does not provide higher sensitivity.

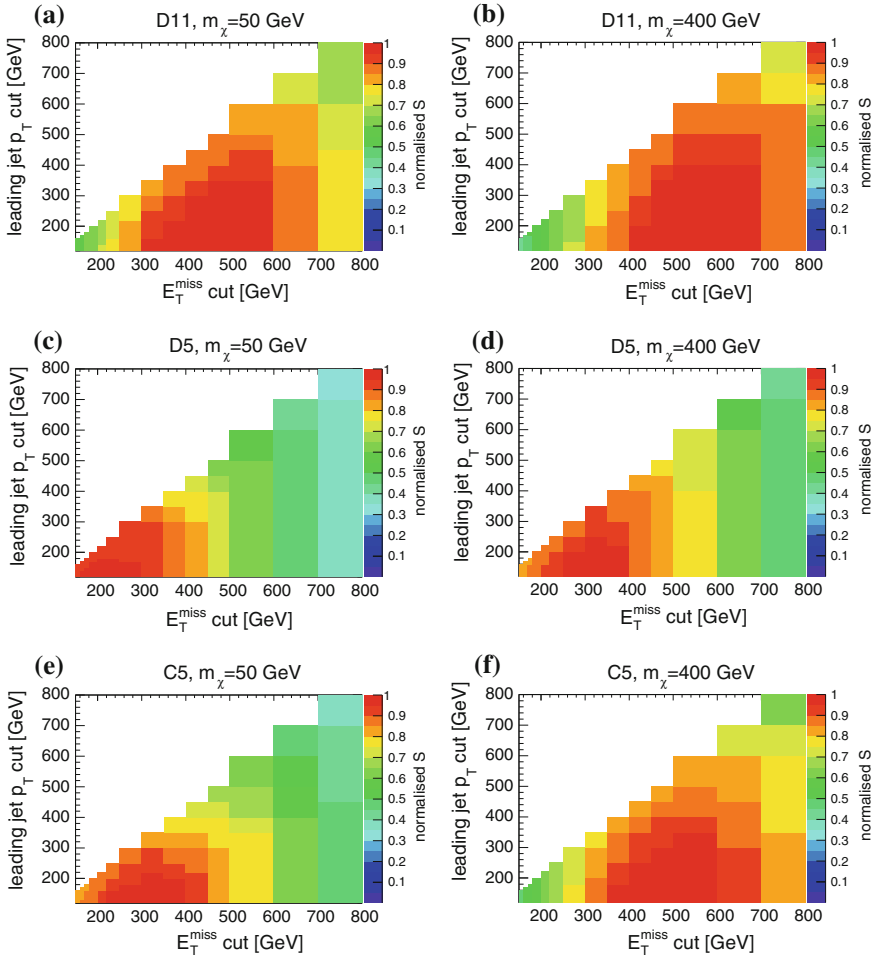


Fig. 13.9 Sensitivity S as a function of the cuts on the jet transverse momentum and E_T^{miss} for three operators at $m_\chi = 50$ GeV (left) and $m_\chi = 400$ GeV (right). Only configurations with $E_T^{\text{miss}} > p_T$ are considered. D11 is shown in the *top* row, D5 in the *middle* and C5 at the *bottom*. Histograms are normalised such that the maximum is 1. **a** D11, $m_\chi = 50$ GeV. **b** D11, $m_\chi = 400$ GeV. **c** D5, $m_\chi = 50$ GeV. **d** D5, $m_\chi = 400$ GeV. **e** C5, $m_\chi = 50$ GeV. **f** C5, $m_\chi = 400$ GeV

Instead of applying fixed cuts on the leading jet p_T , another possibility is to apply a ‘dynamic’ cut on the ratio of leading jet p_T and E_T^{miss} , since Fig. 13.5a suggests some potential discriminating power for this variable. The (normalised) sensitivity measure S in the $p_T/E_T^{\text{miss}} - E_T^{\text{miss}}$ plane is shown in Fig. 13.10 for $m_\chi = 50$ GeV and $m_\chi = 400$ GeV. These distributions demonstrate that there is no improvement on the sensitivity achieved by cutting on the leading jet p_T relative to the E_T^{miss} .

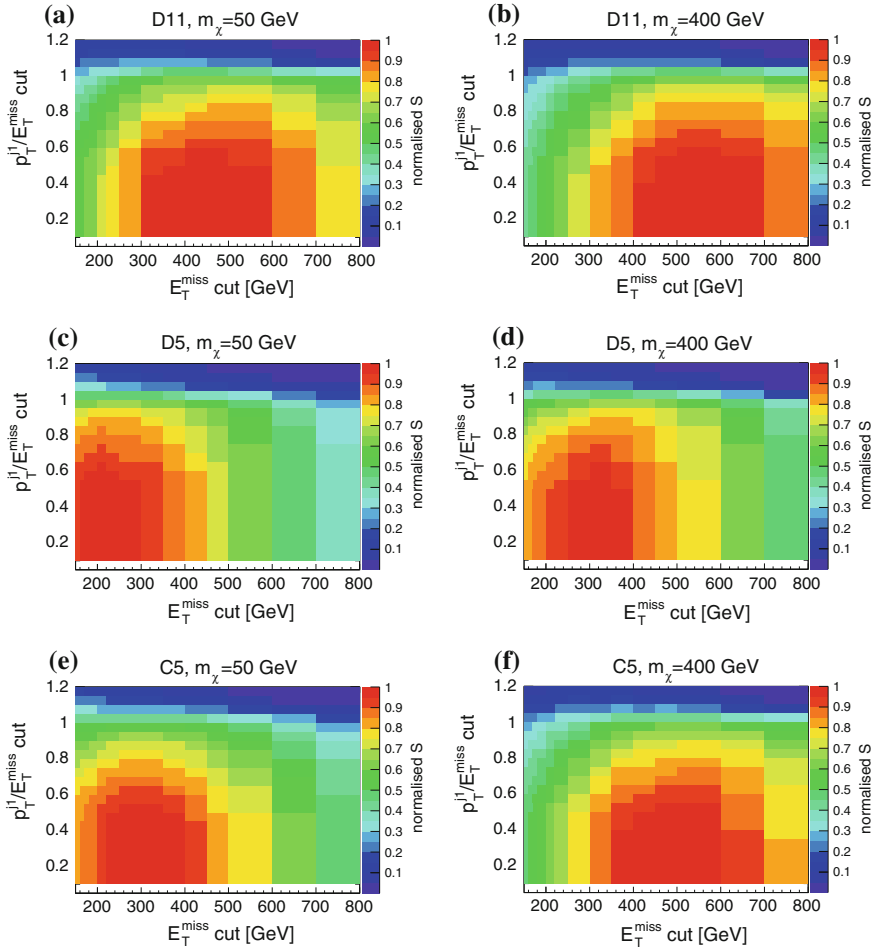


Fig. 13.10 Sensitivity S as a function of the cuts on the ratio of jet p_T over E_T^{miss} and E_T^{miss} for three operators at $m_\chi = 50$ GeV (*left*) and $m_\chi = 400$ GeV (*right*). D11 is shown in the *top* row, D5 in the *middle* and C5 at the *bottom*. Histograms are normalised such that the maximum is 1. **a** D11, $m_\chi = 50$ GeV. **b** D11, $m_\chi = 400$ GeV. **c** D5, $m_\chi = 50$ GeV. **d** D5, $m_\chi = 400$ GeV. **e** C5, $m_\chi = 50$ GeV. **f** C5, $m_\chi = 400$ GeV

Figure 13.11 shows the comparison of S for various cut values on leading jet p_T over E_T^{miss} and a fixed cut value at 120 GeV for the leading jet p_T . For all operators and mass values the best sensitivity is achieved for the fixed jet p_T cut. The optimal cut value on E_T^{miss} depends on the operator and mass point.

In conclusion, the following choices for the signal region selection promise the best sensitivity: No restriction on the jet multiplicity, applying a cut on the leading jet at 120 GeV and scanning the E_T^{miss} cuts in order to define signal regions that provide improved sensitivity for different operators.

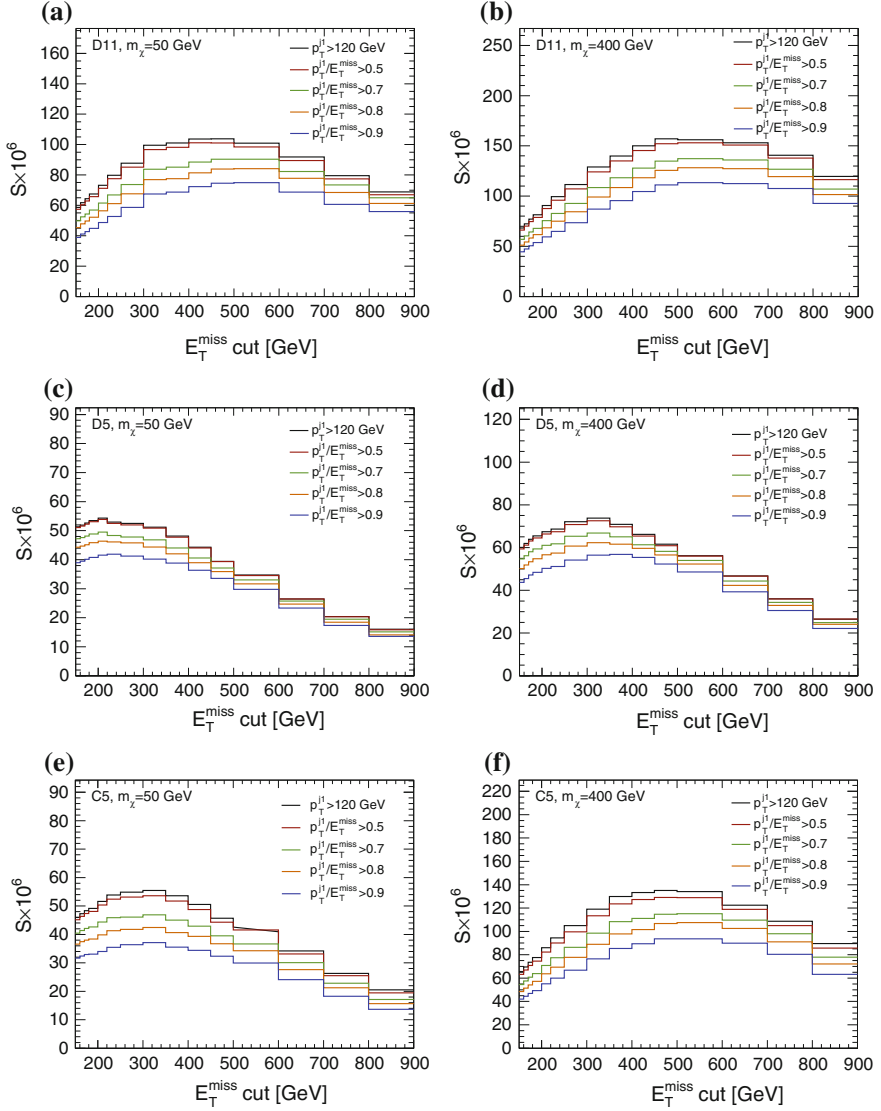


Fig. 13.11 Sensitivity S as a function of E_T^{miss} for different cuts on the jet p_T for three operators at $m_\chi = 50$ GeV (left) and $m_\chi = 400$ GeV (right). D11 is shown in the top row, D5 in the middle and C5 at the bottom. S is scaled by the arbitrary factor of 10^6 for the sake of readability. **a** D11, $m_\chi = 50$ GeV. **b** D11, $m_\chi = 400$ GeV. **c** D5, $m_\chi = 50$ GeV. **d** D5, $m_\chi = 400$ GeV. **e** C5, $m_\chi = 50$ GeV. **f** C5, $m_\chi = 400$ GeV

13.3 Complete Signal Region Selection

As an outcome of the optimisation studies presented in Sect. 13.2 a major change in the signal region definition with respect to previous versions of the mono-jet analysis [3–5] is introduced: previously, signal regions were defined by applying the same cut on leading jet p_T and E_T^{miss} . In this analysis, the cut on the leading jet p_T is kept fixed at 120 GeV, and different signal regions are defined by scanning the E_T^{miss} spectrum only. The first signal region starts at 150 GeV of E_T^{miss} and for the higher signal regions the cut is increased in steps of 50 GeV up to 400 GeV, followed by larger steps with cuts at 400, 500, and 600 GeV. The regions are labeled SR1..SR8, cf. Table 13.1.

The E_T^{miss} cuts were not refined further for the following reasons: As can be seen from Fig. 13.11, the maxima in sensitivity are rather broad, meaning that a moderate change in the E_T^{miss} cut will not change the sensitivity significantly. Since there are in total 45 signal points for the effective operators alone, an optimisation for each point separately with only small changes in the sensitivity seems impractical. Moreover, the optimisation was done in the context of the ATLAS mono-jet analysis [5], which contains not only the dark matter interpretation but also other signals like large extra dimensions or gravitino production. Thus, the signal region cuts were chosen more generally. Finally, in order to judge which is the optimal cut value, systematic uncertainties have to be considered, which was beyond the scope of the studies detailed in Sect. 13.2, since therefore the complete analysis would have to be re-run numerous times. However, the systematic uncertainties will not alter the general conclusion that asymmetric cuts on leading jet p_T and E_T^{miss} are beneficial in terms of sensitivity, although the finally best cut value will depend on their effect. Therefore, the final choice of the best signal region will be made based on the expected limits after running the complete analysis for each of the cuts in Table 13.1.

Another important difference with respect to the past mono-jet publications is the removal of the jet veto, which was also found to improve the sensitivity in Sect. 13.2.

While a cut on the ratio of leading jet p_T and E_T^{miss} does not have an influence on the sensitivity for the WIMP signal in the signal region, it ensures a ‘mono-jet like’ topology by forcing the leading jet to have a p_T of at least a certain amount of the E_T^{miss} . Thus, a cut value of $p_T^{\text{jet1}}/E_T^{\text{miss}} > 0.5$ is adopted.

The complete event selection is summarised in Table 13.2.

Table 13.1 Cuts on E_T^{miss} defining the different signal regions

Name	SR1	SR2	SR3	SR4	SR5	SR6	SR7	SR8
E_T^{miss} cut (GeV)	150	200	250	300	350	400	500	600

Table 13.2 Cuts for the signal region selection except for the E_T^{miss} cut

GRL	Standard GRL for complete 2012 dataset
Trigger	EF_xe80_tclcw
Primary vertex	≥ 1 vertex with $N_{trk} > 1$
Event cleaning	LArError!=2, TileError!=2, coreFlags&0x40000==0, TileTripReader::checkEvent
Jet cleaning	<i>looser</i> cleaning for any jet with $p_T > 20$ GeV
BCH cleaning	<i>Tight</i> for 2 hardest jets ($p_T > 30$ GeV) <i>medium</i> for additional jets
Lepton veto	Veto events with identified electrons or muons
Track veto	Veto events with isolated tracks
Leading jet	$p_T > 120$ GeV, $f_{ch} > 0.1 \cdot f_{max}$, $ \eta < 2.0$
$ \Delta\phi_{\min}(\text{jet}_l, E_T^{\text{miss}}) $	> 1.0
$p_T^{\text{jet}1} - E_T^{\text{miss}}$ balance	$p_T^{\text{jet}1} / E_T^{\text{miss}} > 0.5$

References

1. The ATLAS Collaboration. Search for new phenomena in final states with an energetic jet and large missing transverse momentum in pp collisions at $\sqrt{s} = 8$ TeV with the ATLAS detector. In: submitted to EPJC (2015). [arXiv:1502.01518](https://arxiv.org/abs/1502.01518) [hep-ex]
2. Abdallah J et al (2013) Search for new phenomena with mono-jet plus missing transverse energy signature in proton-proton collisions at $\sqrt{s} = 8$ TeV with the ATLAS detector. Tech. rep. ATLCOM-PHYS-2013-1578. Geneva: CERN
3. The ATLAS Collaboration. Search for new phenomena with the monojet and missing transverse momentum signature using the ATLAS detector in $\sqrt{s} = 7$ TeV proton-proton collisions. Phys. Lett. B705, pp 294–312 (2011). doi:[10.1016/j.physletb.2011.10.006](https://doi.org/10.1016/j.physletb.2011.10.006). [arXiv:1106.5327](https://arxiv.org/abs/1106.5327) [hep-ex]
4. The ATLAS Collaboration. Search for new phenomena in monojet plus missing transverse momentum final states using 10fb-1 of pp Collisions at $\sqrt{s} = 8$ TeV with the ATLAS detector at the LHC
5. The ATLAS Collaboration. Search for dark matter candidates and large extra dimensions in events with a jet and missing transverse momentum with the ATLAS detector. JHEP, vol 1304, 075 p (2013). doi:[10.1007/JHEP04\(2013\)075](https://doi.org/10.1007/JHEP04(2013)075). [arXiv:1210.4491](https://arxiv.org/abs/1210.4491) [hep-ex]
6. Punzi G (2003) Sensitivity of searches for new signals and its optimization. In: eConf, C030908, MODT002. [arXiv:physics/0308063](https://arxiv.org/abs/hep-ph/0308063) [physics]
7. Aaltonen T et al (2012) A Search for dark matter in events with one jet and missing transverse energy in $p\bar{p}$ collisions at $\sqrt{s} = 1.96$ TeV. In: Phys. Rev. Lett. vol 108, p 211804. doi:[10.1103/PhysRevLett.108.211804](https://doi.org/10.1103/PhysRevLett.108.211804). [arXiv:1203.0742](https://arxiv.org/abs/1203.0742) [hep-ex]
8. The CMS Collaboration. Search for dark matter and large extra dimensions in monojet events in pp collisions at $\sqrt{s} = 7$ TeV. JHEP, vol 1209, p 094 (2012). doi: [10.1007/JHEP09\(2012\)094](https://doi.org/10.1007/JHEP09(2012)094). [arXiv:1206.5663](https://arxiv.org/abs/1206.5663) [hep-ex]

Chapter 14

Background Estimation

In this chapter, the estimation of the Standard Model background contributions in the signal region will be presented. First, Sect. 14.1 gives an overview of the sources of systematic uncertainties that will be considered and the way they are propagated to the final result. Sections 14.2.1–14.2.4 describe the estimation of the $Z(\rightarrow \nu\bar{\nu})$ +jets contribution from four different control regions, their combination is presented in Sect. 14.2.5. The estimates for $W^\pm(\rightarrow \mu^\pm\bar{\nu})$ +jets, $W^\pm(\rightarrow e^\pm\bar{\nu})$ +jets and $W^\pm(\rightarrow \tau^\pm\bar{\nu})$ +jets are given in Sects. 14.3.1 and 14.3.2. The estimation of $Z(\rightarrow \ell^+\ell^-)$ +jets backgrounds from simulation is described in Sect. 14.4. In Sect. 14.5 the determination of top and diboson from simulation is presented, and Sect. 14.6 summarises the data driven estimation of QCD multi-jet and non-collision backgrounds.

As was detailed in Chap. 10, the $W^\pm(\rightarrow \ell^\pm\bar{\nu})$ +jets and $Z(\rightarrow \nu\bar{\nu})$ +jets backgrounds in the signal region are estimated from orthogonal control regions defined by explicitly selecting good leptons but keeping all other signal region cuts. In particular, this means that for each control region process, there are 8 control regions defined by the same missing E_T cuts as the signal regions, c.f. Table 13.1.

Plots will mostly be shown for the lowest (most inclusive) regions, with an E_T^{miss} cut at 150 GeV. The plots will compare distributions in data to the ones from simulation. To facilitate shape comparisons, the simulation is scaled to match the number of entries in data. This is legitimate since the normalisation difference will be corrected for by the transfer factor method. Data are shown as black points, the Standard Model simulation as coloured histograms. The ratio of data to the sum of simulated processes is displayed in a panel beneath the actual distributions. Systematic uncertainties due to the sources discussed in Sect. 14.1 are indicated as a light blue band, centred at 1 for the ratio. Statistical uncertainties are presented as error bars.

14.1 Systematic Uncertainties

14.1.1 Trigger

As the trigger is 100 % effective at E_T^{miss} values above 200 GeV, both in data and simulation, there is no systematic uncertainty considered, except for the lowest regions with $E_T^{\text{miss}} > 150$ GeV, where a 1 % uncertainty is considered.

14.1.2 Jet Energy Scale and Resolution

There are in total 55 baseline sources of systematic uncertainties (or nuisance parameters) on the jet energy scale (JES), most of which (47) are related to the in-situ calibration. In addition, there are contributions from the η inter-calibration, the behaviour of high- p_T jets and the pile-up corrections. Apart from those baseline uncertainties, further nuisance parameters for topology and flavour uncertainties are considered. Some typical values of the jet energy scale uncertainty are displayed in Fig. 14.1 [1]: on the left-hand side as a function of p_T for central jets at $|\eta| = 0$, on the right hand side as a function of η for jets with a p_T of 40 GeV. It is seen that in the central region the uncertainty is smallest for a p_T -range from approximately 200 GeV to 1 TeV and has a value of ~ 1.5 %. It increases to ~ 3 % at larger p_T and up to ~ 4 % at small values of p_T . From the plot on the right it is observed that in the central region the JES uncertainty is approximately constant at a value of ~ 3 % and increases at higher absolute values of η to up to ~ 7 %. The resulting global JES uncertainty for each jet is obtained via centrally provided software tools.¹ The uncertainty on the background estimations is obtained by rerunning the selection while shifting the JES in simulation once up and once down, respectively, and propagating the corrections of the jet energy and direction to the E_T^{miss} calculation. The complete analysis chain is repeated for the data driven estimates.

The jet energy resolution uncertainty is derived from comparisons between data and simulation. In simulation, the resolution is fitted as a function of the jet p_T , where each point is obtained as the width of the distribution of $p_T^{\text{reco}}/p_T^{\text{part}}$ divided by its mean. Here, p_T^{reco} is the reconstructed jet p_T and p_T^{part} is the p_T of the jet reconstructed from stable simulated particles. In addition, the bisector method (see for example [2]) is used for an in-situ measurement of the JER both in data and in simulation. Again, fits to the obtained resolution as a function of p_T are performed. The uncertainties obtained from the differences between data and simulation are of the order of a few %, and depend on p_T as well as the detector region. The uncertainty on the background estimation is obtained by smearing the jet energy in simulation according to the 1σ variation on the resolution (by pulling a smearing factor from a Gaussian with that width) and propagating the effects to the E_T^{miss}

¹<https://twiki.cern.ch/twiki/bin/view/AtlasProtected/JetUncertainties>.

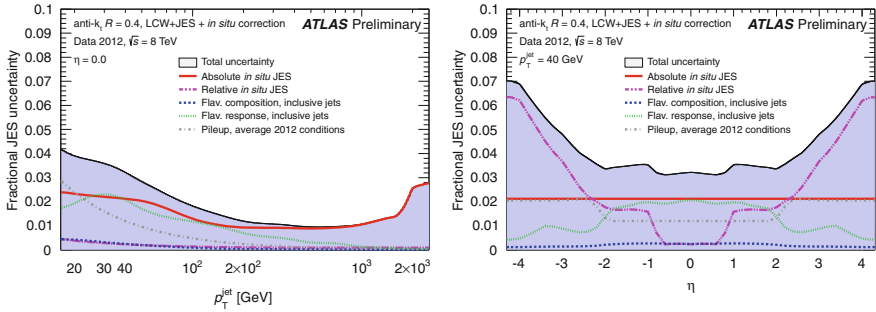


Fig. 14.1 Typical values of the JES uncertainty in 2012. *Left* as a function of p_T for constant $\eta = 0$. *Right* as a function of η for $p_T = 40$ GeV [1]

calculation, rerunning the complete analysis chain. This is done with the help of centrally provided software tools that contain the fits to the resolutions.²

14.1.3 Lepton Uncertainties

The uncertainties on lepton quantities can be grouped into two categories: The uncertainties on energy scales and resolution on the one hand and the uncertainties on the efficiency scale factors on the other hand. In general, it should be noted, that the lepton uncertainties do not cancel in the same way as uncertainties on jets or E_T^{miss} , since the leptons are treated differently in control and signal regions and the variations may lead to a migration of events from one into the other.

Energy Scales and Resolution

A number of uncertainties is associated with the measurement of the electron energy scale and resolution, as detailed in [3], and their effect is evaluated on the simulated samples and propagated to the data driven estimates with the help of software tools provided by the performance group.³ The scale uncertainty contains contributions associated to the estimation from $Z \rightarrow ee$ events, including statistical uncertainties, choice of the generator and method, contributions from the presampler scale uncertainty, material effects and an additional uncertainty for electrons with p_T below 20 GeV. The total uncertainty varies slightly as a function of $|\eta|$, but is at most 1.1 %, and this is expected to be valid up to energies of 500 GeV.

In addition to the absolute scale uncertainty, there is an uncertainty on the electron energy resolution due to potential mis-modelling of the resolution sampling term, the electronics and pile-up noise term, the asymptotic resolution at high energies and the effect of passive material in front of the calorimeter. This uncertainty amounts

²<https://twiki.cern.ch/twiki/bin/viewauth/AtlasProtected/ApplyJetResolutionSmearing>.

³https://twiki.cern.ch/twiki/bin/view/AtlasProtected/EGammaCalibrationGEO20#2013_Set_1_Recommendations_Septe.

to less than 10% at energies below 50 GeV and rises to up to 40% at high energies. Its impact on the background estimation is obtained by varying the energy smearing applied to the simulation up and down within the resolution uncertainty.

The muon momentum scale and resolution correction factors that are applied to the simulation are derived from template fits to the di-muon mass in large samples of $Z \rightarrow \mu^+\mu^-$, $\Upsilon \rightarrow \mu^+\mu^-$ and $J/\Psi \rightarrow \mu^+\mu^-$ events [4]. One of the largest uncertainties is due to the choice of the fit range, The relative scale uncertainty is largest in detector regions with $|\eta| > 2.3$ and amounts to $\lesssim 0.2\%$ there. The relative uncertainty on the momentum resolution ranges from 3 to 10% depending on η and p_T .

The effect of the scale uncertainty on the background estimates is studied by varying the energy scale up and down within its uncertainty with the help of a software package provided by the performance group.⁴ The same package provides also the functionality to vary the resolution of the momentum measurement within its uncertainty. The effects are again propagated through the analysis, including the E_T^{miss} calculation.

Efficiency Scale Factors

Scale factors are derived by the performance groups to account for differences in the reconstruction and identification efficiencies in data and simulation. The uncertainties are provided in software tools. In Ref. [5], the uncertainty on the electron scale factors are found to be mostly below the order of a few percent, except only for low transverse energy or high η -regions. The uncertainty on the muon reconstruction efficiency scale factor is less than 1% over almost the entire detector region when considering muons with a p_T greater than 10 GeV [4]. For the electrons, the total uncertainty (as a function of p_T and η) is obtained by adding the total (i.e. combined statistical and systematic) uncertainties on the trigger, reconstruction and identification efficiencies in quadrature. The muon reconstruction efficiency scale factor uncertainty is given by the linear sum of statistical and systematic uncertainty. The analysis is repeated for each of the up and down variations, respectively, using the nominal scale factor shifted by the corresponding uncertainty as an event weight in the simulation.

14.1.4 Soft Terms in Missing Transverse Energy

As detailed in the previous sections, the systematic uncertainties on lepton and jet scales and resolutions are propagated to the E_T^{miss} calculation via the `Missing-ETUtility` tool and the effect of the resulting variation on the E_T^{miss} is included in the respective scale or resolution uncertainty on the backgrounds instead of being considered as an E_T^{miss} uncertainty.

Another source of systematic uncertainties on the missing E_T arises from the soft terms, i.e. the soft jets and *cellOut* terms. This uncertainty is due to the MC modelling and the effects of pile-up, as described in Ref. [6]. There is one contribution due to

⁴https://twiki.cern.ch/twiki/bin/viewauth/AtlasProtected/MCPAnalysisGuidelinesData2012#Muon_Momentum_Corrections_on_MC.

the resolution of the soft terms terms and one due to their scale uncertainty; both are found to be of the order of a few percent. The effects are propagated through the complete analysis chain to the final background estimates.

14.1.5 *Pile-Up*

The pile-up re-weighting was optimised to reproduce the vertex multiplicity in minimum bias events which led to the introduction of a scale factor for the average number of interactions $\langle\mu\rangle$ to be applied in the simulation. This scale factor is given as 1.09 ± 0.04^5 by the dedicated performance group, i.e. in the simulation, for events with a certain $\langle\mu\rangle$ the number of primary vertices corresponds to that of data events with $1.9 \times \langle\mu\rangle$. The effect of varying the scaling up and down within its margin was studied in [7] and found to be negligible.

14.1.6 *Track Veto*

The uncertainties on the track veto efficiency are taken from Ref. [8]. It was estimated as the difference in efficiency between data and simulation and amounts to about 0.4%. A conservative estimate of 0.5% is used for the $Z(\rightarrow \nu\bar{\nu})$ +jets background, 1% for the others.

14.1.7 *Luminosity*

The uncertainty on the integrated luminosity is $\pm 2.8\%$, cf. Sect. 7.10. Since the main backgrounds (W/Z +jets) are estimated from data, their normalisation is not affected by the luminosity uncertainty. This uncertainty only plays a role for the backgrounds that are taken from simulation, i.e. the top, di-boson and $Z(\rightarrow \ell^+\ell^-)$ +jets backgrounds. Those are, however, covered by large conservative uncertainties already and the luminosity uncertainty is small in comparison and can be neglected.

14.1.8 *Background Subtraction in the Control Regions*

The contributions of single top, $t\bar{t}$ and diboson processes in the control regions are removed by subtracting the event number obtained in simulation directly from the

⁵https://twiki.cern.ch/twiki/bin/viewauth/AtlasProtected/InDetTrackingPerformanceGuidelines#Pile_up_rescaling.

Table 14.1 Parametrisation of the normalisation uncertainty for the diboson samples depending on the control and signal regions [7]

Region	Normalisation uncertainty
$Z(\rightarrow \ell^+\ell^-)+\text{jets}$ CRs and SR	$E_T^{\text{miss}} \leq 400 \text{ GeV}$: $\frac{1}{2500 \text{ GeV}} E_T^{\text{miss}} + \frac{7}{50}$
	$E_T^{\text{miss}} > 400 \text{ GeV}$: $\frac{3}{2000 \text{ GeV}} E_T^{\text{miss}} - \frac{3}{10}$
$W^\pm(\rightarrow \ell^\pm\nu)+\text{jets}$ CRs	$E_T^{\text{miss}} \leq 500 \text{ GeV}$: $\frac{1}{875 \text{ GeV}} E_T^{\text{miss}} + \frac{8}{35}$
	$E_T^{\text{miss}} > 500 \text{ GeV}$: 0.8

data. Thus, normalisation uncertainties on the corresponding samples will affect the background estimation in the signal region. A dedicated study was performed [8] using *b-tag information* to define a top control region. Jets originating from *b*-quarks can be identified as such by exploiting the fact that the *b*-quark decays quickly, resulting in a secondary vertex. Several algorithms exist for the classification of jets as *b*-jets, referred to as *b*-tagging. The one with the best performance used in ATLAS is the MV1 algorithm [9, 10], which is based on an artificial neural network to derive tag-weights for each jet. Different working points in terms of efficiency are defined by the dedicated performance group. In Ref. [8], the 90% working point is used to define the control region. The following uncertainty estimate was obtained: For lower cuts on E_T^{miss} up to 300 GeV, the uncertainty is 20%, then it increases to 50% and above $E_T^{\text{miss}} = 500 \text{ GeV}$ the statistical uncertainty becomes too large and a 100% uncertainty is assumed. Within these uncertainties the simulation normalisation agrees with data and therefore no additional normalisation factor is applied.

The uncertainty on the diboson sample normalisation is also taken from Ref. [8], where it was studied in detail and found to amount to 10–40% in the lower E_T^{miss} regions and up to 70% in the higher regions. A parametrisation as function of the cut on E_T^{miss} was derived and found to differ between $W^\pm(\rightarrow \ell^\pm\nu)+\text{jets}$ control regions on the one hand and $Z(\rightarrow \ell^+\ell^-)+\text{jets}$ control regions and the signal regions on the other hand. The parametrisations are given in Table 14.1.

The contamination of top and diboson processes in the control regions is varied independently within these uncertainties and the effect is propagated to the data-driven signal region estimates. The contributions of top and diboson production in the signal region are also varied accordingly, resulting in another variation of the total background estimate.

14.1.9 PDF

The uncertainties due to the choice of the PDF used in the simulation is estimated using the LHAPDF library, cf. Sects. 4.2 and 11.2.1. The result for the nominal PDF

CT10 (NLO) is compared to the results after reweighting to MSTW2008nlo68cl and NNPDF23_nlo_as_0119, respectively, and the largest difference is taken as a symmetric uncertainty around the CT10 value. The effect on a single sample is typically of the order of a few percent, but the uncertainty on the transfer factors (and therefore the data driven W and Z estimates) is typically less than 1% due to the cancellation effects.

14.1.10 Shower Modeling

The uncertainties due to the shower modeling were estimated for the analysis documented in Ref. [8] by comparing two $Z(\rightarrow \mu^+\mu^-)+\text{jets}$ samples with different modeling schemes at truth level. By using the truth p_T of the Z -boson as a measure of the E_T^{miss} in $Z(\rightarrow \nu\bar{\nu})+\text{jets}$ events, the effect on the transfer factor for $Z(\mu^+\mu^-) \rightarrow Z(\nu\bar{\nu})$ was estimated and found to be of the order of 0.4%.

14.1.11 Matching Scale

For the estimation of the matching scale uncertainty for the electroweak background samples, a similar procedure as for the shower modeling was applied, see Ref. [7]. Again, two $Z(\rightarrow \mu^+\mu^-)+\text{jets}$ truth samples with different CKKW matching scales were used to study the effect on the $Z(\mu^+\mu^-) \rightarrow Z(\nu\bar{\nu})$ transfer factor. The nominal value for the matching scale is 20 GeV and in the alternative sample it is 30 GeV. This translates into an uncertainty of 0.4% on the transfer factor [8].

14.1.12 Renormalisation and Factorisation Scales

In Ref. [8], the uncertainty due to the choice of renormalisation and factorisation scales in the electroweak SHERPA samples is estimated following a procedure that was developed in [11] and relies on the use of samples generated with Alpgen [12] to derive scale factors associated with the scale variations. These scale factors are then used for a reweighting based on the number of truth jets with $p_T > 30$ GeV which is applied to the SHERPA samples. The resulting uncertainty on the transfer factor are at most 0.6%.

Table 14.2 Electroweak radiative correction uncertainties on the transfer factor for $W^\pm(\rightarrow \ell^\pm\bar{\nu})+\text{jets}\rightarrow Z(\rightarrow \nu\bar{\nu})+\text{jets}$ for the different E_T^{miss} cuts, as provided by the authors of [13] for the analysis in [8]

E_T^{miss} cut (GeV)	150	200	250	300	350	400	500	600
$\Delta(TF)$ (%)	1	1	1	1	2	2	3	5

14.1.13 Electroweak Radiative Corrections on the W to Z Ratio

Since this analysis uses not only Z but also W control regions (taking advantage of the higher statistics) to estimate the dominant $Z(\rightarrow \nu\bar{\nu})+\text{jets}$ background in the signal region, electroweak radiative corrections on the W production have to be taken into consideration. Their effect can become significant for high p_T , as was shown in Ref. [13]. The authors give LO to NNLO corrections (as a function of the boson p_T which is equivalent to the E_T^{miss} in this analysis) at $\sqrt{s} = 14\text{ TeV}$, but they state that those are valid at 8 TeV as well. In this analysis, the corrections are not applied directly, but a corresponding uncertainty is considered, following what was done in Ref. [8]. The authors of Ref. [13] were contacted and provided uncertainty estimations for the mono-jet analysis signal regions that are to be used in this work as well and are summarised in Table 14.2. The uncertainty amounts to about 1% at low E_T^{miss} and grows to up to 5% in the highest considered signal region with $E_T^{\text{miss}} > 600\text{ GeV}$.

14.2 Estimation of $Z(\rightarrow \nu\bar{\nu})+\text{jets}$ Background

The $Z(\rightarrow \nu\bar{\nu})+\text{jets}$ background is estimated from four orthogonal control regions and the individual estimates are combined in order to get a precise estimate of the largest background in this analysis.

14.2.1 Estimation from a $Z+\text{jets}$ Control Region with Two Muons

Since muons are not included in the missing E_T definition used here (cf. Sect. 12.4), the closest approximation for emulating $Z(\rightarrow \nu\bar{\nu})+\text{jets}$ events is given by $Z(\rightarrow \mu^+\mu^-)+\text{jets}$ events. In both cases, the calorimeter E_T^{miss} is equivalent to the boson p_T , except for small energy losses by the muons in the calorimeter in the case of $Z(\rightarrow \mu^+\mu^-)+\text{jets}$. Given that muons are also not included in the missing E_T calculation at the trigger level, the same E_T^{miss} trigger as in the signal region can be used to

Table 14.3 Event yields for data and simulated processes in the lowest $Z(\rightarrow \mu^+\mu^-)+\text{jets}$ control region. The numbers in parenthesis are the fractions of the total number of simulated events

$E_{\text{T}}^{\text{miss}} > 150 \text{ GeV}$	
$Z(\rightarrow \mu^+\mu^-)+\text{jets}$	20489.74 (95.3)
Diboson	680.72 (3.2)
$t\bar{t}$	268.43 (1.2)
Single top	43.12 (0.2)
$Z(\rightarrow \tau^+\tau^-)+\text{jets}$	19.82 (0.1)
$W^\pm(\rightarrow \mu^\pm\ell)+\text{jets}$	3.95 (0.0)
$W^\pm(\rightarrow \tau^\pm\ell)+\text{jets}$	1.24 (0.0)
Total simulation	21507.01
Data	19746
Ratio	0.92

select events from the `JetTauEtmiss` stream. To further select $Z(\rightarrow \mu^+\mu^-)+\text{jets}$ events, exactly two good quality muons (c.f. Sect. 12.3) are required and no additional muons or electrons of *veto* quality are allowed in the event. In addition, the range of the invariant mass of the two muons, $m_{\ell\ell}$, is restricted to the interval 66–116 GeV, which are standard cuts for Z selection in ATLAS,⁶ optimised to reject the γ^* contribution.

The event numbers selected in the $Z(\rightarrow \mu^+\mu^-)+\text{jets}$ control region for data and the simulated processes are given in Table 14.3. As expected, the di-muon selection yields a very high purity: about 95% of all selected simulated events are $Z(\rightarrow \mu^+\mu^-)+\text{jets}$ events. The remaining contributions are essentially diboson and top production, with the diboson processes being the dominant background contamination with 3.2%.

Figure 14.2a shows that the level of purity stays the same for all $E_{\text{T}}^{\text{miss}}$ cuts. The top contribution becomes negligible from control region 6 ($E_{\text{T}}^{\text{miss}} > 400 \text{ GeV}$). The diboson contamination, however, increases from ~ 3 to $\sim 5\%$. In Fig. 14.2b, the change of the data to simulation ratio when increasing the $E_{\text{T}}^{\text{miss}}$ cut is shown. At low missing E_{T} , the ratio is about 0.9, and it decreases to roughly 0.6 in the highest control region, although with a large statistical uncertainty of approximately 20%. This already indicates that it will be beneficial to combine different $Z(\rightarrow \nu\bar{\nu})+\text{jets}$ estimates to increase sensitivity in the highest signal regions. The value of this ratio is applied as a scale factor to the simulation in plots to make shape comparisons easier. The normalisation difference will be corrected in the background estimation via the transfer factors.

For the estimation of signal region contributions from control regions, it is important that the variables used to specify the control region are well modelled by the simulation. Otherwise, the normalisation and hence the signal region estimate will

⁶<https://twiki.cern.ch/twiki/bin/view/AtlasProtected/WZElectroweakCommonTopics2011>.

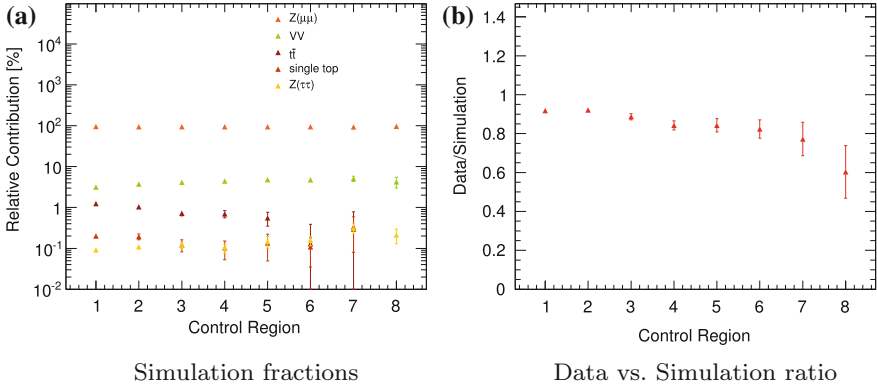


Fig. 14.2 Relative simulation fractions (a) and ratio of data versus simulation (b) in the $Z(\rightarrow \mu^+\mu^-)+\text{jets}$ control regions. The error bars show statistical uncertainties only

change. Mis-modelling of variables used in the same way in signal and control region, on the other hand, is not a concern as this is absorbed in the transfer factor, cf. Eq. (10.4). In the following, therefore, first the data-simulation comparisons for the lepton kinematic variables and the invariant mass will be presented, before also jet and missing E_T variables are discussed. The discussion will mostly focus on the lowest, most inclusive control region.

Figure 14.3 shows kinematic variables of the leading muon. For all of them the data to simulation ratio is compatible with 1 within the uncertainties, except for the tail of the p_T spectrum above 350 GeV. The η and ϕ distributions (Fig. 14.3a, b) show no unexpected features. The small dip at 0 in the pseudo-rapidity distribution is explained by the gaps in coverage that were left open for services to the inner detector parts, cf. Sect. 7.4. Otherwise, the η distribution shows the expected shape for highly energetic events, which are typically central: most of the entries at small absolute values and the distributions falls towards larger absolute values. The ϕ -distribution is expected to be approximately flat between $-\pi$ and π since there is no preferred direction in ϕ . Deviations from a flat distribution can be explained by inefficiencies in the corresponding detector regions and are well described by the simulation.

Between approximately 50 and 100 GeV, the p_T spectrum has a turn-on and falls from about 150 GeV. The position of the maximum and also the lowest occurring value depend on the boson p_T and hence on the E_T^{miss} cut, as is illustrated in Fig. 14.4, which shows the leading muon p_T for the four lowest $Z(\rightarrow \mu^+\mu^-)+\text{jets}$ CRs. The distribution is shifted to higher values for higher E_T^{miss} , the maximum always lying slightly below the E_T^{miss} cut value. This shows that the leading muon typically carries almost the entire boson transverse momentum. This is confirmed by the p_T distribution of the second leading muons, shown in Fig. 14.5a, which exhibits a monotonously falling shape, most of the values below about half the boson p_T . Above that, the spectrum falls steeply since the sub-leading muon cannot carry much more than half of the boson p_T . Figure 14.6 underlines this further: It shows the sub-leading muon p_T

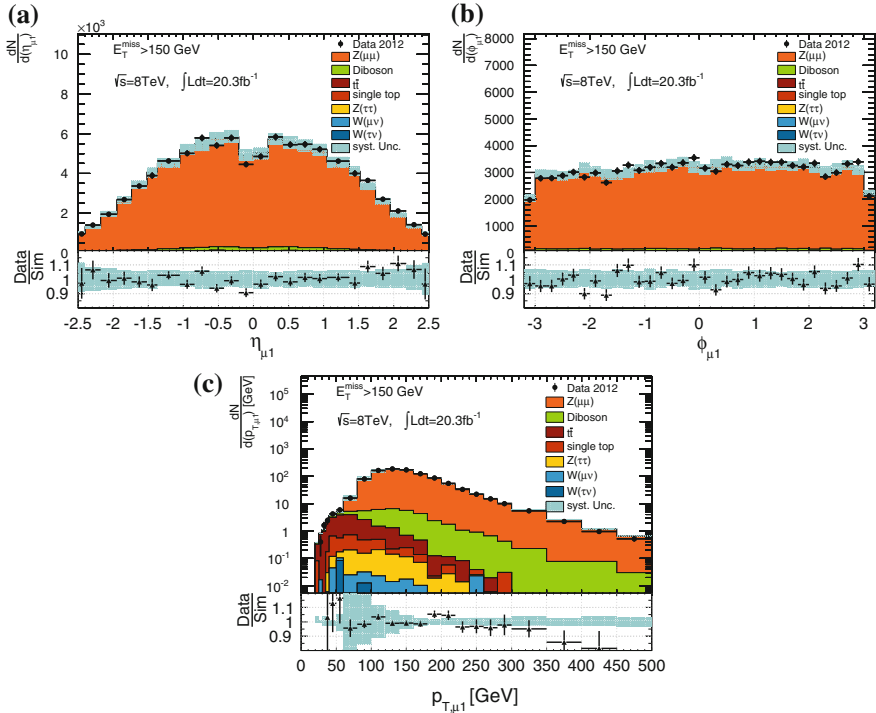


Fig. 14.3 Kinematic variables of the leading muon in the lowest $Z(\rightarrow \mu^+\mu^-)+\text{jets}$ control region. **a** Pseudo-rapidity. **b** Azimuthal angle. **c** Transverse momentum

spectra for the four lowest control regions. It can clearly be seen that the ‘shoulder’ shifts towards higher values, always corresponding to about half the cut value on E_T^{miss} , and therefore half the boson p_T .

The η - and ϕ -distribution for the sub-leading muon are shown in Fig. 14.5b, c. Apart from what has been discussed for the leading muon, there are no unexpected features in either of the distributions. The ratio of data to simulation is compatible with 1 within the uncertainties for the complete range. The same holds for the p_T spectrum up to 250 GeV, however, beyond 150 GeV the statistical uncertainties become large and there are only few events in data.

Figure 14.7 shows the difference in ϕ for the two selected muons for various E_T^{miss} cuts. In the rest frame of the boson, the two muons are back-to-back, i.e. the azimuthal difference is $|\Delta\phi| = \pi$. Since the Z is not at rest in the events considered here, the decay angle in the laboratory frame will be smaller than π , the more so, the higher the boson p_T . This is indeed observed from the different plots in Fig. 14.7: The distribution clearly shifts towards lower values with increasing E_T^{miss} cut. Within uncertainties the simulation models the data well, especially in the bulk of the distributions.

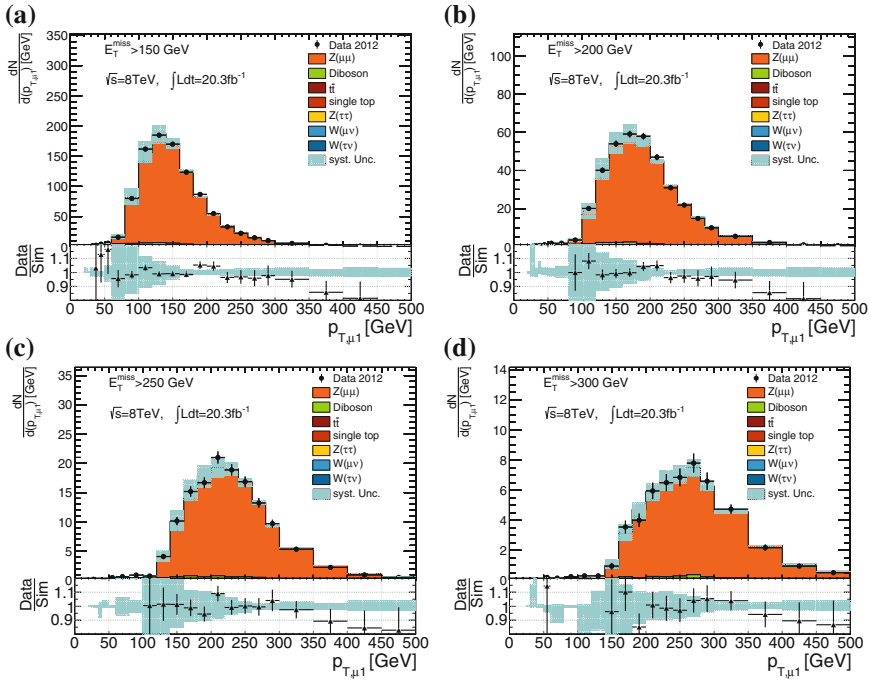


Fig. 14.4 Leading muon p_T in $Z(\rightarrow \mu^+\mu^-)+\text{jets}$ control regions with different E_T^{miss} cuts. **a** $E_T^{\text{miss,calo}} > 150 \text{ GeV}$. **b** $E_T^{\text{miss,calo}} > 200 \text{ GeV}$. **c** $E_T^{\text{miss,calo}} > 250 \text{ GeV}$. **d** $E_T^{\text{miss,calo}} > 300 \text{ GeV}$

Figure 14.8 shows the invariant mass distribution of the muon pair, before the cut at 66 and 116 GeV. The peak at the Z -mass is clearly visible. The excess in data at low values of m_Z is caused by the generator cut applied in the $Z(\rightarrow \ell^+\ell^-)+\text{jets}$ samples. It can be seen that the $Z(\rightarrow \tau^+\tau^-)+\text{jets}$ background is almost completely removed by the cut at 66 GeV. The invariant mass for the diboson processes naturally also features a peak at the Z -mass and is thus not reduced to the same extent by the cut on $m_{\ell\ell}$. The top processes have a flat distribution in $m_{\ell\ell}$. The simulation is compatible with the data within uncertainties.

After having demonstrated that the control region specific cuts are modelled reasonably well within the uncertainties, in the following, distributions for variables that are used in the signal region definition in the same way will be presented. Shape differences in these variables are tolerable, since they will be corrected for by the transfer factor method, cf. Eq. (10.4).

In Fig. 14.9 the $|\Delta\phi_{\text{min}}(\text{jet}_i, E_T^{\text{miss}})|$ variable before the cut at 1.0 is shown. As is to be expected, the distribution peaks at values close to π : the ISR jet recoils against the Z -boson approximately back-to-back balancing the boson p_T which is equivalent to the missing E_T . The data to simulation ratio is flat and compatible with 1 within

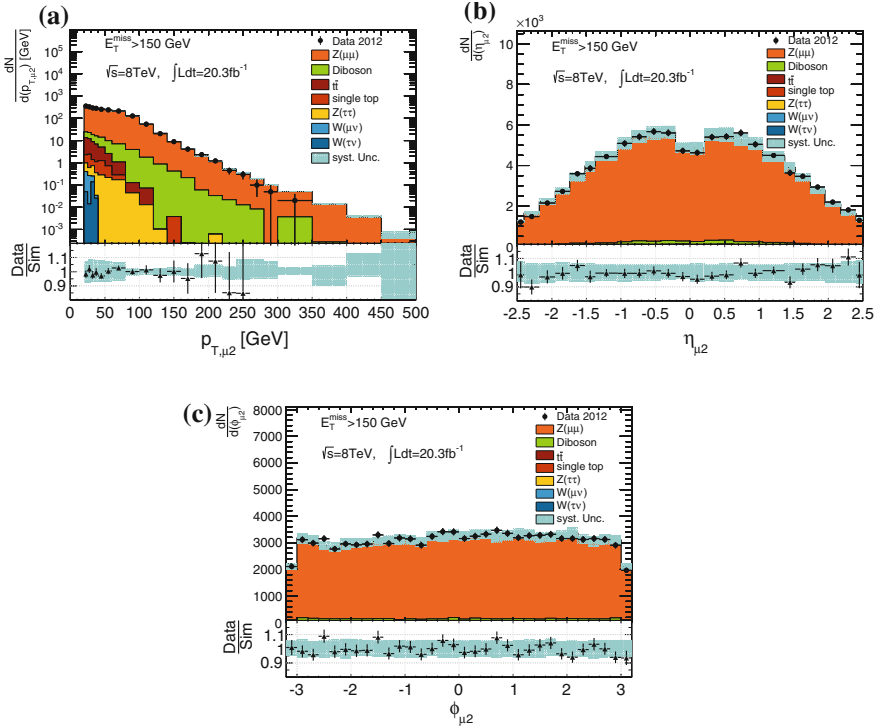


Fig. 14.5 Kinematic variables of the sub-leading muon in the lowest $Z(\rightarrow \mu^+\mu^-)+\text{jets}$ control region. **a** Transverse momentum. **b** Pseudo-rapidity. **c** Azimuthal angle

the uncertainties. In particular, there is no excess in data at values close to 0, which would indicate a QCD multi-jet contamination.

The missing E_T spectrum is displayed in Fig. 14.10a. Especially in the tail the simulation overshoots the data. Up to 600 GeV the deviations are covered by the total uncertainty, the larger deviations in the high E_T^{miss} tail affect only a small fraction of events and will be corrected for by the transfer factors. Figure 14.10b presents the transverse momentum of the di-muon system. It peaks at the cut value of E_T^{miss} at 150 GeV and has a small turn-on at lower values. The description by the simulation is comparable with that for the calorimeter E_T^{miss} .

The kinematic variables of the leading jet are displayed in Fig. 14.11. The ratios of data and simulation for η and ϕ (Fig. 14.11a and b, respectively) are flat over the full acceptance. The pseudo-rapidity is concentrated at small absolute values, which is to be expected given the large transverse momentum required for the leading jet. In the ϕ distribution, the effect of the dead tile modules at roughly 0.5 and 1.5 is clearly visible. The ratio stays approximately flat in those regions, showing that the corrections applied to the simulation emulate the detector very well. The leading jet p_T has a maximum at about 150 GeV which is explained by the cut on E_T^{miss} at this

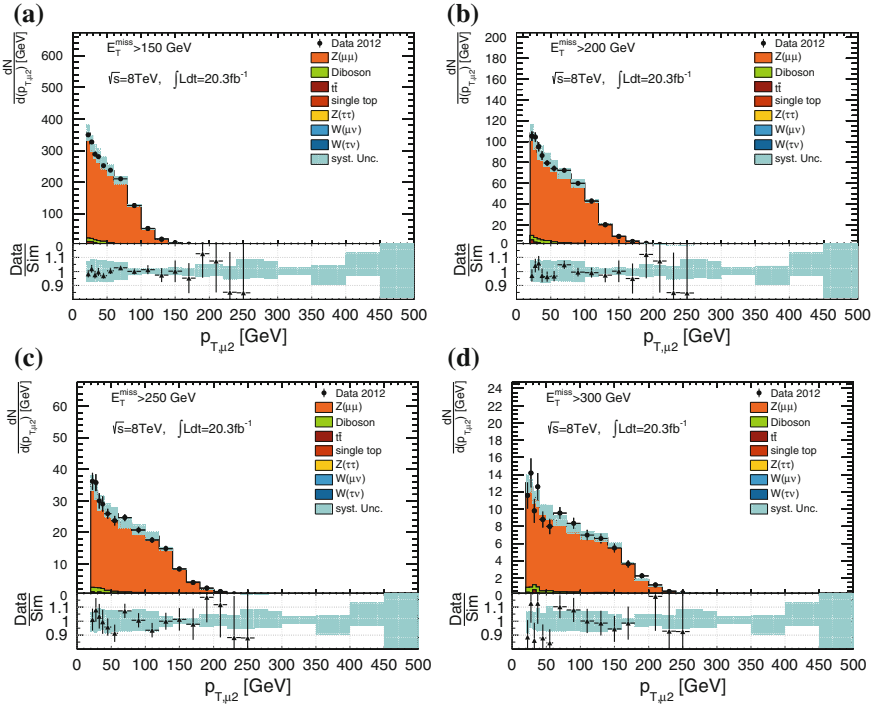


Fig. 14.6 Sub-leading muon p_T in $Z(\rightarrow \mu^+ \mu^-) + \text{jets}$ control regions with different E_T^{miss} cuts. **a** $E_T^{\text{miss,calo}} > 150 \text{ GeV}$. **b** $E_T^{\text{miss,calo}} > 200 \text{ GeV}$. **c** $E_T^{\text{miss,calo}} > 250 \text{ GeV}$. **d** $E_T^{\text{miss,calo}} > 300 \text{ GeV}$

value and the fact that the jet approximately balances the missing E_T . The ratio of data and simulation is compatible with 1, except for the tail of the p_T distribution, where there are only very few events in data. The ratio of leading jet p_T to E_T^{miss} as presented in Fig. 14.11d also illustrates the mono-jet like topology: in the lowest control region considered here, in basically all events the ratio is greater than 0.5, meaning that the jet carries at least half the amount of E_T^{miss} as transverse momentum. In fact, the bulk of the distribution is close to 1, indicating that the jet indeed carries a p_T very similar to the amount of E_T^{miss} .

Figure 14.12 shows the η -, ϕ - and p_T -distributions for the sub-leading jet. The η spectrum in Fig. 14.12a is broader than for the leading jet since there is no hard cut on the jet p_T , and it is well described within $|\eta| < 1.0$ with larger deviations in the tails at higher absolute values. The ratio of data and simulation for the ϕ -distribution in Fig. 14.12b is flat over the complete range, in particular also in the region of the dead tile modules, which can be seen as dips in the distribution. The dips are less pronounced than for the leading jet, since the average (absolute) η for the sub-leading jets is larger and the dead modules are located in the central region. Hence, a smaller fraction of sub-leading jets is affected. The p_T spectrum is steeply falling as expected,

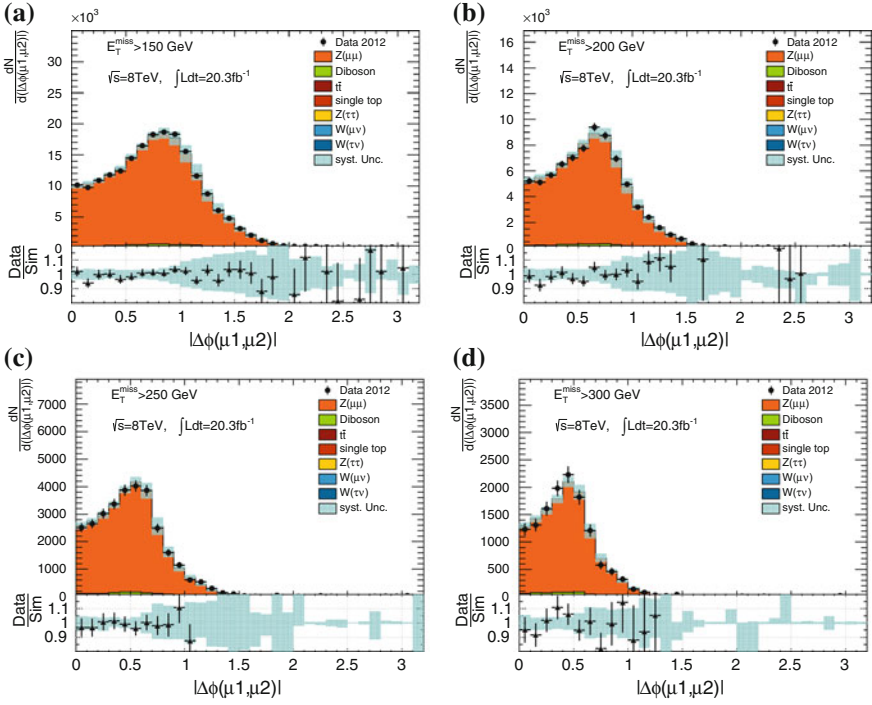
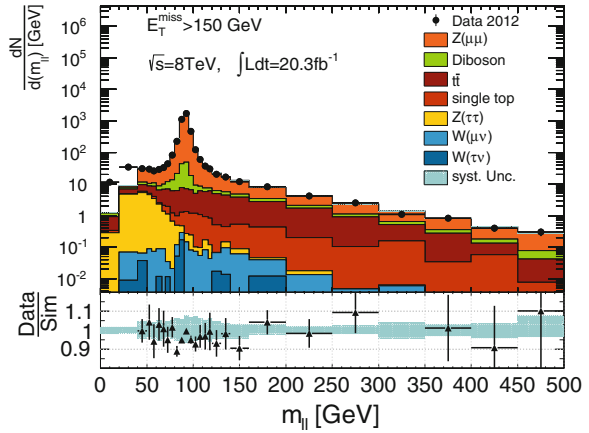


Fig. 14.7 Azimuthal separation of the two muons in $Z(\rightarrow \mu^+\mu^-)+\text{jets}$ control regions with different E_T^{miss} cuts. **a** $E_T^{\text{miss,calo}} > 150 \text{ GeV}$. **b** $E_T^{\text{miss,calo}} > 200 \text{ GeV}$. **c** $E_T^{\text{miss,calo}} > 250 \text{ GeV}$. **d** $E_T^{\text{miss,calo}} > 300 \text{ GeV}$

Fig. 14.8 Di-muon invariant mass distribution in the lowest $Z(\rightarrow \mu^+\mu^-)+\text{jets}$ control region



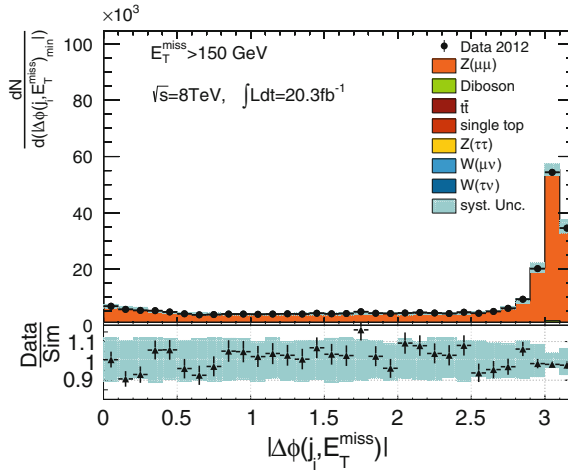


Fig. 14.9 Minimum azimuthal difference between E_T^{miss} and any jet in the lowest $Z(\rightarrow \mu^+ \mu^-) + \text{jets}$ control region

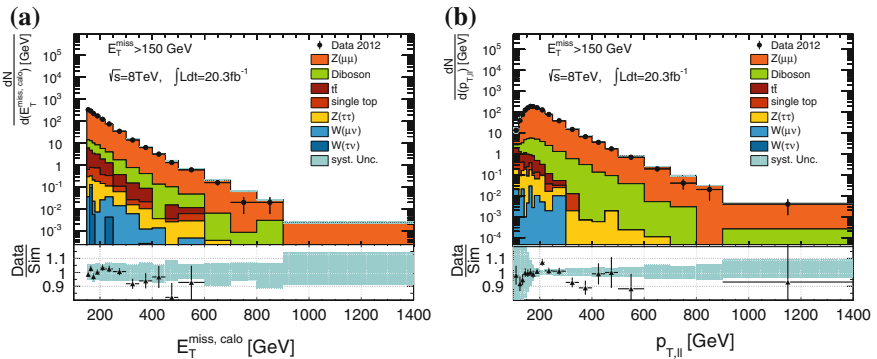


Fig. 14.10 Missing transverse energy and reconstructed di-muon p_T in the lowest $Z(\rightarrow \mu^+ \mu^-) + \text{jets}$ control region. **a** Calorimeter missing E_T . **b** Transverse momentum of the di-lepton system

with a small shoulder at ~ 150 GeV. The ratio is not flat, but compatible with 1 within the uncertainties up to about 300 GeV. Beyond that, there are only very few events.

The jet multiplicity in the $Z(\rightarrow \mu^+ \mu^-) + \text{jets}$ control region can be seen in Fig. 14.13. About 84 % of the events have less than 3 jets, i.e. they are mostly mono-jet like. The data to simulation ratio is within 10 % from 1 up to a jet multiplicity of 5 and the deviations are covered by the uncertainties.

Figure 14.14a shows the acceptance (cf. Eq. (10.3)) of the muon and invariant mass cuts on top of the signal region selection cuts. For the lowest missing E_T bin, the acceptance is ~ 67 %, and it increases to roughly 300 GeV until it stabilises around a value of 75 %, with a slightly falling tendency at $E_T^{\text{miss}} > 700$ GeV. In the highest

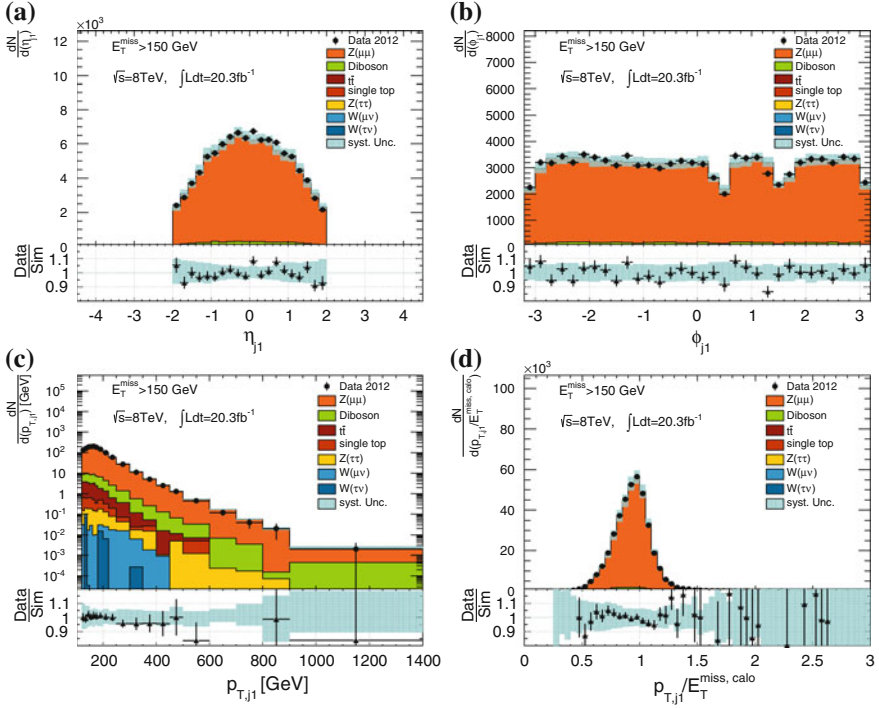


Fig. 14.11 Kinematic variables of the leading jet in the lowest $Z(\rightarrow \mu^+\mu^-)+\text{jets}$ control region. **a** Pseudo-rapidity. **b** Azimuthal angle. **c** Transverse momentum. **d** $p_{T,j1}/E_T^{\text{miss}}$

bin the acceptance is only 50%. The increase of acceptance can be explained by the correlation of muon p_T and η with the boson- p_T : higher calorimeter missing E_T means higher boson- p_T and hence more central muons with higher p_T which are more likely to pass the muon selection cuts.

The ratio of $Z(\rightarrow \mu^+\mu^-)+\text{jets}$ over the sum of all W and Z processes (c.f. Eq. 10.1) in Fig. 14.14b is essentially 1 over the complete E_T^{miss} range, indicating the high purity of the control region after the subtraction of top and diboson processes (c.f. Eq. 10.2). It also shows that the shapes of the E_T^{miss} spectra for all the W and Z processes are similar.

The transfer factor (c.f. Eq. 10.4) for estimating $Z(\rightarrow \nu\bar{\nu})+\text{jets}$ in the control region is shown in Fig. 14.15a. The errors shown are only statistical uncertainties and within those the TF is flat as a function of E_T^{miss} . This indicates that the $Z(\rightarrow \nu\bar{\nu})+\text{jets}$ background indeed can be modelled by $Z(\rightarrow \mu^+\mu^-)+\text{jets}$ events. The ratio of $Z(\rightarrow \nu\bar{\nu})+\text{jets}$ events after the signal region cuts over all W and Z (i.e. essentially only $Z(\rightarrow \mu^+\mu^-)+\text{jets}$) events in the control region is shown in Fig. 14.15b. Corresponding to the upward trend in the acceptance at low E_T^{miss} , this distribution shows a downward trend and then flattens out, except for the highest bin, where the TF is considerably larger, accounting for the lower acceptance.

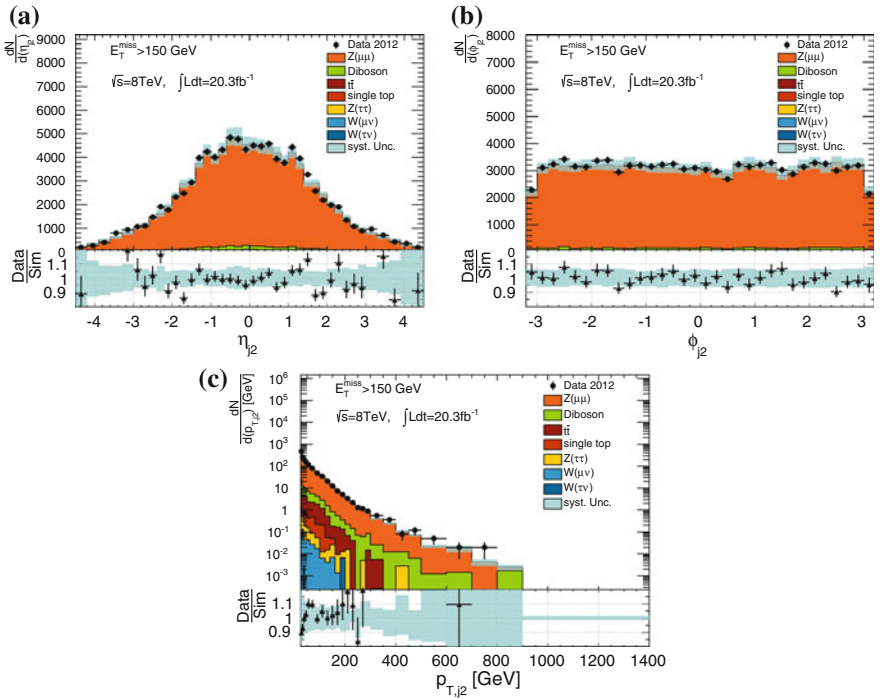


Fig. 14.12 Kinematic variables of the sub-leading jet in the lowest $Z(\rightarrow \mu^+\mu^-)+\text{jets}$ control region. **a** Pseudo-rapidity. **b** Azimuthal angle. **c** Transverse momentum

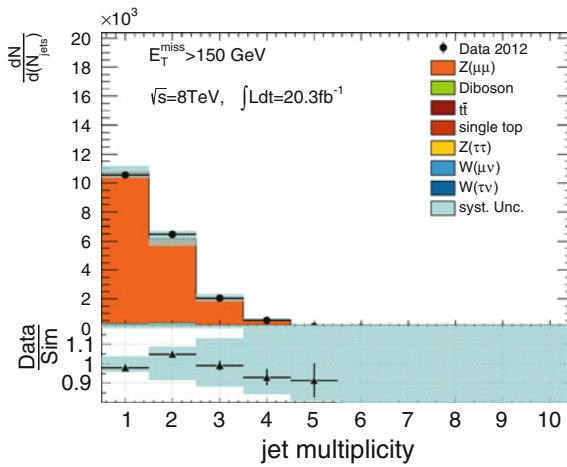


Fig. 14.13 Jet multiplicity in the lowest $Z(\rightarrow \mu^+\mu^-)+\text{jets}$ control region

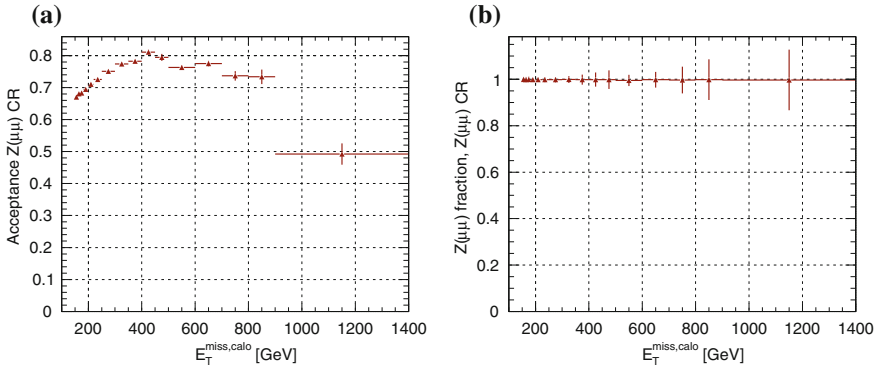


Fig. 14.14 Acceptance and purity in the $Z(\rightarrow \mu^+\mu^-)+\text{jets}$ control regions as a function of E_T^{miss} . The error bars are statistical uncertainties only. **a** Acceptance. **b** Purity

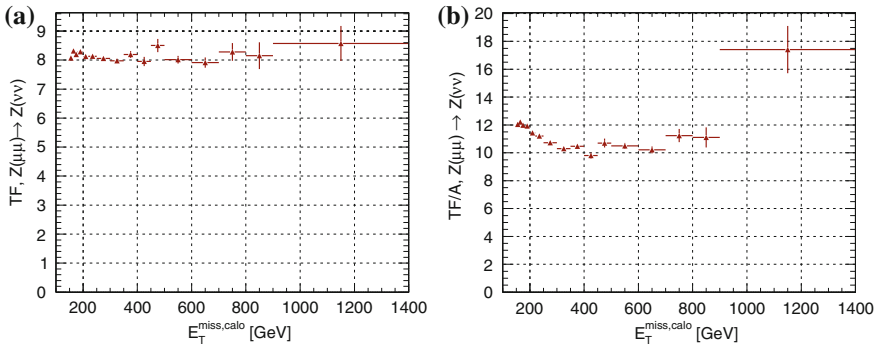


Fig. 14.15 Transfer factors before and after applying the lepton selection in the $Z(\rightarrow \mu^+\mu^-)+\text{jets}$ control region. Error bars are statistical uncertainties only. **a** Transfer factor. **b** Transfer factor with acceptance

The systematic uncertainties on the $Z(\rightarrow \nu\bar{\nu})+\text{jets}$ estimate obtained from the application of the transfer factor to the data corrected for processes other than $Z(\rightarrow \mu^+\mu^-)+\text{jets}$ are listed in Table 14.4. It is found that especially at low missing E_T the systematic uncertainties are remarkably small—at the level of 1% or below. They grow towards higher E_T^{miss} regions, the dominating one being the subtraction of top and diboson processes in the control region, which amounts to almost 5% in the highest signal region. This is about the same level as the uncertainties due to the limited simulation statistics. As is to be expected for a muon control region, the uncertainties due to the electron scales and identification are negligible. Uncertainties from the muon reconstruction and scales are of the order of 1%. The dominating uncertainty at large E_T^{miss} is by far $\sim 24\%$ from the limited data statistic. Again, this motivates the use of in total four control regions for the estimate of $Z(\rightarrow \nu\bar{\nu})+\text{jets}$ especially at large missing E_T . The theory uncertainties includes the

Table 14.4 Relative uncertainties (in %) from different sources on the estimate of $Z(\rightarrow \nu\bar{\nu})$ +jets from the $Z(\rightarrow \mu^+\mu^-)$ +jets control regions

$Z(\rightarrow \nu\bar{\nu})$ from $Z(\rightarrow \mu^+\mu^-)$	SR1	SR2	SR3	SR4	SR5	SR6	SR7	SR8
Data Stat (%)	0.7	1.2	1.9	2.9	4.3	6.1	12.0	23.8
MC Stat (%)	0.5	0.7	1.0	1.3	1.8	2.4	2.8	4.5
JES (%)	0.7	0.6	0.5	0.9	0.4	0.4	1.4	2.1
JER (%)	0.5	0.4	0.4	0.9	0.0	0.1	1.3	1.0
E_T^{miss} (%)	0.2	0.0	0.0	0.0	0.0	0.1	0.2	0.1
CR bkg. (%)	0.8	1.0	1.2	1.5	1.8	1.9	3.4	4.9
Muon (%)	0.9	0.9	1.0	1.0	1.0	1.1	1.1	1.4
Electron (%)	0.0	0.0	0.0	0.1	0.0	0.1	0.1	0.1
Track veto (%)	0.6	0.6	0.6	0.6	0.6	0.6	0.6	0.6
Theory (%)	0.8	0.8	0.8	0.8	0.8	0.8	1.0	2.5

contributions from shower modelling, matching, renormalisation and factorisation scales and choice of PDF. The PDF uncertainty is below 0.5 in the first six regions and increases to 2.3 % in SR8, which illustrates the cancellation of systematic uncertainties due to the transfer factor method.

14.2.2 Estimation from a Z+jets Control Region with Two Electrons

Also in the electron channel, a Z+jets control region is used to get another estimate of the $Z(\rightarrow \nu\bar{\nu})$ +jets background. Exactly two good electrons fulfilling the slightly looser criteria given in Sect. 12.2 are required. Events with additional *veto* quality electrons or muons are discarded. As for the $Z(\rightarrow \mu^+\mu^-)$ +jets control region, a cut on the invariant mass of the two electrons selects events in a range of 66–116 GeV.

A difference to the $Z(\rightarrow \mu^+\mu^-)$ +jets CR follows from the fact, that electrons are part of the missing E_T calculation both at the trigger and the reconstruction level, since they deposit (most of) their energy in the calorimeter. The calorimeter missing E_T in this control region accordingly will be small. Therefore, instead of the E_T^{miss} trigger a logical OR of the two single electron triggers introduced in Sect. 11.1 is used to select data from the E_{gamma} stream.

In order to estimate the $Z(\rightarrow \nu\bar{\nu})$ +jets process, the decay into invisible particles has to be emulated. Thus, the electrons are treated as missing transverse energy by removing them from the E_T^{miss} calculation, cf. Sect. 12.4. The missing E_T corrected in this way corresponds again to the boson p_T as for the $Z(\rightarrow \nu\bar{\nu})$ +jets process. This is illustrated in Figs. 14.16: 14.16a shows the transverse momentum of the di-electron system. The distribution is very similar to the one in the muon channel, see

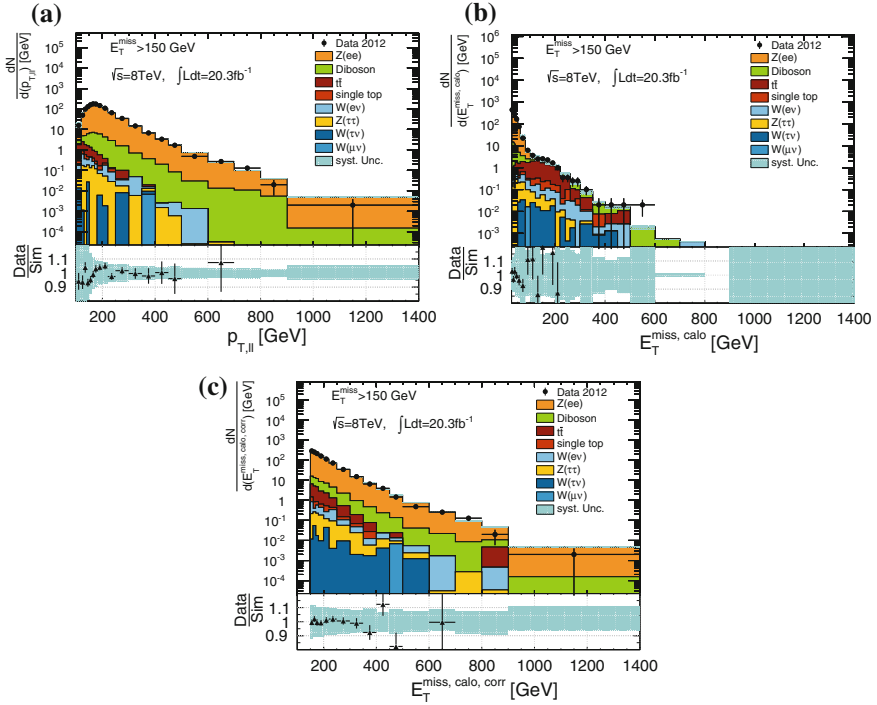


Fig. 14.16 E_T^{miss} and di-electron p_T in the lowest $Z(\rightarrow e^+e^-)+\text{jets}$ control region. **a** Transverse Momentum of the di-lepton system. **b** Uncorrected missing E_T . **c** Missing E_T corrected for the good electrons

Fig. 14.10b, which gives confidence in the electron removal procedure. The recalculated E_T^{miss} is displayed in Fig. 14.16c and is modelled well up to approximately 400 GeV. The differences in the tail will be corrected by the TF application.

For comparison, the uncorrected E_T^{miss} is displayed in Fig. 14.16b. As is to be expected, this variable is close to 0 for the majority of events. The cuts on jets and E_T^{miss} are the same as in the signal regions.

The numbers of selected events in the lowest control region for the various processes are given in Table 14.5. The purity is similar to the one in the $Z(\rightarrow \mu^+\mu^-)+\text{jets}$ control region (c.f. Table 14.3): $Z(\rightarrow e^+e^-)+\text{jets}$ events make up 94% of the simulated processes. The dominant background is diboson production with 4%, $t\bar{t}$ amounts to 1.4% and all other processes contribute less than 1%. The data to simulation ratio is also very similar to the $Z(\rightarrow \mu^+\mu^-)+\text{jets}$ CR with a value of 0.92.

The plots in Fig. 14.17 show the relative contributions of the different simulated processes (Fig. 14.17a) and the data to simulation ratio (Fig. 14.17b) for all 8 control regions. The composition shows a similar picture as in the $Z(\rightarrow \mu^+\mu^-)+\text{jets}$ control region (c.f. Fig. 14.2a): The fraction of the control region process is stable as a function of the E_T^{miss} cut, the top fraction decreases in the higher control regions

Table 14.5 Event yields for data and simulated processes in the lowest $Z(\rightarrow e^+e^-)+\text{jets}$ control region. The numbers in parenthesis are the fractions of the total number of simulated events

$E_T^{\text{miss}} > 150 \text{ GeV}$	
$Z(\rightarrow e^+e^-)+\text{jets}$	19200.54 (94.2)
Diboson	805.52 (4.0)
$t\bar{t}$	294.47 (1.4)
$W^\pm(\rightarrow e^\pm\nu)+\text{jets}$	35.27 (0.2)
Single top	32.26 (0.2)
$Z(\rightarrow \tau^+\tau^-)+\text{jets}$	19.89 (0.1)
$W^\pm(\rightarrow \tau^\pm\nu)+\text{jets}$	3.31 (0.0)
$W^\pm(\rightarrow \mu^\pm\nu)+\text{jets}$	0.36 (0.0)
Total simulation	20391.62
Data	18720
Ratio	0.92

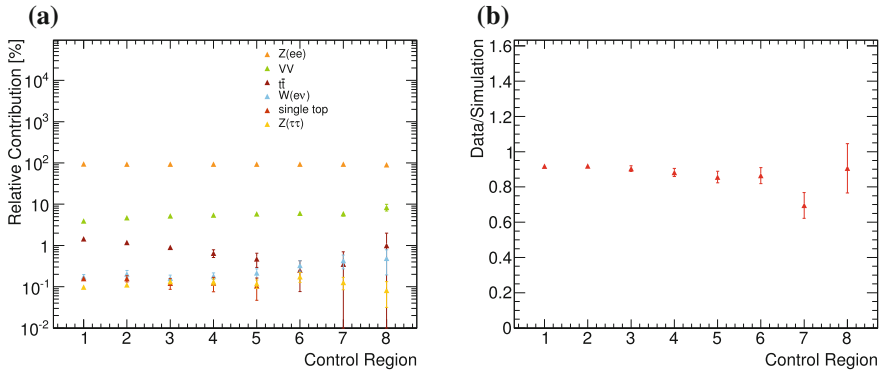


Fig. 14.17 Relative simulation fractions (a) and ratio of data versus simulation (b) in the $Z(\rightarrow e^+e^-)+\text{jets}$ control regions. The error bars show statistical uncertainties only

while the diboson contamination grows. The ratios of data over the sum of the simulated processes is more stable than for the $Z(\rightarrow \mu^+\mu^-)+\text{jets}$ control region: Within the statistical uncertainties it is mostly at the level of 90% with the exception of region 7 ($E_T^{\text{miss}} > 500 \text{ GeV}$) where it is only around 70%. However, as for the $Z(\rightarrow \mu^+\mu^-)+\text{jets}$ CR, the statistical uncertainties become large at high E_T^{miss} , which makes it preferable to not rely on the $Z(\rightarrow \ell^+\ell^-)+\text{jets}$ control regions alone.

Figure 14.18 summarises kinematic variables of the leading electron. All distributions are modelled well by the simulation given the systematic and statistical uncertainties. In the η -distribution, the calorimeter transition regions that have been explicitly removed in the good electron definition are clearly visible. The leading electron p_T has a similar distribution as the leading muon p_T in the $Z(\rightarrow \mu^+\mu^-)+\text{jets}$ control region (c.f. Fig. 14.3c).

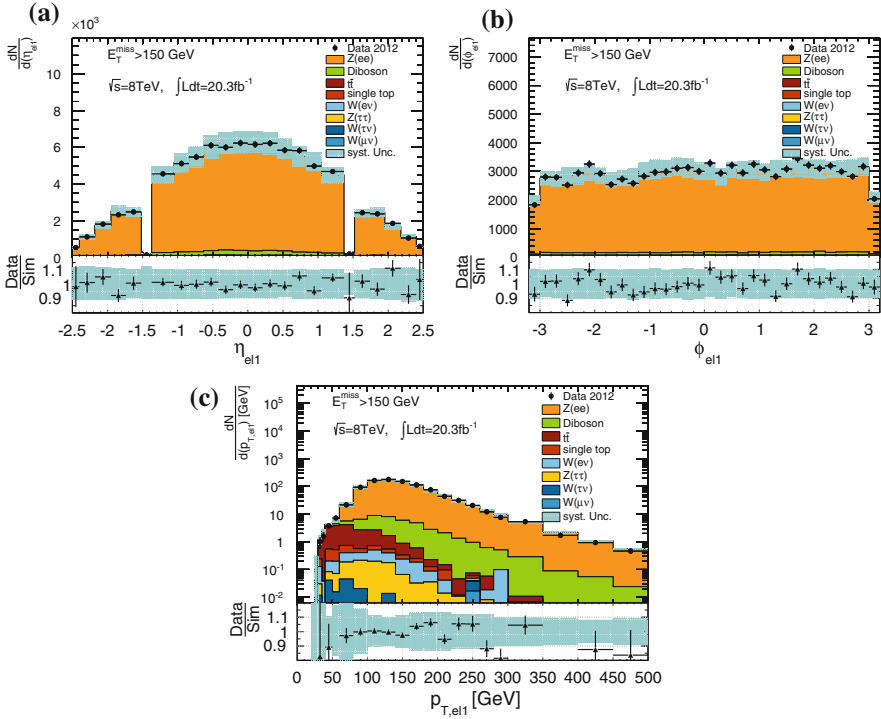


Fig. 14.18 Kinematic variables of the leading electron in the lowest $Z(\rightarrow e^+e^-)+\text{jets}$ control region. **a** Pseudo-rapidity. **b** Azimuthal angle. **c** Transverse momentum

The corresponding variables for the sub-leading electron are displayed in Fig. 14.19. The description by the simulation is accurate within the uncertainties. No unexpected features in either of the distributions is observed.

Also not protected by the transfer factor method is the invariant mass of the di-electron system, see Fig. 14.20. As for the $Z(\rightarrow \mu^+\mu^-)+\text{jets}$ control region (c.f. Fig. 14.8), the Z -mass peak is clearly visible, also for the diboson processes. The excess of data in the low mass region is due to the generator cut at 40 GeV in the SHERPA samples. The cut at 66 and 116 GeV efficiently reduces most backgrounds, except diboson. The simulation does not model the peak very well, but within the uncertainties the ratio is still compatible with 1.

Figure 14.21 illustrates the mono-jet like topology of the $Z(\rightarrow e^+e^-)+\text{jets}$ events: Most of the events have 2 jets at most, as can be seen in Fig. 14.21a. The $|\Delta\phi_{\min}(\text{jet}_i, E_T^{\text{miss}})|$ distribution (before the cut) in Fig. 14.21b shows a clear peak close to π , which means that E_T^{miss} and jets are back-to-back. Again, there is no visible excess of data at low values of $|\Delta\phi_{\min}(\text{jet}_i, E_T^{\text{miss}})|$, indicating that the QCD multi-jet contamination is negligible. While the ratio shows deviations of 10–15%

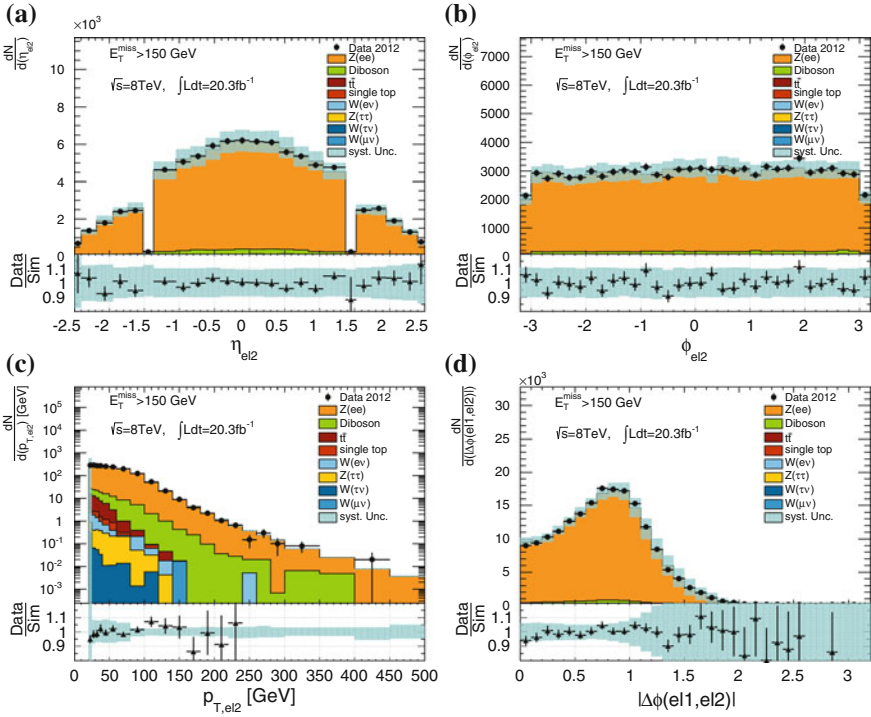
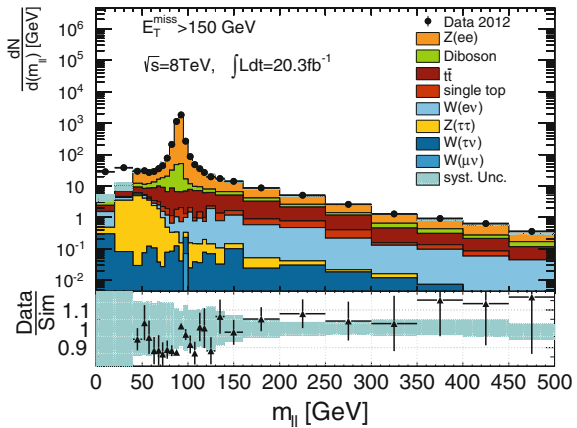


Fig. 14.19 Kinematic variables of the sub-leading electron in the lowest $Z(\rightarrow e^+e^-)+\text{jets}$ control region. **a** Pseudo-rapidity. **b** Azimuthal angle. **c** Transverse momentum. **d** Azimuthal distance to leading electron

Fig. 14.20 Di-lepton mass distribution in the lowest $Z(\rightarrow e^+e^-)+\text{jets}$ control region



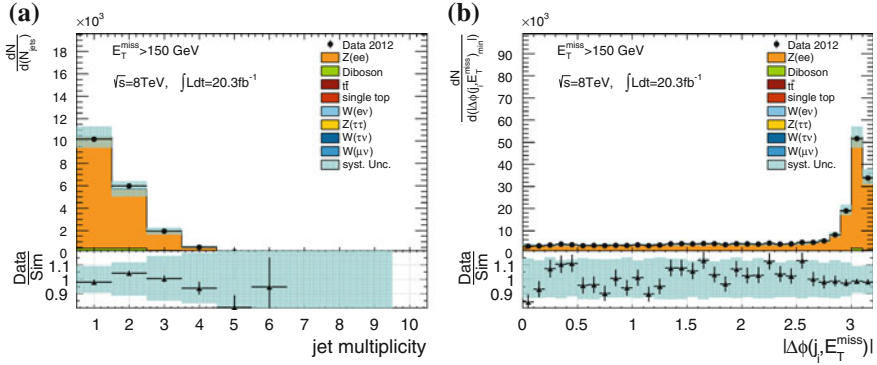


Fig. 14.21 Jet multiplicity and $|\Delta\phi_{\min}(\text{jet}_i, E_T^{\text{miss}})|$ in the lowest $Z(\rightarrow e^+e^-)+\text{jets}$ control region. **a** Jet multiplicity. **b** $|\Delta\phi_{\min}(\text{jet}_i, E_T^{\text{miss}})|$

from 1, this is covered by the systematic uncertainties and will be corrected by the transfer factor method, since this variable is also used to cut on in the signal region.

As any mis-modelling in the jet variables will be corrected by the transfer factor method the respective distributions will be not further discussed here.

The acceptance and purity after subtraction of top and diboson contaminations (see Fig. 14.22a, b) show a very similar behaviour as those in the $Z(\rightarrow \mu^+\mu^-)+\text{jets}$ control region (c.f. Fig. 14.14). The acceptance has an upward trend at low E_T^{miss} , since increasing the boson- p_T leads to more central electrons with higher p_T . The fraction of $Z(\rightarrow e^+e^-)+\text{jets}$ events out of all W - and Z -processes in the control region is close to 100% and stable versus E_T^{miss} .

The transfer factor for the $Z(\rightarrow \nu\bar{\nu})+\text{jets}$ estimation is not flat, see Fig. 14.23a. It shows a falling trend at low E_T^{miss} values and becomes flat only above 400 GeV.

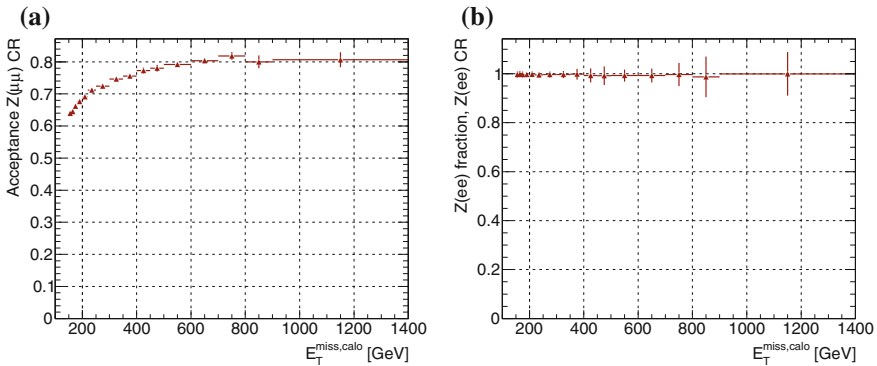


Fig. 14.22 Acceptance and purity in the $Z(\rightarrow e^+e^-)+\text{jets}$ control regions as a function of E_T^{miss} . The error bars are statistical uncertainties only. **a** Acceptance. **b** Purity

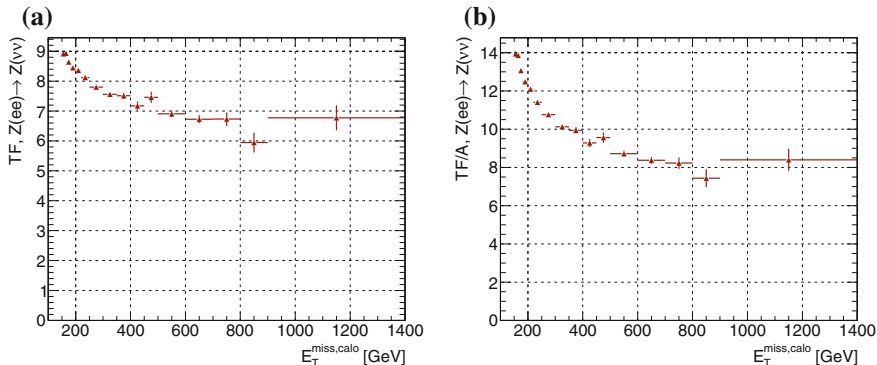


Fig. 14.23 Transfer factors before and after applying the lepton selection in the $Z(\rightarrow e^+e^-)$ +jets control region. Error bars are statistical uncertainties only. **a** Transfer factor. **b** Transfer factor with acceptance

This can again be explained by the different lepton phase space in signal and control region: In the control region, the electrons are restricted to the central region, which leads to a higher boson p_T on average than in the signal region, where there is no such restriction for the neutrinos. Thus, the ratio is larger at lower values of E_T^{miss} .

Table 14.6 summarises the uncertainties on the $Z(\rightarrow \nu\bar{\nu})$ +jets estimate obtained from the $Z(\rightarrow e^+e^-)$ +jets CR. As expected, the statistical uncertainties grow to large values in the higher E_T^{miss} region. The dominant uncertainty is the subtraction of top and diboson in the control region, especially at high E_T^{miss} . The uncertainties due to the lepton scales and reconstruction are analogue to what was observed in the $Z(\rightarrow \mu^+\mu^-)$ +jets control region: here, the muon uncertainties are negligible, while the electron uncertainties are at the level of 2%, i.e. a bit larger than the muon uncertainties in the $Z(\rightarrow \mu^+\mu^-)$ +jets CR. The theoretical uncertainty include again the showering, matching, scale and PDF uncertainties. All of them are of similar size, of the order of 0.5% in all regions.

14.2.3 Estimation from a W +jets Control Region with a Muon

A $W^\pm(\rightarrow \mu^\pm\nu)$ +jets control region is defined by requiring exactly one good muon as defined in Sect. 12.3. Events with additional muons of *veto* quality are rejected, as are events with a *veto* electron (c.f. Sect. 12.2). In addition, the transverse mass⁷ m_T is required to be between 40 and 100 GeV. In the calculation of the transverse mass

⁷The transverse mass m_T of a W boson decaying into a charged lepton ℓ and a neutrino ν is calculated as $m_T = \sqrt{2p_T^\ell p_T^\nu (1 - \cos \Delta\phi(\ell, \nu))}$, using the two transverse momenta of the decay products as well as the angle between them.

Table 14.6 Relative uncertainties (in %) from different sources on the estimate of $Z(\rightarrow \nu\bar{\nu})+\text{jets}$ from the $Z(\rightarrow e^+e^-)+\text{jets}$ control regions

$Z(\rightarrow \nu\bar{\nu})$ from $Z(\rightarrow e^+e^-)$	SR1	SR2	SR3	SR4	SR5	SR6	SR7	SR8
Data Stat (%)	0.8	1.2	1.9	2.8	4.1	5.6	11.5	17.2
MC Stat (%)	0.5	0.8	1.1	1.3	1.9	2.4	2.5	3.7
JES (%)	0.4	0.4	0.2	0.4	0.5	0.4	0.9	1.2
JER (%)	0.1	0.3	0.1	0.3	0.8	0.5	0.5	0.8
E_T^{miss} (%)	0.1	0.0	0.0	0.1	0.1	0.1	0.2	0.1
CR bkg. (%)	1.0	1.2	1.5	1.7	2.1	2.3	4.2	6.2
Muon (%)	0.0	0.0	0.0	0.1	0.1	0.1	0.1	0.1
Electron (%)	1.9	2.0	2.0	2.1	2.1	2.1	2.1	2.1
Track veto (%)	0.6	0.6	0.6	0.6	0.6	0.6	0.6	0.6
Theory (%)	0.9	0.9	0.9	0.9	0.8	0.8	0.8	0.8

Table 14.7 Event yields for data and simulated processes in the lowest $W^\pm(\rightarrow \mu^\pm\bar{\nu})+\text{jets}$ control region. The numbers in parenthesis are the fractions of the total number of simulated events

$E_T^{\text{miss}} > 150 \text{ GeV}$	
$W^\pm(\rightarrow \mu^\pm\bar{\nu})+\text{jets}$	130438.7 (84.8%)
$W^\pm(\rightarrow \tau^\pm\bar{\nu})+\text{jets}$	7313.96 (4.8%)
$t\bar{t}$	7435.24 (4.8%)
Diboson	4165.15 (2.7%)
$Z(\rightarrow \mu^+\mu^-)+\text{jets}$	2176.72 (1.4%)
Single Top	1952.35 (1.3%)
$Z(\rightarrow \tau^+\tau^-)+\text{jets}$	249.99 (0.2%)
$Z(\rightarrow \nu\bar{\nu})+\text{jets}$	2.73 (<0.1%)
$W^\pm(\rightarrow e^\pm\bar{\nu})+\text{jets}$	0.62 (<0.1%)
Total simulation	153735.46
Data	141531
Ratio	0.92

the full detector missing E_T is used, i.e. it includes the muon information, such that it corresponds to the neutrino p_T . All other selection criteria are the same as in the signal region, see Sect. 13.3. In particular, the calorimeter based E_T^{miss} is used, such that, as in the $Z(\rightarrow \mu^+\mu^-)+\text{jets}$ control region, both in the control as well as in the signal region, the missing E_T corresponds to the boson p_T (cf. Sect. 12.4) and the same E_T^{miss} trigger and the JetTauEtmiss data stream can be used.

Table 14.7 gives an overview of the composition in the lowest $W^\pm(\rightarrow \mu^\pm\bar{\nu})+\text{jets}$ control region. The purity is considerably lower than in the very clean di-lepton control regions: About 85% of the simulation events is $W^\pm(\rightarrow \mu^\pm\bar{\nu})+\text{jets}$, the largest background contamination stems from $W^\pm(\rightarrow \tau^\pm\bar{\nu})+\text{jets}$ and $t\bar{t}$ events, with about

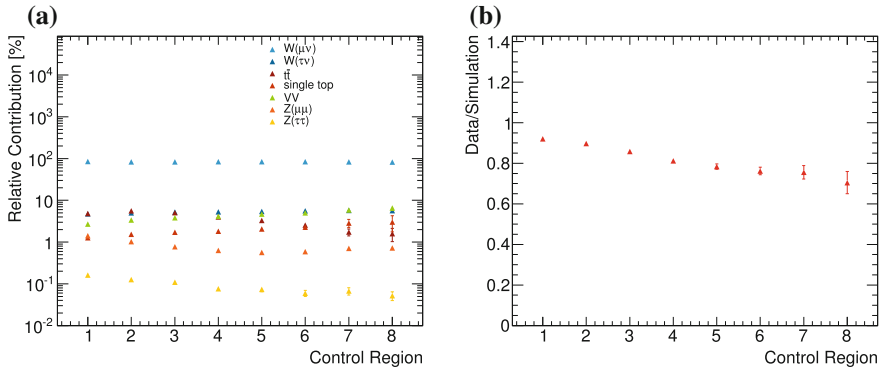


Fig. 14.24 Relative simulation fractions (a) and ratio of data versus simulation (b) in the $W^\pm(\rightarrow \mu^\pm \bar{\nu})+\text{jets}$ control regions. The error bars show statistical uncertainties only

5% each. Diboson, single top and $Z(\rightarrow \mu^+ \mu^-)+\text{jets}$ backgrounds amount to 1-3%, the remaining contributions from Z and W processes are at the sub-percent level. From Fig. 14.24a it can be seen that the fractions of $W^\pm(\rightarrow \mu^\pm \bar{\nu})+\text{jets}$ and $W^\pm(\rightarrow \tau^\pm \bar{\nu})+\text{jets}$ events stay constant when increasing the E_T^{miss} cut, while the other background contaminations vary slightly: While $t\bar{t}$ and $Z(\rightarrow \tau^+ \tau^-)+\text{jets}$ decrease, the contribution of single top and diboson processes grows, leaving the overall level of background contamination unchanged.

The ratio of data to simulation is 0.92 for a cut of $E_T^{\text{miss}} > 150 \text{ GeV}$ (see Table 14.7) and Fig. 14.24b shows how this ratio evolves with increasing E_T^{miss} cut: It decreases from 0.92 to roughly 0.7 at $E_T^{\text{miss}} > 600 \text{ GeV}$, exhibiting a very similar behaviour as was observed in the $Z(\rightarrow \mu^+ \mu^-)+\text{jets}$ CR. However, already from comparing Figs. 14.24b and 14.2b it is apparent that the W control region provides much smaller statistical errors, which is the main reason for using $W^\pm(\rightarrow \ell^\pm \bar{\nu})+\text{jets}$ events to estimate $Z(\rightarrow \nu \bar{\nu})+\text{jets}$.

As before, the control region specific cut variables have to be well modelled by the simulation. Figure 14.25 shows the muon charge, p_T , η and ϕ distributions for data and simulation. Apart from the normalisation difference which is compensated for in the plots by scaling the simulation to the number of entries in data, the η and ϕ distributions agree well between data and simulation, the ratio is flat over the complete acceptance in those variables. The η distributions features the again a dip at 0 due to the service gaps as was explained for the $Z(\rightarrow \mu^+ \mu^-)+\text{jets}$ control region already (see Fig. 14.3a).

The lepton charge distribution is modelled very well by the simulation. The asymmetry between positive and negative charge is expected: The charge of the decay lepton corresponds to the charge of the original boson, and at a pp -collider, the cross section for W^+ production is larger, since this requires (for example) a u - and a \bar{d} -quark, and there are two valence u -quarks in a proton. To produce a W^- , on the other hand, a d -quark is required (in addition to the sea \bar{u} -quark), of which there is only one in the valence quark content of the proton.

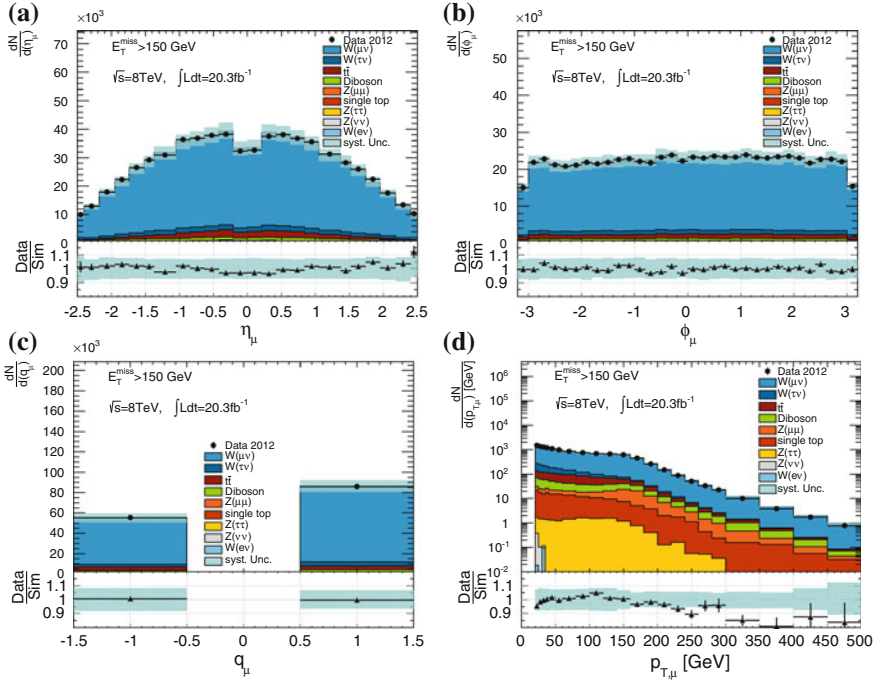


Fig. 14.25 Muon kinematic variables in the lowest $W^\pm(\rightarrow \mu^\pm\nu)$ +jets control region. **a** Pseudo-rapidity. **b** Azimuthal angle. **c** Charge. **d** Transverse momentum

The muon transverse momentum (Fig. 14.25d) exhibits a similar shape as the sub-leading muon p_T distribution in Fig. 14.5a, with the difference that the shoulder in this case is at roughly 150 GeV, i.e. the boson p_T , instead of half the boson p_T (by definition) in the case of the sub-leading muon in $Z(\rightarrow \mu^+\mu^-)+\text{jets}$ events. The data-to-simulation ratio shows deviations from a flat shape, but with the exception of a few bins, the ratio of data and simulation is within 5% around the central value in the bulk of the distribution, showing a falling trend in the tail. This affects, however, only a small fraction of events and can be tolerated. Up to about 300 GeV the deviations are within the total uncertainties.

Figure 14.26 illustrates—similar to Fig. 14.6 for the sub-leading muon in $Z(\rightarrow \mu^+\mu^-)+\text{jets}$ events—how the muon p_T is softly bounded from above by the E_T^{miss} cut: The shoulder is shifted when increasing the E_T^{miss} cut in the control region and beyond that value the spectrum falls steeply. In most of the cases, the muon has a p_T below 100 GeV, indicating that the neutrino typically carries most of the boson momentum.

Figure 14.27a shows the azimuthal separation between the muon and the calorimeter E_T^{miss} (boson p_T). As is to be expected for a boosted topology, the muon direction is typically aligned with the boson p_T . The transverse mass distribution is shown in Fig. 14.27b. The peak around the W -mass at about 80 GeV is clearly visible. The

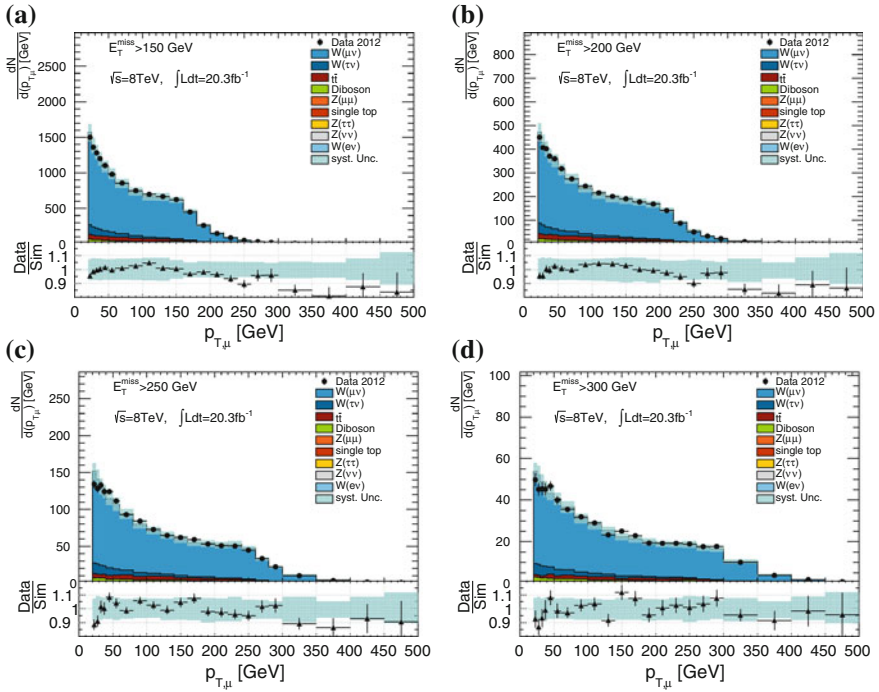


Fig. 14.26 Muon p_T in $W^\pm(\rightarrow \mu^\pm\nu)+\text{jets}$ control regions with different E_T^{miss} cuts. **a** $E_T^{\text{miss,calo}} > 150 \text{ GeV}$. **b** $E_T^{\text{miss,calo}} > 200 \text{ GeV}$. **c** $E_T^{\text{miss,calo}} > 250 \text{ GeV}$. **d** $E_T^{\text{miss,calo}} > 300 \text{ GeV}$

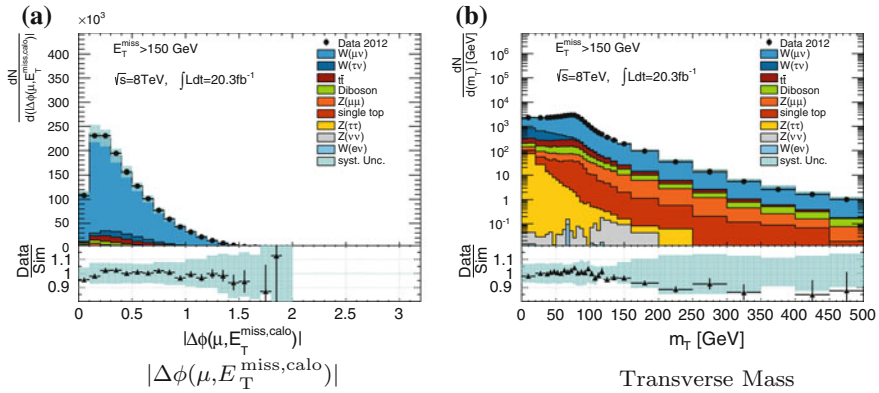


Fig. 14.27 Azimuthal separation of muon and E_T^{miss} **(a)** and transverse mass distribution **(b)** in the lowest $W^\pm(\rightarrow \mu^\pm\nu)+\text{jets}$ control region

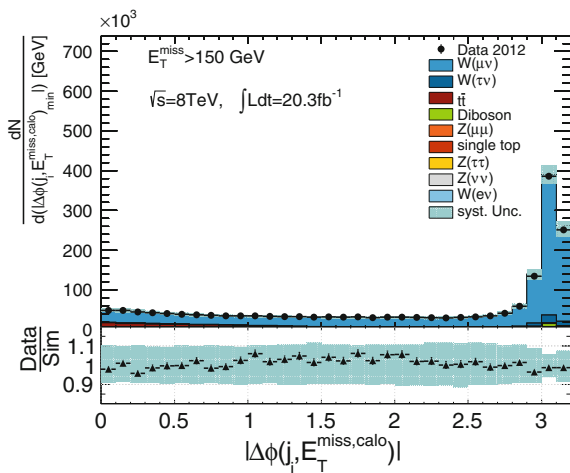
ratio is approximately flat in the window around that peak (between 40 and 100 GeV), which is the range considered in order to increase the purity of the control region. As can be seen from the plot this cut removes a large fraction of $W^\pm(\rightarrow \tau^\pm\nu)$ +jets events, which are the largest background. $Z(\rightarrow \tau^+\tau^-)+\text{jets}$ events are also removed efficiently. Moreover, QCD multi-jet events would—if at all—appear at small values of m_T and would be suppressed by this cut. The ratio does, however, not show an upwards trend at low m_T , which would indicate the presence of multi-jet background which are not included in the simulation in the plot. This indicates that the control region selection even before the cut on m_T provides good QCD suppression. This is partly because of the isolation requirement for the muons which reduces contributions from QCD jets with heavy flavour decays.

The plot in Fig. 14.28a compares the minimal azimuthal distance of the calorimeter E_T^{miss} to any jet in the event for data and simulation before the cut at 1.0. As is to be expected for the mono-jet topology, the distribution has a large maximum at values close to π , i.e. jet and E_T^{miss} are back-to-back. The flat ratio indicates again that there is no significant contamination from multi-jet events which would be visible as an excess in data at low values of $|\Delta\phi_{\text{min}}(\text{jet}_i, E_T^{\text{miss}})|$. It can also be seen that cutting at a value of 1.0 removes a large fraction of the top backgrounds.

In Fig. 14.29a the calorimeter based missing E_T is presented. The ratio of the data and the sum of simulations is flat up to about 300 GeV and starts falling beyond that. This explains the falling trend observed in the ratio of data to simulation for the different control regions in Fig. 14.24b. The deviation is beyond what is covered by the combined systematic (light blue band) and statistical (error bars) uncertainties. However, this mis-modelling of the E_T^{miss} distribution in the tail will be corrected for by the bin-by-bin application of the transfer factor method.

Figure 14.29b shows the boson p_T as reconstructed from the muon and the full-detector missing E_T (i.e. the neutrino p_T). The comparison with Fig. 14.29a shows

Fig. 14.28 $|\Delta\phi_{\text{min}}(\text{jet}_i, E_T^{\text{miss}})|$ in the lowest $W^\pm(\rightarrow \mu^\pm\nu)+\text{jets}$ control region



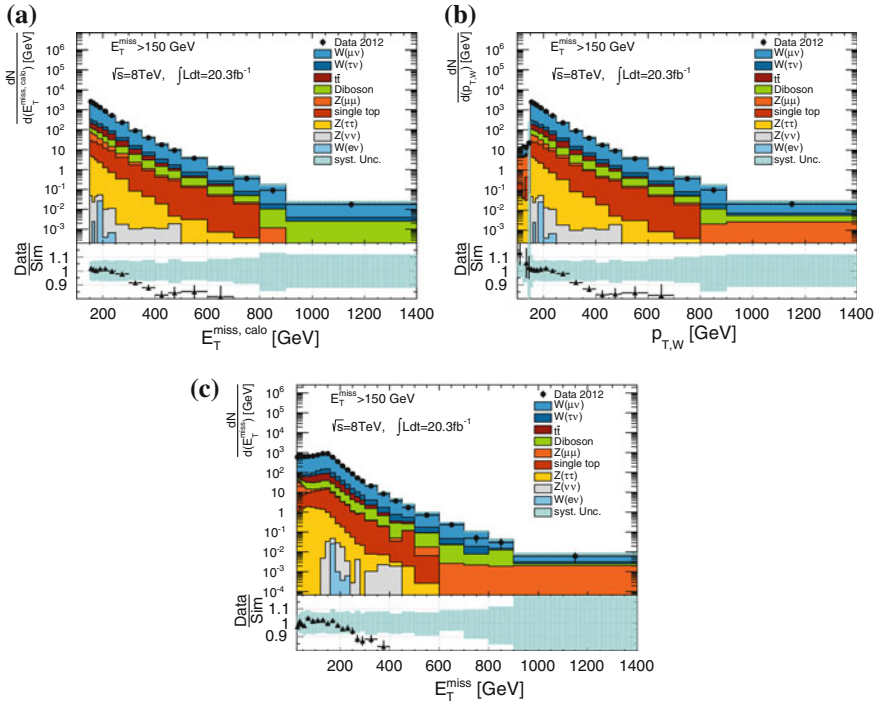


Fig. 14.29 Calorimeter based E_T^{miss} (a), boson- p_T (b) and full-detector E_T^{miss} (c) in the lowest $W^\pm(\rightarrow \mu^\pm\nu)$ +jets control region

that the calorimeter based missing E_T gives a very good approximation of the boson p_T spectrum. The neutrino p_T , taken as the E_T^{miss} including the muon information, is presented in Fig. 14.29c. Here as well, the simulation does not describe the tail very well, at lower values of E_T^{miss} the ratio is essentially flat. This neutrino p_T spectrum has a similar behaviour as the leading muon p_T in the $Z(\rightarrow \mu^+\mu^-)$ +jets CR: It can be seen that the distribution has a maximum roughly at the value of the cut on the boson p_T , indicating that on average the neutrino has higher transverse momentum than the decay muon.

The distributions for leading and sub-leading jets exhibit the same features as described for the $Z(\rightarrow \mu^+\mu^-)$ +jets CR. Thus, the discussion shall not be repeated here. Moreover, discrepancies there are protected by the transfer factor method.

In Fig. 14.30a the jet multiplicity in the control region can be seen. Most of the events have 1 or 2 jets, but close to 20% have higher jet multiplicities and in these events the top contribution amounts to approximately 30%. In total, including the higher jet multiplicities yields a top contamination ($t\bar{t}$ and single top) of roughly 6% in the control region, as is seen in Table 14.7, which makes the top processes the dominating background. The direct subtraction of this background from data (c.f. Eq. 10.2) relies on the correct normalisation of the simulation. It was thus decided

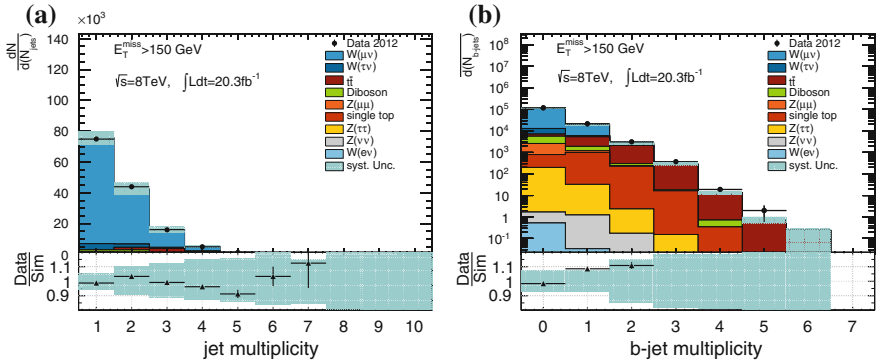


Fig. 14.30 Jet multiplicities in the lowest $W^\pm(\rightarrow \mu^\pm\bar{\nu})+\text{jets}$ control region. **a** Jet multiplicity. **b** b-jet multiplicity

to assess the normalisation uncertainty from a dedicated control region.⁸ In order to estimate this systematic uncertainty, in the mono-jet analysis [8] a control region was defined by requiring a b-tagged jet in order to enhance the top fraction, as outlined in Sect. 14.1.8. The b-tagged jet multiplicity is shown in Fig. 14.30b. In the 2-bjet bin and above, the events are almost all $t\bar{t}$ events, as is to be expected, the 1-bjet bin is still dominated by other processes but provides more statistics. For the definition of the top control region in [8], in addition the cut on $|\Delta\phi_{\min}(\text{jet}_i, E_T^{\text{miss}})|$ was softened to 0.5 and the cut on the ratio of leading jet p_T and E_T^{miss} was removed, as this also suppresses the top background. The uncertainties obtained in [8] are summarised in Sect. 14.1.8.

Figure 14.31 shows the acceptance (Fig. 14.31a) of the cuts specific to the control region selection, i.e. the muon p_T and η cuts as well as the transverse mass cut, estimated from the $W^\pm(\rightarrow \mu^\pm\bar{\nu})+\text{jets}$ simulation (c.f. Eq. 10.3), as a function of the calorimeter missing E_T^{miss} . The acceptance is close to 50% over the complete E_T^{miss} range. At E_T^{miss} of about up to 200 GeV, it is roughly 48%, then increasing up to 300 GeV and remaining flat within the statistical uncertainties. The slight increase in the beginning can be explained by the fact that with higher (calorimeter) E_T^{miss} , the boson p_T increases and thus also the muon p_T on average increases and the muon becomes more central. Hence, the cuts on muon p_T and η remove slightly less events.

Figure 14.31b shows the ratio of $W^\pm(\rightarrow \mu^\pm\bar{\nu})+\text{jets}$ events over the sum of all W and Z processes in the control region as a function of E_T^{miss} (c.f. Eq. 10.1). This ratio is flat at about 92%, i.e. the residual background contamination after the subtraction of top and diboson processes is of the order of 8% over the full E_T^{miss} range. This indicates that the shape of the E_T^{miss} spectrum is the same for all the W and Z processes, justifying the usage of this ratio to correct for the W and Z contamination in the control region, as done in Eq. 10.1.

⁸In previous versions of the mono-jet analysis, a conservative uncertainty of 20% was assumed, but there the veto on a third jet reduced the top contamination to 1–2%.

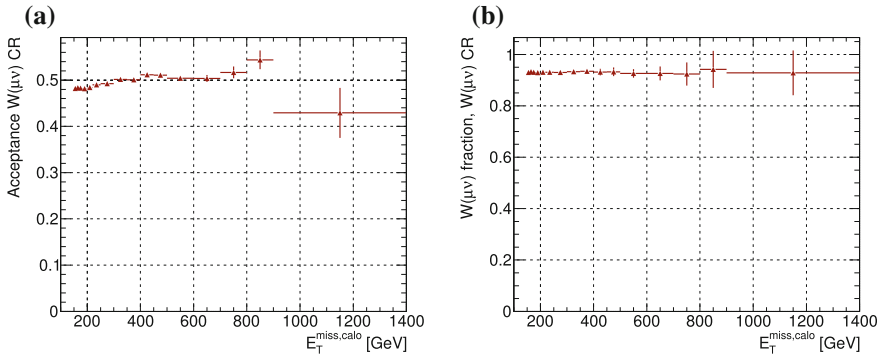


Fig. 14.31 Acceptance and purity in the $W^\pm(\rightarrow \mu^\pm \bar{\nu}) + \text{jets}$ control regions as a function of E_T^{miss} . The error bars are statistical uncertainties only. **a** Acceptance. **b** Purity

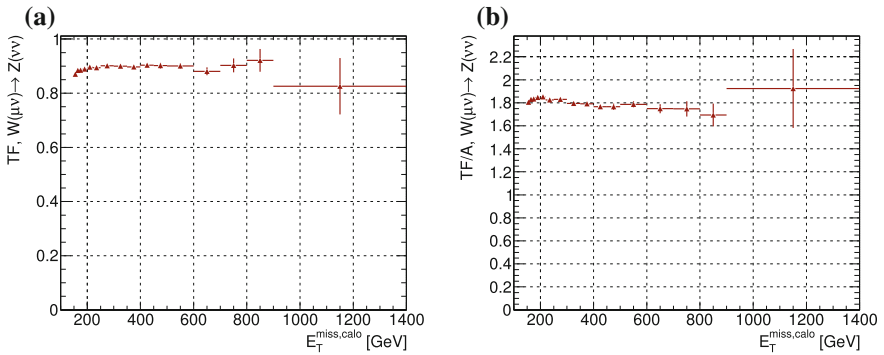


Fig. 14.32 Transfer factors before and after applying the lepton selection in the $W^\pm(\rightarrow \mu^\pm \bar{\nu}) + \text{jets}$ control region. **a** Transfer factor. **b** Transfer factor with acceptance

The transfer factor is shown in Fig. 14.32a. It can be seen that the TF for the estimation of $Z(\rightarrow \nu\bar{\nu}) + \text{jets}$ in the signal region is flat within statistical uncertainties to a very good approximation, only the first bins from 150 to 200 GeV deviate to slightly smaller values. This gives confidence that the emulation of the $Z(\rightarrow \nu\bar{\nu}) + \text{jets}$ process from $W^\pm(\rightarrow \mu^\pm \bar{\nu}) + \text{jets}$ events works well. Figure 14.32b displays the ratio of signal region process over control region process after the full control region selection, i.e. the transfer factor divided by the acceptance of the CR cuts. Given the mostly flat acceptance (c.f. Fig. 14.31a), these distribution shows essentially the same features as discussed for Fig. 14.32a.

In Table 14.8 the relative uncertainties on the $Z(\rightarrow \nu\bar{\nu}) + \text{jets}$ estimate are summarised. Again statistical uncertainties become significant with increasing missing E_T cut. However, the uncertainty due to the data statistic in the control region is considerably smaller than for the $Z(\rightarrow \ell^+ \ell^-) + \text{jets}$ control regions, motivating the use of $W^\pm(\rightarrow \ell^\pm \bar{\nu}) + \text{jets}$ control regions also for the estimation of $Z(\rightarrow \nu\bar{\nu}) + \text{jets}$.

Table 14.8 Relative uncertainties (in %) from different sources on the estimate of $Z(\rightarrow \nu\bar{\nu})$ +jets from the $W^\pm(\rightarrow \mu^\pm\bar{\nu})$ +jets control regions

$Z(\rightarrow \nu\bar{\nu})$ from $W^\pm(\rightarrow \mu^\pm\bar{\nu})$	SR1	SR2	SR3	SR4	SR5	SR6	SR7	SR8
Data Stat (%)	0.3	0.5	0.8	1.3	1.9	2.7	5.0	9.1
MC Stat (%)	0.3	0.5	0.6	0.7	0.9	1.3	2.2	4.1
JES (%)	1.4	1.9	2.0	1.6	2.5	1.7	1.0	3.9
JER (%)	0.4	0.3	0.3	0.1	0.4	0.6	0.1	2.1
E_T^{miss} (%)	0.8	0.6	0.5	0.5	0.5	0.6	0.7	0.6
CR bkg. (%)	2.0	2.6	3.1	3.7	5.8	6.3	9.9	11.6
Muon (%)	0.5	0.5	0.5	0.6	0.7	0.7	0.7	0.8
Electron (%)	0.1	0.1	0.1	0.1	0.4	0.2	0.1	0.1
Track veto (%)	0.6	0.6	0.6	0.6	0.7	0.7	0.7	0.7
Theory (%)	1.3	1.3	1.3	1.3	2.2	2.2	3.2	5.1

The theoretical uncertainties in this case are larger than for the estimation from $Z(\rightarrow \ell^+\ell^-)$ +jets control regions due to the additional uncertainty from the electroweak corrections on the ratio of W and Z cross sections. The other theoretical uncertainties are again at the per-mille level. The dominating uncertainty for all regions is the subtraction of top and diboson in the control region, which is larger than for the $Z(\rightarrow \ell^+\ell^-)$ +jets due to the larger contamination from these processes.

14.2.4 Estimation from a W +jets Control Region with an Electron

Similar as in the muon channel, a control region with W -bosons decaying to an electron and a neutrino can be used to estimate $Z(\rightarrow \nu\bar{\nu})$ +jets in the signal region. This control region will be referred to as $W^\pm(\rightarrow e^\pm\bar{\nu})$ +jets control region A. As in the $Z(\rightarrow e^+e^-)$ +jets control region, the electron is treated as missing transverse energy, i.e. it is removed from the missing E_T calculation, such that the corrected missing E_T again corresponds to the boson p_T , as does the E_T^{miss} in the signal region for $Z(\rightarrow \nu\bar{\nu})$ +jets, (cf. Sect. 12.4).

Special care has to be taken with regard to the multi-jet background in this case: When a high p_T jet is misidentified as an electron and this electron is then treated as E_T^{miss} , the event will enter the control region. To prevent this from happening, the tighter selection criteria listed in Sect. 12.2 are applied for the good electron and additional cuts are applied: The transverse mass reconstructed from the electron and the uncorrected E_T^{miss} has to be within the range of 40–100 GeV and the uncorrected E_T^{miss} (i.e. the neutrino p_T) has to be greater than 25 GeV. In order to have enough statistics, events selected with either of the two single electron triggers also used in the $Z(\rightarrow e^+e^-)$ +jets CR are used.

The residual QCD multi-jet contamination in this $W^\pm(\rightarrow e^\pm\bar{\nu})+\text{jets}$ CR is estimated from data via a matrix method. Let N_{tight} be the number of events in the actual control region, which is composed of events with real electrons, N_{real} , and events with jets faking electrons, N_{fake} :

$$N_{tight} = N_{real} + N_{fake} \quad (14.1)$$

The unknown N_{real} can be eliminated by defining a second region with looser cuts, with an event number N_{Loose} and the corresponding numbers of real and fake electrons, N_{real}^{Loose} and N_{fake}^{Loose} :

$$N_{Loose} = N_{real}^{Loose} + N_{fake}^{Loose} \quad (14.2)$$

To select these events, the same cut as for the actual control region are applied, except for the electron isolation cuts and the *tight* electron quality, instead, *medium* quality electrons are required. Defining ε_{real} as the efficiency of a real electron in the looser region to also pass the tighter requirements, and ε_{fake} the corresponding efficiency for a fake electron, yields $N_{fake} = \varepsilon_{fake} \cdot N_{fake}^{Loose}$ and $N_{real} = \varepsilon_{real} \cdot N_{real}^{Loose}$. This results in the following set of equations:

$$\begin{pmatrix} N_{tight} \\ N_{Loose} \end{pmatrix} = \begin{pmatrix} 1 & 1 \\ 1/\varepsilon_{real} & 1/\varepsilon_{fake} \end{pmatrix} \begin{pmatrix} N_{real} \\ N_{fake} \end{pmatrix}. \quad (14.3)$$

Solving for N_{fake} yields

$$N_{fake} = \varepsilon_{fake} \cdot \frac{\varepsilon_{real} N_{Loose} - N_{tight}}{\varepsilon_{real} - \varepsilon_{fake}}. \quad (14.4)$$

The efficiency for real electrons is estimated from the simulation of $W^\pm(\rightarrow e^\pm\bar{\nu})+\text{jets}$ events as the ratio of events passing the tighter criteria and those passing the loose criteria. The scale factors for reconstruction, trigger and identification efficiencies as provided by the performance group are applied to match the efficiency in data. The efficiency is found to be $\varepsilon_{real} = 0.871 \pm 0.004(\text{stat})$.

For the estimation of ε_{fake} , a QCD enriched control region is defined by inverting the cut on the neutrino p_T and requiring $m_T < 40 \text{ GeV}$. Contributions from other processes are taken from simulation and subtracted from the data. This yields an efficiency $\varepsilon_{fake} = 0.0161 \pm 0.0006(\text{stat})$. Again, this efficiency is calculated as the number of electrons passing the tighter cuts divided by the number of those that pass the looser cuts. The numbers obtained for the different E_T^{miss} cuts are listed in Table 14.9. As in [8], an uncertainty of 100 %. Within these uncertainties the numbers found in this work are compatible with those obtained in Ref. [8].

It should be pointed out that in the distributions shown for the $W^\pm(\rightarrow e^\pm\bar{\nu})+\text{jets}$ CRA, the QCD contamination is not considered since there are no simulation samples with sufficient statistics available. However, the contribution is at the level of 1 % and the impact of neglecting it in the plots is thus assumed to be marginal.

Table 14.9 Estimate of multi-jet contamination in $W^\pm(\rightarrow e^\pm\bar{\nu})+\text{jets}$ control regions A

	Multi-jet events in $W^\pm(\rightarrow e^\pm\bar{\nu})+\text{jets}$ CRA
CR1	904 ± 13 (0.9%)
CR2	338 ± 7 (0.8%)
CR3	146 ± 4 (0.9%)
CR4	70 ± 3 (0.9%)
CR5	36 ± 2 (1%)
CR6	19 ± 1 (1.1%)
CR7	6 ± 0.7 (1.2%)
CR8	2 ± 0.4 (1.3%)

Table 14.10 lists the contributions of the various simulated processes to the $W^\pm(\rightarrow e^\pm\bar{\nu})+\text{jets}$ CRA. The fraction of control region process events is about 84%, comparable to that of the $W^\pm(\rightarrow \mu^\pm\bar{\nu})+\text{jets}$ control region (c.f. Table 14.7). $W^\pm(\rightarrow \tau^\pm\bar{\nu})+\text{jets}$ and $t\bar{t}$ events make up 4.3 and 5.2%, respectively. The diboson contribution is 2.7%, single top and $\gamma+\text{jets}$ both amount to 1.4%. All other contributions are at the sub-percent level. The ratio of data to simulation is 0.94, similar to what was observed for the other control regions. Again, this will be applied as a scale factor to the simulation in the shape comparison plots.

Figure 14.33a demonstrates that the $W^\pm(\rightarrow e^\pm\bar{\nu})+\text{jets}$ fraction is stable over all control regions. The diboson and single top contributions increase towards higher E_T^{miss} , while the other processes show a falling tendency. The ratio of data (including QCD multi-jet) to simulation for all the $W^\pm(\rightarrow e^\pm\bar{\nu})+\text{jets}$ control regions is shown in Fig. 14.33b. Similarly to what was observed in the $W^\pm(\rightarrow \mu^\pm\bar{\nu})+\text{jets}$ control regions, it falls from 0.94 to about 0.75.

The properties of the selected electron are displayed in Fig. 14.34. The η - and ϕ -distributions are very similar to the ones observed in the $Z(\rightarrow e^+e^-)+\text{jets}$ control region, see Fig. 14.18a, b. The removal of the transition region in $1.37 < |\eta| < 1.52$ is clearly visible, the ϕ distribution is approximately flat. The description of the data by the simulation is very good in both distributions within the uncertainties. The charge distribution shows the same asymmetry as discussed in the $W^\pm(\rightarrow \mu^\pm\bar{\nu})+\text{jets}$ control region (Fig. 14.25c) and is reproduced very well by the simulation. The electron p_T spectrum is very similar to what is observed for the muon in the $W^\pm(\rightarrow \mu^\pm\bar{\nu})+\text{jets}$ CR (Fig. 14.25d) or the sub-leading leptons in the $Z(\rightarrow \ell^+\ell^-)+\text{jets}$ CRs: It falls steeply beyond 150 GeV due to the cut on the boson p_T . The description by the simulation is very good, except for the tail beyond 300 GeV.

In Fig. 14.35a, the transverse mass of the W -boson, reconstructed from the uncorrected E_T^{miss} is shown. While the region around the peak which is considered for this control region is very well described, the deviations in the tail are large. The angle between corrected missing E_T and electron is presented in Fig. 14.35b. Similar to what is observed in the $W^\pm(\rightarrow \mu^\pm\bar{\nu})+\text{jets}$ CR (Fig. 14.27a), the electron typically points in the direction of the boson p_T . The shape is reproduced well by the simulation.

Table 14.10 Event yields for data and simulated processes in the lowest $W^\pm(\rightarrow e^\pm\bar{\nu})$ +jets control region A. The numbers in parenthesis are the fractions of the total number of simulated events

$E_T^{\text{miss}} > 150 \text{ GeV}$	
$W^\pm(\rightarrow e^\pm\bar{\nu})$ +jets	92029.6 (84.3)
$t\bar{t}$	5702.0 (5.2)
$W^\pm(\rightarrow \tau^\pm\bar{\nu})$ +jets	4677.4 (4.3)
Diboson	2943.5 (2.7)
Single top	1523.9 (1.4)
γ +jets	1493.0 (1.4)
$Z(\rightarrow e^+e^-)$ +jets	653.6 (0.6)
$Z(\rightarrow \tau^+\tau^-)$ +jets	198.2 (0.2)
$W^\pm(\rightarrow \mu^\pm\bar{\nu})$ +jets	10.5 (<0.1)
$Z(\rightarrow \mu^+\mu^-)$ +jets	0.3 (<0.1)
$Z(\rightarrow \nu\bar{\nu})$ +jets	0.2 (<0.1)
Total simulation	109232.6
Data	102901
Ratio	0.94

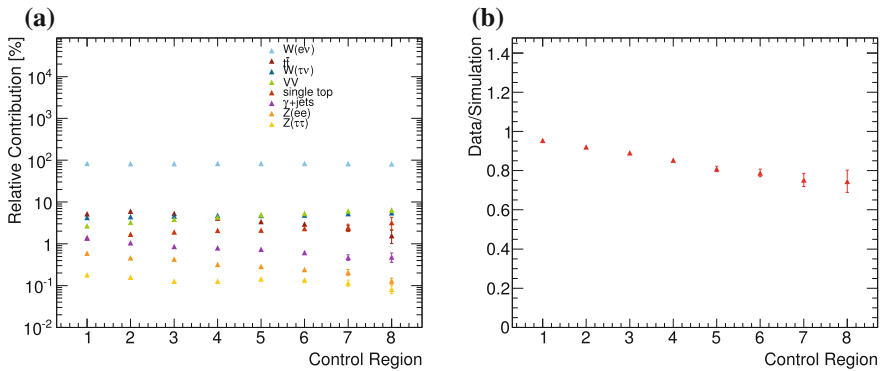


Fig. 14.33 Relative simulation fractions (a) and ratio of data versus simulation (b) in the $W^\pm(\rightarrow e^\pm\bar{\nu})$ +jets control regions A. The error bars show statistical uncertainties only

Figure 14.36a shows the E_T^{miss} distribution with the electron included. The shape is very similar to the full-detector missing E_T in the $W^\pm(\rightarrow \mu^\pm\bar{\nu})$ +jets CR (Fig. 14.29c), as expected. The description by the simulation is good up to 200 GeV, beyond that it drops below 1. Up to 400 GeV this is still within the total uncertainty, the remaining tail contains only very few events. The corrected E_T^{miss} is shown in Fig. 14.36b. Discrepancies between data and simulation—which are not covered by the uncertainties above 350 GeV—explain the trend in Fig. 14.33b and will be corrected by the transfer factors. Since the same holds for the jet distributions and they show no unexpected features, a detailed discussion is omitted here.

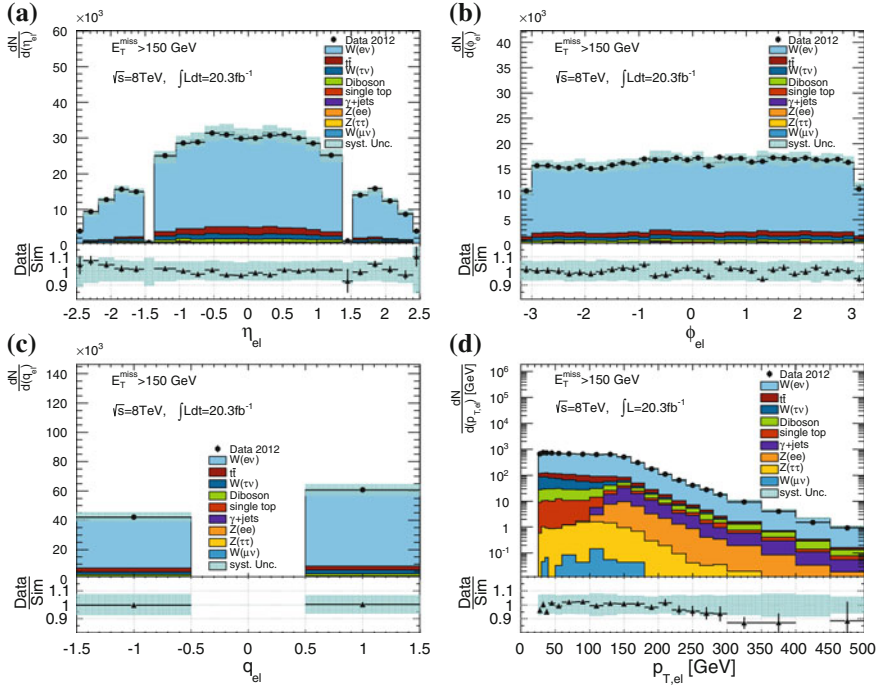


Fig. 14.34 Electron variables in the lowest $W^\pm(\rightarrow e^\pm\bar{\nu})$ +jets control region A **a** Pseudo-rapidity. **b** Azimuthal angle. **c** Charge. **d** Transverse momentum

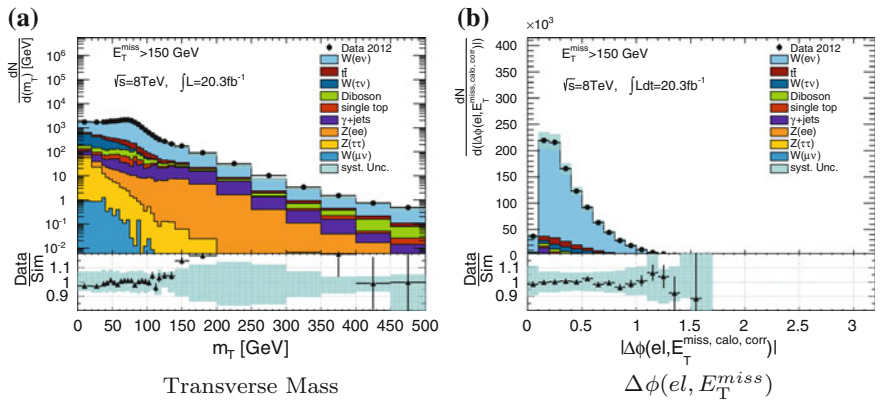


Fig. 14.35 Transverse mass (a) and azimuthal separation of electron and E_T^{miss} (b) in the lowest $W^\pm(\rightarrow e^\pm\bar{\nu})$ +jets control region A

For the jet multiplicity presented in Fig. 14.37a, agreement within the uncertainties is found for multiplicities up to 9. Most of the events, however, have 3 or less jets, in accordance with the mono-jet like topology. The $|\Delta\phi_{\min}(\text{jet}_i, E_T^{\text{miss}})|$ distribution

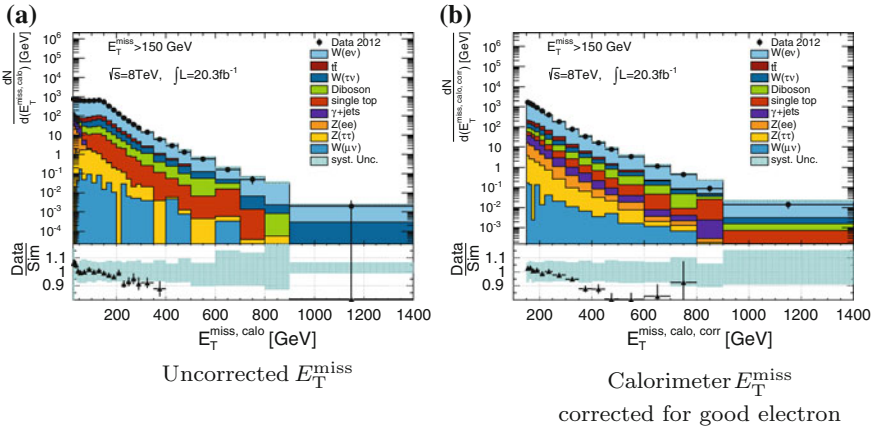


Fig. 14.36 Calorimeter based E_T^{miss} before (a) and after (b) the electron is removed in the lowest $W^\pm(\rightarrow e^\pm\nu)+\text{jets}$ control region A

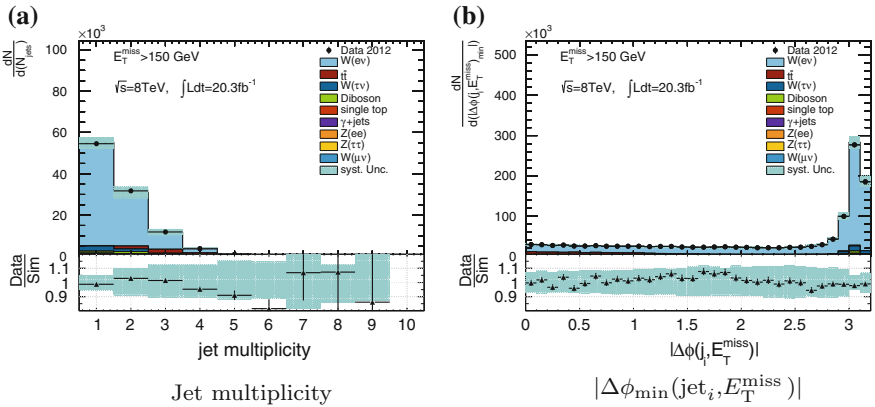


Fig. 14.37 Jet multiplicity (a) and minimum azimuthal separation of calorimeter E_T^{miss} and any jet (b) in the lowest $W^\pm(\rightarrow e^\pm\nu)+\text{jets}$ control region A

(before the cut) in Fig. 14.37b shows a clear peak at $\sim\pi$ and no excess in data at small values, indicating that there is no significant contamination from mis-measured multi-jet events. As for the $W^\pm(\rightarrow \mu^\pm\nu)+\text{jets}$ CR, the top background is reduced by the cut at 1.0. The ratio is flat within uncertainties over the entire region.

The acceptance of the control region cuts in the $W^\pm(\rightarrow e^\pm\nu)+\text{jets}$ region A is at the level of 52 %, as can be seen from Fig. 14.38a. The fraction of $W^\pm(\rightarrow e^\pm\nu)+\text{jets}$ events out of all W and Z events in the control region is also flat as a function of missing E_T and at the level of 94 %. The shape of the corrected E_T^{miss} is thus not altered by the residual background contaminations.

The transfer factor obtained for the estimation of $Z(\rightarrow \nu\bar{\nu})+\text{jets}$ from $W^\pm(\rightarrow e^\pm\nu)+\text{jets}$, Fig. 14.39, reveals differences in the E_T^{miss} shapes for

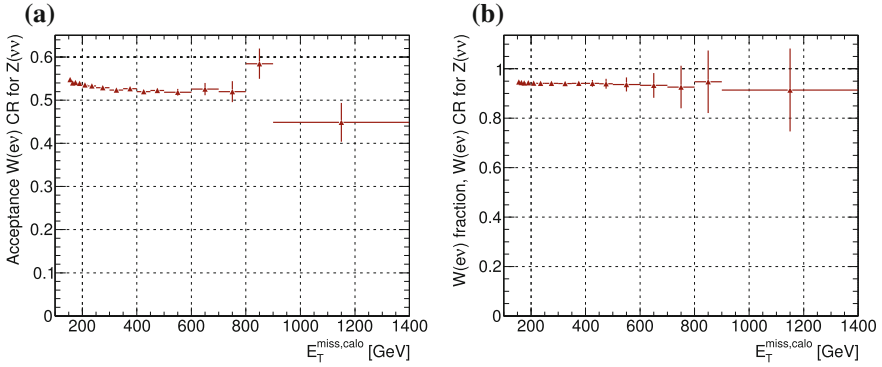


Fig. 14.38 Acceptance and purity in the $W^\pm(\rightarrow e^\pm\bar{\nu})+\text{jets}$ control regions A as a function of E_T^{miss} . The error bars are statistical uncertainties only. **a** Acceptance. **b** Purity

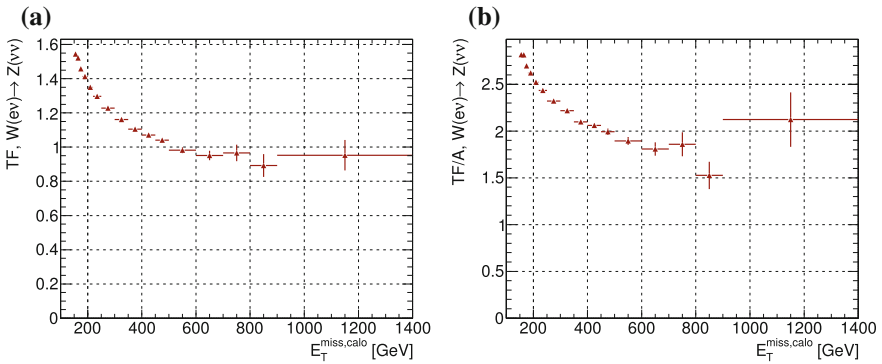


Fig. 14.39 Transfer factors before and after applying the lepton selection in the $W^\pm(\rightarrow e^\pm\bar{\nu})+\text{jets}$ control regions A. Error bars are statistical uncertainties only. **a** Transfer factor. **b** Transfer factor with acceptance

$Z(\rightarrow \nu\bar{\nu})+\text{jets}$ in the signal region and $W^\pm(\rightarrow e^\pm\bar{\nu})+\text{jets}$ in the control region. This is to be expected, since in the signal region, the direction of the neutrinos from the Z is arbitrary, while in the $W^\pm(\rightarrow e^\pm\bar{\nu})+\text{jets}$ control region the electron is restricted to the central region. More central decay products typically result in a higher boson p_T , which is why the differences are most striking at low values of E_T^{miss} .

Table 14.11 summarises the uncertainties on the $Z(\rightarrow \nu\bar{\nu})+\text{jets}$ estimate, which are very similar to what is obtained in the $W^\pm(\rightarrow \mu^\pm\bar{\nu})+\text{jets}$ control region. As seen there, the uncertainty from the background subtraction in the CR is the dominant uncertainty. The JES is at the level of 2–3% in all regions, theoretical and statistical uncertainties increase considerably with higher E_T^{miss} and can be as large as 5–9%. As for the estimation from $W^\pm(\rightarrow \mu^\pm\bar{\nu})+\text{jets}$, the theoretical uncertainty is dominated by the electroweak corrections.

Table 14.11 Relative uncertainties (in %) from different sources on the estimate of $Z(\rightarrow \nu\bar{\nu})+\text{jets}$ from the $W^\pm(\rightarrow e^\pm\bar{\nu})+\text{jets}$ control regions A

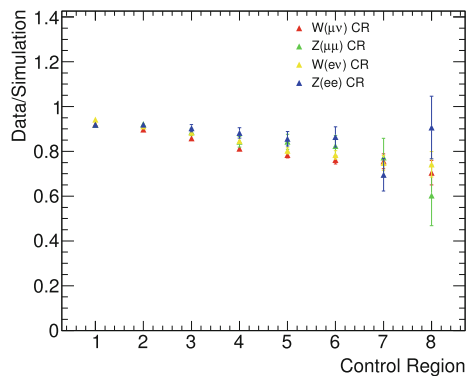
$Z(\rightarrow \nu\bar{\nu})$ from $W^\pm(\rightarrow e^\pm\bar{\nu})$	SR1	SR2	SR3	SR4	SR5	SR6	SR7	SR8
Data Stat (%)	0.4	0.6	0.9	1.4	2.0	2.9	5.2	9.0
MC Stat (%)	0.4	0.5	0.7	0.8	1.1	1.6	3.3	5.9
JES (%)	2.5	2.8	3.0	3.2	3.8	2.3	3.2	3.5
JER (%)	0.1	0.0	0.1	0.2	0.1	0.2	1.1	1.4
E_T^{miss} (%)	0.4	0.4	0.6	0.5	0.8	0.8	1.2	2.3
CR bkg. (%)	2.0	2.7	3.2	3.8	6.1	6.8	10.8	11.1
Muon (%)	0.0	0.0	0.0	0.0	0.1	0.1	0.1	0.1
Electron (%)	1.3	1.4	1.4	1.4	1.4	1.4	1.4	1.8
Track veto (%)	0.6	0.7	0.7	0.7	0.7	0.7	0.7	0.7
Theory (%)	1.3	1.3	1.3	1.3	2.2	2.2	3.2	5.2

14.2.5 Combination of $Z(\rightarrow \nu\bar{\nu})+\text{jets}$ Estimates

The four estimates of the $Z(\rightarrow \nu\bar{\nu})+\text{jets}$ background are combined following the BLUE method as described in Sect. 10.2.2. Figure 14.40 shows a first check of the compatibility of the estimates from the different control regions: The numerator of the transfer factor (c.f. Eq. 10.4) is the same in all cases (the number of simulated $Z(\rightarrow \nu\bar{\nu})+\text{jets}$ events in the signal region), and this number is essentially scaled by the ratio of data (with top and diboson removed) over the sum of W - and Z - backgrounds (c.f. Eq. 10.6), which is what is presented in Fig. 14.40. The uncertainties shown are only statistical.

Figure 14.41 shows the weights that each of the four estimates receives in the eight signal regions (left) and the total uncertainty (statistical and systematic) for each of the single estimates as well as the combined result (right). It is observed that in the lower signal regions, the estimates from Z processes contribute more due to

Fig. 14.40 Data to simulation ratio for all control regions. Error bars are statistical uncertainties only



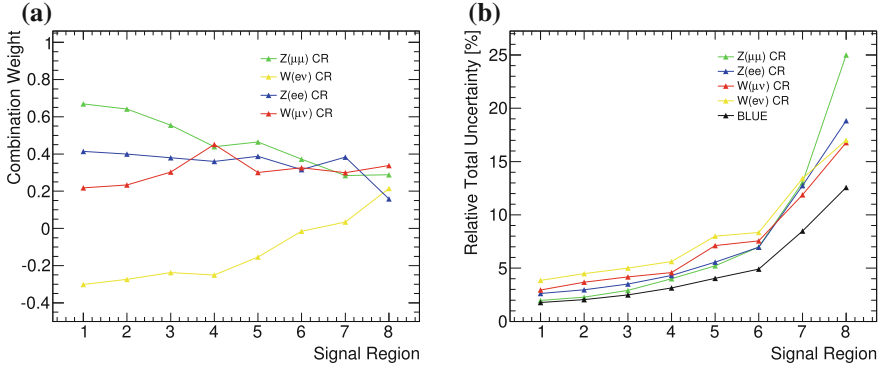


Fig. 14.41 Combination weights (a) and total errors (b) for the four inputs and the combined result

the lower systematic uncertainties. With increasing E_T^{miss} cut, the estimates from W regions become more important as the uncertainties grow more rapidly for the Z regions, as is seen in Fig. 14.41b. The estimate from $W^\pm(\rightarrow e^\pm\nu)$ +jets suffers from larger uncertainties and receives a negative weight up to SR5. Figure 14.41b also shows that the error on the combined estimate is smaller than any of the individual errors, as is to be expected. The gain is particularly large in the higher signal regions where the statistical uncertainties can be decreased considerably by using all four estimates. In the lowest signal regions, the total error on the BLUE result is not much smaller than that for the estimation from $Z(\rightarrow \mu^+\mu^-)$ +jets, which is most important contribution in these regions, as the weights in Fig. 14.41a indicate.

Table 14.12 lists the uncertainties on the combination result, split into different categories. The statistical uncertainties become larger in the higher E_T^{miss} regions, but

Table 14.12 Relative uncertainties (in %) from different sources on the combination result for $Z(\rightarrow \nu\bar{\nu})+\text{jets}$

$Z(\rightarrow \nu\bar{\nu})+\text{jets}$, BLUE combination	SR1	SR2	SR3	SR4	SR5	SR6	SR7	SR8
Data Stat (%)	0.6	0.9	1.3	1.8	2.7	3.1	5.7	7.6
MC Stat (%)	0.4	0.6	0.7	0.9	1.2	1.3	1.5	2.4
JES (%)	0.1	0.2	0.2	0.5	0.6	0.8	1.1	2.8
JER (%)	0.5	0.4	0.3	0.5	0.4	0.4	0.6	1.4
E_T^{miss} (%)	0.2	0.0	0.0	0.1	0.1	0.2	0.4	0.8
Electron (%)	0.5	0.5	0.5	0.5	0.7	0.7	0.8	0.8
Muon (%)	0.7	0.7	0.7	0.7	0.6	0.6	0.6	0.6
Track veto (%)	0.6	0.6	0.6	0.6	0.6	0.6	0.6	0.6
CR Bkg (%)	0.8	1.0	1.4	1.9	2.3	3.1	5.7	8.6
Theory (%)	0.8	0.8	0.8	0.8	0.8	1.0	1.4	3.1

are significantly reduced compared to the individual measurements. The dominant systematic uncertainty especially in the higher signal regions is the subtraction of the top and diboson backgrounds in the control regions. Many of the other uncertainties are below 1 %.

14.3 Estimation of $W^\pm(\rightarrow \ell^\pm \bar{\nu})$ +jets Backgrounds

The $W^\pm(\rightarrow \ell^\pm \bar{\nu})$ +jets backgrounds are also estimated from control regions, cf. Sect. 10.2.1. The results obtained are described in this section.

14.3.1 $W^\pm(\rightarrow \mu^\pm \bar{\nu})$ +jets Estimation from a W +jets Control Region with a Muon

For estimating the $W^\pm(\rightarrow \mu^\pm \bar{\nu})$ +jets background, the same $W^\pm(\rightarrow \mu^\pm \bar{\nu})$ +jets control region as described in Sect. 14.2.3 for the $Z(\rightarrow \nu \bar{\nu})$ +jets estimation is used. The only difference occurs in the transfer factor, since the signal region process is a different one, cf. Eq. 10.4.

The resulting TF is presented in Fig. 14.42a. It shows a steeply falling slope up to about 500 GeV and then flattens out. However, in this case the transfer factor is not expected to be flat as a function of E_T^{miss} . In the signal region, there is a veto on identified muons, so only $W^\pm(\rightarrow \mu^\pm \bar{\nu})$ +jets events where the muon is lost survive the selection. This is mostly the case when the muon does not fall into the acceptance of the veto selection cuts, as do for example forward muons, which typically occur for events with low boson p_T , i.e. low calorimeter E_T^{miss} . Thus, the application of the muon veto in the signal region enhances the fraction of W events with lower E_T^{miss} .

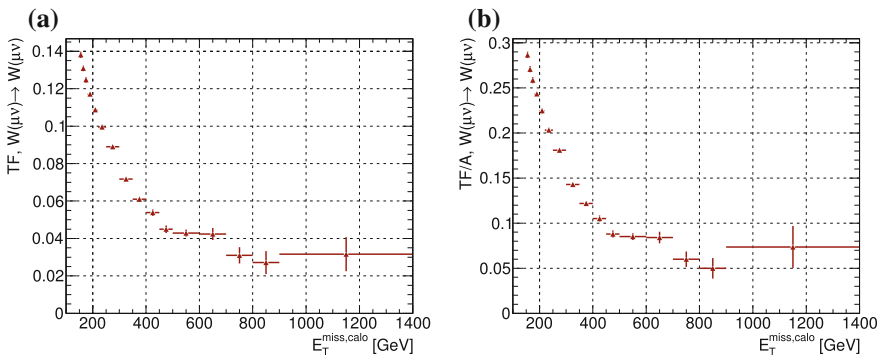


Fig. 14.42 Transfer factors before and after applying the lepton selection in the $W^\pm(\rightarrow \mu^\pm \bar{\nu})$ +jets control region. **a** Transfer factor. **b** Transfer factor with acceptance

Table 14.13 Relative uncertainties (in %) from different sources on the estimate of $W^\pm(\rightarrow \mu^\pm\bar{\nu})+\text{jets}$ from the $W^\pm(\rightarrow \mu^\pm\bar{\nu})+\text{jets}$ control regions

$W^\pm(\rightarrow \mu^\pm\bar{\nu})$ from $W^\pm(\rightarrow \mu^\pm\bar{\nu})$	SR1	SR2	SR3	SR4	SR5	SR6	SR7	SR8
Data Stat (%)	0.3	0.5	0.8	1.3	1.9	2.7	5.0	9.3
MC Stat (%)	0.4	0.6	0.9	1.0	1.4	2.1	3.6	6.2
JES (%)	0.8	0.4	0.5	0.4	0.9	2.9	3.7	9.2
JER (%)	0.6	0.7	0.1	0.0	1.0	1.9	0.4	3.5
E_T^{miss} (%)	0.8	0.6	0.5	0.5	0.5	0.7	0.6	0.7
CR bkg. (%)	1.9	2.6	3.1	3.6	5.8	6.2	10.0	11.8
Muon (%)	0.8	0.9	0.9	1.0	1.0	1.0	1.2	1.6
Electron (%)	0.1	0.1	0.2	0.1	0.3	0.1	0.1	1.0
Track veto (%)	0.1	0.1	0.1	0.1	0.1	0.1	0.2	0.2
Theory (%)	2.4	2.2	1.6	1.2	0.8	0.9	1.0	0.9

This explains why the ratio in Fig. 14.42a is larger for the low E_T^{miss} regions and flattens out at higher values. Figure 14.42b shows the ratio of signal region process over control region process after the full control region selection, i.e. the transfer factor divided by the acceptance of the CR cuts. Given the mostly flat acceptance (c.f. Fig. 14.31a), this distribution exhibits essentially the same features as discussed for Fig. 14.42a.

Table 14.13 lists the relative uncertainties on the $W^\pm(\rightarrow \mu^\pm\bar{\nu})+\text{jets}$ estimate due to various sources. While the statistical uncertainties are negligible in the lower regions, they increase significantly and become some of the largest uncertainties at higher E_T^{miss} . In general, also the systematic uncertainties increase with increasing E_T^{miss} . Dominant in the most signal regions are the uncertainties due to the subtraction of top and diboson processes in the control region. The theoretical uncertainties contribute significantly in the lower regions and are dominated there by the PDF uncertainties. In the higher regions, all theoretical uncertainties are at the per-mille level. Especially in the highest region also the JES uncertainties can be of the order of 10%.

14.3.2 $W^\pm(\rightarrow e^\pm\bar{\nu})+\text{jets}$ and $W^\pm(\rightarrow \tau^\pm\bar{\nu})+\text{jets}$ Estimation from a $W+\text{jets}$ Control Region with an Electron

The background contributions from $W^\pm(\rightarrow e^\pm\bar{\nu})+\text{jets}$ and $W^\pm(\rightarrow \tau^\pm\bar{\nu})+\text{jets}$ events in the signal region are estimated from a control region with W -bosons decaying to an electron and a neutrino. There are differences in the control region selection compared to the one used for the estimation of $Z(\rightarrow \nu\bar{\nu})+\text{jets}$ that is

described in Sect. 14.2.4 ($W^\pm(\rightarrow e^\pm\bar{\nu})+\text{jets}$ CR A), and the control region is therefore labelled $W^\pm(\rightarrow e^\pm\bar{\nu})+\text{jets}$ CR B. The differences are mainly related to the treatment of the missing transverse energy, cf. Sect. 12.4. Both for $W^\pm(\rightarrow e^\pm\bar{\nu})+\text{jets}$ and $W^\pm(\rightarrow \tau^\pm\bar{\nu})+\text{jets}$, the charged decay leptons are part of the E_T^{miss} calculation, since their energy is deposited in the calorimeters, as discussed before for the $Z(\rightarrow e^+e^-)+\text{jets}$ and $W^\pm(\rightarrow e^\pm\bar{\nu})+\text{jets}$ CRs. Accordingly, in the signal as well as in the control regions, the calorimeter based missing E_T corresponds to the neutrino p_T and the same E_T^{miss} and the same trigger as in the signal region is used in the control region. One good electron fulfilling the less stringent selection criteria detailed in Sect. 12.2 is required and events with additional *veto* electrons or muons are rejected. All other cuts (data quality, cleaning, jet variables) are the same as for the signal region. In particular, there is no cut on the transverse mass in this control region. The tight cut on the E_T^{miss} —and hence the neutrino p_T —effectively reduces multi-jet and also other backgrounds as for example $Z(\rightarrow \ell^+\ell^-)+\text{jets}$.

The contributions of different processes in the lowest $W^\pm(\rightarrow e^\pm\bar{\nu})+\text{jets}$ control region B is detailed in Table 14.14: The control region process accounts for about 71 % of the events, the largest contribution are $W^\pm(\rightarrow \tau^\pm\bar{\nu})+\text{jets}$ events (15.5 %). Top and diboson processes contribute with about 8 % and 4 %, respectively. The other contributions are all less than 1 %. The ratio of data to the sum of the simulated processes is 0.89. As for the other control regions, this scale factor is applied to the simulation in the plots. The evolution of the scale factor for the eight control regions is shown in Fig. 14.43b: It decreases with increases E_T^{miss} cut from approximately 0.9 in CR1 to roughly 0.65 in CR8. Figure 14.43a shows the relative contributions of the different simulated processes. The purity of the control regions remains mostly the same, $W^\pm(\rightarrow \tau^\pm\bar{\nu})+\text{jets}$ and diboson production increase, while the $t\bar{t}$ contamination decreases.

Table 14.14 Event yields for data and simulated processes in the lowest $W^\pm(\rightarrow e^\pm\bar{\nu})+\text{jets}$ control region B. The numbers in parenthesis are the fractions of the total number of simulated events

$E_T^{\text{miss}} > 150 \text{ GeV}$	
$W^\pm(\rightarrow e^\pm\bar{\nu})+\text{jets}$	45091.92 (71.1)
$W^\pm(\rightarrow \tau^\pm\bar{\nu})+\text{jets}$	9813.73 (15.5)
$t\bar{t}$	4180.56 (6.6)
Diboson	2496.33 (3.9)
Single top	1021.93 (1.6)
$Z(\rightarrow \tau^+\tau^-)+\text{jets}$	545.86 (0.9)
$W^\pm(\rightarrow \mu^\pm\bar{\nu})+\text{jets}$	161.95 (0.3)
$Z(\rightarrow \nu\bar{\nu})+\text{jets}$	92.89 (0.1)
$Z(\rightarrow \mu^+\mu^-)+\text{jets}$	6.11 (<0.1)
$Z(\rightarrow e^+e^-)+\text{jets}$	0.15 (<0.1)
Total simulation	63411.43
Data	56518
Ratio	0.89

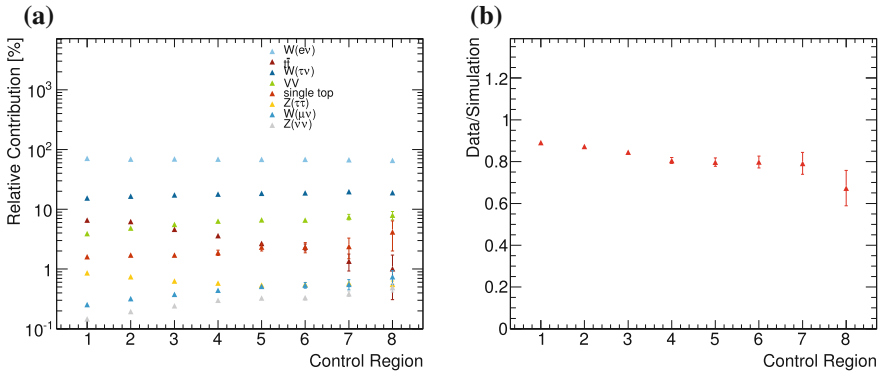


Fig. 14.43 Relative simulation fractions (a) and ratio of data versus simulation (b) in the $W^\pm(\rightarrow e^\pm\bar{\nu})$ +jets control regions B. The error bars show statistical uncertainties only

In comparison to the $W^\pm(\rightarrow \mu^\pm\bar{\nu})$ +jets control region or the $W^\pm(\rightarrow e^\pm\bar{\nu})$ +jets CR used to estimate $Z(\rightarrow \nu\bar{\nu})$ +jets, the purity is poorer, see for example Fig. 14.24, and also statistics are much lower (roughly a factor of 3). This can be understood from the fact that for the $W^\pm(\rightarrow \mu^\pm\bar{\nu})$ +jets CR, the calorimeter based missing E_T corresponds to the boson p_T , which is required to be larger than 150 GeV at least. In the $W^\pm(\rightarrow e^\pm\bar{\nu})$ +jets control region, the neutrino p_T has to be greater than 150 GeV, which typically requires an even higher boson p_T . In order to not decrease statistics further, no cut is applied on the transverse mass, although this would reduce the $W^\pm(\rightarrow \tau^\pm\bar{\nu})$ +jets contamination as can be seen in Fig. 14.44a. The description of the transverse mass by the simulation is consistent with the data within uncertainties except for a few bins in the tail. However, since this variable is not used to cut on in the control region, a good modeling is not as essential as in the other $W^\pm(\rightarrow \ell^\pm\bar{\nu})$ +jets control regions.

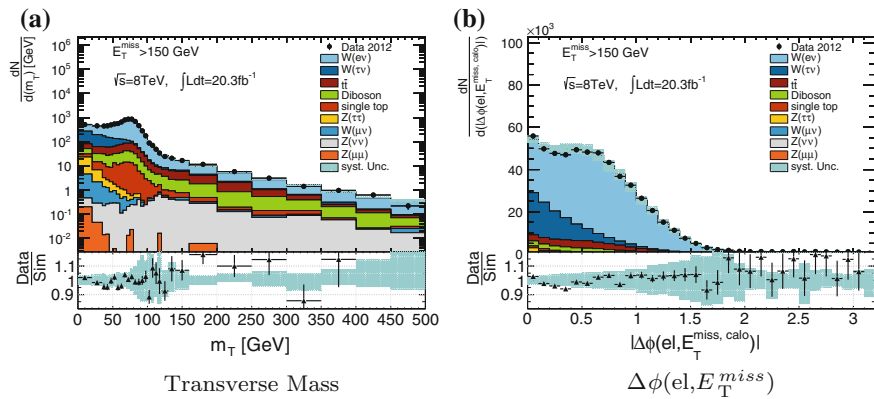


Fig. 14.44 Transverse mass (a) and azimuthal separation between electron and E_T^{miss} (b) in the lowest $W^\pm(\rightarrow e^\pm\bar{\nu})$ +jets control region B

Figure 14.44b shows the difference in ϕ between the electron and the calorimeter missing E_T , i.e. essentially between electron and neutrino. The data is well described by the simulation. The $W^\pm(\rightarrow e^\pm\bar{\nu})$ +jets events show a similar distribution to what is observed in the $W^\pm(\rightarrow e^\pm\bar{\nu})$ +jets control region A, with a peak at values slightly above 0.5. The distribution for $W^\pm(\rightarrow \tau^\pm\bar{\nu})$ +jets on the other hand has its maximum at 0 and falls steadily.

Figure 14.45 gives an overview of other properties of the selected good electron. The ϕ - and η - distributions in Fig. 14.45a, b agree well within uncertainties between data and simulation and show the same features as discussed for Fig. 14.34. It can be noted that there is no shoulder in the p_T distribution Fig. 14.45c as was observed for the charged lepton p_T in the other W CRs (c.f. Fig. 14.25d). The reason is that in this case the E_T^{miss} is the neutrino p_T and not the boson p_T as before. This shows that the neutrino carries a larger transverse momentum than the electron in most of the events. The ratio of data and simulation in the p_T spectrum shows a falling trend above 100 GeV, but the deviation from 1 is for some bins still covered by the uncertainties. The bulk of the distribution is described well, the ratio is flat.

The asymmetric charge distribution displayed in Fig. 14.45d is modelled well by the simulation.

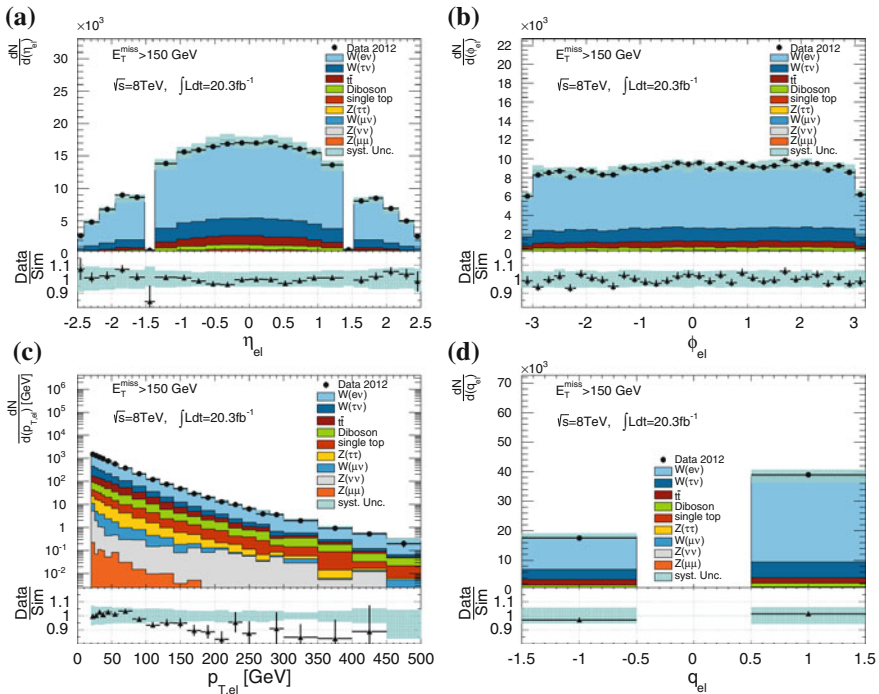


Fig. 14.45 Electron variables in the lowest $W^\pm(\rightarrow e^\pm\bar{\nu})$ +jets control region B. **a** Pseudo-rapidity. **b** Azimuthal angle. **c** Transverse momentum. **d** Charge

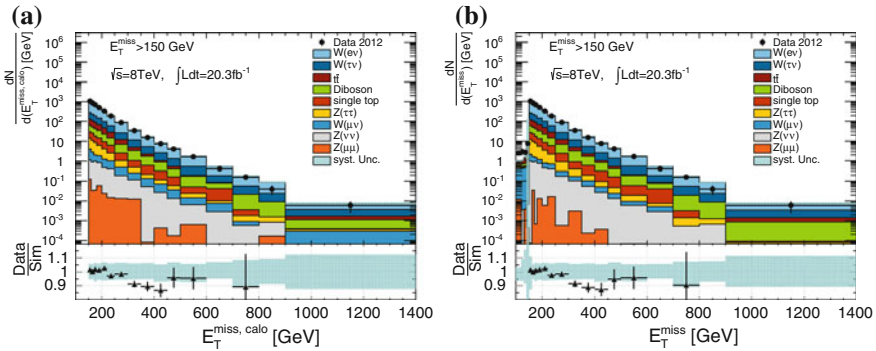


Fig. 14.46 Calorimeter based (a) and full-detector based E_T^{miss} (b) in the lowest $W^\pm(\rightarrow e^\pm\bar{\nu})+\text{jets}$ control region B

The shape of the calorimeter E_T^{miss} spectrum is displayed in Fig. 14.46a. This can be compared to the full-detector E_T^{miss} in Fig. 14.46b. Both distributions are very similar, which is to be expected, as there should not be much activity in the muons system in the events considered in this control region. There are a couple of bins in which the simulation deviates further from the data than the uncertainties cover. However, since the same quantity is used to cut on also in the signal region, differences in the shape will be corrected by the transfer factor method.

The plot in Fig. 14.47a shows the distribution of $|\Delta\phi_{\min}(\text{jet}_i, E_T^{\text{miss}})|$. The ratio of data to simulation is compatible with 1 within the uncertainties except for the region close to 0, where a slight excess in data, can be seen due to a QCD multi-jet contamination. This is however removed when cutting at $|\Delta\phi_{\min}(\text{jet}_i, E_T^{\text{miss}})| > 1.0$. The large peak at $|\Delta\phi_{\min}(\text{jet}_i, E_T^{\text{miss}})| \sim \pi$ shows that in most of the events the jets and E_T^{miss} are back-to-back. The distribution in Fig. 14.47 demonstrates that approximately 80% of the events have less than 3 jets. In the 1- and 2-jet bin the largest background is $W^\pm(\rightarrow \tau^\pm\bar{\nu})+\text{jets}$ (16%), for the higher jet multiplicities the top background becomes dominant (24%). Data and simulation agree within the uncertainties up to multiplicities of 7; there are only very few events with larger jet multiplicities.

The variables for the leading and subleading jet show no features that differ from what has been described in earlier sections; they are hence not further discussed here.

Figure 14.48 shows the acceptance (left) of the control region specific cuts, obtained from the $W^\pm(\rightarrow e^\pm\bar{\nu})+\text{jets}$ simulation⁹ and the purity (right) after the subtraction of top and diboson processes. The acceptance increases from 50% to about 80% with increasing E_T^{miss} , i.e. neutrino p_T . The fraction of $W^\pm(\rightarrow e^\pm\bar{\nu})+\text{jets}$ events in the total W and Z contributions decreases roughly from 82 to 75% at higher E_T^{miss} . This is consistent with the growing fraction of $W^\pm(\rightarrow \tau^\pm\bar{\nu})+\text{jets}$ events, c.f. Fig. 14.43a and indicates a harder missing E_T spectrum for the $W^\pm(\rightarrow \tau^\pm\bar{\nu})+\text{jets}$ production. A qualitative explanation is given by the decay modes of the τ -lepton

⁹With the performance groups' reconstruction and identification scale factors applied to match the data efficiency.

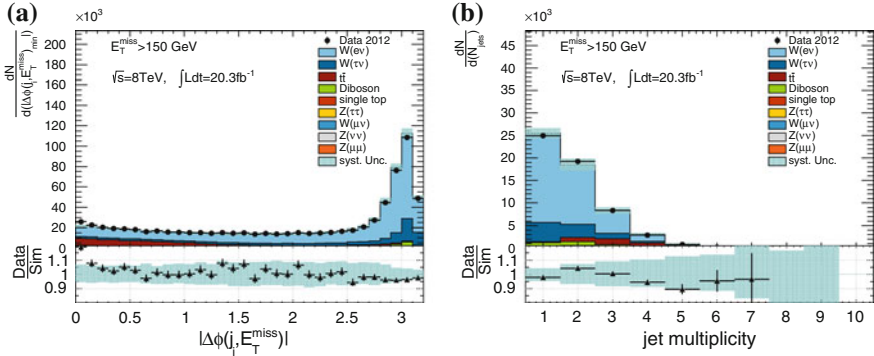


Fig. 14.47 $|\Delta\phi_{\min}(\text{jet}_i, E_T^{\text{miss}})|$ and jet multiplicities in the lowest $W^\pm(\rightarrow e^\pm\nu)$ +jets control region B. **a** $|\Delta\phi_{\min}(\text{jet}_i, E_T^{\text{miss}})|$. **b** Jet multiplicity

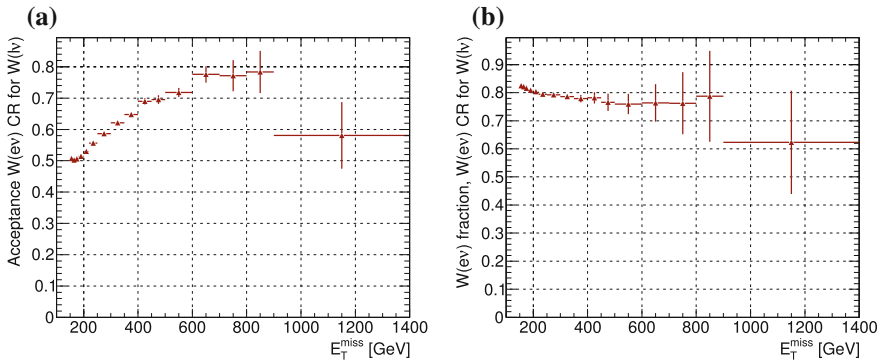


Fig. 14.48 Acceptance and purity in the $W^\pm(\rightarrow e^\pm\nu)$ +jets control regions B as a function of E_T^{miss} . The error bars are statistical uncertainties only. **a** Acceptance. **b** Purity

[14]: When the tauon decays into an electron, electron-neutrino and τ -neutrino, the electron which is identified in the control region will have a smaller p_T with respect to the E_T^{miss} than in a real $W^\pm(\rightarrow e^\pm\nu)$ +jets event. In other words, if an electron with a given p_T is selected in the control region, the E_T^{miss} in the event will be higher due to the additional neutrinos if the electron stems from a τ -decay rather than a W -decay.

Figure 14.49 shows the transfer factors (c.f. Eq. 10.4) for the estimation of $W^\pm(\rightarrow e^\pm\nu)$ +jets (top) and $W^\pm(\rightarrow \tau^\pm\nu)$ +jets (bottom) before and after applying the control region specific cuts. They show a similar shape as a function of E_T^{miss} as the TF for estimating $W^\pm(\rightarrow \mu^\pm\nu)$ +jets from the $W^\pm(\rightarrow \mu^\pm\nu)$ +jets CR, see Fig. 14.42a. The explanation is essentially the same: $W^\pm(\rightarrow e^\pm\nu)$ +jets and $W^\pm(\rightarrow \tau^\pm\nu)$ +jets enter the signal region mostly when the decay lepton is outside of the veto acceptance or—in case of the τ —decays hadronically. In the control region, on the other hand, a good lepton is explicitly selected. Due to the correlation

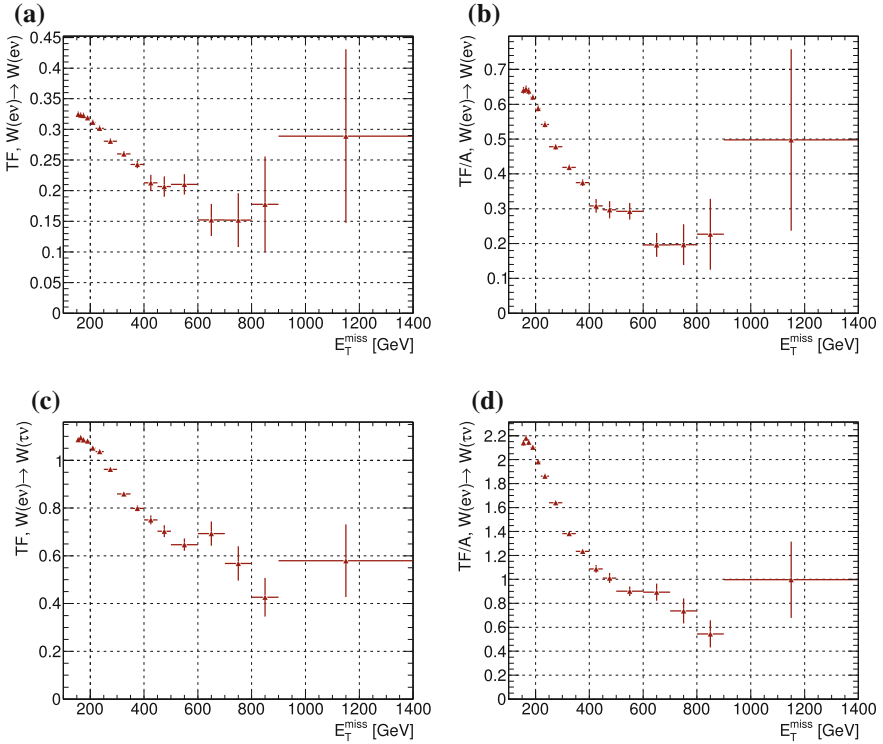


Fig. 14.49 Transfer factors before and after applying the lepton selection in the $W^\pm(\rightarrow e^\pm\bar{\nu})+\text{jets}$ control region B. Error bars are statistical uncertainties only. **a** Transfer Factor, $W(e\nu) \rightarrow W(e\nu)$. **b** Transfer factor with acceptance, $W(e\nu) \rightarrow W(e\nu)$. **c** Transfer Factor, $W(e\nu) \rightarrow W(\tau\nu)$. **d** Transfer factor with acceptance, $W(e\nu) \rightarrow W(\tau\nu)$

between neutrino p_T and charged lepton variables, it is thus to be expected that the E_T^{miss} shapes will be different between signal and control region.

The uncertainties for the $W^\pm(\rightarrow e^\pm\bar{\nu})+\text{jets}$ and $W^\pm(\rightarrow \tau^\pm\bar{\nu})+\text{jets}$ estimate are given in Tables 14.15 and 14.16, respectively. For the $W^\pm(\rightarrow e^\pm\bar{\nu})+\text{jets}$ estimate, in most of the control regions, the background subtraction for top and diboson, electron related uncertainties and the JES uncertainty are the dominating systematics. In the higher E_T^{miss} regions, theoretical uncertainties, which are dominated by PDF uncertainties, increase as well, as do the statistical uncertainties. The picture is mostly the same for the $W^\pm(\rightarrow \tau^\pm\bar{\nu})+\text{jets}$ estimate, except that the lepton systematics are not as large.

Table 14.15 Relative uncertainties (in %) from different sources on the estimate of $W^\pm(\rightarrow e^\pm\bar{\nu})+\text{jets}$ from the $W^\pm(\rightarrow e^\pm\bar{\nu})+\text{jets}$ control regions B

$W^\pm(\rightarrow e^\pm\bar{\nu})$ from $W^\pm(\rightarrow e^\pm\bar{\nu})$	SR1	SR2	SR3	SR4	SR5	SR6	SR7	SR8
Data Stat (%)	0.5	0.8	1.3	2.1	3.0	4.1	7.8	15.9
MC Stat (%)	0.5	0.7	1.0	1.3	2.1	3.8	6.3	12.6
JES (%)	1.3	2.2	2.1	2.0	1.9	4.0	2.6	14.1
JER (%)	0.3	0.5	0.1	0.8	0.3	0.1	0.5	4.5
E_T^{miss} (%)	0.3	0.0	0.1	0.0	0.1	0.2	0.3	0.0
CR bkg. (%)	2.9	3.6	4.3	5.5	7.2	7.4	10.0	15.4
Muon (%)	0.0	0.0	0.0	0.0	0.1	0.1	0.1	0.1
Electron (%)	3.4	3.3	3.1	2.9	2.9	2.8	2.7	3.5
Track veto (%)	0.2	0.2	0.2	0.2	0.2	0.2	0.2	0.2
Theory (%)	0.9	0.8	1.1	1.2	1.2	1.2	2.1	3.1

Table 14.16 Relative uncertainties (in %) from different sources on the estimate of $W^\pm(\rightarrow \tau^\pm\bar{\nu})+\text{jets}$ from the $W^\pm(\rightarrow e^\pm\bar{\nu})+\text{jets}$ control regions B

$W^\pm(\rightarrow \tau^\pm\bar{\nu})$ from $W^\pm(\rightarrow e^\pm\bar{\nu})$	SR1	SR2	SR3	SR4	SR5	SR6	SR7	SR8
Data Stat (%)	0.5	0.8	1.3	2.1	3.0	4.1	7.7	15.7
MC Stat (%)	0.3	0.4	0.5	0.6	0.8	1.1	1.9	3.3
JES (%)	1.6	2.2	2.5	2.0	3.7	4.2	4.1	4.3
JER (%)	0.2	0.2	0.5	0.8	0.7	1.1	2.0	1.0
E_T^{miss} (%)	0.4	0.0	0.1	0.0	0.1	0.2	0.1	0.2
CR bkg. (%)	2.9	3.6	4.3	5.5	7.2	7.4	10.3	15.3
Muon (%)	0.0	0.1	0.1	0.1	0.1	0.1	0.2	0.1
Electron (%)	1.4	1.4	1.4	1.4	1.4	1.4	1.4	1.8
Track veto (%)	0.2	0.2	0.2	0.2	0.2	0.2	0.2	0.2
Theory (%)	0.8	0.8	1.0	1.2	1.4	1.7	2.2	2.3

14.4 $Z(\rightarrow \ell^+\ell^-)+\text{jets}$ Backgrounds Taken from Simulation

The contributions of $Z+\text{jets}$ events where the Z decays to two charged leptons is not estimated in the semi-data driven way used for the other W - and Z -backgrounds, since the $Z(\rightarrow \ell^+\ell^-)+\text{jets}$ contamination in the signal region is very small. The number of $Z(\rightarrow e^+e^-)+\text{jets}$ events is 0 in all signal regions.

The uncertainties on the estimates from simulation for $Z(\rightarrow \tau^+\tau^-)+\text{jets}$ and $Z(\rightarrow \mu^+\mu^-)+\text{jets}$ are given in Tables 14.17 and 14.18, respectively. In the highest signal regions, statistical uncertainties dominate. JES and JER uncertainties can also be of the order of or larger than 10%, depending on the signal region. The theoretical

Table 14.17 Relative uncertainties (in %) from different sources on the number of $Z(\rightarrow \tau^+\tau^-)+\text{jets}$ events, taken from simulation

$Z(\rightarrow \tau^+\tau^-)+\text{jets}$	SR1	SR2	SR3	SR4	SR5	SR6	SR7	SR8
MC Stat (%)	2.2	7.2	5.0	7.8	11.1	16.1	15.4	25.8
JES (%)	9.5	7.9	9.2	16.9	14.8	6.3	4.9	15.1
JER (%)	0.3	0.3	8.7	3.0	3.1	3.5	10.9	11.2
E_T^{miss} (%)	3.0	0.1	0.3	0.1	0.0	0.0	0.2	0.6
Muon (%)	0.0	0.1	0.2	0.4	0.0	0.0	0.0	0.0
Electron (%)	0.1	0.1	0.2	0.7	1.8	4.0	0.0	0.0
Track veto (%)	1.0	1.0	1.0	1.0	1.0	1.0	1.0	1.0
Theory (%)	2.5	2.8	2.3	1.5	1.9	1.6	2.3	3.2

Table 14.18 Relative uncertainties (in %) from different sources on the number of $Z(\rightarrow \mu^+\mu^-)+\text{jets}$ events, taken from simulation

$Z(\rightarrow \mu^+\mu^-)+\text{jets}$	SR1	SR2	SR3	SR4	SR5	SR6	SR7	SR8
MC Stat (%)	1.9	3.7	7.0	9.1	10.2	10.5	7.1	8.6
JES (%)	13.1	14.7	10.8	3.8	4.0	6.7	2.2	2.1
JER (%)	1.0	0.1	1.9	5.5	0.5	7.8	6.0	1.0
E_T^{miss} (%)	4.0	0.1	0.5	0.0	0.0	0.0	0.0	0.0
Muon (%)	0.0	0.0	0.0	0.1	0.2	0.3	0.4	0.5
Electron (%)	0.0	0.1	0.1	0.1	0.2	0.3	0.4	0.3
Track veto (%)	1.0	1.0	1.0	1.0	1.0	1.0	1.0	1.0
Theory (%)	5.8	6.7	6.9	6.8	2.2	3.4	4.9	4.5

uncertainties (PDF essentially) are also a source of considerable uncertainty. This illustrates the cancellation of such uncertainties in the TF method, when comparing for example to the theoretical uncertainties on the $Z(\rightarrow \nu\bar{\nu})+\text{jets}$ estimate from the $Z(\rightarrow e^+e^-)+\text{jets}$ control region (Table 14.6).

14.5 Top and Diboson Backgrounds

Top and diboson processes in the signal region are estimated from the simulation directly, since their contribution is fairly small. The associated uncertainties are given in Tables 14.19, 14.20 and 14.21. The theoretical uncertainties on the normalisation are dominating. Especially for the top processes, the statistical uncertainties become very large in the highest signal regions. JER and especially JES are additional sources of large uncertainties.

Table 14.19 Relative uncertainties (in %) from different sources on the number of $t\bar{t}$ events, taken from simulation

$t\bar{t}$	SR1	SR2	SR3	SR4	SR5	SR6	SR7	SR8
MC Stat (%)	0.9	1.5	2.9	5.6	8.6	13.7	36.3	55.0
JES (%)	7.3	9.5	11.1	9.7	4.0	12.0	18.1	27.7
JER (%)	0.4	1.0	0.6	2.9	1.2	11.7	2.1	27.7
E_T^{miss} (%)	1.8	0.3	0.1	1.2	1.3	4.3	0.0	0.0
Muon (%)	0.1	0.1	0.1	0.4	0.8	0.0	0.0	0.0
Electron (%)	0.0	0.1	0.2	0.4	0.8	0.0	0.0	0.0
Track veto (%)	1.0	1.0	1.0	1.0	1.0	1.0	1.0	1.0
Theory (%)	20.0	20.0	20.0	20.0	50.0	50.0	100.0	100.0

Table 14.20 Relative uncertainties (in %) from different sources on the number of single top events, taken from simulation

Single top	SR1	SR2	SR3	SR4	SR5	SR6	SR7	SR8
MC Stat (%)	2.4	4.3	7.1	12.4	21.4	30.0	64.4	0
JES (%)	8.5	10.1	8.8	11.6	19.9	5.8	42.0	0
JER (%)	0.5	3.3	2.7	11.1	9.2	0.4	14.2	0
E_T^{miss} (%)	2.7	0.2	0.9	0.4	0.0	0.0	0.0	0
Muon (%)	0.1	0.3	0.1	0.0	0.0	0.0	0.0	0
Electron (%)	8.5	6.6	7.7	3.1	11.1	1.8	42.0	0
Track veto (%)	1.0	1.0	1.0	1.0	1.0	1.0	1.0	0
Theory (%)	20.0	20.0	20.0	20.0	50.0	50.0	100.0	0

Table 14.21 Relative uncertainties (in %) from different sources on the number of diboson events, taken from simulation

Diboson	SR1	SR2	SR3	SR4	SR5	SR6	SR7	SR8
MC Stat (%)	0.6	0.9	1.4	2.0	2.8	3.8	6.4	10.5
JES (%)	5.2	5.9	5.7	5.4	7.0	5.6	8.5	13.4
JER (%)	0.0	0.5	0.0	1.1	0.8	1.0	1.2	6.6
E_T^{miss} (%)	1.5	0.1	0.1	0.1	0.1	0.2	0.1	0.0
Muon (%)	0.0	0.1	0.1	0.3	0.3	0.3	0.0	0.0
Electron (%)	0.1	0.1	0.1	0.2	0.3	0.4	0.6	0.0
Track veto (%)	1.0	1.0	1.0	1.0	1.0	1.0	1.0	1.0
Theory (%)	20.0	22.0	24.0	26.0	28.0	30.0	45.0	60.0

14.6 Multi-jet and Non-collision Background

The multi-jet background is determined from data with the help of a *jet smearing* method described in more detail in Ref. [7]. The basic idea is to mimic the mis-measurement of jets that leads to multi-jet events entering the signal region. In a first step, a sample of *seed events* with low E_T^{miss} is selected from events triggered by

single jet triggers with p_T thresholds ranging from 55 to 460 GeV that are combined according to their prescales. The p_T of the jets in the events is smeared according to response functions obtained from simulation and adapted to data, creating events with large missing E_T . A control region is defined by inverting the $|\Delta\phi_{\min}(\text{jet}_i, E_T^{\text{miss}})|$ cut and used to normalise the multi-jet contribution. For this work, the results from Ref. [8] are used. The uncertainties given there are a conservative estimate of 100%.

The non-collision background is estimated in a data driven way that is detailed in Ref. [7]. To identify events potentially originating from beam backgrounds, the beam-induced background tagger [15] is used. It uses information from muon segments on both sides of the detector in combination with the position of calorimeter clusters. The tagging efficiency is estimated using the jet timing distribution. All events with $t < -5$ ns ($N_{t < -5 \text{ ns}}$) are assumed to be NCB events. With the number of events out of this sample that are identified by the tagger, $N_{t < -5 \text{ ns}}^{\text{tag}}$, the efficiency is estimated as $\varepsilon = \frac{N_{t < -5 \text{ ns}}^{\text{tag}}}{N_{t < -5 \text{ ns}}}$. The number of beam background events is then obtained as $N_{\text{NCB}} = N^{\text{tag}} \times \frac{N_{t < -5 \text{ ns}}}{N_{t < -5 \text{ ns}}^{\text{tag}}}$. The results are taken from [8]. The non-collision background is suppressed efficiently by the cleaning cuts, in particular those for the leading jet: There is only a contamination in the lowest SRs, namely 449 events in SR1 and 47 events in SR2. The uncertainty is estimated in Ref. [8] to be 100%, as a conservative estimate.

References

1. The ATLAS Collaboration. ATLAS experiment—public results. <https://twiki.cern.ch/twiki/bin/view/AtlasPublic/JetEtmisssApproved2013JESUncertainty>. Accessed Sept 2014
2. The ATLAS Collaboration (2013) Jet energy resolution in proton-proton collisions at $\sqrt{s} = 7$ TeV recorded in 2010 with the ATLAS detector. Eur Phys J C73:2306. doi:10.1140/epjc/s10052-013-2306-0. arXiv:1210.6210 [hep-ex]
3. The ATLAS Collaboration (2014) Electron and photon energy calibration with the ATLAS detector using LHC Run 1 data. ArXiv Pre-Prints. arXiv:1407.5063 [hep-ex]
4. The ATLAS Collaboration (2014) Measurement of the muon reconstruction performance of the ATLAS detector using 2011 and 2012 LHC proton-proton collision data. ArXiv Pre-Prints. arXiv:1407.3935 [hep-ex]
5. The ATLAS Collaboration (2014) Electron efficiency measurements with the ATLAS detector using the 2012 LHC proton-proton collision data. Technical report ATLAS-CONF-2014-032. Geneva: CERN
6. The ATLAS Collaboration (2013) Performance of Missing Transverse Momentum Reconstruction in ATLAS studied in Proton-Proton Collisions recorded in 2012 at 8 TeV. Technical report ATLAS-CONF-2013-082. Geneva: CERN
7. Abdallah J et al (2013) Search for new phenomena with mono-jet plus missing transverse energy signature in proton-proton collisions at $\sqrt{s} = 8$ TeV with the ATLAS detector. Technical report ATL-COM-PHYS-2013-1578. Geneva: CERN
8. The ATLAS Collaboration (2015) Search for new phenomena in nal states with an energetic jet and large missing transverse momentum in pp collisions at $\sqrt{s} = 8$ TeV with the ATLAS detector. In: submitted to EPJC. arXiv:1502.01518 [hep-ex]
9. The ATLAS Collaboration (2014) Calibration of the performance of b-tagging for c and light-flavour jets in the 2012 ATLAS data. Technical report ATLAS-CONF-2014-046. Geneva: CERN

10. The ATLAS Collaboration (2014) Calibration of b-tagging using dileptonic top pair events in a combinatorial likelihood approach with the ATLAS experiment. Technical report ATLAS-CONF-2014-004. Geneva: CERN
11. The ATLAS Collaboration (2012) Search for squarks and gluinos using final states with jets and missing transverse momentum with the ATLAS experiment in $\sqrt{s} = 8$ TeV proton-proton collisions: supporting documentation. Technical report ATL-PHYS-INT-2012-063. Geneva: CERN
12. Mangano M et al (2003) ALPGEN, a generator for hard multiparton processes in hadronic collisions. JHEP 07:001. [arXiv:hep-ph/0206293](https://arxiv.org/abs/hep-ph/0206293)
13. Kuhn JH et al (2008) Electroweak corrections to hadronic production of W bosons at large transverse momenta. Nucl Phys B797:27–77. doi:[10.1016/j.nuclphysb.2007.12.029](https://doi.org/10.1016/j.nuclphysb.2007.12.029). [arXiv:0708.0476](https://arxiv.org/abs/0708.0476) [hep-ph]
14. Beringer J et al (2012) Review of particle physics. Phys Rev D 86:010001. doi:[10.1103/PhysRevD.86.010001](https://doi.org/10.1103/PhysRevD.86.010001)
15. The ATLAS Collaboration (2013) Characterisation and mitigation of beam-induced backgrounds observed in the ATLAS detector during the 2011 proton-proton run. JINST 8:07004. doi:[10.1088/1748-0221/8/07/P07004](https://doi.org/10.1088/1748-0221/8/07/P07004). [arXiv:1303.0223](https://arxiv.org/abs/1303.0223) [hep-ex]

Chapter 15

Results and Interpretation

In this chapter, first, the Standard Model background estimation obtained in Chap. 14 is compared to the event numbers observed in data for each signal region and model-independent limits on the cross section for new physics will be derived in Sect. 15.1. In Sect. 15.2 the signal inputs to the limit calculation are described, in particular, the effect of different sources of experimental and theoretical uncertainties is discussed. The actual limits on Dark Matter pair production are given in Sect. 15.3, both for the EFT in Sect. 15.3.1 as well as for the simplified model in Sect. 15.3.2. In Sect. 15.3.1, the EFT limits are also compared to results from direct and indirect search experiments. Finally, Sect. 15.4 summarises the obtained results.

15.1 Background Summary and Model Independent Results

The background expectations derived in Chap. 14 are to be compared to the observed data event numbers for each signal region. Table 15.1 gives the event numbers at each step of the selection (see Sect. 13.3) for the first signal region ($E_T^{\text{miss}} > 150 \text{ GeV}$). It can be seen that about 95 % of the collected data in the `JetTauEtmiss` stream are of good quality. Approximately 60 % of the remaining events pass the trigger requirement. The various jet and event cleaning criteria together remove about 5 %. After the cut on the E_T^{miss} , only 3.6 % of the total events are left, the further requirements reduce this to 0.8 %, corresponding to 364378 events for the first signal region. This is in good agreement with the background expectation as can be seen from Table 15.2, which summarises the final results for all background contributions in comparison with the observed event numbers in data. The uncertainties given are the total uncertainties, calculated as the quadratic sum of data statistical uncertainty (if applicable), simulation statistical uncertainty and systematic uncertainties. For the calculation

Table 15.1 Event numbers after each cut of the event selection outlined in Sect. 13.3, here for the first signal region. For numbers in the higher SRs, see Table 15.2. The efficiency of each cut with respect to the previous ones is given as well as the fraction of events with respect to the total for each selection step

Cut	Number of events	ε (%)	Fraction (%)
None	42,355,348	100	100
GRL	39,976,488	94.3	94.3
E_T^{miss} trigger	23,921,936	59.8	56.4
Primary vertex	23,921,488	99.9	56.4
Jet cleaning	22,703,856	94.9	53.6
Event cleaning	22,631,280	99.6	53.4
Leading jet	13,660,827	60.3	32.2
BCH cleaning	11,613,279	85.0	27.4
$E_T^{\text{miss}} > 150$ GeV	1,525,497	13.1	3.6
$ \Delta\phi_{\min}(\text{jet}_i, E_T^{\text{miss}}) > 1.0$	881,296	57.7	2.0
Electron veto	771,571	87.5	1.8
Muon veto	413,878	53.6	0.9
Track veto	365,738	88.3	0.8
$p_{T,j1}/E_T^{\text{miss}} > 0.5$	364,378	99.6	0.8

of the uncertainty on the total background, correlations are taken into account. Systematic uncertainties of a given source are treated fully correlated between different background estimates, uncertainties from different sources are treated uncorrelated. For the data driven estimates, the statistical uncertainties are split into different components: one is the uncertainty due to the limited statistic in data in the control region, the others are due to the simulation statistical uncertainties. These are split further into one contribution from the numerator of the transfer factor, one from the denominator and one from the background subtraction, i.e. the statistical uncertainties of the samples for all the other processes. This allows one to consider the correlations between the data driven estimates. For processes estimated from the same control region,¹ all statistical uncertainties are treated as correlated, with the exception of those on the TF numerator. For example, the statistical uncertainty from data in the $W^\pm(\rightarrow \mu^\pm\bar{\nu}) + \text{jets}$ control region on the $Z(\rightarrow \nu\bar{\nu}) + \text{jets}$ combination result is correlated with the data statistical uncertainty on the $W^\pm(\rightarrow \mu^\pm\bar{\nu}) + \text{jets}$ estimate. (The uncertainty on the combined $Z(\rightarrow \nu\bar{\nu}) + \text{jets}$ estimate due to a given source in a given control region is obtained from the BLUE method, cf. Eq.(10.11).)

The decomposition of the total background uncertainty into the separate contributions is given in Table 15.3. Many of the uncertainties are less than 1% in most of the signal regions. The uncertainty due to the limited statistic in the simulation becomes 1% in SR5 and grows to 3% in SR8. The statistical uncertainty from data amounts to 1% in SR3 and reaches 6.7% in SR8. The statistical uncertainties are

¹ $Z(\nu\bar{\nu})$ and $W(\mu\nu)$ from $W(\mu\nu)$, $Z(\nu\bar{\nu})$, $W(\tau\nu)$ and $W(e\nu)$ from $W(e\nu)$.

Table 15.2 Observed number of events and background estimations for all signal regions. The errors are the total uncertainties. For the total background estimate the combination of the four $Z(\nu\bar{\nu})$ estimates is used

	SR1	SR2	SR3	SR4	SR5	SR6	SR7	SR8
$Z(\nu\bar{\nu})$ from $Z(\mu^+\mu^-)$	218082 ± 4313	80579 ± 1842	30258 ± 880	12648 ± 506	5959 ± 310	2915 ± 203	781 ± 101	195 ± 48
$Z(\nu\bar{\nu})$ from $Z(e^+e^-)$	217899 ± 5721	80301 ± 2378	30861 ± 1082	13298 ± 572	6073 ± 337	3091 ± 215	701 ± 89	310 ± 58
$Z(\nu\bar{\nu})$ from $W(\mu^{\pm}\bar{\nu})$	217736 ± 6437	78159 ± 2871	29066 ± 1216	12068 ± 553	5466 ± 389	2659 ± 200	760 ± 90	230 ± 38
$Z(\nu\bar{\nu})$ from $W(e^{\pm}\bar{\nu})$	221368 ± 8512	78888 ± 3534	29759 ± 1490	12528 ± 704	5546 ± 443	2707 ± 225	752 ± 101	247 ± 42
$Z(\nu\bar{\nu})$ from BLUE	216936 ± 3862	80367 ± 1643	30246 ± 751	12652 ± 397	5918 ± 239	2890 ± 142	743 ± 63	236 ± 29
$W(\tau^{\pm}\bar{\nu})$ from $W(e^{\pm}\bar{\nu})$	79387 ± 3027	23834 ± 1114	7709 ± 426	2746 ± 182	1151 ± 104	534 ± 54	131 ± 19	32 ± 8
$W(e^{\pm}\bar{\nu})$ from $W(e^{\pm}\bar{\nu})$	23505 ± 1132	7016 ± 391	2273 ± 137	826 ± 59	343 ± 31	156 ± 17	40 ± 6	8 ± 2
$W(\mu^{\pm}\bar{\nu})$ from $W(\mu^{\pm}\bar{\nu})$	28513 ± 999	8265 ± 309	2538 ± 99	858 ± 37	332 ± 22	142 ± 11	35 ± 4	10 ± 1
$Z(e^+e^-)$ from MC	0 ± 0	0 ± 0	0 ± 0	0 ± 0	0 ± 0	0 ± 0	0 ± 0	0 ± 0
$Z(\tau^+\tau^-)$ from MC	786 ± 83	184 ± 20	44 ± 6	14 ± 2	5 ± 0	2 ± 0	0 ± 0	0 ± 0
$Z(\mu^+\mu^-)$ from MC	528 ± 79	96 ± 16	18 ± 2	7 ± 0	3 ± 0	2 ± 0	2 ± 0	1 ± 0
$t\bar{t}$ from MC	5218 ± 1117	1803 ± 400	511 ± 118	141 ± 32	54 ± 27	21 ± 11	3 ± 3	0 ± 0
Single top from MC	1352 ± 315	398 ± 95	132 ± 32	45 ± 13	15 ± 9	8 ± 4	2 ± 3	0 ± 0
Diboson from MC	8060 ± 1671	3539 ± 807	1522 ± 376	694 ± 185	354 ± 103	181 ± 55	61 ± 28	22 ± 13
γ +jets from MC	1010 ± 682	248 ± 475	24 ± 17	24 ± 17	22 ± 17	20 ± 17	1 ± 4	1 ± 1
Multi-jet from data	6453 ± 6453	785 ± 785	177 ± 177	44 ± 44	15 ± 15	6 ± 6	1 ± 1	0 ± 0
Non-collision from data	449 ± 456	47 ± 51	0 ± 0	0 ± 0	0 ± 0	0 ± 0	0 ± 0	0 ± 0
Total	373264 ± 10034	126739 ± 2682	45239 ± 964	18070 ± 465	8223 ± 270	3968 ± 157	1026 ± 63	315 ± 29
Data	364378	123228	44715	18020	7988	3813	1028	318

Table 15.3 Breakdown of relative uncertainties (in %) on the total background estimate in all signal regions

Total Bkg	Relative uncertainties (%)							
	SR1	SR2	SR3	SR4	SR5	SR6	SR7	SR8
Data Stat	0.4	0.7	1.0	1.4	2.1	2.4	4.4	6.7
MC Stat	0.4	0.5	0.6	0.7	1.0	1.2	1.6	3.0
JES	0.7	0.7	0.2	0.2	0.5	1.0	0.6	1.2
JER	0.3	0.6	0.3	0.2	0.0	0.4	0.8	0.5
E_T^{miss}	0.2	0.1	0.1	0.1	0.1	0.2	0.2	0.5
Electron	0.8	0.7	0.7	0.7	0.8	0.8	0.9	0.8
Muon	0.5	0.5	0.5	0.5	0.5	0.5	0.4	0.5
Track veto	0.3	0.4	0.4	0.4	0.4	0.4	0.4	0.4
Top/Diboson	0.8	1.0	1.2	1.6	1.9	2.4	3.7	5.2
QCD	2.0	0.7	0.5	0.3	0.2	0.2	0.3	0.5
NCB	0.1	0.0	0.0	0.0	0.0	0.0	0.0	0.0
Theory	0.9	0.7	0.7	0.7	0.7	0.8	1.0	2.2

dominating in the higher signal regions, together with the uncertainty coming from the uncertainties on top and diboson processes. As was found in the control regions, they are by far the largest systematic uncertainties, amounting to up to 5.2% in the highest signal region. In the lowest signal region, the uncertainty on the multi-jet background is the largest uncertainty on the total background, amounting to 2%. This is quickly reduced when going to regions of larger E_T^{miss} . The theoretical uncertainties are dominated by the electroweak corrections on the W and Z cross section ratio.

In Table 15.2, agreement between data and simulation is observed in all signal regions.

Figure 15.1 shows for illustration the calorimeter missing E_T and the leading jet kinematic variables in the first signal region: Data is compared to the Standard Model prediction after the bin-by-bin application of the transfer factors to the respective distributions. For $Z(\rightarrow \nu\bar{\nu}) + \text{jets}$, the estimate from the $W^\pm(\rightarrow \mu^\pm\bar{\nu}) + \text{jets}$ CR is used, since the combination of the four $Z(\rightarrow \nu\bar{\nu}) + \text{jets}$ estimates is done only for the inclusive numbers, not bin-by-bin. In contrast to what was done in the control regions, no scale factor is applied to the simulation here, such that normalisation and shape can be compared. Especially in the lowest signal region shown here, no large excess is expected, since a signal would show up in the tail of the E_T^{miss} distribution. Therefore, this region can be used as a validation region for the transfer factor method.

The leading jet ϕ - and η -distributions (Fig. 15.1c, d) are reproduced very well by the data within the statistical uncertainties. (Systematic uncertainties are not included in these plots.) The ratio is mostly flat and compatible with 1 over the complete range. This is in accordance with the fact that there is no excess observed in signal region 1. The leading jet p_T in Fig. 15.1b is well described, especially up to 400 GeV. Above

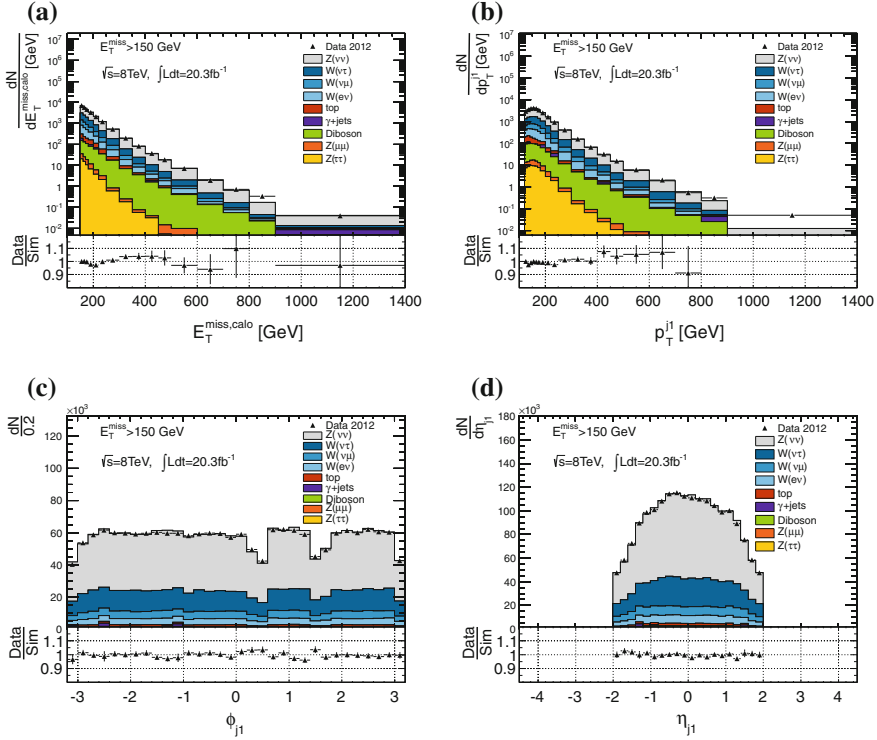


Fig. 15.1 E_T^{miss} and leading jet variables in the signal region. The $Z(\rightarrow \nu\bar{\nu}) + \text{jets}$ and $W^\pm(\rightarrow \ell^\pm\bar{\nu}) + \text{jets}$ backgrounds are estimated via the transfer factor method, the $Z(\rightarrow \nu\bar{\nu}) + \text{jets}$ estimate is taken from the $W^\pm(\rightarrow \mu^\pm\bar{\nu}) + \text{jets}$ CR. **a** E_T^{miss} , SR1. **b** Leading jet p_T , SR1. **c** Leading jet ϕ , SR1. **d** Leading jet η , SR1

that, the deviations become of the order of 10% and even larger than 20% above 800 GeV, but also the statistical uncertainties are large there. Figure 15.1a displays the missing E_T distribution. The ratio of data and simulation is compatible with 1 within statistical uncertainties, in particular there is no significant excess observed, as was deduced already from the inclusive numbers in Table 15.2. Since no shape information but only the integrated event numbers will be used in the limit setting, these plots are mostly a sanity check, demonstrating that the data-driven transfer factor method reliably reproduces the relevant shapes and corrects the normalisation of the simulation to the data.

As seen from Table 15.2, no significant deviation from the Standard Model prediction is observed in any of the signal regions. Thus, exclusion limits can be set on the visible cross section for new physics. The CL_s limits (cf. Sect. 10.4) on this visible cross section are listed in Table 15.4 for both 90 and 95% confidence level. Since for most signal regions the observed number of events is lower than the central value of

Table 15.4 Model independent upper limits on the visible cross section in fb both for 90 and 95 % confidence level

	95 % CL (fb)		90% CL (fb)	
	Expected	Observed	Expected	Observed
SR1	915.95	684.35	771.57	559.99
SR2	227.07	143.78	190.82	115.94
SR3	72.05	57.44	60.59	47.19
SR4	31.07	29.49	26.12	24.64
SR5	14.72	9.05	12.36	7.28
SR6	9.83	6.09	8.26	4.9
SR7	3.52	3.57	2.94	3.0
SR8	3.04	3.14	2.5	2.6

the Standard Model prediction, the observed limits are in most cases stronger than the expected limits.

15.2 Inputs for Limit Calculation

The results can also be interpreted in terms of dark matter pair production and limits on $\sigma \times A \times \varepsilon$ can be calculated. Here, σ is the cross section for the WIMP pair production (via a given operator), A is the acceptance of the corresponding sample, defined as the ratio of events selected at truth level over the total number of generated events, $A = \frac{N_{truth}}{N_{gen}}$, and ε is the reconstruction efficiency, given by $\varepsilon = \frac{N_{reco}}{N_{truth}}$, where N_{reco} is the number of events selected at reconstruction level. The detailed acceptances and efficiencies for all samples described in Sect. 11.2.1 are presented in Tables B.1 and B.2 for the Dirac fermionic and complex scalar dark matter operators, respectively, only the main features are summarised here. As expected, the acceptances increase with WIMP mass and decrease with tighter E_T^{miss} cut (higher SR), the more so, the softer the E_T^{miss} spectrum for the respective operator. The highest acceptance is about 40 % for the C5 operator in SR1, the lowest in SR1 is about 11 % for C1. The dependence of the acceptance on the WIMP mass is more pronounced for scalar WIMPs. The efficiencies vary only slightly between roughly 75 and 80 % for all signal points in all SRs. Similar numbers are found for the simplified model (Tables B.3, B.4).

For the limits on $\sigma \times A \times \varepsilon$, the systematic uncertainties on the signal have to be taken into account and the correlations with the background uncertainties have to be considered. The statistical uncertainties are of course uncorrelated between signal and background. Experimental systematic uncertainties, however, are treated as fully correlated between signal and background, since the detector is the same in both cases. This applies to the JES, JER and E_T^{miss} systematic uncertainties. Lepton uncertainties are negligible for the signal, as are those for the track veto (since there

are no leptons in the signal). An additional source of uncertainty for the signal is the beam energy uncertainty. Due to the data driven estimation of the main backgrounds this uncertainty is negligible for the background. The statistical uncertainty from the simulation is treated as a systematic uncertainty for the background, only the data statistic is considered in the statistical uncertainty.

The theoretical uncertainties on the signal, i.e. PDF, ISR/FSR and scale uncertainties, are not included as nuisance parameters in the limit setting. Instead, their impact on the observed limit will be indicated as an error band in the plots. The reasoning for this procedure is the following: The expected limit is meant to give information about the sensitivity of the experiment on its own, assuming a perfect theory. Thus, uncertainties not related to the experiment are not included in the calculation of the limits. Moreover, the signal samples are produced with a leading order generator and PDF, and for LO, uncertainties due to scales and PDFs are not well defined. Including them in the limit calculation might be misleading. It seems preferable to have a clear separation between the purely experimental result and “external” theoretical uncertainties and effects.

The various sources of systematic uncertainties for the signal samples are discussed in the following sections. One note has to be made concerning the axial-vector operator D8: As discussed in Sect. 11.2.1, only truth level samples were generated for this operator, since it results in the same kinematic distributions as the vector operator D5, just with a different cross section. For the same reason, no dedicated study of the systematic uncertainties is done, but the values for D5 are adopted.

15.2.1 Luminosity

The luminosity uncertainty amount to 2.8% for 2012 data taking, cf. Sect. 14.1.7. As discussed there, it cancels in the semi-data driven estimation of the main backgrounds. Thus, the uncertainty is not considered for the background in the limit setting procedure.

15.2.2 Jet Energy Scale and Resolution

The jet energy scale and resolution uncertainties are estimated in the same way as for the background simulation, cf. Sect. 14.1.2. The resulting relative uncertainties on $\sigma \times A \times \varepsilon$ are listed in details in Tables B.5–B.8 for the samples of the EFT operators and the light mediator simplified model. In summary, the jet energy scale uncertainty for the EFT samples is found to grow with increasing E_T^{miss} cut and to decrease with higher WIMP mass. The uncertainties are largest for the C1-operator, ranging up to roughly 10%. Similar trends are observed for the JES uncertainty for the light mediator samples. There is no strong dependence on the mediator mass or width.

In Table B.7 the uncertainties on $\sigma \times A \times \varepsilon$ for the EFT samples due to the jet energy resolution uncertainty are summarised. There are no clear trends visible, the uncertainties are mostly of the order of 1–2%. A similar picture for the light mediator samples gives Table B.8: The uncertainties are in most cases $\sim 2\%$ or below and no obvious dependence on either of the parameters is observed.

15.2.3 E_T^{miss} Soft Terms

The Tables B.9 and B.10 list the uncertainties on $\sigma \times A \times \varepsilon$ due to the uncertainties from the E_T^{miss} soft terms for both the EFT and the light mediator samples, respectively. They are estimated as for the background samples, cf. Sect. 14.1.4. As is expected and was also seen for the background samples, the uncertainty is below 1% with the exception of very few signal points.

15.2.4 Beam Energy

The beam energy in 2012 was not exactly 4 TeV, but estimated as $3988 \pm 5(\text{stat}) \pm 26(\text{syst})$ GeV [1]. In order to estimate the effect of this uncertainty on $\sigma \times A \times \varepsilon$, additional samples were produced with beam energies at 3988, 3962 and 4014 GeV. The uncertainty is taken as the mean of the absolute values of the differences resulting from the up- and down-variation, respectively. Table B.11 presents the resulting uncertainties for all EFT operator samples. The uncertainties tend to increase with higher SR and larger WIMP mass, which is to be expected since the average momentum transfer (Q_{tr}) increases accordingly. For low Q_{tr} , the differences in beam energy are not as important, but at larger momentum transfer they have an effect. The uncertainties are at a similar level for all the operators.

On the timescale of this work no such additional samples for the simplified model were available. Therefore, the beam energy uncertainty in this case is approximated by the uncertainties for the D5 operator, which is the pendant in the EFT to the light vector mediator. For each WIMP mass, a conservative estimate is taken by taking a number a bit larger than the maximum uncertainty for D5, see Table 15.5. This does, however, not take into account possible effects due to the mass of the mediator itself, but without additional samples, this cannot be estimated reliably.

Table 15.5 Relative beam energy uncertainty on $\sigma \times A$ in % for the light mediator operator samples

m_χ (GeV)	10	50	200	400	1000	1300
$\Delta(\sigma \times A)$ (%)	4	3	5	5	6	8

15.2.5 Factorisation and Renormalisation Scale

To estimate the uncertainty due to the choice of factorisation and renormalisation scales, additional samples for each EFT operator are produced, varying the scales simultaneously by a factor of 2 and 0.5, respectively.² The uncertainty is estimated as the mean of up- and down-variation.

The effect on $\sigma \times A$ is summarised in Table B.12. The uncertainties are found to grow both with increasing E_T^{miss} cut and WIMP mass, i.e. they are again largest in configurations with high momentum transfer, as is expected. They range roughly from 5 to 20% for the $q\bar{q}$ -operators and can be as high as about 40% for the gg -operators D11 and C5.

15.2.6 PDF

As already discussed in Chap. 11, all signal samples are reweighted to the LO variant of MSTW2008, using the LHAPDF library [2]. A prescription by the PDF4LHC group describes how to estimate PDF uncertainties for NLO signal samples [3]. It says to use the full error sets for CT10 and MSTW2008NLO and the 100 NNPDF23NLO sets and construct an envelope from those, using half of the envelope as the uncertainty around the central value for the PDF the samples were produced with. A similar approach was followed here, but using the LO sets for MSTW2008 and NNPDF21, as there is no LO variant of NNPDF23.

It should be noted that the way of constructing the uncertainty bands is conceptually different for the two families: For MSTW, there is one central PDF set and 40 error sets, from which the uncertainties are constructed following the asymmetric Hessian procedure [4], as was introduced in Sect. 4.2. The asymmetric errors are calculated using the following formulas:

$$\Delta X^+ = \sqrt{\sum_i (X_i - X_0)^2} \quad , \quad X_i > X_0 \quad (15.1)$$

$$\Delta X^- = \sqrt{\sum_i (X_i - X_0)^2} \quad , \quad X_i < X_0. \quad (15.2)$$

Here, X_0 is the central value and X_i corresponds to the i th error set.

The NNPDF sets, on the other hand, are 100 independent sets, so that the central value is given by the mean value (X_0) of this ensemble and the (symmetric) error by its standard deviation:

²The scales are defined event by event in MadGraph as the central m_T^2 scale after k_T -clustering of the event, i.e. in the case of pair production it is the geometric mean of $m^2 + p_T^2$ for each particle.

$$\Delta X = \sqrt{\frac{1}{100-1} \sum_{i=1}^{100} (X_i - X_0)^2} . \quad (15.3)$$

The uncertainties are constructed from the envelope of the above uncertainties:

$$\Delta X = \frac{1}{2} [\max(X_0^{NNPDF} + \Delta X, X_0^{MSTW} + \Delta X^+) - \min(X_0^{NNPDF} - \Delta X, X_0^{MSTW} - \Delta X^-)] \quad (15.4)$$

Table B.13 lists the obtained relative uncertainties. The numbers quoted are the uncertainties at 68 % confidence level. Similar trends as for the scale and beam energy uncertainty are observed: The uncertainties increase with higher E_T^{miss} cut and WIMP mass. This is plausible since this corresponds to regions of phase space where the PDFs are less well constrained. The size of the uncertainties for the different operators moreover depends on the initial states they correspond to: For the $q\bar{q}$ -operators D5 and D9 the cross section is dominated by light (valence) quark interactions, while for C1 and D1, due to the additional quark mass factor, the cross section is dominated by interactions involving heavier sea quarks for which the PDFs are less well known. Accordingly, D1 and C1 have much higher PDF uncertainties, ranging from 13 % to 75 %. The uncertainties for the gg -operators D11 and C5 are at a similar level, 23–65 %, which is reasonable given the limited constraints on gluon PDFs.

15.2.7 ISR and FSR

The uncertainty due to the ISR/FSR description is split into two components: one due to the value of the coupling α_s , and one due to the matching scale between MadGraph and PYTHIA.

Matching scale The matching scale can have an impact on the signal yield since events are removed if there is a jet created in the shower with a p_T larger than the value of the matching scale. This is more likely to happen for high p_T jets and a low matching scale. For example, from a 500 GeV jet, a 80 GeV jet can be produced in the showering relatively easily. For a matching scale of 80 GeV, such an event would be removed, while it would be kept for a matching scale of 300 GeV. Thus, the population in the tail of the jet p_T spectrum (or E_T^{miss} spectrum) is potentially different for different choices of the matching scale.

In order to estimate this effect, samples with a matching scale of $q_{\text{cut}} = 190$ GeV (QCUT190) were produced in addition to the ones with $q_{\text{cut}} = 80$ GeV (QCUT80) and $q_{\text{cut}} = 300$ GeV (QCUT300). An estimate of the uncertainty is derived by combining the QCUT80 and QCUT300 samples as well as the QCUT80 and QCUT190 samples and compare these combined samples in two regions of missing E_T : in the region $E_T^{\text{miss}} > 250$ GeV this compares mostly QCUT80 to QCUT190, whereas

for $E_T^{\text{miss}} > 350\text{GeV}$ the comparison is mostly sensitive to differences between QCUT190 and QCUT300. The resulting values are summarised in Table B.14. For signal regions 1 to 4 a conservative estimate of 3% will be used. For the higher signal regions, 5% will be used for the limit setting.

Coupling α_s The contribution of the α_s uncertainty is estimated by comparing samples with different PYTHIA tunes (370, 371, 372), which vary the relevant ISR and FSR variables from $\alpha_s(p_T/2)$ to $\alpha_s(2p_T)$. One subtlety here is that the nominal samples were produced with the ATLAS underlying event tune AUET2B, as was recommended at the time, while the aforementioned tunes are part of the Perugia2012 [5] family. It was however checked that the nominal samples are within the range of the 3 Perugia tunes [6]. The uncertainties on $\sigma \times A$ given in Table B.15 are again the mean of the two variations (370 vs. 371 and 370 vs. 372). They are found to be smaller than 2% in most cases.

15.3 Dark Matter Limits

15.3.1 Effective Operator Limits

Limits on the suppression scale of the effective field theory are calculated both at 90 and 95% confidence level in order to be able to compare to a variety of other search experiments which use different defaults for the confidence level of their limits. The direct detection experiments typically quote 90% confidence level, while the limits on the annihilation cross section are given at 95% CL. Since the latter is also the default for LHC and other collider searches, most of the results in this section will be at 95% confidence level, the exception being the comparison to the direct searches.

Figure 15.2 shows the expected (solid lines) and observed (dashed lines) 95% CL lower limits on the suppression scale as a function of the signal region for the seven operators and various WIMP masses. In regions where the data is overestimated by the simulation, the observed limit is stronger than the expected and vice versa.

For most points, signal region 7 ($E_T^{\text{miss}} > 500\text{GeV}$) or 8 ($E_T^{\text{miss}} > 600\text{GeV}$) is the strongest in terms of expected limits. An exception is the operator C1, for which the strongest region is signal region 4 ($E_T^{\text{miss}} > 300\text{GeV}$) for the lowest masses. For higher masses the curves are relatively flat for regions 4 to 7. In the following, only the limits from the region with the best expected limits will be considered for further comparisons, i.e. signal region 4 for C1, signal region 7 for D1, D5 and D8, and signal region 8 for the other operators.

In Fig. 15.3, the 95% CL limits on the suppression scale for these signal regions are shown as a function of the WIMP mass for each operator, the corresponding values are listed in Table 15.6. The solid red line is the observed limit, the dashed red lines mark the impact of the theoretical uncertainties discussed in Sect. 15.2. The expected limit is displayed as a dashed black line, with the $\pm 1\sigma$ - ($\pm 2\sigma$)-error bands due to the experimental uncertainties in grey (blue). The green lines (taken

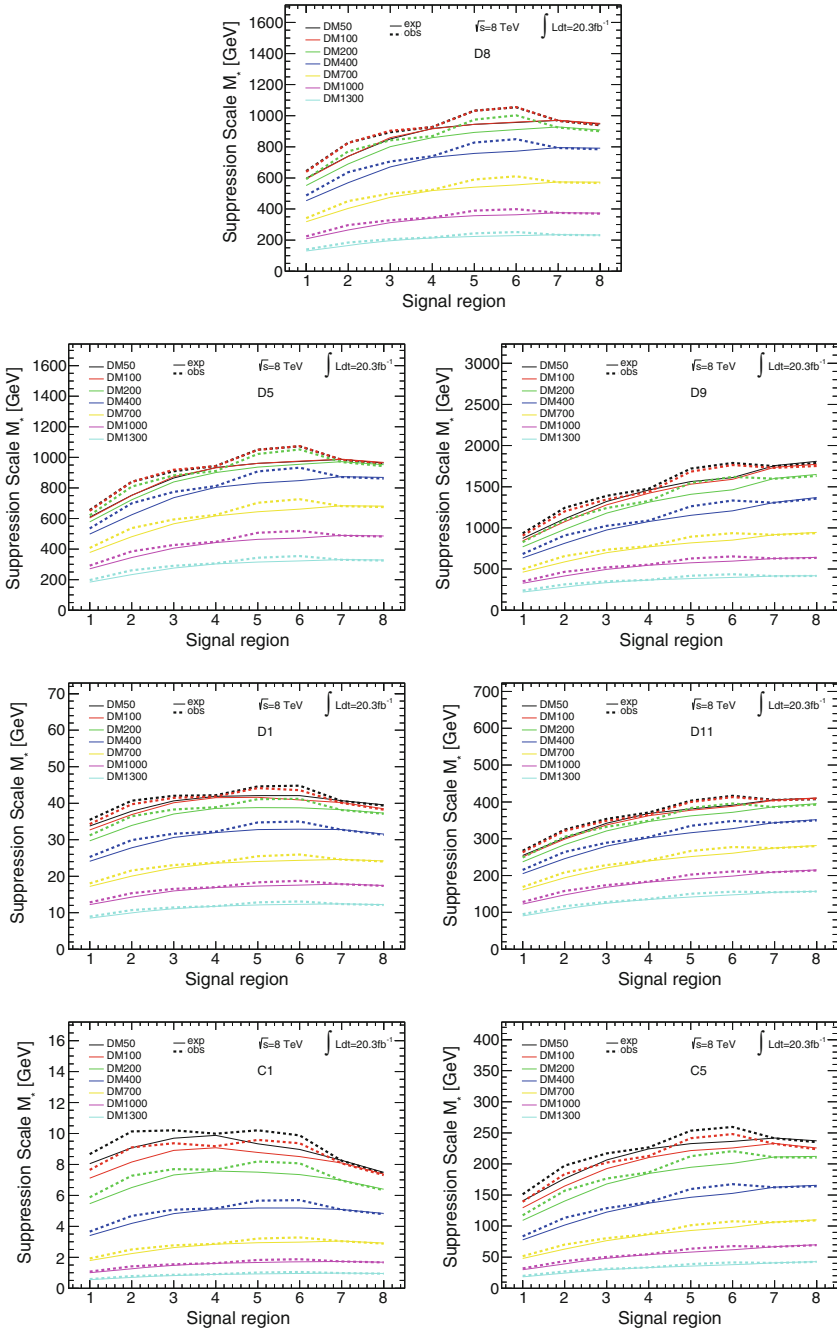


Fig. 15.2 95% CL lower limits on the suppression scale M_* as a function of the signal region for all operators and WIMP mass points. *Solid lines* are expected, *dashed lines* observed limits

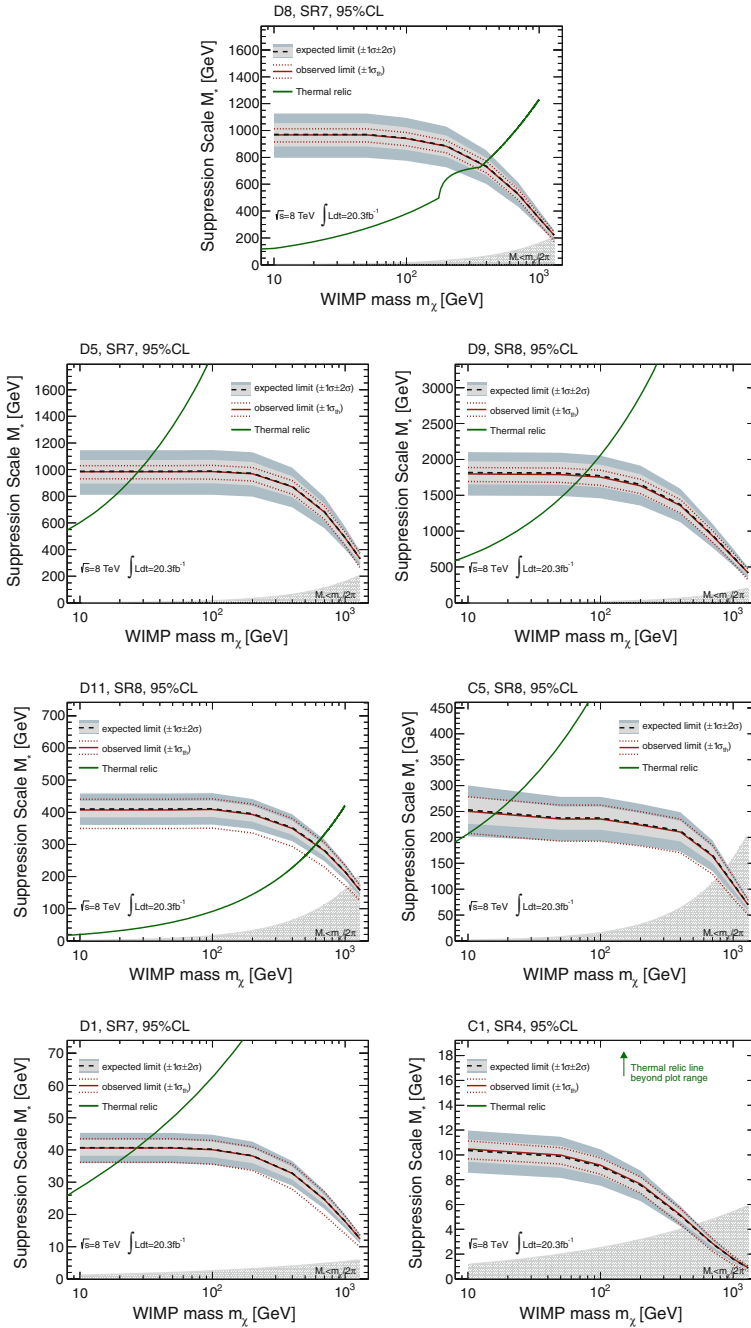


Fig. 15.3 95 % CL lower limits on the suppression scale M_* for the best signal region as a function of the WIMP mass for all operators

Table 15.6 Observed (expected) 95 % confidence level lower limits on the suppression scale M_* in GeV. The signal region used for each operator is indicated

m_χ (GeV)	95 % CL limits on M_* (GeV)						
	D1, SR7	D5, SR7	D8, SR7	D9, SR8	D11, SR8	C1, SR4	C5, SR8
10	40 (40)	983 (986)	967 (970)	1788 (1808)	407 (409)	9 (9)	235 (237)
50	40 (40)	983 (986)	967 (970)	1788 (1808)	407 (409)	9 (9)	235 (237)
100	40 (40)	984 (987)	939 (942)	1753 (1772)	408 (410)	9 (9)	223 (225)
200	38 (38)	969 (971)	882 (885)	1631 (1649)	392 (395)	7 (7)	210 (212)
400	32 (32)	870 (873)	731 (733)	1355 (1369)	349 (351)	5 (5)	164 (165)
700	24 (24)	681 (683)	523 (525)	935 (944)	280 (281)	2 (2)	109 (110)
1000	17 (17)	487 (489)	345 (346)	635 (641)	214 (215)	1 (1)	69 (69)
1300	12 (12)	330 (331)	220 (220)	415 (419)	156 (157)	0 (0)	42 (42)

from Ref. [7]) indicate those pairs of m_χ and M_* that result in the observed relic density, as measured by WMAP [8],³ assuming that annihilation into SM particles in the early universe proceeded via the considered operator exclusively. In regions where the limit on M_* lies above the green line, the results are in conflict with this assumption: The values of M_* that would give the observed relic density are excluded, only higher values are still allowed. Higher values of M_* correspond to lower values of the cross section—in other words, the cross section for the annihilation via this operator only is too small to account for the observed value, i.e. there have to be other annihilation channels or operators.

The grey shaded area (in the bottom right corner) marks regions, in which the effective theory is not valid according to the simple kinematic constraints considered for Eq. (5.12). This is a stronger requirement than previous publications used, as for example Ref. [11]. The limits for the operators D11, C1 and C5 violate this condition for WIMP masses close to 1 TeV. These points will therefore not be considered in comparison plots to other experiments in the following.

The limits are found to depend on the initial state: the $q\bar{q}$ -operators D5 and D9, which mostly couple to light quarks, provide the strongest limits of the order of TeV, for the gg -operators (D11, C5) the limits are of the order of a few hundred GeV and for the heavy-quark dominated operators the limits are on the 10–50 GeV scale.⁴

At this point, further comments on the validity of the effective theory in the high-energy LHC environment, which was introduced in Sect. 5.2.1, are necessary. In

³The most recent measurement of the relic density is the one from PLANCK [9], however, the slightly different value of Ωh^2 will not cause a visible change of the line in these plots [10].

⁴For C1, therefore, the relic density line does not lie within the plot range any more, this is indicated by the green arrow.

Refs. [6, 12], studies have been performed on the fractions of valid events for each operator in the range of allowed couplings. As discussed in Sect. 5.2.1, this range can vary for different operators. In the aforementioned studies, it was found that for the operators for scalar DM there are no events left, even with the maximum allowed coupling. In the following, the scalar DM operators (C1 and C5) will therefore not be used in the comparisons to other experiments. For the D-operators, there exist couplings for which the EFT approach is considered valid under the condition $Q_{tr} < M_{Med}$, in some cases well below the maximum allowed coupling value. The operator D9, which gives the strongest M_* limits, for example, remains valid even for a coupling product of 1.

Apart from omitting the C-operators in the comparisons, it was decided for this work to not rescale the limits based on one particular choice of couplings, but instead use the unscaled limits as long as there exist couplings for which the theory is valid and to not draw comparisons to other experiments for cases where the EFT is not valid.

The limits on M_* can be translated into limits on the WIMP-nucleon scattering cross section, following the Eqs. (5.1)–(5.6). As seen in Sect. 5.2, the axial-vector (D8) and tensor (D9) operators describe spin-dependent interactions, the others are spin-independent. For these comparisons the limits on M_* are recomputed at 90% CL, the corresponding values are given in Table 15.7.

Figure 15.4 presents the limits on the WIMP-nucleon scattering cross section obtained in this work in comparison to previous ATLAS results with $\sqrt{s} = 7$ TeV [11]. All limits show an improvement, it is largest for the operators D1, D5 and D8 and more moderate for D9 and D11.

Table 15.7 Observed (expected) 90% confidence level lower limits on the suppression scale M_* in GeV. The signal region used for each operator is indicated

m_χ (GeV)	90% CL limits on M_* (GeV)						
	D1, SR7	D5, SR7	D8, SR7	D9, SR8	D11, SR8	C1, SR4	C5, SR8
10	41 (42)	1031 (1034)	1013 (1017)	1871 (1894)	420 (423)	10 (10)	246 (249)
50	41 (42)	1031 (1034)	1013 (1017)	1871 (1894)	420 (423)	10 (10)	246 (249)
100	41 (41)	1032 (1035)	984 (987)	1834 (1857)	421 (424)	9 (9)	234 (237)
200	39 (39)	1016 (1019)	925 (928)	1708 (1728)	405 (408)	8 (7)	220 (222)
400	33 (33)	912 (915)	766 (769)	1419 (1435)	361 (363)	5 (5)	172 (173)
700	25 (25)	714 (716)	548 (550)	981 (991)	289 (291)	3 (2)	114 (115)
1000	18 (18)	511 (513)	362 (363)	667 (673)	221 (222)	1 (1)	72 (73)
1300	12 (12)	346 (347)	230 (231)	436 (440)	161 (162)	0 (0)	44 (44)

Fig. 15.4 Inferred 90% CL upper limits on the spin-independent WIMP-nucleon scattering cross section as a function of the WIMP mass in comparison to the previous ATLAS results at $\sqrt{s} = 7$ TeV [11]

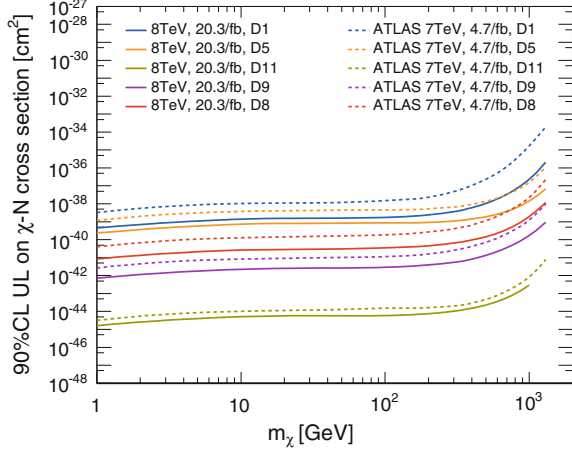
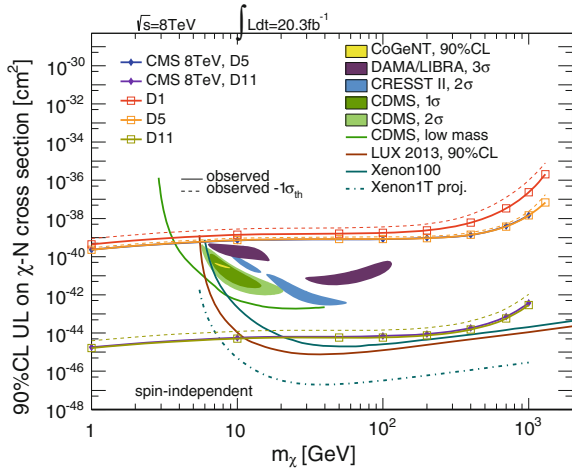


Fig. 15.5 Inferred upper limits on the spin-independent WIMP-nucleon scattering cross section as a function of the WIMP mass in comparison to other recent results from CDMS [13], SuperCDMS [14], CoGeNT [15], DAMA/LIBRA [16] (as interpreted in [17]), CRESST II [18], LUX [19], Xenon100 [20] and CMS [21]. Data courtesy of [22]



In Fig. 15.5, the converted limits for the effective operators are shown in comparison to recent results from direct detection and other collider experiments, similar to what was shown in Fig. 3.8. The results are also summarised in Table 15.8. For a more detailed discussion of the direct detection results, the reader is referred to Sect. 3.5.1. As mentioned there, in the region of WIMP masses of the order of a few GeV, the direct detection experiments suffer from kinematic suppression not allowing them to set strong limits. Here, the colliders provide stronger limits and thus valuable complementary information. The CMS results for 8 TeV [21] are displayed as solid lines with filled diamond symbols (blue and violet). They include the theoretical uncertainties, and therefore, the observed limits obtained in this work (solid lines and open squares) are shown together with the theoretical uncertainties which are indicated by dashed lines. For D5, where the impact of the theoretical uncertainties is small,

Table 15.8 Inferred 90% CL upper limits on the spin-independent WIMP-nucleon scattering cross section in cm^2

m_χ (GeV)	$\sigma_{\chi N}^{D5}$ (cm^2)	$\sigma_{\chi N}^{D11}$ (cm^2)	$\sigma_{\chi N}^{C5}$ (cm^2)
10	7.3×10^{-40} (7.2×10^{-40})	5.1×10^{-45} (4.9×10^{-45})	1.9×10^{-41} (1.8×10^{-41})
50	8.4×10^{-40} (8.3×10^{-40})	5.9×10^{-45} (5.7×10^{-45})	8.8×10^{-43} (8.4×10^{-43})
100	8.5×10^{-40} (8.4×10^{-40})	5.9×10^{-45} (5.7×10^{-45})	2.7×10^{-43} (2.6×10^{-43})
200	9.2×10^{-40} (9.1×10^{-40})	7.5×10^{-45} (7.2×10^{-45})	8.8×10^{-44} (8.5×10^{-44})
400	1.4×10^{-39} (1.4×10^{-39})	1.5×10^{-44} (1.5×10^{-44})	6×10^{-44} (5.8×10^{-44})
700	3.8×10^{-39} (3.7×10^{-39})	5.8×10^{-44} (5.5×10^{-44})	1×10^{-43} (9.6×10^{-44})
1000	1.4×10^{-38} (1.4×10^{-38})	2.9×10^{-43} (2.8×10^{-43})	3×10^{-43} (2.9×10^{-43})
1300	6.8×10^{-38} (6.8×10^{-38})	1.9×10^{-42} (1.8×10^{-42})	1.3×10^{-42} (1.2×10^{-42})

both collider experiments find almost identical limits. For D11, the limit obtained in this work is slightly weaker than the CMS limit when including the theoretical uncertainties. However, it has to be noted that the limits compared here are observed limits. While the expected and observed limits in SR7 and SR8 in this analysis are very similar, CMS observes a downward fluctuation in data in the signal region they use for the limits, yielding observed limits that are roughly 30% stronger than the expected ones. When comparing the expected limits on M_* , the results obtained in this work are approximately 8% stronger than those from CMS. D1 gives the weakest limits of the three operators considered. (There is no corresponding result from CMS at the time of writing.)

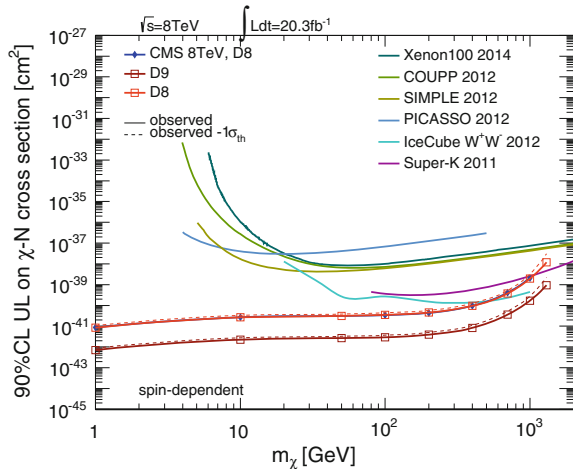
For the operator D5 (vector $q\bar{q}$ interaction), the limits are on the verge of cutting into the region with claims by other experiments but are not yet competitive. In the low mass range, however, limits can be obtained for these operators while the direct detection experiments can make no statement there. The limits for D5 are much weaker than those for the gg operator D11. D11 provides the strongest limits at low WIMP masses (below 10 GeV) and is close to becoming competitive in the higher mass range as well. But the greatest strength of the collider limits remains their coverage in the GeV mass range.

The limits for spin-dependent interaction are listed in Table 15.9 and in Fig. 15.6, the results from this work (solid lines with open squares) are compared to other collider limits from CMS [21] (blue line with diamonds) as well as to results from XENON100 [23], COUPP [24], SIMPLE [25], PICASSO [26], Super-K [27] and IceCube [28] (solid lines without markers). The collider limits are stronger by up to 4

Table 15.9 Inferred 90%CL upper limits on the spin-dependent WIMP-nucleon scattering cross section in cm^2

m_χ (GeV)	$\sigma_{\chi N}^{D8}$ (cm^2)	$\sigma_{\chi N}^{D9}$ (cm^2)
10	2.7×10^{-41} (2.6×10^{-41})	2.3×10^{-42} (2.2×10^{-42})
50	3.1×10^{-41} (3×10^{-41})	2.6×10^{-42} (2.5×10^{-42})
100	3.5×10^{-41} (3.5×10^{-41})	2.9×10^{-42} (2.8×10^{-42})
200	4.5×10^{-41} (4.5×10^{-41})	3.9×10^{-42} (3.7×10^{-42})
400	9.7×10^{-41} (9.6×10^{-41})	8.2×10^{-42} (7.9×10^{-42})
700	3.7×10^{-40} (3.6×10^{-40})	3.6×10^{-41} (3.5×10^{-41})
1000	1.9×10^{-39} (1.9×10^{-39})	1.7×10^{-40} (1.6×10^{-40})
1300	1.2×10^{-38} (1.2×10^{-38})	9.2×10^{-40} (8.9×10^{-40})

Fig. 15.6 Inferred upper limits on the spin-dependent WIMP-nucleon scattering cross section as a function of the WIMP mass in comparison to other recent results from XENON100 [23], COUPP [24], SIMPLE [25], PICASSO [26], Super-K [27], IceCube [28] and CMS [21]. Data courtesy of [22]



orders of magnitude (for the operator D9) in the mass range up to a few hundred GeV, even when taking the effect of theoretical uncertainties into account, as indicated by the dashed lines. The results for D8 found here are again almost identical to the ones from the CMS publication [21]. The same comment on the difference between expected and observed limits as for the spin-independent interactions applies here. At the time of writing there is no corresponding result for D9 by CMS.

A compilation of the ATLAS results from various mono-X search channels in terms of observed limits is shown in Fig. 15.7. The channels considered in addition to the mono-jet results from this work (solid lines with square, filled markers) are mono-W and mono-Z, both with leptonic and hadronic decays [29–31], as well as the mono-photon [32] and heavy-flavour [33] search. All results correspond to the full 2012 data set of 8 TeV data. The plot for spin-independent interactions (left) illustrates that by now there is a large number of results from the ATLAS experiment, spanning multiple orders of magnitude. Shown in blue are the limits obtained for

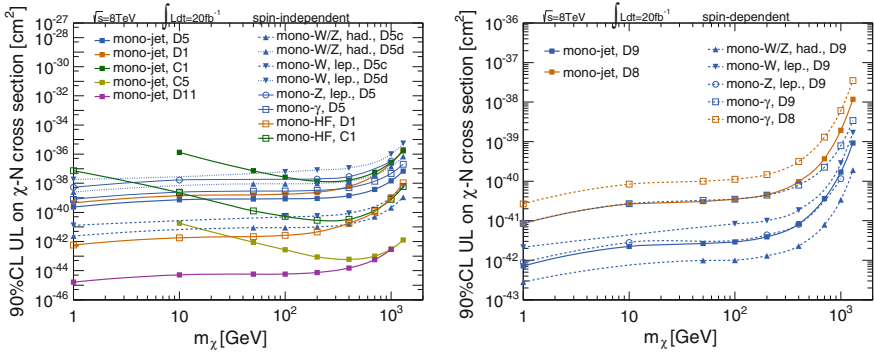


Fig. 15.7 Comparison of ATLAS mono-X observed limits for spin-independent (*left*) and spin-dependent (*right*) WIMP-nucleon scattering. Shown in comparison to the limits from this work are results from the hadronic mono- W/Z [29], the leptonic mono- W [30] and mono- Z [31], the mono-photon [32] and the heavy-flavour analysis [33]

the vector operator D5. For the analyses involving a W -boson, there are two lines each—one for constructive and one for destructive interference (labelled ‘c’ and ‘d’, respectively), depending on whether couplings to up- and down-quarks have opposite sign or not. In case of constructive interference (dashed lines), these analyses provide the most stringent limits for D5, the analysis of hadronically decaying bosons sets stronger limits than the one using leptonic decays. The latter also holds in case of destructive interference (dotted lines), but in this case the limits are weaker than the mono-jet ones. Compared to the mono-photon and the leptonic mono- Z analyses, the limits derived in this work are also stronger. For the operators involving a quark mass factor (D1 and C1, orange and green lines, respectively), the mono-jet results, which consider only light quarks, are surpassed by several orders of magnitude by the heavy-flavour analysis, as is to be expected. The gluon-gluon operators C5 (light green) and D11 (magenta) are only probed by the mono-jet analysis and set the strongest limits over the entire WIMP mass range in case of D11 and at high masses for C5. This demonstrates the usefulness of multiple search channels that each have specific strength and sensitivities to different scenarios. Depending on the character of Dark Matter, one or the other might be more sensitive.

On the right-hand side of Fig. 15.7, the limits for the spin-dependent operators from this work are compared to the results from the same set of analyses as for the spin-independent case except for the heavy-flavour search which has no competitive sensitivities to the involved operators. The limits for D8 are shown in orange and it is observed that the mono-jet limits are considerably stronger than the ones from mono-photon (open squares). This is even more the case for D9, while the limits from the leptonic mono- Z analysis (open circles) are very close to the corresponding mono-jet limits. The strongest limits are obtained in the hadronic mono- W/Z analysis, while the leptonic mono- W search obtains limits that are weaker than the mono-jet ones.

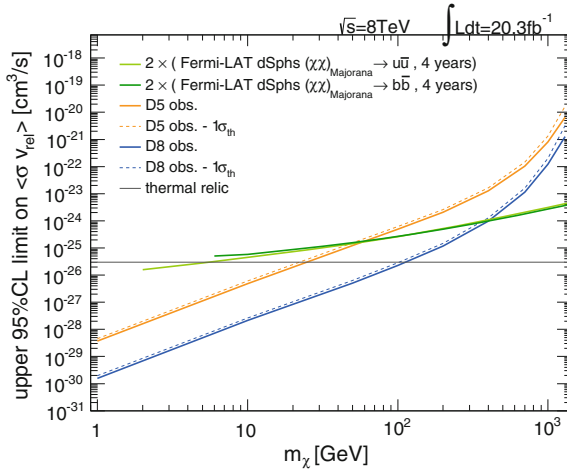


Fig. 15.8 Inferred 95 % CL upper limits on the velocity-averaged $\chi\text{-}\chi$ annihilation cross section as a function of the WIMP mass. Limits for the effective operators are calculated for annihilation into light quarks [36]. Shown in comparison are results from Fermi-LAT [34] for annihilation into $u\bar{u}$ and $b\bar{b}$. The factor of 2 accounts for the rate difference between Dirac and Majorana fermions [35]. Also shown is the annihilation cross section resulting in the observed relic density [8]

The limits on the suppression scale can also be converted into limits on the annihilation rate $\langle \sigma v_{rel} \rangle$ of two WIMPs into a quark-antiquark pair, where the product of cross section and relative velocity of the WIMPs is averaged over the dark matter velocity distribution. Formulas are given for D5 and D8 in Eqs. (5.7) and (5.8), respectively. Figure 15.8 shows the 95 % CL limits in comparison to results obtained from the observation of highly-energetic galactic gamma-rays from dwarf spheroidal satellite galaxies (dSphs) by the Fermi-LAT [34]. For the effective operator limits, both the central observed limit (solid lines) as well as the effect of the theoretical uncertainties (dashed lines) are displayed. The Fermi-LAT limits were calculated assuming the WIMPs are Majorana fermions, however, the difference in the rate compared to the case where WIMPs are Dirac fermions is a simple factor of 2. This is due to the fact that for not self-conjugated particles, σv_{rel} must be averaged over particles and antiparticle, yielding a factor of 1/2 compared to the rate for self-conjugate particles (see for example the comment on Eq. (34) of Ref. [35]). Fermi-LAT limits are shown both for annihilation into $b\bar{b}$ and $u\bar{u}$, the limits for the effective operators are for annihilation into light quarks, since the production at the collider is dominated by interactions between those. All limits assume 100 % branching fraction for WIMP annihilation into quarks. It is observed that Fermi-LAT is approximately equally sensitive to annihilation in heavy and light quarks.

The collider bounds exhibit a much stronger dependence on the dark matter mass than the indirect search limits: In the mass range considered, the collider limits vary over 9 orders of magnitude, the Fermi-LAT limits only over 2–3 orders of magnitude. For WIMP masses of 70 (400) GeV, the Fermi-LAT result is stronger than the limit

obtained for D5 (D8). Below these values, the collider limits become stronger. With higher center-of-mass energies at the LHC, the limits at higher WIMP masses are expected to improve as well.

The grey line in Fig. 15.8 presents the annihilation rate required to make up the observed relic density as measured by WMAP [8]. For dark matter masses smaller than approximately 30 (100) GeV, the collider bounds are below this value. The conclusion is analogue to the one for Fig. 15.3: The annihilation rate is too small, i.e. assuming that annihilation proceeded via the respective operator only results in a value for the relic density larger than the one from the WMAP data. Hence, other annihilation channels or operators must exist if the relic abundance is due to WIMPs of masses in this range.

The above comparisons reveal another point worth keeping in mind in the context of EFT validity: The validity typically will be less critical for small DM masses. Larger DM mass in general requires larger momentum transfer which leads to a larger fraction of events failing the requirement (5.10). In Fig. 15.5, however, it was observed that the collider limits for spin-independent interactions are most interesting at WIMP masses below 10 GeV. For the spin-dependent interactions, it was seen in Fig. 15.6 that the collider searches provide limits competitive over a large mass range. While the region of O(100 GeV) is more problematic in terms of validity, the collider limits here are much stronger than those from direct detection experiments. Even if only 10% of the original events were valid (for a given coupling), which would translate in a change of the WIMP-nucleon cross section limit by one order of magnitude, the collider limits would still be stronger in most cases. Thus, while the applicability of the EFT for LHC searches certainly has to be studied case-by-case and should be considered carefully, the conclusions and comparisons drawn here will not be altered greatly.

In the light of the concerns about the validity of the effective field theory, a natural next step—as discussed in Sects. 5.2 and 5.3—is to move towards a simplified model in which the mediator is not integrated out. One example will be discussed in the following section.

15.3.2 Simplified Model

As described in Sect. 5.3, the simplified model assumes an s -channel vector mediator with a mass M_{Med} and couplings g_χ and g_{SM} to the dark matter and Standard Model fermions, respectively. The EFT pendant to this would be the vector-operator D5, and in analogy to the suppression scale of the EFT the scale Λ is defined as $\Lambda = M_{Med}/\sqrt{g_{SM}g_\chi}$. The cross section for a given mediator mass depends on $g_\chi^2 g_{SM}^2$. In the sample generation, the value was set to $\sqrt{g_\chi g_{SM}}|_0 = 1$. The limits on the signal strength μ obtained by HistFitter in the same way as for the EFT samples can thus be translated into limits on the product of the couplings ($\sqrt{g_\chi g_{SM}}|_L$) in the following way: $\sqrt{g_\chi g_{SM}}|_L = \mu^{1/4} \sqrt{g_\chi g_{SM}}|_0 = \mu^{1/4}$. This can be used to obtain

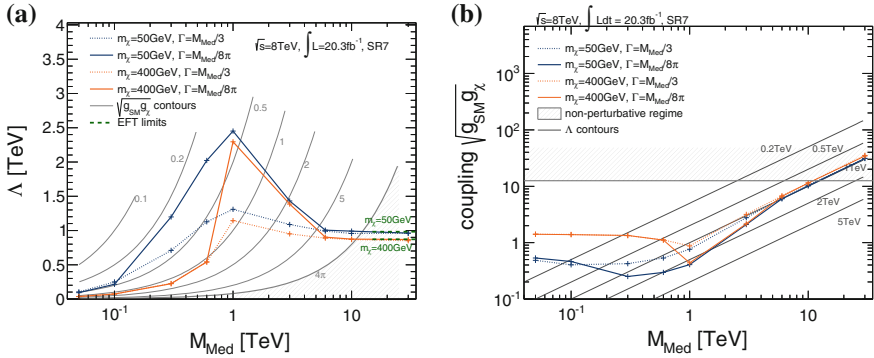


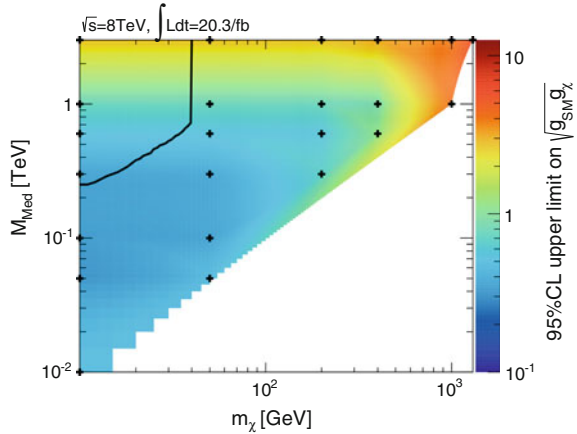
Fig. 15.9 95% CL observed lower limits from SR7 on the scale Λ (a) and upper limit on the coupling (b) in the simplified model as a function of the mediator mass. *Blue lines* are for $m_\chi = 50$ GeV, *orange lines* for $m_\chi = 400$ GeV. Limits for $\Gamma = M_{Med}/3$ are shown as *dashed*, limits for $\Gamma = M_{Med}/(8\pi)$ as *solid* lines. *Grey lines* give the contours of constant $\sqrt{g_\chi g_{SM}}$ (a) and constant Λ (b). The non-perturbative regime with couplings larger than 4π is indicated as a *dark shaded area*

the corresponding limit on Λ . The observed limits are presented in Fig. 15.9a as a function of the mediator mass for two different WIMP masses (50 and 400 GeV) and both choices of the width of the mediator, Γ . No theoretical uncertainties are shown in these plots since they are not necessary for the points that are to be illustrated and discussed here.

Three regions can be distinguished in Fig. 15.9a: At mediator masses below twice the WIMP mass, the mediator has to be produced off-shell and hence cross sections are low and the limits are weak. Once the mediator mass is of the order of $2m_\chi$ the limits start to become stronger and show a resonant-like peak around 1 TeV.⁵ The peak is more pronounced for mediators with a smaller width, as is to be expected. Beyond that, the cross sections (and accordingly the limits) decrease again, on the one hand because the mediator has to be off-shell again, on the other hand because the mediator mass approaches the maximum centre-of-mass energy. This second effect is clearly visible in the third regime, above roughly 6 TeV: The limits stay almost constant, illustrating the transition to a contact interaction with a very heavy mediator, as in the EFT. For comparison, the limits obtained for the effective vector-operator are shown as well, underlining the analogy. It should, however, be noted that for the highest mediator masses the obtained limits are too weak, resulting in couplings larger than 4π , as can also be seen from Fig. 15.9b, which shows the upper limits on the couplings. For low mediator masses the couplings are of the order of 1 and below, for mediator masses between 1 and 10 TeV they begin to approach the perturbativity boundary, surpassing it for even larger mediator masses. This means that the analysis

⁵The actual maximum will most likely be between 1 and 3 TeV and will be at different values for the different WIMP masses, but no samples for mediator masses between 1 and 3 TeV were available at the time of writing.

Fig. 15.10 95 % CL upper limits on the coupling in the simplified model as a function of the mediator and WIMP mass. The grid points used are marked by *black crosses*. The *black line* indicates where the lower limits derived from the relic density become larger than the upper limits obtained in this work. Values of $M_{Med} < m_\chi$ are not considered



is not sensitive enough to make sensible statements about this parameter space. It also illustrates again the question of validity of the effective theory: If the mediator is too heavy (above 10 TeV), the limits obtained with the current sensitivity would require couplings beyond what is possible in a perturbative theory.

While Fig. 15.9a is useful for illustrating the different regimes and the transition to the contact interaction, the scale Λ is not actually a parameter of the simplified model and the information contained in Fig. 15.9a is equivalent to that in Fig. 15.9b. The coupling is the actual model parameter that limits are set on. In Fig. 15.10, therefore, the 95 % CL upper limit on the coupling is shown for a grid of mediator and WIMP masses. The width considered here is $\Gamma = M_{Med}/3$. The grid points are indicated by black crosses, the colours in between are an automatic extrapolation. The limits for each of the grid points (and also all other sample points) are given in the appendix (Table B.16). The lower right half of the grid parameter space was not populated since no corresponding simulation samples were available at the time of writing. However, in this case, the mediator would be lighter than the WIMP, the process hence strongly suppressed and the limits correspondingly weak. Thus, the potentially more interesting part of the parameter space has been covered by the available samples. For mediator masses below 1 TeV and WIMP masses below 400 GeV the couplings are of the order of 1 or below. They increase both with mediator as well as with WIMP mass, in the most extreme case considered here ($M_{Med} = 3$ TeV, $m_\chi = 1.3$ TeV), the limit is 5.4. For the mass ranges considered here, the couplings all remain well within the region of perturbativity.

The black line in Fig. 15.10 demarcates where the lower limits derived from the relic density [6] become larger than the upper limits derived in this work. This poses a conflict with the relic density measurement in the upper left corner of the plot.

15.4 Results Summary

No significant deviation between background expectations and observed data is found in either of the signal regions. The largest systematic uncertainty on the total background estimate in many regions, especially the ones used for the limit setting, is the uncertainty on top and diboson processes, which is at the same level as the statistical uncertainties. The transfer factor method and combination of $Z(\rightarrow \nu\bar{\nu}) + \text{jets}$ estimates reduces the remaining uncertainties considerably, to below 1% in many cases.

Limits on the suppression scale have been derived for five effective operators for Dirac fermionic Dark Matter and two operators for scalar Dark Matter, which are new compared to the previous version of the mono-jet analysis [11]. Following EFT validity considerations described in detail in [6], the latter are not considered in comparisons with other experiments. In comparison to the previous 7 TeV ATLAS results [11], the limits obtained in this work improve for all operators.

For spin-independent WIMP-nucleon scattering, collider limits provide complementary information in the region of low WIMP mass ($< 10 \text{ GeV}$), where the direct detection experiments are not sensitive. The observed collider bounds are very similar for CMS and the analysis presented in this work. The expected limits on M_* found in this work, however, are about 8% stronger than those from CMS.

In the plane of spin-dependent WIMP-nucleon scattering, the collider bounds are competitive over a large mass range, surpassing most of the direct detection experiments by several orders of magnitude. The CMS results are again very similar to the limits found in this work.

The limits on the annihilation cross section obtained in this analysis are stronger than the ones from the Fermi-LAT [34] below WIMP masses of $\mathcal{O}(100 \text{ GeV})$.

These observations will not change greatly under the rescaling procedure to take into account the fraction of valid events for a specific coupling choice, which was therefore not performed. Nevertheless, it is instructive to also consider simplified models where the question of validity does not arise. One such model is considered here, assuming an s -channel vector mediator. Limits are derived on the coupling product and the scale $\Lambda \equiv M_{Med}/\sqrt{g_{SM}g_\chi}$. The strongest limits are obtained for mediator masses at the TeV scale, for very heavy mediators the EFT limits are reproduced. In regions of WIMP mass below approximately 50 GeV and mediator masses above 300 GeV, the upper limits on the couplings obtained in this work are in conflict with the lower bounds derived from the relic density.

References

1. Wenninger J (2013) Energy calibration of the LHC beams at 4 TeV. Technical report. CERN-ATS-2013-040. Geneva: CERN
2. Whalley MR, Bourilkov D, Group RC (2005) The Les Houches accord PDFs (LHAPDF) and LHAGLUE. ArXiv Pre-Prints. [arXiv:hep-ph/0508110](https://arxiv.org/abs/hep-ph/0508110) [hep-ph]

3. Botje M et al (2011) The PDF4LHC working group interim recommendations. ArXiv Pre-Prints. [arXiv:1101.0538](https://arxiv.org/abs/1101.0538) [hep-ph]
4. Campbell JM, Huston J, Stirling W (2007) Hard interactions of quarks and gluons: a primer for LHC physics. Rep Prog Phys 70:89. doi:[10.1088/0034-4885/70/1/R02](https://doi.org/10.1088/0034-4885/70/1/R02). [arXiv:hep-ph/0611148](https://arxiv.org/abs/hep-ph/0611148) [hep-ph]
5. Skands PZ (2010) Tuning Monte Carlo generators: the Perugia tunes. Phys Rev D82:074018. doi:[10.1103/PhysRevD.82.074018](https://doi.org/10.1103/PhysRevD.82.074018). [arXiv:1005.3457](https://arxiv.org/abs/1005.3457) [hep-ph]
6. Abdallah J et al (2013) Search for new phenomena with mono-jet plus missing transverse energy signature in proton-proton collisions at $\sqrt{s} = 8\text{TeV}$ with the ATLAS detector. Technical report. ATL-COM-PHYS-2013-1578. Geneva: CERN
7. Goodman J et al (2010) Constraints on dark matter from colliders. Phys Rev D82:116010. doi:[10.1103/PhysRevD.82.116010](https://doi.org/10.1103/PhysRevD.82.116010). [arXiv:1008.1783](https://arxiv.org/abs/1008.1783) [hep-ph]
8. Komatsu E et al (2011) Seven-year Wilkinson microwave anisotropy probe (WMAP) Observations: cosmological interpretation. Astrophys J Suppl Ser 192.2:18. [arXiv:1001.4538](https://arxiv.org/abs/1001.4538) [astro-ph.CO]. <http://stacks.iop.org/0067-0049/192/i=2/a=18>
9. The PLANCK collaboration (2013) Planck 2013 results. XVI. Cosmological parameters. ArXiv Pre-Prints. [arXiv:1303.5076](https://arxiv.org/abs/1303.5076) [astro-ph.CO]
10. Tait T, Private communication
11. The ATLAS collaboration (2013) Search for dark matter candidates and large extra dimensions in events with a jet and missing transverse momentum with the ATLAS detector. JHEP 1304:075. doi:[10.1007/JHEP04\(2013\)075](https://doi.org/10.1007/JHEP04(2013)075). [arXiv:1210.4491](https://arxiv.org/abs/1210.4491) [hep-ex]
12. The ATLAS Collaboration (2014) Sensitivity to WIMP dark matter in the final states containing jets and missing transverse momentum with the ATLAS detector at 14 TeV LHC. Technical report. ATL-PHYS-PUB-2014-007. Geneva: CERN
13. CDMS Collaboration (2013) Silicon detector dark matter results from the final exposure of CDMS II. Phys Rev Lett 111:251301. doi:[10.1103/PhysRevLett.111.251301](https://doi.org/10.1103/PhysRevLett.111.251301). [arXiv:1304.4279](https://arxiv.org/abs/1304.4279) [hep-ex]
14. Agnese R et al (2014) Search for low-mass WIMPs with SuperCDMS. Phys Rev Lett 112:241302. doi:[10.1103/PhysRevLett.112.241302](https://doi.org/10.1103/PhysRevLett.112.241302). [arXiv:1402.7137](https://arxiv.org/abs/1402.7137) [hep-ex]
15. Aalseth CE et al (2013) CoGeNT: a search for low-mass dark matter using p-type point contact germanium detectors. PRD 88.1:012002. doi:[10.1103/PhysRevD.88.012002](https://doi.org/10.1103/PhysRevD.88.012002). [arXiv:1208.5737](https://arxiv.org/abs/1208.5737) [astro-ph.CO]
16. Bernabei R et al (2008) First results from DAMA/LIBRA and the combined results with DAMA/NaI. Eur Phys J C56:333–355. doi:[10.1140/epjc/s10052-008-0662-y](https://doi.org/10.1140/epjc/s10052-008-0662-y). [arXiv:0804.2741](https://arxiv.org/abs/0804.2741) [astro-ph]
17. Savage C et al (2009) Compatibility of DAMA/LIBRA dark matter detection with other searches. JCAP 0904:010. doi:[10.1088/1475-7516/2009/04/010](https://doi.org/10.1088/1475-7516/2009/04/010). [arXiv:0808.3607](https://arxiv.org/abs/0808.3607) [astro-ph]
18. Angloher G et al (2012) Results from 730 kg days of the CRESST-II dark matter search. Eur Phys J C 72:1971. doi:[10.1140/epjc/s10052-012-1971-8](https://doi.org/10.1140/epjc/s10052-012-1971-8). [arXiv:1109.0702](https://arxiv.org/abs/1109.0702) [astro-ph.CO]
19. Akerib D et al (2014) First results from the LUX dark matter experiment at the Sanford underground research facility. Phys Rev Lett 112:091303. doi:[10.1103/PhysRevLett.112.091303](https://doi.org/10.1103/PhysRevLett.112.091303). [arXiv:1310.8214](https://arxiv.org/abs/1310.8214) [astro-ph.CO]
20. Aprile E et al (2012) Dark matter results from 225 live days of XENON100 data. Phys Rev Lett 109.18:181301. doi:[10.1103/PhysRevLett.109.181301](https://doi.org/10.1103/PhysRevLett.109.181301). [arXiv:1207.5988](https://arxiv.org/abs/1207.5988) [astro-ph.CO]
21. The CMS collaboration (2014) Search for dark matter, extra dimensions, and unparticles in monojet events in proton-proton collisions at $\sqrt{s} = 8\text{ TeV}$. ArXiv Pre-Prints. [arXiv:1408.3583](https://arxiv.org/abs/1408.3583) [hep-ex]
22. Gaitskell RJ, Mandic V (2014) The dark matter community website. <http://dmtools.brown.edu/>. Accessed July 2014
23. Aprile E et al (2013) Limits on spin-dependent WIMP-nucleon cross sections from 225 live days of XENON100 data. Phys Rev Lett 111.2:021301. doi:[10.1103/PhysRevLett.111.021301](https://doi.org/10.1103/PhysRevLett.111.021301). [arXiv:1301.6620](https://arxiv.org/abs/1301.6620) [astro-ph.CO]
24. Behnke E et al (2012) First dark matter search results from a 4-kg CF3I bubble chamber operated in a deep underground site. Phys Rev D 86.5:052001. doi:[10.1103/PhysRevD.86.052001](https://doi.org/10.1103/PhysRevD.86.052001). [arXiv:1204.3094](https://arxiv.org/abs/1204.3094) [astro-ph.CO]

25. Felizardo M et al (2012) Final analysis and results of the phase II SIMPLE dark matter search. *Phys Rev Lett* 108.20:201302. doi:[10.1103/PhysRevLett.108.201302](https://doi.org/10.1103/PhysRevLett.108.201302). [arXiv:1106.3014](https://arxiv.org/abs/1106.3014)
26. Archambault S et al (2012) Constraints on low-mass WIMP interactions on 19F from PICASSO. *Phys Lett B* 711:153–161. doi:[10.1016/j.physletb.2012.03.078](https://doi.org/10.1016/j.physletb.2012.03.078). [arXiv:1202.1240](https://arxiv.org/abs/1202.1240) [hep-ex]
27. The Super-Kamiokande collaboration (2011) An indirect search for weakly interacting massive particles in the sun using 3109.6 days of upward-going muons in Super-Kamiokande. *Astrophys J* 742:78. doi:[10.1088/0004-637X/742/2/78](https://doi.org/10.1088/0004-637X/742/2/78). [arXiv:1108.3384](https://arxiv.org/abs/1108.3384) [astro-ph.HE]
28. The IceCube collaboration (2012) Search for dark matter annihilations in the sun with the 79-string IceCube detector. ArXiv Pre-Prints. [arXiv:1212.4097](https://arxiv.org/abs/1212.4097) [astro-ph.HE]
29. The ATLAS collaboration (2014) Search for dark matter in events with a hadronically decaying W or Z Boson and missing transverse momentum in pp collisions at ps = 8 TeV with the ATLAS detector. *Phys Rev Lett* 112:041802. doi:[10.1103/PhysRevLett.112.041802](https://doi.org/10.1103/PhysRevLett.112.041802)
30. The ATLAS collaboration (2014) Search for new particles in events with one lepton and missing transverse momentum in pp collisions at ps = 8 TeV with the ATLAS detector. *JHEP* 1409:037. doi:[10.1007/JHEP09\(2014\)037](https://doi.org/10.1007/JHEP09(2014)037). [arXiv:1407.7494](https://arxiv.org/abs/1407.7494) [hep-ex]
31. The ATLAS collaboration (2014) Search for dark matter in events with a Z Boson and missing transverse momentum in pp collisions at ps = 8 TeV with the ATLAS detector. *Phys Rev D* 90:012004. doi:[10.1103/PhysRevD.90.012004](https://doi.org/10.1103/PhysRevD.90.012004)
32. The ATLAS collaboration (2015) Search for new phenomena in events with a photon and missing transverse momentum in pp collisions at ps = 8 TeV with the ATLAS detector. *Phys Rev D* 91:012008. doi:[10.1103/PhysRevD.91.012008](https://doi.org/10.1103/PhysRevD.91.012008)
33. The ATLAS collaboration (2015) Search for dark matter in events with heavy quarks and missing transverse momentum in pp collisions with the ATLAS detector. *Eur Phys J C* 75.2:92. issn:1434-6044. doi:[10.1140/epjc/s10052-015-3306-z](https://doi.org/10.1140/epjc/s10052-015-3306-z)
34. Ackermann M et al (2014) Dark matter constraints from observations of 25 Milky Way satellite galaxies with the fermi large area telescope. *Phys Rev D* 89:042001. doi:[10.1103/PhysRevD.89.042001](https://doi.org/10.1103/PhysRevD.89.042001). [arXiv:1310.0828](https://arxiv.org/abs/1310.0828) [astro-ph.HE]
35. Cirelli M et al (2011) PPPC 4 DM ID: a poor particle physicist cookbook for dark matter indirect detection. *JCAP* 1103:051. doi:[10.1088/1475-7516/2012/10/E01](https://doi.org/10.1088/1475-7516/2012/10/E01), doi:[10.1088/1475-7516/2011/03/051](https://doi.org/10.1088/1475-7516/2011/03/051). [arXiv:1012.4515](https://arxiv.org/abs/1012.4515) [hep-ph]
36. Fox PJ et al (2012) Missing energy signatures of dark matter at the LHC. *Phys Rev D* 85:056011. doi:[10.1103/PhysRevD.85.056011](https://doi.org/10.1103/PhysRevD.85.056011). [arXiv:1109.4398](https://arxiv.org/abs/1109.4398) [hep-ph]

Chapter 16

Prospects with Future LHC Data

In the light of the LHC run-II starting in early 2015, a simulation study has been performed to investigate the sensitivity of the mono-jet analysis to Dark Matter pair production at 14 TeV.¹ The simulation based estimation of the Standard Model backgrounds and signal yields is summarised in Sect. 16.1.² In Sect. 16.2, the expected limits derived in the EFT framework for the operator D5 and WIMP masses of $m_\chi = 50$ GeV and $m_\chi = 400$ GeV are presented, and in Sect. 16.3 the results for the same simplified model as discussed in Sect. 5.3 are described.

16.1 Estimation of Event Yields

At the time the study was conducted, there was only a limited set of simulation samples with $\sqrt{s} = 14$ TeV available. This necessitated a number of approximations to be made in order to obtain the background estimate at 14 TeV. Moreover, a few changes compared to the 8 TeV analysis are required to account for the different running conditions in run-II. All samples used were produced with the full ATLAS detector simulation.

For 14 TeV, only simulations for $W^\pm(\rightarrow \tau^\pm \bar{\nu})$ +jets, $W^\pm(\rightarrow \mu^\pm \bar{\nu})$ +jets and $t\bar{t}$ were available. The $Z(\rightarrow \nu\bar{\nu})$ +jets background is emulated from $W^\pm(\rightarrow \mu^\pm \bar{\nu})$ +jets events, adjusting the cross section accordingly. For $W^\pm(\rightarrow e^\pm \bar{\nu})$ +jets, it is assumed that the relative contributions of $W^\pm(\rightarrow \mu^\pm \bar{\nu})$ +jets and $W^\pm(\rightarrow e^\pm \bar{\nu})$ +jets will stay approximately the same as for 8 TeV. Thus, the $W^\pm(\rightarrow e^\pm \bar{\nu})$ +jets contribution is estimated by scaling the $W^\pm(\rightarrow \mu^\pm \bar{\nu})$ +jets background by the ratio at 8 TeV. Similarly,

¹The initial centre-of-mass energy in 2015 will be 13 TeV, which was not yet decided at the time of the study. However, this will not alter the general conclusions obtained.

²This part of the study was not done by the author personally. However, all results and plots shown in the following sections are produced by the author.

Table 16.1 Centre-of-mass energy, average number of interactions per bunch crossing $\langle\mu\rangle$ and integrated luminosity \mathcal{L} assumed for each upgrade phase considered. The years in brackets indicate the shutdown periods needed for the upgrade, not the duration of data taking [1]

	\sqrt{s} (TeV)	$\langle\mu\rangle$	\mathcal{L} (fb $^{-1}$)
2012	8	20	20
After phase-0 upgrade (2015)	14	60	25
After phase-1 upgrade (2018)	14	60	300
After phase-2 upgrade (2022)	14	140	3000

the total top contribution is obtained by scaling the $t\bar{t}$ background according to the relative amount of single top and $t\bar{t}$ at 8 TeV. Other backgrounds ($Z(\rightarrow \ell^+\ell^-)+$ jets, multi-jet, NCB, diboson) are assumed to be negligible. This is certainly valid to a good approximation—especially at large E_T^{miss} —for the first three, which contribute significantly less than 1% in these regions. The diboson processes are of slightly larger at 8 TeV and are expected to be at a similar level at 14 TeV. Thus, omitting the diboson contribution is still considered a justified approximation.

Different pile-up conditions in terms of average number of interactions per bunch-crossing, $\langle\mu\rangle$, and plausible luminosity milestones are considered, as summarised in Table 16.1.

At the time the 14 TeV study was performed, the selection for the final 8 TeV mono-jet analysis [2] (which is the same as used in this work) was not finalised yet, and instead a selection close to what was done for previous versions of the analysis [3, 4] has been adopted. In the study described here, the background estimate for 8 TeV is also taken from simulation only for simplicity and to allow for a more straight forward comparison of the 8 and 14 TeV results. The selection is summarised in Table 16.2 and details are given in [1]. Here, just the most important points are highlighted.

No trigger is required for the 14 TeV study as it is not clear yet what the trigger thresholds will be. Instead, the lowest signal region thresholds were set to 300 GeV for leading jet p_T and 400 GeV for E_T^{miss} , to be in the regime where the triggers will most likely be fully efficient. No data quality requirements—except of at least one primary vertex (with more than 2 tracks)—are applied for the 14 TeV samples as there is no detailed information on the state and performance of the detector during run-II yet. Similarly, there were no recommended standard lepton definitions for 14 TeV yet, but the selection efficiencies are expected to stay the same [5, 6]. Therefore, for the 14 TeV selection no cuts are actually applied to the leptons but the number of events is scaled according to the efficiencies estimated for 8 TeV (as a function of E_T^{miss}).

In the 14 TeV samples, jet properties and E_T^{miss} at reconstruction level are obtained by smearing the final state particle-level quantities depending on the pile-up scenario, to emulate the reconstruction and energy calibration [5, 6]. The smearing factors for

Table 16.2 Event selection for 8 and 14 TeV [1]

	$\sqrt{s} = 8 \text{ TeV}$	$\sqrt{s} = 14 \text{ TeV}$
Data quality	E_T^{miss} trigger primary vertex jet cleaning	Primary vertex
Lepton veto	Muons: $p_T > 7 \text{ GeV}$, $ \eta < 2.5$	Emulated using lepton selection efficiency from 8 TeV
	Electrons: $p_T > 7 \text{ GeV}$, $ \eta < 2.47$	
Jet and E_T^{miss} cuts	Jet definition: $p_T > 30 \text{ GeV}$, $ \eta < 4.5$	$p_T > 50 \text{ GeV}$, $ \eta < 3.6$
	Leading jet: $p_T > 300 \text{ GeV}$, $ \eta < 2.0$ $E_T^{\text{miss}} > 400, 600, 800 \text{ GeV}$ $\Delta\phi(\text{jet}, E_T^{\text{miss}}) > 0.5$ $N_{\text{jet}} < 3$	

jets are only provided up to $|\eta| < 3.6$ because the performance of jet reconstruction in the forward region is difficult to predict precisely. Thus, jets are only considered for the more central region in pseudo-rapidity. The minimum jet p_T threshold is increased to 50 GeV for 14 TeV to ensure the same level of pile-up suppression as was achieved at 8 TeV.

As in the previous mono-jet analyses, a veto on events with more than two jets is applied and a looser cut with respect to what is used in this work on the minimal azimuthal separation of 0.5 is used.

The resulting event yields for 20 fb^{-1} at both 8 and 14 TeV for the two EFT samples and the $Z(\rightarrow \nu\bar{\nu})$ +jets background are listed in Table 16.3. The event yields increase significantly with higher centre-of-mass energy and this increase is more pronounced for regions of higher E_T^{miss} and stronger for the signal process than for the main $Z(\rightarrow \nu\bar{\nu})$ +jets background. This already indicates two trends: the sensitivity can be expected to improve with the higher centre-of-mass energy and the gain will be largest at high E_T^{miss} . This will be quantified more in the next section.

16.2 Reach of the Mono-Jet Search in the EFT Framework

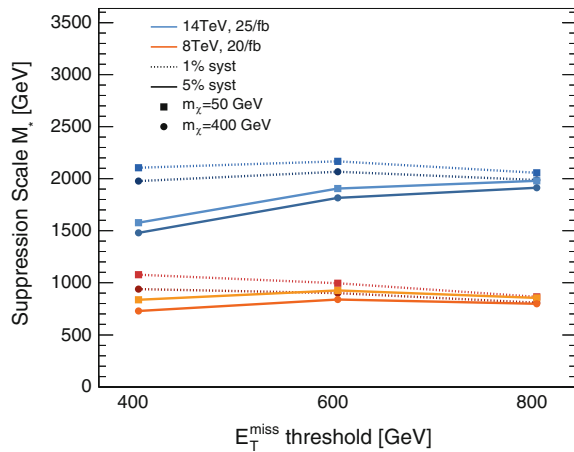
Based on the background estimation outlined above, 95 % CL limits on the suppression scale are calculated with the same framework as used for the limit determination in Sect. 15.3. Different scenarios for the total background systematic uncertainty are considered: A plausible value of 5 % and the assumption for an ultimate precision of 1 %. The luminosity uncertainty is omitted for the background as in the analysis of run-II data again a data driven approach for the background estimation will be used. Figure 16.1 compares the limits for the two signal points (squares and circles, respectively) for both centre-of-mass energies: the 8 TeV results are displayed in

Table 16.3 The number of events in Monte Carlo simulation for the dominant background from $Z(\rightarrow \nu\bar{\nu})+\text{jets}$ and Dark Matter signal processes assuming the D5 operator with the suppression scale $M_* = 1 \text{ TeV}$

		$\sqrt{s} = 8 \text{ TeV}$ $L = 20 \text{ fb}^{-1}$	$\sqrt{s} = 14 \text{ TeV } L = 20 \text{ fb}^{-1}$	
			Phase-I $\mu = 60$	Phase-II $\mu = 140$
$E_T^{\text{miss}} > 400 \text{ GeV}$	$Z(\rightarrow \nu\bar{\nu})+\text{jets}$	2800	3600	3900
	D5, $m_\chi = 50 \text{ GeV}$	200	3300	3300
	D5, $m_\chi = 400 \text{ GeV}$	120	2500	2600
$E_T^{\text{miss}} > 600 \text{ GeV}$	$Z(\rightarrow \nu\bar{\nu})+\text{jets}$	260	510	580
	D5, $m_\chi = 50 \text{ GeV}$	39	1100	1100
	D5, $m_\chi = 400 \text{ GeV}$	26	910	960
$E_T^{\text{miss}} > 800 \text{ GeV}$	$Z(\rightarrow \nu\bar{\nu})+\text{jets}$	37	100	110
	D5, $m_\chi = 50 \text{ GeV}$	8.5	390	400
	D5, $m_\chi = 400 \text{ GeV}$	6.6	340	350

Equivalents of 20 fb^{-1} are compared in different ATLAS upgrade phases. All numbers are given with a precision of two significant digits [1]

Fig. 16.1 Projected EFT limits for 20 fb^{-1} of 8 TeV (orange) and 25 fb^{-1} of 14 TeV (blue) data. The solid lines correspond to the assumption of 5% systematic uncertainty, the dashed lines to 1%. Different WIMP masses are indicated by different marker symbols: The squares denote $m_\chi = 50 \text{ GeV}$, the circles $m_\chi = 400 \text{ GeV}$. The plots is identical to the ones in Ref. [1], except for notation and style changes



orange colours, the ones for 14 TeV in blue. In both cases, the integrated luminosity corresponds to one year of data taking, i.e. 20 fb^{-1} for 8 TeV and 25 fb^{-1} for 14 TeV. Solid lines indicate 5% total systematic, dashed lines 1%.

The plot demonstrates that the behaviour for both WIMP masses is very similar for all scenarios. Comparing the different colours shows that the increase in centre-of-mass energy will lead to an increase in the limits by roughly a factor of two. The gain from reducing systematic uncertainties depends strongly on the signal region considered: At the lowest E_T^{miss} cut, where the expected number of events is fairly large, the measurement is dominated by systematic uncertainties and therefore a considerable gain in sensitivity is observed for reduced uncertainties. This is more pronounced at

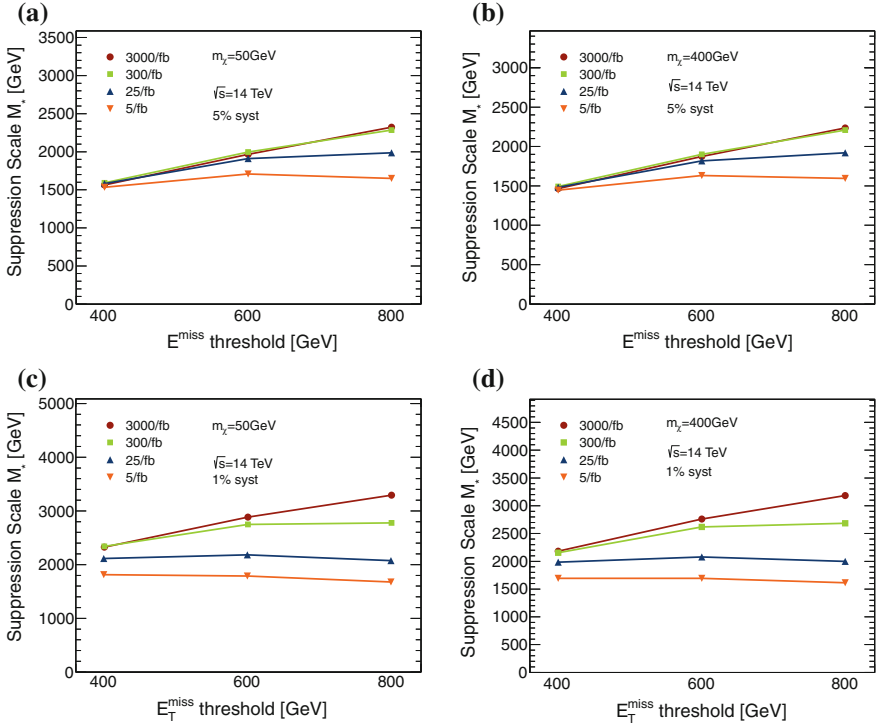


Fig. 16.2 Limit projection in the EFT framework for different integrated luminosities of 14 TeV data in the 3 signal regions. The *top* plots are for the assumption of 5% systematic uncertainty, the *bottom* plots for 1% systematic uncertainty. On the *left-hand side* are the plots for a WIMP mass of $m_\chi = 50$ GeV, on the *right-hand side* for $m_\chi = 400$ GeV. The plots are identical to the ones in Ref. [1], except for notation and style changes

14 TeV since here the first region suffers even less from statistical uncertainties. With increasing E_T^{miss} cut, the benefit is diminished as the results become statistically limited. For a total systematic uncertainty of 1%, the best limits are obtained in the first region for 8 TeV and in the second region for 14 TeV, mirroring the influence of the statistical uncertainties. With a total systematic uncertainty of 5%, the best limits are obtained in SR2 (SR3) for 8 TeV (14 TeV). Thus, an additional improvement in the high E_T^{miss} regions can be expected from accumulating more integrated luminosity.

This is found to be confirmed in the projections presented in Fig. 16.2a which shows the change in the limits when increasing the collected data set. Curves are shown for 5 fb^{-1} , corresponding to the first few months of data taking in 2015, and for the three milestones of 25, 300, and 3000 fb^{-1} listed in Table 16.1. The left hand side shows the expected limits for a WIMP mass of 50 GeV, the right hand side for 400 GeV, the top row is for a total systematic uncertainty of 5% and the bottom row for 1%. Again, the general behaviour is found to be mostly independent of the WIMP mass. For a 5% systematic uncertainty, it is observed that increasing the

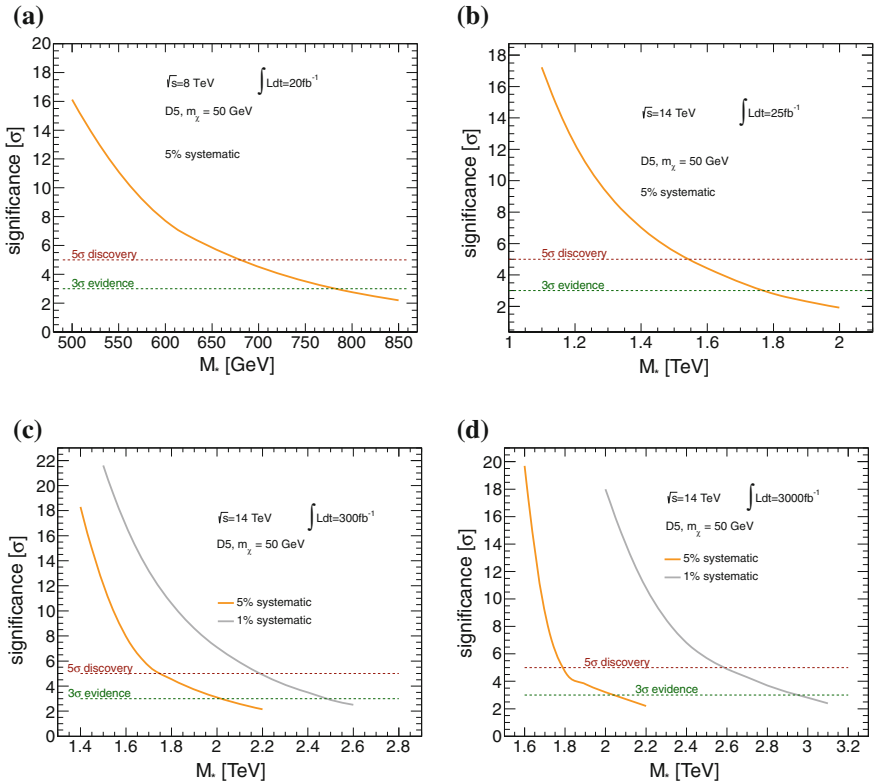


Fig. 16.3 Projected expected significance of a signal as a function of the suppression scale M_* for 20fb^{-1} of 8 TeV data (a), as well as for 25fb^{-1} (b), 300fb^{-1} (c) and 3000fb^{-1} (d) at 14 TeV. 5σ (red) and 3σ (green) are indicated as dashed lines. For 300fb^{-1} and 3000fb^{-1} , two different systematic uncertainties are considered: 5% (orange) and 1% (grey). The plots (b)–(d) are identical to the ones in Ref. [1], except for notation and style changes, (a) was produced only for this work

luminosity up to 300fb^{-1} yields higher sensitivity by roughly a factor of 1.5 in the highest signal region. For $E_T^{\text{miss}} > 600$ GeV the increase is less significant and for the lowest region there is nothing to be gained by gathering more data. It is interesting to note that the limits do not improve further beyond an accumulated luminosity of 300fb^{-1} for the signal regions considered here, not even at $E_T^{\text{miss}} > 800$ GeV. However, with more data, regions of even higher E_T^{miss} become populated as well such that signal regions with tighter lower cuts on the E_T^{miss} could be used and might provide stronger limits. In addition, reducing the systematic uncertainty also leads to a slight additional improvement especially at large E_T^{miss} , as can be seen from the lower plots in Fig. 16.2.

Another way to quantify the sensitivity is to investigate which model parameters would lead to a 5σ discovery at a given integrated luminosity by performing corresponding hypothesis tests (cf. Sect. 10.4) for different values of the parameters. This

has been studied for a WIMP mass of 50 GeV (as seen before the sensitivity has no strong mass dependence for the two values considered here) by scanning the value of the suppression scale. The results are presented in Fig. 16.3 in terms of the obtained significance as a function of the suppression scale M_* for SR3. Figure 16.3a shows that for 20 fb^{-1} of 8 TeV data, the discovery potential reaches up to roughly 700 GeV. The luminosities considered for 14 TeV in Fig. 16.3b–d are again the three milestone values from Table 16.1. Assuming a 5% systematic uncertainty for the first year of data taking in run-II the LHC could detect a signal within the EFT framework up to a value of $M_* \sim 1.5 \text{ TeV}$. With 300 fb^{-1} this reach is extended to about 1.8 TeV. Again, for the case of 5% systematic, no further improvement is obtained with more luminosity. Additional sensitivity might be achieved, however, by extending the search regions to higher E_T^{miss} . If ultimately a systematic uncertainty of 1% is reached, the range will be extended to $M_* \sim 2.2$ and $M_* \sim 2.6 \text{ TeV}$ for 300 and 3000 fb^{-1} , respectively.

16.3 Comparison to a Simplified Model

In all of the studies discussed in the previous section, full validity of the EFT is assumed. The validity was investigated in the same fashion as outlined in Sect. 5.2.1. It was found that the theory is valid for couplings above π , which leaves a reasonable fraction of phase space. However, given the concerns that have been raised with respect to the use of an EFT, the results of the 14 TeV simulation study are also interpreted in terms of the simplified model introduced in Sect. 5.3.

Figure 16.4 shows the limits on $\Lambda = M_{Med} / \sqrt{g_{SM} g_\chi}$ as a function of the mediator mass for the first signal region ($E_T^{\text{miss}} > 400 \text{ GeV}$). The left plot is for 8 TeV, the right one for 14 TeV, both correspond to one year of data taking, 20 and 25 fb^{-1} . The general features are the same as discussed for Fig. 15.9: At low mediator masses the production cross section is small and hence limits are weak, a resonant enhancement is obtained for intermediate mediator masses and for high mediator masses the EFT limits are reproduced. Here, the focus is on the comparison between the results for 8 and 14 TeV. As was observed for the EFT, limits improve by roughly a factor of two. Moreover, the mediator mass for which the strongest limits are obtained shifts to higher values, as is to be expected for an increase in the average partonic centre-of-mass energy.

Figure 16.5 presents the corresponding limits on the coupling strengths. It is observed that at 8 TeV, the limits begin to deteriorate quickly above a mediator mass of roughly 1 TeV. For 14 TeV, this is shifted to about 1.2 TeV. In all cases, the coupling limits remain well below the 4π boundary for perturbativity.

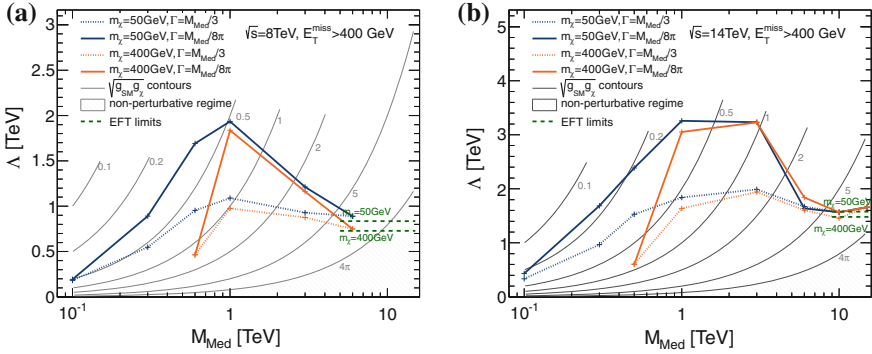


Fig. 16.4 Limits on the scale Λ in the simplified model as a function of the mediator mass, M_{Med} , at 8 TeV (a) and 14 TeV (b). Two WIMP masses are considered: $m_\chi = 50\text{ GeV}$ (blue) and $m_\chi = 400\text{ GeV}$ (orange). The dashed lines are for a width $\Gamma = M_{Med}/3$, the solid lines for $\Gamma = M_{Med}/8\pi$. The contours of constant coupling are shown as grey lines. The beginning of the non-perturbative regime is indicated by the shaded area. The plots are identical to the ones in Ref. [1], except for notation and style changes

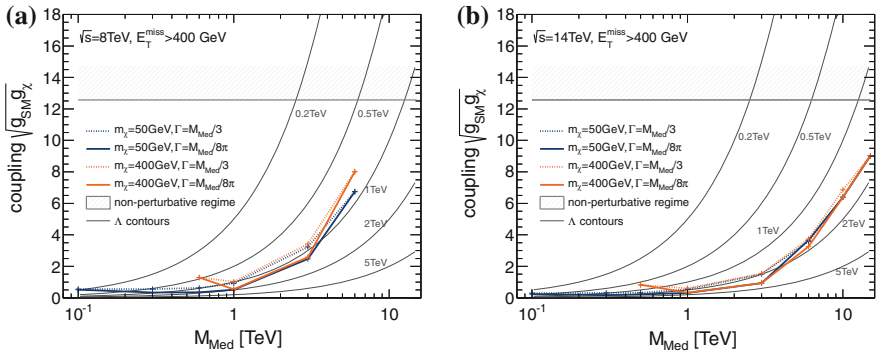


Fig. 16.5 Limits on the coupling strengths in the simplified model as a function of the mediator mass, M_{Med} , at 8 TeV (a) and 14 TeV (b). Two WIMP masses are considered: $m_\chi = 50\text{ GeV}$ (blue) and $m_\chi = 400\text{ GeV}$ (orange). The dashed lines are for a width $\Gamma = M_{Med}/3$, the solid lines for $\Gamma = M_{Med}/8\pi$. The contours of constant Λ are shown as grey lines. The beginning of the non-perturbative regime is indicated by the shaded area. The plots are identical to the ones in Ref. [1], except for notation and style changes

16.4 Summary of 14 TeV Studies

The simulation based sensitivity studies performed for a centre-of-mass energy of 14 TeV demonstrate that already with the first few fb^{-1} of run-II data, current limits on Dark Matter pair production from the mono-jet analysis will be superseded by roughly a factor of two. Even though the centre-of-mass energy in 2015 will probably be 13 TeV, this conclusion is not greatly altered. Further improvements can be achieved

by a combination of gathering more luminosity, reducing the systematic uncertainties and extending the search reach to higher E_T^{miss} .

The potential for a 5σ discovery at 14 TeV (assuming a WIMP mass of 50 GeV) extends from the order of 1.5–2.6 TeV in M_* , for 25 fb^{-1} and 5 % systematic uncertainty and 3000 fb^{-1} and 1 % systematic uncertainty, respectively. At 8 TeV, this value is of the order of 700 GeV.

Limits on the parameters of the simplified model show a similar general behaviour for both centre-of-mass energies. The limits increase again by approximately a factor of two and the region of strongest limits is shifted to slightly higher mediator masses.

References

1. The ATLAS collaboration (2014) Sensitivity to WIMP dark matter in the final states containing jets and missing transverse momentum with the ATLAS detector at 14 TeV LHC. Technical report ATL-PHYS-PUB-2014-007. Geneva: CERN
2. The ATLAS collaboration (2015) Search for new phenomena in final states with an energetic jet and large missing transverse momentum in pp collisions at $\sqrt{s} = 8$ TeV with the ATLAS detector. In: submitted to EPJC. [arXiv:1502.01518](https://arxiv.org/abs/1502.01518) [hep-ex]
3. The ATLAS collaboration (2013) Search for dark matter candidates and large extra dimensions in events with a jet and missing transverse momentum with the ATLAS detector. In: JHEP 1304, p. 075. doi:[10.1007/JHEP04\(2013\)075](https://doi.org/10.1007/JHEP04(2013)075), [arXiv:1210.4491](https://arxiv.org/abs/1210.4491) [hep-ex]
4. The ATLAS collaboration (2012) Search for new phenomena in monojet plus missing transverse momentum final states using 10 fb^{-1} of pp collisions at $\sqrt{s} = 8$ TeV with the ATLAS detector at the LHC. Technical report ATLAS-CONF-2012-147. Geneva: CERN
5. The ATLAS collaboration (2013) Performance assumptions for an upgraded ATLAS detector at a high-luminosity LHC. Technical report ATL-PHYS-PUB-2013-004. Geneva: CERN
6. The ATLAS collaboration (2013) Performance assumptions based on full simulation for an upgraded ATLAS detector at a high-luminosity LHC. Technical report ATL-PHYS-PUB-2013-009. Geneva: CERN

Part V

Conclusion

Chapter 17

Conclusion

The Standard Model of particle physics is one of the best tested and most successful theories in the history of science. It leaves, however, a number of observed phenomena unexplained and many theories exist that propose extensions to the Standard Model in order to remedy the situation. To date, direct experimental evidence for either of these theories is still pending and it is one of the goals of the Large Hadron Collider project at CERN to provide it.

One of the open questions the Standard Model does not answer concerns the matter (and energy) content of the universe: A large number of observations on largely different cosmological scales constitute compelling evidence for the existence of Dark Matter, for which the Standard Model provides no viable particle candidate. A generic class of candidates are WIMPs—weakly interacting massive particles, with cross sections and masses that naturally allow to account for the observed relic abundance of Dark Matter. Many experiments searching for Dark Matter try either to detect the nuclear recoil in a target material due to a WIMP scattering off the nucleus or to detect the annihilation of WIMPs into Standard Model particles. Particle colliders can provide complementary information to these approaches and have become the third pillar of Dark Matter searches. The interest in collider searches for Dark Matter has been growing constantly since the beginning of the LHC operation.

The LHC started physics data taking with proton-proton collisions in March 2010 at a centre-of-mass energy of 7 TeV. With understanding of and confidence in the accelerator growing, the instantaneous luminosities have been increased over the first years of running. In 2012, the centre-of-mass energy was increased to 8 TeV and a data set corresponding to roughly 20 fb^{-1} was collected by the ATLAS detector, exceeding the 2011 data set by a factor of 4.

Essential for an efficient detector operation and data taking is a reliably functioning trigger system. Extensive online monitoring of the system is crucial to allow for quickly isolating a problem and solving it. Especially the Central Trigger has to be monitored closely as it constitutes a single point of failure, and without it no data can be recorded. Two new timing monitoring features have been developed and

implemented as part of this work: the orbit and the bunch group monitoring. Both have been deployed in 2011 and have been active throughout the remainder of run-I data taking. No timing problems were observed during this time, underlining the extremely stable performance of the Central Trigger. The monitoring has, however, proven useful to exclude misalignment of the timing signals in the CTP as possible cause of problems.

The data collected with the ATLAS detector in 2012 are used in this thesis to perform a search for WIMP dark matter candidates in events with a highly energetic jet and missing transverse momentum. The event selection is optimised with respect to the sensitivity for a signal of WIMP pair production; the most drastic changes compared to previous versions of the analysis are the release of the veto on events with more than two jets and the use of asymmetric cuts on the transverse momentum of the leading jet and the missing transverse energy.

The largest and irreducible Standard Model background is the production of Z bosons in association with jets with the Z decaying into a neutrino-antineutrino pair. Another source of large background contributions are $W^\pm(\rightarrow \ell^\pm\bar{\nu})$ +jets events. A precise estimate of these backgrounds is required in order to compare the data to the theory prediction and to draw conclusions about the probability for a signal to be present. Therefore, the processes mentioned above are estimated in a semi-data driven way from control regions selecting well-understood events of $W^\pm(\rightarrow \ell^\pm\bar{\nu})$ +jets and $Z(\rightarrow \ell^+\ell^-)$ +jets events. In this approach, the simulation is used only in the form of ratios (transfer factors) which corrects the normalisation and the shape of distributions to the one observed in data and leads to a considerable reduction of various experimental and theoretical uncertainties. Four estimates for the dominant $Z(\rightarrow \nu\bar{\nu})$ +jets background are obtained from $W^\pm(\rightarrow \ell^\pm\bar{\nu})$ +jets and $Z(\rightarrow \ell^+\ell^-)$ +jets control regions in both the electron and the muon channel and are combined, further reducing the total uncertainty. $W^\pm(\rightarrow \ell^\pm\bar{\nu})$ +jets events are estimated from W control regions either in the electron or the muon channel. The transfer factor method reproduces the shapes in the signal region very well and—together with the combination for the $Z(\rightarrow \nu\bar{\nu})$ +jets backgrounds—results in very small uncertainties, many of them at the per-mille level. This procedure is expected to perform equally well for run-II data, provided that the simulation continues to adequately model the Standard Model processes in the control regions. A veto on τ -leptons could help in the future to suppress the second largest background of $W^\pm(\rightarrow \tau^\pm\bar{\nu})$ +jets events and to increase the purity in the W control regions.

Due to lack of precise simulations with sufficient statistics, the QCD multi-jet and non-collision backgrounds are estimated in a data driven way. Although both have a 100% uncertainty assigned, the effect on the total background is negligible since these contributions are very small at large missing transverse energy. Consequently, not much will be gained by a refined estimation technique. This also holds for the $Z(\rightarrow \ell^+\ell^-)$ +jets backgrounds which are taken directly from the simulation. The remaining backgrounds consisting of top and diboson processes are also estimated purely simulation based. In case of the top background a systematic uncertainty on the normalisation is obtained from a data control region; the systematic uncertainty on the diboson normalisation is derived from modified simulated samples. It turns

out that these uncertainties are the dominating systematic uncertainties especially in the higher signal regions. One goal for the next round of the analysis will therefore be to improve the selections in particular in the control regions to better suppress these backgrounds, and to reduce their uncertainties. The statistical uncertainties are approximately of the same order as the combined top and diboson uncertainty. This will be reduced when more data at higher centre-of-mass energies will be collected in LHC run-II.

The search for Dark Matter candidates is performed in eight signal regions with increasing lower thresholds on the missing transverse energy. No significant excess over the Standard Model prediction is observed and CL_s exclusion limits on the visible cross section for new physics are computed. At 95% confidence level the limits in the eight signal regions range from 684.3 to 3.1 fb.

Moreover, the results are interpreted in an effective field theory for WIMP pair production in terms of limits on the suppression scale of the theory for various operators describing different types of interactions. For each operator, the limits from the signal region with the best expected limit are considered. Compared to previous ATLAS results, the limits improve by 30–70%. The strongest limits are obtained for the tensor operator and are of the order of 1.8 TeV for WIMP masses below 100 GeV, which is the region particularly interesting for collider searches as the direct and indirect search experiments are less sensitive at small WIMP masses. For spin-independent interactions, this analysis sets stronger limits than the direct searches for WIMP masses below roughly 10 GeV. In the case of spin-dependent interaction, the results obtained in this work are competitive over the entire WIMP mass range considered. The limits on the annihilation cross section this analysis provides are stronger than those from the Fermi-LAT experiment below $\mathcal{O}(100)$ GeV.

While the merit of the effective theory is to allow for a straight forward comparison to direct and indirect searches, its validity at LHC energies has to be considered carefully. A natural next step towards a more ultra-violet complete model is to consider a model where the mediator is not integrated out. In this analysis, a Z' -like s -channel mediator is considered. It is found that at low mediator masses of $\mathcal{O}(100)$ GeV and below the production is kinematically suppressed, leading to small cross sections and weak limits. For mediator masses around 1 TeV, the production cross sections increase and the strongest limits are obtained. At very large mediator masses, $\mathcal{O}(10)$ TeV, the limits of the effective theory are reproduced.

In 2015, the LHC will resume operation at centre-of-mass energies of initially 13 TeV but going up to 14 TeV. The sensitivity of the mono-jet analysis to the WIMP signal at 14 TeV has been investigated in a simulation study and expected limits and discovery potentials have been calculated as part of this work. It is found that already with the first months of run-II data the limits on the suppression scale of the effective theory will be improved by approximately a factor of two. The reach can be further extended once more luminosity is collected and systematics are reduced. Depending on the luminosity and systematic uncertainties the potential for a 5σ discovery extends from 1.5 to 2.6 TeV in M_* . It should be kept in mind, however, that a positive signal could be caused by various BSM physics and does not automatically

mean that Dark Matter has been detected. Limits on the parameters of the simplified model are also found to improve by about a factor of two.

Given the questionability of the EFT validity at large momentum transfer, future versions of the mono-jet analysis will probably involve studies of a more complete set of simplified models, while still providing limits in the EFT framework which remains a useful benchmark model. While the choice of different signal regions provides the means to optimise for individual operators, considering only one region and performing a shape analysis might prove beneficial for future versions of the analysis.

In order to prepare the detector for run-II operation, several systems of the ATLAS experiment undergo upgrades during the two years shutdown of the LHC in which the machine is upgraded as well. The decision taking and output boards of the Central Trigger as well as the backplane for the trigger signals will be replaced. The main goal is to remove hardware limitations in the number and complexity of trigger items. The new system will allow for more than three times the number of inputs and double the number of trigger items. The corresponding changes to the event format and in the Central Trigger simulation have been implemented as part of this work.

Appendix A

Signal Simulation Samples

Table A.1 Cross section, generated number of events, corresponding integrated luminosity and sample ID for the signal points for the effective operators for complex scalar DM

Operator	m_χ (GeV)	QCUT (GeV)	σ (nb)	N_{gen}	\mathcal{L}_{int} (fb $^{-1}$)	ID
C1	10	80	$5.5e - 11$	20000	$3.6e + 20$	159637
		300	$4.3e - 13$	20000	$4.7e + 22$	159645
	50	80	$3.1e - 11$	20000	$6.5e + 20$	159638
		300	$3.6e - 13$	20000	$5.6e + 22$	159646
	100	80	$1.4e - 11$	20000	$1.5e + 21$	159639
		300	$2.5e - 13$	20000	$7.9e + 22$	159647
	200	80	$3.2e - 12$	20000	$6.2e + 21$	159640
		300	$1.1e - 13$	20000	$1.9e + 23$	159648
	400	80	$3e - 13$	20000	$6.7e + 22$	159641
		300	$1.8e - 14$	19500	$1.1e + 24$	159649
	700	80	$1.5e - 14$	20000	$1.4e + 24$	159642
		300	$1.3e - 15$	20000	$1.5e + 25$	159650
	1000	80	$9.7e - 16$	20000	$2.1e + 25$	159643
		300	$1e - 16$	20000	$1.9e + 26$	159651
	1300	80	$7e - 17$	20000	$2.9e + 26$	159644
		300	$8.2e - 18$	20000	$2.4e + 27$	159652
C5	10	80	$2.4e - 06$	20000	$8.3e + 15$	159669
		300	$1.6e - 07$	20000	$1.3e + 17$	159677
	50	80	$1.8e - 06$	20000	$1.1e + 16$	159670
		300	$1.4e - 07$	20000	$1.4e + 17$	159678
	100	80	$1.1e - 06$	20000	$1.7e + 16$	159671
		300	$1.2e - 07$	20000	$1.7e + 17$	159679

(continued)

Table A.1 (continued)

Operator	m_χ (GeV)	QCUT (GeV)	σ (nb)	N_{gen}	\mathcal{L}_{int} (fb $^{-1}$)	ID
	200	80	$4.9e - 07$	20000	$4.1e + 16$	159672
		300	$6.7e - 08$	20000	$3e + 17$	159680
	400	80	$1.1e - 07$	20000	$1.9e + 17$	159673
		300	$2e - 08$	20000	$1e + 18$	159681
	700	80	$1.4e - 08$	20000	$1.4e + 18$	159674
		300	$3.1e - 09$	20000	$6.5e + 18$	159682
	1000	80	$2e - 09$	9999	$4.9e + 18$	159675
		300	$4.6e - 10$	20000	$4.3e + 19$	159683
	1300	80	$2.8e - 10$	20000	$7.2e + 19$	159676
		300	$6.5e - 11$	20000	$3.1e + 20$	159684

Table A.2 Cross section, generated number of events, corresponding integrated luminosity and sample ID for the signal points for the effective operators for Dirac fermionic DM

Operator	m_χ (GeV)	QCUT (GeV)	σ (nb)	N_{gen}	\mathcal{L}_{int} (fb $^{-1}$)	ID
D1	50	80	$5.9e - 12$	20000	$3.4e + 21$	159565
		300	$1.7e - 13$	20000	$1.2e + 23$	159572
	100	80	$4.2e - 12$	20000	$4.8e + 21$	159566
		300	$1.5e - 13$	20000	$1.4e + 23$	159573
	200	80	$1.9e - 12$	19500	$1.1e + 22$	159567
		300	$8.9e - 14$	20000	$2.2e + 23$	159574
	400	80	$3.5e - 13$	20000	$5.7e + 22$	159568
		300	$2.6e - 14$	20000	$7.8e + 23$	159575
	700	80	$3.1e - 14$	20000	$6.4e + 23$	159569
		300	$3e - 15$	20000	$6.6e + 24$	159576
	1000	80	$3e - 15$	20000	$6.7e + 24$	159570
		300	$3.3e - 16$	20000	$6.1e + 25$	159577
	1300	80	$2.8e - 16$	20000	$7.2e + 25$	159571
		300	$3.3e - 17$	20000	$6e + 26$	159578
D5	50	80	0.00057	20000	$3.5e + 13$	159593
		300	$4e - 05$	20000	$5e + 14$	159600
	100	80	0.00053	20000	$3.8e + 13$	159594
		300	$4e - 05$	20000	$5.1e + 14$	159601
	200	80	0.00041	20000	$4.8e + 13$	159595
		300	$3.5e - 05$	20000	$5.7e + 14$	159602
	400	80	0.00021	20000	$9.3e + 13$	159596
		300	$2.1e - 05$	20000	$9.4e + 14$	159603

(continued)

Table A.2 (continued)

Operator	m_χ (GeV)	QCUT (GeV)	σ (nb)	N_{gen}	\mathcal{L}_{int} (fb $^{-1}$)	ID
D9	700	80	$6.5e - 05$	20000	$3.1e + 14$	159597
		300	$7.2e - 06$	20000	$2.8e + 15$	159604
	1000	80	$1.6e - 05$	20000	$1.2e + 15$	159598
		300	$1.9e - 06$	20000	$1.1e + 16$	159605
	1300	80	$3.5e - 06$	20000	$5.7e + 15$	159599
		300	$4e - 07$	20000	$5e + 16$	159606
	10	80	0.0021	20000	$9.5e + 12$	159607
		300	0.00025	20000	$8e + 13$	159615
	50	80	0.0019	20000	$1e + 13$	159608
		300	0.00024	20000	$8.3e + 13$	159616
100	80	0.0016	20000	$1.3e + 13$	159609	
	300	0.00021	20000	$9.3e + 13$	159617	
200	80	0.0011	20000	$1.9e + 13$	159610	
	300	0.00015	20000	$1.3e + 14$	159618	
400	80	0.00049	20000	$4.1e + 13$	159611	
	300	$6.9e - 05$	20000	$2.9e + 14$	159619	
700	80	0.00014	20000	$1.4e + 14$	159612	
	300	$1.9e - 05$	20000	$1.1e + 15$	159620	
1000	80	$3.4e - 05$	20000	$5.9e + 14$	159613	
	300	$4.4e - 06$	20000	$4.6e + 15$	159621	
1300	80	$7.2e - 06$	20000	$2.8e + 15$	159614	
	300	$8.8e - 07$	20000	$2.3e + 16$	159622	
D11	50	80	$9.3e - 07$	20000	$2.2e + 16$	159623
		300	$1.4e - 07$	19000	$1.4e + 17$	159630
	100	80	$8e - 07$	20000	$2.5e + 16$	159624
		300	$1.3e - 07$	20000	$1.6e + 17$	159631
	200	80	$5.4e - 07$	20000	$3.7e + 16$	159625
		300	$9.6e - 08$	20000	$2.1e + 17$	159632
	400	80	$2.1e - 07$	19000	$9.1e + 16$	159626
		300	$4.3e - 08$	20000	$4.7e + 17$	159633
	700	80	$4.5e - 08$	20000	$4.4e + 17$	159627
		300	$1e - 08$	19500	$1.9e + 18$	159634
	1000	80	$8.5e - 09$	20000	$2.3e + 18$	159628
		300	$2e - 09$	20000	$1e + 19$	159635
	1300	80	$1.4e - 09$	5000	$3.4e + 18$	159629
		300	$3.2e - 10$	20000	$6.2e + 19$	159636

Table A.3 Cross section, generated number of events, corresponding integrated luminosity and sample ID for the signal points for the simplified model and mediator masses below 1 TeV

m_{Med}	Width	m_χ (GeV)	QCUT (GeV)	σ (nb)	N_{gen}	\mathcal{L}_{int} (fb^{-1})	ID		
10 GeV	$m_{Med}/3$	10	80	0.26	20000	$7.8e + 10$	188605		
			300	0.0044	20000	$4.6e + 12$	188606		
50 GeV	$m_{Med}/3$	10	80	0.48	20000	$4.2e + 10$	188607		
			300	0.0082	20000	$2.4e + 12$	188608		
		50	80	0.097	20000	$2.1e + 11$	182328		
			300	0.0015	20000	$1.3e + 13$	182337		
		400	80	0.00012	20000	$1.7e + 14$	182364		
			300	$1.1e - 05$	20000	$1.9e + 15$	182373		
	$m_{Med}/8\pi$	50	80	0.096	20000	$2.1e + 11$	182346		
			300	0.0015	20000	$1.3e + 13$	182355		
		400	80	0.00012	20000	$1.7e + 14$	182382		
			300	$1.1e - 05$	20000	$1.9e + 15$	182391		
100 GeV	$m_{Med}/3$	10	80	0.21	20000	$9.4e + 10$	188609		
			300	0.0044	20000	$4.5e + 12$	188610		
		50	80	0.3	20000	$6.7e + 10$	182329		
			300	0.0038	20000	$5.2e + 12$	182338		
		400	80	0.00012	20000	$1.6e + 14$	182365		
			300	$1.1e - 05$	20000	$1.8e + 15$	182374		
		$m_{Med}/8\pi$	50	80	1.2	20000	$1.6e + 10$	182347	
				300	0.013	20000	$1.6e + 12$	182356	
	400		80	0.00012	20000	$1.6e + 14$	182383		
			300	$1.1e - 05$	20000	$1.8e + 15$	182392		
	300 GeV		$m_{Med}/3$	10	80	0.028	20000	$7.1e + 11$	188611
					300	0.0013	19999	$1.5e + 13$	188612
		50		80	0.072	20000	$2.8e + 11$	182330	
				300	0.0023	20000	$8.7e + 12$	182339	
200		80		0.0018	20000	$1.1e + 13$	188619		
		300		0.00014	20000	$1.5e + 14$	188620		
400		80		0.00015	20000	$1.3e + 14$	182366		
		300		$1.3e - 05$	20000	$1.5e + 15$	182375		
$m_{Med}/8\pi$		50		80	0.71	20000	$2.8e + 10$	182348	
				300	0.022	20000	$9e + 11$	182357	
		400	80	0.00015	20000	$1.4e + 14$	182384		
			300	$1.3e - 05$	20000	$1.6e + 15$	182393		
600 GeV		$m_{Med}/3$	10	80	0.004	20000	$5e + 12$	188613	
				300	0.00034	20000	$6e + 13$	188614	
	50		80	0.0095	20000	$2.1e + 12$	182331		
			300	0.00055	20000	$3.6e + 13$	182340		

(continued)

Table A.3 (continued)

m_{Med}	Width	m_χ (GeV)	QCUT (GeV)	σ (nb)	N_{gen}	\mathcal{L}_{int} (fb^{-1})	ID
		200	80	0.003	20000	$6.7e + 12$	188621
			300	0.00027	20000	$7.3e + 13$	188622
		400	80	0.00031	20000	$6.5e + 13$	182367
			300	$2.6e - 05$	20000	$7.6e + 14$	182376
	$m_{Med}/8\pi$	50	80	0.089	20000	$2.3e + 11$	182349
			300	0.0055	20000	$3.6e + 12$	182358
		400	80	0.00032	20000	$6.3e + 13$	182385
			300	$2.8e - 05$	20000	$7.2e + 14$	182394

Table A.4 Cross section, generated number of events, corresponding integrated luminosity and sample ID for the signal points for the simplified model and mediator masses from 1 TeV

m_{Med}	Width	m_χ (GeV)	QCUT (GeV)	σ (nb)	N_{gen}	\mathcal{L}_{int} (fb^{-1})	ID		
1 TeV	$m_{Med}/3$	10	80	0.00065	20000	$3.1e + 13$	188615		
			300	$7.3e - 05$	20000	$2.7e + 14$	188616		
		50	80	0.0015	20000	$1.3e + 13$	182332		
			300	0.00011	20000	$1.8e + 14$	182341		
		200	80	0.00058	20000	$3.5e + 13$	188623		
			300	$6.8e - 05$	20000	$2.9e + 14$	188624		
				400	80	0.00071	20000	$2.8e + 13$	182368
					300	$6.3e - 05$	20000	$3.2e + 14$	182377
				1000	80	$3.7e - 07$	20000	$5.4e + 16$	188627
					300	$5.9e - 08$	20000	$3.4e + 17$	188628
$m_{Med}/8\pi$	50			80	0.013	20000	$1.6e + 12$	182350	
				300	0.0011	20000	$1.8e + 13$	182359	
	400		80	0.0093	20000	$2.2e + 12$	182386		
			300	0.00081	20000	$2.5e + 13$	182395		
3 TeV	$m_{Med}/3$		10	80	$3.9e - 06$	20000	$5.2e + 15$	188617	
				300	$4.5e - 07$	20000	$4.4e + 16$	188618	
		50	80	$8.8e - 06$	20000	$2.3e + 15$	182333		
			300	$7e - 07$	20000	$2.9e + 16$	182342		
		200	80	$3.2e - 06$	20000	$6.3e + 15$	188625		
			300	$4.2e - 07$	20000	$4.8e + 16$	188626		

(continued)

Table A.4 (continued)

m_{Med}	Width	m_χ (GeV)	QCUT (GeV)	σ (nb)	N_{gen}	\mathcal{L}_{int} (fb^{-1})	ID		
		400	80	$4.5e - 06$	20000	$4.5e + 15$	182369		
			300	$4.7e - 07$	15000	$3.2e + 16$	182378		
		1000	80	$4.6e - 07$	20000	$4.4e + 16$	188629		
			300	$7.6e - 08$	20000	$2.6e + 17$	188630		
		1300	80	$1.4e - 07$	20000	$1.4e + 17$	188631		
			300	$2.3e - 08$	20000	$8.6e + 17$	188632		
	$m_{Med}/8\pi$	50	80	$1.8e - 05$	20000	$1.1e + 15$	182351		
			300	$1.7e - 06$	20000	$1.2e + 16$	182360		
		400	80	$1.3e - 05$	20000	$1.5e + 15$	182387		
			300	$1.5e - 06$	20000	$1.4e + 16$	182396		
6 TeV	$m_{Med}/3$	50	80	$4.3e - 07$	20000	$4.6e + 16$	182334		
			300	$3e - 08$	20000	$6.6e + 17$	182343		
		400	80	$1.7e - 07$	20000	$1.2e + 17$	182370		
			300	$1.7e - 08$	20000	$1.2e + 18$	182379		
	$m_{Med}/8\pi$	50	80	$4.7e - 07$	20000	$4.2e + 16$	182352		
			300	$3.4e - 08$	20000	$5.9e + 17$	182361		
		400	80	$1.9e - 07$	20000	$1.1e + 17$	182388		
			300	$1.9e - 08$	20000	$1.1e + 18$	182397		
		10 TeV	$m_{Med}/3$	50	80	$5.4e - 08$	20000	$3.7e + 17$	182335
					300	$3.7e - 09$	20000	$5.4e + 18$	182344
400	80			$2.1e - 08$	20000	$9.6e + 17$	182371		
	300			$2e - 09$	20000	$1e + 19$	182380		
$m_{Med}/8\pi$	50		80	$5.8e - 08$	20000	$3.4e + 17$	182353		
			300	$4.1e - 09$	20000	$4.8e + 18$	182362		
	400		80	$2.2e - 08$	20000	$9e + 17$	182389		
			300	$2.2e - 09$	20000	$9e + 18$	182398		
	30 TeV		$m_{Med}/3$	50	80	$6.6e - 10$	20000	$3e + 19$	182336
					300	$4.5e - 11$	20000	$4.4e + 20$	182345
400		80		$2.5e - 10$	20000	$8.1e + 19$	182372		
		300		$2.4e - 11$	20000	$8.4e + 20$	182381		
$m_{Med}/8\pi$		50	80	$7e - 10$	20000	$2.8e + 19$	182354		
			300	$5e - 11$	20000	$4e + 20$	182363		
		400	80	$2.7e - 10$	20000	$7.5e + 19$	182390		
			300	$2.6e - 11$	20000	$7.6e + 20$	182399		

Appendix B

Signal Tables

This appendix contains the efficiency and acceptance information for the various signal simulation samples as well as tables listing the experimental and theoretical systematic uncertainties.

Table B.1 Acceptance \times efficiency (both in %) for all signal regions for the operators for Dirac fermionic WIMPs

Operator	m_χ (GeV)	SR1	SR2	SR3	SR4	SR5	SR6	SR7	SR8
D1	50	20.5 \times 81.1	11.1 \times 79.1	6.0 \times 76.7	3.2 \times 79.4	2.0 \times 75.7	1.2 \times 79.7	0.4 \times 71.9	0.0 \times 0.0
	100	22.4 \times 80.3	12.8 \times 78.9	7.1 \times 78.7	4.1 \times 80.1	2.5 \times 75.8	1.4 \times 77.5	0.6 \times 71.3	0.2 \times 74.1
	200	25.6 \times 80.3	15.7 \times 77.0	8.9 \times 77.9	5.5 \times 76.9	3.3 \times 76.7	2.0 \times 77.5	0.8 \times 77.1	0.3 \times 77.3
	400	30.0 \times 79.8	19.6 \times 77.5	11.9 \times 77.0	7.5 \times 75.2	4.8 \times 76.7	3.2 \times 74.5	1.3 \times 74.2	0.5 \times 72.7
	700	31.7 \times 81.5	21.8 \times 79.8	14.3 \times 78.4	9.5 \times 76.8	6.3 \times 74.5	4.2 \times 76.5	1.9 \times 75.3	0.9 \times 75.5
	1000	33.1 \times 80.6	23.0 \times 79.2	15.3 \times 79.2	10.2 \times 78.3	6.8 \times 78.3	4.7 \times 77.1	2.2 \times 76.3	1.0 \times 72.6
	1300	33.5 \times 81.0	23.6 \times 78.4	15.6 \times 77.0	10.4 \times 76.8	7.0 \times 78.7	4.8 \times 78.2	2.2 \times 76.1	1.1 \times 74.7
D5 (D8)	50	27.6 \times 81.8	17.1 \times 82.1	10.6 \times 78.2	6.6 \times 79.6	4.4 \times 76.1	2.8 \times 77.1	1.2 \times 75.7	0.0 \times 0.0
	100	28.9 \times 81.6	18.5 \times 79.5	11.6 \times 79.7	7.2 \times 77.4	4.6 \times 77.7	3.0 \times 79.3	1.3 \times 77.8	0.6 \times 77.0
	200	30.5 \times 81.7	19.8 \times 80.5	12.6 \times 79.4	7.9 \times 78.0	5.3 \times 77.4	3.5 \times 77.4	1.6 \times 77.2	0.7 \times 77.1

(continued)

Table B.1 (continued)

Operator	m_χ (GeV)	SR1	SR2	SR3	SR4	SR5	SR6	SR7	SR8
	400	32.3 × 81.3	21.8 × 79.3	14.2 × 79.4	9.6 × 78.4	6.3 × 77.8	4.3 × 76.4	2.0 × 76.7	0.9 × 78.5
	700	35.0 × 80.8	24.6 × 78.9	16.3 × 78.6	11.0 × 78.7	7.4 × 78.4	5.1 × 77.6	2.5 × 76.5	1.2 × 76.1
	1000	35.8 × 81.6	25.4 × 79.8	16.9 × 78.7	11.6 × 77.2	7.8 × 78.7	5.4 × 76.8	2.6 × 76.0	1.3 × 77.6
	1300	35.4 × 81.3	24.7 × 79.9	16.8 × 78.6	11.4 × 79.2	7.8 × 78.1	5.3 × 78.0	2.5 × 76.9	1.2 × 77.0
D9	10	34.1 × 82.4	23.1 × 81.2	15.9 × 79.7	10.8 × 80.1	7.5 × 79.3	5.3 × 79.2	2.7 × 78.8	1.4 × 80.0
	50	34.7 × 82.2	24.2 × 81.6	16.5 × 80.5	11.4 × 79.5	7.9 × 80.0	5.6 × 78.8	2.8 × 78.7	1.6 × 77.8
	100	36.1 × 82.2	25.4 × 80.9	17.4 × 80.7	12.3 × 79.3	8.9 × 79.2	6.4 × 78.6	3.3 × 78.6	1.8 × 75.9
	200	36.4 × 82.2	25.7 × 81.3	18.5 × 80.6	13.1 × 79.8	9.5 × 79.0	6.9 × 78.0	3.6 × 78.3	1.9 × 79.6
	400	36.9 × 82.2	26.6 × 81.2	19.0 × 79.9	13.2 × 80.2	9.7 × 79.6	7.0 × 81.0	3.8 × 80.0	2.2 × 78.7
	700	36.0 × 82.8	25.2 × 81.1	17.6 × 79.8	12.3 × 79.2	8.7 × 79.7	6.4 × 78.5	3.6 × 78.8	2.0 × 77.1
	1000	36.4 × 81.8	26.1 × 79.7	18.2 × 79.1	12.6 × 79.9	9.0 × 77.8	6.4 × 78.3	3.4 × 77.0	1.8 × 77.8
	1300	36.0 × 81.0	25.5 × 79.2	17.5 × 79.8	12.0 × 78.5	8.3 × 79.1	6.0 × 78.7	3.0 × 77.9	1.5 × 80.0
D11	50	30.8 × 82.4	23.2 × 80.0	17.1 × 79.2	12.6 × 79.5	9.0 × 76.9	6.6 × 76.8	3.5 × 76.8	1.9 × 75.4
	100	32.6 × 80.9	24.8 × 79.9	17.9 × 79.8	13.3 × 78.2	9.6 × 78.5	7.1 × 78.0	3.8 × 78.5	2.2 × 78.0
	200	34.1 × 80.8	26.7 × 79.7	19.8 × 78.5	14.6 × 79.1	11.0 × 78.0	8.0 × 77.9	4.3 × 76.8	2.5 × 77.0
	400	35.7 × 82.2	28.6 × 80.0	21.9 × 78.0	16.5 × 77.9	12.4 × 77.1	9.4 × 77.6	5.4 × 76.7	3.2 × 77.1
	700	37.5 × 81.8	30.7 × 80.4	23.5 × 79.8	17.8 × 80.4	13.8 × 79.4	10.7 × 78.8	6.3 × 78.0	3.7 × 77.9
	1000	38.1 × 81.9	31.2 × 79.9	24.4 × 78.9	18.8 × 78.5	14.5 × 77.1	11.1 × 78.0	6.6 × 77.5	3.9 × 77.6
	1300	37.5 × 83.5	30.9 × 79.7	24.3 × 77.5	18.7 × 79.1	14.5 × 79.0	11.0 × 77.8	6.5 × 77.0	3.7 × 75.4

Table B.2 Acceptance \times efficiency (both in %) for all signal regions for the operators for scalar WIMPs

Operator	m_χ (GeV)	SR1	SR2	SR3	SR4	SR5	SR6	SR7	SR8
C1	10	10.8 \times 85.0	4.5 \times 77.4	2.0 \times 79.1	1.0 \times 77.2	0.5 \times 76.1	0.3 \times 67.4	0.0 \times 0.0	0.0 \times 0.0
	50	13.8 \times 81.3	5.9 \times 81.4	2.9 \times 72.7	1.4 \times 76.3	0.7 \times 70.5	0.4 \times 71.5	0.0 \times 0.0	0.0 \times 0.0
	100	16.7 \times 83.2	8.3 \times 78.0	4.0 \times 77.3	2.0 \times 78.7	1.0 \times 77.2	0.6 \times 78.6	0.2 \times 77.7	0.0 \times 0.0
	200	21.9 \times 81.8	12.3 \times 78.9	6.8 \times 75.7	3.7 \times 77.1	2.1 \times 74.5	1.2 \times 74.3	0.4 \times 74.0	0.0 \times 0.0
	400	27.9 \times 81.0	17.5 \times 79.9	10.4 \times 79.6	6.4 \times 77.5	3.9 \times 76.4	2.4 \times 78.4	0.9 \times 77.3	0.4 \times 73.6
	700	30.8 \times 81.3	20.9 \times 78.6	13.6 \times 78.0	8.7 \times 78.0	5.8 \times 77.3	3.8 \times 75.9	1.7 \times 77.7	0.7 \times 77.2
	1000	33.1 \times 81.9	23.0 \times 79.5	15.0 \times 78.1	10.0 \times 77.0	6.8 \times 76.8	4.6 \times 76.5	2.1 \times 75.8	0.0 \times 0.0
	1300	34.1 \times 80.9	24.1 \times 78.7	15.9 \times 76.9	10.6 \times 76.8	7.1 \times 77.6	5.0 \times 76.2	2.3 \times 76.2	1.1 \times 75.1
C5	10	21.8 \times 80.6	13.9 \times 80.4	8.8 \times 80.1	5.8 \times 78.9	3.8 \times 76.5	2.5 \times 75.6	1.1 \times 76.0	0.6 \times 74.8
	50	24.5 \times 81.4	16.4 \times 80.1	10.8 \times 78.0	7.0 \times 79.3	4.7 \times 78.2	3.1 \times 78.0	1.5 \times 75.6	0.7 \times 76.2
	100	27.2 \times 80.4	19.1 \times 78.5	12.7 \times 77.3	8.5 \times 77.4	6.0 \times 77.6	4.1 \times 76.2	1.9 \times 76.7	0.9 \times 73.5
	200	31.0 \times 81.6	23.0 \times 79.8	16.2 \times 79.6	11.5 \times 77.7	8.1 \times 78.2	5.8 \times 77.6	2.9 \times 79.6	1.5 \times 81.2
	400	34.2 \times 82.0	26.7 \times 80.2	19.9 \times 79.7	14.8 \times 79.3	10.9 \times 79.8	8.2 \times 77.5	4.5 \times 78.5	2.5 \times 77.0
	700	36.5 \times 81.9	29.6 \times 79.5	22.8 \times 79.4	17.5 \times 77.7	13.4 \times 78.6	10.3 \times 78.5	6.1 \times 78.3	3.6 \times 77.2
	1000	37.0 \times 81.9	30.7 \times 79.0	23.7 \times 79.4	18.3 \times 79.2	14.2 \times 78.2	11.0 \times 78.3	6.5 \times 77.5	3.9 \times 78.8
	1300	39.1 \times 81.7	31.9 \times 80.6	25.0 \times 80.1	18.7 \times 79.3	14.6 \times 77.6	11.2 \times 77.9	6.6 \times 78.1	4.0 \times 77.9

Table B.3 Acceptance \times efficiency (both in %) for all signal regions for simplified model for mediator masses below 1 TeV

m_{Med}	Width	m_χ (GeV)	SR1	SR2	SR3	SR4	SR5	SR6	SR7	SR8
10 GeV	$m_{Med}/3$	10	19.1 \times 85.7	7.5 \times 84.4	3.0 \times 80.3	1.3 \times 77.4	0.6 \times 75.9	0.3 \times 76.7	0.1 \times 79.7	0.0 \times 78.0
		50 GeV	$m_{Med}/3$	10	22.2 \times 84.8	8.5 \times 84.6	3.2 \times 81.7	1.3 \times 86.6	0.6 \times 82.3	0.3 \times 80.2
50	13.7 \times 83.9	6.4 \times 83.6		2.9 \times 81.4	1.4 \times 79.9	0.7 \times 73.2	0.4 \times 76.9	0.1 \times 78.2	0.0 \times 82.1	
400	31.2 \times 82.0	20.3 \times 80.5		12.8 \times 80.8	8.4 \times 79.3	5.6 \times 78.2	3.7 \times 76.9	1.6 \times 76.3	0.8 \times 77.1	
$m_{Med}/8\pi$	50	13.7 \times 84.9		6.2 \times 81.0	2.7 \times 81.0	1.4 \times 81.9	0.7 \times 88.4	0.4 \times 80.8	0.1 \times 77.4	0.0 \times 78.4
	400	31.3 \times 82.8		20.7 \times 80.1	13.2 \times 80.1	8.5 \times 79.3	5.5 \times 79.6	3.7 \times 78.6	1.6 \times 78.8	0.7 \times 78.4
100 GeV	$m_{Med}/3$	10		34.4 \times 82.4	13.7 \times 82.0	5.7 \times 79.4	2.6 \times 78.1	1.2 \times 78.3	0.7 \times 74.5	0.2 \times 77.7
		50	11.8 \times 84.8	4.9 \times 82.8	2.0 \times 83.7	0.9 \times 80.0	0.5 \times 77.9	0.3 \times 76.4	0.1 \times 80.0	0.0 \times 78.1
		400	31.8 \times 81.1	20.9 \times 79.6	13.3 \times 77.6	8.3 \times 79.8	5.5 \times 78.3	3.6 \times 78.5	1.6 \times 78.3	0.7 \times 81.1
	$m_{Med}/8\pi$	50	10.4 \times 85.2	4.1 \times 84.5	1.6 \times 80.9	0.7 \times 79.3	0.4 \times 76.6	0.2 \times 75.1	0.1 \times 90.7	0.0 \times 84.0
		400	30.9 \times 82.3	20.3 \times 81.6	12.9 \times 80.8	8.4 \times 79.1	5.6 \times 79.0	3.7 \times 79.0	1.7 \times 78.1	0.8 \times 77.9
		300 GeV	$m_{Med}/3$	10	50.5 \times 82.5	25.8 \times 81.6	13.4 \times 79.7	6.7 \times 79.4	3.8 \times 76.1	2.1 \times 77.6
50	21.0 \times 83.2	10.8 \times 82.6		5.5 \times 81.0	3.0 \times 78.5	1.7 \times 78.5	1.0 \times 74.0	0.3 \times 71.7	0.1 \times 70.9	
200	57.5 \times 82.5	34.4 \times 82.4		19.7 \times 81.0	11.5 \times 80.7	6.7 \times 80.9	4.2 \times 78.8	1.7 \times 79.7	0.7 \times 79.0	
400	33.0 \times 83.5	21.6 \times 82.6		14.0 \times 82.0	9.1 \times 80.0	5.9 \times 78.7	3.8 \times 78.4	1.6 \times 76.7	0.8 \times 76.3	
$m_{Med}/8\pi$	50	21.2 \times 83.1		11.0 \times 82.3	5.7 \times 78.9	2.9 \times 80.7	1.6 \times 79.5	0.9 \times 75.7	0.3 \times 76.3	0.1 \times 78.6
	400	31.2 \times 82.0		20.6 \times 80.9	13.2 \times 79.8	8.6 \times 78.6	5.5 \times 80.2	3.5 \times 80.5	1.6 \times 79.8	0.7 \times 79.4
600 GeV	$m_{Med}/3$	10	57.2 \times 81.6	33.5 \times 80.9	19.2 \times 80.5	11.3 \times 78.5	6.9 \times 80.4	4.2 \times 80.5	1.7 \times 78.8	0.7 \times 79.8
		50	27.0 \times 81.4	15.8 \times 80.1	9.4 \times 79.3	5.6 \times 77.5	3.2 \times 78.3	2.0 \times 79.4	0.8 \times 79.2	0.3 \times 78.6
		200	59.5 \times 82.2	35.8 \times 81.6	21.0 \times 80.4	12.4 \times 80.2	7.7 \times 80.3	4.9 \times 79.1	1.9 \times 78.5	0.8 \times 77.0
		400	32.3 \times 83.6	21.0 \times 81.4	13.3 \times 80.7	8.6 \times 78.3	5.5 \times 78.9	3.6 \times 77.4	1.6 \times 76.7	0.7 \times 78.1
	$m_{Med}/8\pi$	50	28.3 \times 83.8	17.0 \times 80.7	9.8 \times 81.4	6.0 \times 79.7	3.7 \times 78.1	2.3 \times 77.6	0.9 \times 78.6	0.4 \times 75.5
		400	31.1 \times 82.5	20.2 \times 80.1	12.8 \times 80.2	8.1 \times 77.9	5.3 \times 77.7	3.5 \times 78.3	1.5 \times 79.5	0.7 \times 77.8

Table B.4 Acceptance \times efficiency (both in %) for all signal regions for simplified model for mediator masses starting from 1 TeV

m_{Med}	Width	m_χ (GeV)	SR1	SR2	SR3	SR4	SR5	SR6	SR7	SR8	
1 TeV	$m_{Med}/3$	10	61.3 \times 82.7	38.2 \times 82.0	23.4 \times 81.1	14.8 \times 80.2	9.4 \times 79.6	6.2 \times 80.0	2.7 \times 80.5	1.2 \times 80.2	
		50	30.6 \times 83.6	19.4 \times 83.0	12.1 \times 80.5	7.4 \times 81.0	4.7 \times 80.9	3.0 \times 80.8	1.3 \times 79.0	0.6 \times 79.7	
		200	62.0 \times 82.6	39.8 \times 81.8	24.9 \times 81.0	15.6 \times 80.0	9.9 \times 80.7	6.6 \times 79.9	2.9 \times 78.3	1.3 \times 77.7	
		400	33.7 \times 83.1	21.9 \times 81.6	13.7 \times 81.1	8.9 \times 79.0	5.7 \times 79.1	3.7 \times 78.4	1.6 \times 79.5	0.7 \times 79.4	
		1000	67.3 \times 83.1	46.5 \times 81.6	31.4 \times 81.0	21.4 \times 80.2	14.9 \times 78.8	10.3 \times 78.4	4.8 \times 78.7	2.4 \times 78.8	
	$m_{Med}/8\pi$	50	32.5 \times 82.5	20.7 \times 79.4	12.8 \times 79.5	8.1 \times 77.8	5.2 \times 78.1	3.4 \times 78.5	1.5 \times 79.5	0.7 \times 76.8	
		400	32.7 \times 83.2	20.8 \times 81.6	13.0 \times 81.9	8.3 \times 79.6	5.4 \times 80.3	3.7 \times 78.6	1.6 \times 80.0	0.7 \times 80.2	
	3 TeV	$m_{Med}/3$	10	61.5 \times 82.6	39.4 \times 81.1	24.5 \times 80.9	15.8 \times 80.0	10.3 \times 79.9	6.9 \times 78.9	3.1 \times 77.7	1.4 \times 78.4
			50	31.1 \times 82.5	19.5 \times 79.9	12.0 \times 79.6	7.7 \times 80.0	5.0 \times 78.7	3.4 \times 76.9	1.5 \times 78.8	0.7 \times 80.5
			200	63.5 \times 82.6	41.2 \times 81.8	26.6 \times 79.9	17.0 \times 79.8	11.3 \times 79.0	7.6 \times 79.0	3.5 \times 79.6	1.6 \times 81.1
400			34.3 \times 84.7	22.5 \times 82.2	13.8 \times 81.6	8.9 \times 78.2	5.6 \times 78.9	3.7 \times 77.5	1.7 \times 78.8	0.8 \times 80.4	
1000			67.5 \times 82.7	46.8 \times 81.2	31.2 \times 80.5	21.0 \times 79.9	14.4 \times 79.3	9.9 \times 78.8	4.7 \times 79.2	2.4 \times 78.3	
1300			68.6 \times 83.4	46.8 \times 82.4	31.3 \times 80.1	21.0 \times 79.3	14.3 \times 79.3	10.0 \times 79.3	4.8 \times 81.0	2.4 \times 78.6	
$m_{Med}/8\pi$		50	33.9 \times 83.1	22.3 \times 82.4	14.4 \times 81.8	9.7 \times 79.1	6.6 \times 79.7	4.4 \times 80.2	2.1 \times 79.0	1.0 \times 77.2	
		400	37.3 \times 83.5	25.3 \times 81.5	16.6 \times 80.6	11.2 \times 81.3	7.6 \times 79.8	5.2 \times 80.5	2.5 \times 78.5	1.2 \times 78.6	
6 TeV		$m_{Med}/3$	50	29.3 \times 83.9	18.6 \times 80.2	11.4 \times 80.4	7.3 \times 79.3	4.6 \times 80.3	3.0 \times 78.6	1.3 \times 78.7	0.6 \times 78.0
			400	34.7 \times 83.4	23.4 \times 81.9	15.3 \times 80.8	10.0 \times 80.5	6.6 \times 77.5	4.3 \times 78.4	2.0 \times 80.9	1.0 \times 78.6
	$m_{Med}/8\pi$	50	28.8 \times 82.0	18.1 \times 80.5	11.0 \times 79.2	7.0 \times 78.3	4.4 \times 80.1	2.8 \times 80.0	1.3 \times 78.0	0.6 \times 78.0	
		400	33.0 \times 81.9	22.4 \times 81.2	14.6 \times 79.2	9.7 \times 79.4	6.5 \times 79.3	4.3 \times 79.8	2.0 \times 80.5	1.0 \times 79.7	

(continued)

Table B.4 (continued)

m_{Med}	Width	m_χ (GeV)	SR1	SR2	SR3	SR4	SR5	SR6	SR7	SR8
10 TeV	$m_{Med}/3$	50	29.4×83.6	18.6×80.9	11.1×81.7	7.1×79.2	4.5×80.9	2.9×81.0	1.2×78.6	0.5×77.8
		400	35.1×83.1	24.0×80.1	15.6×79.8	10.3×79.3	6.7×78.3	4.5×77.4	2.1×78.7	0.9×78.3
	$m_{Med}/8\pi$	50	27.8×82.4	17.5×80.8	10.8×79.5	6.9×79.2	4.4×78.7	2.8×80.1	1.3×80.0	0.6×78.0
		400	33.1×82.0	22.2×81.9	14.7×80.1	9.6×80.7	6.6×78.8	4.5×77.6	2.0×78.4	0.9×76.8
30 TeV	$m_{Med}/3$	50	29.6×83.2	18.5×81.7	11.3×79.2	7.1×79.8	4.7×75.5	2.9×78.3	1.2×77.8	0.6×76.6
		400	35.1×82.3	23.4×78.8	15.3×79.0	10.1×79.5	6.8×79.2	4.6×77.8	2.0×77.8	1.0×76.9
	$m_{Med}/8\pi$	50	27.7×83.3	17.3×80.8	10.6×79.8	6.7×80.2	4.3×76.3	2.7×77.8	1.2×76.7	0.5×78.1
		400	32.6×81.8	22.0×80.9	14.3×80.1	9.6×79.3	6.4×78.7	4.3×78.2	2.0×77.4	0.9×75.8

Table B.5 Relative JES uncertainty on $\sigma \times A \times \varepsilon$ in % for the EFT samples

Operator	m_χ (GeV)	SR1	SR2	SR3	SR4	SR5	SR6	SR7	SR8
D1	50	3.81	4.61	2.68	3.45	3.51	2.95	4.67	6.03
	100	3.19	4.71	3.6	5.37	5.1	6.64	5.37	8.05
	200	3.13	3.68	4.22	5.16	5.15	3.72	4.7	8.14
	400	2.51	3.1	2.84	3.84	2.86	3.69	4.86	5.73
	700	2.21	2.21	2.64	2.6	3.41	4.07	3.86	5.26
	1000	1.72	2.44	2.61	3.29	3.7	3.06	4.95	5.34
	1300	1.68	2.54	2.31	2.61	2.73	3.7	3.88	4.24
D5 (D8)	50	2.78	3.24	3.44	3.52	4.5	4.51	4.74	5.2
	100	3.06	2.91	3.71	3.01	3.16	4.03	4.53	4.94
	200	2.4	1.98	3.01	3.14	3.08	3.8	5.01	5.33
	400	1.95	2.54	2.32	2.64	3.49	2.79	3.6	4.99
	700	1.86	1.92	2.48	3.21	2.81	2.57	3.47	3.32
	1000	1.5	2.24	2.37	2.34	2.5	3.77	4.23	4.69
	1300	1.91	2.03	1.78	1.94	3.42	3.39	4.58	4.64
D9	10	1.76	2.15	2.36	2.75	2.28	2.38	3.64	3.11
	50	1.94	1.95	2.17	2.68	3.04	3.14	3.7	2.63
	100	1.09	1.78	1.91	1.48	1.99	2.19	3.56	3.9
	200	1.27	1.42	1.28	1.82	1.94	2.51	3.1	3.45
	400	1.69	1.82	2.4	2.74	2.42	2.63	2.81	3.23
	700	2.09	1.83	1.59	2.3	2.22	2.11	3.3	3.36
	1000	1.33	1.74	1.62	2.09	2.1	2.87	2.99	4.36
1300	1.69	1.86	2.47	2.38	2.6	3.08	3.48	3.92	

(continued)

Table B.5 (continued)

Operator	m_χ (GeV)	SR1	SR2	SR3	SR4	SR5	SR6	SR7	SR8
D11	50	1.12	1.32	1.38	1.65	2.2	2.56	3.14	3.01
	100	0.24	0.64	1.02	1.35	1.34	2.46	3.06	3.89
	200	0.19	0.11	0.82	1.25	1.99	2.9	2.48	3.54
	400	0.38	0.76	0.64	1.63	1.14	1.95	2.56	2.98
	700	0.21	0.43	0.65	0.7	1.4	2.19	3.23	3.26
	1000	0.15	0.15	0.48	1.12	1.61	1.49	2.69	2.95
	1300	1.36	0.44	1.01	1.02	1.32	1.18	2.23	2.61
C1	10	6.76	7.43	9.75	6.68	5.1	6.73	8.64	7.74
	50	6.19	7.34	7.52	8.12	8.67	6.39	8.23	8.7
	100	5.43	5.01	6.6	3.25	8.17	5.58	5.94	8.85
	200	3.87	4.51	5.12	5.64	4.49	4.19	5.32	7.9
	400	2.97	3.8	3.22	4.76	4.03	4.98	6.24	5.39
	700	2.49	2.67	2.84	3.38	3.02	3.23	4.5	5.69
	1000	1.8	2.35	2.98	2.46	2.54	2.7	3.64	4.21
	1300	1.33	1.9	2.56	2.79	1.78	2.53	3.58	4.78
C5	10	2.15	2.66	2.83	3.98	3.28	3.37	4.56	6.03
	50	1.49	1.53	1.92	2.73	2.04	3.03	4.4	4.76
	100	1.66	1.83	2.24	2.28	2.61	3.32	4.75	4.61
	200	0.82	1.38	1.66	1.68	2.95	3.66	3.08	3.58
	400	0.3	0.33	0.98	2.11	2.03	2.13	2.64	3.62
	700	0.3	0.27	0.93	1.41	2.33	1.97	2.44	3.55
	1000	0.43	0.31	0.57	1.12	1.37	1.85	2.31	2.04
	1300	0.36	0.24	0.63	1.21	1.28	1.63	2.39	2.78

Table B.6 Relative JES uncertainty on $\sigma \times A \times \varepsilon$ in % for the light mediator samples

M_{Med}	Width	m_χ (GeV)	SR1	SR2	SR3	SR4	SR5	SR6	SR7	SR8
10 GeV	$M_{Med}/3$	10	5.14	7.92	5.89	8.73	4.06	7.27	6.32	4.47
50 GeV	$M_{Med}/3$	10	5.23	7.42	10.41	6.96	4.89	3.56	12.08	7.82
		50	5.23	5.72	7.19	8.77	3.68	5.82	6.8	7.07
		400	2.76	3.09	2.75	3.28	3.54	3.93	5.4	4.83
	$M_{Med}/8\pi$	50	5.73	7.45	6.35	6.7	5.0	6.34	10.61	7.61
		400	2.05	3.31	2.9	3.5	3.19	3.73	4.53	4.69
100 GeV	$M_{Med}/3$	10	4.88	7.14	7.82	6.01	10.24	7.45	7.55	5.62
		50	5.93	7.13	7.17	6.37	5.74	6.16	7.66	7.39
		400	2.23	2.46	3.04	3.09	2.96	3.87	3.63	4.44
	$M_{Med}/8\pi$	50	6.72	6.73	9.03	5.08	4.6	5.0	16.01	7.25
		400	2.41	2.64	2.51	3.36	3.29	4.78	5.0	6.61

(continued)

Table B.6 (continued)

M_{Med}	Width	m_χ (GeV)	SR1	SR2	SR3	SR4	SR5	SR6	SR7	SR8	
300 GeV	$M_{Med}/3$	10	3.17	4.26	5.22	5.52	5.16	8.09	5.77	9.19	
		50	4.26	4.81	3.89	6.41	4.53	5.97	7.35	6.52	
		200	2.42	3.49	4.22	4.72	4.84	5.08	5.14	6.46	
		400	2.57	3.23	3.76	3.61	3.95	3.71	5.04	4.79	
	$M_{Med}/8\pi$	50	4.19	4.92	5.6	4.01	4.78	5.21	4.77	7.72	
		400	2.1	2.74	2.22	3.22	4.03	3.8	4.32	5.74	
600 GeV	$M_{Med}/3$	10	2.6	3.63	3.52	4.02	4.1	5.23	6.76	5.21	
		50	3.12	3.25	3.41	3.81	4.29	3.74	5.38	6.05	
		200	2.25	3.1	4.04	4.43	3.63	4.16	4.79	4.71	
		400	2.36	2.66	3.36	3.5	4.01	4.32	5.04	5.62	
	$M_{Med}/8\pi$	50	3.11	3.67	4.12	3.99	5.04	5.15	4.66	5.67	
		400	2.62	2.51	2.92	3.85	3.58	3.79	4.64	4.46	
1 TeV	$M_{Med}/3$	10	2.51	3.15	3.73	3.32	3.58	4.1	4.15	5.09	
		50	2.5	1.88	3.49	3.41	3.88	4.63	5.4	4.87	
		200	1.84	2.48	3.42	3.35	3.28	4.14	4.95	5.27	
		400	2.5	3.05	2.99	3.83	3.99	4.3	5.02	4.42	
		1000	1.43	2.34	2.76	2.95	2.91	3.5	4.13	4.15	
	$M_{Med}/8\pi$	50	2.59	3.02	3.14	3.7	2.47	4.18	4.43	4.92	
400		2.19	2.79	3.14	3.27	3.08	4.47	4.22	4.92		
3 TeV	$M_{Med}/3$	10	1.9	2.91	3.43	3.26	3.4	3.56	4.26	3.79	
		50	2.97	3.38	3.54	3.54	3.36	5.51	4.82	5.4	
		200	1.94	2.82	3.05	3.64	3.39	3.49	4.38	4.57	
		400	2.03	2.83	3.54	3.4	3.36	3.77	3.94	4.38	
		1000	1.42	2.32	2.64	2.85	3.17	3.62	3.78	4.44	
		1300	1.4	2.29	2.44	2.55	2.49	3.01	3.54	4.08	
6 TeV	$M_{Med}/3$	50	2.64	2.86	2.52	4.13	3.2	4.58	4.28	3.91	
		400	2.07	2.79	3.26	3.97	3.46	4.0	3.82	4.6	
	$M_{Med}/8\pi$	50	3.03	3.48	3.66	4.51	3.54	4.08	5.04	6.24	
		400	2.47	3.19	2.9	2.55	3.68	4.05	3.59	3.58	
	10 TeV	$M_{Med}/3$	50	2.84	3.42	3.48	3.92	4.26	4.88	6.82	5.26
			400	1.98	2.68	2.72	2.95	2.88	2.96	4.89	5.31
$M_{Med}/8\pi$		50	2.99	3.05	3.02	3.26	4.48	3.57	4.66	4.22	
		400	2.13	3.23	3.02	3.21	3.05	3.9	4.65	3.94	
30 TeV	$M_{Med}/3$	50	2.96	3.41	3.68	4.0	5.26	3.96	5.46	5.58	
		400	2.64	2.68	3.5	3.13	3.5	4.09	4.24	3.88	
	$M_{Med}/8\pi$	50	3.0	3.85	3.07	3.98	4.12	4.14	5.1	4.11	
		400	2.38	3.07	2.42	2.89	3.45	3.49	3.45	5.15	

Table B.7 Relative JER uncertainty on $\sigma \times A \times \varepsilon$ in % for the EFT samples

Operator	m_χ (GeV)	SR1	SR2	SR3	SR4	SR5	SR6	SR7	SR8
D1	50	0.86	0.39	2.99	2.48	0.6	3.96	2.08	2.38
	100	1.25	0.15	0.37	0.02	2.86	1.15	0.46	7.23
	200	0.5	0.17	0.47	0.25	0.37	0.6	0.33	1.16
	400	0.52	0.8	0.25	0.74	0.27	1.03	0.15	1.4
	700	0.79	1.4	1.18	0.89	0.0	0.81	1.47	0.87
	1000	0.86	0.92	1.16	2.53	2.59	1.48	2.29	1.07
	1300	0.34	0.26	0.6	0.98	1.4	0.07	0.73	1.3
D5 (D8)	50	1.22	1.32	0.73	0.25	0.4	0.05	0.35	0.87
	100	0.18	0.09	0.67	0.96	0.95	0.42	0.32	0.93
	200	1.32	0.79	1.32	0.87	0.21	0.64	1.29	0.85
	400	1.22	1.7	0.59	1.35	0.78	1.14	0.03	2.45
	700	0.67	0.87	0.85	1.47	0.53	1.39	0.98	0.3
	1000	0.96	1.23	0.36	0.66	0.86	0.55	1.12	0.19
	1300	0.69	0.91	0.85	1.25	0.2	0.27	0.22	0.36
D9	10	0.58	0.77	0.69	1.3	1.16	0.37	0.83	0.06
	50	0.87	1.12	0.92	0.49	1.48	0.18	1.39	1.46
	100	1.0	0.4	0.63	0.82	1.42	1.12	0.88	0.24
	200	0.66	1.1	1.33	0.42	1.05	0.45	1.6	1.07
	400	0.49	0.79	0.29	0.59	0.95	1.21	0.85	0.13
	700	0.79	1.16	0.99	0.51	0.4	0.12	0.95	0.18
	1000	1.3	0.47	0.77	0.73	1.34	0.95	0.54	0.17
	1300	1.21	0.97	1.64	0.61	1.18	1.01	0.85	1.05
D11	50	1.44	0.95	1.36	1.99	0.37	1.15	1.09	1.55
	100	1.37	0.96	0.84	0.6	0.02	0.1	0.43	0.67
	200	1.22	1.45	1.48	0.9	1.07	0.91	0.75	0.9
	400	1.29	1.33	0.06	0.6	0.19	0.38	0.53	0.57
	700	1.66	1.51	1.48	1.61	0.99	0.37	0.59	0.26
	1000	0.46	0.49	0.71	0.77	0.18	0.46	0.06	0.99
	1300	1.81	1.09	1.09	2.07	2.8	1.19	0.15	0.6
C1	10	0.97	0.39	3.45	2.08	1.77	0.6	0.12	0.0
	50	1.89	0.16	0.32	3.81	2.98	4.87	0.96	1.58
	100	0.3	1.3	3.07	1.77	2.02	3.71	1.06	0.29
	200	0.65	0.12	0.23	1.24	0.13	1.46	1.3	0.47
	400	0.15	0.06	1.0	1.27	0.85	0.06	0.69	1.77
	700	1.16	0.93	1.55	0.93	0.37	0.03	0.06	2.37
	1000	0.91	0.19	0.18	0.21	0.72	0.39	0.7	1.56
	1300	0.77	0.48	0.94	0.88	0.95	1.17	0.72	0.56

(continued)

Table B.7 (continued)

Operator	m_χ (GeV)	SR1	SR2	SR3	SR4	SR5	SR6	SR7	SR8
C5	10	0.08	0.38	1.04	0.65	0.02	0.2	0.92	0.84
	50	1.18	1.87	1.85	1.39	2.36	1.99	0.4	1.52
	100	0.59	0.3	1.41	0.58	0.96	2.06	1.23	0.16
	200	2.3	1.97	1.49	2.24	1.13	1.04	1.77	0.88
	400	1.32	1.1	1.71	0.74	1.0	0.61	0.88	1.31
	700	0.96	0.74	1.01	0.52	0.51	1.35	0.95	1.16
	1000	0.88	1.07	1.63	0.62	1.0	1.23	1.23	1.25
1300	0.79	1.01	0.86	1.18	0.71	0.88	1.31	1.21	

Table B.8 Relative JER uncertainty on $\sigma \times A \times \varepsilon$ in % for the light mediator samples

M_{Med}	Width	m_χ (GeV)	SR1	SR2	SR3	SR4	SR5	SR6	SR7	SR8
10 GeV	$M_{Med}/3$	10	0.96	0.01	0.17	5.12	6.89	0.98	1.98	4.47
50 GeV	$M_{Med}/3$	10	0.47	0.77	1.93	2.64	0.94	4.85	1.75	0.0
		50	0.03	0.74	0.52	0.15	0.17	1.86	2.23	2.02
		400	0.17	0.63	0.05	0.18	1.35	0.52	0.19	1.18
	$M_{Med}/8\pi$	50	1.26	0.42	3.07	0.9	1.35	0.7	1.66	0.54
		400	0.73	0.25	0.93	0.9	1.72	1.9	0.61	2.15
100 GeV	$M_{Med}/3$	10	0.99	0.5	0.68	1.2	2.02	1.74	0.07	3.15
		50	1.59	0.32	5.49	0.38	0.93	2.1	0.32	1.89
		400	0.5	0.71	0.05	0.36	0.15	0.58	0.93	1.07
	$M_{Med}/8\pi$	50	0.22	0.12	1.12	0.2	0.37	0.38	1.17	0.38
		400	0.44	0.77	0.65	0.94	0.62	1.14	0.78	1.02
300 GeV	$M_{Med}/3$	10	0.68	0.77	0.35	1.7	0.89	0.19	0.66	4.33
		50	0.01	0.26	1.76	0.15	1.07	2.8	4.33	0.2
		200	1.42	1.05	0.73	0.96	0.49	0.33	0.44	1.58
	$M_{Med}/8\pi$	400	0.11	0.64	0.71	0.18	0.12	0.61	0.23	1.05
		50	0.72	1.3	0.31	0.71	1.86	0.1	1.03	0.0
	$M_{Med}/8\pi$	400	0.74	0.87	0.8	0.3	1.3	1.16	0.31	0.34
		50	1.12	0.4	0.78	0.77	1.16	0.9	0.89	0.07
600 GeV	$M_{Med}/3$	50	0.15	1.32	0.77	2.86	0.38	0.61	1.03	0.38
		200	0.55	0.45	1.01	0.52	0.69	0.12	0.0	1.14
		400	0.39	0.08	1.19	0.51	0.84	0.25	0.9	0.08
	$M_{Med}/8\pi$	50	0.32	0.42	1.15	0.19	0.93	0.2	0.81	1.34
		400	0.14	0.88	0.72	0.16	0.73	0.28	1.32	0.36

(continued)

Table B.8 (continued)

M_{Med}	Width	m_χ (GeV)	SR1	SR2	SR3	SR4	SR5	SR6	SR7	SR8	
1 TeV	$M_{Med}/3$	10	0.78	0.61	0.82	1.13	0.61	0.77	1.01	1.14	
		50	0.73	1.25	1.06	1.94	1.84	1.2	0.62	0.91	
		200	0.98	0.58	0.93	0.05	0.59	0.35	1.11	0.44	
		400	1.37	0.81	1.31	0.46	0.57	0.29	0.29	0.84	
		1000	0.65	0.01	0.82	0.36	0.61	0.11	0.49	0.41	
	$M_{Med}/8\pi$	50	0.58	1.13	0.2	0.3	0.18	0.46	1.16	0.6	
		400	0.67	0.18	0.65	0.33	2.43	1.3	0.23	1.47	
	3 TeV	$M_{Med}/3$	10	0.62	0.73	0.65	1.1	1.43	0.09	0.07	0.13
			50	0.02	0.3	0.74	1.32	0.12	0.29	0.55	1.03
			200	0.91	0.37	0.32	0.63	0.6	0.31	0.85	1.02
400			0.6	0.84	0.47	0.15	1.12	1.39	0.31	0.4	
1000			0.33	0.13	0.3	0.49	0.71	0.67	0.68	1.02	
1300			0.31	0.39	0.24	0.13	0.43	0.62	0.9	0.15	
$M_{Med}/8\pi$		50	0.23	0.44	0.77	0.39	0.28	0.31	0.24	0.45	
		400	0.75	0.6	0.92	0.06	0.3	0.68	0.64	0.64	
6 TeV		$M_{Med}/3$	50	1.21	1.45	1.02	0.08	0.36	0.2	1.56	0.64
			400	0.58	1.28	0.26	0.71	0.37	0.73	0.01	0.13
	$M_{Med}/8\pi$	50	0.64	0.45	0.76	0.63	0.61	2.38	0.1	1.69	
		400	0.44	1.07	0.99	0.69	0.62	0.26	0.42	0.79	
10 TeV	$M_{Med}/3$	50	0.5	0.49	0.83	0.48	0.31	2.48	2.53	1.03	
		400	0.96	0.43	0.68	1.68	0.71	0.26	1.65	0.07	
	$M_{Med}/8\pi$	50	0.49	0.39	0.78	0.83	1.21	0.03	1.0	1.92	
		400	0.06	0.26	0.22	1.88	0.66	0.13	0.39	0.35	
30 TeV	$M_{Med}/3$	50	0.53	1.03	1.1	1.16	0.24	0.57	1.19	1.17	
		400	1.25	0.1	1.15	1.08	1.96	0.23	0.76	0.74	
	$M_{Med}/8\pi$	50	1.8	1.24	0.96	0.17	1.15	1.27	0.16	0.71	
		400	1.41	1.34	0.94	1.62	0.83	0.06	1.65	0.5	

Table B.9 Relative E_T^{miss} soft term uncertainty on $\sigma \times A \times \varepsilon$ in % for the EFT samples

Operator	m_χ (GeV)	SR1	SR2	SR3	SR4	SR5	SR6	SR7	SR8
D1	50	0.29	0.59	0.4	0.48	0.55	0.87	0.54	0.78
	100	0.22	0.78	0.53	0.39	1.13	0.26	0.52	1.31
	200	0.29	0.42	0.34	0.39	0.54	0.28	0.57	0.38
	400	0.19	0.08	0.33	0.4	0.49	0.12	0.37	0.5
	700	0.22	0.33	0.39	0.28	0.57	0.49	0.35	0.4
	1000	0.2	0.37	0.42	0.37	0.49	0.23	0.29	0.59
	1300	0.21	0.17	0.46	0.4	0.35	0.51	0.57	0.28

(continued)

Table B.9 (continued)

Operator	m_χ (GeV)	SR1	SR2	SR3	SR4	SR5	SR6	SR7	SR8
D5 (D8)	50	0.28	0.56	0.62	0.54	0.75	0.17	0.5	0.45
	100	0.23	0.48	0.08	0.35	0.39	0.43	0.18	0.26
	200	0.11	0.12	0.27	0.43	0.54	0.34	0.12	0.16
	400	0.1	0.43	0.46	0.15	0.16	0.14	0.31	0.31
	700	0.12	0.31	0.29	0.43	0.3	0.31	0.25	0.29
	1000	0.16	0.34	0.43	0.39	0.15	0.31	0.35	0.57
	1300	0.22	0.4	0.42	0.21	0.5	0.31	0.26	0.52
D9	10	0.16	0.16	0.24	0.24	0.19	0.2	0.35	0.34
	50	0.18	0.16	0.18	0.38	0.27	0.25	0.25	0.26
	100	0.17	0.27	0.16	0.29	0.07	0.11	0.36	0.21
	200	0.08	0.14	0.15	0.16	0.27	0.29	0.19	0.34
	400	0.1	0.29	0.2	0.39	0.19	0.27	0.25	0.3
	700	0.12	0.18	0.17	0.53	0.39	0.3	0.22	0.24
	1000	0.15	0.24	0.22	0.17	0.28	0.16	0.21	0.27
	1300	0.19	0.15	0.37	0.49	0.17	0.32	0.67	0.23
D11	50	0.25	0.28	0.06	0.24	0.28	0.24	0.12	0.33
	100	0.14	0.29	0.37	0.31	0.17	0.3	0.1	0.23
	200	0.27	0.25	0.19	0.23	0.17	0.07	0.29	0.36
	400	0.14	0.25	0.37	0.23	0.14	0.12	0.19	0.19
	700	0.24	0.08	0.17	0.2	0.19	0.16	0.33	0.25
	1000	0.11	0.18	0.19	0.14	0.33	0.16	0.16	0.15
	1300	0.3	0.53	0.24	0.48	0.85	0.23	0.26	0.14
C1	10	0.47	0.39	1.52	1.43	1.83	0.32	1.22	0.83
	50	0.26	0.63	1.99	1.89	2.64	0.45	0.87	1.02
	100	0.44	0.74	0.44	0.81	1.25	0.23	0.64	0.82
	200	0.2	0.43	0.73	0.28	1.06	0.61	0.6	0.95
	400	0.27	0.38	0.63	0.31	0.82	0.29	0.72	2.02
	700	0.15	0.29	0.31	0.32	0.45	0.33	0.33	0.3
	1000	0.1	0.12	0.53	0.32	0.52	0.25	0.11	0.51
	1300	0.21	0.2	0.39	0.2	0.43	0.38	0.29	0.12
C5	10	0.15	0.24	0.21	0.42	0.51	0.48	0.51	0.31
	50	0.26	0.48	0.35	0.47	0.12	0.81	0.18	0.57
	100	0.11	0.29	0.17	0.5	0.29	0.54	0.45	0.38
	200	0.26	0.24	0.2	0.39	0.36	0.27	0.24	0.2
	400	0.16	0.1	0.13	0.12	0.3	0.28	0.18	0.17
	700	0.22	0.1	0.11	0.18	0.23	0.09	0.16	0.35
	1000	0.31	0.35	0.22	0.32	0.34	0.39	0.21	0.13
	1300	0.08	0.11	0.11	0.29	0.25	0.35	0.22	0.15

Table B.10 Relative E_T^{miss} soft term uncertainty on $\sigma \times A \times \varepsilon$ in % for the light mediator samples

M_{Med}	Width	m_χ (GeV)	SR1	SR2	SR3	SR4	SR5	SR6	SR7	SR8
10 GeV	$M_{Med}/3$	10	0.14	0.71	1.07	3.74	1.23	0.26	0.47	0.66
50 GeV	$M_{Med}/3$	10	0.37	0.94	1.14	0.67	0.78	1.01	4.21	1.0
		50	0.5	0.33	1.31	0.55	1.16	1.1	0.46	0.89
		400	0.19	0.35	0.42	0.62	0.21	0.19	0.57	0.3
	$M_{Med}/8\pi$	50	0.53	0.66	0.84	0.65	0.64	0.15	3.04	1.0
		400	0.25	0.19	0.21	0.44	0.31	0.16	0.23	0.41
100 GeV	$M_{Med}/3$	10	0.32	0.99	1.21	1.23	0.52	1.56	0.55	0.66
		50	0.56	0.97	1.21	1.49	1.66	1.92	0.43	0.35
		400	0.09	0.4	0.05	0.45	0.26	0.59	0.26	0.27
	$M_{Med}/8\pi$	50	0.43	0.72	1.17	0.05	0.98	0.2	0.38	1.43
		400	0.23	0.63	0.35	0.26	0.8	0.55	0.25	0.69
300 GeV	$M_{Med}/3$	10	0.13	0.45	0.45	0.33	0.66	0.71	0.23	2.71
		50	0.37	0.32	0.27	0.73	0.39	1.07	0.33	0.67
		200	0.08	0.38	0.36	0.45	0.31	0.54	0.21	0.8
		400	0.23	0.27	0.42	0.74	0.23	0.43	1.03	0.27
	$M_{Med}/8\pi$	50	0.3	0.44	0.48	1.14	0.52	0.9	0.27	0.62
			400	0.12	0.27	0.26	0.37	0.5	0.08	0.18
600 GeV	$M_{Med}/3$	10	0.23	0.37	0.24	0.33	0.35	0.28	0.42	0.38
		50	0.15	0.46	0.28	0.52	0.64	0.63	0.37	0.28
		200	0.1	0.22	0.35	0.33	0.51	0.45	0.52	0.3
		400	0.16	0.22	0.34	0.49	0.28	0.54	0.65	0.64
	$M_{Med}/8\pi$	50	0.15	0.44	0.85	0.98	0.42	0.46	1.17	0.44
			400	0.18	0.27	0.39	0.36	0.82	0.63	0.31
1 TeV	$M_{Med}/3$	10	0.11	0.18	0.08	0.28	0.34	0.34	0.35	0.31
		50	0.14	0.23	0.57	0.54	0.29	0.59	0.47	0.39
		200	0.14	0.35	0.27	0.43	0.27	0.37	0.19	0.36
		400	0.18	0.5	0.17	0.85	0.67	0.33	0.67	0.2
		1000	0.15	0.29	0.14	0.17	0.21	0.29	0.15	0.17
	$M_{Med}/8\pi$	50	0.21	0.13	0.35	0.58	0.28	0.43	0.6	0.35
			400	0.13	0.41	0.47	0.18	0.4	0.28	0.35
3 TeV	$M_{Med}/3$	10	0.09	0.34	0.29	0.45	0.4	0.38	0.23	0.3
		50	0.26	0.47	0.76	0.66	0.24	0.52	0.47	0.34
		200	0.21	0.2	0.33	0.41	0.28	0.25	0.17	0.17
		400	0.12	0.32	0.41	0.36	0.23	0.67	0.17	0.59
		1000	0.2	0.24	0.3	0.23	0.16	0.2	0.35	0.33
		1300	0.04	0.34	0.27	0.44	0.1	0.33	0.17	0.44
	$M_{Med}/8\pi$	50	0.2	0.33	0.37	0.85	0.62	0.35	0.31	0.22
			400	0.12	0.45	0.39	0.29	0.24	0.25	0.18

(continued)

Table B.10 (continued)

M_{Med}	Width	m_χ (GeV)	SR1	SR2	SR3	SR4	SR5	SR6	SR7	SR8
6 TeV	$M_{Med}/3$	50	0.32	0.18	0.17	0.44	0.27	0.23	0.68	0.6
		400	0.11	0.37	0.41	0.42	0.24	0.3	0.23	0.17
	$M_{Med}/8\pi$	50	0.26	0.51	0.34	0.2	0.95	0.45	0.25	0.49
		400	0.41	0.41	0.27	0.4	0.38	0.43	0.25	0.54
10 TeV	$M_{Med}/3$	50	0.4	0.53	0.3	0.51	0.35	0.53	0.53	0.37
		400	0.2	0.15	0.42	0.35	0.23	0.21	0.63	0.7
	$M_{Med}/8\pi$	50	0.14	0.41	0.31	0.28	0.37	0.17	0.55	0.4
		400	0.26	0.41	0.29	0.43	0.5	0.3	0.29	0.19
30 TeV	$M_{Med}/3$	50	0.2	0.45	0.34	0.59	0.66	0.45	0.73	0.13
		400	0.13	0.31	0.4	0.33	0.46	0.81	0.39	0.54
	$M_{Med}/8\pi$	50	0.16	0.34	0.25	0.31	0.35	0.17	0.59	0.38
		400	0.39	0.3	0.12	0.22	0.13	0.37	0.51	0.57

Table B.11 Relative beam energy uncertainty on $\sigma \times A \times \varepsilon$ in % for the EFT operator samples

Operator	m_χ (GeV)	SR1	SR2	SR3	SR4	SR5	SR6	SR7	SR8
D1	50	2.51	3.57	1.77	4.06	0.67	1.44	2.82	3.93
	100	2.77	2.93	3.82	5.01	2.74	3.82	4.92	5.52
	200	3.22	3.6	2.47	1.55	3.26	4.24	5.69	6.77
	400	3.35	3.3	3.64	4.56	5.22	4.68	5.87	6.58
	700	5.21	5.43	6.07	4.6	5.11	4.42	6.61	6.25
	1000	6.46	5.98	5.64	6.7	6.38	7.77	7.43	6.17
	1300	8.29	8.48	7.99	8.13	8.6	9.48	9.84	14.29
D5 (D8)	50	2.25	2.69	2.58	3.28	3.25	2.36	1.96	3.9
	100	1.96	1.51	1.65	1.89	2.56	1.38	1.94	2.04
	200	3.04	3.34	2.42	1.42	1.56	3.57	3.63	4.17
	400	2.54	2.6	2.79	1.99	2.65	3.19	4.51	4.14
	700	3.81	3.94	4.42	5.23	4.81	5.1	5.19	6.72
	1000	5.02	5.81	5.81	5.51	5.98	5.9	5.7	5.28
	1300	5.88	6.47	6.79	6.92	7.51	7.68	7.78	6.15
D9	10	2.32	1.83	1.39	2.44	1.6	2.05	2.55	3.25
	50	0.74	1.3	1.04	0.99	1.95	2.57	4.0	2.97
	100	2.45	1.88	2.15	1.99	1.81	2.33	2.62	3.64
	200	2.17	1.9	2.19	2.72	3.82	3.34	4.57	4.06
	400	2.78	2.63	3.63	3.59	3.43	3.53	3.04	3.66
	700	4.15	4.26	4.46	4.64	4.48	4.7	5.1	4.72
	1000	5.3	5.43	5.34	5.02	5.93	6.33	6.48	7.91
	1300	7.7	8.6	8.8	8.57	8.32	8.1	8.28	8.98

(continued)

Table B.11 (continued)

Operator	m_χ (GeV)	SR1	SR2	SR3	SR4	SR5	SR6	SR7	SR8
D11	50	2.98	3.23	3.01	2.69	3.05	2.98	4.16	5.59
	100	3.3	3.74	3.7	4.11	4.06	4.19	3.33	4.09
	200	2.5	2.36	2.07	1.73	1.9	1.14	1.74	0.61
	400	4.73	4.52	4.26	4.21	4.24	4.07	5.62	5.37
	700	4.48	4.38	4.14	4.84	4.57	4.81	5.08	5.78
	1000	5.88	6.45	5.96	6.88	6.58	6.69	6.67	6.57
	1300	7.28	6.96	7.89	7.28	7.82	8.75	8.49	8.66
C1	10	1.97	1.57	3.6	3.47	5.87	2.37	11.79	6.63
	50	2.92	3.95	5.13	5.25	4.12	4.27	11.6	4.34
	100	3.53	4.1	4.51	4.19	3.11	3.41	5.43	6.61
	200	2.22	2.71	3.55	3.86	1.71	5.21	1.85	2.43
	400	2.92	3.62	4.03	2.68	3.06	3.44	4.92	6.04
	700	4.46	4.93	6.04	5.61	5.69	6.99	7.23	7.4
	1000	4.77	4.46	5.1	5.72	6.44	6.49	7.78	6.34
	1300	7.51	7.84	7.54	8.05	9.16	9.2	9.98	8.41
C5	10	1.86	2.08	3.1	3.48	3.25	3.04	3.25	6.14
	50	2.01	2.44	3.56	4.27	3.79	3.69	4.75	4.04
	100	1.3	2.5	2.79	3.35	3.07	3.91	3.33	3.85
	200	1.69	1.5	1.56	0.83	1.26	1.54	2.77	4.95
	400	2.7	2.66	2.59	2.46	3.29	3.31	3.7	4.78
	700	3.32	3.55	3.48	3.63	4.66	4.67	4.27	5.09
	1000	5.02	4.99	5.41	5.39	6.56	6.08	6.23	5.86
	1300	7.65	7.77	8.05	7.63	7.99	8.62	8.65	10.12

Table B.12 Relative renormalisation and factorisation scale uncertainties on $\sigma \times A$ in % for EFT operators

Operator	m_χ (GeV)	SR1	SR2	SR3	SR4	SR5	SR6	SR7	SR8
D1	50	4.76	6.64	7.6	9.21	9.91	6.76	8.0	6.74
	100	4.39	5.81	5.09	5.6	6.92	7.23	10.47	9.79
	200	6.54	8.34	9.29	8.35	8.57	8.18	7.82	6.64
	400	8.23	8.99	10.21	9.64	9.84	9.1	9.58	10.0
	700	12.18	12.54	12.25	12.12	12.42	13.0	10.89	12.1
	1000	14.51	14.95	15.8	16.03	15.76	15.7	18.15	18.54
	1300	17.18	16.9	17.66	17.35	17.69	17.59	18.55	18.82
D5 (D8)	50	7.09	7.53	7.98	8.44	8.79	8.8	8.83	10.44
	100	7.23	8.06	8.37	7.22	6.9	9.28	10.8	11.71
	200	8.29	8.66	8.27	9.21	8.15	9.04	9.9	9.12
	400	9.06	9.26	10.08	9.73	10.91	11.31	11.95	12.36
	700	11.27	11.33	10.99	11.46	11.17	13.02	13.48	14.11
	1000	13.67	13.25	13.15	13.35	12.64	13.72	12.95	11.9
	1300	16.08	16.23	15.43	15.56	15.62	16.41	15.25	14.79

(continued)

Table B.12 (continued)

Operator	m_χ (GeV)	SR1	SR2	SR3	SR4	SR5	SR6	SR7	SR8
D9	10	7.18	7.79	7.79	9.04	9.04	9.66	9.56	10.57
	50	7.47	8.14	8.94	9.02	10.18	9.83	9.19	11.07
	100	7.46	8.06	8.66	9.63	9.76	9.71	10.33	11.45
	200	7.87	8.1	8.49	8.52	9.64	9.87	10.21	11.84
	400	9.39	9.66	9.54	10.02	10.9	10.87	11.33	11.98
	700	12.26	12.56	12.52	12.54	11.67	10.97	12.04	12.37
	1000	12.22	13.21	13.7	14.49	13.42	13.66	14.78	17.36
	1300	14.16	14.16	14.47	14.9	14.72	15.18	15.58	15.36
D11	50	35.98	34.99	35.27	34.74	35.79	35.22	35.46	35.11
	100	35.72	35.26	35.91	36.09	36.2	36.78	35.63	35.52
	200	35.72	35.72	35.44	35.08	34.74	35.79	35.54	35.77
	400	36.53	36.53	37.09	36.56	36.73	36.9	37.21	37.49
	700	37.58	37.48	37.01	37.53	38.76	37.99	38.34	38.71
	1000	39.4	39.34	38.94	39.27	38.69	39.29	39.04	40.39
	1300	42.0	41.69	41.42	41.86	41.61	41.49	40.63	41.55
	C1	10	6.39	4.7	10.65	13.76	22.73	15.3	6.07
50		6.91	6.73	4.84	3.95	3.12	4.25	8.44	12.31
100		3.58	6.12	3.5	5.9	3.85	6.58	6.98	7.64
200		4.44	5.11	6.13	5.72	6.93	6.34	6.64	7.28
400		6.3	6.89	8.28	8.52	9.03	8.62	10.76	14.32
700		10.33	10.03	10.08	12.0	11.75	11.33	10.89	12.89
1000		13.56	13.31	13.27	13.67	14.24	12.83	12.47	13.47
1300		15.7	16.43	17.06	15.96	16.47	15.82	16.98	17.03
C5	10	36.38	36.5	36.65	36.91	36.14	36.18	33.98	33.6
	50	36.79	36.83	35.6	36.81	35.8	37.11	36.55	37.79
	100	36.68	37.09	36.73	36.42	36.35	36.64	34.54	36.32
	200	35.72	36.45	37.1	36.76	36.3	35.99	34.96	36.74
	400	35.94	36.35	36.39	36.75	36.92	38.09	37.91	37.58
	700	37.71	37.54	37.37	37.53	38.49	38.4	38.46	39.77
	1000	39.29	39.18	40.12	39.59	38.13	38.35	38.55	38.23
	1300	41.55	40.7	40.94	40.59	40.22	38.87	38.44	38.75

Table B.13 Relative PDF uncertainties on $\sigma \times A$ in % for the EFT operators

Operator	m_χ (GeV)	SR1	SR2	SR3	SR4	SR5	SR6	SR7	SR8
D1	50	24	28.2	32.5	36.1	39.6	42.8	49.2	53
	100	27	30.8	34.9	38.5	41.7	44.7	49.7	54.7
	200	33.9	37.3	40.8	43.4	45.6	47.6	52.7	58.1
	400	46.9	49.2	51.4	53.2	55.5	57.6	61.6	65.2
	700	63.3	64.7	66.2	67.7	68.9	70.1	72.3	73.6

(continued)

Table B.13 (continued)

Operator	m_χ (GeV)	SR1	SR2	SR3	SR4	SR5	SR6	SR7	SR8
D5 (D8)	1000	72.8	73	73.4	73.7	74.1	74.4	74.5	73.9
	1300	73	72.6	72.3	71.8	71.2	71	72.3	75.1
	50	6.35	7.68	9.17	10.7	12.3	13.9	17.3	20.7
	100	6.68	8.1	9.74	11.2	12.8	14.2	17.6	20.8
	200	7.48	8.7	10.2	11.5	12.8	14.4	17.6	21.3
	400	9.63	10.4	12.1	13.4	15.2	16.6	19.7	22.9
	700	15.4	16.8	18.5	19.4	20.7	22.2	24.8	28.7
	1000	24.2	25.7	27.8	29.2	31.1	32.3	37	40.3
D9	1300	38.9	41.1	44.6	47.3	49.6	52.4	59	64.1
	10	6.81	8.04	9.38	10.5	11.9	13.1	15.9	18.7
	50	7.05	8.25	9.59	10.8	12	13.3	16.2	19
	100	7.62	8.93	10.3	11.5	12.9	14.2	17.2	20.6
	200	8.59	9.95	11.2	12.7	14.2	15.6	18.3	21
	400	11	12.3	14	15.6	17.3	19	22.2	24.5
	700	16.2	17.7	19.1	21	22.4	24.2	27.5	30.1
	1000	24.5	25.8	27.9	29.6	31	32.1	36.1	40.4
D11	1300	39	40.5	42.5	45.9	48.6	51.2	56.3	64.2
	50	38.9	40.2	41.5	42.2	43.7	44.5	46.3	48.3
	100	40.3	41.1	42	42.9	43.8	44.6	46.9	48.2
	200	44.2	44.7	44.8	45.4	45.8	46.5	48	49.4
	400	51.8	51.6	51.4	51.3	51.6	52.2	52.7	52.8
	700	60.5	59.8	58.8	58.3	57.7	57.9	58.2	57.8
	1000	63.6	63.1	62	61.5	61.5	61.2	61.7	60.7
C1	1300	64.3	63.6	62.7	61.8	62.1	62.1	61.4	60.4
	10	13.1	15.7	20.2	22.9	27.6	31	37.8	45.6
	50	14.6	17.5	20.9	24.8	28.7	31.7	38.1	47
	100	17	19.8	23.8	27.4	30.5	33.4	41.1	49.5
	200	23.5	26.6	29.9	32.8	35.8	38.9	45.2	50
	400	38.3	40.6	43.6	46.5	48.5	51.1	55.2	59
	700	56.6	58.3	60.4	62.5	64.3	65.6	68.7	70.5
	1000	71	71.7	72.5	73	73.5	74.2	74.9	74.8
C5	1300	74.8	74.7	74.7	74.6	74.6	74.3	73.8	73
	10	23.6	26	28.3	30.2	32.3	34.1	36.7	40
	50	25.4	27.5	29.2	31.1	32.4	34.2	37.2	39.8
	100	27.8	29.3	30.7	32.5	33.7	35.6	38.4	40.9
	200	33.9	34.6	35.6	36.3	37.4	38.7	41.4	43.6
	400	44.7	44.9	45.3	45.2	45.7	46	47.6	49
	700	56.7	56.2	55.5	55.2	54.6	54.9	55.4	55
	1000	63.1	62.2	61.1	60.5	60.6	60.6	60.2	59.5
1300	64.6	63.7	62.6	62.1	61.6	61.6	61	59.5	

Table B.14 Relative matching scale uncertainty on $\sigma \times A$ in % for the EFT operator samples

Operator	m_χ (GeV)	SR3	SR5
D1	50	0.25	1.02
	100	1.58	1.52
	200	0.88	3.37
	400	1.43	1.97
	700	0.76	2.8
	1000	0.38	3.18
	1300	1.16	3.2
D5 (D8)	50	2.36	2.85
	100	0.61	1.61
	200	2.21	4.03
	400	0.16	0.74
	700	1.27	3.68
	1000	1.4	3.53
	1300	0.3	2.2
D9	10	1.32	1.64
	50	0.17	1.39
	100	1.18	1.79
	200	1.15	1.9
	400	2.34	4.66
	700	0.08	3.38
	1000	0.68	3.86
	1300	3.17	3.3
D11	50	0.83	2.77
	100	0.43	1.89
	200	2.28	4.69
	400	1.18	3.67
	700	2.08	4.3
	1000	1.78	3.89
	1300	1.45	3.14
C1	10	0.39	5.46
	50	1.86	2.29
	100	0.6	2.74
	200	1.49	3.55
	400	0.66	0.44
	700	1.68	4.61
	1000	0.74	2.5
	1300	0.73	3.93

(continued)

Table B.14 (continued)

Operator	m_χ (GeV)	SR3	SR5
C5	10	0.28	4.71
	50	0.22	3.6
	100	1.41	2.99
	200	0.32	2.57
	400	1.47	2.82
	700	2.39	3.27
	1000	0.84	3.66
	1300	2.35	3.46

Table B.15 Relative α_s uncertainty on $\sigma \times A$ in % for the EFT operator samples

Operator	m_χ (GeV)	SR1	SR2	SR3	SR4	SR5	SR6	SR7	SR8
D1	50	0.31	1.19	2.27	1.03	1.36	2.01	4.19	3.44
	100	0.64	1.14	1.28	0.89	3.06	1.93	0.92	7.77
	200	0.81	1.13	0.44	1.12	2.15	2.52	1.16	7.55
	400	0.74	0.86	1.89	2.35	1.95	1.86	1.14	1.52
	700	0.73	1.28	1.31	1.51	1.31	1.12	3.04	0.41
	1000	1.09	1.19	0.25	0.58	0.02	0.92	1.57	2.89
	1300	0.49	0.47	0.79	1.24	3.22	2.49	1.89	0.25
D5 (D8)	50	1.44	1.43	1.82	2.3	0.5	0.48	3.96	2.2
	100	0.31	0.18	1.34	0.83	0.46	0.48	1.63	2.61
	200	0.85	1.13	0.65	0.92	0.78	0.88	1.55	2.87
	400	0.78	0.87	1.31	2.13	2.15	1.24	1.97	0.46
	700	0.54	0.54	0.26	0.1	0.36	0.79	1.18	0.92
	1000	0.86	0.83	0.52	0.5	0.87	1.46	0.36	0.49
	1300	0.19	0.11	0.5	0.35	0.66	1.15	1.35	2.19
D9	10	0.35	0.34	0.31	0.57	0.35	0.19	0.33	0.97
	50	0.26	0.49	0.2	0.37	0.24	0.39	0.96	1.47
	100	0.74	0.43	0.11	0.16	0.33	0.27	0.97	0.84
	200	1.0	0.8	0.78	1.22	0.69	0.62	1.13	0.21
	400	0.8	0.87	0.7	0.87	0.41	0.36	0.48	1.23
	700	0.47	0.53	0.38	0.51	0.14	0.35	0.17	0.33
	1000	1.39	1.2	0.48	1.4	2.2	1.31	0.39	0.31
	1300	0.42	0.39	0.12	1.14	0.83	0.21	0.93	0.83

(continued)

Table B.15 (continued)

Operator	m_χ (GeV)	SR1	SR2	SR3	SR4	SR5	SR6	SR7	SR8
D11	50	0.49	0.59	0.84	1.42	0.67	0.93	0.55	2.31
	100	0.9	0.62	0.4	1.04	0.7	1.01	1.09	2.31
	200	0.42	1.4	1.17	0.6	1.39	1.14	0.94	1.27
	400	0.48	0.94	0.63	0.55	0.94	1.0	0.82	1.33
	700	1.09	1.14	0.09	0.5	0.87	0.6	0.32	0.13
	1000	1.28	1.39	1.51	0.9	0.89	1.34	0.11	1.17
	1300	0.45	1.05	0.37	0.53	0.28	0.42	0.84	2.12
C1	10	1.7	1.7	1.28	2.22	9.07	8.74	1.38	1.18
	50	1.0	1.15	3.23	5.7	3.51	8.1	1.79	5.15
	100	0.59	2.22	1.98	2.22	2.5	2.4	5.08	6.7
	200	0.59	1.26	3.27	0.61	1.23	1.91	0.47	1.85
	400	1.21	1.43	1.99	1.09	2.04	1.98	2.36	2.44
	700	0.73	0.95	0.35	2.56	0.63	0.42	0.63	1.7
	1000	1.33	0.77	0.59	1.86	1.46	0.83	0.56	2.58
	1300	0.15	0.32	0.22	0.62	1.07	2.14	0.86	1.77
C5	10	0.78	0.6	0.4	1.3	1.11	0.74	1.8	1.52
	50	0.18	0.53	1.52	1.0	1.59	1.91	2.48	1.9
	100	0.28	0.36	0.91	0.29	0.6	1.54	0.43	0.29
	200	0.7	0.5	0.51	1.23	0.2	1.08	0.74	0.66
	400	1.44	0.49	0.93	0.32	0.73	0.74	0.69	0.67
	700	0.48	0.79	0.77	1.24	1.58	0.06	0.31	1.1
	1000	0.55	1.04	1.32	0.87	0.06	0.28	1.08	0.19
	1300	0.13	0.34	0.75	0.27	0.15	0.93	0.86	0.8

Table B.16 95%CL observed (expected) limits on the coupling and scale Λ for the simplified model in signal region 7

M_{Med}	Width	m_χ (GeV)	$\sqrt{g_\chi g_{SM}}$	Λ (GeV)
10 GeV	$m_{Med}/3$	10	0.51 (0.51)	19 (19)
50 GeV	$m_{Med}/3$	10	0.36 (0.36)	140 (140)
		50	0.49 (0.48)	103 (103)
		400	1.41 (1.4)	35 (35)
	$m_{Med}/8\pi$	50	0.53 (0.53)	93 (94)
		400	1.41 (1.4)	35 (35)
100 GeV	$m_{Med}/3$	10	0.38 (0.38)	264 (265)
		50	0.4 (0.4)	248 (248)
		400	1.4 (1.39)	71 (71)
	$m_{Med}/8\pi$	50	0.46 (0.46)	216 (216)
		400	1.39 (1.38)	72 (72)

(continued)

Table B.16 (continued)

M_{Med}	Width	m_χ (GeV)	$\sqrt{g_\chi g_{SM}}$	Δ (GeV)
300 GeV	$m_{Med}/3$	10	0.4 (0.4)	742 (744)
		50	0.42 (0.42)	709 (711)
		200	0.67 (0.66)	450 (452)
		400	1.33 (1.33)	225 (225)
	$m_{Med}/8\pi$	50	0.25 (0.25)	1197 (1200)
		400	1.34 (1.34)	223 (224)
600 GeV	$m_{Med}/3$	10	0.53 (0.52)	1139 (1143)
		50	0.53 (0.53)	1127 (1131)
		200	0.55 (0.55)	1092 (1096)
		400	1.12 (1.11)	537 (539)
	$m_{Med}/8\pi$	50	0.3 (0.3)	2020 (2027)
		400	1.11 (1.1)	541 (543)
1 TeV	$m_{Med}/3$	10	0.76 (0.76)	1318 (1322)
		50	0.76 (0.76)	1307 (1311)
		200	0.77 (0.77)	1299 (1303)
		400	0.87 (0.87)	1144 (1147)
		1000	4.35 (4.34)	229 (230)
	$m_{Med}/8\pi$	50	0.41 (0.41)	2451 (2460)
	400	0.44 (0.43)	2293 (2301)	
3 TeV	$m_{Med}/3$	10	2.76 (2.75)	1086 (1089)
		50	2.76 (2.75)	1087 (1090)
		200	2.78 (2.77)	1080 (1083)
		400	3.16 (3.15)	949 (952)
		1000	4.12 (4.11)	727 (729)
		1300	5.48 (5.46)	547 (549)
$m_{Med}/8\pi$	50	2.1 (2.09)	1429 (1433)	
	400	2.17 (2.16)	1383 (1387)	
6 TeV	$m_{Med}/3$	50	6.06 (6.04)	989 (992)
		400	6.76 (6.75)	886 (889)
	$m_{Med}/8\pi$	50	5.97 (5.96)	1004 (1007)
		400	6.65 (6.63)	902 (905)
10 TeV	$m_{Med}/3$	50	10.45 (10.42)	956 (959)
		400	11.53 (11.5)	867 (869)
	$m_{Med}/8\pi$	50	10.1 (10.08)	989 (992)
		400	11.44 (11.41)	873 (876)
30 TeV	$m_{Med}/3$	50	31.31 (31.23)	958 (960)
		400	35.19 (35.09)	852 (854)
	$m_{Med}/8\pi$	50	31.17 (31.09)	962 (964)
		400	34.57 (34.48)	867 (870)

Curriculum Vitae

Contact Details

Name Ruth Pöttgen
Address 139, Chemin des deux Hameaux
01710 Thoiry, France
E-Mail ruth.poettgen@cern.ch



Personal Data

Born February 23, 1986, Neuwied, Germany
Nationality German
Civil Status Single

Education and Academic Career

1992–1996 Primary School, Wehr, Germany
1996–2005 Secondary School (Bertha-von-Suttner-Gymnasium),
Andernach, Germany
March 2005 “Allgemeine Hochschulreife”; Grade: “sehr gut” (1.0)
Main subjects: Physics, Maths, English
2005–2011 Study of Physics, Johannes Gutenberg—University, Mainz,
Germany
Jan.–Aug. 2008 ERASMUS exchange student, Lund, Sweden
Jul.–Sep. 2009 Summer Student, CERN, Geneva, Switzerland, 12 Weeks
April/May 2010 Diploma Exam; Grade: “sehr gut” (1.0)
2010–2011 Diploma Thesis; Grade: “sehr gut” (1.0)
“Messung der Rapiditätsabhängigkeit der Reaktion $pp \rightarrow Z/(e^+e^-) + X$ bei $\sqrt{s} = 7$ TeV mit dem ATLAS-Experiment”
09/2011–05/2015 Ph.D Student, Johannes Gutenberg—University, Mainz

09/2011–08/2014 Wolfgang-Gentner-Stipendiate, CERN, Geneva
 Since 03/2015 Post-Doc, Stockholm University, Stockholm, Sweden
 May 2015 Ph.D, Grade: “summa cum laude” (with distinction, 0.7)

Selected Publications

- [1] *Measurement of inclusive W^\pm and Z/γ cross sections in the electron and muon decay channels in pp collisions at $\sqrt{s} = 7$ TeV with the ATLAS detector*
 The ATLAS Collaboration, *Phys. Rev. D* **85** (2012) 072004
- [2] *Search for dark matter candidates and large extra dimensions in events with a jet and missing transverse momentum with the ATLAS detector*
 The ATLAS Collaboration, *JHEP* 04 (2013) 075
- [3] *Search for New Phenomena in Monojet plus Missing Transverse Momentum Final States using 10 fb^{-1} of pp Collisions at $\sqrt{s} = 8$ TeV with the ATLAS detector at the LHC*
 The ATLAS Collaboration, ATLAS-CONF-2012-147,
<https://cdsweb.cern.ch/record/1493486>
- [4] *Sensitivity to WIMP Dark Matter in the Final States Containing Jets and Missing Transverse Momentum with the ATLAS Detector at 14 TeV LHC*
 The ATLAS Collaboration, ATL-PHYS-PUB-2014-007
<https://cds.cern.ch/record/1708859/>
- [5] *Search for new phenomena in final states with an energetic jet and large missing transverse momentum in pp collisions at $\sqrt{s} = 8$ TeV with the ATLAS detector*
 The ATLAS Collaboration
 submitted to EPJC, arXiv Preprint: [1502.01518](https://arxiv.org/abs/1502.01518)
- [6] *An upgraded ATLAS Central Trigger for post-2014 LHC luminosities*
 G. Anders et al., *J. Inst.* 8 02 C02031
 Proceedings to *International Workshop on Radiation Imaging Detectors (iWoRID) 2012*
- [7] *Searches for Physics Beyond the Standard Model in Monojets- and Monophoton-Events with the ATLAS Detector*
J. Phys.: Conf. Ser. 455 011001
 Proceedings to *Workshop on Discovery Physics at the LHC* (Kruger 2012)
- [8] *An upgraded ATLAS central trigger for 2015 luminosities*
 IEEE xplora 10.1109/ANIMMA.2013.6728025
 Proceedings to *Conference on Advancements in Nuclear Instrumentation and Measurement Methods and their Applications (ANIMMA) 2013*
- [9] *Exotics Searches at ATLAS*
 arXiv Preprint: [1411.4292](https://arxiv.org/abs/1411.4292)
 Proceedings to *Interplay between Particle and Astroparticle Physics (IPA) 2014*